



Eclogitic breccias from Monviso (W. Alps): structural, petrographic and geochemical evidence for multiple rupture stages at intermediate depths in subduction zones

Michele Locatelli

► To cite this version:

Michele Locatelli. Eclogitic breccias from Monviso (W. Alps): structural, petrographic and geochemical evidence for multiple rupture stages at intermediate depths in subduction zones. Earth Sciences. Université Pierre et Marie Curie - Paris VI; Università degli studi (Gênes, Italie), 2017. English. NNT : 2017PA066349 . tel-01875132

HAL Id: tel-01875132

<https://theses.hal.science/tel-01875132>

Submitted on 17 Sep 2018

HAL is a multi-disciplinary open access archive for the deposit and dissemination of scientific research documents, whether they are published or not. The documents may come from teaching and research institutions in France or abroad, or from public or private research centers.

L'archive ouverte pluridisciplinaire **HAL**, est destinée au dépôt et à la diffusion de documents scientifiques de niveau recherche, publiés ou non, émanant des établissements d'enseignement et de recherche français ou étrangers, des laboratoires publics ou privés.

Université Pierre et Marie Curie

Ecole doctorale: Géoscience, Ressources Naturelles et Environnement

Laboratoire : IStEP/Equipe : Lithosphère, Structure Déformation

Eclogitic breccias from Monviso (W. Alps): structural, petrographic and geochemical evidence for multiple rupture stages at intermediate depths in subduction zones

Par Michele LOCATELLI

Thèse de doctorat en Science de la Terre

Dirigée par Anne Verlaquet, Philippe Agard et Laura Federico

Présentée et soutenue publiquement le 15 Septembre 2017

Devant un jury composé de :

M. Agard Philippe	Professeur - Université Pierre et Marie Curie	Directeur de thèse
Mme. Verlaquet Anne	Maître de conférences - Université Pierre et Marie Curie	Co-directeur de thèse
Mme. Federico Laura	Professore associato - Università degli Studi di Genova	Co-directeur de thèse
M. Raimbourg Hugues	Maître de conférences - Université d'Orléans	Rapporteur
M. Guillot Stéphane	Directeur de recherche 1 - Université Grenoble Alpes	Rapporteur
Mme. Penniston-Dorland Sarah	Associate Professor - University of Maryland	Examineur
M. Jolivet Laurent	Professeur - Université Pierre et Marie Curie	Examineur

Résumé

Les séismes intermédiaires (40-325 km de profondeur) ont été largement documentés dans les plaques océanique en subduction mais leur mécanismes déclencheurs restent énigmatiques et très peu compris en raison (I) des incertitudes instrumentales sur l'acquisition des données géophysiques et (II) de la rareté des exemples de roches métamorphisées dans des conditions du faciès éclogites et préservant (sans ambiguïté) les structures produites par des séismes intermédiaires.

Bien que toujours limité, il y a de plus en plus de preuves que les lambeaux « fossiles » de lithosphère océanique exhumée de taille pluri-kilométrique peuvent enregistrer les processus chimiques et mécaniques caractéristiques de la sismicité de profondeur intermédiaire.

Ce projet de doctorat étudie l'impact de la libération et de l'infiltration des fluides métamorphiques sur la génération des brèches éclogitiques disséminées dans une zone de cisaillement de 15 km de long, exposée dans un fragment presque intact de lithosphère océanique Téthysienne, subduite jusqu'à 80 km de profondeur (2.6 GPa - 550 ° C, unité du Lago Superiore): le complexe métaophiolitique du Mont Viso (W Alps, Italie).

Trois zones de cisaillement majeures ont été étudiées, et en particulier la Lower Shear Zone (LSZ), dans laquelle des blocs de métagabbros mylonitiques éclogitisés et bréchifiés (potentiellement lors d'une phase sismique) sont dispersés, avec des blocs métasédimentaires, dans la matrice serpentineuse de la zone de cisaillement.

Dans cette dernière zone de cisaillement, une attention particulière a été portée à la caractérisation pétrologique et structurale de 196 blocs exhibant ces brèches (dans lesquels plus de 100 échantillons ont été récoltés), notamment à travers l'étude (i) de leur répartition dans la zone de cisaillement et (ii) de leurs caractéristiques morphologiques (longueur, largeur, hauteur, volumétrie relative de la matrice par rapport aux clastes et nature des clastes). Ces données ont été synthétisées dans une nouvelle carte géologique détaillée des méta-ophiolites du Mont Viso à l'échelle 1 : 20.000.

L'étude pétro-structurale a permis de montrer que la formation des brèches résulte de passages transitoires de la déformation ductile à cassante dans le faciès éclogitique, comme le montre la foliation mylonitique des métagabbros (composée de l'assemblage omphacite + rutile \pm grenat et quartz) recoupé par des plans de brèches cimentées par des matrices riches en omphacite \pm grenat et lawsonite. Elle montre également que la formation des brèches n'est pas liée à des événements pré-alpins (brèches sédimentaires ou tectoniques superficielles) comme d'autres auteurs l'ont proposé (Balestro et al. 2013; Festa et al. 2015). L'analyse des éléments en trace (in-situ et dans la roche totale), en lien avec une caractérisation rigoureuse des microstructures dans les blocs de brèches, a permis de mettre en évidence un changement progressif des fluides circulant pendant la bréchification. Les premières ruptures fragiles (locales, M1) ont été déclenchées par des fluides dérivés localement (e.g. métagabbros) avec une injection progressive de fluides « exotiques » (dérivés de la déshydratation de serpentine) provoquant la bréchification dans l'intégralité des LSZ and ISZ (avec la cristallisation de M2 et M3). En raison de l'extension limitée des affleurements, l'origine sismique des brèches éclogitiques reste spéculative. Néanmoins, plusieurs preuves (par exemple, les minéraux fracturés et décalés le long des niveaux micrométriques riches en omphacite) suggèrent que les brèches d'éclogite du Monviso ont été générées par rupture fragile instantanée.

Abstract

Intermediate-depth earthquakes (40-325 km depth) have been extensively documented within subducting oceanic slab but their triggering mechanisms remain enigmatic due to (I) the instrumental uncertainties on geophysical data acquisition and (II) the scarcity of examples of exhumed (and unambiguously recognized) eclogite-facies earthquake-derived rocks.

Although still limited, there is growing evidence that large-scale, “fossil” exhumed portions of subducted lithosphere may record both chemical and mechanical processes operating in the depth range of intermediate-depth seismicity.

This thesis project investigates the role of metamorphic fluids in the formation of the eclogitic breccias (resulting from potentially seismic deformation) found in a 15 km-long shear zone developed in an almost intact fragment of Tethyan oceanic lithosphere metamorphosed to eclogite-facies peak metamorphic conditions (2.6 GPa - 550 °C) during Alpine subduction: the *Monviso metaophiolite complex (W. Alps)*. Three major shear zones cutting across the complex at low angle were studied, with a major focus on the Lower Shear Zone -LSZ-, where blocks of variably brecciated (and potentially seismically-derived) Fe-Ti and Mg-Al metagabbros are embedded, together with metasedimentary blocks, in a talc and tremolite-rich serpentinite matrix.

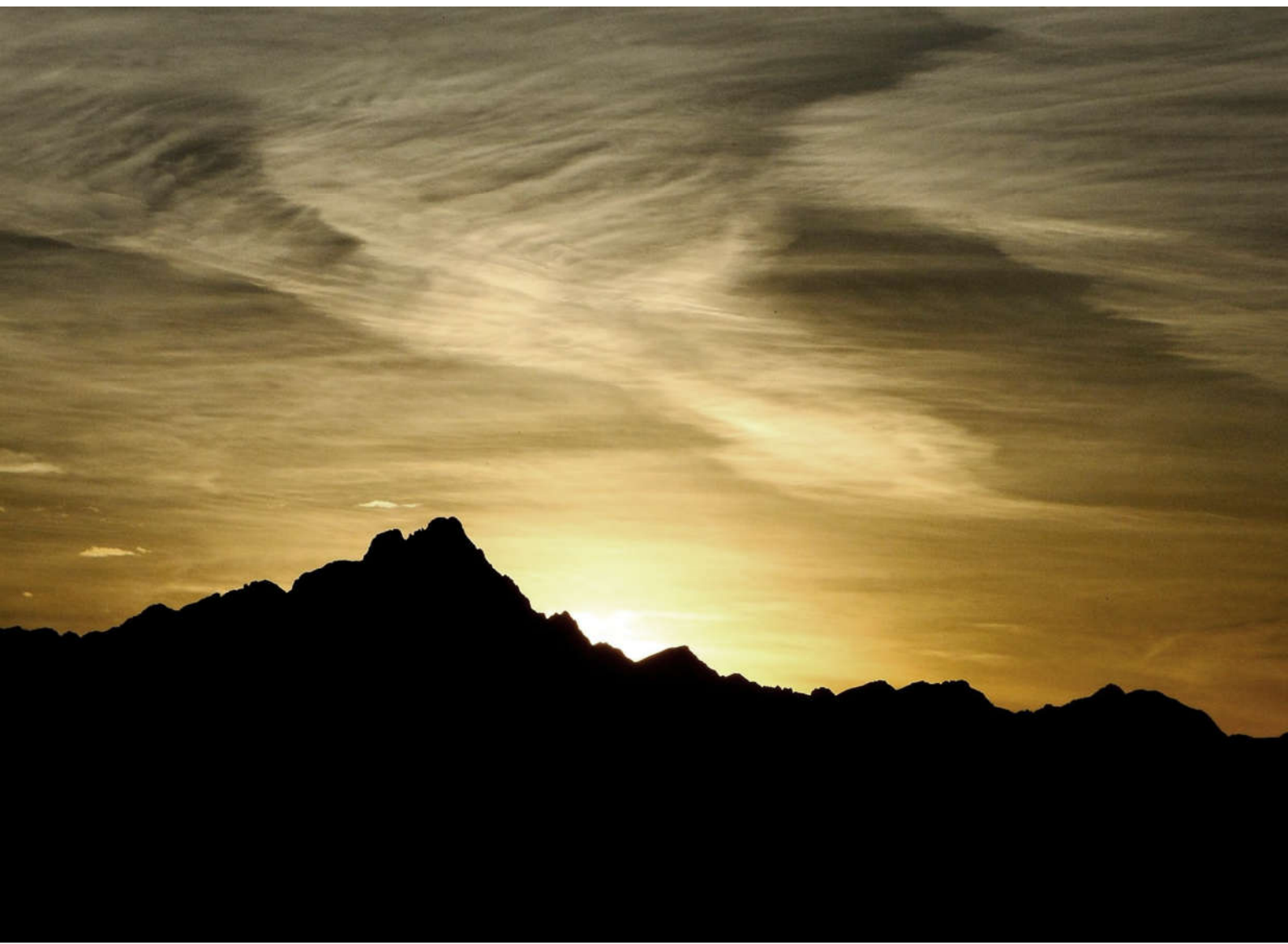
Particular attention was paid to the petrological and structural characterization of 196 breccia blocks (in which more than 100 samples were collected), with (i) detailed analysis and mapping of their distribution in the LSZ and (ii) morphological characterization (block size, relative volume of matrix with respect to clasts and matrix-clast composition). These data have been synthesized in a new detailed geological map of Monviso meta-ophiolite at a scale of 1: 20,000.

The mylonitic foliation of intact Mg-Al-rich metagabbros (composed of omphacite + rutile ± ex-lawsonite ± quartz and locally garnet) cut by breccia planes (cemented by omphacite + garnet ± ex-lawsonite) univocally indicates brecciation at eclogite facies conditions. In the breccias the occurrence of a first omphacite-rich matrix (M1) cut by a second matrix rich in garnet + lawsonite pseudomorphs (M2) witnesses multiple brittle rupture events (probably shortly spaced in time) prior to a stage of massive eclogite facies fluid ingression (matrix M3). Trace elements analysis (in-situ and bulk) coupled to rigorous microstructural characterization of samples suggest a progressive change of fluids circulating during the brecciation. First brittle event M1 was triggered by locally-buffered fluids (e.g., from metagabbros) with later ingression of “exotic” fluids (e.g., from serpentinites) triggering the brecciation events M2 and M3.

Due to the limited extension of outcrops, the coseismic origin of the eclogitic breccia remains somehow speculative; nevertheless several evidences (e.g., minerals fractured and offset along omphacite-bearing planes) suggest that Monviso eclogite breccias were generated by instantaneous brittle rupture.

Keywords:

Eclogite-facies breccia, plate interface, Monviso, Western Alps, fluid-rock interaction



« Actus aper, multos Vesulus quem pinifer annos defendit multosque palus Laurentia? »

(Virgilio, Eneide, X)

« Est ad Italie latus occiduum Vesullus ex Apenini iugis mons unus altissimus, qui, vertice nubila superans, liquido sese ingerit etheri, mons suapte nobilis natura, Padi ortu nobilissimus, qui eius e latere fonte lapsus exiguo, orientem contra solem fertur, mirisque mox tumidus incrementis brevi spatio decurso, non tantum maximorum unus amnium sed fluviorum a Virgilio rex dictus Liguriam gurgite violentus intersecat; dehinc Emiliam atque Flaminiam Venetiamque disternans multis ad ultimum et ingentibus hostiis in Adriacum mare descendit. »

(Francesco Petrarca, de insigni obedientia et fide uxoria)

Table of Contents

Chapter 1 - Introduction.....	1
1.1 The Link between subduction zones and earthquakes.....	2
1.2 The seismicity along subduction zones.....	6
1.3 Fluids in subduction zones and their link to seismicity.....	11
1.4 Potential mechanism triggering intermediate-depth seismicity.....	17
1.5 The key-role of field to unravel deep processes in subduction zones.....	19
Chapter 2 - Geological overview of the Monviso meta-ophiolite complex.....	22
2.1 Geological overview of the Alps and the Monviso metaophiolite complex.....	23
2.2 Geological setting of Monviso Metaophiolite.....	26
2.3 Brief historical overview of the geological knowledge of the area.....	27
2.4 The modern interpretation of the intra-slab shear zones within the Lago Superiore unit: the Lower and Intermediate shear zones (LSZ, ISZ).....	34
2.5 Evidences for deep fluid circulation in subduction zone: the case-study of Monviso metaophiolite.....	36
2.6 The Monviso brecciated metagabbros: evidence for brittle rupture at eclogite-facies conditions?.....	40
2.7 Aims of the thesis.....	42
Chapter 3 - A new geological map of Monviso metaophiolite complex.....	45
3.1 Tectonostratigraphy.....	48
3.2 Structures.....	64
Chapter 4 - Characterization of eclogite-facies brecciation along the subduction plate interface...45	
Brief overview of the adopted work flow.....	74
Eclogite-facies rupture along the subduction plate interface (Monviso meta-ophiolite complex, W. Alps) - Submitted paper to Lithos.....	77
4.1 Introduction.....	78
4.2 Geological setting.....	80
4.3. Field mapping, sampling and methodology.....	85
4.4. Block types and distribution within shear zones.....	88
4.5. Brecciation patterns.....	95

4.6 Clast and matrix: mineralogy and microstructure.....	102
4.7 Mineral chemistry.....	110
4.8. Discussion.....	117
4.9. Conclusions.....	131
4.10 Supplemetary Material to the submitted paper.....	132
4.11 The identification of dynamic fracture networks in coseismic breccia.....	153
4.11.1 - Dynamic fracturing: fracture geometry and spacing.....	154
4.11.2 - Dynamic fracturing summary.....	157
Chapter 5 - The Geochemical Signature of Eclogitic Breccia.....	169
5.1. Introduction.....	170
5.2 Analytical techniques.....	172
5.2.1 Bulk-rock geochemical analysis.....	172
5.2.2 X-ray mapping and mineral major element analysis.....	173
5.2.3 Mineral trace-element analysis.....	174
5.3. Outcrops and samples description.....	176
5.3.1 Eclogitic breccias in the LSZ.....	176
5.3.2 Eclogitic breccias in the ISZ.....	180
5.4 Brecciation patterns.....	181
5.4.1 Outcrop scale: structural patterns of eclogitic breccia-bearing blocks.....	181
5.4.2 Decimeter- to millimeter-scale structures of eclogitic breccia layers.....	184
5.5. Bulk-rock geochemistry.....	188
5.6. Textural generations and mineral geochemistry: major elements.....	194
5.6.1 – Clast mineral chemistry: Major elements.....	195
5.6.2 – Matrix mineral chemistry: Major elements.....	196
5.6.3 – Intermediate Shear Zone.....	199
5.6.4 – Note on omphacite composition.....	200
5.7. Mineral geochemistry: trace elements.....	201
5.7.1 Lower Shear Zone - LSZ.....	201
5.7.2 Intermediate Shear Zone.....	217
5.8 Discussion.....	220

5.8.1 Formation of Veins 1 and Matrix M1: evidences for closed-system fluid circulation.....	220
5.8.2 Matrices M2, M3 and late-stage veins: evidences for dm- to km-scale external fluid infiltration.....	222
Chapter 6 - Discussion.....	227
6.1 - Monviso metabreccia: evidence for brittle rupture at eclogite-facies conditions.....	228
6.1.2 Eclogitic or Pre-Alpine breccias?.....	228
6.2 Chronology of brecciation steps and origin of fluids.....	233
6.2.1 - STEP (I) Pre-brecciation eclogitization, mylonitization and veining.....	233
6.2.2 - STEP (II) Brecciation M1.....	234
6.2.3 - STEP (III) Brecciation M2.....	237
6.2.4 - STEP (IV) Brecciation M3.....	240
6.2.5 - STEP (V) Post-brecciation evolution.....	242
6.3 – Strain localization in Fe-Ti gabbro horizons.....	244
6.4 – Strain localization in the LSU.....	247
6.5 - Are Monviso eclogite-breccia seismically derived?.....	251
Chapter 7- Conclusions and Perspectives.....	255
7.1 – Conclusions.....	256
7.2 – Perspectives.....	259
Bibliography.....	261
Appendix 1 - Complete LA-ICP-MS dataset.....	281

*« A proem to describe those lands renowned,
Saluzzo, Piedmont, and the region round,
And speaks of Apennines, those hills so high
That form the boundary of West Lombardy,
And of Mount Viso, specially, the tall,
Whereat the Po, out of a fountain small,
Takes its first springing and its tiny source
That eastward ever increases in its course
Toward Emilia, Ferrara, and Venice;
The which is a long story to devise. »*

(Geoffrey Chaucer, The Clerk's Tale, da The Canterbury Tales)

Chapter 1

Introduction

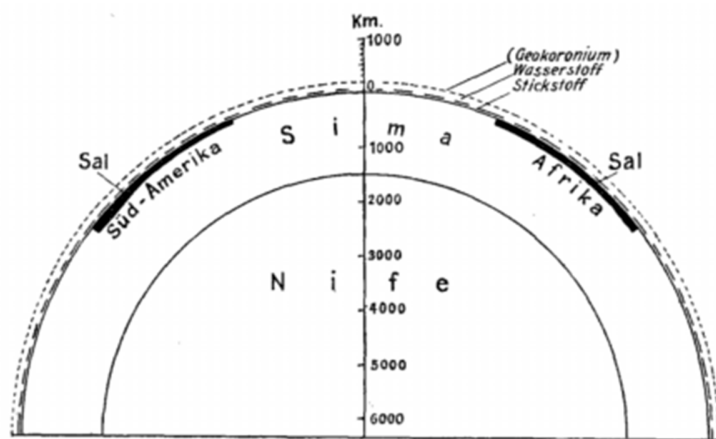


Fig. 2. Schnitt im größten Kreise durch Südamerika und Afrika, in getrennten Größeverhältnissen.

The first modern representation of “plate tectonics” by Wagner (1912), a spectacular example of how much the study of the earth “peel” can give to the understanding of its interior. From the paper “Die Entstehung der Kontinente”.

1.1 The Link between subduction zones and earthquakes

The distribution of earthquakes doesn't show a random pattern, instead most of them are aligned along a continuous belt that wraps around the Earth (Figure 1). The explanation for such a seismic pattern is linked to the theory of the plate tectonics (introduced for the first time by McKenzie & Parker, 1967, on the basis of the observations made by Wagner in the paper “*Die Entstehung der Kontinente*”, 1912), which proposes that the surface of the Earth is covered with large, rigid mosaic-like plates that move relative to each other causing tectonic activity at their boundaries. In the zone of convergence one plate is dragged down or overridden by another one along the subduction zone, the “junctions” between two plates.

The recognition, since the first decade of 20th century, of oceanic crust-derived rocks stacked on a non-cylindrical orogen such as the European Alps (described in classical geological literature as “*Verschluckungszonen*”, literally “swallowing-areas”) put the basis for development of the modern plate tectonics theory (e.g., Ampferer & Hammer 1911; Ampferer, 1925, 1941 and Amstutz, 1951; Figure 2). Indeed, these evidences were indicating that orogens were developed mainly by horizontal rather than vertical “rocks-movement” (e.g., Bertrand, 1894; Schardt, 1898; Lugeon, 1902; Argand, 1911; Wegener, 1912) allowing to overcome the eighteenth century concept of “vertical-orogeny” or “lifting crater” theory (e.g., Von Humboldt & Von Buch). In the review work of White et Al. (1971) the Authors trace the origin of the emergent plate-tectonics theory back to the paper by Ampferer, 1906 “*Über das Bewegungsbild von Faltengebirgen*”. Anyhow, the first “modern-view” models of asymmetrical subduction zones were proposed more recently by Dewey & Bird (1970), who described them as the direct result of lateral buoyancy contrasts

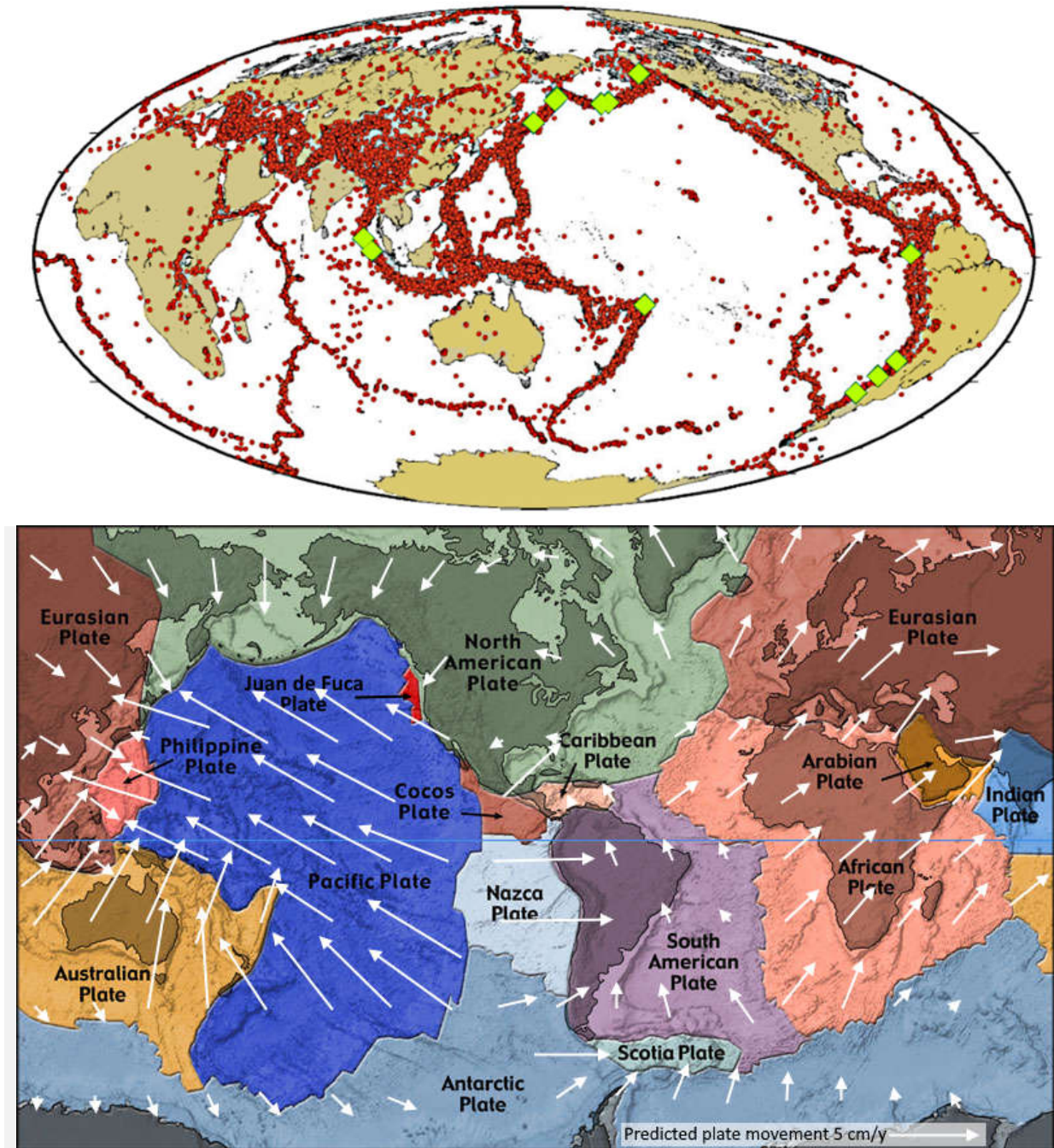


Figure 1: Global seismicity ($M \geq 4$, depth < 70 km, 1964–1998) shown as red circles (Engdahl et al., 1998) and very great M8.5 subduction earthquakes, shown as green diamonds (Engdahl & Villaseñor, 2002; Lay et al., 2005). Modified after Gutscher and Westbrook 2009 (in Lallemand and Funiciello, 2009). (b) Earth's surface subdivision with the major tectonic plates; the independent movement of every plate (with the sense of motion) is shown by the white arrows (Credit: USGS. Figure modified for this work).

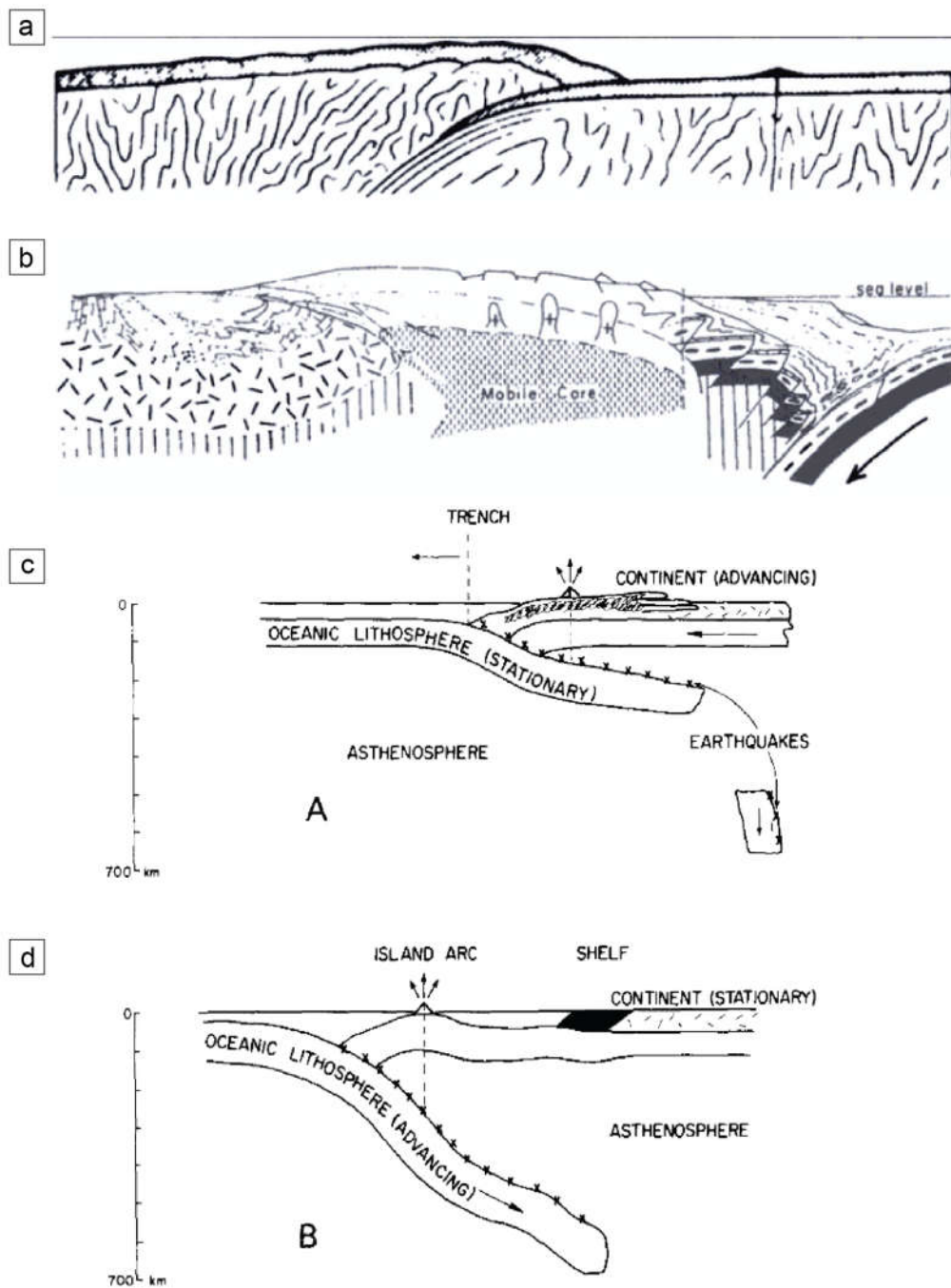


Figure 2: a compilation of the first 2D models of subduction-zones. In Figure 2A it is shown the first attempt by Amstutz to describe a "Verschluckungszonen": the position of the magmatic arc is, interestingly, on the lower plate. On Figure 2B the subduction structures as presented by Dewey and Bird (1972): all the structures and lithologies expected on a transect across subduction zones are already

recognized and depicted. The age of “subduction zone” is open! One year later Wilson (1973) will improve the description of subduction-zones dynamics focusing his attention on the rate and geometries of convergence to explain the occurrence of volcanic-Arc islands, back-arc extensions and active orogeny (Figure 2C-D). Interestingly, in this study, elements such as the slab break-off, plate-interface seismicity are already introduced. The link between superficial structures VS slab geometry will be extensively studied in the next decades.

between convergent plates (Figure 2). One year later, Wilson (1973) suggested that an additional factor could play a key-role to describe the geometries of subduction zone both at depth and at the surface: the differential convergence rates and geometries between plates. In his work he also introduced the direct correlation between subduction zones and seismicity, pointing out the earthquake generation in correspondence to the plates' interface (Figure 2).

This correlation explain the fact that most of the earthquakes concentrate and form a narrow, belt-shaped seismic zones along approximately 55.000 km over the tectonic plates margins (Figure 2). Way different is the case of subduction zones: as clearly shown in Figure 1, subduction zones are generally intimately linked to the occurrence of coastal lines and, thus, of human activities. Moreover, the seismic events linked to subduction processes can exceed the magnitude of 9 in the Richter scale. Famous examples are the earthquakes of Tohoku in 2011 (M~9.0: Simons et Al., 2011), Alaska 1964 (M~9.4: Plafker, 1965) and the 1960 Valdivia earthquake (considered as the most powerful earthquake ever registered, with M~9.5: Moreno et Al., 2009).

The study of active processes in subduction zones is, therefore, a major challenge to understand the interplate mechanical coupling, the fluids generation and their migration pathways through the slab. All the new findings would thus compete to unravel the driving mechanism generating margin-plate seismicity and to define new seismic-risk mitigation methodologies.

1.2 The seismicity along subduction zones

The seismicity in subduction zones can be subdivided into four major zones (Figure 3): (I) the **Upper-Seismogenic** zone (from the surface up-to 15/30 km-depth), (II) the **ETS** (*Episodic Tremor Slips*, from 30 to 45 Km-depth) zone, (III) the **IDS** (*Intermediate Depth Seismicity*, from 40/45 to 300 km-depth) zone and (IV) the **DSZ** (*Deep Seismic Zone, below 300 km-depth*) zone . The shallower **Upper-Seismogenic** zone, located at depths between 15 and 30 kilometers (Lyakhovsky et al., 2001) is characterized by mechanical coupling between upper and lower plate. Most of the field studies, geophysical investigations and mechanical models have focused on processes acting here, where megathrusts nucleation is responsible for the most powerful earthquakes ever recorded (Ikesawa et al., 2003; Rowe et al., 2005; Bachmann et al., 2009; Meneghini et al., 2010; Vannucchi et al., 2012).

By contrast, there is a general lack of data on the mechanical and geochemical processes acting at deeper slab levels. The observation by continuously recording Global Positioning System (GPS) network allowed in recent years to identify transient surface deformation as the direct result of aseismic-slip processes acting at the subduction zone interface at depths between 25- to 45-km (e.g. Dragert et Al., 2001; Roger and Dragert, 2003). The slip events here recognized (called **ETS**: “*Episodic Tremor Slips*”) occur down-dip from the seismogenic portion of the subduction and are not followed by seismic events, but instead are identified by non-earthquake signals that accompany the occurrence of slip (eg., Shelly et Al., 2006). The origin of these aseismic tremors is debated, being either linked to (I) fluid migration along the slab (which origin would be related to metamorphic reaction on-going at deeper levels in the slab; e.g. Obara, 2002) or (II) to generation by shearing source (e.g. Rogers and Dragert, 2003).

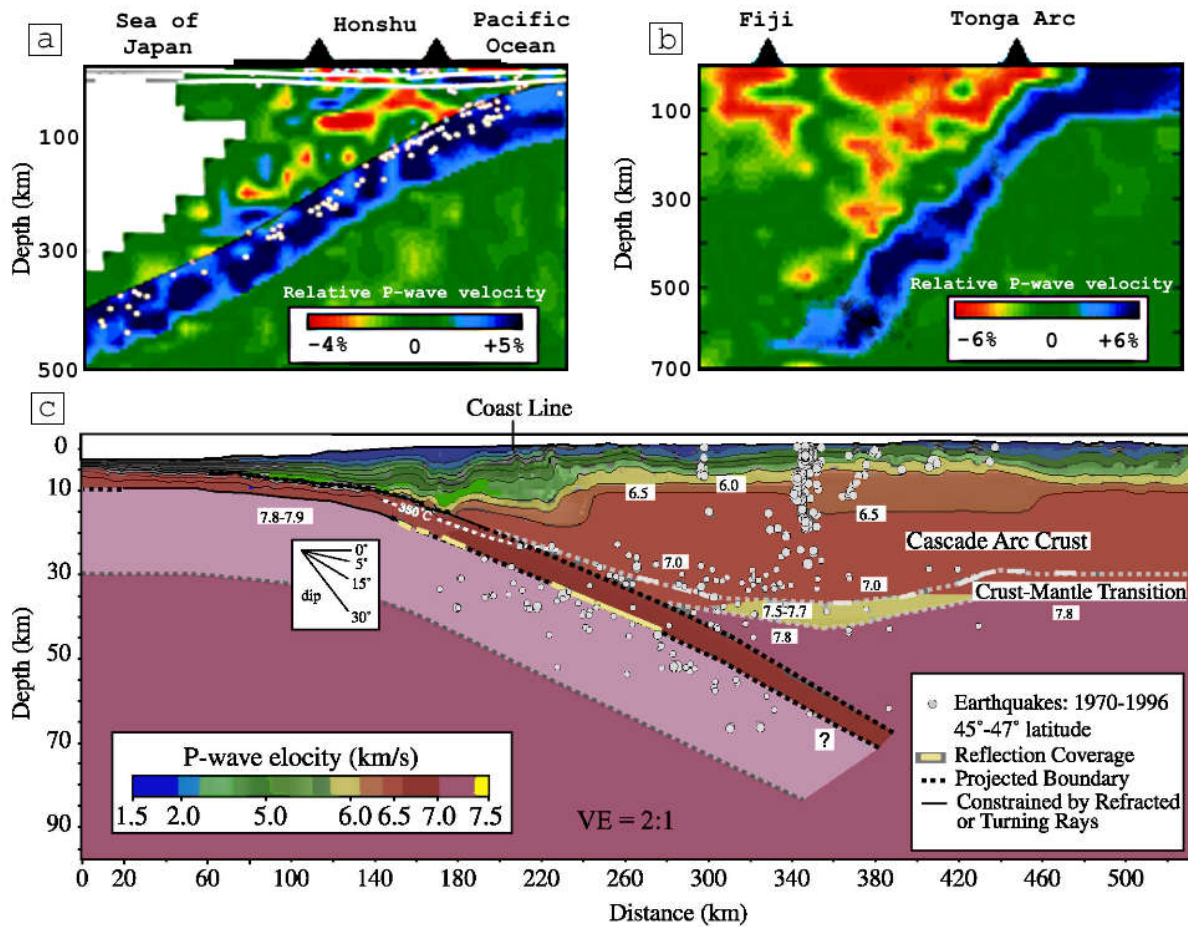


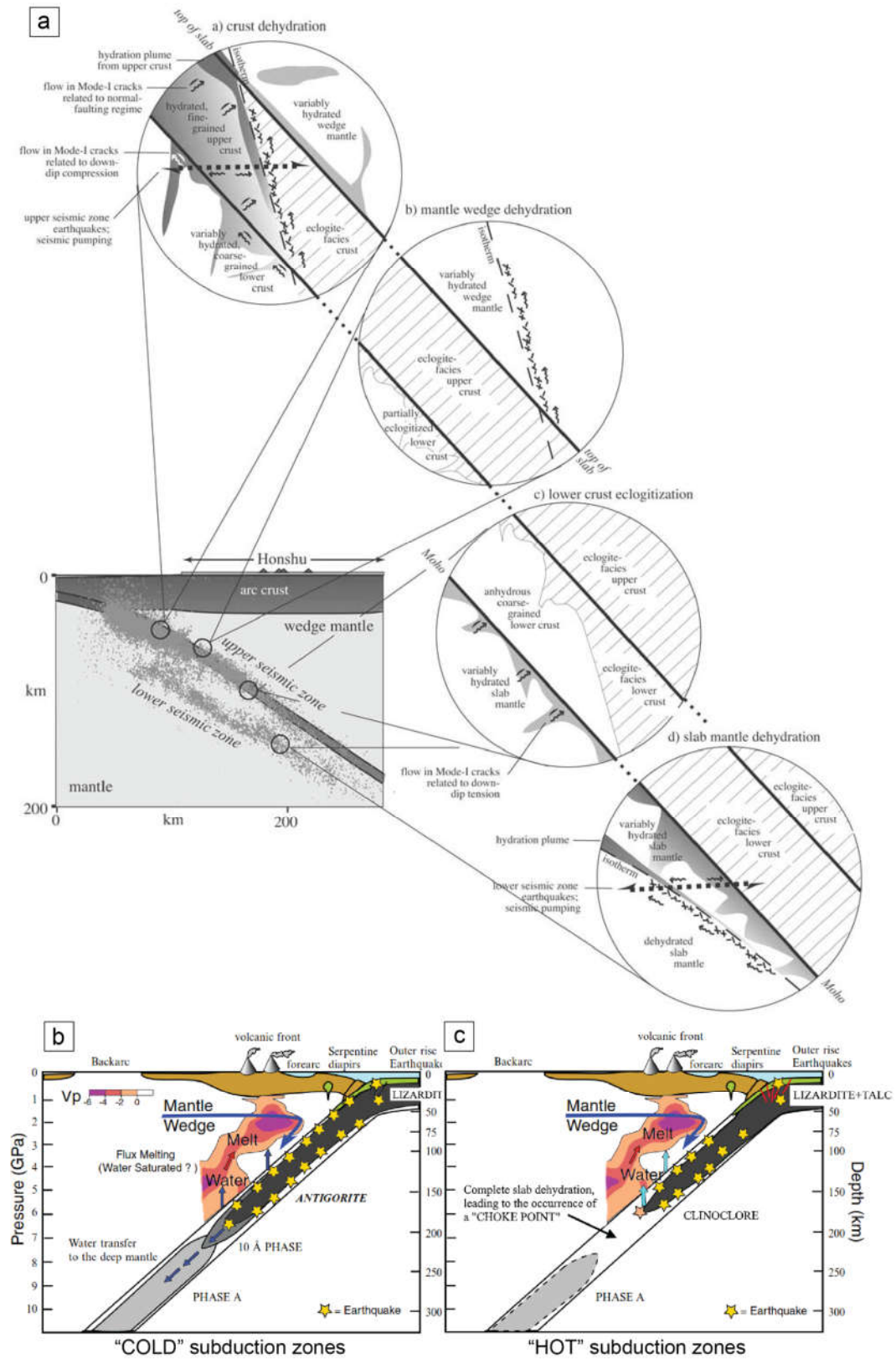
Figure 3: Thermal models of young (and hot) versus old (and cold) subduction zones. (a) NE Japan arc, a good example of a cold subduction zone. (b) SW Japan arc, a good example of a hot subduction zone. It is possible to see the great difference in the T° of the slab interface at 50 km depth and beneath the volcanic front versus the small difference in the maximum T° of the mantle wedge beneath the volcanic front. (c) P wave velocity structure across the Cascadia Subduction zone depicting the structure and the expected depth for typical seismic events in subduction zones. Figure modified after Parsons et al. (1998) and Stern (2002). Grey dots show earthquakes during 1970–1996 between 45° and 47° latitude. Seismic events with magnitude >1 are more frequent at depths deeper than 25 km, while more powerful events (e.g., $>4M$ - megathrust earthquakes) usually take place at shallower depths. The vertical exaggeration is 2x. Note that expected depths of seismic zones are variable from a subduction zone to another.

Several authors (e.g. Thatcher, 1982; Linde et Al, 1989; Roger and Dragert, 2003) suggest that ETS could be used as precursor for the nucleation of megathrust earthquakes, based on the fact that slip events, on the deep slab interface, increase the stress across the locked plate interface.

At depth $> \sim 40$ km the PT conditions reached by the slab and the overriding mantle wedge do not enable mechanical coupling anymore, nevertheless, seismic activity is here well recorded and documented (**IDS**: “*Intermediate Depth Seismicity*”; Figure 4), thus requiring triggering processes different respect to those observed in the shallower *seismogenic zone*. High-resolution seismic imaging has revealed a spatial correlation between low-velocity zones (where fluids may be present) and intermediate-depth earthquakes (e.g., Preston et al., 2003; Tsuji et al., 2008; Nakajima et al., 2009a; Shiina et al., 2013). It is thus expected that in response to P and T increase, rocks undergo a series of dehydration reactions forming progressively less hydrated phases, and therefore releasing a free fluid phase in the rocks.

Next page:

Figure 4: Schematic (not to scale) illustration of subducting crust, depicting the major phase transformation from hydrated basalt and gabbro to eclogite under equilibrium conditions. No horizontal or vertical scale is implied. The boundary between upper and lower crust is actually not sharp because the transformation from basalt/gabbro to eclogite involves a complex series of intermediate mineralogical changes. Also grains size and hydration state change throughout the crust, resulting in heterogeneous time/space mineral transformation. Picture after Hacker et al, 2003b. To note how the subduction zone cross-section from Tohoku (true scale) shows the double seismic zone (or Wadati-Benioff double seismic layer. Data of Igarashi et al. [2001]). (b) and (c) show the major phase transformations at the expenses of the serpentine polymorphs throughout idealized “cold” and “warm” subduction zones. Fluids expulsion from subducting plate results in major decreasing of V_p velocity in the mantle wedge due to fluid-induced melting (feeding the volcanic front). Simplified scenarios after Fumagalli and Poli (2005) and Poli and Schmidt (2002). The V_p seismic velocities are from Nakajima et al. (2001). Figure modified after Mainprice and Ildefonse (2009).



Continuous mineral re-equilibration is also required to explain the seismicity interesting subducted slab at depth $> \sim 325$ km (the *Deep Seismic Zone*). Here geophysical evidence shows a rapid increase of seismic velocity up-to 690 km-depth, likely induced by sudden failure on localized superplastic shear bands (e.g., Kirby et Al., 1996) at the predicted depth of the *olivine* \rightarrow *spinel* and *clinoenstatite* \rightarrow *ilmenite* transition. At this depth all the invoked processes involve anhydrous mineral phase, indicating that the slab already totally dehydrated at shallower depth. Noteworthy several studies predict that down-going plate in subduction zones would release almost totally their H₂O content (up-to 98 wt%-loss) at depth ranging between 80 to 150 km, where *Intermediate Depth Seismicity* take place (Schmidt & Poli, 1998; Van Keken et Al., 2011). It is thus fundamental to focus the attention on the fate of H₂O in slab at depth between 60 to 290 km, to unravel the processes leading to (I) the depth and the processes of mineral dehydration, (II) fluid migration along slab, (III) fluid hydration/fertilization of the mantle wedge, (IV) rheological variation of subducted rocks and, thus, (V) their link to intermediate-depth seismicity triggering.

1.3 Fluids in subduction zones and their link to seismicity

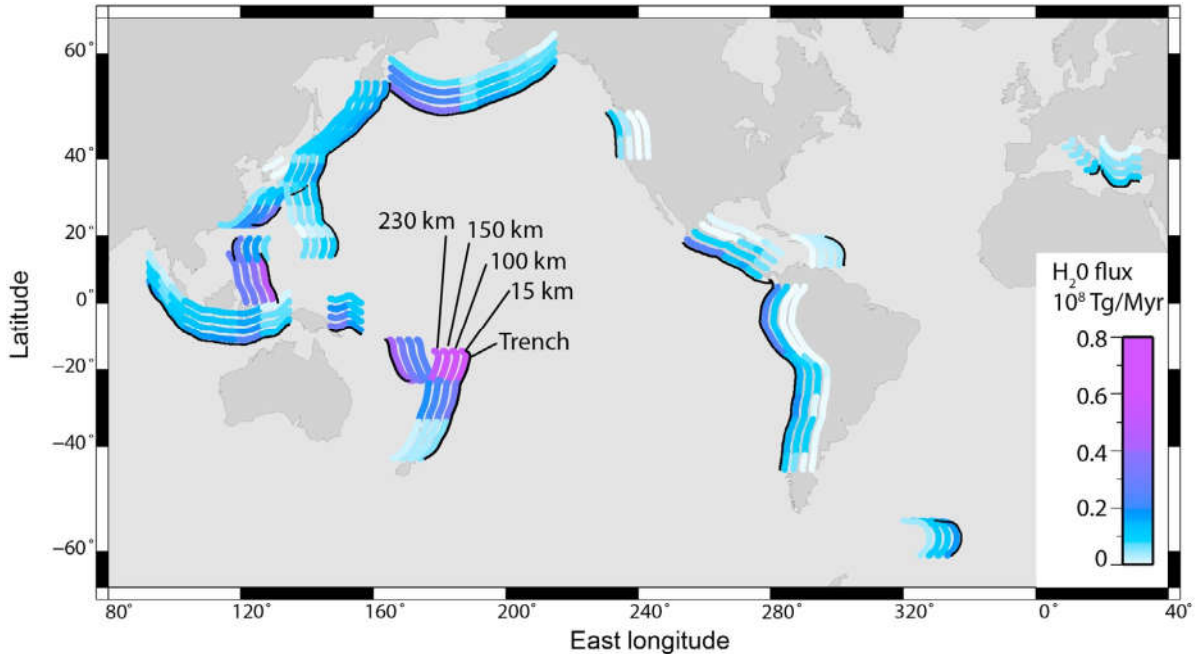


Figure 5: predicted H₂O in-flux at variable depth in the world's subduction zones, evaluated as tons-per-million years. The black lines represent the present-day position of the trench; subsequent parallel lines represent the approximate position of the slab and its H₂O content moving away from the trench. The water release / production is highlighted from the forearc to the volcanic front (100 km). Horizontal distances of slab projection to the surface are not in scale. Picture from Van Keken et Al., 2011

The release of a fluid in a rock (and, in general, in a subduction zone) is related to the thermodynamic definition of “saturation” and controlled by assemblages buffering the chemical potential of water (e.g., Bolfan-Casanova, 2005). Anyhow, the relationships between the total amount of water expected in a rock (as intercrystalline H₂O and chemically bounded H₂O in crystals) and the presence of free water (as saturated media) are not straightforward.

A key role in the H₂O influx in slabs (Figure 5) is played by the subduction of hydrated minerals (Figure 6 Figure 7 Figure 8). During this process the temperature of the subducting plate (controlled essentially by its age and subduction rate, as already postulated by Wilson, 1973) controls the

metamorphic processes resulting in the progressive hydrous minerals breakdown (e.g., Scambelluri et Al., 1991; Arcay et al., 2005; Fumagalli & Poli, 2005; Van Keken et Al, 2011).

It is difficult to exhaustively list the hydrous phases involved in the H₂O recycling inside the subduction zones; we can however subdivide them into 3 main groups with increasing depth (from Mainprice & Hildefonse, 2009):

1. *Low pressure* ($P < 5$ Gpa) minerals, such as *antigorite* (13.0 wt% H₂O, dehydrating at $\sim 600^{\circ}\text{C}$), *clinochlore* (13 wt% H₂O), *talc* (4.8 wt% H₂O), *Ca-amphibole tremolite* or *pargasite* (2.3 wt% H₂O) are commonly observed in exposed metamorphic rocks.
2. *Moderate pressure* (5–7 Gpa) minerals, such as *phlogopite* (4.8 wt% H₂O), *10Å phase* (10–13 wt% H₂O), *clinohumite* (2.8 wt% H₂O) in hydrated peridotites, *lawsonite* (11.5 wt% H₂O) and *zoisite* (2.0 wt% H₂O) in hydrated metamorphosed basalts and *potassium rich phengite* (4.6 wt% H₂O) in metamorphosed sediments.
3. *High pressure* (>7 Gpa) minerals such as the K-amphibole *richterite* (2.1 wt% H₂O), *topaz-OH* (10.0 wt% H₂O), *phase Egg* (11–18 wt% H₂O) and the DHMS or alphabet phases, *phase A* (12 wt% H₂O), *phase B* (3 wt% H₂O), *phase superhydrous B* (2 wt% H₂O), *phase D* (10 wt% H₂O), and *phase E* (11 wt% H₂O).

The general mineral-breakdown trend shows a decrease in the water content in the hydrated slab with depth (e.g., Van Keken et Al., 2011) as the hot surrounding mantle raises the slab temperature by thermal conduction, resulting in the breakdown and reduction of the volume fraction of hydrous minerals and in the release of a free fluid phase to the surrounding rocks and the adjacent mantle (*Figure 6* and *Figure 7*). In “warm” subduction zones (*Figure 4*) the hydrous phases may be completely de-hydrated at some critical depth, called a choke point

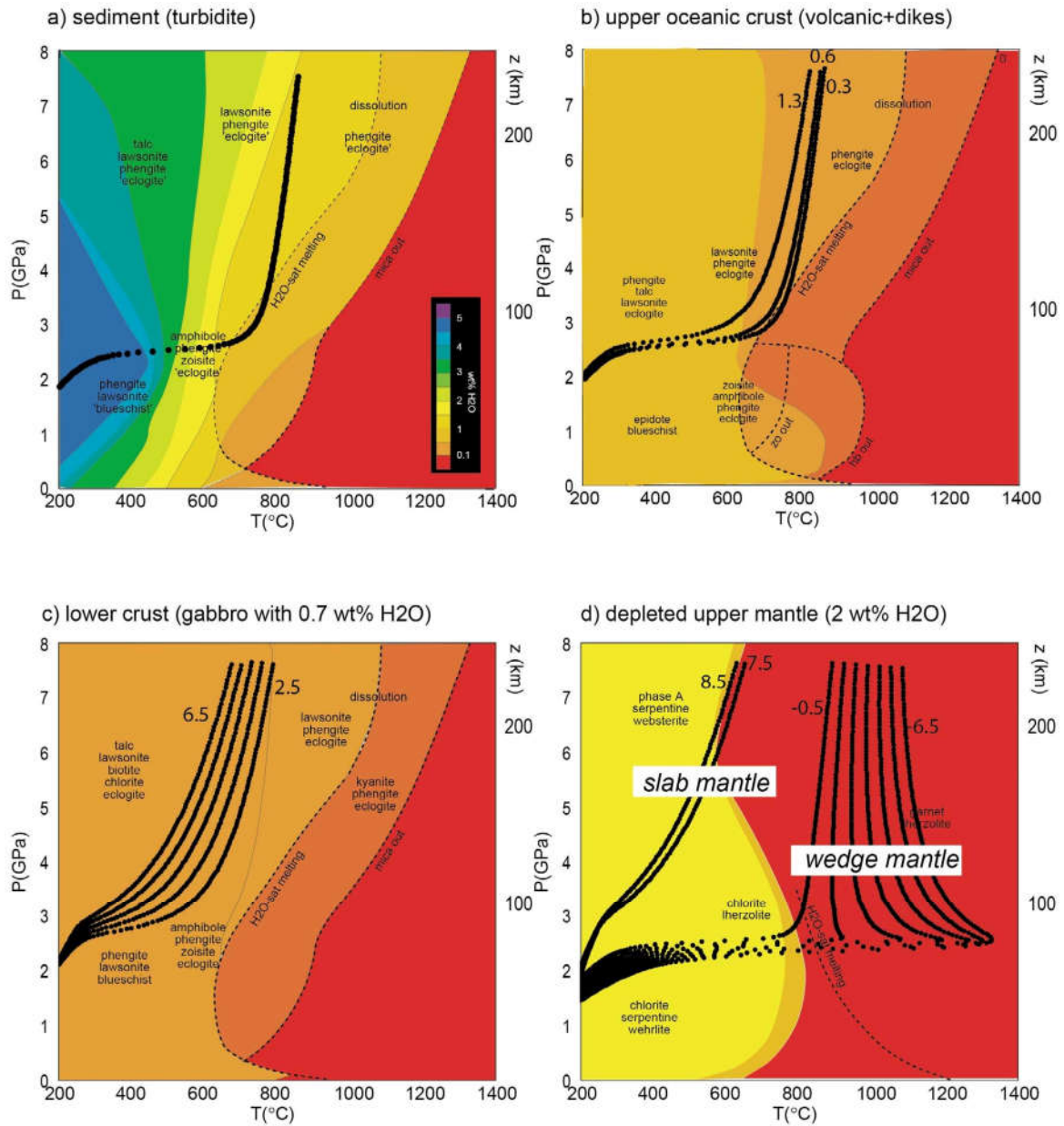


Figure 6: Example from Van Keken et Al., (2011) of P- T paths for the southern Mariana subduction zone in and directly on top of the slab and expected water content retained in the slab (mineral-bounded H_2O). The numbers next to the P- T paths indicate the depth in km below sediments (positive numbers) or the height in km above the sediments (negative numbers). (a) The P- T path in the middle of sediment pile (here as turbidite). (b) The P- T paths in the uppermost 2 km of the oceanic crust. (c) The P- T paths in lowermost 5 km of the oceanic crust. (d) P- T paths in the slab mantle (to 2 km below Moho) and wedge mantle (to 6.5 km above the slab). In general, sediments reach the H_2O -saturated solidus, but the high-temperature gradients allow parts of the volcanic crust and gabbros to retain H_2O . The wedge mantle below the subducting crust is in all cases too hot to retain hydrated phases. The serpentinized upper mantle below the crust is expected to be dehydrated in all but the coldest subduction zones. The pressure-temperature curves are derived from the thermal model for paths that run parallel to the top of the slab.

(Kawamoto et al., 1996). The process of continuous phase transformation into less and less hydrated phases and associated fluid release can continue up-to-the depth of the transition zone and the lower mantle (e.g., Kawamoto et al., 1996).

Conversely, where slab temperatures are sufficiently low (e.g., N.E. Japan) the stabilization of hydrous minerals containing large amounts of water as hydroxyl groups (e.g., antigorite, chlorite, lawsonite), increases the content of H₂O in the slabs. Here hydrous minerals are stable over a significant depth range in the slab (Figure 7 and Figure 8) and their breakdown likely triggers earthquakes in the form of the double Wadati-Benioff zone (e.g., Fumagalli and Poli, 2005; Brudzinski et al., 2007a).

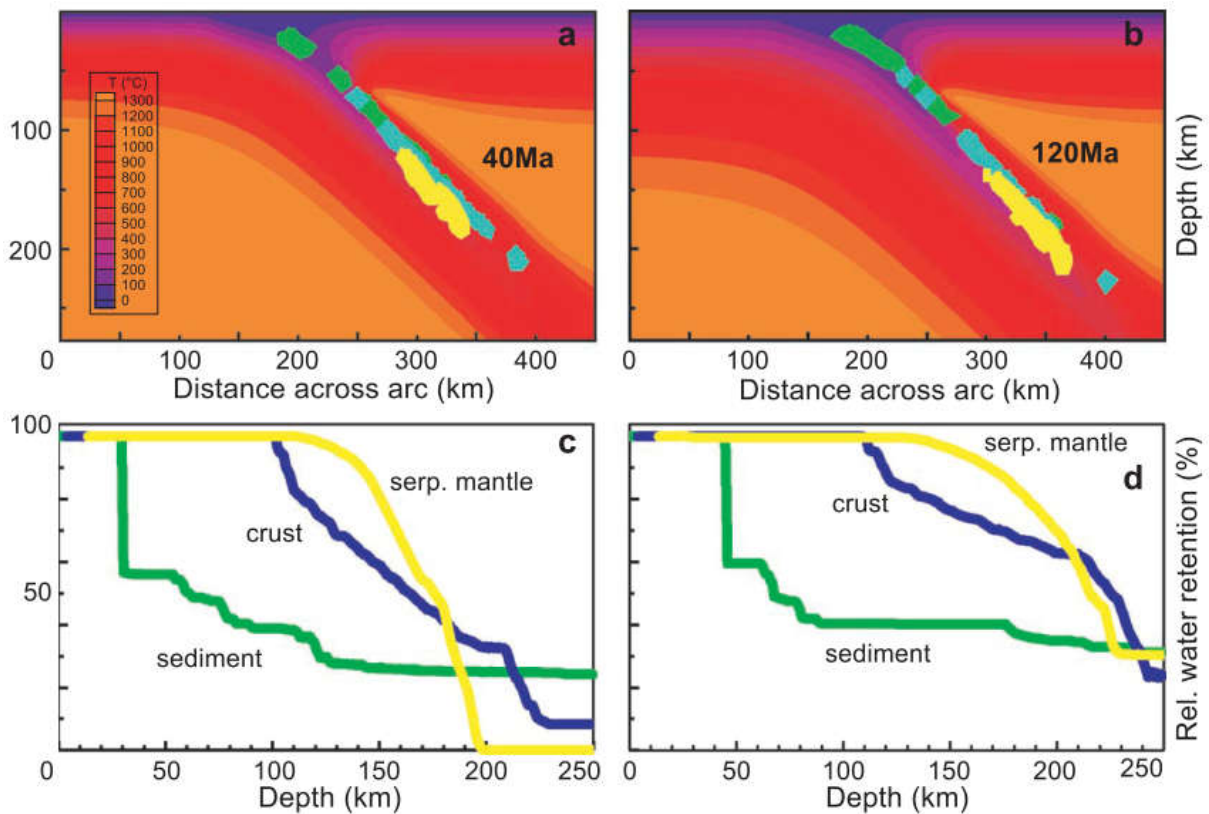


Figure 7 Modeled water release in subduction zone. In (a) and (b), the modeled regions of water release from subducting sediments (green), oceanic crust (cyan), and serpentinized mantle (yellow) are shown for 40- and 120-Ma-old slabs, respectively. (b) and (c) show the relative degrees of water retention at 8 GPa for the three different lithologies. Picture from Rupke et Al., 2004.

This double seismic layers are geophysically imaged at depth between 60 to 250 km-depth, corresponding to the IDS zone (Figure 4; Hacker et al., 2003a, 2003b; Yamasaki & Seno, 2003) and are vertically separated by a 10 to 40 km-thick aseismic area (Rietbrock & Waldhauser, 2004; Abers et al., 2006). Geophysical and petrological data suggest that the upper layer may correlate with the topmost, previously hydrothermalized crustal part of the slab ongoing massive metamorphic dehydration (Figure 4 and Figure 7; Bostock et al., 2002; Green & Houston, 1995; Hacker et al., 2003b; Rondenay et al., 2008). Indeed, the subducted oceanic lithosphere is largely hydrated by extensive hydrothermal circulation taking place both at the ridge and at the outer rise. This intense hydration can reach mantle rocks when they are exhumed (i.e., oceanic detachments at slow spreading ridges); moreover, the oceanic lithosphere is capped by sediments bearing both hydrated phases (clays) and free fluids in pores (sediments, hydrated oceanic crust and upper mantle; e.g. Scambelluri et al., 1995; Schmidt and Poli, 1998; Hacker et al., 2003a; Omori et al., 2004; Hermann et al., 2006; Kita et al., 2006; Van Keken et al., 2011; John et al., 2012; Abers et al., 2013). The lower low-velocity layer, instead, correspond to serpentinitized peridotite of oceanic crust (Figure 4) and would thus correlate to progressive antigorite breakdown (e.g., Fumagalli and Poli, 2005; Brudzinski et al., 2007).

In addition, the study of focal mechanism solutions suggests that intermediate-depth earthquakes may be locally associated to the reactivation of hydrated faults that formed by bending-related tensional faulting at the outer trench slope (e.g., Jiao et al., 2000; Marot et al., 2012; Nakajima et al., 2011a; Shiina et al., 2013; Ranero et al., 2003). This latter evidence makes even more complex to precisely define the structures and mechanism at the base of IDS, suggesting a complex interplay between phase-changes and inherited, pre-subduction structures.

1.4 Potential mechanism triggering intermediate-depth seismicity

As shown in section 1.3, numerous evidences support the origin of IDS by free-fluid liberation due to the breakdown of hydrous minerals phase in subducted slabs (e.g., Figure 4Figure 5Figure 6). Several studies (both experimental and field-based) tried to depict the key-reactions leading to phase change at intermediate depth (e.g., 40/45 to 300 km-depth) and the resulting rheological change on slab rocks.

Raleigh and Paterson (1965) were the first to prove by experiments that antigorite dehydration during shear-deformation culminates in fracturing accompanied by a sudden stress drop. At high-pressure, the experiments have shown that dehydration embrittlement of serpentinite could be a plausible mechanism for the genesis of IDS (e.g., Dobson et al., 2002; Jung et al., 2004). However, stick-slip instabilities are not expected to develop during the dehydration of antigorite (Chermak & Hirth, 2010), raising a debate on the link between dehydration and (induced) brittle failure. The occurrence in natural rocks (e.g. in the Voltri massif, Scambelluri et Al., 1991) of olivine veins as the product of antigorite dehydration, however, confirms that serpentinite dehydration reaction could be a key to explain *IDEs* through episodic fluid-pulses (e.g., John et al., 2011; Ferrand et al., 2017). Another key-mineral to study subduction zones water recycling is lawsonite (whose H₂O content reaches up-to 11.5 wt%). Several examples of lawsonite-bearing (as fresh- or pseudomorphosed-crystals) rocks have been described in the majority of HP terrains of worldwide orogens (Pawley, 1996; Tsujimori et Al., 2006) and it is demonstrated that its stability field may cover a range up to eclogitic-conditions (e.g., Ravna et Al., 2010; Angiboust & Agard, 2011; Brovarone et Al., 2011). From experiments with a Griggs-type apparatus, Okazaki & Hirth (2016) proposed that dehydration embrittlement enhanced by lawsonite breakdown reactions at 2-2.5 Gpa

/ 600°C could be the trigger for upper-seismic plane *IDEs* in cold subduction zones (in addition to antigorite breakdown in the lower-seismic plane).

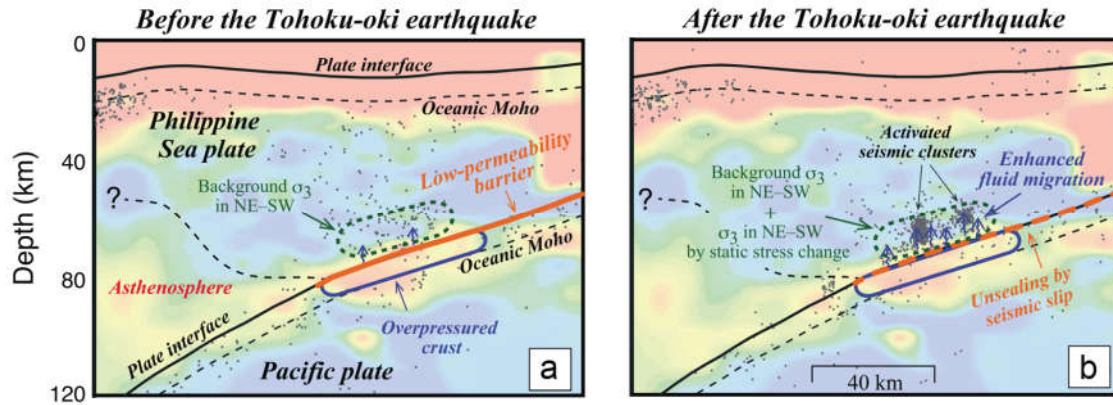


Figure 9: Schematic model of the activation of seismicity in the lowermost part of the Philippine Sea plate after the Tohoku-oki earthquake (2011) as presented by Nakajima et al. (2013). (a) Before the seismic event, the low-permeability barrier is attested along the interface between Pacific plate (lower-plate) and the Philippine plate (upper-plate). (b) The seismic-slips associated with the Tohoku-oki earthquake would be the driving force producing the break of the seal, resulting in fluid migration from the lower- to the upper-plate. Geophysical evidence for fluid migration, however, cannot exclude that H_2O release at intermediate depth could be “active” part in the variation of the permeability of the rocks and not only “passive” occurrence by shallower earthquake destabilization of the slab

This theory is however challenged by other studies: in detail, Incel et al. (2016) suggest that grain-size reduction (resulting in transformational faulting/shear fracturing) during the transition from *lawsonite–blueschist* to *lawsonite–eclogite* is the effective process leading to AEs (acoustic emission = seismic emission) at pressure and temperature comparable to intermediate-depth seismicity. Previously, self-localizing shear instability onset of highly localized viscous creep in preexisting, fine-grained shear zones had been proposed by Kelemen & Hirth (2007) and John et al. (2009) as a potential mechanism for intermediate-depth earthquakes (further details?).

In addition, open discussion exists about the *fluid migration induced* intermediate-depth seismicity. As noted by Nakajima et al. (2013) and Shiina et al. (2013), after the big Tohoku earthquake of 2011 a swarm of a minor seismic event was detected migrating from the subducting

Pacific plate into the mantle wedge of the Philippine plate. The authors interpreted it as the consequence of the migration of fluids liberated by the down-going plate by seismic-waves destabilization (Figure 9).

Moreover, the fate of the fluids produced by hydrous-phase breakdown remains unclear. Good agreement exists on the chemical consequences of fluid release/migration into the mantle wedge, as triggering melting and subsequent feeding of back-arc magmatism (e.g., Ulmer & Trommsdorff, 1995; Schmidt and Poli, 1998; John et al., 2012) and the linked reduction of seismic velocities (e.g., V_p -6%; Nakajima et al., 2001).

On the contrary, much debate exists on the effects, kinematics and expected fluid migration pathways in the slab (e.g. Scambelluri & Philippot, 2001; Bebout, 2007; Kawano et Al., 2011; Angiboust et Al., 2014). The predicted processes associated to deep fluid circulation in the slab like (I) hydraulic fracturing, (II) dehydration embrittlement, (III) mineral transformation induced faulting and potentially (IV) partial melting recorded by pseudotachylites (e.g. Davies, 1999; Hacker et al., 2003b; Jung & Green., 2004) are actually still largely debated.

1.5 The key-role of field to unravel deep processes in subduction zones

The debate presented above is fueled by both the lack of direct observations of pristine subduction-derived rocks (“... *it is easier to send a man to the moon, 384.400 km away from home than sampling rocks at 70 km-depth!*”) and by instrumental uncertainties on geophysical data acquisition (e.g., Kuge et al., 2010). Indeed, uncertainties in the range of several hundred meters to a few kilometers affect the relocation of earthquake hypocenter, with depth even more poorly constrained than the epicenter (e.g., Waldhauser & Schaff, 2008). These errors, due to (I) inaccuracies in seismic waves phase picks and (II) errors in the adopted relocation model, are

larger than the spatial dimension of the earthquakes themselves (~10 m to 1000 m for M1–4 earthquakes).

The investigations on subducted materials encompass petrological studies on rocks subsequently exhumed at the surface, samples drilled from the ocean floor (e.g., Michibayashi et Murakami, 2007) and xenoliths (e.g., Michibayashi et al., 2006b), thermodynamic calculations (e.g., Hacker et al., 2003a; Bousquet et al., 2005) and laboratory experiments (e.g., Ohtani et al., 2004; Iwamori, 2004; Fumagalli & Poli, 2005). A major critical issue in the experiments and thermodynamic calculations is the water-saturated conditions at which they are run, with free water present (which may only be true transiently, while water activity may most often be much lower than 1; e.g., Fumagalli & Poli, 2005; Schmidt & Poli, 1998). Actually, in natural samples, mineral assemblages normally show evidence for water-undersaturated conditions at HP and UHP conditions (e.g., Chinner & Dixon, 1973; etc).

Although still limited, there is growing evidence that large-scale, “fossil” exhumed portions of subducted lithosphere (Agard et al., 2009) may record both chemical and mechanical processes operating in the depth range of intermediate-depth seismicity (WM White et al., 1985a-b; Kirby, 1985; Handy et al., 1999; Montesi et al., 2003; John et al., 2009; Plat et al., 2011; Angiboust et al., 2011, 2012b). In the past, many studies on fluid circulation in subduction zones focused on the veins and mineral assemblages of eclogitic terrains (e.g. Philippot, 1987; Philippot & Kienast, 1989; Philippot & Selverstone, 1991; Spandler et Al., 2003 and 2011). Nevertheless, the link between fluids and deformation and their significance in the optic of subducted plate evolution was less studied, particularly their role in the transient switch between ductile and brittle deformation (eg., Philippot and Van Roermund, 1992). This is due to the fact that few examples of exhumed (and unambiguously recognized) eclogite-facies earthquake-derived rocks are known.

Pseudotachylites are described in deeply subducted continental crust from Lofoten (Norwegian Caledonides, i.e., Terry & Heidelbach, 2006; Raimbourg et al., 2007a), Zambia (John and Schenk, 2006) and Musgrave range in Australia (Hawemann et al., EGU General Assembly 2015-poster), whereas more discussed is the example from Corsica (Andersen & Austrheim, 2006). Cataclastic rocks ascribed to eclogite-facies conditions are even rarer: examples are found in Yangkou bay, China (Yang et al., 2014), in the Etna/Levaz nappe, Western Alps (Erwelin et al., EGU General Assembly 2013-poster) and in Monviso metaophiolite, Western Alps (Angiboust et al., 2012b).

The recent report of oceanic crust brecciation at eclogite facies conditions (in the Lago Superiore Unit of the Monviso meta-ophiolite, Western Alps; Angiboust et al., 2012b) opens the possibility of retrieving patterns of intermediate-depth seismic rupture from a well-preserved slab fragment. This finding was challenged, however, by authors who interpret these breccias as inherited pre-Alpine detachment fault rocks from an oceanic core complex or as sedimentary-derived breccias (e.g., Balestro et al., 2014a-b; Festa et al., 2015). The feasibility of brittle rock failure at eclogite-facies conditions, and thus HP brecciation processes, is actually lively debated both for subduction-zone settings (e.g., with relative low temperature gradients: Raleigh et al., 1965, 1967; Kirby et al., 1996; Jin et al., 2001; Jung & Green., 2004; Zhang et al., 2007) and also for other HP terrains with higher temperature gradients (e.g., in the Limpopo granulites: Roering et al., 1995).

Chapter 2

Geological overview of the Monviso meta-ophiolite complex



Drawing representing the measurements realized by Valeriano da Castiglione to evaluate the elevation of the Monviso, probably the first scientific research done in the area (1627). The Lakes Chiaretto (12) and Lago Superiore (7) are easily recognizable. From the “Relatione di Monviso et dell'origine di fiume Po”.

2.1 - Geological overview of the Alps and the Monviso metaophiolite complex

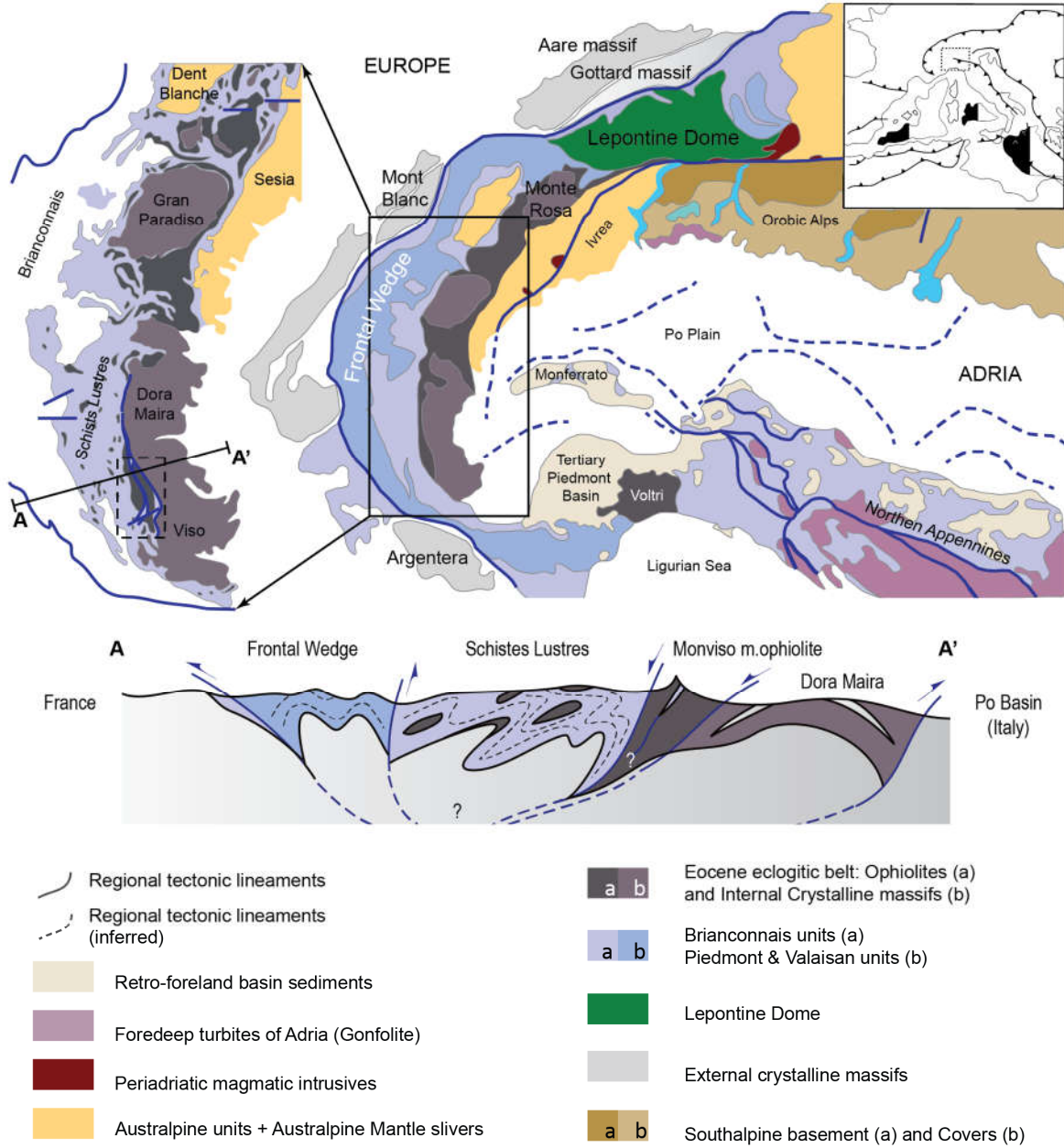


Figure 10: Tectonic sketch of the Western Alps. The Eocene eclogitic belt (deep-grey) is exposed on the upper-plate side of the orogen, between the Frontal wedge (light blue) and the remnants of a Late Cretaceous doubly-vergent wedge (yellow). In the inset, a detail of the eclogite belt and the frontal wedge with the localization of the Monviso metaophiolite. The simplified geological cross section AA' depict the major structures and tectonic units across the Alpine edifice, color-code as in the geological map.

Maps modified after Malusá et Al. (2011) and Agard et Al. (2009). The geological cross-section is derived from Guillot et Al. (2004).

The study area belongs to the Monviso meta-ophiolite complex, extending in the Western Alps for over 30 km between Piedmont (Italy) and Provence-Alpes-Cote d'Azur (France); it is part of the larger Liguro-Piemontese domain, which extends from the Voltri complex (Ligurian Alps, Italy) to the Zermatt-Saas zone (Valais, Switzerland, *Figure 10*). The Western Alps represent the result of the convergence and subsequent collision between Adria microplate and the European continental margin, with the Liguro-Piemontese oceanic-crust domain interposed (Ricou & Siddans 1986; Coward & Dietrich 1989; Laubscher, 1991; Schmid & Kissling 2000). The inner part of the Western Alps is structurally composed of a double-verging stack of oceanic and continental nappes belonging to the slow-spreading Jurassic Tethyan oceanic seafloor and the associated European thinned continental margin respectively; these nappes are bounded by major-scale, poly-metamorphic tectonic contacts (Platt et al. 1989; Polino et al. 1990; Lardeaux et al. 2006; Butler et al. 2013). Four main geodynamic steps led to the building of the actual Western Alps edifice: (I) the Late Jurassic opening of the slow-spreading Tethyan ocean, followed during Eocene (II) by E-dipping subduction of the paleo-European plate resulting in up-to eclogite-facies peak metamorphic conditions, then (III) continental collision promoting W-verging accretion and later (IV) Oligocene-to-Miocene crust/mantle indentation leading the partial exhumation of the alpine orogen (Lagabrielle & Cannat, 1990; Schmid et al., 1996; Lagabrielle & Lemoine, 1997).

In detail, the Liguro-Piemontese domain is formed by exhumed remnants of tens of kilometres-wide eclogite-facies tectonic slices, such as the Monviso meta-ophiolite, juxtaposed to lower grade (blueschist facies) sedimentary-derived terrains belonging to the fossil accretionary wedge, such as the Schistes Lustrés. In the Monviso area this domain exhibits structural and metamorphic characteristics comparable to those observed in the Zermatt-Saas and Lanzo metaophiolite (e.g. Pelletier & Muntener, 2006; Angiboust & Agard, 2010; Debret et al., 2012).

In the Monviso area, the stack of nappes shows, from the West to the East, the succession of (a) the Schistes Lustrés complex and (b) The Monviso metaophiolite complex tectonically overlaying the (c) Dora Maira massif (*Figure 10*). The Queyras schistes Lustrés represent a former fossil accretionary wedge, with mafic and ultramafic blocks disseminated in a dominantly carbonate-rich metasedimentary matrix with metamorphic grade increasing from the West to the East up-to blueschist facies (e.g. Goffé & Chopin, 1986; Agard et al., 2001; Oberhänsli & Goffé, 2004). A major west-dipping ductile normal fault system separates the Schistes Lustré from the Monviso meta-ophiolite (*Figure 10*), exhibiting a metamorphic gap between the two units (Balleve et al., 1990; Philippot, 1990). To the East, the Dora Maira massif consists of a Paleozoic continental basement overlain by Mesozoic carbonate sedimentary cover; it was part of the thinned continental European distal margin involved in the Alpine subduction. The Dora Maira coesite-bearing massif is made of several slices detached from the downgoing slab at different depths (and therefore PT conditions) and ages (metamorphic peak of 120 km-depth at 39-33 Ma; e.g. Chopin, 1984, 2003; Schertl et al., 1991; Tilton et al., 1991; Gebauer et al., 1997; Castelli et al., 2007; Groppo et al., 2007), whereas the analogous terrains of Monte Rosa and Gran Paradiso massif were subducted to 80 km depth at 43-37 Ma (e.g. Meffan-Main et al., 2004; Lapen et al., 2007; Gabudianu Radulescu et al., 2009). The contact between the Monviso meta-ophiolite and Dora Maira massif consists of a ductile, W-dipping, normal fault (Blake & Jayko, 1990, Schwartz et al., 2000); all these major W-dipping tectonic structures are ascribed to the Oligocene-to-Early Miocene crust/mantle indentation, leading to the doming of the Dora Maira massif, which promoted the late-stage westward tilting of the Monviso metaophiolite complex and overlying Queyras Schistes Lustrés (Balleve et al. 1990; Philippot 1990; Lardeaux et al. 2006; Schwartz et al., 2000).

2.2 – Geological setting of Monviso Metaophiolite

The Monviso metaophiolite complex represents a well-preserved fragment of Tethyan oceanic lithosphere, with recognizable lithostratigraphic successions. It used to be subdivided into several tectonometamorphic units (Lombardo et al., 1978) and more recently in two main units: the Monviso s.s. unit (MU) and the Lago Superiore Unit (LSU; Angiboust et al., 2011). For the *Monviso unit*, a peak of 480°C–22 kbar was proposed by Angiboust et al. (2012a), whereas slightly different eclogitic P–T peaks were calculated for the Lago Superiore Unit by different authors: 580°C–19 kbar (Schwartz et al., 2000), 650°C–26 kbar (Messiga et al., 2000), 545°C–20 kbar (Castelli et al., 2002), 550°C–25 kbar (Groppo & Castelli, 2010) and 550°C–26 kbar (Angiboust et al., 2012a).

This study focuses mainly on the LSU, which comprises, from bottom to top: serpentinized lherzolitic mantle intruded and/or capped by late Jurassic Mg-Al and/or Fe-Ti gabbros (152 Ma; Lombardo et al., 2002; 163 Ma, Rubatto and Hermann, 2003); banded tholeiitic basalts (with locally preserved pillow structures); diabases and mixed calcareous/pelitic Cretaceous metasediments (Lombardo et al. 1978, 2002; Balestro et al. 2011, 2013). Strong lateral variations in lithostratigraphy, with one or more of the above horizons missing, were attributed to an irregular seafloor structure typical of slow spreading oceans (Lagabriele & Lemoine, 1997).

The original stratigraphic sequence is partly disrupted by shear zones (Lombardo et al., 1978; Philippot & Kienast, 1989; Angiboust et al., 2011, 2012a; Festa et al., 2015); we particularly focus on two of them: the Lower Shear Zone (LSZ) and the Intermediate Shear Zone (ISZ), which locally mark the metagabbros – serpentinites and metabasalts - metagabbros boundaries, respectively. Since P-T conditions are undistinguishable on either side of the shear zones (Angiboust et al., 2012a), vertical displacements along them are probably less than km-scale.

The LSU is therefore an almost intact, well-preserved fragment of oceanic lithosphere coherently subducted to 80 km-depth and subsequently crosscut by poly-metamorphic km-scale shear zones (Angiboust et al. 2011, 2014).

2.3 - Brief historical overview of the geological knowledge of the area.

The first detailed study of the geology of the Monviso meta-ophiolite complex dates back to the first year of the unified Reign of Italy. In those years, Gastaldi (1876) and Zaccagna (1887) provide the first geological observation resulting in the first coherent description of the lithologies and the regional West-dipping of the ophiolitic sequences of the Monvsio area (*Figure 11*). A few years later, during the first systematic geological survey by the Italian Geological Office, Stella (1895) and Novarese (1896) performed the first detailed mapping of this sector (respectively of the *Po-Varaita valleys* and of the *Pellice Valley*). Their work was the basis for the subsequent redaction of the geological maps of the area at the scale 1:100.000, resulting in the “*Foglio 67 – Pinerolo*” (edited in-between 1912-1930, reprinted in 1951) and “*Foglio 78/79 – Dronero/Argentera*” (edited in-between 1912-1930, reprinted with substantial improvement in 1971; *Figure 12*). The more recent reprint, unfortunately, is characterized by the loss of significant distinctions, in particular between Mg-Al vs Fe-Ti metagabbros (present, in example, on the older geological cross-section of Zaccagna and Stella, *Figure 11*).

The first modern interpretation of the Monviso meta-ophiolite as a remnant slice of the former Tethys Ocean separating Africa and Europe has to be assigned to Lombardo et Al. (1978) who carefully re-mapped all the area with the integration of the unedited maps of G. Cavallera (1978), F. Dutto (Valle Varaita e Vallone delle Forciolline, 1976-1977), L. Fiora (1970), P. Leporati (1968), B. Lombardo (1969), G. Migliardi (1969) and P. F. Sorzana (1969). In their work, Lombardo et al. provided a careful description of all the lithologies and performed also the first geochemical

analysis of metabasalts, metasediments, serpentinites and metagabbros. This work also proposed the first lithostratigraphical subdivision of the Monviso metaophiolite in six different units: (1) *Unit of Vallone di Vallanta*, (2) *Series of Costa Ticino*, (3) *Serpentinites of Colle di Viso and Complesso di Passo Gallarino*, (4) *Unit of Viso Mozzo*, (5) *Unit of the Smaragdite-bearing metagabbros of Lago Superiore* and the (6) *Basal Serpentinites and eclogites of Colle Gianna and Verni*. At the base of the basal serpentinites the unit of the “*basal calcshists*” was recognized, composed by Triassic metasedimentary slivers pinched-out during the juxtaposition of the Monviso metaophiolite and the

Dora Maira massif. This unit was later assigned to the Dora Maira massif, being largely composed of metasediments of continental rather than oceanic affinity (e.g., Michard, 1967; Lombardo, 1969 and Cavallera, 1978).

Next Page:

Figure 11: (a) geological cross-section between the Costa Savaresch (Vallanta valley) and Crissolo, drawn by Zaccagna (1987) and edited by Franchi (1904, tav. III, Fig. 4). gs: gneiss; qzm: quartzite; cs: calcschist; ms: micaschist; cm: marble; s: massive serpentinite; ss: serpentinite-schist; ef: gabbro “eufotide”; anf: amphibolite; mo: moraine. Scale 1:100.000. (b) Geological cross-section from the Vallanta valley to the Po valley (south of the precedent cross-section), drawn by Stella and edited by Franchi (1898, Tav. IX, profile VII). gng: augen gneiss; ms: micaschist; Ti: lower triassic; Tm: middle Triassic; Li: lower Lias; cs: calcschist; c: crystalline/dolomitized limestones; cg: carniole; s: massive serpentinite; ss: serpentinite schists; eu: gabbro “eufotide”; a: amphibolite; pr: prasinite; pf: porphyrite; ct: layered limestones; dt: quaternary covers; mo: moraine. Scale 1:100.000. (c) Geological cross-section through the Monviso from Lombardo et Al. (1978). 1a: calcschist; 1b Qtz-bearing micaschist; 2: antigorite serpentinite schists; 3: metagabbros; 4: eclogitic Fe-Ti metagabbros; 5: massive metabasalts; 6: pillowed metabasalts; 7a: latered metabasites; 7b: brecciated metabasites; 8: “zona a scaglie”. VU: Vallanta unit; CT: Costa Ticino series; VM: Viso Mozzo Unit; MG: Lago Superiore unit; BS: basal serpentinites.

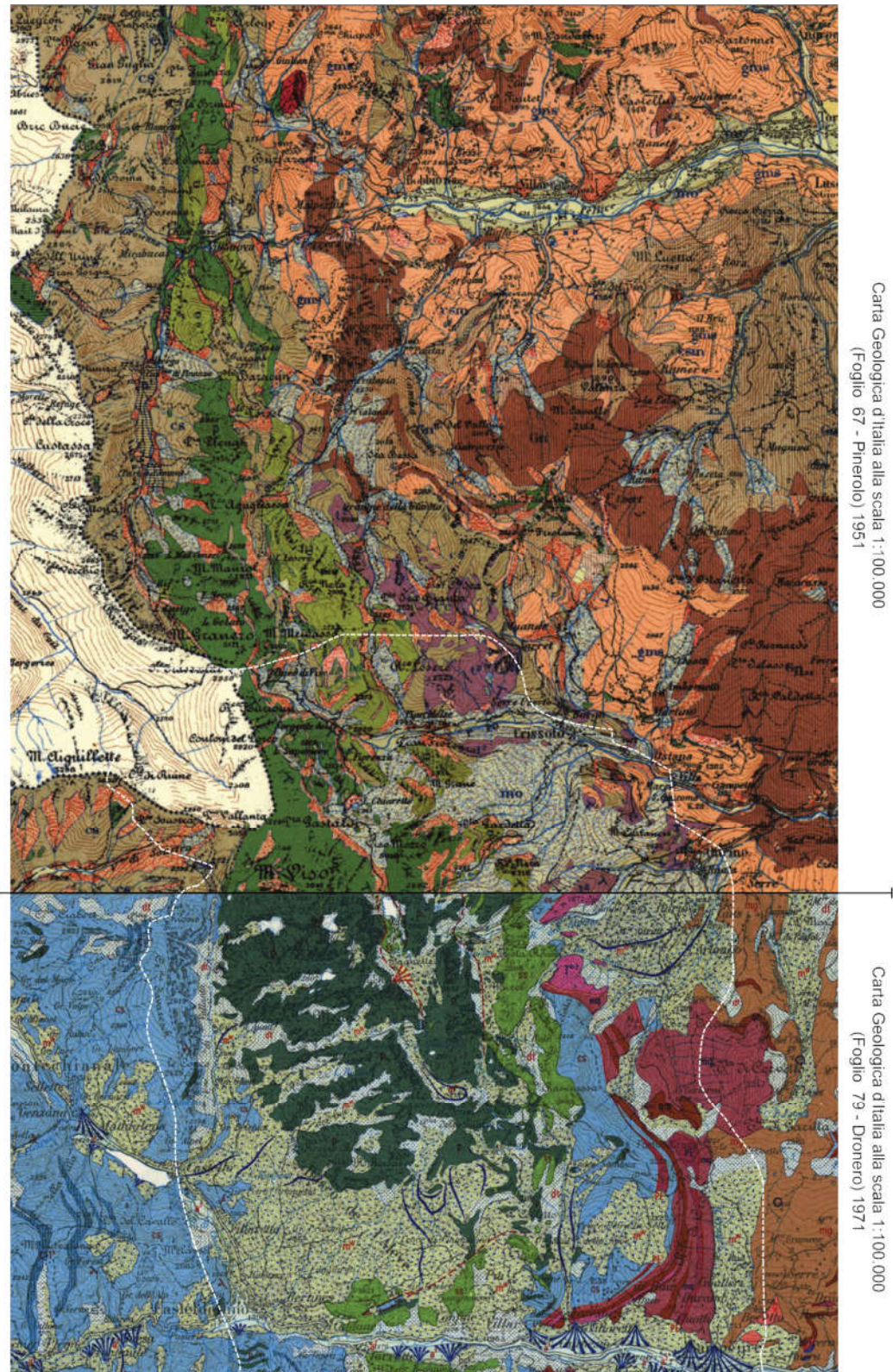


Figure 12

Figure 13

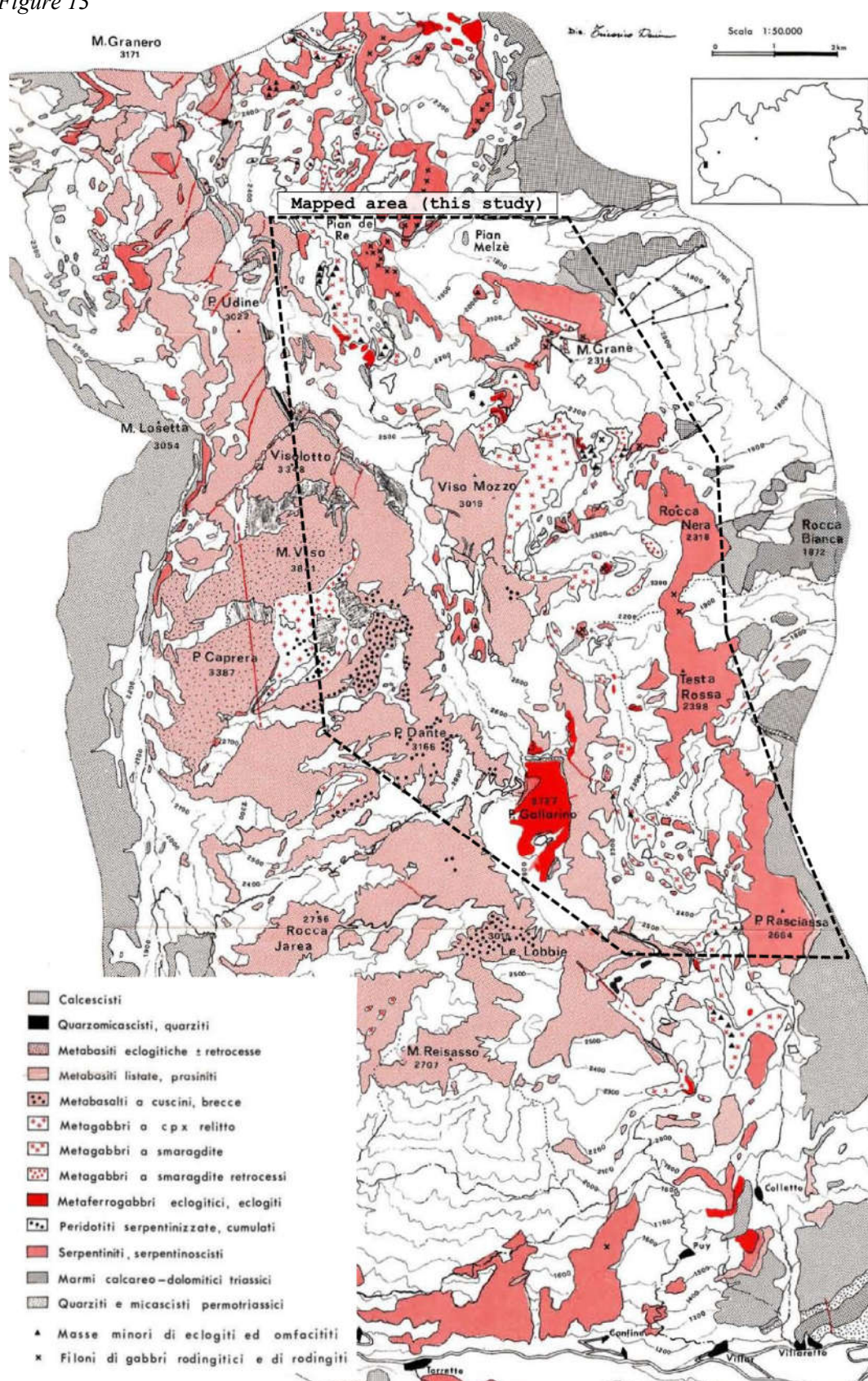


Figure 12: assemblage of the Foglio 67 (Pinerolo) and Foglio 79 (Dronero) from the official Geological Map of Italy at the scale 1:100.000, covering the area of Monviso metaophiolite complex. Note the absence, in the Monviso metaophiolite, of any differentiation between metagabbros, metabasite, metasediments, etc. The presence of the LSZ, ISZ and USZ is deduced only by the over-impression of quaternary covers.

Figure 13: Geological map of the Monviso ophiolite edited by Lombardo et al. (1978). Differently from the official Geological Map of Italy at the scale 1:100.000, the lithologies constituting the metaophiolite complex are differentiated. The major shear zones (LSZ, ISZ and USZ) are not recognized, being the entire complex still considered as a tectonic *mélange*.

After Lombardo (1978), several studies focused on the P-T characterization of the different units leading to variable estimates ranging from c. 450 °C/12 kbar to 620 °C/24 kbar (Blake et al., 1995 -in Coleman & Wang, 2005-; Messiga et al., 1999; Schwartz et al., 2000; Table 1). Based on both these petrological evidences and structural arguments, the Monviso metaophiolite complex was interpreted as a deep subduction *mélange* where tectonic slices detached from different depths accumulated in a weak, serpentinitized subduction channel along which they were exhumed to the surface (e.g., Schwartz et al., 2000; Guillot et al., 2004).

This theory was challenged by Angiboust et al. (2011 and 2012a) who suggested (on the basis of new petrographic evidences and PT estimates) that the Monviso ophiolite was rather formed by two main coherent tectono-metamorphic units, the first one being overturned on the second one:

- (I) the *Monviso Unit (or MU)*, peak PT conditions at ca. 480 °C/22 kbar (comprising the units of *Vallone di Vallanta* and *Costa Ticino* ref. Lombardo et al., 1978)
- (II) the *Lago Superiore Unit*, peak PT condition at ca. 550 °C/26 kbar (comprising the *Unit of Viso Mozzo*, the *Unit of the Smaragdite-bearing metagabbros of Lago Superiore* and the *Basal Serpentinites + eclogites of Colle Gianna and Verni* ref. Lombardo et al., 1978), crosscut by the *Intermediate* and *Lower shear zones* (respectively *ISZ* and *LSZ*).

The two tectono-metamorphic units come in contact along a ductile shear zone named “Upper Shear Zone” (or USZ) that corresponds to the *Serpentinities of Colle di Viso* and the *Complesso di Passo Gallarino* (ref. Lombardo et al., 1978). On this basis, the *Lago Superiore Unit (LSU)* was recognized as an almost preserved fragment of Tethyan oceanic lithosphere (Angiboust et Al., 2011 and 2012a), with the lithostratigraphical sequence only partly reworked during the subduction-burial-exhumation path; the major shear zones, in turn, developed at the metamorphic peak conditions (Angiboust et al., 2011).

As predicatable, this theory opened a huge debate in the geological community. In 2013 Balestro et al. published the geological maps of *Upper Pellice Valley* and *Monviso Massif* at the scale 1:25.000, followed by a series of publications (e.g., Balestro et al., 2013, 2014 and 2015; Festa et al., 2015) that analyse the occurrence of block-in-matrix structures both at the top of Dora Maira Massif and in the Basal Shear Zone (the latter named “Baracun shear zone”). Both the works of Balestro and Festa proposed (essentially from structural and microstructural evidence) the occurrence in the Monviso metaophiolite complex of a reworked OCC (Oceanic Core Complex). In this optic, the metaophiolite internal structure was revisited as a series of units juxtaposed across major shear zones not developed at high-pressure but resulting of the reactivation of pre-alpine structures (e.g. oceanic detachment and/or slab-inherited bending faults), rehabilitating the theory of Monviso metaophiolite as a tectonic-melange *s.s.* (Festa et al., 2010).

	Lago Superiore Unit (LSU)		Monviso Unit (MU)	
	Max P (Kbar)	Max T (°C)	Max P (Kbar)	Max T (°C)
Angiboust et Al. (2012)	26	550	22	480
Groppo & Castelli (2010)	25	550		
Schwartz et Al. (200)	19	580		
Messiga et Al. (2000)	26	650		
Blacke et Al. (1995) ¹	12 ÷ 19	400 ÷ 600	?	480 ÷ 530
Philippot (1987) ²	≥ 12	500 ÷ 550		
	Lago Superiore Unit (LSU) ³			
	Max P (Kbar)	Max T (°C)		
Balestro et Al. (2014)	2.5 ÷ 2.7	550 ÷ 570		
	Magmatic Zr	HP-veins Zr	Block-rind Zr ⁴	
	Ma	Ma	Ma	
Rubatto & Hermann (2003)	163 ± 2	45 ± 1		
Rubatto & Angiboust (2015)	~ 163	45-46	~ 46	

Table 1: (a) Compilation of the Pressure – Temperatures estimate for the Lago Superiore Unit (LSU) and the Monviso Unit (MU). (b) Ages of magmatic crystallization, peak-metamorphism and metasomatic-rind development from U/Pb analysis on zircons.

Notes: (1) The large range of temperatures and pressures obtained by Blake et Al. (1995) support the hypothesis of the Monviso metaophiolite as a mélange of different units exhumed from various depths in the subduction channel during the exhumation stage. (2) Philippot (1987) inferred the pressure-temperature condition leading to the crystallization of the HP veins (Omp+Grt) hosted in the Fe-Ti metagabbros emplaced near the Lago Superiore. Indication of PT condition were indirectly derived by the observation of Kienast (1983) and Lombardo et Al. (1978). (3) Balestro et Al. (2014) estimate the maximum pressure-temperature condition for the metagabbros emplaced in the Upper Pellice valley, in the northern portion of Monviso metaophiolite.

2.4 - The modern interpretation of the intra-slab shear zones within the Lago Superiore unit: the Lower and Intermediate shear zones (LSZ, ISZ)

Two main km-scale shear zones partially disrupt the LSU unit of the Monviso meta-ophiolite, both made of a serpentinite-rich matrix embedding several kinds of blocks. The LSZ separates the main Mg-Al metagabbro body (to the west) from the underlying massive serpentinite sole that crops out in the eastern cliff of the meta-ophiolite Monviso massif (Figure 12 and Figure 13). In the study area, the shear zone has an extension along strike of over 15 km from the south (Colle di Luca pass) to the north (Rocce Fons) with a variable thickness ranging from ~300 m at Colle di

Luca pass or Lago Superiore area to ~500 m at Pian Radice (refer to Geological Map chapter for more details). The LSZ matrix is made of strongly deformed mylonitic serpentinite with locally interbedded cm to dm-thick layers of strongly sheared antigorite schists (with subordinate talc and magnesite-rich levels). Serpentinite mainly consists of fine-grained, strongly-deformed antigorite (+/- magnetite, talc, magnesite and secondary olivine), whereas talc- and chlorite-schists contain lawsonite pseudomorphs, clinozoisite, light-green amphibole, rutile, apatite and rare quartz. Foliation inside the LSZ generally dips 20° to 40° to the W, and rotates to the W-SW in the area around Ghincia Pastour and Lago Superiore. The mylonites usually show internal chaotic geometries with dragged, disharmonic folds (particularly around blocks and slices) progressively turning into mylonitic shear bands near the shear zone boundaries. Blocks of eclogite-facies gabbros, eclogitic metasediments and massive serpentinite (the first type being the most abundant) are embedded in the antigorite schist serpentinite matrix of the LSZ.

The ISZ cuts across the topmost part of the gabbroic sequence and extends for over 4 km from the Lago Superiore area to the north flank of Viso Mozzo, where it connects to the LSZ and pinches-out under the cover of Quaternary glacier deposits. Its thickness varies between 1 and 10 m and contains much less serpentinite matrix than the LSZ. Fe-Ti metagabbros crop out along the ISZ directly at the top of Mg-Al metagabbros (notably in the Lago Superiore area; they underwent mylonitization during eclogite-facies deformation, leading to the formation of a characteristic planar fabric dominated by an omphacitic clinopyroxene, garnet and rutile assemblage (Philippot & Van Roermund, 1992). Eclogitic omphacite crack-seal veins, which occasionally crosscut these mylonitized gabbros, are believed to form by incremental opening associated with mylonitization (Philippot and Kienast, 1989).

Structural characteristics, petrography and distribution of the blocks inside the LSZ (and partly the ISZ) are described and discussed in the next chapters.

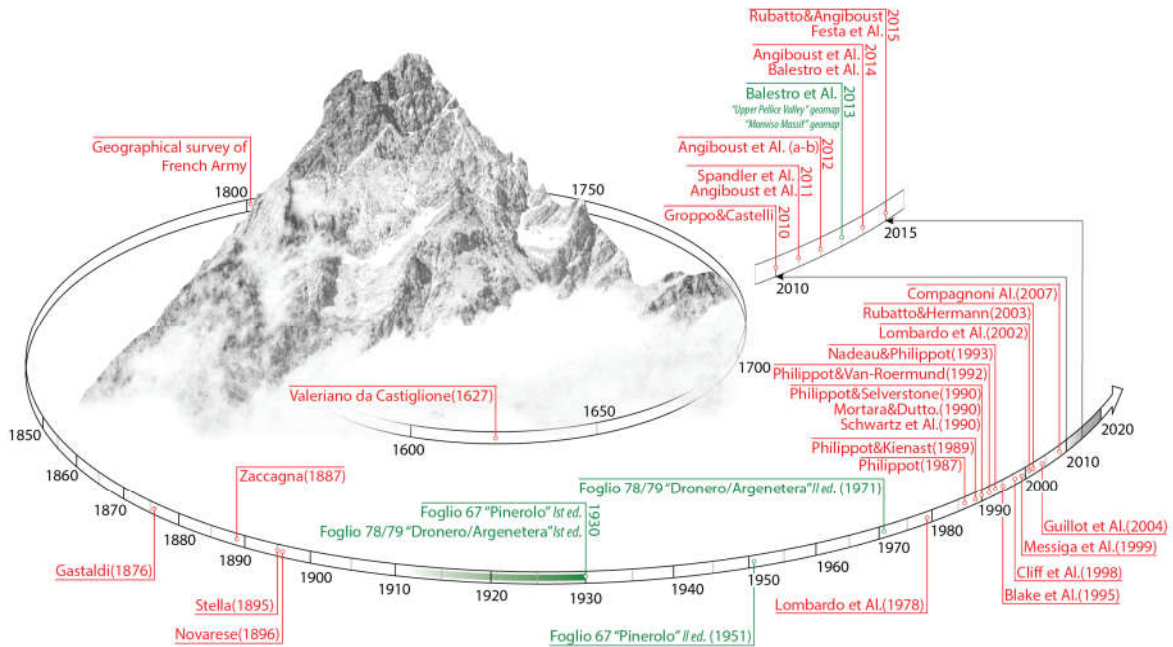


Figure 14: Timeline of the geological works developed in the Monviso area. The study of Valeriano di Castiglione (Abbot from Milan) was the first to evaluate the elevation of Monviso: 1664 meters above the Chiaretto Lake (~3925 meters above the sea level... an amazing result considering that the elevation of the "Re di Pietra" is actually 3841 meters a.s.l.!). The list could miss some papers, I apologize for that.

2.5 - Evidences for deep fluid circulation is subduction zone: the case-study of Monviso metaophiolite

In 1987, Philippot published the first paper about the omphacite/garnet-bearing HP veins crosscutting the Fe-Ti metagabbros near the Lago Superiore ("Unit of the Smaragdite-bearing metagabbros of Lago Superiore" sensu Lombardo et al., 1978). In this paper, he first documented the occurrence of repeated cycles of crack-seal veining at high-pressure conditions, symptomatic of transient switch between brittle and ductile deformation styles. The detailed characterization of these veins was accomplished in the paper by Philippot & Kienast (1989), who carefully dealt with the composition of omphacites in terms of major-elements and first proposed a possible external

source for the fluids circulating during the crystallization of later-stage HP veins. This external source, however, was later challenged in the paper by Philippot & Selverstone (1990): here, through the analysis of trace element-rich brines trapped in HP vein minerals, the hypothesis of "exotic" fluids entering the system was demonstrated to be unlikely in the eclogitic metagabbros from the Monviso. Indeed the evidences of mm- to cm-scale trace elements transfer by fluids does not support any large-scale fluid migration from different rock types (e.g. from serpentinite or metasediments dehydration), which was confirmed a few years later (1993) by Nadeau & Philippot (that first applied stable isotope analysis – $\delta^{18}\text{O}$ and $\delta^{13}\text{C}$ - on Monviso metaophiolite). The above listed evidences for fluid-induced transient switch between ductile and brittle regime were summarized by Philippot & Van Roermund (1992) in a comprehensive work on the mechanisms of deformation of omphacite at eclogite-facies condition. One of the major conclusions of this work was that the development of km-scale eclogitic shear zones (e.g. in the Lago superiore area) could be a suitable way to promote the delamination of oceanic crust from the subducting plate.

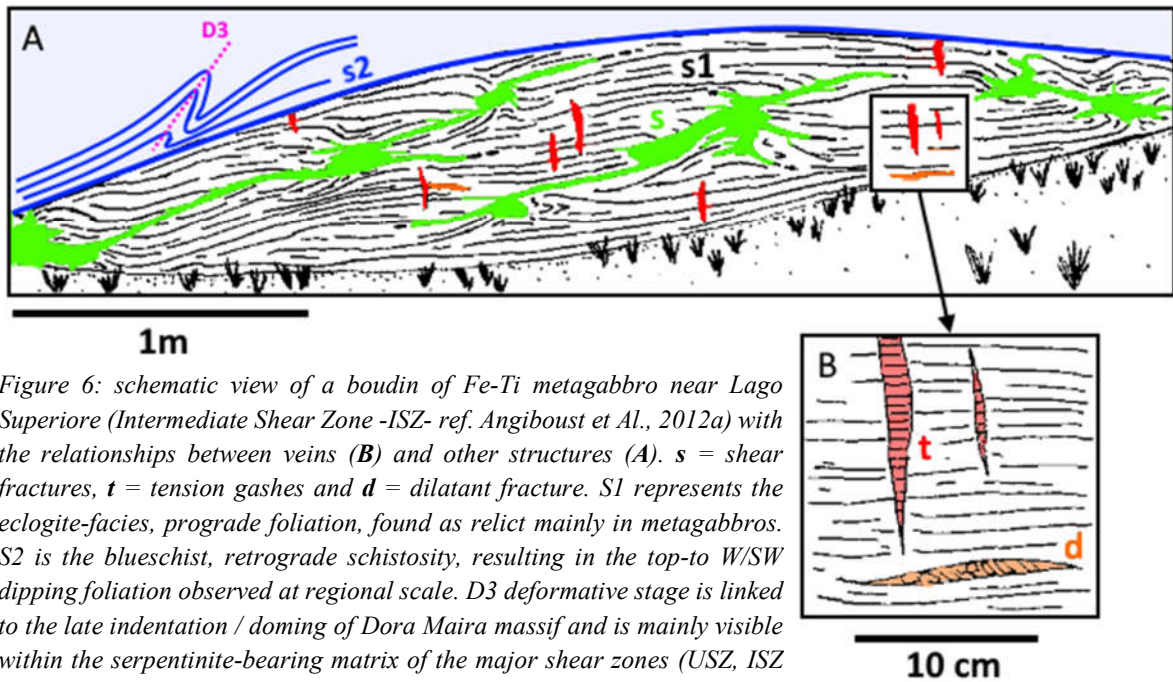


Figure 6: schematic view of a boudin of Fe-Ti metagabbro near Lago Superiore (Intermediate Shear Zone -ISZ- ref. Angiboust et Al., 2012a) with the relationships between veins (B) and other structures (A). *s* = shear fractures, *t* = tension gashes and *d* = dilatant fracture. S1 represents the eclogite-facies, prograde foliation, found as relict mainly in metagabbros. S2 is the blueschist, retrograde schistosity, resulting in the top-to W/SW dipping foliation observed at regional scale. D3 deformative stage is linked to the late indentation / doming of Dora Maira massif and is mainly visible within the serpentinite-bearing matrix of the major shear zones (USZ, ISZ and LSZ) crosscutting the Monviso metaophiolite complex. Figure modified after Philippot & Selverstone (1991).

From the study of the Mg-bearing chloritoid hosted in the metatroctolite from Lago Superiore area, Messiga et al. (1999) pointed out that pre-orogenic metasomatization of oceanic floor played a key-role in the hydration of oceanic crust. Furthermore, the development of OH-bearing minerals and carbonates (e.g., at the expenses of chloritoid) was interpreted as witness of local dehydration at about peak metamorphic conditions (estimated by the same authors at 2.45 GPa, $620\pm 20^{\circ}\text{C}$).

Thanks to the new in-situ trace element analytical technique (LA-ICP-MS apparatus), Spandler et al. (2011) gave new insights into fluid composition and potential sources at eclogitic PT conditions. Similarly to previous studies, they concluded that the first vein generations were formed under closed system conditions. However, late sectorial Cr- and Nb-enrichments in omphacite crystals from the last vein generation suggests the influx of limited amounts of serpentinite-derived fluids (*Figure 16*).

Further analytical improvements permit also to perform in situ geochronological analyses on zircons hosted by the mylonitic eclogites and HP veins from the Lago Superiore area. Rubatto & Hermann (2003) proposed an age of 163 ± 2 Ma for the primary crystallization of magmatic-inherited zircons in mylonites and an age of metamorphic recrystallization of 45 ± 1 My for those hosted in the HP veins. More recently, Rubatto & Angiboust (2015) refined the age of metamorphic recrystallization of zircons hosted in garnet from metasomatized blocks in LSZ around 45-46 Ma. In addition, they also showed evidence for circulation of fluids derived by serpentinites and metasediments during the development of LSZ at HP conditions, thus confirming that “exotic” fluid phases circulated in the subduction channel near peak-metamorphic conditions (as already proposed in Angiboust et al., 2014).

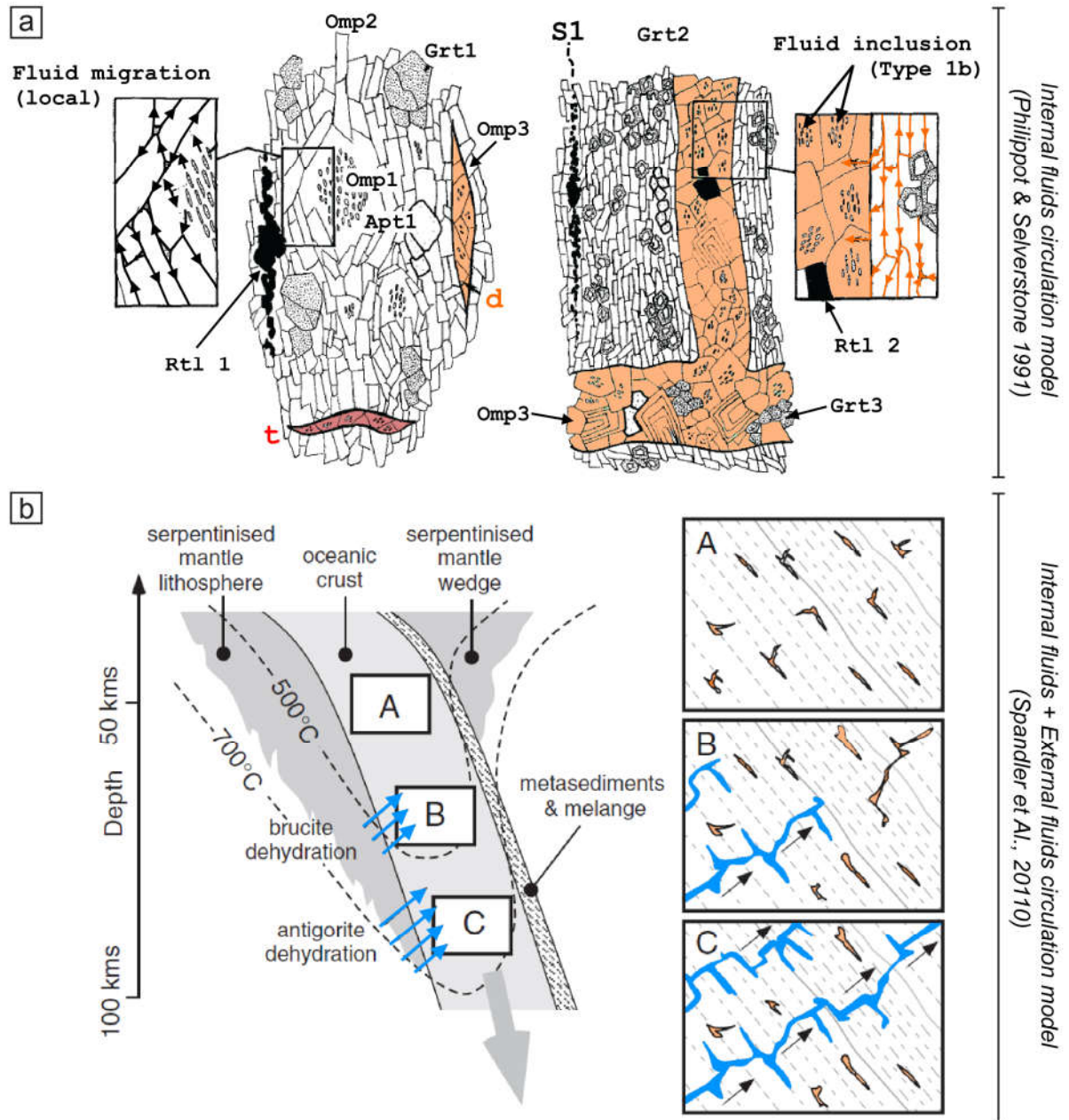


Figure 16: (a) detailed drawing depicting the expected "internal" fluids circulation predicted by Philipot & Selverstone (1991) for the Fe-Ti metagabbro from Lago Superiore area. Note that authors inferred cm- to m-scale elements transport by fluids from the study of fluid-inclusions in Omp, Grt and Apt. (b) Schematic draw from Spandler et Al. (2011) modeling the fluids circulation leading to the formation of the HP-veins in Fe-Ti metagabbro from Lago Superiore area (the same of Philipot & Selverstone). From in-situ trace element analysis (on Omp, Grt and Rtl) Spandler depicted a first stage of HP veining by in-situ fluid circulation followed by veining promoted by external fluids. The latter was likely released from antigorite breakdown. Figures modified from original papers; colors were added to be consistent with the tension gashes (red, "t") and dilatant fractures (orange, "d") presented in figure 11.

2.6 - The Monviso brecciated metagabbros: evidence for brittle rupture at eclogite-facies conditions?

In recent year, a series of blocks with peculiar clast-in-matrix structures were identified in the Lower Shear Zone (LSZ) along the southern part of Monviso metaophiolite. These breccias correspond to meter-sized blocks composed by 1 to 10 cm-long fragments of eclogite mylonite cemented by interstitial eclogite-facies matrix. The mylonitic fabrics of the clasts, together with the composition of the interclast matrix (composed by omphacite + garnet + lawsonite pseudomorphs) suggested the occurrence of a brittle event at eclogite-facies conditions (Angiboust et al., 2012a), potentially linked to intermediate-depth seismic events (Angiboust et al., 2012b). These findings were further supported by the occurrence, at the mineral scale, of omphacite crack-seal veins and garnet zoning patterns, likely an evidence for polyphased fracturing-healing events (Angiboust et al., 2012b). The later-stage embedding of breccia-blocks in the serpentinite-rich LSZ likely happened just after the peak metamorphic conditions reached by the LSU (ca. 550 °C/26 kbar; Angiboust et al., 2012a; Angiboust et al., 2014).

Nevertheless, this finding was challenged by other authors: Festa et al. (2015) and Balestro et al. (2015) recognized, in the northern part of Monvio metaophiolite (in the “Baracun Shear Zone”), structures and mineral phases interpreted to be the remnant of a core complex formed in an embryonic ocean (i.e., the Ligurian-Piedmont Ocean) as the products of rift-drift processes. By the occurrence of heterogeneous lithostratigraphy subsequently overprinted by subduction zone tectonics and leading to the complex structural architecture, these authors identified the breccia blocks disseminated in the “Baracun Shear Zone” (corresponding to the LSZ of Angiboust et al.,

2012a) as either inherited pre-Alpine detachment fault rocks or sedimentary-derived breccias (Balestro et al., 2013 and Festa et al., 2015).

The contrast between these two interpretations for metagabbro breccia block origin (and their significance at the regional scale, e.g. their link with respect to the evolution of the LSZ) is therefore the “holy grail” from which this PhD thesis originated.

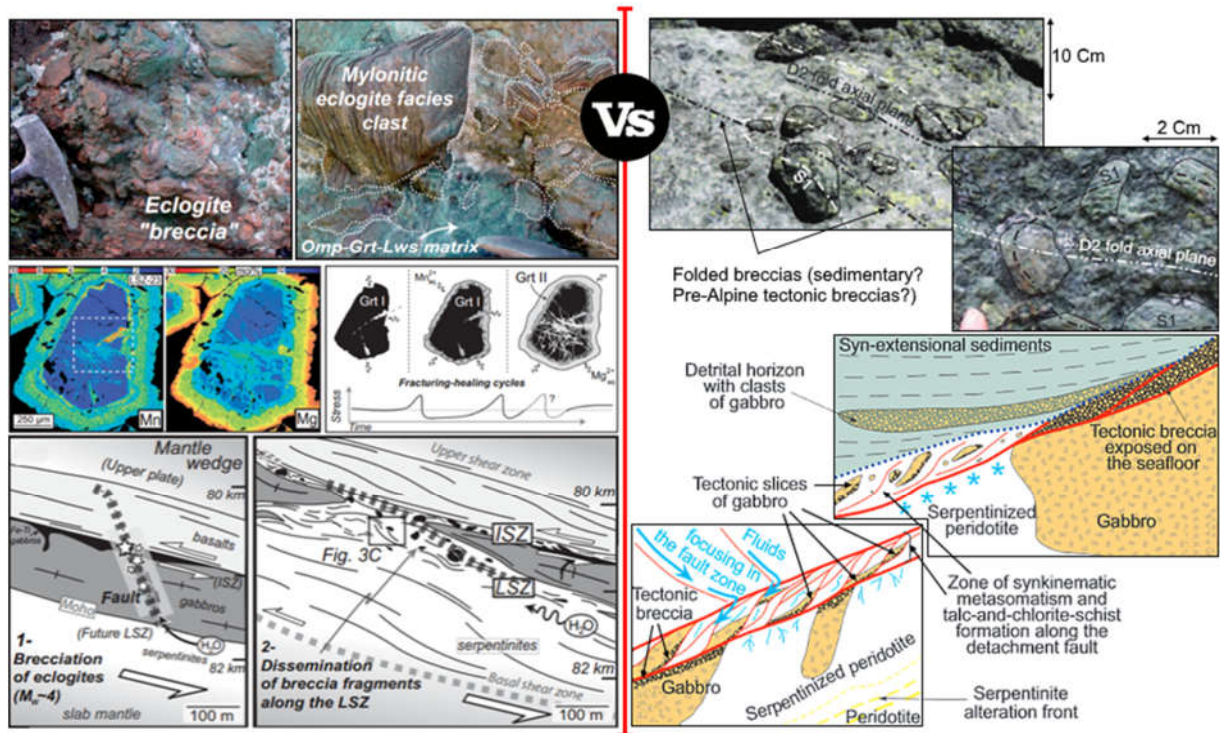


Figure 17: (a) summary of the main evidences used by Angiboust et al. (2012a-b) to ascribe Monviso metabreccias to brittle rupture at eclogite-facies conditions. The clast-in-matrix structures of the breccia, with mylonitic clast cemented by Omp+Grt±Lws matrix, and the occurrence of early-stage fractured garnets sealed by a newly-formed Mg-rich generation were interpreted to be developed by dynamic, co-seismic brittle deformation at eclogite facies conditions. Thus the dissemination of breccia blocks was ascribed to post-peak deformation in the newly-formed LSZ. (b) Nevertheless, in breccia-blocks from the Upper Pellice valley, Balestro et al. (2013) and Festa et al. (2014) found the evidences of mylonitization and polyphasic deformation of the matrix cementing clasts. By occurrence of polymictic breccia, deformed detrital matrices and field evidences, the authors ascribed the metabreccias of Monviso to pre-subduction stage, potentially to (i) brecciation in OCC detachment faults or to (ii) Pre-Alpine syn-extensional sedimentation processes. More details in the text and Chapter 4.

2.7 - Aims of the thesis

Despite the numerous and detailed studies developed on the Monviso metaophiolite, many questions still remain open to investigation and further discussion. The aims of this PhD thesis are (I) to characterize the metabreccia blocks occurring in the shear zones of Monviso metaophiolite (particularly in the LSZ and subordinately in the ISZ and USZ) and investigate the significance of their distribution, (II) to understand the processes leading to episodes of brittle deformation at peak metamorphic conditions and their link with fluid liberation / circulation at depth in subduction zones and (III) to investigate the potential links between eclogite-facies brecciation and Intermediate Depth Seismicity.

In detail, the main “steps” leading the course of the thesis were:

- 1.** To map the occurrence (representativeness) and distribution (chaotic or ordered?) of brecciated eclogite-facies bodies inside the Monviso metaophiolite complex.
- 2.** To analyze the structures recorded in the breccia planes at the macro- to micro-scale, with detailed focus on (i) the morphology and organization of breccia planes, (ii) clast and matrix composition. Additionally, the potential similarities with respect to analogue structures developed in shallow-crustal (<20 km-depth) by seismic activity were investigated.
- 3.** To constrain the P-T conditions of brecciation (thanks to clast and matrix mineral composition) to prove that these breccias are a reliable example of brittle-rupture occurring at eclogite-facies condition.

4. To describe the succession of the reactions/events taking place in the metagabbros (mineral appearance and/or destabilization, fluid production/ingress) during the transition from ductile to brittle deformation and provide a relative chronology of the events leading to brecciation (pure mechanical brecciation or hydraulic fracturing?)
5. To define the origin of the fluids circulating at the time of brecciation -as attested by the presence of veins and different types of matrix- discriminating between internally derived (i.e. local dehydration) or externally derived (i.e. fluid infiltration) sources.
6. To identify the rheological parameters that lead to brecciation preferential localization in Fe-Ti metagabbro levels, i.e. the potential role of rheological contrasts and evolving rheology through time (vein formation, matrix crystallization, ...), fluid presence...
7. To understand the influence of breccia-plane formation in the dissemination of metagabbro blocks inside the LSZ and ISZ (and, consequently, understand the consequences on the post-metamorphic peak evolution of the shear zones)
8. To investigate if structural and microstructural evidences could demonstrate/infirm the co-seismic origin of Monviso metaophiolite eclogitic breccia.
9. To evaluate if the evidence for fluid-release/fluid-rock-interactions on Monviso natural rocks may provide new constraints to the thermo-mechanical models for subduction dynamics and Intermediate Depth Seismicity.

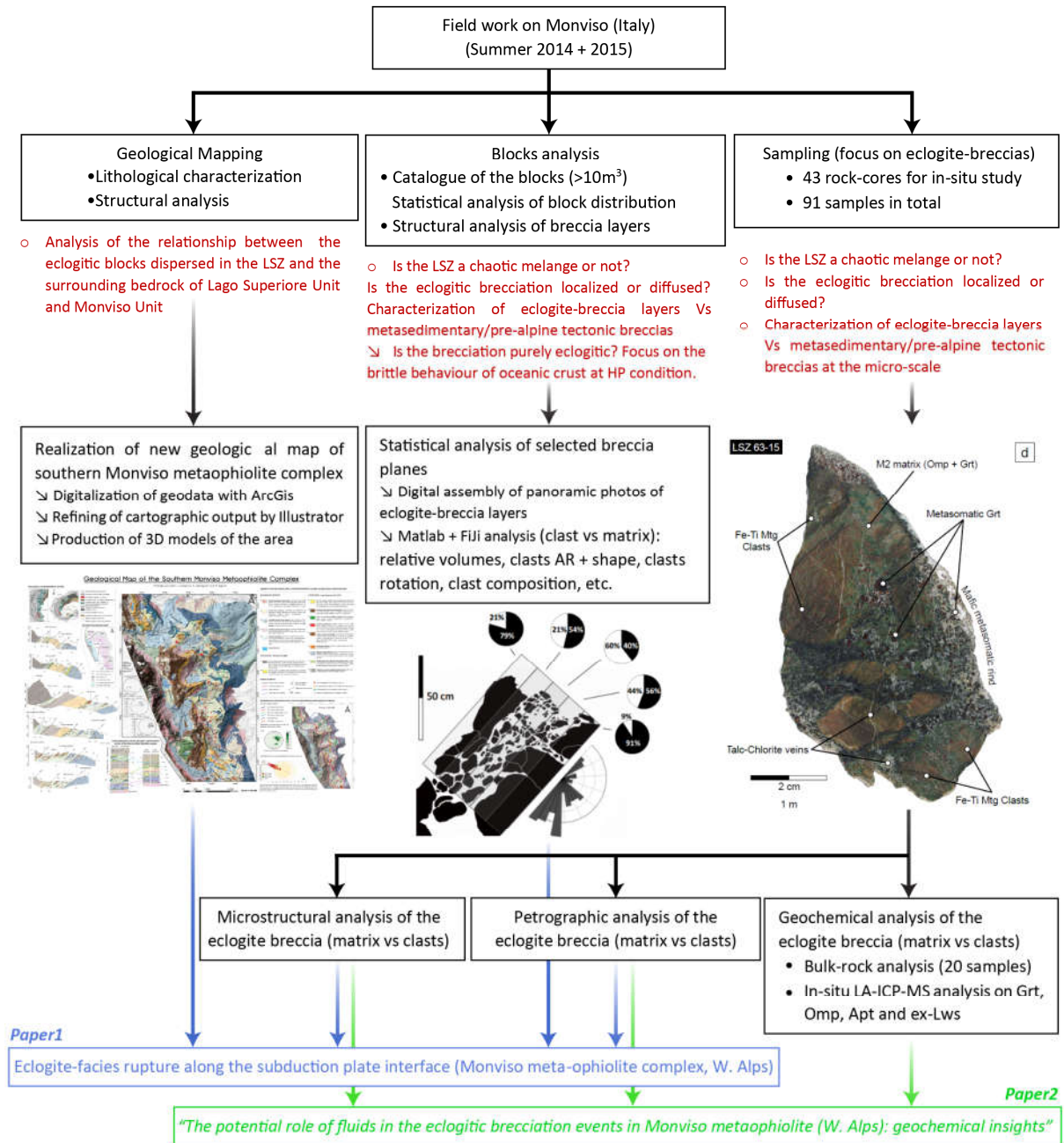



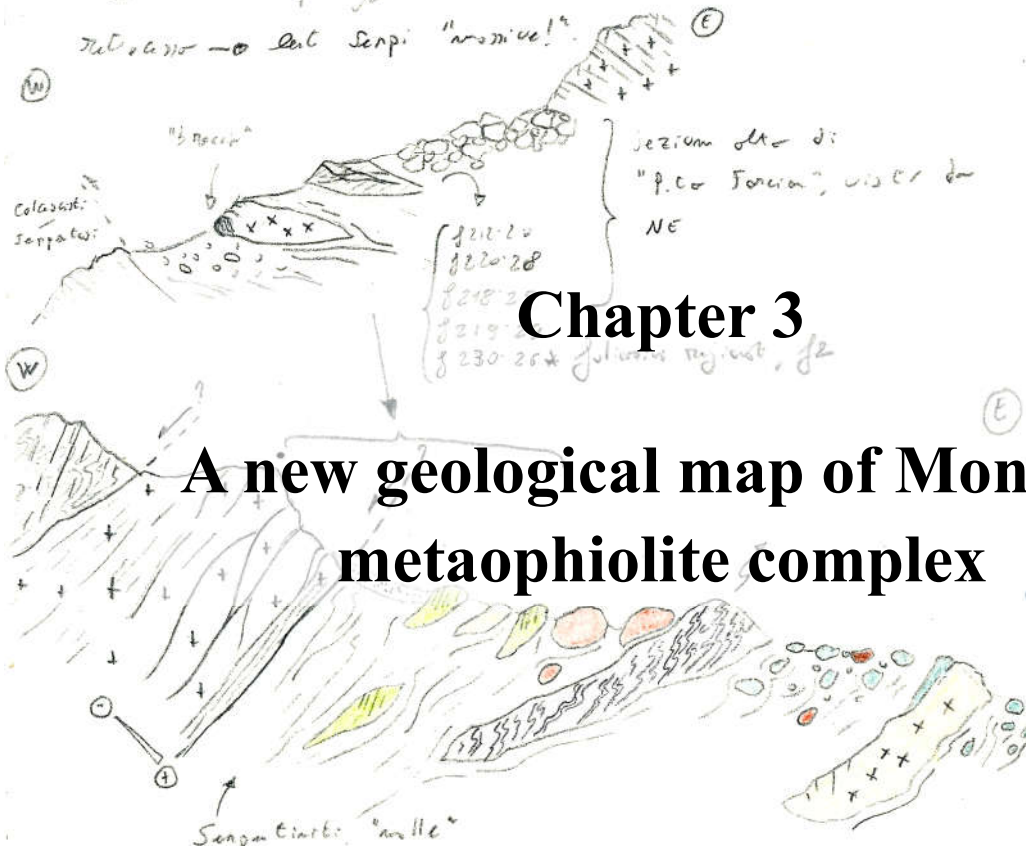
Figure 18: simplified master-plan of the present thesis, with the workflow followed. The approach was field-work based, with a rigorous characterization of the eclogitic blocks dispersed in the LSZ, ISZ and USZ. The study of the eclogite breccia spans the statistical analysis of block distribution in the LSZ, the (micro-) structural characterization of breccia layers, the petrographic characterization of the clasts Vs matrices and the geochemical analysis on bulk-rock and in-situ trace elements in minerals. The latter, run by LA-ICP-MS, was possible thanks to the collaboration with Thomas Pettke (Bern Universität, Switzerland).

$$9. [VI - 14 + 29 - 7 + 1] 6 \text{ ps.}$$

$L_1 \in \text{padr. Munk.}$ 2 entropije existant e shqyhet (7)

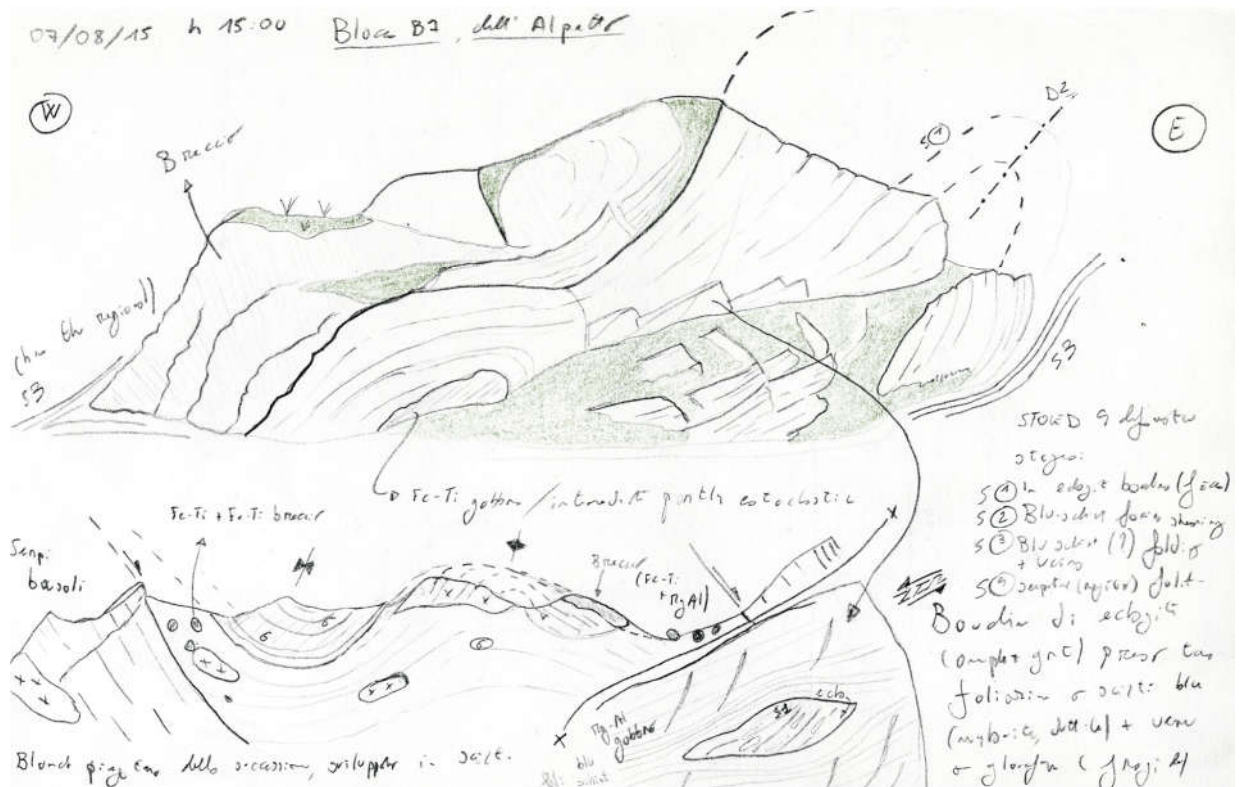
Abbiamo un po' di serpi bravi → luti mal

Redondo - Ent Serpi "nomine!"  (E)



Chapter 3

A new geological map of Monviso metaophiolite complex



The presented geological map is at 1:20.000 scale and covers an area of ~35 km². It results from original fieldwork at 1:10.000 scale using the topographic base of the CTR maps (Carta Tecnica Regionale) provided by the geographical database (<http://www.geoportale.piemonte.it/cms/>) of the Regione Piemonte. Field data were digitalized using the software ESRI ArcGis® (Coordinate System WGS 1984, UTM Zone 32N) and projected (using Adobe illustrator) on a digital topographic base derived by the DTM of Regione Piemonte. The new lithological, structural and geomorphological data were compared and locally integrated with those from the works of Lombardo et al. (1978), Angiboust et al. (2012) and Balestro et al. (2013). The structural data were analysed with the software OpenStereo (Schmidt net, lower-area projection). The quaternary geology has been mapped during field seasons 2014 and 2015; geomorphological analysis and interpretation were later implemented by aerial image analysis (Google-Earth Pro, Bing-Maps and Ortophoto of Regione Piemonte). The tectonostratigraphic units were defined following the work of Angiboust et al., (2012) as Lago Superiore Unit -LSU- and Monviso Unit -MU-. Applying the definition of tectonostratigraphic units after De La Pierre et al., (1997) we additionally introduced three subdomains to the LSU: the (I) *Basal Serpentinite* subdomain, the (II) *Lower Shear Zone* subdomain and the (III) *Lago Superiore s.s* subdomain (including the Intermediate -ISZ- and Upper? -USZ- Shear Zones¹).

¹ The LSZ, ISZ and USZ show similar antigorite-rich matrix, with comparable D1 and D2 structures. Is anyhow worth of mention the different block-in-matrix structure, with the ISZ and USZ showing substantial absence of Eclogite-Breccia -Eg- blocks (even-if recorded as dm-thick layers on the footwall of the shear-zones) or Fe-Ti metagabbro -Fg- blocks. In addition the thickness of LSZ is on average three-times bigger than the ISZ and USZ, with well-developed D3 structures. Please refer to the text for more details.

The two units of the Monviso metaophiolite show a similar tectono-metamorphic history (Lombardo et Al., 1978; Angiboust et al., 2011) and recorded four main tectono-metamorphic events:

I. The **Pre-Alpine**, oceanic-stage event, leading to the primary lithostratigraphical structuration of the ophiolite.

Three successive Alpine stages, describing the (II) *peak* to (III) *exhumation* to (IV) *continental collision* events:

- II. Peak-metamorphism **Eclogitic** event, leading to the formation of **S1**. Peak mineral-assemblage in Fe-Ti-oxydes metagabbros is characterized by *omphacite*, *almandine-rich garnet*, *Fe-poor epidote* and *rutile*, with minor *talca*, phengite and locally glaucophane.
- III. Exhumation-stage **Blueschist** event, characterized by the regional development of the W/WSW-dipping **S2** foliation underlined by *blue-amphiboles* (glaucophane and crossite)
- IV. Continental-collision event, recorded by **D3** greenschist-facies structures such as the W-verging drag-folds and SC-structures. Typical is the irregular development of albite, chlorite, Fe-rich epidotes and tremolite/actinolite in Fe-Ti-oxydes metagabbros.

3.1 Tectonostratigraphy

3.1.1 The Lago Superiore Tectonostratigraphic Unit

- The Basal Serpentine subdomain (BSU)

The *basal serpentinite unit* crops out continuously in the studied area from the *Colle della Gianna* (where it is up to 1000-m thick) to the Punta Rasciassa area (where its thickness decreases to 500-m), and corresponds to the lowest unit of the Monviso Metaophiolite complex.

It is composed of **medium-grained serpentinites -Bs-** mainly made up of antigorite and with pervasive foliation underlined by magnetite beds (*Figure 19a*). The peridotite pre-alpine mineral assemblage is preserved as relics of pyroxenes only in the poorly deformed areas (Lombardo et al., 1978; Balestro et al., 2013).

Variable size (dm- to m-thick) rodingitic-metagabbro dykes are continuously observed aligned along the foliation from the Lago Fiorenza to the Costiera dell' Alpetto cliff (*Figure 19b*). Constant symmetric shape and high aspect-ratio don't permit to appreciate any shear-sense indicator. Other Authors indicate also the presence of rare omphacitite and jadeitite (Compagnoni et al., 2012).

Meter- to hectometer-size boudins composed of **Mg-Al** and **Fe-Ti metagabbros** (the latter much less abundant; **-Mg-** and **-Fe-** respectively) are discontinuously scattered in the basal serpentinites (e.g. east of Lago Fiorenza or east of Gruppo dell' Alpetto cliff, *Figure 19c*). Mg-Al metagabbros are mainly composed of albite, clinozoisite and actinolite (as result of static retrogression under greenschist facies conditions) with minor eclogite-facies 'smaragdite'-bearing boudins. The eclogite-facies Fe-Ti metagabbros are discontinuously associated to the Mg-Al metagabbros. These were found as decimetre-sized boudins outcropping east of Costiera dell' Alpetto Cliff. Their texture progressively varies from cm-sized "pegmatitic-like" cores composed of deep-green clinopyroxene and garnet (ideally replacing the pre-existing igneous assemblage) to mylonitic

bands composed of apple-green omphacite, garnet and rare Na-amphibole-rich bands with abundant rutile underlying the foliation. Meter-sized blocks with same fabrics and mineralogy crop out at the base of the LSZ (see later for more details). Other authors (Lombardo et al., 1978 and Balestro et al., 2015) recognized similar Fe-Ti metagabbros at the base of the basal serpentinite near Colle della Gianna and Punta Sea Bianca.

The contact between the *Monviso metaophiolite* and the underlying *Dora-Maira* consists in a variable-thick sequence of *metasedimentary slivers* pinched-out between the two units (*Figure 19c*). These slivers are composed of marbles and calcschists (e.g. Rocca Bianca - supposed ages span from Middle Triassic to Early Jurassic) with at the base quartzites and micaschists of Permian age (e.g. the “Sampeyre Ensemble” of Vialon, 1966).

Other Authors (Balestro et Al., 2013 and 2015) report the occurrence of an overtuned metasedimentary sequence between Rocca Nera and Punta Rasciassa (corresponding to the “*Roccenie Complex*” by Mondino et Al., 2004) stratigraphically laying between the Monviso metaophiolite complex and the Dora Maira unit. It is described as a calchshist composed by variable amounts of calcite, white mica and quartz and hosting dm- to m-sized levels and bodies of metabasite. Balestro et Al. (2013) suggest that these overtuned calchshist would correspond to the sedimentary-cover originally deposited on the denudated mantle peridotite rocks of Tethyan Ocean.

- *The Lower Shear Zone subdomain (LSZ)*

The LSZ mark the boundary between the basal serpentinites and the Lago Superiore Unit. Its thickness strongly varies along the shear zone, from a minimum of ~250 m in the Punta Forcion area (*Figure 19d*) and a maximum of 600 m in the Pian Radice area. A bit further to the north, out of the main area of study, the LSZ reaches a maximum thickness of ~800 m.

Its internal structure corresponds to a *tectonic melange* (*sensu* Festa et Al., 2010, *Figure 20a*), where a pervasively foliated antigorite schists matrix (intercalated with cm-thick magnesite-rich layers) encloses blocks of variable size (decimetre to decametre) composed of (I) *retrogressed Mg-Al metagabbro -Rg-*, (II) *eclogitic Fe-Ti metagabbro -Fg-*, (III) *eclogitic Breccia -Eb-*, (IV) *metaperidotite -Mp-*, (V) *metasediment -Ms-*, (V) *rodingitic metagabbro dykes -Rd-* (VI) and rare jadeitite.

The *retrogressed Mg-Al metagabbros -Rg-* consist of five main lenticular sheets (up to 50-m thick) outcropping at *M.te Ghincia Pastour*, *M.te Granè*, east of *P.ta Forcion* and *Lago Bulé* areas respectively. They are generally NNE-SSW striking north of Prà Fiorito Valley, and NNW-SSE striking in the Lago Bulé area. These bodies have medium-to-fine grained mylonitic fabrics with clinozoisite-rich and omphacite-rich beds defining a pervasive foliation (*Figure 20b*). Glaucophane-rich levels statically recrystallize along the eclogitic foliation plane (*Figure 20c*), with pervasive retrogression at greenschist facies leading to albite and actinolite recrystallization. A large number of boudins with Fe-Ti metagabbro composition are embedded in the foliation (*Figure 20d*). A first generation of veins (up-to 5 cm thick) filled by fibrous glaucophane (*Figure 20e*) postdated by (I) epidote + actinolite + albite and (II) quartz-bearing veins (*Figure 20f*) crosscut at various angle the entire blocks. It is worth mentioning that HP, omphacite- and garnet-bearing veins are developed only in the Fe-Ti metagabbros boudins, with peculiar “tapering-like” geometry at the transition with Mg-Al metagabbros (*Figure 21a*). Other smaller (decametre to meter scale) Mg-Al metagabbro blocks show the same fabrics but some of them contain levels composed by metabreccia (*Eclogite-Breccia -Eg-*) unconformably crosscutting the eclogite-facies foliation of the blocks (Type2 blocks, see chapter for more details).

The ***Fe-Ti metagabbros -Fg-*** (Type3 blocks, hereafter) represent the 16% of mapped blocks (Min Vol. 1.56 m³, Max Vol. 6.00 m³, *Figure 21b*). They show fabrics ranging from finely-foliated to massive; coarse grained “pegmatite-like” fabrics are preserved in the core of the largest blocks (> 10 m³, e.g., *Pian Radice area*) and consist in almost undeformed coronitic garnet (< 6 mm) crystallizing around megacrystals of omphacite (< 8 mm), which were interpreted as pseudomorphs after magmatic pyroxene or plagioclase (Lombardo et al., 1978; Pognante & Kienast, 1987; Philippot & van Roermund., 1992; Groppo & Castelli, 2010; Angiboust et al., 2011). Block rinds show a progressive increase in deformation, with finely-foliated mm-thick bands of omphacite and garnet underlined by rutiles beds.

The ***eclogite-breccia -Eb-*** (*Figure 21c-d*) occurs either as layers locally crosscutting the HP foliation of Mg-Al metagabbros blocks or as single blocks (Type1 blocks, hereafter). It shows peculiar clast-in-matrix structure consisting almost exclusively of mylonitic Fe-Ti metagabbros with rare Mg-Al gabbros (10% of modal amount) clasts cemented by an omphacite-rich matrix (+/- garnet and lawsonite). Matrix proportions vary, from block to block, from less than 10 vol% to up to more than 50 vol%. Dimension and extent of rotation of the clasts are also variable (*Figure 21e*). For more details on eclogite-breccia, please refer to chapter 4.

The ***metaperidotites -Mp-*** consist either in minor dm- to m-sized levels interlayered with the *retrogressed Mg-Al metagabbros* (e.g., NE of Lago Bulè), and bigger dam-sized slivers embedded in the antigorite-schists matrix of the LSZ (e.g. E of Rocce Sbiasere and Punta Murel). They are almost completely serpentized: the bulk of the rock is actually made-up almost exclusively of antigorite and minor magnetite. Their fabric varies from massive to foliated, with magnetite describing pervasive foliation in the more deformed bodies. The original mineral assemblage of the peridotite is locally preserved in less deformed portions and consists of relics of pyroxenes.

Veins of fibrous serpentinite-minerals are locally associated to calcite-bearing serpentinites (*Figure 21f*).

The **metasediments -ms-** are discontinuously scattered in the LSZ lacking a well-defined stratigraphical position. Locally they lay either at the contact with the metaperidotite blocks (e.g., E of Lago Fiorenza and W of Lago dell'Alpetto) or at the base of the Mg-Al metagabbro cliff of the Lago Superiore Unit (e.g., E of Truc Bianco) or as isolated sliver in the antigorite schist of the LSZ (e.g., Prà Fiorito valley) or associated to the retrogressed Mg-Al metagabbro (e.g., Ghincia Pastour). They mainly consist of calcschists (locally lawsonite-bearing) intercalated with levels of micaceous marbles, phengite- and garnet-bearing metacherts and minor talcschist levels (*Figure 22a-e*). Metabasite-rich layers (in places with conglomeratic texture, highly deformed) are locally found (e.g., Prà Fiorito valley and Alpetto). Here, the occurrence of metabasalt, metagabbro and metaperidotite clasts suggest a detrital input from an ophiolite-derived source.

Dm-thick **rodingitic-metagabbro dykes -Rd-** are discontinuously scattered in the LSZ matrix, usually associated to massive **metaperidotite -mp-** blocks. Strong metasomatism is observed at the expenses of the dykes, leading to talc and chlorite recrystallization at their rims (*Figure 23*).

Jadeitite is rarely found as dm-thick layers at the contact between metaperidotite -mp- and the retrogressed Mg-Al metagabbros -Rg-, especially NE of the Lago Bulé. Compagnoni et al. (2012) suggest that the jadeitite found in the Monviso metaophiolite derives from former felsic dykes originally intruded into upper mantle peridotite, which experienced a significant metasomatism during the serpentinization of the peridotite.

- The Lago Superiore S.S. subdomain (LSU)

The Lago Superiore Unit is made up of metabasites (locally with preserved basalt textures), Mg-Al metagabbros and metasediments, with minor Fe-Ti metagabbros. It has a non-cylindrical shape, with a maximum thickness of ~ 1200-m along the section across the Viso Mozzo and thinning southward and northward. It is bounded at the top by the Upper Shear Zone (USZ) defined by the occurrence of chlorite- and talc-bearing antigorite schists.

The eclogitic ***Fe-Ti metagabbros -Fg-*** of the Lago Superiore Unit consist in dm- to m-sized masses found at the top both of the Mg-Al metagabbros (e.g., NW of Lago Chiaretto) and metabasites (e.g. W of Rocche Sbiasere). The texture vary from dm-sized coarse “low-strain” domains (composed of deep-green clinopyroxene + garnet ± lawsonite-pseudomorphs) to progressively more deformed, m-thick mylonitic bands composed of omphacite, garnet and rare ex-lawsonite rich bands with abundant rutile aligned along the pervasive foliation. Locally, especially in the area of Lago Superiore, eclogites-facies breccia blocks-***Eb-*** crop out in the LSZ.

The ***foliated metabasites -Mb-*** show a medium-to-fine grained banded texture consisting in alternate, cm-thick, albite- and epidote-rich levels; Na-amphibole and actinolite-rich levels are frequently intercalated (*Figure 23b*). Boudins of eclogitic metabasites (*Figure 24c*), with relict omphacite and clinozoisite crystals, are locally observed (e.g., SW of Lago Gallarino) wrapped in the pervasive glaucophane-rich foliation. Yellowish/pistache-colored epidote-rich levels are diffused. Brecciated and pillowed textures (the latter dm-sized) are locally preserved (e.g. SE of Rifugio Quintino Sella or S-flank of Viso Mozzo).

The **Mg-Al metagabbros -Mg-** correspond to the “smaragdite-bearing metagabbros” of the literature of Monviso metaophiolite complex (e.g., Lombardo et al. 1978). They crop out at the base of the metabasites between the NE flank of the Viso Mozzo to the Colle di Luca. These

medium-to-fine grained mylonitic metagabbros are mainly composed of alternate clinozoisite-rich and omphacite-rich bands with subordinate glaucophane. Garnet is present only in the vicinity of Fe-Ti metagabbro boudins (*Figure 21a*). The greenschist retrogression, pervasive at the contact with the LSZ, lead to the massive crystallization of albite, epidote and tremolite / actinolite (*Figure 23d*). Layered to massive metatroctolites crop out as m-thick boudins in the cliff W of Lago Fiorenza, intercalated to finely crenulated, decimeter- to meter-thick metaperidotites (*Figure 23e*).

The **metasediments -Ms-** mainly crop out at the top of the Lago Superiore as dam- to m-thick slivers stratigraphically at the top of the metabasites. Minor m-thick bodies crop out discontinuously E of Passo Gallarino between the metabasites and the Fe-Ti metagabbros.

From the Lago Grande di Viso to Colle Di Luca they mainly consist of mylonitic calcschists interlayered to minor micaceous-rich levels. To the W of Lago Chiaretto, the metasedimentary sliver exceeds thickness of 20m - interlayered to the metabasites - and consist of calcschists with interbedded levels of micaceous marbles and quartz/phengite-rich garnet-bearing micaschists (*Figure 23f*).

3.1.2 The Monviso Tectonostratigraphic Unit

The Monviso Unit reaches a maximum thickness of ~900-m across the E flank of Monviso and is bounded to the W by the overlying Queyras Schistes Lustres (the latter not directly studied during the mapping). It is an overturned sequence of metagabbros and basalt-deriving metabasites (Lombardo et al., 1978; Balestro et al., 2013), with minor metasediments discontinuously outcropping W of Lago Grande di Viso and W of Passo Gallarino. The metabasites are mainly composed by aphyric and porphyritic metabasalts; additionally, brecciated and pillowed metabasalts outcrops in the area between Punta Barracco, Punta Michelis and Laghi delle Forciolline (Lombardo et Al., 1978; Balestro et Al., 2013). The metasediments consist of m-sized

levels of phengite- and garnet-bearing metacherts (e.g., at the base of the cliff W of Lago Pellegrina) overlaying calcshist interbedded to quartz/phengite-rich garnet-bearing micaschists. The metabasites of the MU show a well-developed metamorphic layering with cm-thick yellowish/pistache colored epidote-rich levels alternate to dark-green Na-amphibole and tremolite/actinolite-rich layers.

3.1.3 Geomorphology and Quaternary Geology

Glacial processes deeply affected the morphology of the Monviso metaophiolite massif. The N-S valleys (located in correspondence to the incoherent antigorite-rich matrix of LSZ, ISZ and USZ) are evidently carved by glacial erosion (Figure 24a). Sheepback morphologies are recorded on the smoothed outcrops of Basal serpentinites -Bs- located E of the Alpetto Lake (Figure 24b). The rock-wall E of Costiera dell'Alpetto (nice glacial striations are here preserved, Figure 19b) appear to be the product of enhanced rock-plucking. *Lateral* and *end* moraine, some of them up-to 50–70 meters-high and 1.5 km-long, are mainly located on the E-side of the Monviso massif and partly cover also the underlying Doira Maira massif (e.g. E of Rocca Nera, P.ta Gardetta and Monte Grané). The related tills deposits are made up of chaotic and unsorted angular blocks with sandy-silty matrix and subordinate diamicton. Characteristically abundant lichens cover the blocks. The above listed structures are linked to the Last Glacial Maximum (or *LIA*) of Upper Pleistocene (Lombardo et Al., 1978; Balestro et al., 2013).

At the E/NE of Cadreghe di Viso, on the Costa Piatta Gelata, a well-developed end-moraine system occurs (Figure 24a) with blocks characterized by only incipient lichen cover. This till deposits (related to the Little Ice Age, or *LIA*) are made up of diamicton with abundant silty-sandy. A thin layer of supraglacial debris made up of unsorted angular blocks and rock fragments cover the till, with at the top abundant rock-fall deposits (Figure 25a).

Several **rock glaciers -Rg-** have been mapped, mainly located on the NE flank of Monviso metaophiolite, with a covered area of ~13Km². Single rock-glaciers can reach length up-to ~1.3 km and width of ~400 m (e.g. the one located SE of Lago Pellegrino). Lobate to tongue-shaped planar morphology characterize a complex system of longitudinal and transverse arcuate ridges that locally exceed heights of 10 meters. In the mapped area, only inactive rock glacier were identified, nevertheless active rock-glacier are reported at altitude exceeding 2490 meters s.l.m (NW of Monviso peak; Balestro et Al., 2013). Interestingly, rock glaciers are mainly located on the LSZ, at the base of the hectometer-high rock walls at the E of the Monviso Unit.

Gravitational phenomena deeply affect the rock massif of Monviso metaophiolite (Figure 24 and Figure 25): **rock falls** (generally extended all-over the mapped area), **earth flows** (e.g. the large flows localized NE of Rocce Sbiasere, SE of Peiro Jauno or NW of Monte Grané) and massive **rock slides** (e.g. S of Lago dell'Alpetto or NW of P.ta Rasciassa, Figure 25a). The nature of the deposits varies from chaotic accumulation of angular blocks with abundant sandy-silty matrix (rock-falls and earth-flows) to large sliced slivers of bedrock (e.g. the rock slides S of Alpetto Lake).

All these gravitational phenomena appear to be linked to the incoherent antigorite-rich matrix of the shear-zones, in particular in the LSZ. Three conjugate sets of fractures (dipping at high-angle toward N/NW, E and S/SW respectively) cut the Rocce Sbiasere ridge, likely linked to gravitate collapse of the more-rigid Mg-Al metagabbros over the LSZ matrix (Figure 24c). The elongated ridge north of Punta Rasciassa (the “Costa Pelata”) appears to be affected by a *deep seated gravitational slope deformation* (or DSGSD) producing impressive antislope-scarps and trenches (Figure 25a).

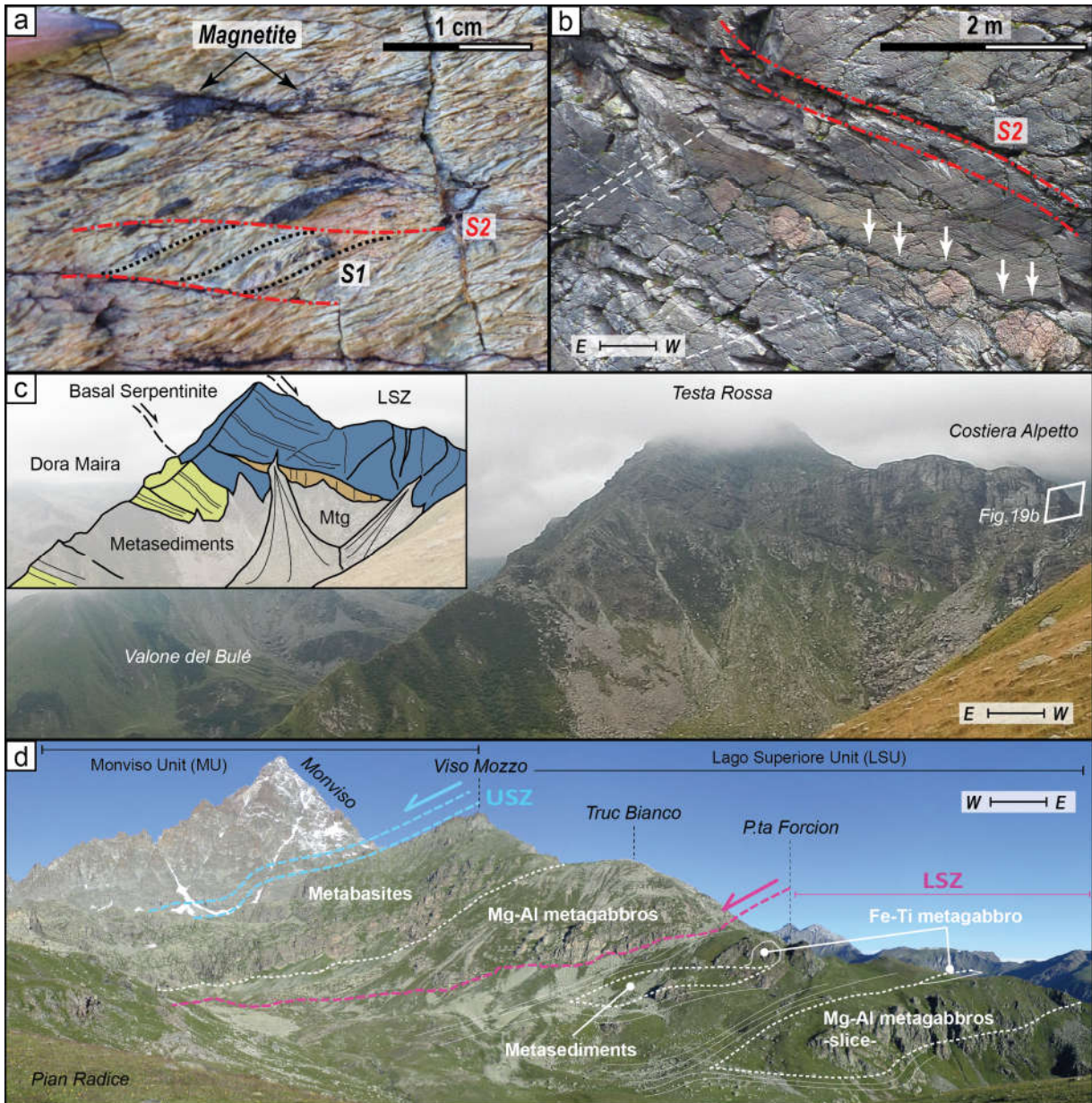


Figure 19: (a) close-up view of the basal metaperidotite. In evidence the SC-structure with S1 foliation (underlined by magnetite-beds) transposed by the S2 foliation. (b) Boudinated rodingitic dyke (white arrows) E of Alpetto lake. In evidence the W-dipping S2 foliation and the glacial striations carved on the glacier-polished basal serpentinites (white dashed lines). (c) Panoramic view of the basal serpentinite cliff E of Alpetto lake. The cartoon highlights the metagabbro mega-boudin (note its lighter colour in the photo) and the metasediments pinched in-between the Monviso metaophiolite (W) and the Dora Maira massif (E). The pertinence of metasediments to the Monviso metaophiolite or to Dora Maira massif is unclear and was not studied in this work (d) Panoramic view from Pian Radice depicting the inner structuration of the Lago Superiore Unit (LSU). Retrogressed Mg-Al metagabbro slices are continuously enveloped in the LSZ from P.ta Forcion to Colle di Luca, together with peridotite slivers and minor bodies of Fe-Ti metagabbros and breccia blocks. Metabasites and metabasalts are always underlined by Mg-Al metagabbros up-to 300 meters thick. At the top of the LSU, the Upper Shear Zone (USZ) marks the boundary with the Monviso Unit (MU). The latter is constituted by a thick (up-to 500 meters), overturned sequence of metabasites with minor metagabbros capped by a thin (max 15 meters thick) metasediments cover (the latter largely outcropping W of Lago Grande di Viso).

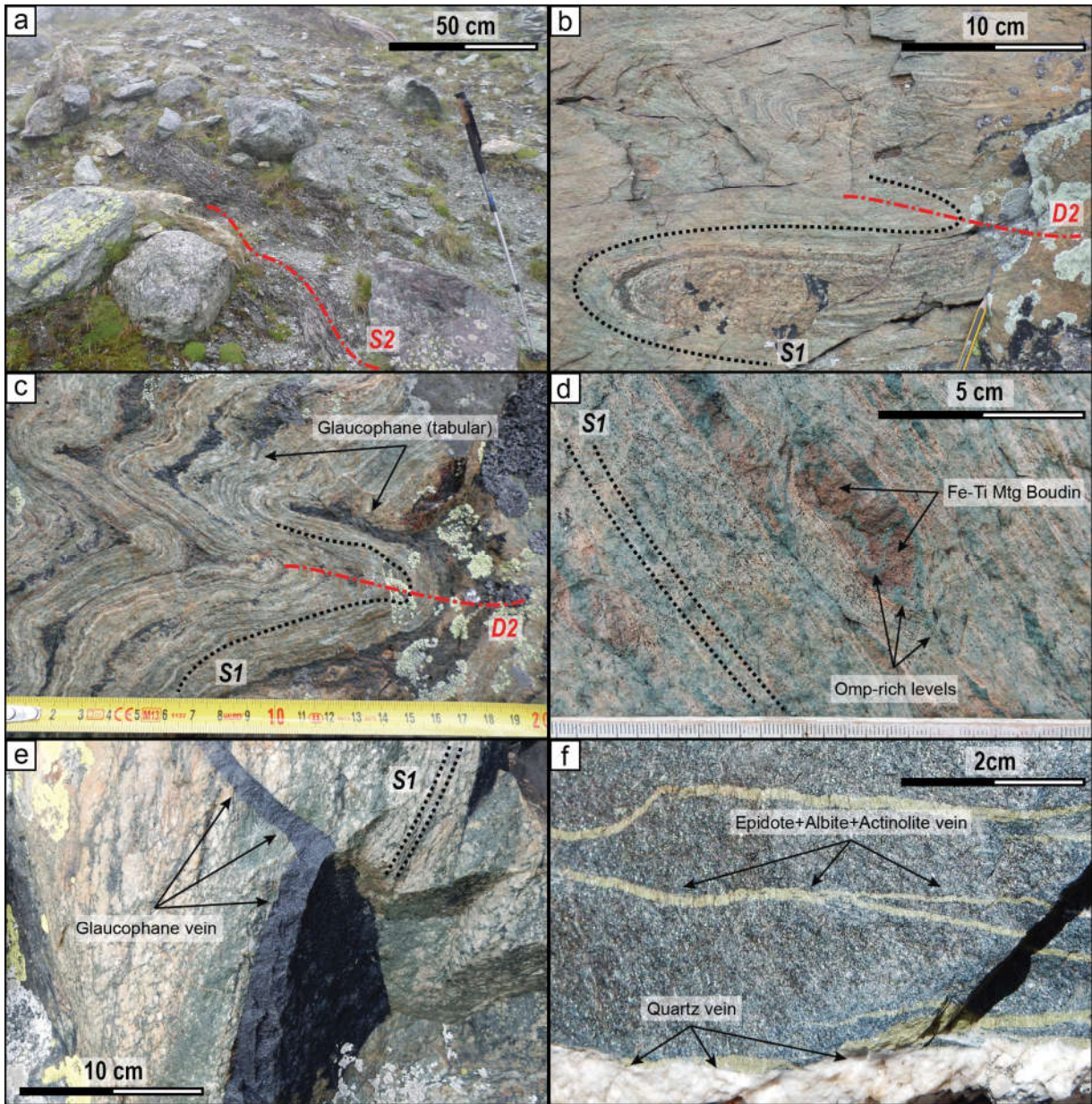


Figure 20: (a) the usual appearance of the antigorite-rich serpentinite constituting the bulk of the LSZ. The finely-crenulated serpentinites envelope numerous blocks of variable size composed of metagabbros, massive metaperidotite and, locally, metasediment slivers. The blocks distribution is only apparently chaotic, as shown in chapter 4. (b) Example of the recumbent syn-D2 folds recorded in the retrogressed Mg-Al metagabbro slivers dispersed in the LSZ (photo from Ghincia Pastour). (c) Close-up view of a retrogressed Mg-Al metagabbro with static crystallization of glaucophane at the hinge of syn-D2 folds (Rg east of Alpetto lake, block B7). (d) Close-up view of Fe-Ti Mtg boudins ($Grt+Rtl\pm Omp$) aligned along the S1 foliation of a Mg-Al metagabbro block. Note how the omphacite growth results in the dismemberment of the more-rigid Fe-Ti Mtg boudin in che senso la crescita dell'omph smembra i boudins? (block SW of P.ta Forcion). (e) cm-thick vein sharply crosscutting a Mg-Al metagabbro block. The vein is exclusively made up of fibrous, syntaxial glaucophane crystals (photo from a block N of P.ta Murel). (f) Example of two sets of greenschist veins developed in a retrogressed metabasite from Viso Mozzo. The first generation of fibrous, syntaxial epidote-rich veins is sharply cut by the thicker, massive quartz vein.

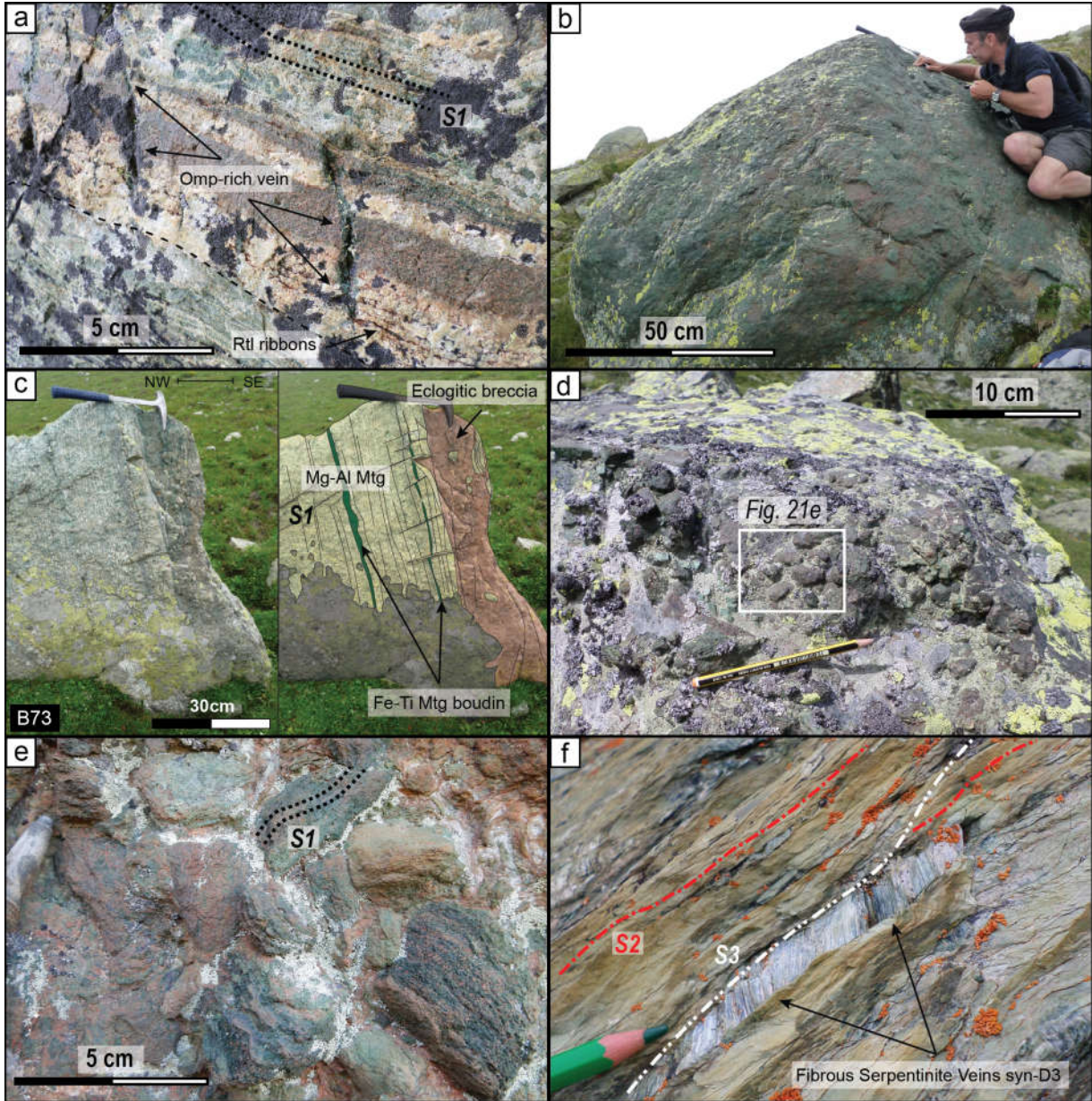


Figure 21: (a) highly-deformed Fe-Ti metagabbro boudin ($\text{Grt}+\text{Rtl}\pm\text{Omp}$) embedded in the S_1 schistosity of a Mg-Al metagabbro ($\text{Omp}+\text{Ep}\pm\text{Rtl}$) block. In evidence the Omp-rich veins, developed sub-perpendicularly to the Mg-Al Mtg foliation, crosscutting the boudin and disappearing on the first centimeters of the Mg-Al metagabbro. The latter in the portions around the boudins (evidenced in the figure by dotted lines) have a composition enriched in Ep (brownish ribbons subparallel to S_1) and Grt. Block B70, NE of Rocce Sbiasere. (b) massive block of Fe-Ti metagabbro at the base of the LSZ. This type of blocks (Type3) is characterized by the absence of breccia structures. Block B12, SW of Rocca Nera. (c) structures of a Type2 block, with the breccia layer crosscutting (here subparallelly) the S_1 foliation of the Mg-Al metagabbro block. Block B63, Pra Fiorito valley. (d) A Type1, eclogite-breccia block. The clast-in-matrix structure is well preserved under the pervasive lichen cover. Block B50, E of Peiro Jauno peak. (e) close-up view of an eclogite-breccia: the clast-in-matrix structure is emphasized by the foliated clasts of Fe-Ti metagabbro composition, with the S_1 well preserved and underlined by $\text{Grt}+\text{Rtl}+\text{Omp}$ beds. Block B50, E of Peiro Jauno peak. (f) close-up view of the antigorite-rich serpentinites of the LSZ. Here, in detail, the S_3 foliation crosscut subparallelly the S_2 with development of disjunctive surfaces recrystallizing fibrous, syntaxial serpentinite. LSZ, S of Lago Fiorenza.

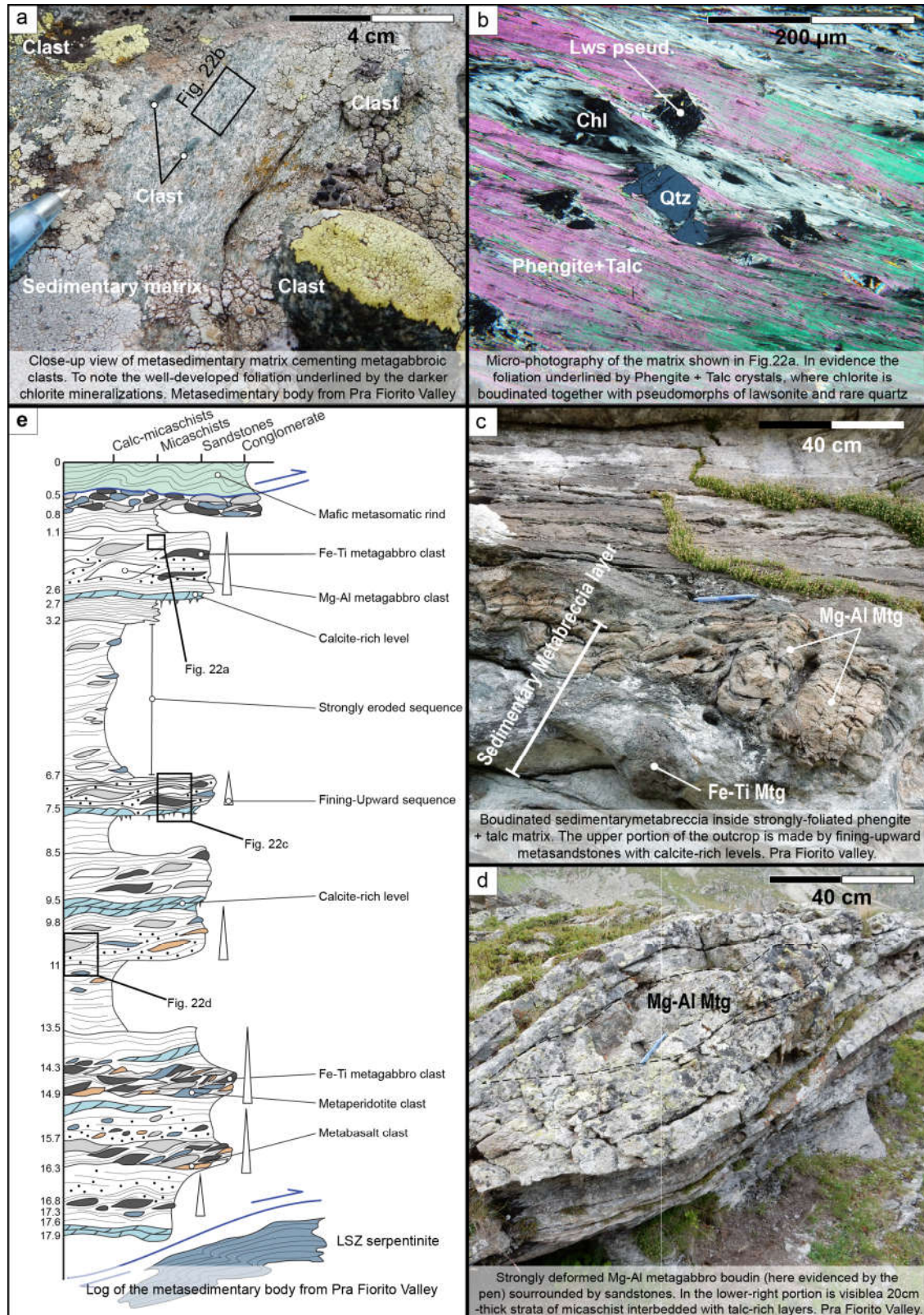


Figure 22

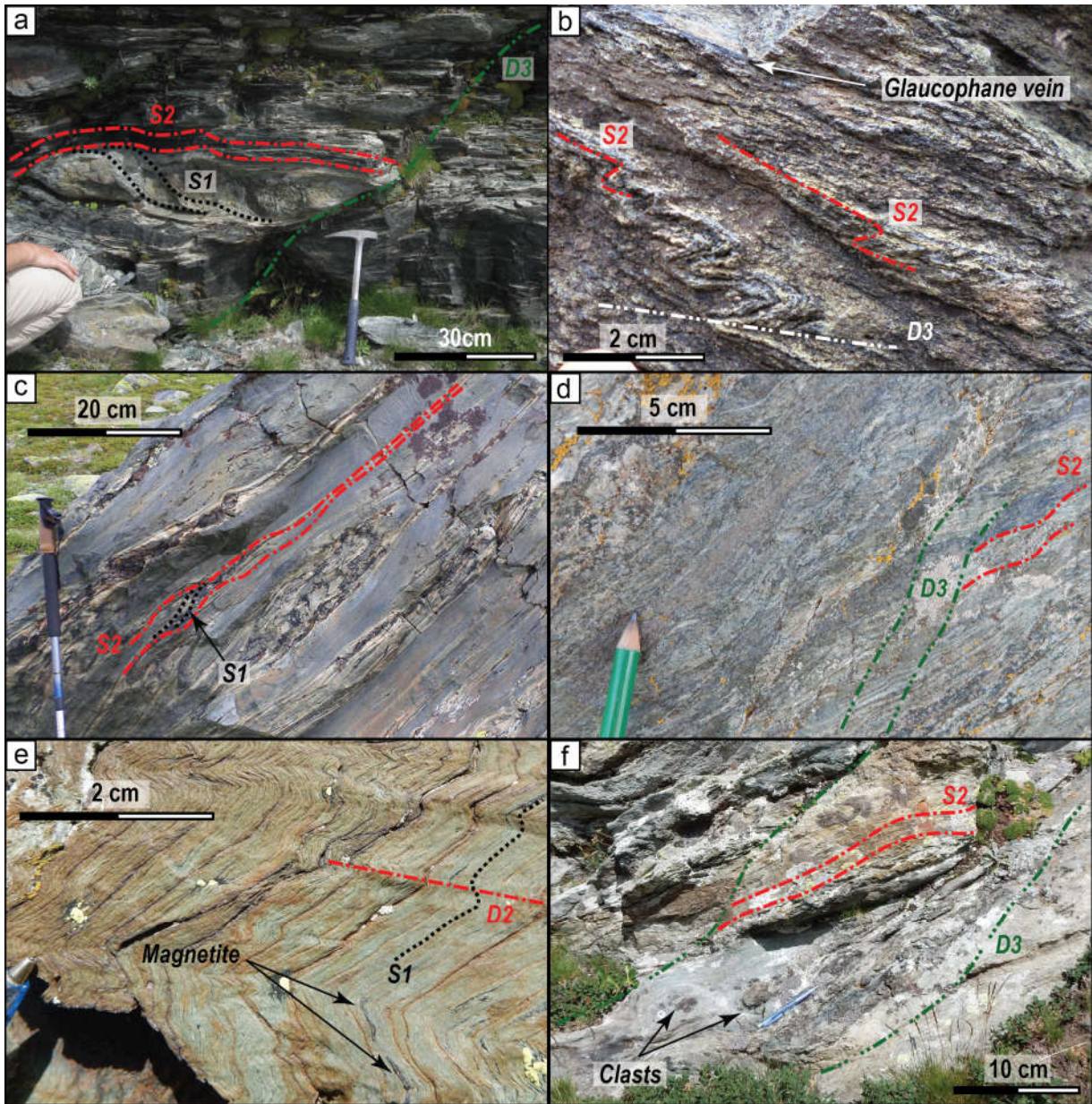


Figure 23: (a) Rodingitic dyke embedded in a foliated metaperidotite block from the LSZ. The pervasive foliation developed in the metaperidotite is coeval to the stage D2. D3 deformation leads to the development of disjunctive surfaces crosscutting at high-angle the S2. Photo taken W of Rocce Sbiasere. (b) Close-up view of the recumbent folds W-verging, syn-D3, developed in the finely foliated metabasites outcropping at the base of the NE flank of Viso Mozzo. (c) Eclogitic boudins (with preserved S1: paragenesis Omp+Ep) embedded in the S2 foliation of metabasites outcropping SSE of the Gallarino lake. (d) “S-C” structures developed at the expenses of the S2 foliation of Mg-Al metagabbro; the outcrop is at E of the Truc Bianco, at the base of the thick sequence of Mg-Al metagabbros between the LSZ and the metabasites. (e) Finely-crenulated serpentinites of a metaperidotite block near Colle di Luca. The preserved S1 (enlightened by the occurrence of magnetite ribbons) is folded during syn-D2 deformation. (f) Metasediments outcropping between the metabasites of the Lago Superiore Unit and the Lower Shear Zone. Meter-scale “SC” structures displace the S2 foliation, where dm-scale clast are enveloped in finely-grained quartz- and mica-bearing calcshists. Photo taken SE of Lago Grande di Viso.

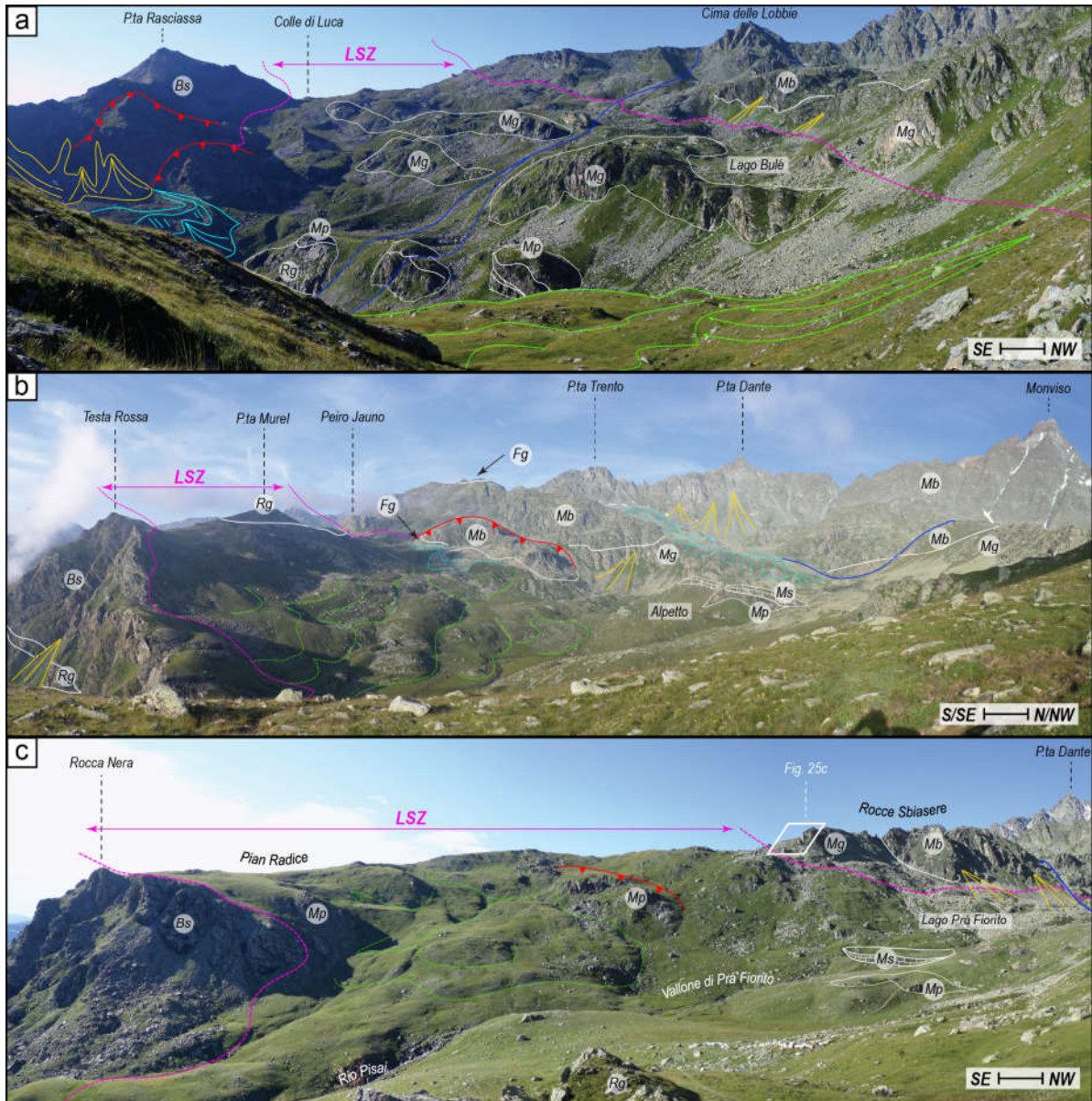


Figure 24: (a) Panoramic of the Viso Mozzo, with highlighted the limits of the Lower Shear Zone (LSZ, pink dashed line) and the Upper Shear Zone (USZ, light blue dashed line). On the left of the figure, the terminal moraine developed during the maximum advance of the NE Monviso “Pyrenean-Type” glacier in the Little Ice Age (LIA). The “heart” shape of Chiaretto lake is derived by the accumulation of rock-fall debris produced by the collapse of the Coolidge glacier in 1989 (Mortara and Dutto, 1990). (b) Panoramic view from the Monte Grané peak to the N, highlighted the inferred position of the LSZ and the outcropping lithologies. In evidence, at the W of Rocce Losere, the impressive antislope-scarps and trenches linked to deep seated gravitational slope deformations (DSGSD). (c) Typical rock-fall developed at the expenses of Mg-Al metagabbros at the contact with the LSZ. The cyclopic blocks (sizes up-to 15 meters) are produced by the interaction of three sets of joints dipping at high-angle respectively to NNW, NNE and SSW as shown by the stereographic plot (Schmidt net, lower hemisphere). This type of geometry suggests that gravitational collapse is the main force driving this rock falls. Picture taken E of the Rocce Sbiassere ridge.

The adopted acronyms are from the legend to the geological map of Monviso metaophiolite complex.

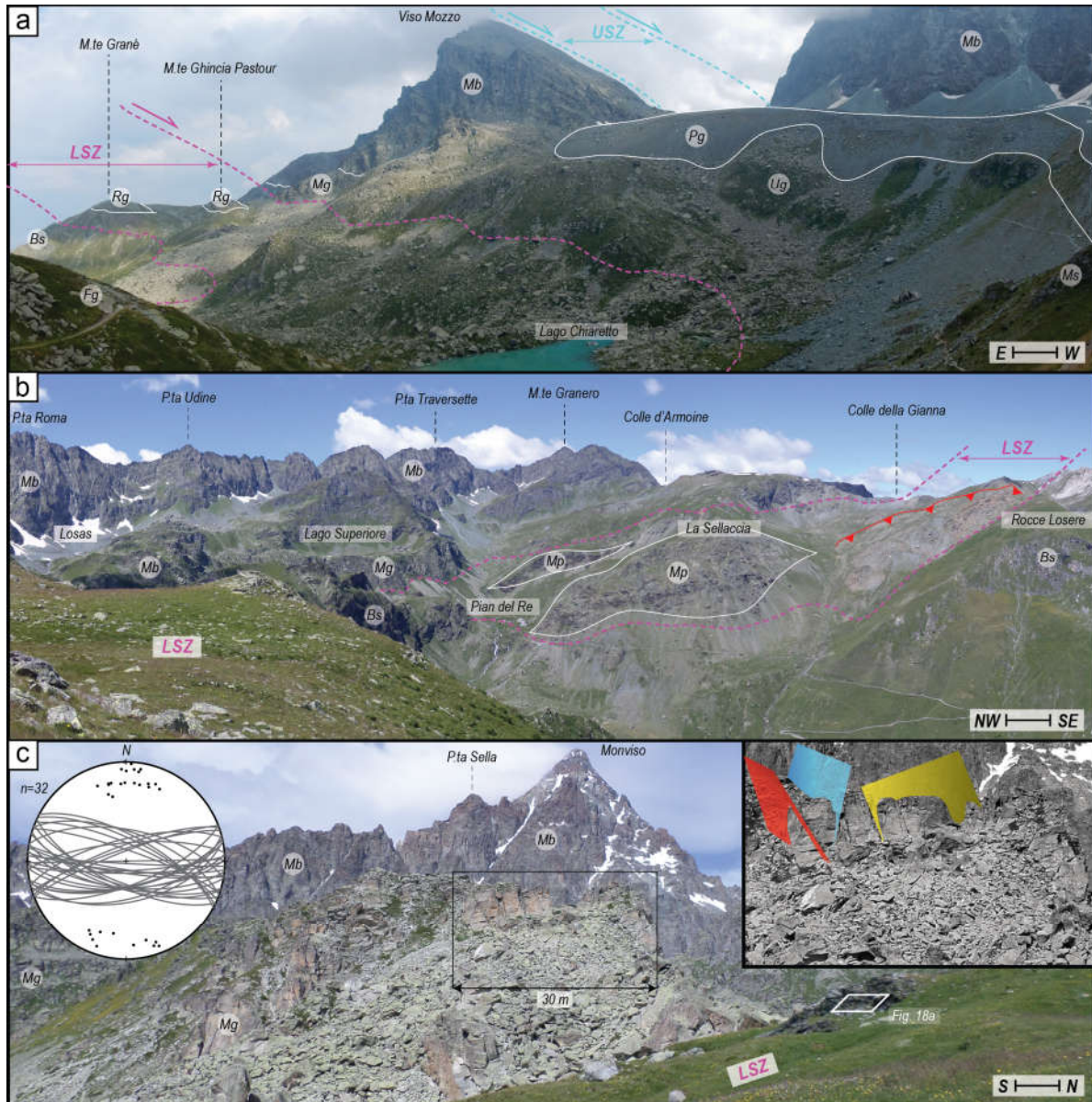


Figure 25: (a) Panoramic view to the S of the Bulé valley taken from the base of the eastern flank of the Peiro Jauno flank. The blue, continuous lines highlight the inferred faults system that crosscuts the Bulé valley resulting in the apparent dextral displacement of pre-existing structures. On the left of the figure we highlighted the trenches produced by the deep seated gravitational slope deformations (DSGSD) occurring at the western flank of Costa Pelata (N of P.ta Rasciassa). The volume of the DSGSD is able to deviate the underlying rock-glacier (now inactive). (b) panoramic view of the valley of the Alpetto. On the flank NNW of the Testa Rossa peak numerous scarp-trench structures suggest the presence of inactive rock-glacier, locally eroded by massive earth-flows giving the typical "lobate-like" shape. NW of Peiro Jauno peak a massive rock-slide is present, involving both the metabasites and the metagabbros. On the middle-right of the picture the blue line shows the inferred dextral fault passing through the Rocce Sbiasere ridge. (c) Panoramic view from Punta Forcion to Prá Fiorito valley. NW of Pian radice a massive earth-flow developed at the expenses of the incoherent antigorite-rich serpentinite schists of the LSZ occurs. The latter likely activated also the rock-slide NE of Rocce Sbiasere ridge by gravitative collapse. At the up-right side of the figure, the blue line shows the same dextral fault presented in Fig. 20b.

3.2 Structures

Three main tectonometamorphic phases are recognized in the Monviso meta-ophiolite complex (Figure 26 and Figure 29). To be consistent to the literature they are classified as D1, D2 and D3, respectively. The primary surfaces (i.e., the “S0” corresponding to magmatic foliation and sedimentary bedding) was never observed in the studied Monviso metaophiolite lithologies. Nevertheless, other Authors report its occurrence both in the Monviso metaophiolite and in the Dora Maira metasediments cover (e.g., Lardeaux et al. 1987; Balestro et al., 2014) and in the upper Val Varaita area (e.g., Balestro et al., 2014).

The **D1** phase (Figure 26 and Figure 27) is only locally preserved in the Fe-Ti metagabbros - *Fg*- (Figure 21a), Mg-Al metagabbros (in both “pristine” -*Mg*- and “retrogressed” -*Rg*-, Figure 20a, b and c) and as dm-sized boudins in metabasites -*Mb*- (Figure 23c), in metaperidotite lenses -*Mp*- from LSZ (Figure 19a) and rodingitic dykes (Figure 25a). In the different lithologies the **S1** is characterized by a layering made up of peculiar mineral assemblages, in detail: (I) in Fe-Ti metagabbros of mm-thick omphacite-rich and garnet-rich layers plus rutile ribbons (thickness up to 1 mm) that mark the foliation. Where visible, the related stretching lineation (**L1**) is marked by garnet-rich ribbons. (II) In Mg-Al metagabbros (both “pristine” and “retrogressed”) of mm-thick omphacite-rich layers and rutile-poor ribbons surrounded by static clinozoisite likely pseudomorphing lawsonite. At the contact with Fe-Ti metagabbro boudins, rare garnets are aligned along the S1. No appreciable lineation L1 was observed in this lithology. (III) In metabasites alternating mm-thick layers respectively omphacite-rich and clinozoisite-rich define the S1. Rarer interbedded garnet-rich levels also occur.

Where preserved, the S1 foliation is mostly NW-SE striking and dips to S/SW at variable angles (Figure 26).

The **D2** stage (leading to the development of **S2** and **L2**) is the most pervasive deformation event recorded in the Monviso metaophiolite. The lithological contacts, as well as the syn-metamorphic shear zones bounding the W- to SW-dipping units (e.g. the LSZ, ISZ and USZ), are parallel to the **S2** pervasive foliation. The latter is generally N/NW-S/SE striking with SW-dip and corresponds to the axial plane of non-cylindrical tight to isoclinal syn-S2 folds (Figure 26). The S2 overprints the S1, forming a composite regional foliation coeval to the metamorphic re-equilibration of Monviso rocks during the exhumation stage (Schwartz et al., 2000; Balestro et al., 2014). The L2 lineation has constant NE-SW trend and SW-WSW dip. Macroscopically, in the metabasites and the metagabbros from the Lago Superiore Unit, the S2 is defined by pervasively developed, strongly deformed mm-thick beds of glaucophane \pm clinozoisite alternated to levels richer in clinozoisite + chlorite + actinolite. SE of Passo Gallarino, the D2 phase brings about boudinage of eclogite-facies metabasites and development of S-C structures. At the opposite, in the retrogressed Mg-Al metagabbro scattered along the LSZ, no dynamic recrystallization under blueschist/greenschist facies is observed. It is rather recorded, along the foliation and in the hinge of the recumbent folds, the static recrystallization of glaucophane \pm epidote and actinolite (*Figure 20c*).

Within the pervasively foliated antigorite-schist matrix of the shear zones (e.g., the LSZ, ISZ and USZ) the **S2** results in cm- to dm-long disjunctive shear surfaces. On the studied area, no univocal evidences of L2 lineation was observed in the antigorite-schist.

The last deformation event (the **D3** stage) is characterized by open to close folds that deformed the **S2** foliation. In the metabasites and metagabbros from the Lago Superiore unit, the **D3** results in W-SW-verging drag-folds (Figure 18b) and local development of SC-structures where the **S2** is dragged on newly-formed epidote-, actinolite- and chlorite-bearing **S3** schistosity (Figure 23d). The antigorite-rich schists of the shear zones have similar structures: in less deformed areas the **D3** defines a finely banded crenulation with W-WSW verging folds; increasing deformation results in disharmonic folding with rootless geometries progressively flattening into W-dipping shear bands. Development of high-angle spaced cleavage inside less competent rocks is also recorded.

All the listed structures are finally crosscut by a network of high-angle transtensive faults, clearly postdating the metamorphic stages (Figure 24 and Figure 25). A major NE/SW-striking fault system, apparently crosscutting both the primary lithological contacts and the syn-metamorphic shear zones (e.g., the LSZ and the USZ), has been inferred in the Bulé Valley. As highlighted by the dextral displacement of Mg-Al metagabbros and metaperidotite, it is characterized by decametre-sized throw. Another high-angle, W-dipping fault was inferred E of Lago Grande di Viso. At the present state of knowledge it can be interpreted as a dextral transtensive fault with meter-sized throw. These structures likely accommodate the late-stage orogenic extension of the Alpine orogen (e.g., Sue et al. 1999; Schwartz et al., 2000; Perrone et al. 2013).

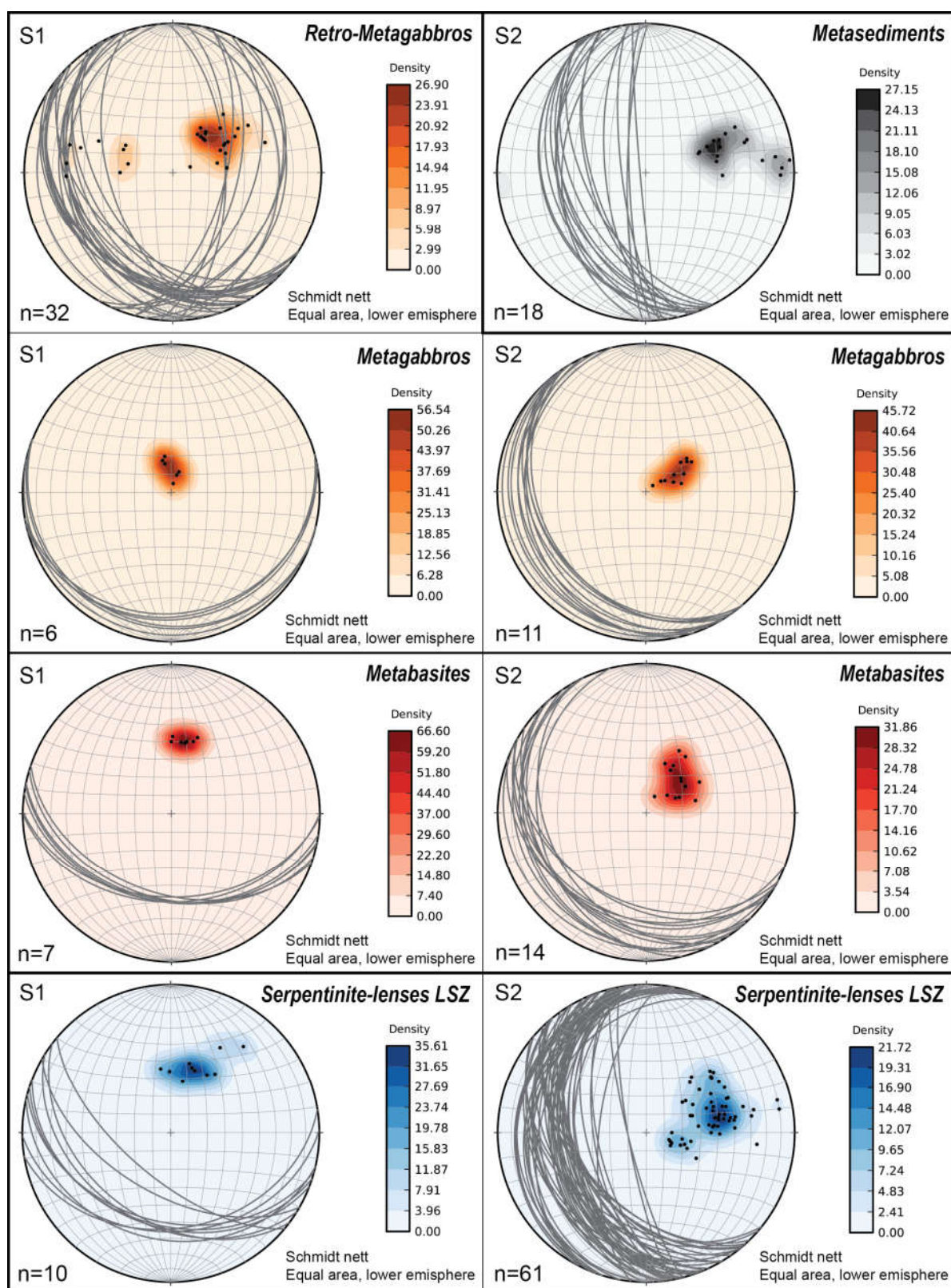


Figure 26: Foliations S1 and S2 sorted by lithology. Schmidt net, lower emisphère.

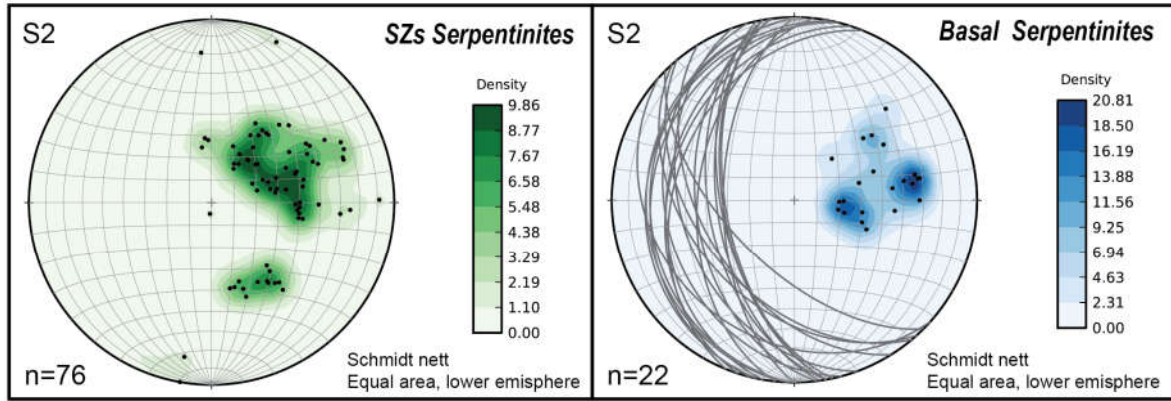


Figure 27: (a) S2 foliations of the antigorite-rich serpentinite of the LSZ and the basal serpentinites. The poles clustering in the LSZ is related to measurements taken in the southern flank of Prá Fiorito valley (N of Pian Radice, figure 20c) and reveals the occurrence of a massive earth-flows that obliterate the pre-existing structures. The clustering of Basal Serpentinite, instead, is linked to the syn-D2 folding

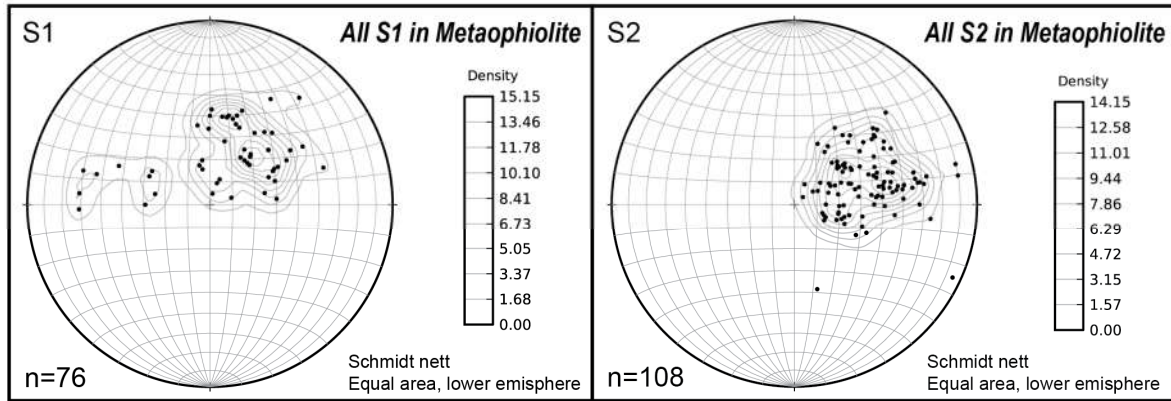


Figure 27: (b) collection of the S1 and S2 foliations for all the analyzed lithologies. For the S1 the clustering of poles is linked to the isoclinal folding observed in the retrogressed Mg-Al metagabbros slivers dispersed in the LSZ. In general, S1 foliations show a common dip-direction towards SSW (see also Fig. 21). The S2 poles, representing the regional foliations, describe a well clustered dip-direction towards SW. Here the data acquired in the Pra Fiorito valley are not plotted (see Fig. 22a).

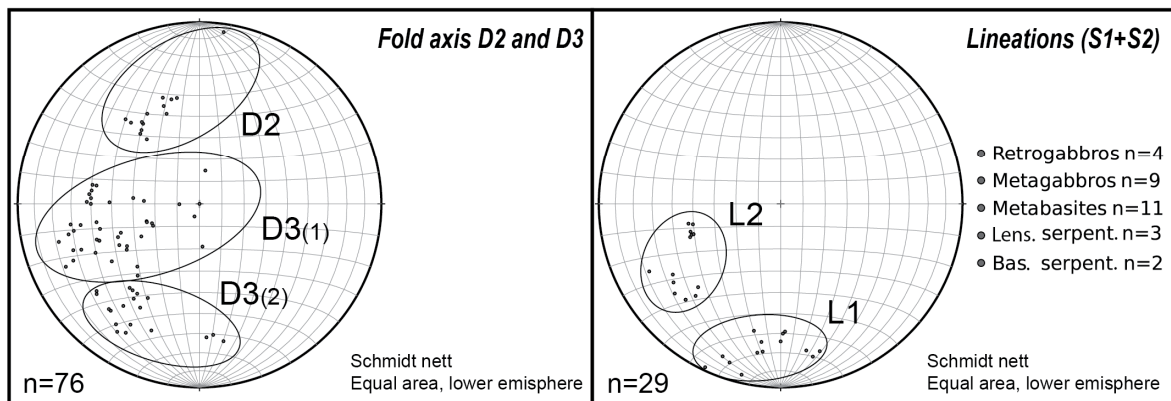


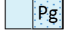







Figure 27: (c) collection of fold axis and lineations poles. Fold axes were observed for the D2 and D3 folding. Lineations were observed only on pristine D1 and D2 foliation planes. For D3, no clear lineations were recognized.

LEGEND TO THE GEOLOGICAL MAPS, LITHOSTRATIGRAPHIC COLUMNS and GEOLOGICAL CROSS-SECTIONS










QUATERNARY DEPOSITS

- Df**  **Alluvial and debris flow deposits**, composed by gravelly cobbles and sandy gravels clast-supported, well stratified to massive, sometimes containing decimetric- to metric-scale boulders. *Late Upper Pleistocene – Present*
- Td**  **Recent talus deposits**, composed by centimetric to decimetric angular fragments and blocks, usually clast supported, without visible stratifications. *Upper Pleistocene – Present*
- Ag**  **Undifferentiated glacial deposits (Ag)**, made up of diamicton with silty-sandy matrix and chaotic blocks accumulation. Blocks are locally devoid of lichens. **Pg**: **Little Ice-Age** moraines. *Holocene-Present*
- Ug**  **Undifferentiated glacial deposits**, made up of diamicton and chaotic blocks accumulation with silty-sandy matrix (Ug). *Upper Pleistocene*
- Rg**  **Inactive rock glacier**, formed by poorly sorted angular to sub-angular blocks at surface, with progressive passage to blocks-in-matrix texture below the surface. Characteristic the coverage of blocks by lichens. *Holocene*
-  **Lakes and ponds**

LITHOLOGIES - Monviso Unit (MU)

- Fb**  **Finely banded epidote-rich metabasites**, with pervasive blueschist foliation, locally retrogressed to greenschist facies. Pillow-structures, generally strongly deformed, are observed NW of Passo delle Segnette. *Middle Jurassic? Late Jurassic?*
- Ms**  **Fine-to-medium grained lawsonite-bearing calcschists** interbedded with quartz-rich (metachert) and mica-rich cm-to-dm levels. *Late Jurassic? Cretaceous?*

LITHOLOGIES - Lago Superiore Unit (LSU)

- Ms**  **Fine-to-medium grained lawsonite-bearing calcschists** (Mc) interbedded with quartz-rich and mica-rich cm-to-dm levels; locally with decimetric to metric-size bodies of metabasite (a). *Late Jurassic? Cretaceous?*
- Mb**  **Finely banded epidote-rich metabasites**, with pervasive blueschist foliation, locally strongly retrogressed to greenschists (Mb). *Middle Jurassic? - Late Jurassic?*
- Fg**  **Blocks of massive-to-foliated Eclogitic Fe-Ti metagabbros**, usually strongly retrogressed to greenschist facies. *Middle Jurassic?*
- Eb**  **Eclogitic metabreccias** (Punta Forcion, SW of Testa Rossa, Colle di Luca, W of Rocca Nera), composed by strongly foliated Fe-Ti and subordinate Mg-Al metagabbros clasts on fine-grained omphacite-matrix, locally with ex-Lawsonite-rich domains. *Middle Jurassic?*
- Rg**  **Bodies of Mg-Al metagabbros**, frequently retrogressed in green-schist facies, with cm-to-meter Fe-Ti gabbro boudins, and locally (W of P.ta Murel, W-NW of R.ca Negra) with preserved eclogitic metabreccias. *Middle Jurassic?*
- Mg**  **Mg-Al metagabbros**, locally strongly foliated and folded. *Middle Jurassic?*
- Mp**  **Massive metaperidotites** (Lago Fiorenza), locally interbedded as slices in the mylonitic serpentinites (N Colle di Luca, W of R.ca Nera, Lago Grande di Viso). *Middle Jurassic?*
- Ss**  **Strongly deformed mylonitic serpentinite schists**, locally interbedded with centimetric to decimetric-thick layers of talcschist. Internal structures are chaotic, usually dismembered by recent erosion. *Middle Jurassic?*
- Bs**  **Foliated to massive antigorite serpentinites** with subordinate antigorite schists. *Middle Jurassic?*

LINEAR ELEMENTS





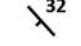






-  **Major tectonic contacts**
-  **Landslide escarpments**
-  **Regional Fault**
-  **Regional Fault (inferred)**
-  **32** **Regional foliation (with dip angle)**
-  **Geological cross-sections**
-  **2000** **Isolines**
-  **Fe-Ti metagabbro breccia blocks (Type 1)**
-  **Mg-Al metagabbro blocks with eclogitic breccia (Type 2)**
-  **Unbrecciated Fe-Ti metagabbro blocks (Type 3)**
-  **Massive rodingite dykes (Rd). Middle Jurassic?**

Figure 28: Legend to the Geological Map of the Southern Monviso metaophiolite complex. For Further detail, please refer to the geological map attached to this thesis.

INTERPRETATIVE GEOLOGICAL MAP of THE SOUTHERN MONVISO METAOPHIOLITE COMPLEX

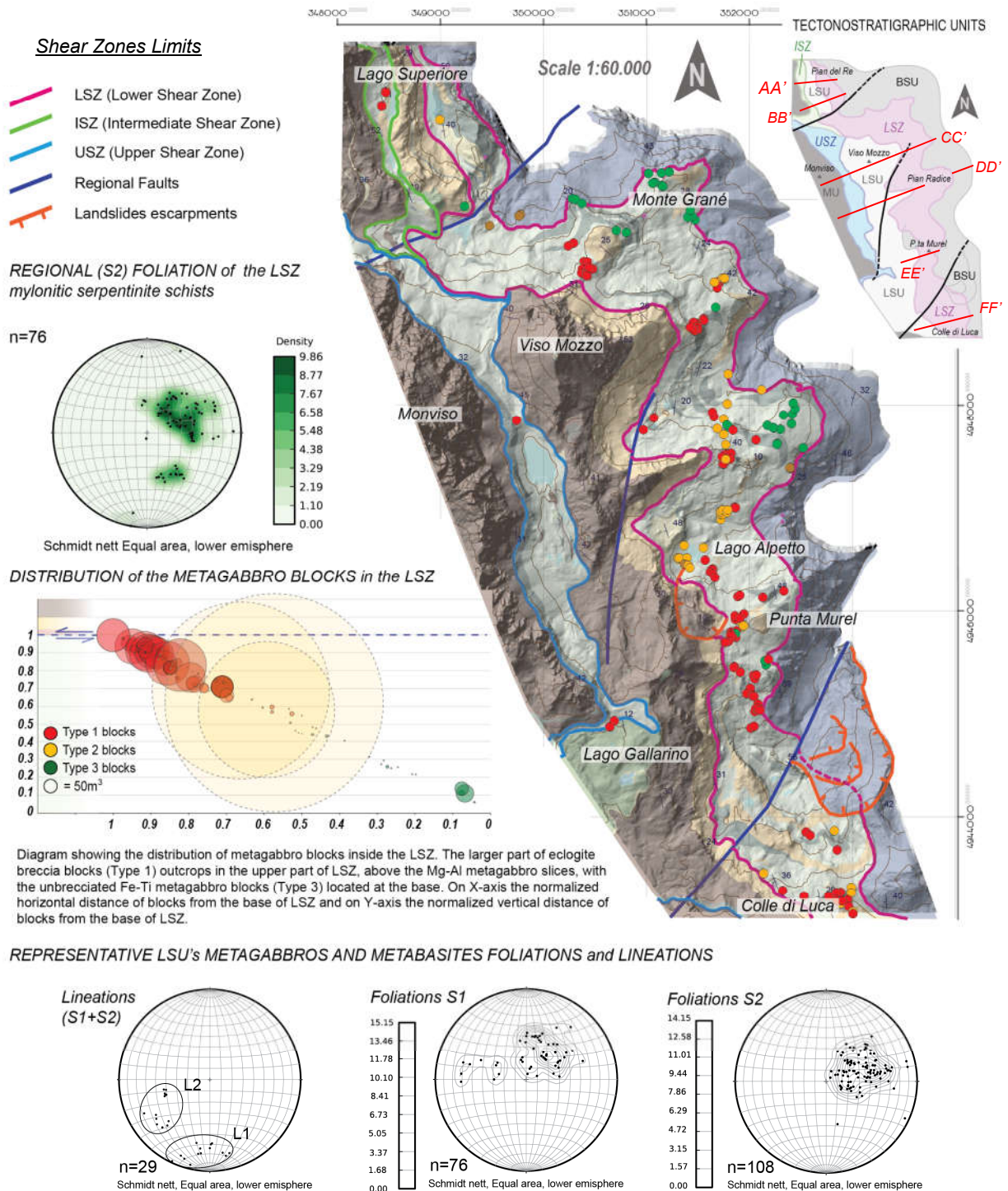
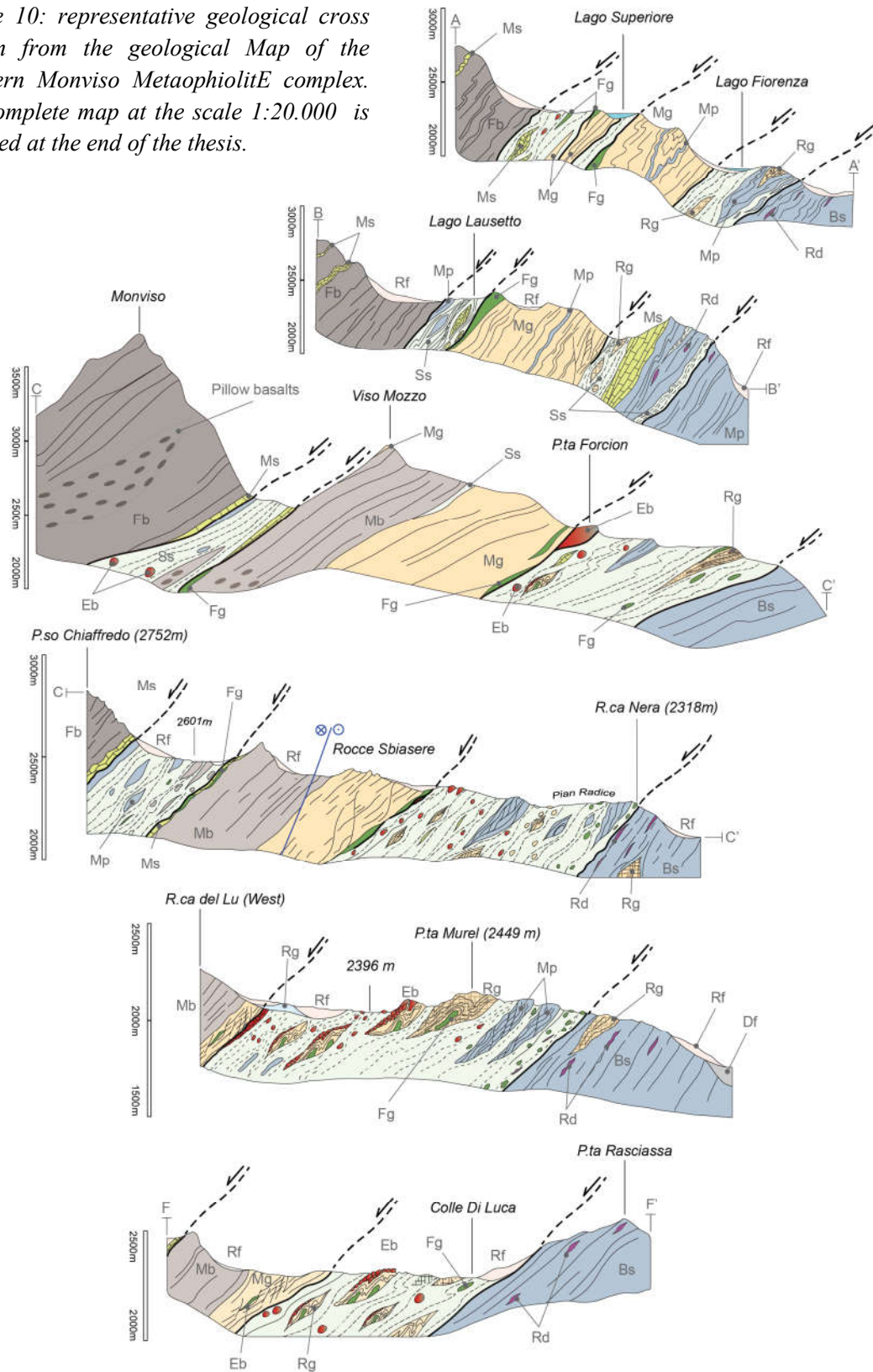
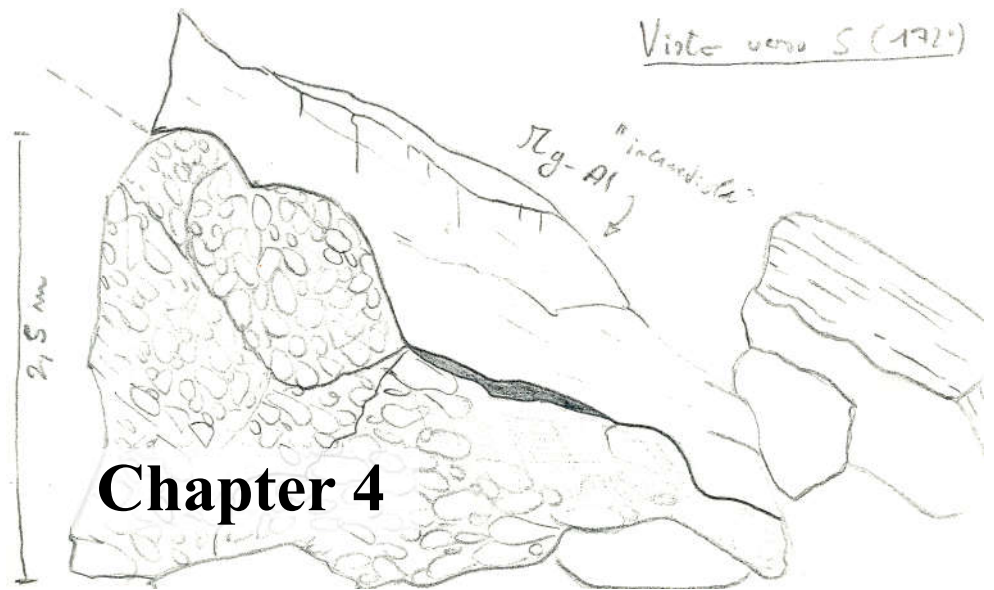


Figure 29: Interpretative geological map of the southern part of the Monviso metaophiolite complex. In evidence the tectonostratigraphic units and the distribution of eclogite-facies metagabbro blocks in the LSZ and ISZ. For further details, please refer to Chapter 4 and the geological map attached to this thesis.

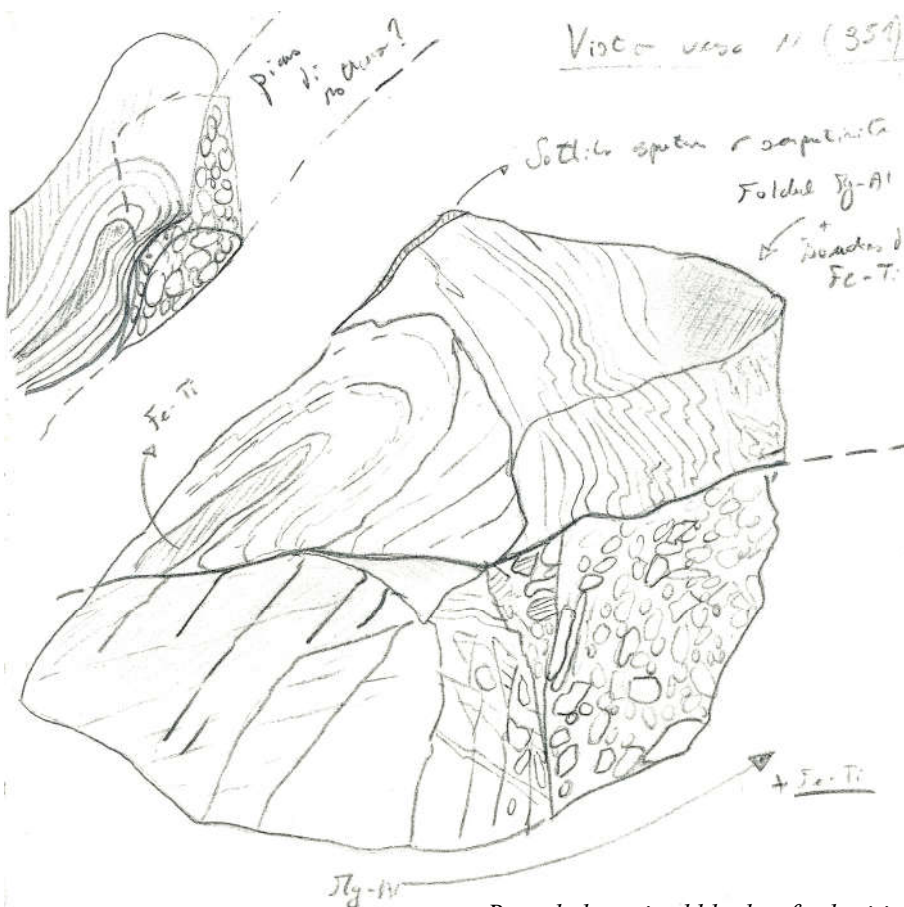
Figure 10: representative geological cross section from the geological Map of the Southern Monviso Metaophiolite complex. The complete map at the scale 1:20.000 is attached at the end of the thesis.





Chapter 4

Characterization of eclogite-facies brecciation along the subduction plate interface



Rounded, m-sized blocks of eclogitic breccia dispersed in serpentinite-matrix shear zones: a challenging topic, full of surprises!

After the redaction of the geological map of the southern part of Monviso metaophiolite (chapter 3), the second step consisted in a detailed (micro) ***structural and petrographic characterization of brecciated metagabbro blocks*** distributed in the LSZ and (to a lesser extent) in the ISZ, in order to better constrain the conditions (P-T, rheological, fluid) and successive steps of brecciation, and the rheological parameters that allowed this brittle rupture phase at eclogitic facies conditions.

Evidences for brittle rupture at eclogite facies conditions in metagabbros were already reported by Angiboust et Al. (2012a-b). Nevertheless, such eclogitic origin for the breccia blocks was fervently discussed in the literature in recent years, raising the need for a more detailed characterization of the breccia microstructures as well as the distribution of brecciated blocks in the LSZ. Indeed, in the northern part of Monviso metaophiolite (upper Pellice Valley), Festa et al. (2015) and Balestro et al. (2013) recognized in the structures and block distribution of the “Baracun Shear Zone” (corresponding in the southern part of Monviso metaophiolite to the LSZ of Angiboust et al., 2012a) the remnant of a core complex formed in an embryonic ocean (i.e., the Ligurian-Piedmont Ocean) as the products of rift-drift processes, thus proposing the origin of breccias as inherited pre-Alpine detachment fault rocks or sedimentary-derived breccias.

To overcome the contradiction of these two theories, which were developed using different methodological approaches (petrography-based for Angiboust et al., structurally-based for Festa et al. and lithostratigraphy-based for Balestro et al.), we adopted a ***multi-methodological approach***, with a work-flow optimized to characterize the brecciation development from the macro to the micro scale. This chapter thus addresses the following questions:

1. What is the distribution of eclogite breccias in the Monviso metaophiolite? Are brecciated blocks randomly distributed in the LSZ or do specific pattern exist?
2. What are the structures recorded in the breccia planes? Are these comparable with analogue structures developed in shallow-crustal (<20 km-depth) fault areas, potentially linked to seismic activity?
3. Are the breccias a reliable example of brittle-rupture occurring at Eclogite-facies conditions?
4. What is the chronology of events leading to the brecciation? What are the mineral reactions (and potential fluid release) occurring synchronously with brecciation, and what is their impact on such brittle rupture?
5. What is the origin of fluids present at the time of brecciation (as attested by presence of veins and different types of matrix): internally (i.e. local dehydration) or externally (i.e. fluid infiltration) derived?
6. What are the implications, at the regional scale, of such metagabbro brecciation on the structural and rheological evolution of the Monviso metaophiolite complex?

Brief overview of the adopted work-flow

As described in chapter 3, the positions of 195 eclogitic metagabbro blocks scattered in the three main shear zones were precisely mapped, in order to study their occurrence and distribution. All the studied blocks were geographically positioned (*latitude*, *longitude* and *altitude*) using **GPS**, taking care to select those with preserved primary contact with the mylonitic serpentinite-schists of the shear zones.

On every block, we measured the descriptive dimensional parameters (*height*, *length* and *thickness*), in order to evaluate their volumes, considering them as ellipsoids. For the biggest blocks, the size measurements were refined with additional evaluations done on aerial images using **GIS** software.

In order to characterize the structures of eclogitic breccias at the mesoscale, on the most representative brecciated surfaces we measured (1) the thickness and geometry of breccia planes, (2) the clasts vs. matrix relative volumetric abundances, (3) the dimension and shape ratio of clasts and (4) the angle of misorientation between clast elongation axes or, where possible, between internal clast foliations. Additionally, on the most representative blocks, we evaluated (5) the number of clasts sorting them by lithological composition.

Careful in-situ drawings and photo-picturing were performed to later reproduce and graphically study the breccia layers/planes and their relationship with unbrecciated gabbros. After that the scaled images were outlined thanks to paint-software, converted to grey-scale images and analyzed by the use of FiJi software in order to obtain the clast areas, perimeters, angles of maximum elongation axis, aspect ratio and roundness. The last parameter was recalculated as adaptation of the Waddel's sphericity, as suggested by Mort & Woodcock (2008). The above described field work was essential to precisely constrain the occurrence of brecciation along the multiple successive deformation stages recorded in these rocks from eclogitic to late-alpine greenschist facies.

During field season 2014 **91** samples were collected (of which **49** are composed by Fe-Ti and Mg-Al metagabbros cores extracted from the best-preserved breccia blocks), with additional **68** samples from season 2015 (**43** cores). The major problems for the largest part of eclogitic blocks outcropping in the Monviso area are the blueschist to greenschist retrogression and the considerable lichen cover, as well as the thick reaction rinds formed at the serpentinite schists-breccia blocks contact, ascribed to the dissemination-phase of the bodies inside the LSZ (Angiboust et al., 2014). As a result, only **37** of the samples collected during season 2014 and **28** samples from season 2015 resulted in fresh eclogite-facies brecciated metagabbros.

On these, microscopic and petrographic analysis of the textures and micro-structures has been performed, allowing to recognize preserved breccia fabrics (e.g., clast-in-matrix structures) developed at eclogite-facies condition. Multiple microprobe and SEM analyses were performed, with particular focus on the analysis of mineral compositions from matrix vs. clasts of breccia samples.

The complete description of the study and the results are presented in the next draft of the paper submitted to *Lithos*, with title “*Eclogite-facies rupture along the subduction plate interface (Monviso meta-ophiolite complex, W. Alps)*”. In paragraph 4.11 of this chapter, the methodology and results of the statistical analysis on selected eclogite-breccia planes from 4 blocks disseminated in the LSZ are presented.

Eclogite-facies rupture along the subduction plate interface (Monviso meta-ophiolite complex, W. Alps)

Michele Locatelli¹, A. Verlaquet¹, P. Agard¹, L. Federico², S. Angiboust³

¹ *Institut des Sciences de la Terre de Paris (ISTeP), Université Pierre et Marie Curie (Paris VI)*

² *Dipartimento di Scienze della Terra, dell'Ambiente e della Vita (DISTAV), Università di Genova*

³ *Institut de Physique du Globe de Paris, Sorbonne Paris Cité, Univ. Paris Diderot, CNRS, F-75005 Paris, France*

Abstract

The Monviso meta-ophiolite complex (Northern Italy, Western Alps) represents an almost intact fragment of Tethyan oceanic lithosphere metamorphosed at ~80 km down (2.6 GPa - 550 °C; Lago Superiore Unit) during the Alpine subduction. We focus our study on a major shear zone cutting across this slab fragment at low angle (the Lower Shear Zone; LSZ), in which blocks of variably brecciated Fe-Ti and Mg-Al metagabbros are embedded, together with metasedimentary blocks, in a talc and tremolite-rich serpentinite matrix. These blocks were either interpreted as eclogitic breccias resulting from (potentially seismic) intermediate-depth rupture or as inherited, overprinted oceanic core complex features. Our new field and petrographic data demonstrate their univocal genesis at eclogite-facies conditions. Three types of eclogitic blocks can be distinguished, with non-random distribution (and decreasing size from top to base) throughout the ~200 meter thick and ~15 km-long LSZ: (1) Fe-Ti-metagabbros, brecciated and scattered in the upper to intermediate levels of the LSZ; (2) meter-size blocks and decameter-scale slivers of intact Mg-Al metagabbros, locally brecciated; (3) un-brecciated blocks of Fe-Ti-metagabbros restricted to the lower part of LSZ. Brecciation at eclogite facies conditions (at ~80 km depth) is univocally demonstrated by: i) the eclogitic foliation of intact Mg-Al-rich metagabbros (composed of omphacite + clinozoisite ± rutile and locally garnet) cut by breccia planes (cemented by omphacite + garnet ± lawsonite) and ii) the occurrence in breccia clasts of minerals that are fractured and offset along peak P-T omphacite-bearing planes. Rupture preferentially affected the Fe-Ti metagabbros, suggesting that rheological contrasts controlled the locus of brecciation. A first set of garnet-bearing, omphacite-rich matrices (crushed+M1+M2) witnesses multiple brittle rupture events, probably shortly spaced in time, prior to a stage of eclogite facies fluid ingression marked by massive lawsonite recrystallization (matrix M3).

Keywords: eclogite-facies breccia, plate interface, Monviso, Western Alps

4.1 Introduction

Documenting processes acting at the plate-slab subduction interface is fundamental for understanding (and modeling) interplate mechanical coupling, fluid migration pathways and/or processes triggering seismicity. Most field studies, geophysical investigations and mechanical models have focused on processes acting within the seismogenic zone (15-30 km-depth, Toyoshima et al., 1990), where megathrusts nucleate (Ikesawa et al., 2003; Rowe et al., 2005; Bachmann et al., 2009; Meneghini et al., 2010; Vannucchi et al., 2012). By contrast, there is a general lack of data on the mechanical and geochemical processes acting at deeper slab levels (> ~40 km).

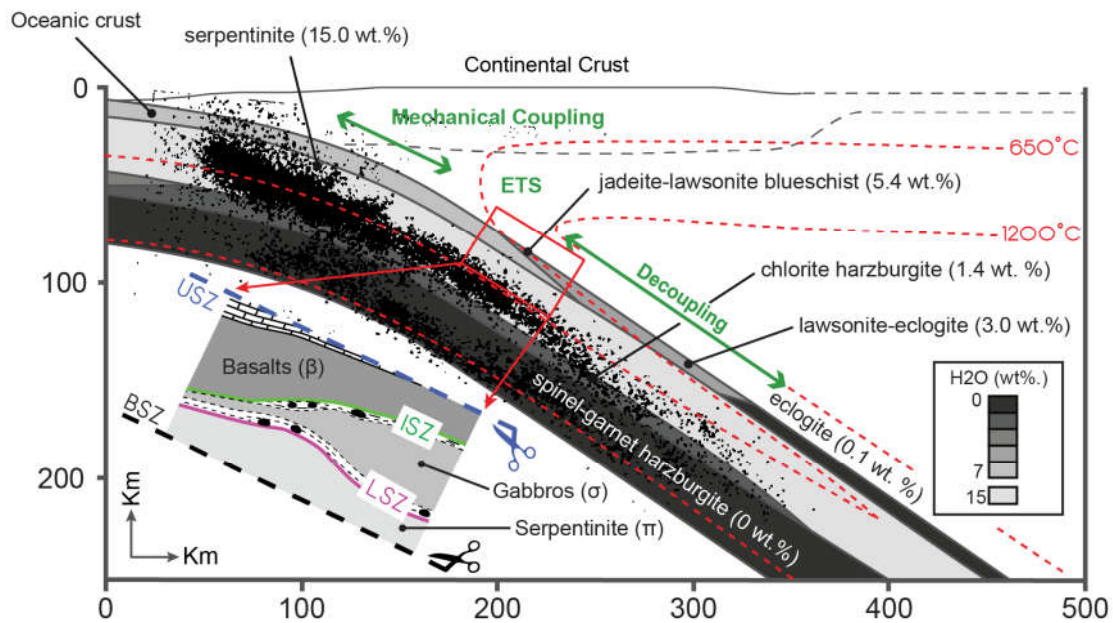


Figure1

Figure 31: Correlation between seismicity and mineral phase transformations in subduction zones (the sketch refers to the Tohoku subduction zone, modified after Hacker et Al., 2003). In the inset, the position of the Lago Superiore Unit (LSU) and its shear zones respect to the inferred P-T condition (from Angiboust et Al., 2012). In the brackets, the estimated water content (wt%). Isotherms from Peacock and Wang, 1999.

Two distinct seismic layers are recognized beyond the seismogenic zone (*Figure 31*; Hacker et al., 2003a, 2003b; Yamasaki and Seno, 2003); of these, geophysical and petrological data suggest that the upper one may correlate with the topmost, previously hydrothermalized crustal part of the slab ongoing massive metamorphic dehydration (*Figure 31*; Bostock et al., 2002; Green & Houston, 1995; Hacker et al., 2003b; Rondenay et al., 2008). However, rheological processes associated with intermediate-depth seismicity and/or deep fluid circulation (e.g., hydraulic fracturing, dehydration embrittlement, mineral transformation induced faulting and partial melting recorded by pseudotachylites; Davies, 1999; Hacker et al., 2003; Jung et al., 2004) are still largely debated due both to the lack of direct observations and to instrumental uncertainties (Kuge et al., 2010).

Although still limited, there is a growing body of evidence that large-scale, “fossil” exhumed portions of subducted lithosphere (Agard et al., 2009) may record both chemical and mechanical processes operating in the depth range of intermediate-depth seismicity (White et al., 1985; Kirby, 1985; Handy et al., 1999; Montesi et al., 2003; John et al., 2009; Plat et al., 2011; Angiboust et al., 2011, 2012b; Yang et al., 2014). The recent report of oceanic crust brecciation at eclogite facies conditions (in the Lago Superiore Unit of the Monviso meta-ophiolite, Western Alps; Angiboust et al., 2012b; *Figure 32*) points to the possibility of retrieving patterns of intermediate-depth seismic rupture from a well-preserved slab fragment (*Figure 31*). This finding was challenged, however, by authors who interpret these breccias as inherited pre-Alpine detachment fault rocks from an oceanic core complex or sedimentary-derived breccias (Balestro et al., 2015). Considerable debate also exists in the literature on the feasibility of brittle rock-failure at eclogite-facies conditions (e.g., Raleigh et al., 1965, 1967; Kirby et al., 1995; Jin et al., 2001; Jung et al., 2004).

The aims of this paper are therefore: i) to demonstrate the eclogite-facies origin of the brecciation recorded by the metagabbro blocks disseminated in the Monviso shear zones (particularly in the Lower Shear Zone; LSZ); ii) to define their spatial extent and distribution across the LSZ; iii) to unravel the detailed chronology of brecciation and associated mechanical/chemical changes and vi) to discuss implications for intermediate-depth processes (whether seismic or not).

4.2 Geological setting

4.2.1 - Regional geological setting

The Western Alps formed as a result of the eastward subduction of a branch of the Tethyan Ocean and of part of the thinned European continental margin beneath Adria, followed by collision from the Oligocene onwards (Coward & Dietrich, 1989; Laubscher, 1991; Lagabrielle & Lemoine, 1997; Schmid & Kissling, 2000). The reader is referred to more comprehensive publications for further details on the alpine geodynamic evolution (Agard et al., 2009; Beltrando et al., 2010a, 2010b).

The study area belongs to the ~30 km long Monviso meta-ophiolite complex (Figure 32), one of the largest slices of oceanic lithosphere among the Liguro-Piemontese domain, which extends from the Voltri complex (Ligurian Alps, Italy) to the Zermatt-Saas zone (Valais, Switzerland and Valle D'Aosta, Italy).

The Liguro-Piemontese domain is formed by the juxtaposition of km to 10 km-long exhumed eclogite-facies tectonic slices to lower grade (blueschist to eclogite facies) fragments of a fossil accretionary wedge, known as the Schistes Lustrés (Agard et al., 2002, 2009; Plunder et al., 2013).

A major westward-dipping ductile normal shear zone system separates the Schistes Lustrés complex from the Monviso meta-ophiolite below (*Figure 32*), exhibiting a metamorphic gap between the two units (Balleve et al., 1990). Below and to the east of the Monviso meta-ophiolite, the Dora Maira massif represents slivers of the thinned continental European distal margin involved in the Alpine subduction

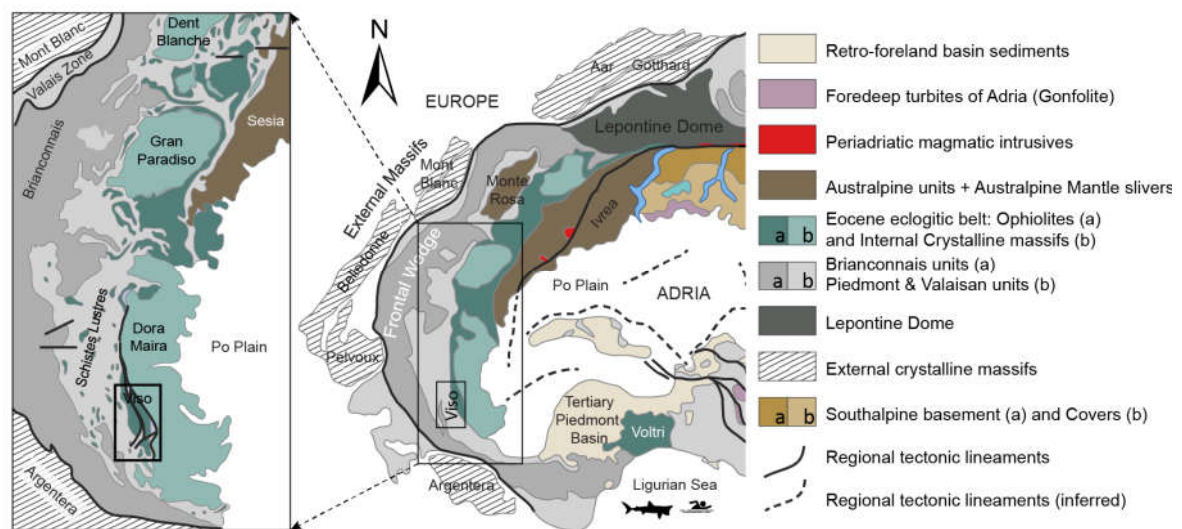


Figure 32: Tectonic sketch of the Western Alps. The Eocene eclogitic belt (Grey) is exposed on the upper-plate side of the orogen, between the Frontal wedge (light blue) and the remnants of a Late Cretaceous doubly-vergent wedge (yellow). In the inset, a detail of the eclogite belt and the frontal wedge with the localization of the Monviso metaophiolite. Maps modified after Malusá et Al. (2011) and Agard et Al. (2009).

and detached from the downgoing slab at different depths during the Late Eocene.

Age constraints indicate that peak burial for the Monviso meta-ophiolite was achieved around 45 Ma (Duchene et al., 1997; Rubatto & Angiboust, 2015).

Noteworthy, the structural and metamorphic characteristics of the Monviso are broadly comparable to those observed in the Zermatt-Saas and Voltri meta-ophiolites (e.g., Dal Piaz et al., 2003; Schmid et al., 2004; Angiboust & Agard, 2010; Pelletier & Muntener, 2006).

4.2.2 - Structure and P-T conditions of the Monviso meta-ophiolite

The Monviso meta-ophiolite provides well-preserved fragments of Tethyan oceanic lithosphere, with recognizable lithostratigraphic successions. It was subdivided in several tectonometamorphic units (Lombardo et al., 1978) and more recently in two main units: the Monviso s.s. unit (MU) and the Lago Superiore Unit (LSU; Angiboust et al., 2011). For the *Monviso unit*, a peak of 480°C–22 kbar was proposed by Angiboust et al. (2012a), while slightly different eclogitic P–T peaks were calculated for the Lago Superiore Unit: 580°C–19 kbar (Schwartz et al., 2000), 650°C–26 kbar (Messiga et al., 2000), 545°C–20 kbar (Castelli et al., 2002), 550°C–25 kbar (Groppo & Castelli, 2010) and 550°C–26 kbar (Angiboust et al., 2012a).

This study focuses on the LSU, which comprises, from bottom to top: serpentinitized lherzolitic mantle intruded or capped by late Jurassic Mg-Al and/or Fe-Ti gabbros (152 Ma; Lombardo et al., 2002; 163 Ma, Rubatto and Hermann, 2003); banded tholeiitic basalts (with locally preserved pillow structures); diabases and mixed calcareous/pelitic Cretaceous metasediments (Lombardo et al. 1978, 2002; Balestro et al. 2011, 2013). Strong lateral variations in lithostratigraphy, with one or more of the above horizons missing, were attributed to an irregular seafloor structure typical of slow spreading oceans (Lagabrielle and Lemoine, 1997).

The original stratigraphic sequence is partly disrupted by shear zones (Lombardo et al., 1978; Philippot & Kienast, 1989; Angiboust et al., 2011, 2012a; Festa et al., 2015); we particularly focus on two of them (*Figure 33a, b, SM1 and SM2*): the Lower Shear Zone (LSZ) and the Intermediate Shear Zone (ISZ), which locally mark the boundaries metagabbros-serpentinites and metabasalts-metagabbros, respectively. Since P-T conditions are undistinguishable on either side of the shear zones (Angiboust et al., 2012a), vertical displacements along them are probably less than km-scale.

The LSU is therefore an almost intact, well-preserved fragment of oceanic lithosphere coherently subducted to 80 km-depth and subsequently crosscut by poly-metamorphic km-scale shear zones (Angiboust et al. 2011, 2014).

4.2.3 - Intra-slab shear zones within the Lago Superiore unit: the Lower and Intermediate shear zones (LSZ, ISZ)

Two main km-scale shear zones partially disrupt the LSU unit of the Monviso meta-ophiolite, both made of a serpentinite-rich matrix embedding several kinds of blocks. The LSZ separates the main Mg-Al metagabbro body (to the west) from the underlying massive serpentinite sole constituting the eastern cliff of the meta-ophiolite Monviso massif (*Figure 33a, b, Figure 34a and SM1*). In the study area, the shear zone has an extension along strike of over 15 km from the south (Colle di Luca pass) to the north (Rocce Fons) with a variable thickness ranging from ~300 m at Colle di Luca pass or Lago Superiore area to ~500 m at Pian Radice (*Figure 33a and SM1*). The LSZ matrix is made of strongly deformed mylonitic serpentinite with locally interbedded cm to dm-thick layers of strongly sheared talc-chlorite schists. Serpentinite mainly consists of fine-grained, strongly-deformed antigorite (+/- magnetite, talc, magnesite and secondary olivine), whereas talc- and chlorite-schists contain lawsonite pseudomorphs, clinozoisite, light-green amphibole, rutile, apatite and rare quartz. Foliation inside the LSZ generally dips 20° to 40° to the W, and rotates to the W-SW in the area around Ghincia Pastour and Lago Superiore. The mylonites usually show internal chaotic geometries with dragged, disharmonic folds (particularly around blocks and slices) progressively turning into mylonitic shear bands near the shear zone boundaries. Blocks of eclogite-facies gabbros, eclogitic metasediments and massive serpentinite (the first type

Figure 33

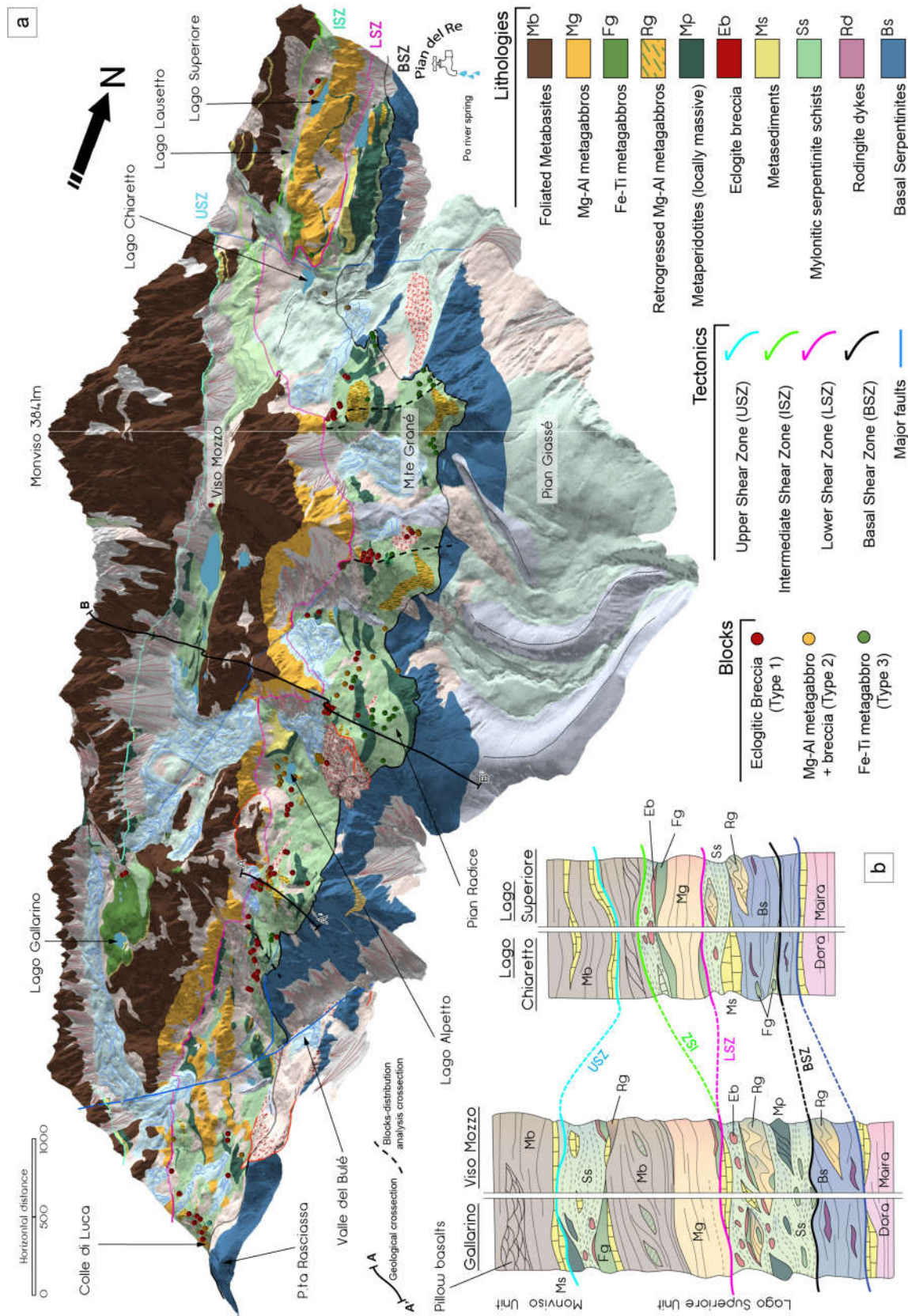


Figure 33: (a) 3D rendering of the geology of the southern portion of the Monviso metaophiolite. Black full-lines represent the traces of the geological cross-section AA', BB', dashed lines are the sections across the Lower shear zone (LSZ) used for the evaluation of block distribution inside the shear zone (more details in Fig. 4b).

(b) Detailed stratigraphic logs across the Lago Superiore Unit (LSU) and the Monviso Unit (MU). From South to North the analyzed sectors are Gallarino, Viso Mozzo, Lago Chiaretto and Lago Superiore. For further details refer to the geological map presented in SMI.

being the most abundant) are embedded in the talc and tremolite-rich serpentinite matrix of the LSZ.

The ISZ cuts across the topmost part of the gabbroic sequence and extends for over 4 km from the Lago Superiore area to the north flank of Viso Mozzo, where it connects to the LSZ and pinches-out under the cover of Quaternary glacier deposits (*Figure 33a and SMI*). Its thickness varies between 1 and 10 m and contains much less serpentinite matrix than the LSZ. Fe-Ti metagabbros outcropping along the ISZ directly at the top of Mg-Al metagabbros (notably in the Lago Superiore area; *Figure 33a, b and SMI*) underwent mylonitization during eclogite-facies deformation, leading to the formation of a characteristic planar fabric dominated by an omphacitic clinopyroxene, garnet and rutile assemblage (Philippot & Van Roermund, 1992). Eclogitic omphacite crack-seal veins, which occasionally crosscut these mylonitized gabbros, are believed to form by incremental opening associated with mylonitization (Philippot and Kienast, 1989).

Structural characteristics, petrography and distribution of the blocks inside the LSZ (and partly the ISZ) are described and discussed in the next paragraphs.

4.3. Field mapping, sampling and methodology

In order to perform an exhaustive characterization of eclogite-facies blocks disseminated in the shear zones developed inside the LSU of Monviso meta-ophiolite, we adopted a “multi-scale”

approach combining detailed fieldwork and meticulous structural and petrographic analysis of collected samples, as described below.

4.3.1 Field mapping of Monviso meta-ophiolites

A new geological map of the area was compiled (Map *SM1*, with 3D model in *Figure 33a*), with a particularly detailed mapping of shear zones crosscutting the LSU (in particular the LSZ) and of the different block types disseminated inside. All field mapping was based on the 1:10.000-scale maps from the Regional Geographic Office of Piedmont (Italian CTR maps).

Four specific lithostratigraphic sequences analyzed along the strike of the LSU are presented in *Fig. 3b* in order to illustrate the important lithostratigraphic lateral variations inside the Monviso meta-ophiolite slice. Detailed logs and structural study were also performed on selected metasedimentary outcrops (West of Alpetto lake and Pra Fiorito Valley; *SM3*) in order to compare structures and compositions to those observed in mafic blocks.

4.3.2 Mapping of blocks: block nature and distribution

We performed a detailed field mapping of the different kinds of blocks, in particular Fe-Ti metagabbro blocks (more detail in section 4), to determine their distribution and representativity inside the LSZ (in particular) and ISZ. To overcome misinterpretation in block position due to erosional problems (i.e., blocks displaced by landslides; e.g., in the upper Bulé valley or north of Rocca del Lu; *Fig. Figure 33a and SM1*), we used trigonometric calculations to re-locate the 3D position of blocks inside the LSZ across 5 preserved cross-sections (only for blocks whose position in the shear zone was preserved, as attested by intact primary contacts with the serpentinite foliation; *Figure 33a and SM1*; see *SM4* for details).

On **SM5** are provided the detailed location, dimensions and structural characteristics of more than 180 blocks (for mapping, we considered a minimum blocks diameter of 1 m). Most of these are brecciated blocks, for which clast and matrix composition and relative proportions were also characterized.

4.3.3 Structural and image analysis of eclogitic brecciated blocks

A structural study at the outcrop scale was performed on brecciated blocks to characterize the rupture planes and was completed by image analysis on dedicated softwares. On fresh eclogite-facies brecciated blocks, we measured (1) block length, width and height, (2) the clasts vs. matrix relative volumetric abundances, (3) the dimension and shape ratio of clasts, (4) the angle of misorientation between clast elongation axes or, where possible, between different clast foliations and (5) the number of clasts of different lithological composition.

Careful in-loco drawings and photographs were then analyzed using FiJi© image-analysis software (*Schindelin et al., 2012*) to retrieve clast areas, perimeters, angles of maximum elongation axis, aspect ratio and roundness. The last parameter was recalculated as adaption of the Waddel's sphericity, as suggested by Mort and Woodcock (2008). Automated clast detection was not feasible due to the poor color contrast between different clasts and matrices, so all clast contours were first manually outlined (paint software) and photographs converted to grey-scale images.

4.3.4 Microstructural and chemical analysis of clast and matrix: analytical techniques

55 samples of brecciated blocks were drilled inside clasts, matrix, and at clast/matrix contacts for subsequent structural and chemical analysis. The microstructural study at the thin section scale was performed using both optical microscope and SEM (Zeiss Supra 55VP associated to SSD

detector PTG Sahara for EDS analysis; ISTE_P, UPMC). Mineral chemical compositions were then analysed by EPMA (CAMECA FIVE and SX100) at CAMPARIS (UPMC, Paris), with analytical conditions for spot analysis of 15kV, 10 nA, wavelength-dispersive spectroscopy (WDS) mode. Used standards were Fe₂O₃ (Fe), MnTiO₃ (Mn, Ti), diopside (Mg, Si), CaF₂ (F), orthoclase (Al, K), anorthite (Ca) and albite (Na).

4.4. Block types and distribution within shear zones

4.4.1 - Eclogitic metagabbros in the LSZ

• Block types

Two end-member lithologies make up the metagabbro blocks distributed in the LSZ: the Fe-Ti metagabbros, with the classical omphacite + garnet (+ rutile +/- lawsonite) paragenesis, and the lighter colored Mg-Al metagabbros with (generally chromium-rich) omphacite and clinozoisite. Their morphology, structure and mineralogy allows to classify the blocks into three different groups:

(1) Type 1 blocks are made of completely brecciated metagabbros and are the most representative and spectacular of the eclogitic bodies dispersed in the LSZ (62% of mapped blocks, Min Vol. 0.05 m³, Max Vol. 2613,81 m³; see *SM4*, 5, 6). They present a peculiar clast-in-matrix structure (*Fig. Figure 34b, c and d*), with clasts almost exclusively made of mylonitic Fe-Ti metagabbros with rare Mg-Al gabbros (10% of modal amount), cemented by an omphacite-rich matrix (+/- garnet and lawsonite). Matrix proportions vary, from block to block, from less than 10 vol.% to up to more than 50 vol.%. Dimension and extent of rotation of the clasts are also variable (for details, *SM4*, 5, 6).

(2) Type 2 blocks (22% of mapped blocks, Min Vol. 1.51 m³, Max Vol. 125663.71 m³) are made of unbrecciated, foliated Mg-Al metagabbros showing strong internal mylonitization and complex folding. They locally embed up to 5 m thick unbrecciated boudins of Fe-Ti metagabbros (*Figure 34e, f, g*). Although relatively rare (only 3% of the mapped blocks; see *SM4, 5, 6*), there are some large hm-scale slivers of Type 2 blocks (Colle Di Luca: B196; Punta Murel: B169; Lago dell'Alpetto: B7; *SM7*). In both cases, Type 2 blocks foliation is in places abruptly truncated by planes of brecciated Type 1 Fe-Ti metagabbros (*Figure 34e, f, g and h*). Noteworthy, these Fe-Ti breccia planes always bound the hm-scale Type 2 blocks on their western flank (*Figure 35a, b*; i.e., facing the Mg-Al metagabbro cliff, dipping 20° to 60° to the W; *Figure 33a, SM7a, b, c, d*) and are absent on the other side.

At the outcrop-scale, the clast-in-matrix structure of eclogite breccias of Type 1 and Type 2 blocks is made of mylonitic clasts rotated to variable degrees and cemented by interstitial matrix (*Figure 34c, d*), with structures comparable to those observed at the micro-scale (i.e., discordant mylonitic foliation underlined by rutile beds; see below). (3) Type 3 blocks are characterized by finely-foliated to massive, unbrecciated Fe-Ti metagabbro blocks (16% of mapped blocks, Min Vol. 1.56 m³, Max Vol. 6.00 m³). Coarse grained fabrics are preserved in the core of the largest blocks (> 10 m³, e.g., Pian Radice area) and consist in almost undeformed coronitic garnet (< 6 mm) crystallizing around megacrystals of omphacite (< 8 mm), which were interpreted as pseudomorphs after magmatic pyroxene or plagioclase (Lombardo et al., 1978; Pognante & Kienast, 1987; Philippot et al., 1992; Groppo et al., 2010; Angiboust et al., 2011). All blocks are coated by late, variably thick metasomatic rinds formed at the expense of the eclogite-facies matrix (*Figure 34b*).

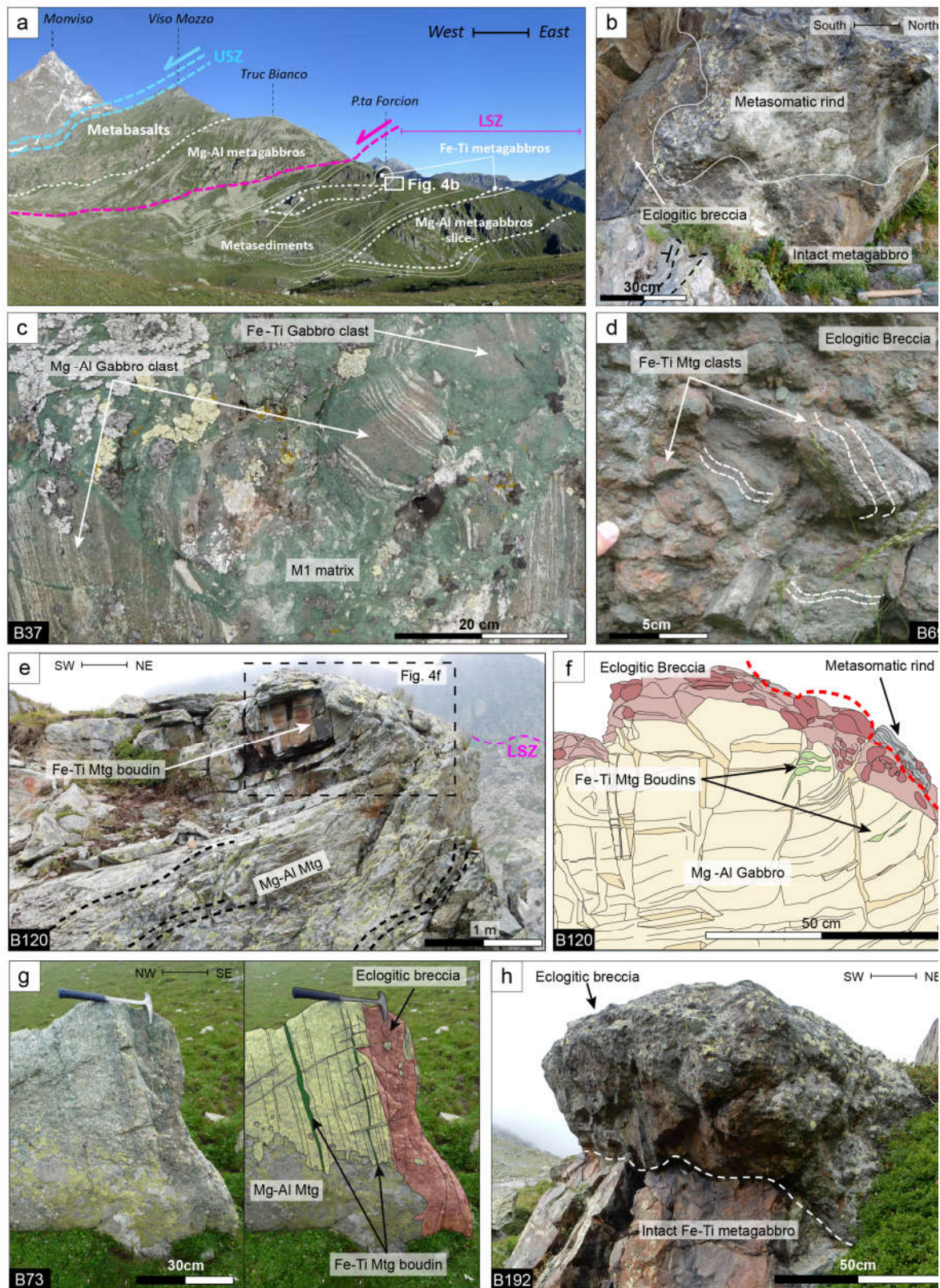


Figure 34

Figure 34: (a) Panoramic view from Pian Radice to the North (Viso Mozzo). We enlightened the internal structural pattern of the LSU with the big detached slices of Mg-Al metagabbro dispersed in the LSZ antigorite-schists matrix.

(b) Detail of a Fe-Ti metagabbro outcrop at the base of the Mg-Al metagabbros constituting the Truc Bianco cliff. Notably, the intact Fe-Ti metagabbro is surrounded by a breccia layer with thickness up-to 50 cm, locally strongly metasomatized. Sampling location of specimen LSZ 63-15 (Fig. 7d).

(c) Typical clast-in-matrix appearance of eclogite-facies breccia on fresh surface. Here the rotated metagabbro clasts are cemented by omphacite-rich matrix (M1). Veins in the clasts are filled by fibrous omphacite \pm apatite. Block B37, NW of Alpetto.

(d) Typical appearance of eclogite breccia with strong weathering patina. The clast-in-matrix structure is still visible, with appreciable clasts rotation enlightened by foliation planes. Block B69, Punta Murel.

(e-f) Example of a folded, mylonitic, eclogite-facies Mg-Al metagabbro unconformably cut by eclogite-facies breccia planes. Serpentine-talcschists metasomatization is focused on the breccia matrix. Block B120, north of Punta Murel.

(g) Typical m-scale Type2 block. The eclogitic breccia develops crosscutting (here at low angle) the pre-existing mylonitic foliation of the intact Mg-Al metagabbro. To be noted the Fe-Ti boudins in the intact metagabbro. Block B73, Prá Fiorito valley.

(h) Transition from intact to brecciated rock recorded in a single Fe-Ti metagabbro block. Here the breccia thickness reach-up 80 cm. B192, south of Colle di Luca.

• **Metagabbro block distribution within the LSZ**

Detailed mapping along the 11 km-long LSZ suggests a non-chaotic distribution of the metagabbro blocks (*Figure 35a and SMI*): Type 1 and Type 2 blocks preferentially crop out in the intermediate-to-upper part of the shear zone, whereas unbrecciated Type 3 blocks are restricted to the lower part of the LSZ (*Figure 35b*).

Block distribution in the shear zone also depends on the volume of the blocks (*Figure 35b*): the largest Type 1 breccia blocks (80% of mapped Type 1 blocks, average volume $> 50 \text{ m}^3$) are restricted to the upper part of the shear zone, whereas smaller blocks (20%, with average volume of 10 m^3) are spread in the first half of the shear zone. Most Type 2 blocks (76 %) and all Type 1 blocks are located stratigraphically above the big slivers of retrogressed Mg-Al metagabbro of Punta Murel, Colle di Luca and Alpetto Lake (Type 2). Unbrecciated Type 3 blocks, which are

restricted to a 30-100 m thick-band at the base of the LSZ, show a general volume increase towards the serpentinite sole, with

eclogitic bodies reaching volumes of 6 m³ SW of Monte Granè (*Figure 35b*; more details in *SM5*).

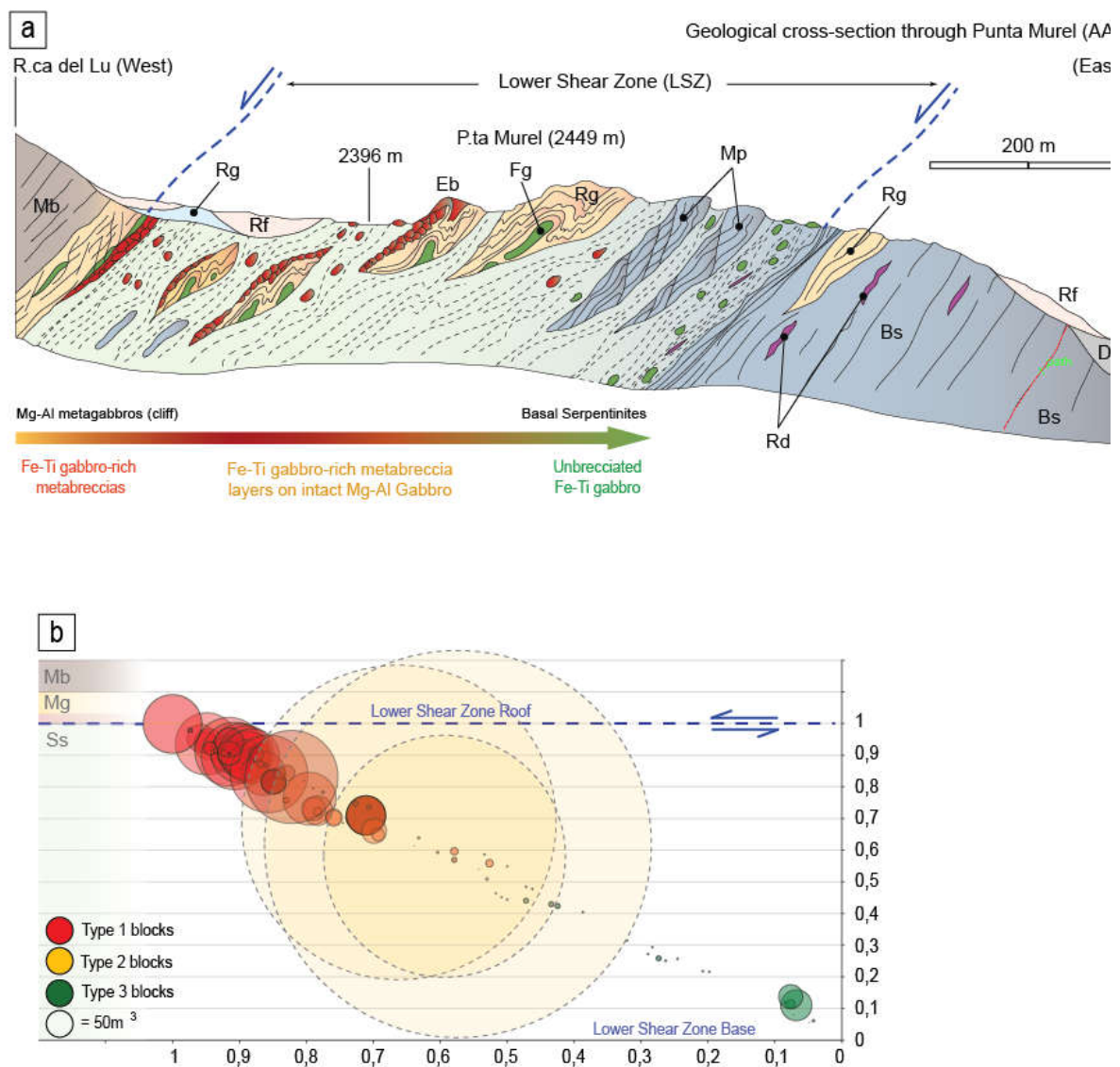


Figure 35

Figure 35: (a) Geological cross-section across the Lower Shear Zone (Punta Murel area). We enlightened the ordered distribution (dip towards West) of the breccia planes in the detached Mg-Al metagabbros slices dispersed in the LSZ. Unbrecciated Fe-Ti metagabbro blocks are concentrated at the base of LSZ.

(b) Diagram showing the distribution of metagabbro blocks inside the LSZ. The larger part of eclogite breccia blocks (Type 1) outcrops in the upper part of LSZ, above the Mg-Al metagabbro slices, with the unbrecciated Fe-Ti metagabbro blocks (Type 3) located at the base. On X-axis the normalized horizontal distance of blocks from the base of LSZ and on Y-axis the normalized vertical distance of blocks from the base of LSZ.

4.4.2 Serpentinite, metasedimentary and jadeitite blocks in the LSZ

Several massive serpentinite blocks and slivers are disseminated in the lower portion of the shear zone (Figure 33a, b and SM1), associated to rounded, unbrecciated Fe-Ti metagabbro blocks (Type 3 blocks) and rare boudins of metasomatized rodingite.

Meter-scale lenses of metasediments are also dispersed within the LSZ, decreasing in abundance from N to S. Large slivers (up to 90 m thick) were only observed in Lago Superiore, Pra Fiorito and Alpetto area (Figure 33a, b and SM1). Metasediments are calcschists and marbles metamorphosed under eclogite facies P-T conditions. Large slivers preserve evidence for alternations of metadolostones, quartz-mica-rich sandstones, garnet-lawsonite-chloritoid-paragonite-rich micaschists and meta-conglomerate strata. The latter, frequently clast-supported, are composed of mm to dm (< 50 cm) clasts of gabbro, basalt and peridotite mixed with a strongly deformed sedimentary matrix (Fig. SM3a, b). Clasts are well rounded and elongated (aspect ratio up to 4), often boudinaged (Fig. SM3c, d) and indicative of strong deformation (e.g., bodies West of Alpetto Lake or in the upper Pra Fiorito Valley). For example, the W-dipping metasedimentary sliver outcropping in the Pra Fiorito Valley (Figure 33a and SM1) shows three clast-supported and four matrix-supported fining-upward conglomerate layers (Fig. SM3e), with a progressive decrease of serpentinite and relative increase of (meta) basaltic clasts from base to top of the outcrop. Metasomatism and mylonitization of the metasedimentary matrix leads to massive growth

of antigorite and talc at the expense of paragonite, omphacite, albite and preexisting chlorite (Fig. SM3c, d).

In the LSZ are also found rare meter-size blocks of jadeitite (especially in the upper Bulé valley and Colle di Luca; see Castelli et al., 2002 and Lombardo et al., 1998 for details). Nevertheless their origin is unclear: the lack of primary contacts with the shear zone mylonite and their uneven distribution in the LSZ may suggest quaternary erosion of the upper Mg-Al metagabbro cliff and the subsequent dissemination of this blocks in the LSZ.

4.4.3 Comparison with block types and distribution in the ISZ

Rare, m-scale Type 1 brecciated blocks crop out chiefly on the western and eastern side of Lago Superiore (*Figure 33a and SM1*). Interestingly, these blocks stratigraphically overlay the Fe-Ti gabbro sills intruded in the eclogitic Mg-Al metagabbros outcropping south-east of the Lausetto Lake, following a stratigraphic scheme also observed in the USZ (*Figure 33b*). Moreover, meter-scale metabasaltic blocks (hanging wall of the ISZ) are found in the ISZ together with scarce metasedimentary blocks. In the southern part of the shear zone, for example North-East of Chiaretto Lake (Fig. SM1), big slivers (up to 60 m long) of massive serpentinite and metasediments are scattered. The latter shows a strong deformation with N/S to NW/SE-trending major fold axis and W-verging fold limbs describing clockwise Z-shaped W-verging parasitic folds. The presence of allocthonous serpentinitized metaperidotite and metasediment slivers in the ISZ suggests the disruption of the preexisting ophiolitic sequence along this shear zone (*Figure 33a, b and SM1, SM2*).

4.5. Brecciation patterns

4.5.1 Outcrop scale structural patterns

The structural study of breccia horizons was limited by the small size ($80\% < 5$ m) of most blocks that do not preserve the full width of breccia planes and by the widespread ultramafic metasomatic coating that hinders the block surfaces. Nevertheless, several blocks from the LSZ exhibit the complete transition from intact metagabbros to breccia cores (*Figure 36a, b, c*): five Type 2 blocks were chosen among them to conduct a detailed structural analysis (in Prà Fiorito valley, north of Alpetto Lake and in the upper Bulè Valley; *Fig. SM1*). Type 2 blocks usually present only one single brecciation horizon, more rarely multiple brecciation planes (*Figure 36d, SM7e, f*), sharply truncating the preexisting eclogite-facies mylonitic foliation (*Figure 34e, f, g*). More than 80% of analyzed clasts have an area smaller than 10 cm^2 and 90% of the clasts in breccia horizons are $< 30\text{ cm}^2$, with a clear power-law distribution (*Fig. SM6c*).

In complete breccia planes, the rim to core sequence is characterized by a strong decrease in clast size and increase in clast rotation angle, clast roundness and matrix vs clast amount (*Figure 36*). The progressive transition from intact rock to crackle, mosaic and finally chaotic-breccia zones in the Fe-Ti breccia planes (*Figure 36a, b, c*) is similar to the classic rim-to-core sequence observed in tectonic breccias (Sibson, 1987; Jébrak, 1997; Mort et al., 2008):

(1) near the rupture surfaces, crackle breccia layers (10-30 cm thick) are characterized by very angular clasts (*Figure 36b*) detached from the fault walls by a complex array of fractures (*Figure 36a, b*), with limited displacement (≤ 2 cm) and almost no rotation. Eclogite clasts, locally with diameters up-to 40 cm, exhibit exploded-jigsaw texture (Sibson, 1986). Matrix represents only 10 vol%.

(2) textures progressively shift to mosaic breccia textures (20-50 cm thick, *Figure 36c*), with a higher matrix content ($< 45\%$ of total volume, with up to 1cm thick matrix layers; Fig. *Figure 36a, c*), smaller clasts (< 20 cm) and slight clast rotation ($< 10^\circ$).

(3) Breccia core portions (20-50 cm thick, “chaotic breccia s.l.”) are matrix supported ($> 55\%$ of total volume). The clasts are smaller (more that 80% of clast < 5 cm²), have aspect ratio < 2 and are randomly oriented (*Figure 36c*), giving rise to chaotic breccia fabrics. The transition from crackle to chaotic breccia shows also a progressive increase in the modal amount of Fe-Ti metagabbro clasts vs Mg-Al metagabbro clasts (*Figure 36a*), the latter absent from breccia cores.

The analysis of the orientation of the maximum-elongation axis of the clasts with respect to the inferred rupture planes (*Figure 36e* and, for comparison, *SM7f*) reveals that in each single breccia horizon, the clast orientations are not totally random: there are preferred orientations, particularly around $20^\circ \pm 10^\circ$ and $70^\circ \pm 10^\circ$ (*Figure 36e*). On the contrary, taking into account all the breccia planes present in one block (when multiple, *Figure 36d*), clast distribution is random, with angles ranging from 0° to 180° (Fig. *SM7f*). In most cases, rotated clasts were cemented after brecciation by a newly-formed matrix. Textural and compositional characteristics of the clasts and the four successive matrix types observed are described below.

Note that in the ISZ, only 4 small brecciated metagabbro blocks were observed (Type1) and thus none of them record a full brecciation plane.

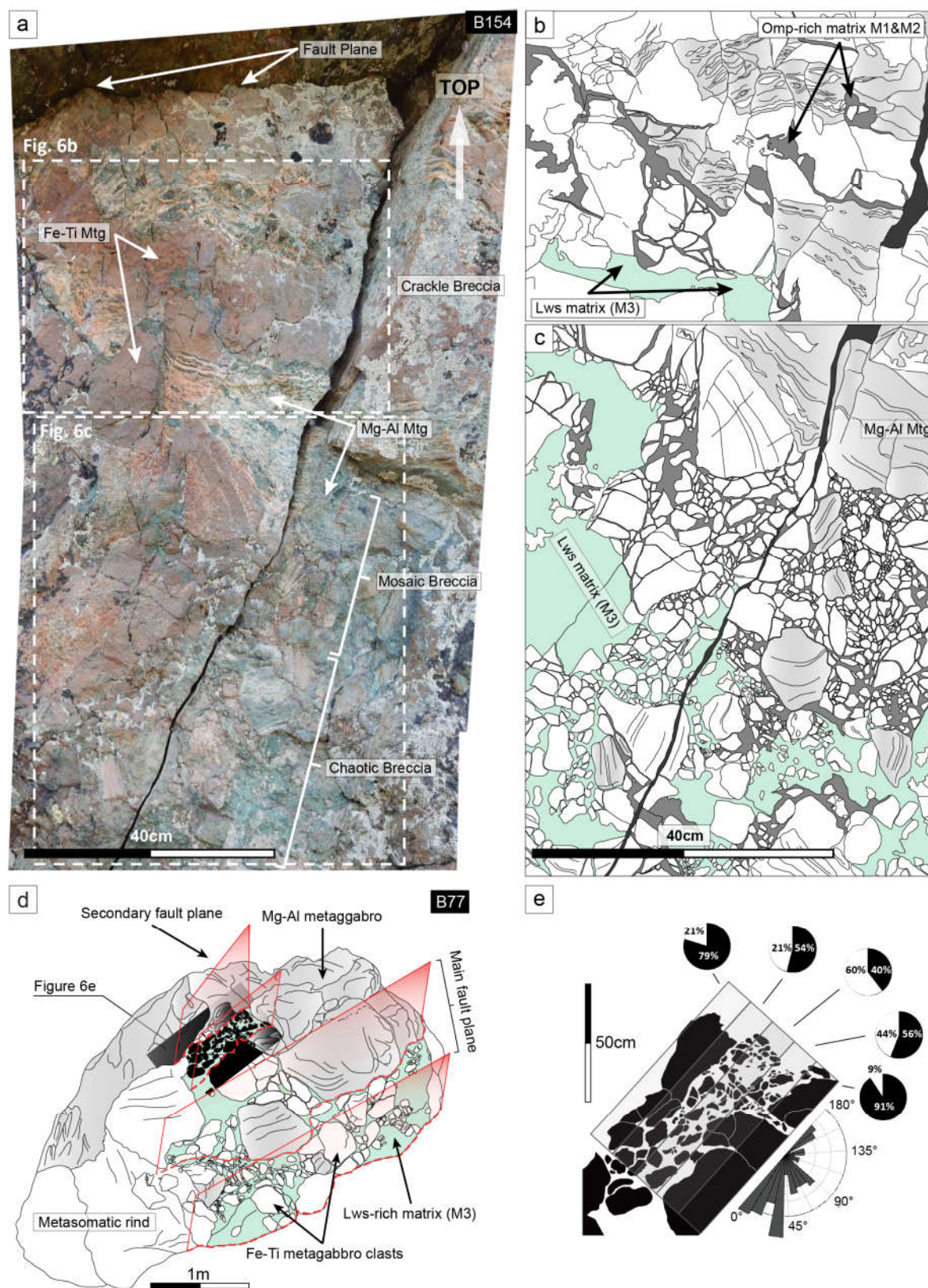


Figure 36

Figure 36: (a) A fully preserved eclogite-breccia fault-plane.) Breccia fabrics show the transition from crackle breccia (at the top) to chaotic breccia (at the core), according to the definitions of Mort and Woodcock (2007). Block B154, Pra Fiorito valley.

(b-c) schematic drawing of the clast-in-matrix structures observed in preserved eclogite-facies breccia planes. Used color-code: Fe-Ti metagabbro clast (white), Mg-Al metagabbro clasts (light gray), Omphacite-rich matrix (dark gray), Lws-rich matrix (light green). Block B154, Pra Fiorito valley.

(d) Sketch of an eclogite-facies breccia block characterized by multiple rupture surfaces. Black area locates Fig. 6e. Original photo of the block in supplementary material SM3a. Block B77, Pra Fiorito Valley.

(e) Schematic sketch of the minor breccia plane in the block B77 with the evaluated volumetric percentage of clasts (black) vs matrix (white) on 5 equal-area sectors. In the inset, the orientation of the maximum elongation axis of the clasts dispersed in the matrix with respect to the single minor breccia plane. Only clasts with $AR > 2$ were analyzed.

4.5.2 At the decimeter to millimeter scale: different types of clast and matrix

In brecciated eclogite-facies blocks (Type1), the clasts are constituted by Fe-Ti metagabbro (90% of modal amount) and rarer Mg-rich metagabbros (mostly close to the unbrecciated rock, 10% of modal amount). Mg-Al metagabbro clasts show the same fabrics and composition than Mg-Al metagabbros constituting the western cliff of the LSZ (Figure 33a) and forming most of Type 2 blocks, whereas mylonitized Fe-Ti metagabbro clasts are comparable to the Fe-Ti metagabbro boudins embedded in Type 2 blocks. The mylonitic foliation of the Fe-Ti gabbro clasts is locally crosscut by omphacite-rich veins (Figure 37a) up-to 1 cm wide, which locally include host-rock fragments. Opening geometries vary from crack-seal to tension gashes, similar to geometries of veins crosscutting the Lago-Superiore Fe-Ti metagabbros (Philippot et al., 1991; Spandler et al., 2011). Some of these veins are crosscut by the matrix sealing the clasts, and thus predate the brecciation event (Veins I; Figure 37a), while others (Veins II) crosscut both clasts and matrix, clearly postdating the brecciation event.

In these brecciated metagabbro blocks, clasts are partly sealed by a matrix whose amount increases from rims to cores of breccia levels (*Figures 34c, 36a, and 37*); crosscutting and textural relationships allow distinguishing four successive matrix types (*Figure 37*):

(1) At the transition between intact rock and crackle brecciated layers, slightly rotated clasts are surrounded by anastomosed, sub-millimetric domains of finely crushed grains ($< 100\ \mu\text{m}$) of Fe-Ti metagabbros (called crushed breccia hereafter).

(2) Such domains are sealed by small amounts of a light green omphacitic cement (hereafter called M1, *Figure 34c*), whose amount increases (up-to 1 cm-thick mantles around clasts; *Figure 36a, b*) while crushed breccia progressively disappears from the inner to outer levels of crackle breccias.

(3) Along the crackle-mosaic breccia transition (*Figure 36a, b, c*), M1 matrix progressively turns into another omphacite- matrix type (M2), which also contains garnet visible in hand-specimen (*Figure 37a*).

(4) In the inner portion of brecciated layers (i.e., chaotic breccia fabrics), crosscutting relationships show that a late matrix M3 postdates both M1 and M2 (*Figures 36a, b, c and 37b*). M3 is the most abundant matrix type (*Figure 37e*) and is characterized by impressive euhedral lozenge-shape pseudomorphs after lawsonite ($< 2\ \text{cm}$; *Figure 37b, c*). Noteworthy, all these matrices lack any evidence of crystal-plastic deformation.

At the contact with the antigorite-rich matrix embedding the blocks in the LSZ, blocks are rimmed by a hydrated metasomatic rind that can locally reach 0.5 meters thick (e.g. in Lago Superiore, Pta. Forcion and Colle di Luca; *Figure 34b*). This metasomatic replacement affects both clasts and matrix, and thus postdates brecciation. Matrix zones are more strongly affected, however, and a complex set of sub-millimeter scale veins filled with hydrous minerals nucleate in

the retrogressed matrix and radially crosscut the surrounding clasts (e.g., *Figure 37d*). The degree of ultramafic metasomatism rapidly decreases from block rims to cores, clearly suggesting an external fluid-assisted metasomatic event postdating both brecciation and block dismembering in the LSZ.

Note that the scarce brecciated metagabbro blocks sampled in the ISZ show similar structures (i.e., clasts locally crosscut by veins and embedded in matrix) but only small amounts of M1 and M2 matrices (*Figure 37a*). Indeed, no extensive M3 lawsonite-rich matrix was observed in the poorly developed brecciated layers of these rocks.

All the structural relationships between clasts and matrices described above are summarized in *Figure 37e*.

Figure 37: Meso-structures of eclogite breccias. (a) Fibrous eclogitic vein (Omp + Apt) developed in an eclogite-facies Fe-Ti metagabbro mylonitic clast. Coarse-grain Omp + Grt matrix (deep-green color) seals all the previous structures. Block B110, Intermediate Shear Zone (West of Lago Superiore). (b) Eclogitic metagabbro clasts (evident the mylonitic foliations) sealed by Lws-rich matrix. Noteworthy, in the upper-center part of the picture, the occurrence of a clast composed by reworked eclogite-facies breccia (mylonitic metagabbro clasts cemented by Omp-rich matrix M1). Block B45, South of Punta Murel. (c) Mylonitic eclogite-facies clasts of Fe-Ti metagabbro sealed by Cr-rich ex-Lws matrix. Ex-Lws crystals locally reach-up lengths of 1cm. Block B50, South of Punta Murel. (d) Polished sample of eclogite breccia evidencing the crosscutting relationship between mylonitic clasts, the Omp + Grt matrix (M2) and the metasomatic rind mineralization (Tlc + Chl + Grt + Amph ± Ca-rich Diop). The darker areas (mainly developed in the matrix portions) are Chl/Amph-rich recrystallization linked to late-stage retrogression under green-schist condition. Sample LSZ 63-15, from the base of Truc Bianco cliff (Fig. 4b). (e) Schematic reconstruction of the structures developed in blocks with fully-preserved transition from intact rock to breccia layers. Such type of blocks correspond to the “Type 2” described in the text (e.g. the big sliver of Punta Murel -B69- or the smaller blocks B154 in Pra Fiorito valley).

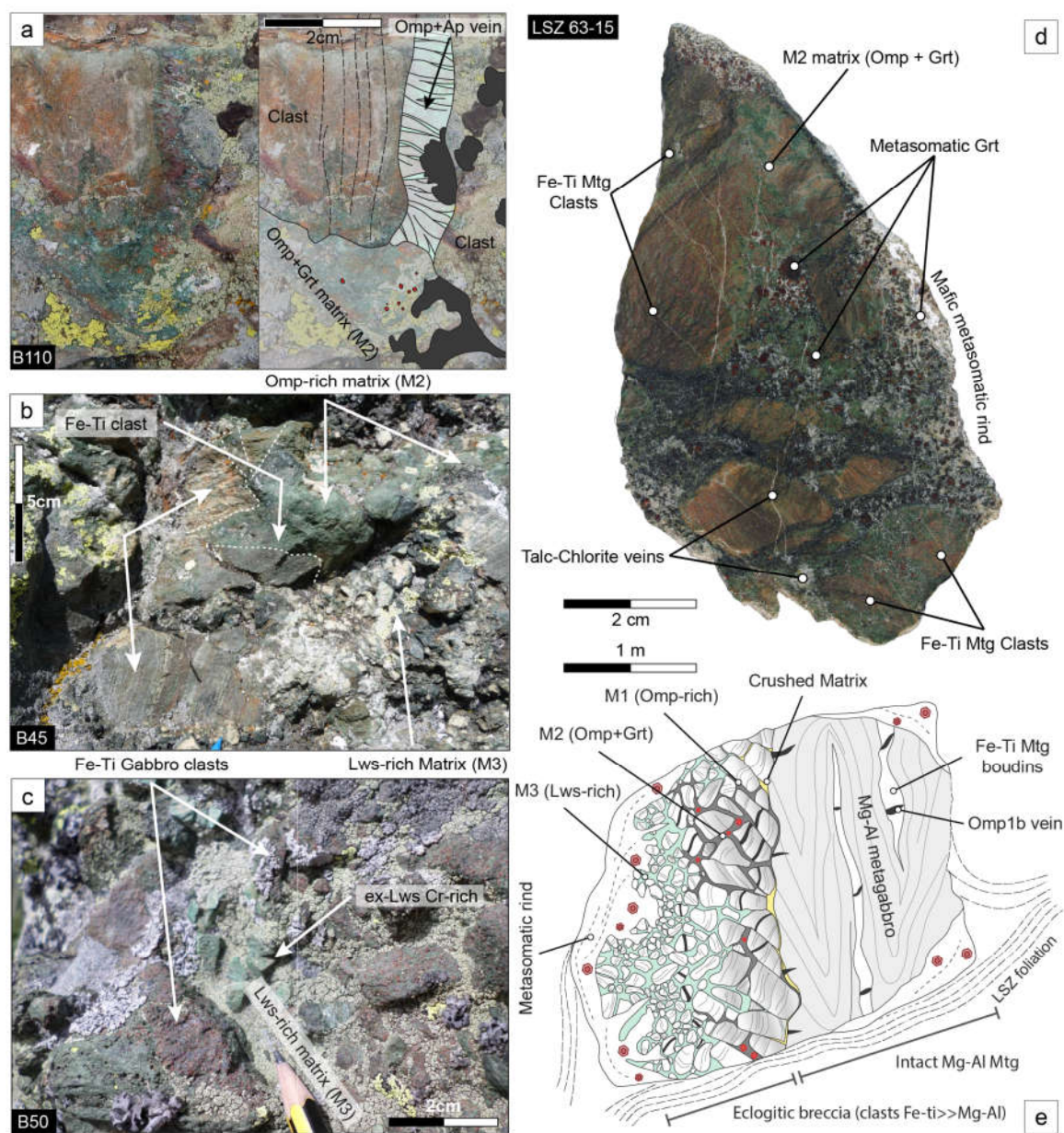


Figure 37

4.6 Clast and matrix: mineralogy and microstructure

4.6.1 – Clast mineralogy and microstructure

Fe-Ti metagabbro clasts are mainly composed of omphacite (up to 60 vol.%) garnet (35 vol.%), and rutile (*Figure 38a, b; Table 2*), i.e., the classical eclogitic paragenesis in mafic rocks. Euhedral omphacite and rutile crystals underline a strong mylonitic foliation. In particular, rutile aggregates, grown at the expense of magmatic ilmenite, locally form polycrystalline ribbons up-to 70 μm -thick aligned in the mylonitic foliation (*Figure 38a*). Sub-idioblastic garnets (200-500 μm) show conspicuous zoning under the microscope, with darker cores and lighter rims (*Figure 38a*). Folded omphacite crystals and rutile trails are included in garnet cores (and rims to a lesser extent; *Figure 38a, b*), thereby underlining garnet syn-kinematic growth. Local occurrence of randomly distributed square or lozenge-shape patches filled with fine grained ($< 20 \mu\text{m}$ size, *SM8a*) clinozoisite and white micas are interpreted as pseudomorphs after lawsonite crystals. Foliation planes folded around these aggregates suggest that lawsonite crystallization was pre- to syn-kinematic with respect to Fe-Ti metagabbro ductile deformation, and thus coeval with the P-T peak eclogitic paragenesis. Other accessory minerals are sub-idiomorphic apatite, randomly distributed acicular glaucophane crystals ($< 1 \text{ vol. } \%$ in these rocks), rare quartz (included in garnet cores) and small paragonite crystals ($< 2 \text{ vol. } \%$, $< 50 \mu\text{m}$ long) parallel to the main foliation (*Table 1*). Locally, sub-mm-sized deep-green porphyroclasts embedded in the foliation are interpreted as relict crystals of magmatic clinopyroxene completely re-equilibrated as omphacite.

The rare Mg-Al metagabbro clasts are made of mm-thick bands of deep-green omphacite alternating with whitish clinozoisite horizons (up-to 1.5 cm; *Figure 34c*). Glaucophane and pseudomorphs after lawsonites are occasionally found in the eclogitic foliation of these clasts

(Table 2). Although garnet is absent in the Mg-richest lithologies, sub-millimetric garnet-rich layers are frequently observed inside gabbro layers showing a composition intermediate between Fe-Ti and Mg-Al metagabbros.

Clasts are locally crosscut by two vein generations, which are both mainly filled with omphacite and secondary apatite (Figure 37a and Figure 39a).

Table 2: Summary of eclogite-facies assemblages, their relative abundance and associated chemistry in eclogitic breccia blocks

		Omp	Grt	Lws	Rt	Czo	Ap	Na-Amp	Ca-Di	Ph	Tlc	Chl
Clasts	Fe-Ti clast	++	++									
	(Chemistry)	(Omp1a+Omp1b)	(Grt1a+Grt1b)	(rare)†	++		(rare)					
	Mg-Al clast	++	(rare)									
	(Chemistry)	(Omp1a+Omp1b)	(Grt1a+Grt1b)	(rare)†	+	++	(rare)			(rare)		(rare)
Clasts	Vein I	++										
	(Chemistry)	(Omp1b)			+		+					
	Vein II	++	(rare)									
	(Chemistry)	(Omp2b)	(Grt2b)							(rare)		
Matrices	Crush Matrix	++	++									
	(Chemistry)	(Omp2a+Omp1a/b*)	(Grt2a overg. on Grt1)		+		+					
	M1	++										
	(Chemistry)	(Omp2b>Omp2a-Omp1a/b)										
Matrices	M2	++	+									
	(Chemistry)	(Omp2b>>Omp2a-Omp1a/b)	(Grt2b)	+						(rare)		
	M3	+	+									
	(Chemistry)	(Omp2b)	(Grt2?)	+								
Matrices	Metasom. Rinds		+									
	(Chemistry)		(Grt3)				(rare)	+	+	+	++	+

† Pseudomorphs after lawsonite (microcrystalline Czo, Ph and Chl) and garnet (Chl aggregates with banded rutile trails)

* Relict crystal fragments derived from clasts and dispersed in vein/matrix

Adopted abbreviations for rock-forming minerals are from Whitney and Evans (2010). *Omp*: omphacite, *Grt*: garnet, *Lws*: lawsonite,

Rt: rutile, *Czo*: clinozoisite, *Ap*: apatite, *Na-Amp*: sodic amphibole, *Ca-Di*: calcic diopside, *Ph*: phengite, *Tlc*: talc, *Chl*: chlorite

4.6.2 - Matrix mineralogy and microstructure

Table 2 summarizes the mineralogy of the four successive matrix types wrapping the eclogitic Fe-Ti and Mg-Al clasts of brecciated metagabbros (Fig. *Figure 37e*).

In rare cases, the absence of matrix between clasts in the levels of crackle breccia nearest to the intact rocks (*Figure 36b*) results in micrometric garnet offset (*Figure 38d, e*) and pressure-solution-like fabrics at sharp clast-clast contacts, with progressive deflection of clast mylonitic foliation, and strong grain-size reduction and reorientation of mylonitic omphacite (*Figure 38f*).

In the outer part of breccia planes (i.e., at the contact with intact rock), clasts are separated by sub-millimetric domains of crushed breccia, composed of sharply-fractured crystals of omphacite, garnet, apatite and rutile, i.e., the mineral assemblage present in the surrounding clasts. There, garnet crystals are fragmented and rounded, whereas rutile and omphacite are crudely reoriented parallel to clast boundaries, with a strong grain size reduction for omphacite (down to 10 μm long vs 200 μm in clasts; *Figure 38f*).

M1 matrix consists of almost pure deep green omphacite (euhedral crystals up to 200 μm -long), with few euhedral apatite crystals (*Figure 39b*), for both LSZ and ISZ samples. Scarce sub-millimetric corroded rutile and pyrite overgrown by iron oxides are dispersed close to clast-matrix borders. Contacts between clasts and matrix are usually sharp (*Figure 38c, d*), but FEG-SEM quantified maps exhibit complex radial infiltration patterns of M1-like omphacite inside clasts (*Figure 39b*). This fabric, characterized by clasts irregularly fractured and cemented by M1, is also well visible at the outcrop scale (*Figure 34c*).

M2 matrix assemblage is omphacite-dominated too, but contains additional garnet and rare rutile and lawsonite pseudomorphs (for LSZ and ISZ; *Figure 39c*), i.e., the classical eclogitic paragenesis in mafic rocks. Omphacite crystals are usually tabular and locally up-to 300 μm -long.

Euhedral garnet (*Figure 39c*) is clearly less fractured than in mylonitic foliation of the clasts, but also shows zoning, with inclusion-rich darker core rimmed by inclusion-poor mantles. Garnet inclusions consist in omphacite and rare rutile. Accessory minerals are titanite and rare deep-blue acicular glaucophane, the latter crystallizing as interstitial phase between omphacite and defining a weak foliation plane. These lawsonite pseudomorphs are indeed surrounded by the following greenschist-facies assemblage: tremolite-actinolite (constituting more than 40% of M3 matrix) + chlorite + calcite + albite + epidote.

However, textural arguments show that this greenschist assemblage replaced a former eclogite-facies paragenesis: occurrence of rare relicts of sub-mm omphacite inside tremolite-actinolite crystals, mm-thick tabular rutile in textural equilibrium with lawsonite crystals, and chlorite filling large (up to 0.2 mm) rounded domains with preserved rutile trails (*Fig. SM8b, c*) are suggestive of garnet pseudomorphs. Therefore, the mineralogy of the M3 matrix may have been very close to that of M2 (i.e., classical eclogitic paragenesis), but with a much higher proportion of lawsonite.

Contrary to the sharp contacts observed between clasts and M1 or M2 matrix, clasts contacts with M3 matrix are smoothed by the overgrowth of the greenschist facies assemblage (*Figure 39d*). This late greenschist retrogression affected all matrix types, but was much more pervasive in M3, ($M3 > M2 > M1$), indicating that retrogression was limited in matrices with less hydrous-rich phases

Figure 38

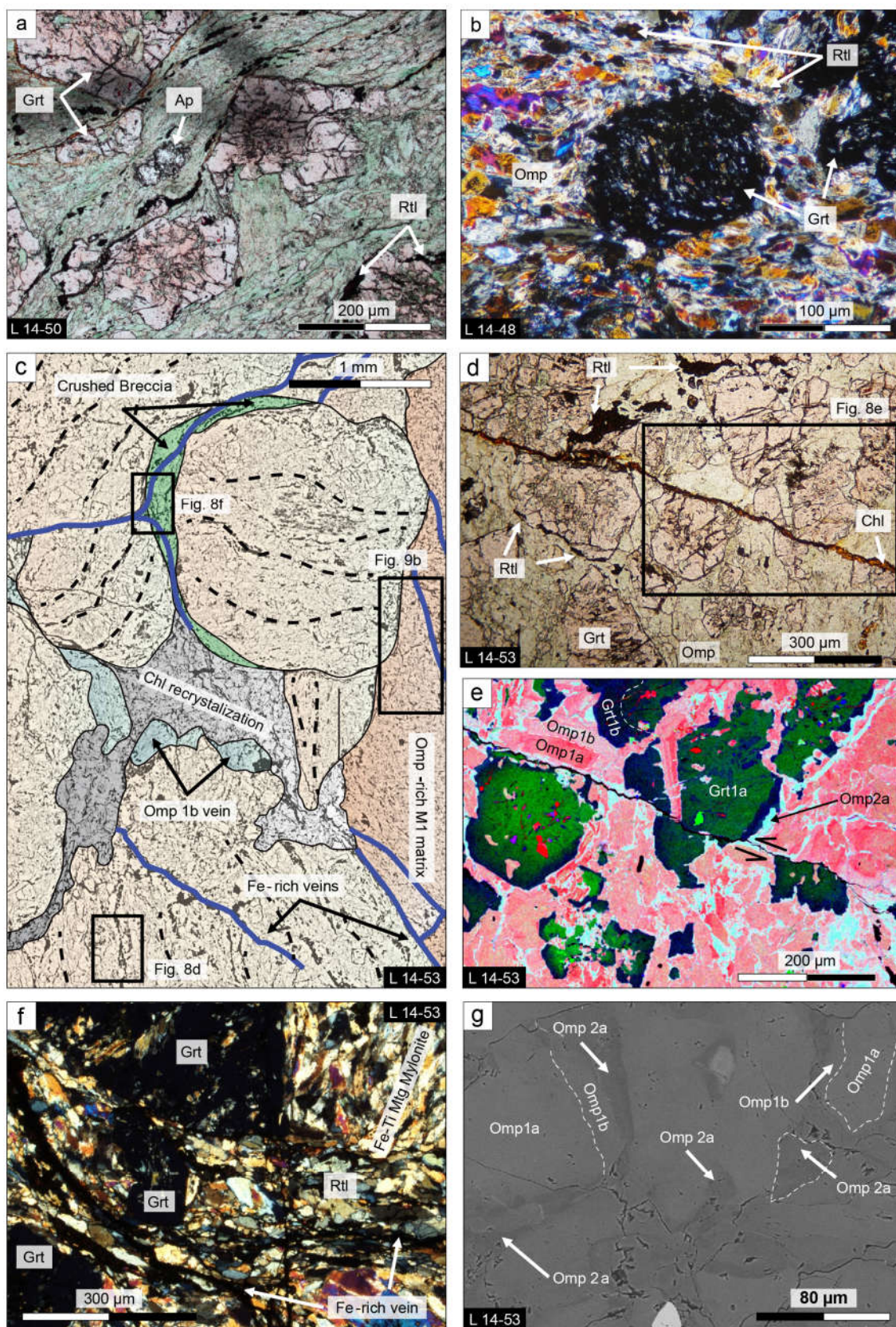


Figure 38: Microstructures of eclogite breccias as seen under optical polarizing microscope, if not otherwise indicated. Pictures (a, c, d) plane polarized light; (b, f) cross polarized light. (a) Mylonitic eclogite-facies foliation of a Fe-Ti metagabbro clasts (sample L14-50, LSZ). (b) Syn-kinematic garnet with preserved omphacite trails inclusions growth in a mylonitic Fe-Ti metagabbro clasts (sample L14-48, LSZ). (c) Clast-in-matrix fabric with evident clasts rotation and eclogite-facies matrix crystallization, totally comparable to those observed at the meso-scale. Sample L14-53, LSZ. (d) Micrometric garnet and omphacite offset along omphacite-bearing microfractures. Sample L14-53, LSZ. (e) FEG-SEM quantified Ca (Green), Na (Red) and Mg (Blue) map of the off-set garnets in sample L14-53 evidencing an apparent displacement of 285 μm . (f) Microfractured Omp, Grt and Rtl crystals crudely re-oriented in the “crushed-breccia” domains in-between clasts. Notably, garnet shapes are sharp-edged. Later-stage Fe-rich veins preferentially infiltrate in these domains. Sample L14-53, LSZ. (g) SEM image of the complex zonation of omphacite crystals in the “crushed-breccia” domains, with mylonitic Omp1a and Omp1b sealed by a third generation of omphacite Omp2a. As observed for garnets, crystals have sharp-edged shapes. Quantified EPMA map of these domains are presented in Fig. SM9a.

(i.e., M1). External fluid ingression is nevertheless attested locally by late veins and interstitial domains (up-to 5 millimeter thick) between clasts filled with greenschist fan-shaped chlorite aggregates (*Figure 38c*). Fe-rich veins (up to 50 wt.% FeO, thickness up-to 50 μm) nucleate in these domains and crosscut the samples, preferentially following the clast-clast or clast-matrix boundaries, again clearly postdating brecciation. In several blocks from LSZ, especially in Type2, a complex array of fibrous glaucophane veins (thickness up-to 2 cm) crosscut both clasts and matrices, postdating the brecciation but predating the greenschist events.

4.6.3 - Metasomatic rinds

At their contact with the surrounding antigorite schist forming the matrix of LSZ, the mafic eclogitic breccias are strongly affected by a widespread ultramafic metasomatism (*Figure 34b*), which affects preferentially matrices. The pre-existing eclogite-facies assemblages are replaced by a mesh of talc and chlorite, a new-generation of brown metasomatic garnet, acicular amphibole and diopside plus very rare phengite. Lawsonite pseudomorphs (now replaced by epidote + paragonite) in textural equilibrium with the surrounding talc and metasomatic-stage chlorite are also observed, together with relicts of omphacite crystals and dispersed rutile. A complex set of sub-millimeter scale veins of syntaxial talc, diopside and chlorite radiates from the hydrated mafic domains into the clasts (*Figure 37d*). Similarly to block matrices, metasomatic rinds were locally replaced by a later, cross-cutting greenschist facies assemblage (chlorite, tremolite-actinolite, calcite, rare quartz).

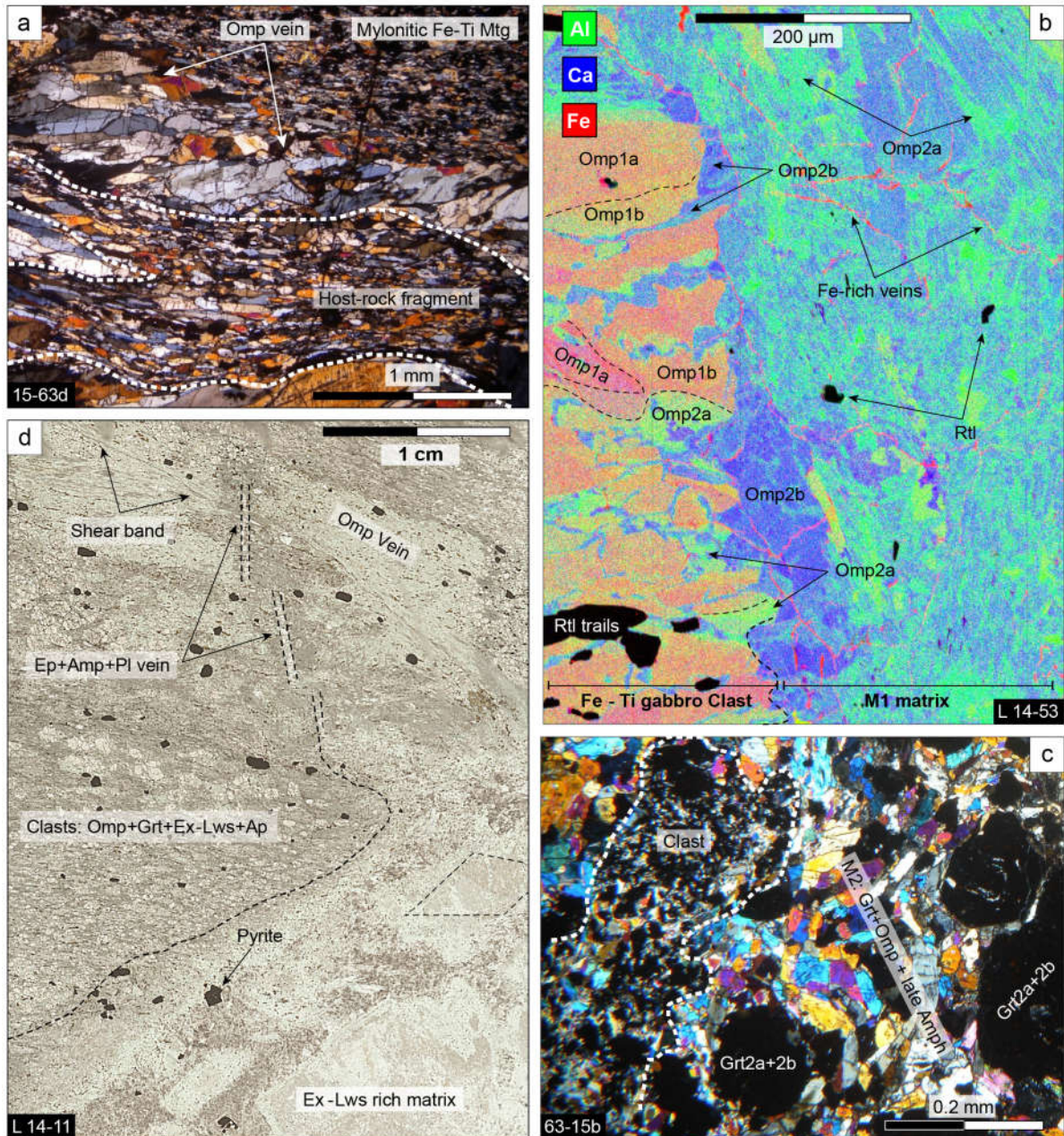


Figure 39: Microstructures of eclogite breccias as seen under optical polarizing microscope, if not otherwise indicated. Picture (b) plane polarized light; (c, d) cross polarized light. (a) Photomicrograph of a sheared omphacite veins growth inside a mylonitic Mg-Al metagabbro clast. Sample 63-15d, LSZ. (b) FEG-SEM quantified Ca (Blue), Fe (Red) and Al (Green) map of the transition between a mylonitic Fe-Ti metagabbro clast and the omphacite-rich matrix M1. In evidence the infiltration-like geometries of Omp2b inside the clast departing from M1. Sample L14-53, LSZ. (c) Photomicrograph of the big hypidiomorphic omphacite crystals and inclusion-poor garnets constituting the bulk of M2 matrix. Note the sharp contact clast-M2 matrix. Sample 63-15b, LSZ. (d) Photomicrograph of the transition between an Mg-Al metagabbro clast and ex-Lws rich matrix M3. The unsharp contact clast-matrix is linked to the massive green-schist recrystallization that partly obliterated the pre-existing structures. Sample L14-11, LSZ. See Fig. SM8a-b for more detail on matrix M3 paragenesis.

4.7 Mineral chemistry

Both clast and matrix mineral compositions are given in Table 2.

4.7.1 Clast mineral chemistry

In the mylonitic Fe-Ti metagabbro clasts, the first generation of omphacite (Omp1a, $\text{Di}_{45}\text{Jd}_{30}\text{Ae}_{25}$; *Figure 40a, b*) forms the bright cores of large, partially dismembered porphyroclasts. These are rimmed by a second omphacite generation (Omp1b, $\text{Di}_{40}\text{Jd}_{38}\text{Ae}_{22}$; *Fig. 10a, b*) crystallizing also as newly formed crystals aligned in the mylonitic foliation. Garnet is also zoned (*Figure 38a*), with dark cores (Grt1a, $\text{Gr}_{24}\text{Prp}_5\text{Alm}_{71}$; *Figure 40c*) and light rims (Grt1b, $\text{Gr}_{17}\text{Prp}_{13}\text{Alm}_{70}$; *Figure 40c*); garnet cores are locally affected by complex radial fractures (*Fig. SM9b*) filled and sealed by Grt1b compositions. Smaller garnets ($< 100\ \mu\text{m}$) with Grt1b composition are also scattered in the foliation. Interestingly, garnet cores (Grt1a) are full of Omp1a inclusions, whereas garnet rims (Grt1b) only contain few inclusions of Omp1b, showing that omphacite and garnet compositions evolved jointly during mylonitization.

In the outer-most clast domains, a third generation of interstitial Al-rich omphacite (Omp2a, peak composition $\text{Di}_{46}\text{Jd}_{48}\text{Ae}_6$; *Fig. 10a, b*) crystallized as rims around the previous omphacite crystals with complex, dissymmetric patterns (*Figs. 8g, 9b, SM8d*). Interestingly, omphacite crystallizing in the pressure-solution planes promoting micrometric garnet offset (*Figure 38d, e*) are in equilibrium with Omp2a (*Figure 40a, b*). Finally, a later generation of omphacite (Omp2b, $\text{Di}_{60}\text{Jd}_{30}\text{Ae}_8$; *Figure 40a, b*), locally replacing all previous omphacite generations, is restricted to less than 1mm at the clast-matrix contact; Omp2b crystals seem to follow radial infiltration patterns from the surrounding matrix into the clasts (*Figure 39b, SM8d*). At the clast borders,

garnet (Grt1a-b) is also overgrown, on the matrix side, by a later garnet generation (up-to 60 μ m-thick mantles, SM8e), richer in FeO and MnO (Grt2a: Grs₁₈Prp₂₈Alm₅₄, Figure 40a).

Veins I (i.e., crosscutting clasts but predating brecciation; Figure 37a) are filled with Omp1b omphacite, whereas omphacite in Veins II (crosscutting both clasts and matrix; Figure 39c) presents an Omp2b composition.

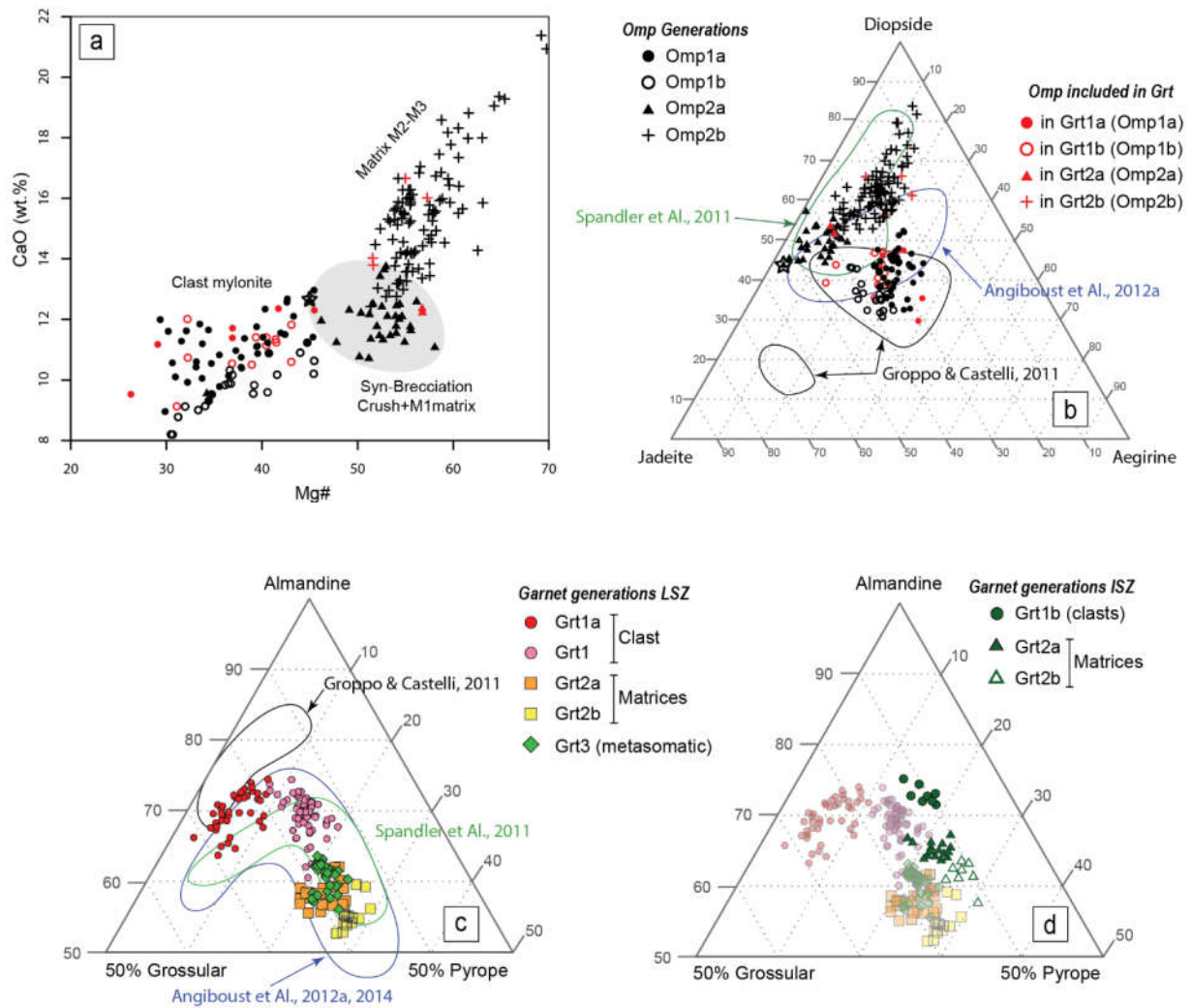


Figure 40: EPMA composition of selected minerals: a) Mg# [$\text{MgO}/(\text{MgO}+\text{FeO}) \times 100$] vs. CaO (wt.%) in LSZ omphacites; b) Ternary-plot (Jad-Diop-Aeg) for selected omphacite from the LSZ; c) Ternary-plot (Grs-Alm-Prp) for selected garnets from the LSZ; d) Ternary-plot (Grs-Alm-Prp) for selected garnets from the LSZ vs. selected garnets from the ISZ. Comparison with previous data (Fig. 10 b, c) from Groppo & Castelli (2011); Spandler et al. (2011); Angiboust et al. (2012a, 2014) is shown.

4.7.2 Matrix mineral chemistry

In the crushed-matrix domains, fragmented omphacite and garnet crystals show compositions similar to clast minerals (i.e., Omp1a cores rimmed by Omp1b compositions and Grt1a rimmed by Grt1b; *Figure 40*). These crushed minerals are locally sealed by interstitial Omp2a omphacite (*Fig. 8g*). Here, fragmented Grt1 garnet in contact with Omp2a layers are rimmed by thin (<20 μm) Mn-rich mantles with Grt2a compositions (*Figure 39b*). Locally, anastomosed layers (< 70 μm thick) of Omp2b seal these microdomains of crushed minerals (*Fig. SM9a*).

The M1 matrix (omphacite only) is composed by about 60 vol.% of Omp2b (*Figs. 9b, 10a, b* and *SM8d*) crystals surrounding flake-shaped remnants of corroded, Al-richer Omp2a crystals (35 vol.%), resulting in an extremely intricate mesh of both generations. The remaining 5 vol.% is composed by crystals of rutiles and rare flakes of Omp1 omphacites close to the clast borders.

M2 matrix is largely made of tabular omphacite crystals of Omp2b composition, with subordinate Omp2a (mainly as crystal cores) and relics of Omp1a-b (*Figure 40a, b*); composition of Omp2b is similar to the one analyzed in clasts, crushed and M1 matrix but locally noticeably enriched in Cr_2O_3 (up to 0.35 wt.% vs < 0.1 wt.% in the mylonitic clasts; *Table 3*). Garnet cores (Grt2a composition, *Figure 40c*) are rimmed by almandine-poorer garnet (Grt2b; $\text{Gr}_{\text{S}20}\text{Pr}_{\text{P}25}\text{Al}_{\text{M}45}$). Both are enriched in Cr_2O_3 (up to 0.30 wt%, *Table 4*, with peculiar sectorial enrichment pattern: *SM8f*) compared to clast mylonitic Grt1 observed in crushed and M1 matrix (up-to 0.1 wt.%). In Grt2a, the included omphacite have Omp2a compositions, while Grt2b appear to be equilibrated with inclusions of Omp2b (*Figure 40b*).

Analysis of M3 matrix eclogite-facies assemblage is difficult due to the strong greenschist retrogression (*Figure 39d*). The rare omphacite relicts dispersed in the tremolite-actinolite mesh have an Omp2b composition (*Fig. 10a, b*). No analysis could be made on lawsonite and garnet

which are now completely pseudomorphosed by clinozoisite and chlorite, respectively. In the metasomatic rinds, the newly-formed garnet is almandine-rich (Grt₃: Grs₁₇Prp₂₁Alm₆₁, *Figure 40c*).

In the next pages:

Table 3: representative major element analysis (wt.%) of omphacite crystals subdivided by microstructural domains.

Table 4: representative major element analysis (wt.%) of garnet crystals subdivided by microstructural domains.

Table 3: representative major elements analysis (wt.%) of omphacite subdivided by microstructural domains

Analysis	Omphacite included in Garnet								Grt offset planes*		Mylonitic Fe-Ti clasts				
	23 / 1	24 / 1	32 / 1	33 / 1	12/15b	12 / 15	19 / 1	20 / 1	13	14	249 / 1	250 / 1	33 / 1	34 / 1	38 / 1
Sample	1450	1453	1450	1453	6315	6315	6315	6315	1453	1453	1450	1450	1450	1450	1450
Generation	Omp1a (In Grt1a)	Omp1a (In Grt1a)	Omp1b (In Grt1b)	Omp1b (In Grt1b)	Omp2a (In Grt2a)	Omp2a (In Grt2a)	Omp2b (In Grt2b)	Omp2b (In Grt2b)	Omp2a	Omp2a	Omp1a	Omp1b	Omp1b	Omp1a	Omp1b
SiO ₂	55.18	54.90	56.10	55.88	57.16	57.16	56.34	55.47	56.52	55.84	55.33	55.43	54.50	55.32	55.51
TiO ₂	0.08	0.03	0.02	0.02	0.03	0.08	0.06	0.00	0.10	0.34	0.06	0.04	0.06	0.05	0.09
Al ₂ O ₃	6.44	6.47	8.25	7.83	9.16	9.22	6.17	4.26	10.32	8.92	7.80	8.89	8.80	6.95	9.02
Cr ₂ O ₃	0.08	0.01	0.04	0.06	0.04	0.07	0.11	0.01	0.08	0.06	0.06	0.04	0.04	0.03	0.02
FeO	14.52	13.95	10.07	10.62	6.39	6.41	8.83	8.83	5.90	7.14	11.02	11.33	10.46	10.18	9.82
MnO	0.07	0.06	0.07	0.07	0.08	0.06	0.18	0.06	0.04	0.10	0.01	0.04	0.03	0.07	0.08
MgO	5.18	5.72	7.14	6.89	8.40	8.42	9.40	10.80	8.17	7.88	6.34	5.66	6.07	7.78	6.20
CaO	9.53	11.18	11.24	11.41	12.22	12.35	14.03	16.66	11.09	12.49	10.14	9.01	9.88	12.10	9.83
Na ₂ O	8.94	7.61	8.17	7.94	7.37	7.45	6.43	5.15	7.72	7.09	8.45	9.07	8.74	7.44	8.66
Total	100.02	99.93	101.10	100.70	100.84	101.23	101.55	101.24	99.92	99.85	99.21	99.51	98.57	99.92	99.03
Mg#	26.28	29.08	41.49	39.37	56.78	56.75	51.57	55.01	58.07	52.46	36.51	33.33	36.73	43.30	39.18
X _{Wo}	33.88	37.17	38.62	38.87	42.22	42.42	41.09	43.13	40.93	42.90	36.77	34.96	37.25	39.13	37.77
X _{En}	25.61	26.47	34.16	32.69	40.35	40.22	38.31	38.90	41.97	37.69	31.99	30.59	31.87	35.00	33.14
X _{Fs}	40.50	36.36	27.22	28.43	17.43	17.36	20.60	17.97	17.10	19.41	31.24	34.46	30.88	25.87	29.09
Total	100.00	100.00	100.00	100.00	100.00	100.00	100.00	100.00	100.00	100.00	100.00	100.00	100.00	100.00	100.00
X _{Aeg}	34.83	24.48	23.67	22.44	8.37	10.01	17.95	21.00	8.02	9.18	24.81	25.88	28.11	23.54	21.11
X _{Jd}	27.65	27.40	34.15	32.65	37.66	37.77	25.43	17.92	41.54	37.22	33.00	37.10	37.69	29.19	38.10
Wo+En+Fs	37.52	48.12	42.19	44.91	53.97	52.22	56.62	61.08	50.44	53.80	42.19	37.02	34.20	47.27	40.79
Total	100.00	100.00	100.00	100.00	100.00	100.00	100.00	100.00	100.00	100.00	100.00	100.00	100.00	100.00	100.00

*Omphacite crystallizing in the fracture planes resulting in micrometric garnet off-set (Fig. 7d, e)

Analysis	Crushed Matrix						Matrix1				Matrix2				
	205 / 1	207 / 1	209 / 1	210 / 1	46 / 1	48 / 1	201 / 1	202 / 1	203 / 1	205 / 1	50 / 1	59 / 1	60 / 1	68 / 1	69 / 1
Sample	1453	1453	1453	1453	1453	1453	1453	1453	1453	1453	6315	6315	6315	6315	6315
Generation	Omp2b	Omp2b	Omp2a	Omp2a	Omp1a	Omp1b	Omp2b	Omp2a	Omp2b	Omp2a	Omp2b	Omp2b	Omp2b	Omp2b	Omp2b
SiO ₂	57.28	55.57	58.08	58.52	55.73	55.92	56.43	56.31	56.86	56.65	55.48	55.19	55.26	55.72	56.33
TiO ₂	0.02	0.05	0.10	0.04	0.00	0.00	0.02	0.06	0.03	0.05	0.01	0.06	0.09	0.04	0.01
Al ₂ O ₃	7.81	7.64	9.95	9.32	10.44	11.03	6.54	9.46	7.49	8.63	7.71	7.87	7.36	7.58	8.65
Cr ₂ O ₃	0.03	0.00	0.13	0.02	0.00	0.01	0.00	0.07	0.11	0.06	0.20	0.29	0.20	0.44	0.04
FeO	7.68	6.79	6.89	7.04	9.38	10.42	7.81	6.88	7.08	6.33	6.23	6.34	5.11	6.23	6.28
MnO	0.05	0.10	0.02	0.07	0.02	0.00	0.11	0.12	0.08	0.07	0.05	0.02	0.03	0.05	0.04
MgO	8.12	8.91	7.55	7.98	5.25	4.58	9.19	7.66	9.14	7.89	7.63	7.48	8.55	7.71	7.07
CaO	12.43	13.36	11.46	12.10	8.87	7.47	14.03	11.47	13.67	11.76	13.57	13.18	14.28	13.82	12.75
Na ₂ O	6.97	6.52	7.84	7.80	9.34	9.88	6.43	7.67	6.76	7.60	7.04	7.33	6.55	6.98	7.56
Total	100.39	98.95	102.02	102.89	99.04	99.32	100.57	99.48	101.22	99.04	97.93	97.76	97.43	98.58	98.73
Mg#	51.38	56.74	52.28	53.12	55.92	50.51	54.05	53.42	56.38	55.51	55.06	54.11	62.56	55.34	52.97
X _{Wo}	41.76	42.91	41.88	42.09	37.72	33.99	42.51	41.80	42.75	42.39	46.65	46.17	47.30	46.92	46.32
X _{En}	37.96	39.81	38.40	38.60	31.09	28.98	38.75	38.85	39.79	39.61	36.50	36.44	39.39	36.44	35.75
X _{Fs}	20.28	17.28	19.71	19.31	31.18	37.03	18.75	19.35	17.46	18.00	16.85	17.39	13.31	16.64	17.92
Total	100.00	100.00	100.00	100.00	100.00	100.00	100.00	100.00	100.00	100.00	100.00	100.00	100.00	100.00	100.00
X _{Aeg}	5.82	10.88	5.37	8.67	20.31	20.81	13.82	9.88	12.61	9.14	11.49	14.64	9.42	11.16	9.47
X _{Jd}	33.19	32.22	40.80	38.18	43.99	45.54	27.60	39.60	31.11	37.35	35.40	36.05	33.76	34.85	39.24
Wo+En+Fs	60.99	56.90	53.82	53.14	55.71	53.65	38.38	50.52	56.28	53.51	55.11	48.32	56.82	53.98	51.29
Total	100.00	100.00	100.00	100.00	100.00	100.00	100.00	100.00	100.00	100.00	100.00	100.00	100.00	100.00	100.00

Table 4: representative major elements analysis (wt.%) of garnet subdivided by microstructural domains

Analysis Sample	Mylonitic Fe-Ti metagabbro clast										Eclogitic matrices Crushed, M1 and M2										Metasomatic Rinds									
	189 / 1	190 / 1	194 / 1	196 / 1	187 / 1	219 / 1	92 / 1	97 / 1	01-Oct	48 / 6	01-Sep	48 / 7	01-Jan	Jan-18	48 / 2	48 / 14	140 / 13	140 / 14	140 / 15	140 / 16										
Generation	LSZ 1453	LSZ 1450	LSZ 1446	LSZ 1446	LSZ 1453	LSZ 1450	LSZ 1453	LSZ 1453	LSZ 6315d	LSZ 6315d	LSZ 6315d	LSZ 6315b	LSZ 6315b	LSZ 6315d	LSZ 6315d	LSZ 6315b	LSZ 6315b	LSZ 6315b	LSZ 6315d	LSZ 6315d										
SiO ₂	37.66	36.64	36.84	37.96	37.95	37.39	37.43	37.54	38.80	38.44	38.44	38.69	39.02	38.81	38.80	39.13	38.45	38.41	38.17	38.32										
TiO ₂	0.06	0.07	0.09	0.09	0.00	0.05	0.00	0.01	0.03	0.01	0.06	0.04	0.06	0.03	0.06	0.05	0.05	0.04	0.06	0.05										
Al ₂ O ₃	21.08	20.99	20.65	20.41	21.24	21.30	20.94	21.14	21.26	21.84	21.58	21.78	22.07	21.81	21.74	22.36	21.07	20.55	20.95	21.15										
Cr ₂ O ₃	0.03	0.01	0.08	0.02	0.02	0.04	0.00	0.01	0.04	0.15	0.06	0.28	0.11	0.12	0.16	0.07	0.55	0.55	0.57	0.61										
Fe ₂ O ₃																														
FeO	30.22	29.68	30.86	29.79	32.48	30.49	31.18	31.48	27.55	27.07	27.41	27.87	28.65	29.26	26.04	26.46	29.97	29.34	29.70	29.42										
MnO	0.44	0.47	0.43	3.64	0.73	1.18	1.08	1.03	1.22	0.77	0.68	0.56	1.14	1.04	1.08	0.58	0.40	0.26	0.44	0.40										
MgO	2.11	1.58	2.35	0.77	3.89	4.36	4.39	4.36	5.32	6.49	5.22	6.01	6.76	6.85	6.95	7.17	5.01	5.14	5.30	5.46										
CaO	9.74	10.08	8.58	8.51	4.83	4.78	4.98	4.79	7.51	6.21	7.62	5.95	6.74	5.17	6.89	6.46	6.81	6.50	6.69	6.78										
NiO									0.15	0.04	0.11	0.03	0.12	0.03	0.01	0.06	0.08	0.06	0.15	0.03										
Total	101.31	99.55	99.90	101.19	101.14	99.51	99.99	100.37	101.60	101.17	101.20	101.26	102.44	103.09	101.77	102.31	102.44	100.76	102.01	102.18										
Mg numb	6.53	5.07	7.07	2.52	10.69	12.50	12.35	12.16	16.19	19.34	15.99	17.75	20.23	18.96	21.07	21.33	14.32	14.90	15.14	15.66										
Norm Grs	26.76	28.36	23.63	25.86	13.48	13.72	13.91	13.40	20.46	16.90	20.85	16.32	18.04	13.52	18.44	17.26	17.88	17.39	17.46	17.66										
Norm Alm	64.68	65.00	66.60	70.84	70.92	68.38	68.00	68.76	58.33	57.29	58.46	60.14	55.23	59.24	53.88	54.88	62.23	62.38	61.28	60.54										
Norm Prp	8.57	6.64	9.77	3.30	15.60	17.90	18.09	17.84	21.21	25.81	20.69	23.54	26.73	27.23	27.68	27.86	19.89	20.23	21.26	21.80										
X Ca	0.26	0.28	0.23	0.24	0.13	0.13	0.13	0.13	0.20	0.16	0.20	0.16	0.17	0.13	0.18	0.17	0.17	0.17	0.17	0.17										
X Mg	0.08	0.06	0.09	0.03	0.15	0.17	0.18	0.17	0.20	0.25	0.20	0.23	0.26	0.26	0.27	0.27	0.19	0.20	0.21	0.21										
X Fe	0.83	0.63	0.65	0.65	0.89	0.66	0.66	0.67	0.56	0.56	0.57	0.59	0.53	0.57	0.52	0.54	0.61	0.61	0.60	0.59										
X Mn	0.01	0.01	0.01	0.08	0.02	0.03	0.02	0.02	0.03	0.02	0.01	0.01	0.02	0.02	0.02	0.01	0.01	0.01	0.01	0.01										

For comparison, in the brecciated Fe-Ti metagabbros of ISZ, mylonitic clasts display the same Omp1a-Omp1b zonation found in the LSZ, with veins crystalizing Omp1b. In contrast to the LSZ, omphacite of M1 matrix is made of Jd-rich Omp1b (*Figure 40a, b*), whereas M2 matrix is composed by Omp2b in equilibrium with garnet, whose composition is comparable to Grt2a (cores) and Grt2b (rims) but slightly depleted in grossular and almandine (*Figure 40d*). Locally, Cr₂O₃ content of M2 omphacite and garnets is enriched respect to those in M1, clasts and veins (1.02 wt.% vs 0.35 wt.% respectively).

4.7.3 Comparison with other existing geochemical data and interpretations in terms of P-T conditions

The mineral analyses presented in this paper compare well with previously published works on Monviso meta-ophiolite. As shown in *Figure 40b*, the mylonitic omphacite generations (Omp1a cores and Omp1b rims) fall in the same compositional field than mylonitic omphacite analysed by Groppo & Castelli (2011) and Angiboust et al. (2012a), and their trend (i.e., towards higher jadeitic content) likely corresponds to the prograde eclogitic path of the Lago Superiore unit (*Figure 41, steps A-B*).

In mylonitic Fe-Ti metagabbros, peak omphacite compositions of Angiboust et al. (2012a; Di₄₅Jd₄₃Ae₁₂) and Spandler et al. (2011; i.e., host-rock omphacite crystals, Di₄₃Jd₄₇Ae₁₀) correspond to the transition between mylonitic Omp1b and Omp2a in our breccia blocks (i.e., highest jadeite content; *Figure 40a, b*). The onset of eclogitic brecciation, characterized by crushed and M1 matrix formation, is associated to Omp2a crystallization in the LSZ, and to Omp1b in the M1 matrix of ISZ. The onset of the first eclogitic brecciation can therefore be ascribed to peak P-T conditions (*Figure 41, Step C*).

Composition of our Omp2a ($\text{Di}_{46}\text{Jd}_{48}\text{Ae}_6$) is in equilibrium with the omphacite of type1 veins of Spandler et al. (2011), whereas the range of composition of Omp2b (*Figure 40b*) is comparable to that observed by Spandler et al. (2011) for their type2 veins (composed mainly by omphacite + garnet, similar paragenesis of our M2 matrix). The decreasing jadeitic content led us to ascribe them to the beginning of the retrograde path (*Figure 41*).

Compositions of garnet from mylonitic clasts (Grt1a and Grt 1b, *Figure 40c*) are comparable to those described by Angiboust et al. (2012a; e.g. mylonitic Fe-Ti metagabbro) and Spandler et al. (2011; e.g. host rock garnets). Furthermore, breccia-coeval Grt2a and Grt2b are comparable to the garnet crystalizing in type2 veins of Spandler et al. (2011), whereas the almandine-rich metasomatic Grt3 have similar composition to those described by Angiboust et al. (2014) crystalizing in the mafic rinds developed around blocks disseminated in the LSZ. In contrast, mylonitic garnet from Groppo et al. (2011) are slightly richer in almandine (up to +5% Alm); this may reflect bulk-chemical variations among the Lago Superiore unit.

4.8. Discussion

4.8.1 Unequivocal evidence for brecciation at eclogite-facies conditions

Breccia blocks equilibrated at eclogite-facies P-T conditions (i.e., clast and matrix both composed of the classical eclogite facies paragenesis omphacite + garnet + rutile) and disseminated in the Monviso ophiolite LSZ have been interpreted, in the literature, as either eclogitic breccias resulting from brittle rupture at 80 km depth (Angiboust et al., 2012b) or as sedimentary breccias inherited from a Tethyan Oceanic Core Complex (Balestro et al., 2015). The main brecciation structures described here are the following:

(i) all the breccia planes preserved in eclogitic blocks (which are found for ~15 km along strike the LSZ) cut across mylonitic eclogite facies foliation. At the outcrop scale, they cut abruptly, at various angles, the eclogitic foliation made of intact Mg-Al metagabbros and Fe-Ti metagabbro boudins (e.g., Type 2 blocks; *Figure 34e, f, g, h and Figure 36a*). At the thin-section scale, brecciation cuts across syn-kinematic garnet (Grt1 to Grt3; *Figure 38d, e*) and rutile trails aligned along the mylonitic foliation (*Figure 38c, f*).

(ii) eclogitic breccias are almost monogenic (90 % of Fe-Ti metagabbros), and clasts of Mg-Al metagabbros (10 %) are restricted to the rims (20-50 cm zones) of breccia planes crosscutting Mg-Al metagabbros, rapidly disappearing towards the core of breccia planes. This points to a sharp rheological contrast between the Fe-Ti and Mg-Al gabbros (as suggested by Angiboust et al., 2012a).

(iii) within the breccia planes, the peculiar clast-in-matrix structure characterized by strong misorientation of the mylonitic foliation between the rotated clasts postdates the eclogitic foliation of the metagabbros (*Figure 34c, d*). Furthermore, the occurrence in the matrices of typical eclogite facies paragenesis (this study; Angiboust et al., 2012b) testifies that brecciation at eclogite facies conditions too. These geometrical relationships are sketched in *Figure 37e*.

This interpretation can in principle be challenged (e.g., Balestro et al., 2015) by considering that the mylonitization of the gabbros is inherited from an earlier stage of ductile deformation and that the whole brecciation event (whether tectonic or sedimentary) happened at shallow depth prior (and is unrelated) to eclogitization. Such mylonitization followed by shallow brecciation could occur during oceanic detachment (such as the mylonitization of flaser gabbros, during initial rifting stages) or during a former episode of eclogitization followed by exhumation and shallow

brecciation (i.e., before a second eclogitic cycle, as for "yo-yo" subduction; e.g., Rubatto et al., 2011).

There are, however, strong objections to such an alternative interpretation:

1) a sedimentary origin of the breccia can be refuted for the following reasons:

— no sedimentary material is found within the breccia horizons of Fe-Ti metagabbros (e.g., *Figures 34, 37a, b, c, d, 38c and 39b, c, d*);

— these breccias are almost monogenic, whereas those formed by oceanic detachment faults exhuming oceanic core complexes exhibit a larger compositional variety in the fragments (metabasalts, metagabbros, metaperidotites, sometimes embedded in metasediments; e.g. Escartin et al., 2013).

— no mineralogical nor structural evidence for multiple eclogitic cycles (such as "yo-yo" subduction; e.g., Rubatto et al., 2011) has been found in this study nor documented in previous works, making the assumption really unlikely.

— preserved breccia planes advocate for dynamic fracturing, as they record the full, undisturbed classical rim-to-core sequence (Jébrak, 1997; Mort & Woodcock, 2008), from intact metagabbro, to fractured rock, crackle breccia, mosaic breccia and chaotic breccia (i.e., blocks B154, B1 and B77; *Figure 36a, b, c*).

2) tectonic brecciation prior to eclogitization (e.g., during oceanic detachment) is (very) unlikely for the following reasons:

— subsequent eclogitization of both clasts and matrix would have to be static, as the matrix is made of euhedral crystals and lacks foliation: any deformation post-dating brecciation would have resulted in a foliation overprinting both clasts and matrix, which is clearly not the case. Static recrystallization at eclogite facies conditions is very unlikely as nearby eclogitized basalts in the

LSU are strongly, plastically deformed. Within the gabbroic foliation itself, rutile stringers are folded. If the foliation was pre-eclogitic, one would have to accept that former folded ilmenite stringers were perfectly pseudomorphed and statically replaced by rutile. Moreover, a static replacement would have produced strain-free eclogite-facies minerals, whereas occurrence of shape preferred orientation (SPO) of omphacite crystals evidences syn-kinematic crystallization (*Figure 38a, b*).

— the occurrence, in between clasts, of crushed (angular) eclogitic minerals (such as syn-kinematic garnets and rutile trails; *Figure 38c, f*) showing grain size reduction with compositions similar to those of the clasts (*Figure 38a, b; Table 2*), demonstrates that part of the already eclogitized Fe-Ti gabbros was finely crushed during brecciation. Moreover, the existence of successive matrix generations with an eclogitic paragenesis (Omp +/- Grt +/- Lws, *Figure 36a, b, c and 37a, b, c, d*), sharply crosscutting each other is, in our view, the best argument for eclogitic brecciation.

It is therefore possible to univocally ascribe the formation of these Fe-Ti metagabbro breccia blocks to processes occurring at eclogite-facies conditions. Distinct blocks (scattered in both the LSZ and ISZ) nevertheless preserve evidence for earlier disruption. Conglomeratic layers, containing well rounded clasts and bodies of metagabbro, metabasalt and serpentinite, were found in metasedimentary slivers (*Fig. SM3*). In contrast to the above metagabbro breccia, however, clasts are embedded in a strongly deformed mylonitic matrix and the foliation is continuous (even if folded) across matrix and clasts, advocating for the coeval eclogitic mylonitization of former clasts and surrounding matrix. These structures could correspond to pre-alpine sedimentary or tectonic breccias, tentatively ascribed to detachment faulting (Festa et al., 2014; Balestro et al., 2015).

4.8.2 Reconstructing the discrete steps of eclogitic brecciation

Structural/microstructural relationships and mineral chemistry data on breccia matrix and clasts (Angiboust et al., 2012a), together with previous observations from the literature (Philippot et al., 1987; 1990; 1991; Schwartz et al., 2000; Spandler et al., 2011), allow to recognize several episodes in the brecciation process at eclogite facies conditions. Based on the successive omphacite and garnet compositions, these steps can be ascribed to prograde to peak mylonitization (*Figure 41*; Omp2a matching compositions used for published P-T evolutions; Groppo & Castelli., 2010; Angiboust et al., 2012a) and early retrograde stage linked to exhumation (as suggested by the jadeite-poorer Omp2b).

→ Eclogitization and mylonitization prior to brecciation (steps A and B; *Figure 41*)

The Fe-Ti and Mg-Al gabbros (either within the crustal sequence or intruded in the peridotitic mantle) underwent prograde eclogitization up to 530-550°C/23-27.5 kbar (Angiboust et al., 2011) associated to intense mylonitization, as inferred from both collected samples and previous works (Lombardo et al., 1979; Philippot et al., 1987, 1990, 1991; Schwartz et al., 2000; Angiboust et al., 2011, 2012a; Balestro et al., 2014). As testified by the less deformed metagabbros, the pre-existing magmatic clinopyroxene crystals were replaced by Omp1a omphacite associated to rutile (growing after magmatic ilmenite) and coronitic garnet Grt1a (as shown by the foliated trails of Omp1a and rutile included in Grt1a garnet cores; *Figure 38a, b*).

Progressive deformation (step B) led to grain size reduction, fracturing and dismembering of the magmatic clinopyroxene relicts into the newly formed mylonitic foliation and to a new generation of omphacite (Omp1b) crystallizing as rims around Omp1a, while Grt1b synchronously formed around Grt1a garnet cores (with Omp1b inclusions in Grt1b). This is accompanied by the progressive flattening of rutile ribbons in extremely elongated trails parallel to the foliation.

Garnet, especially where segregated into bands or lenses, underwent extensive fracturing (*Figure 38a*, potentially linked to indentation between garnet crystal borders and/or to hydrofracturing (as suggested by Spandler et al., 2011). This step was accompanied by the (probably transient) development of tension gashes and dilatant veins with Omp1b omphacite \pm apatite.

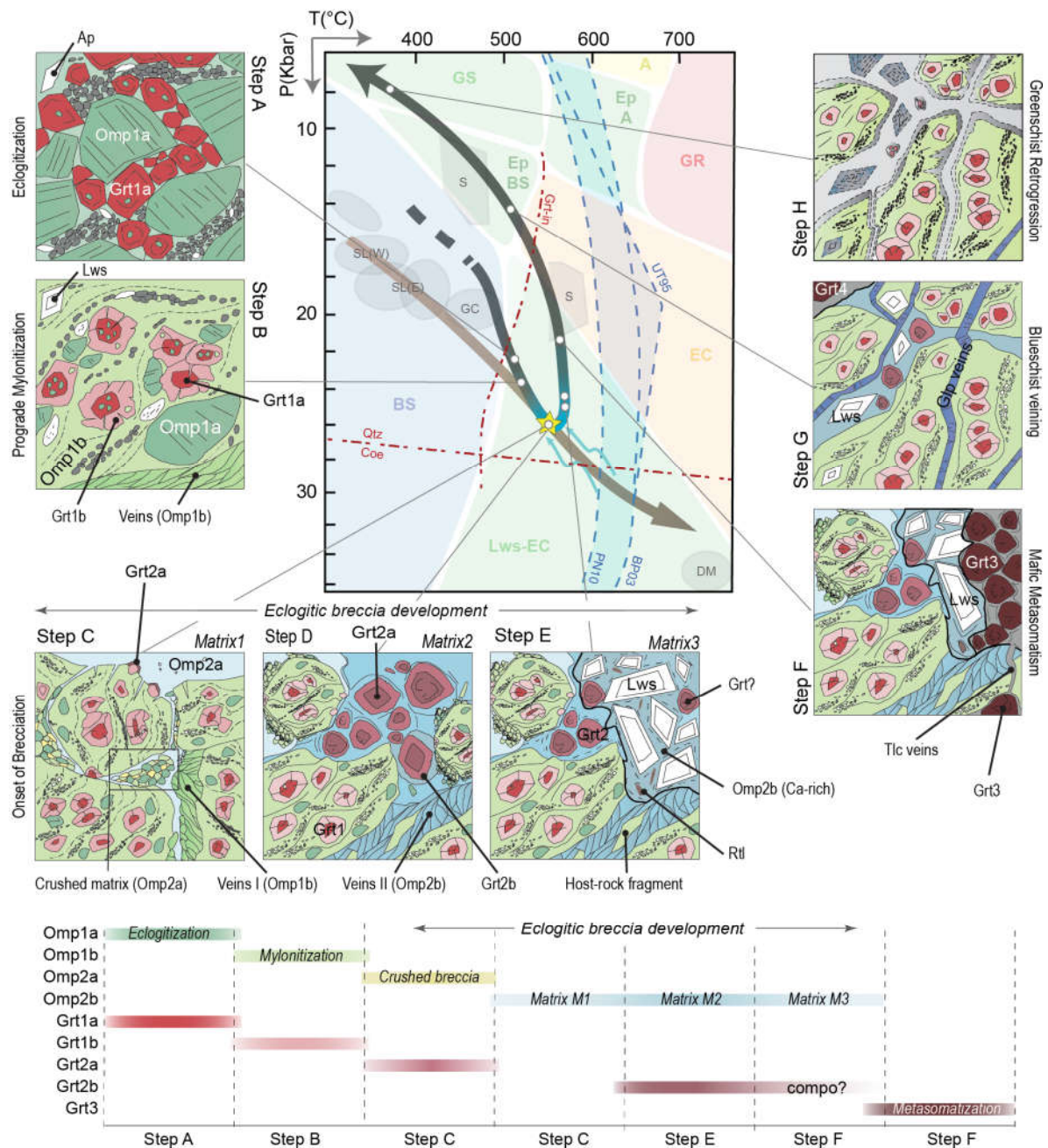


Figure 41

Figure 41: Relative chronology of events (with associated P-T position, from Angiboust et al., 2012) leading to the brecciation of eclogite-facies Fe-Ti metagabbros from the LSZ. Eclogitized igneous texture (step A) are progressively obliterated by mylonitization (step B), with related opening of Omp1b ± apatite veins I. Various amount of hydrous minerals growth at this stage (e.g. Lws). Progressive deformation culminated in the first brecciation event (Step C), with brittle disruption of metagabbros (e.g. formation crackle breccia domains and micro-displacement of garnets), clasts rotation and crystallization of Omp-rich matrix M1. On-going deformation and increasing water-content of circulating fluids lead to the crystallization of matrices M2 (Step D, Omp + Grt) and M3 (Step E, Lws + Omp + Grt). The opening of dilatant veins II with Omp2b ± apatite, either as static or sheared veins, advocate for ongoing shear deformation during step D rather than for hydrofracturation alone. Widespread mafic metasomatism (with crystallization of newly-formed Grt + Tlc + Chl + Amph + Ca-rich Diop) occurs after all the previous events (Step F). Exhumation stages are witnessed by the emplacement of impressive Glp veins (step G) and by the later-stage, massive greenschist retrogression of the matrices eclogitic assemblages. P-T path diagram for the LSU modified after Angiboust et al., 2012.

→ Brecciation (steps C to E)

The first brecciation event (step C) accompanying the relative rotation of clasts of Fe-Ti (and rare Mg-Al) metagabbros is recorded by thin (< 200 µm-thick; *Figure 38f*) inter-clast domains filled with either crushed eclogitic minerals ("crushed matrix") or newly crystallized, idiomorphic omphacite-rich (Omp2a) M1 matrix (with Omp2a composition in LSZ, but Omp1b in ISZ). In both matrix types, this stage is associated to Grt2a overgrowths around mylonitic garnets. In the crushed matrix, fractured and angular omphacite and garnet exhibit strong grain size reduction, obliteration of foliation, and compositions similar to minerals in clasts: all these features show that they correspond to clast pieces crushed during brecciation and subsequently sealed by interstitial omphacite Omp2a (*Figure 38g*) and associated to Grt2a rims (*SM8e*). Newly formed Omp2a and Omp1b (ISZ), which present the highest jadeitic content among all analyzed omphacite crystals, correspond to those ascribed to peak conditions by Angiboust et al. (2012a) and Spandler et al. (2011). Therefore, the onset of brecciation took place at or close to peak P-T conditions.

Crushed matrix domains are nevertheless infiltrated by anastomosed layers (< 70 µm thick; *SM9a*) of Omp2b. Moreover, in M1 matrix, Omp2a seems to be overgrown by Omp2b (*Figure 39b*), both generations forming an intricate mesh, with clast boundaries exhibiting radial-shape

infiltration patterns of Omp2b overgrowing mylonitic omphacite Omp1 (*Figure 39a and SM8d*). All this suggests that both crushed and M1 matrix were later infiltrated by fluids that allowed partial replacement of initial Omp2a by Omp2b omphacite. The same assemblage is also recorded in matrix M2: euhedral Omp2a, locally Cr-rich, is associated to garnets showing Grt2a cores and Grt2b rims (the latter including Omp2b crystals; *Figure 39c*) with sectorial Cr-enrichment patterns. The lower jadeitic content of Omp2b (compared to Omp1b and 2a; *Figure 40a*) and Grt2a low-Mn content suggests that the development of M2 matrix (Step D in *Figure 41*) took place at the onset of the retrograde P-T path. The development of tension gashes and dilatant veins with Omp2b omphacite \pm apatite, either as static or sheared veins (**Fig. 9a**) advocate for ongoing shear deformation during step D rather than for hydrofracturation alone.

A third, volumetrically dominant (80 vol%) lawsonite-rich M3 matrix crosscuts all preexisting structures (Step E *Figure 41*; *Figure 37b, c*). The extreme abundance of lawsonite in M3 (up to ~40 vol% in places), compared to the rather dry assemblages of M1 and even M2, advocates for massive fluid infiltration. Fluids were most probably externally-derived, since no significant dehydration is predicted for Fe-Ti eclogitic metagabbros at such PT conditions (i.e., not until lawsonite breakdown; Angiboust et al., 2011). We speculate that the infiltration of fluids may have been promoted by the first steps of brecciation (steps C and D) by mechanical weakening and porosity increase.

→ Post-brecciation evolution (steps F to H)

Step F corresponds to the extensive ultramafic metasomatism that affected brecciated blocks, and subsequent rind formation (up to 0.5 m thick) at their contact with the antigorite-rich matrix embedding them in the LSZ (*Figures 34b and 37d*). This metasomatic replacement affects both clasts and matrix, and thus postdates brecciation. In metagabbro block rims, the preexisting

eclogitic facies assemblage was replaced by a mafic to ultramafic assemblage (talc, chlorite, metasomatic garnet Grt3, sodic amphibole, diopside, rare phengite and lawsonite pseudomorphs), suggesting an interaction with an ultramafic fluid. The degree of metasomatism rapidly decreases from block rims to cores, suggesting an external fluid-assisted metasomatic event postdating both brecciation and block dismembering in the LSZ: metagabbro brecciated blocks, when embedded in the LSZ matrix, likely interacted with an ultramafic fluid coming from the surrounding serpentinite schist. These mafic rinds are thought to form shortly after peak burial and brecciation, during the onset of exhumation (*Figure 42a*; see also Angiboust et al., 2014).

Steps G and H respectively correspond to the formation of crosscutting cm-thick blueschist veins and to the late-stage retrogression of the eclogite-facies blocks into a greenschist assemblage (i.e., tremolite-actinolite, chlorite, epidote, and mm-thick veins of calcite + albite + quartz + epidote; *Figure 39d* and *SM8b, c*). In M3 matrix, particularly affected by a penetrative retrogression, the massive water release associated with the breakdown of lawsonite into epidote may have partly controlled retrogression progress and allowed for the formation of the greenschist-facies hydrated paragenesis. On the contrary, the dryer matrices (M1 and M2) and the less permeable clasts underwent only partial retrogression at their rims, preserving their pristine eclogite-facies assemblages.

4.8.3 Locus of brecciation and progressive strain localization along the slab interface

• *Strain localization along Fe-Ti gabbro horizons*

Brecciation took place at eclogite-facies conditions preferentially along Fe-Ti metagabbros horizons and in their vicinity, as shown by the largely monogenic nature of breccia blocks. This

suggests that the rupture event affected the most competent layer and/or took place where strong rheological contrasts existed (i.e., along major changes in gabbroic composition).

Field mapping (*Figure 33a, b and SM1*) shows that most of the breccia blocks (88% of Type 2 blocks and all Type 1) are concentrated in the upper part of the LSZ and crop out structurally above the large slivers of Mg-Al metagabbros (*Figures 35a, b and SM2*), all along the strike of the LSZ, from Colle di Luca to Ghincia Pastour (~15 km; *Fig. SM1*). Brecciation therefore either occurred (i) on the Fe-Ti metagabbros located structurally above the Mg-Al metagabbros (and below the metabasalts; i.e., more or less along the ISZ) or (ii) along dykes and sills of Fe-Ti metagabbros emplaced within the Mg-Al metagabbro sequence (*Figures 33b and 42 a, b*). Such Fe-Ti gabbro intrusions, partly rodingitized, are found in the basal peridotite and, more generally, in active slow-spreading oceans such as the Indian Ocean and the Mid-Atlantic ridge (i.e., Lagabrielle et al., 1990, 1997; Lissenberg et al., 2016). Type 3 unbrecciated, coarse grained Fe-Ti metagabbro blocks restricted to the lower part of the LSZ (block size decreasing towards the basal peridotite) may correspond to such sills or dykes intruded into the peridotite sole, and progressively incorporated into the LSZ during shear zone widening.

The observation that Fe-Ti metagabbro brecciation planes included in the Mg-Al metagabbro type 2 blocks and slivers are always located on their upper/western side (*Figures 33b, 34a, 35a, SM1, SM2*), being broadly parallel to the LSZ shear zone walls with W-NW dipping foliations (e.g. Punta Murel, Colle di Luca), advocates for only small displacements and rather supports the second hypothesis: Fe-Ti and Mg-Al blocks would be fragments disrupted within the Mg-Al gabbroic sequence further dismembered and incorporated into the LSZ matrix. Nucleation of brecciation in the ISZ (as envisioned by Angiboust et al., 2012b) would imply km-scale movements and possibly greater disruption.

• ***Progressive strain localization within the slab***

The mechanical behavior of the LSZ through time is shown in *Figure 42*. Brecciation nucleation triggered and controlled strain localization into the Fe-Ti metagabbros (*Figure 42a*, steps I-II), which acted as a major discontinuity. It is suggested that the formation of M1 matrix represents the onset of strain localization at about peak P-T conditions and testifies to changes in porosity/permeability, while the formation of the M3 matrix would correspond to a stage when eclogite breccias became connected, allowing for intense fluid infiltration (*Figure 42a*, step III).

Given the >10 km long extension of breccia distribution in the field and the similarity of brecciation patterns all along the LSZ (i.e., with systematic formation of successive matrix generations), it is more likely than only one rupture event occurred, leading to microcracking. Duration of the various steps recognized here is completely unknown, however.

Subsequent deformation and incorporation of metagabbro blocks and the serpentinite sole into the LSZ (as evidenced by the presence of type 3, unbrecciated Fe-Ti blocks at the base of the LSZ; *Figure 33a, b, 35a, b and SMI*) attest to progressive, fluid-assisted network widening of the shear zone (i.e., Means, 1995; Shrank et al., 2008) and possible tectonic reworking of the crustal organization (*Figure 42a, b*). Strain localization on the weakest layers (brecciated Fe-Ti metagabbros and serpentinitized top of the mantle, *Figure 42a, b*) further promoted the detachment of Mg-Al metagabbro slivers and incorporation in the metasomatic shear zone matrix (*Figures 34 a, 35, 42a -step IV- and SMI*).

Ultramafic metasomatism of the breccia matrix (*Figure 41, step F*) indeed led to massive recrystallization of Cr-rich talc, chlorite, subordinate garnet, serpentinite (plus sodic amphibole and accessory phengite), dramatically decreasing the strength of the rock (e.g. Wassmann et al., 2011). Dissemination of eclogitic metagabbro blocks in the LSZ probably occurred briefly after

the metamorphic peak, during exhumation, at the eclogite to blueschist facies transition (Angiboust et al., 2014).

Noteworthy, a similar and competing process of strain localization must have occurred slightly deeper within the sinking slab, as the final detachment (and later exhumation) of the Lago Superiore ophiolite occurred by strain localization at the base of the peridotite sole (*Figure 42b*). Detachment allowed preserving this remarkable evidence of fossil strain localization along the LSZ.

Next Page:

Figure 42: (a) Localization of the brecciation events inside subducted oceanic crust (corresponding to the Monviso LSU) and its implication. At the pre-subduction stage (I) the slow-spread oceanic crust is characterized by a complex intrusion pattern of Fe-Ti gabbros (as suggested by La Gabrielle et Al., 1999 or Lissemberg et Al., 2016). During subduction it reached the eclogite-facies condition (stage II) and the increasing deformation coupled to the rheological contrast between Fe-Ti and Mg-Al metagabbros culminate at peak-burial conditions in the brittle failure (brecciation) mainly in the Fe-Ti metagabbros. As suggested by the crystalization of matrices progressively richer in water (M1, pure omphacite; M2, Omphacite + Garnet; M3, 70% of volume composed by lawsonites) and the subsequent development of mafic metasomatic rinds and veins, brecciation likely promote the generation the porosity that permitted the successive external fluid infiltration (stage III). The interplay between on-going deformation and massive, fluid-assisted mafic metasomatism dramatically decreased the strength of the rock, generating the shear zones and promoting the detachment and dissemination of blocks and slivers in LSZ and ISZ (stage IV). (b) Schematic 3D view of a plate interface at intermediate depth inferred from the structures observed in the Monviso metaophiolite, with locus of the eclogite-facies brecciation (yellow stars) and the localization of the main shear zones. The subduction-zone sketch with the localization of earthquake ipocenters is modified after Hacker et Al., 2003a.

● **Brecciation mechanism: triggered by earthquake or hydrofracturation?**

The switch from ductile to brittle regime documented by eclogite brecciation (crosscutting the eclogitic mylonitic foliation) could result from either a change in strain rate (i.e., as a consequence of an earthquake) or/and in fluid pressure (whether or not by dehydration embrittlement; Hacker et al., 2003), as evocated by Angiboust et al. (2012a). Massive water ingress, as recorded by the crystallization of the M3 lawsonite-rich matrix (Lws~40 vol%), could thus be seen either as a consequence or as the trigger for strain localization.

Evidence for instantaneous deformation includes the sharp breccia planes crosscutting the eclogitic mylonitic foliation, the formation of crackle-breccia with relative displacement (and the full transition from crackle to chaotic breccia), the formation of a crushed matrix and the existence of minerals fractured and offset along omphacite-bearing planes (e.g., garnets; *Figure 38d, e*).

The formation of the rather fluid-poor crushed and M1 matrices (*Figure 41*, step C) is taken here as an argument in favor of the first hypothesis. The crystallization of euhedral Omp3 omphacite and lawsonite porphyroclasts, or the occurrence of radial infiltration patterns (Omp3) in the clasts as well as in mylonitic garnets nevertheless also testifies to (later) transient fluid infiltration phases (M2 then M3 matrices, steps D and E in *Figure 41*).

Elucidating the nature of infiltrating fluids (work in progress) may provide further information and help decide which of the two processes was most effective.

4.9. Conclusions

This study documents progressive strain localization within the slab into the gabbroic crust during and prior to the detachment of the large Monviso slab fragment:

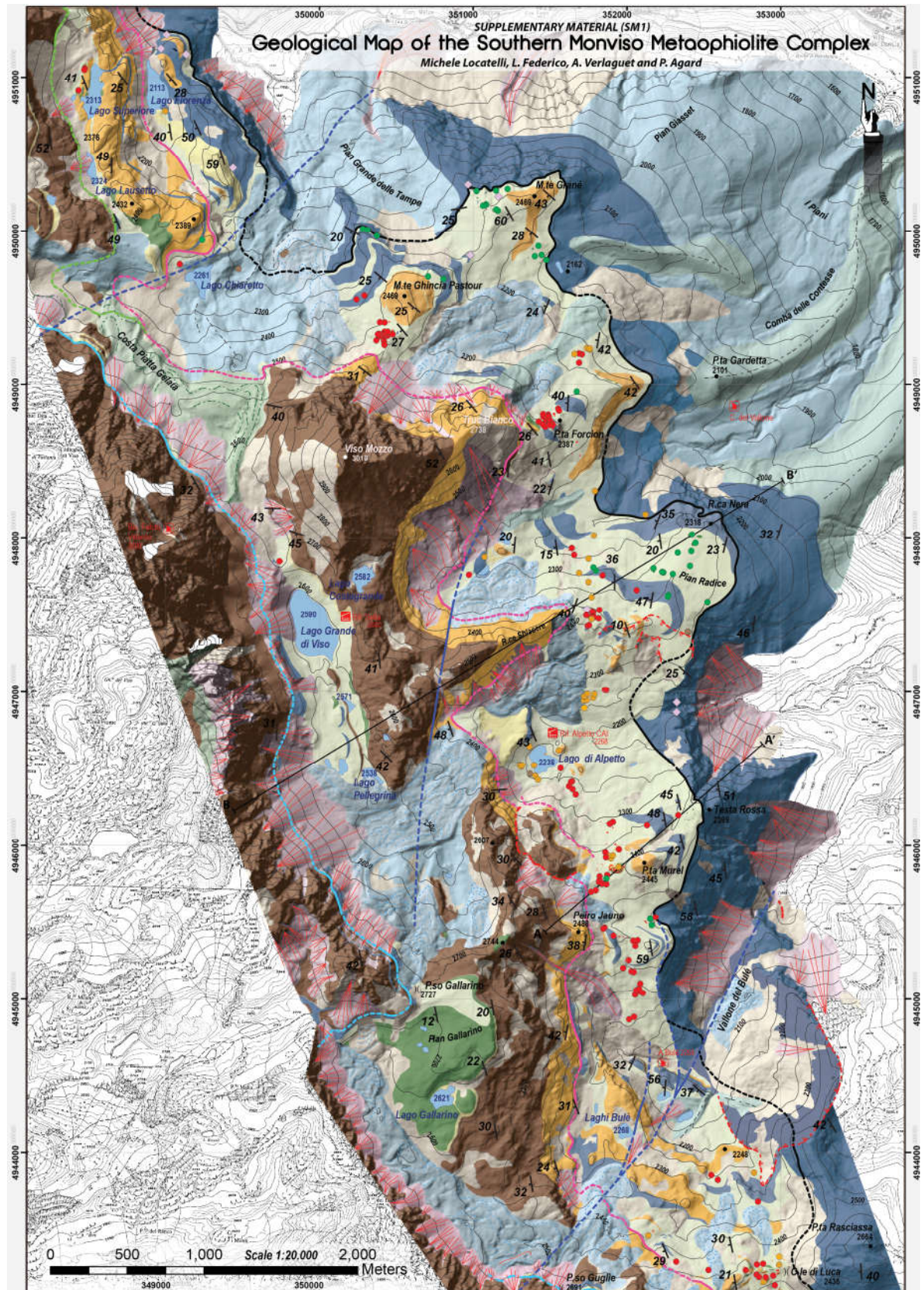
(1) The majority of breccia blocks outcropping inside the LSZ formed by brittle rupture under eclogite-facies conditions. Occurrence of eclogite-facies mylonitic Fe-Ti and Mg-Al metagabbro clasts exclude the origin by sedimentary deposition in paleo-oceanic basins or high-pressure overprinting of breccia formed at shallow crustal depths. The lack of deformation in the matrix between eclogite clasts contrasts with the reworked matrix of other metasedimentary blocks dispersed in the shear zone.

(2) Brecciation controlled the initial stages of strain localization within the LSZ. It preferentially occurred in Fe-Ti gabbros embedded in Mg-Al metagabbros, suggesting that the rheological contrast between the two metagabbros controlled the onset of brecciation.

(3) A complex succession of events accompanies brecciation. The existence of three successive types of matrix, with a sharp increase in fluid-content for the latest, lawsonite-rich one (M3), points to embrittlement then fluid ingress. Observation on preserved breccia planes of the full transition from intact metagabbro to crackle, mosaic and chaotic breccia, together with the presence of crushed matrix and the occurrence of minerals fractured and offset along omphacite-bearing planes support the view that Monviso eclogite breccias were generated by instantaneous brittle rupture.



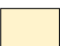
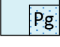



(4) Further strain localization into the LSZ, marked by the incorporation of unbrecciated mafic and ultramafic blocks and by network widening, was promoted by fluids and metasomatism.

4.10 Supplementary Material to the submitted paper
**“Eclogite-facies rupture along the subduction plate interface (Monviso meta-
ophiolite complex, W. Alps)”**











SUPPLEMENTARY MATERIAL (SM1) - Legend to Geological Map, 3D sketch and the Geological cross-sections

QUATERNARY DEPOSITS

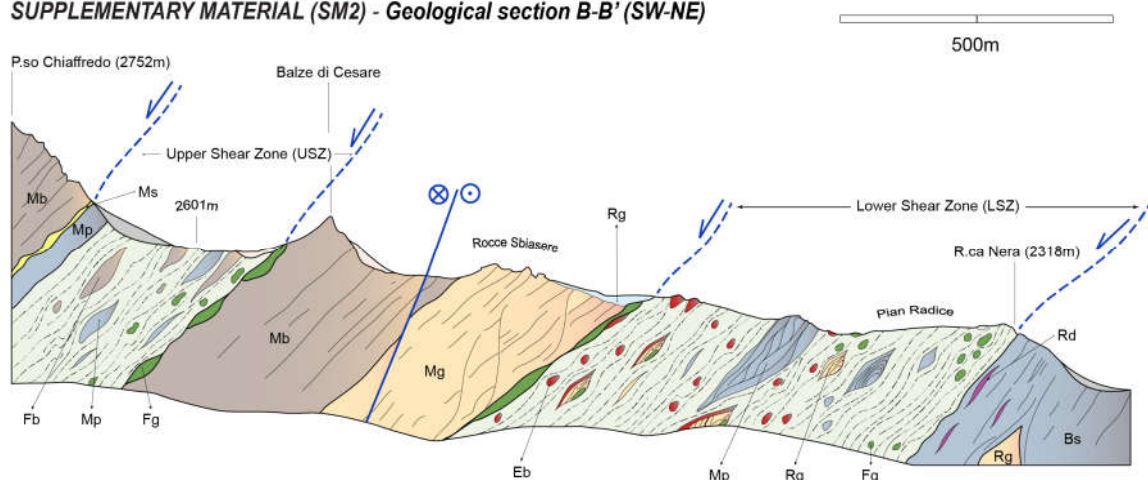
Bs		Foliated to massive antigorite serpentinites with subordinates antigorite schists. <i>Middle Jurassic?</i>
Df		Alluvial and debris flow deposits, composed by gravely cobbles and sandy gravels clast-supported, well stratified to massive, sometimes containing decimetric- to metric-scale boulders. <i>Late Upper Pleistocene – Present</i>
Td		Recent talus deposits, composed by centimetric to decimetric angular fragments and blocks, usually clast supported, without visible stratifications. <i>Late Upper Pleistocene – Present</i>
Ag		Undifferentiated glacial deposits (Ag), made up of diamicton with silty-sandy matrix and chaotic blocks accumulation. Blocks are locally devoid of lichens. Pg: Little Ice-Age moraines. <i>Holocene-Present</i>
Ug		Undifferentiated glacial deposits, made up of diamicton and chaotic blocks accumulation with silty-sandy matrix (Ug). <i>Upper Pleistocene</i>
Rg		Inactive rock glacier, formed by poorly sorted angular to sub-angular blocks at surface, with progressive passage to blocks-in-matrix texture below the surface. Characteristic the coverage of blocks by lichens. <i>Holocene</i>
		Lakes and ponds

Lago Superiore Unit and Monviso Unit LITHOLOGIES

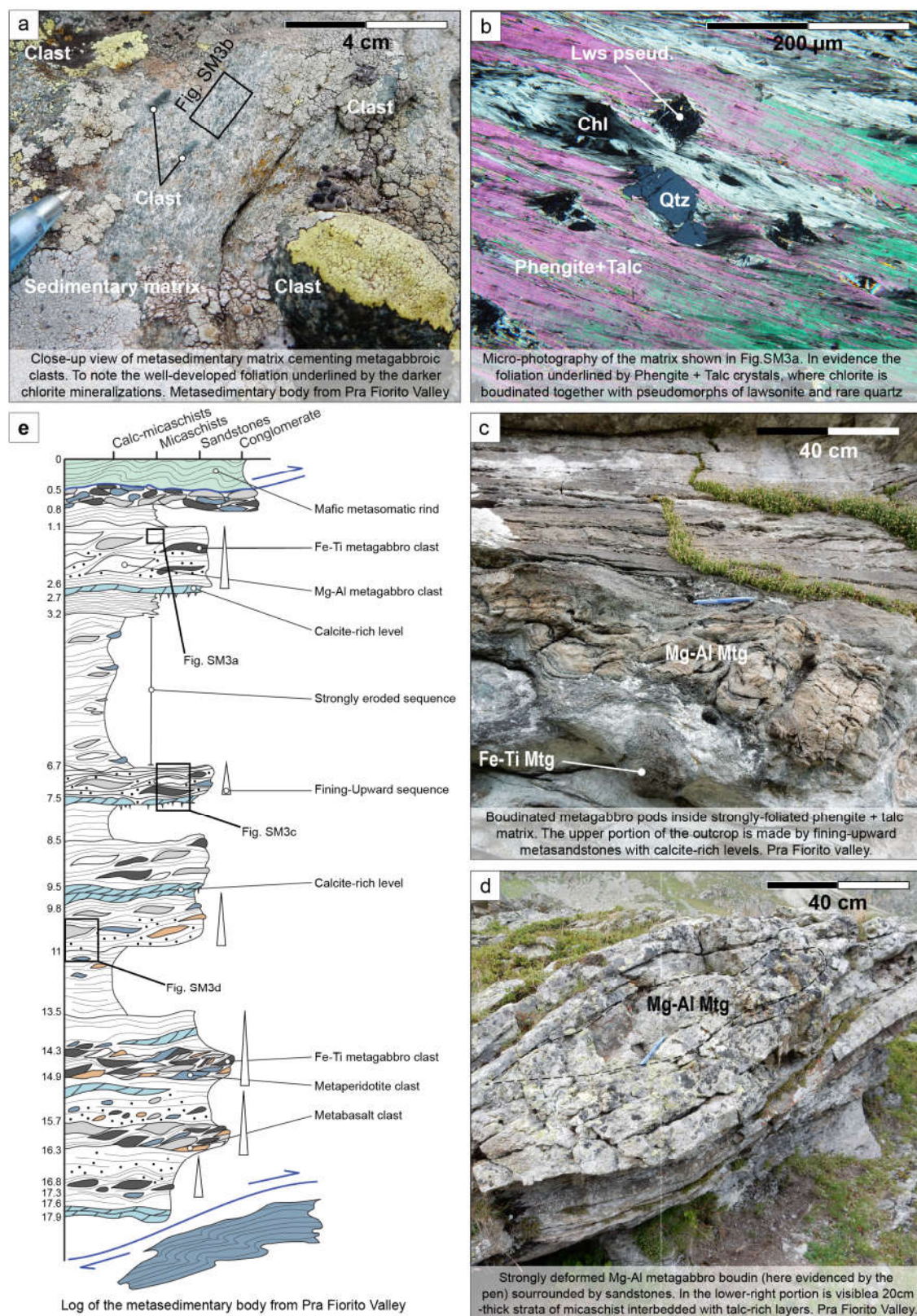
Ms		Fine-to-medium grained lawsonite-bearing calcschists (Mc) interbedded with quart-rich and mica-rich cm-to-dm levels; locally with decimetric to metric-size bodies of metabasite (a). <i>Late Jurassic? - Cretaceous?</i>
Mb		Finely banded epidote-rich metabasites, with pervasive blue-schist foliation, locally strongly retrogressed to greenschists (Mb). <i>Middle Jurassic? - Late Jurassic?</i>
Fg		Blocks of massive-to-foliated Eclogitic Fe-Ti metagabbros, usually strongly retrogressed to greenschist-facies. <i>Middle Jurassic?</i>
Eb		Eclogitic metabreccias (Punta Forcion, SW of Testa Rossa, Colle di Luca, W of Rocca Nera), composed by strongly foliated Fe-Ti and subordinate Mg-Al metagabbros clasts on fine-grained omphacite-matrix, locally with ex-Lawsonite-rich domains. <i>Middle Jurassic?</i>
Rg		Bodies of Mg-Al metagabbros, frequently retrogressed in green-schist facies, with cm-to-meter Fe-Ti gabbro boudins, and locally (W of P.ta Murel, W-NW of R.ca Nera) with preserved eclogitic metabreccias. <i>Middle Jurassic?</i>
Mg		Mg-Al metagabbros, locally strongly foliated and folded. <i>Middle Jurassic?</i>
Mp		Massive metaperidotites (Lago Fiorenza), locally interbedded as slices in the mylonitic serpentinites (N Colle di Luca, W of R.ca Nera, Lago Grande di Viso). <i>Middle Jurassic?</i>
Ss		Strongly deformed mylonitic serpentinite schists, locally interbedded with centimetric to decimetric-thick layers of talcschist. Internal structures are chaotic, usually dismembered by recent erosion. <i>Middle Jurassic?</i>

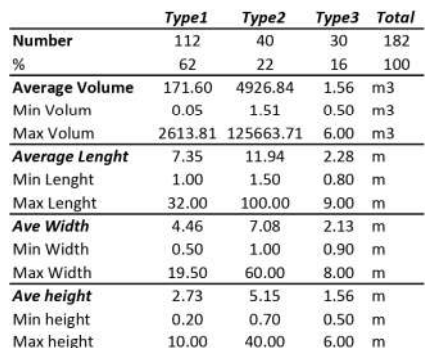
	BSZ (Basal Shear Zone)		32 Regional foliation (with dip angle)		Fe-Ti metagabbro breccia blocks (Type 1)
	LSZ (Lower Shear Zone)		Regional Fault		Mg-Al metagabbro blocks with eclogitic breccia planes (Type 2)
	ISZ (Intermediate Shear Zone)		Regional Fault (inferred)		Unbrecciated Fe-Ti metagabbro blocks (Type 3)
	USZ (Upper Shear Zone)				Massive rodingite dykes (Rd). <i>Middle Jurassic?</i>

SUPPLEMENTARY MATERIAL (SM2) - Geological section B-B' (SW-NE)



SUPPLEMENTARY MATERIAL (SM3) - The metasediments disseminated in the LSZ





SUPPLEMENTARY MATERIAL (SM5)

SUPPLEMENTARY MATERIAL (SM5) - catalog of mapped eclogite-facies Fe-Ti and Mg-Al metagabbro blocks from the LSZ and ISZ											
ZID (GIS)	NAME (Block name)	Typology (Type of block)	(Universal Transverse Mercator)		Elevation	Length	Width	Height	Brief topological description		Volume (ellipsoid)
			X_coord	Y_coord							
0	B105	block	349235.6039	4949941.185	2309	1.8	1.5	1.3	Ftg block		1.8378317
1	B112	Type1	351643.6566	4946415.805	2253	2.3	2	1.5	Breccia		3.6128316
2	B113	Type1	351635.2295	4946411.553	2254	3	3	1.3	Breccia		6.1261057
3	B114	Type1	351623.0876	4946383.713	2261	4	1	1	Breccia		2.0943951
4	B115	Type1	351645.5294	4946366.082	2264	1.5	1.5	0.9	Breccia		1.0602875
5	B116	Type1	351665.7703	4946332.053	2269	1	1.2	0.7	Breccia		0.439823
6	B117	Type1	351888.1673	4946143.349	2314	4.5	3.1	1.6	Breccia		11.686725
7	B118	Type1	351908.8018	4946154.101	2311	3.9	1.2	1.8	Breccia		4.4107961
8	B119	Type1	351947.8738	4945972.381	2376	2.7	1.5	0.8	Breccia		1.69646
9	B121	Type2	351904.7589	4945908.463	2385	8	8	7	Breccia [Ftg] on borders		234.572251
10	B122	Type2	351880.0694	4945930.936	2369	7	4	6	Breccia [Ftg] on borders		87.9645943
11	B123	Type1	351863.3337	4945921.75	2367	4	2.3	0.9	Breccia		4.3353979
12	B124	Type1	351859.0179	4945954.968	2359	3.1	2.7	0.7	Breccia		3.0677652
13	B125	Type1	352010.2073	4945254.215	2312	4.7	2.9	1.2	Breccia		8.5639816
14	B126	Type1	351974.4905	4945201.685	2300	3.1	2.4	0.9	Breccia		3.5060174
15	B127	Type1	352029.2314	4945180.649	2285	3.4	1.8	1.1	Breccia		3.524867
16	B129	Type1	352086.2886	4945101.323	2249	2.5	1.8	1.2	Breccia		2.8274334
17	B130	Type1	352052.4265	4945029.302	2240	2.1	1.8	1.5	Breccia		2.9688051
18	B135	Type1	352012.6637	4944869.394	2208	3.5	2.6	1.1	Breccia		5.2412237
19	B136	Type1	352046.1591	4944883.742	2204	3	1.8	0.8	Breccia		2.2619467
20	B137	Type1	352549.635	4943854.873	2249	1.7	1.2	0.8	Breccia		0.8545132
21	B138	Type1	352590.987	4943823.811	2261	1.2	1	0.5	Breccia		0.3141593
22	B140	Type1	352850.8057	4943684.194	2325	1	0.8	0.5	Breccia		0.2094395
23	B141	Brecciated Mg-Al metagabbro*	352991.4153	4943320.352	2418	60	37	22	Mag "brecciated"		25572.564
24	B142		352320.9992	4943288.281	2430	5	4.2	1.5	Breccia		16.493361
25	B143	Type2	352138.2761	4943457.386	2393	7.6	5	2	Breccia [Ftg] on borders		39.7935069
26	B9	Brecciated Mg-Al metagabbro*	351722.4477	4946893.565	2246	4	4	1.5	Mag "brecciated"		12.566371
27	B10	Brecciated Mg-Al metagabbro*	351721.4367	4946942.823	2257	3	2	2	Mag "brecciated"		6.2831853
28	B11	Type2	351737.8909	4946944.335	2254	2	1.5	1	Breccia [Ftg] on borders		1.57079633
29	B12	Type2	351719.5603	4946968.206	2269	1.8	1.7	1.6	Breccia [Ftg] on borders		2.56353961
30	B13	Type2	351723.7876	4946969.221	2268	2.1	1.9	1.5	Breccia [Ftg] on borders		3.13373867

SUPPLEMENTARY MATERIAL (SM5) - catalog of mapped eclogite-facies Fe-Ti and Mg-Al metagabbro blocks from the LSZ and ISZ										
31	B16	Type2	351742.0156	4946985.807	2266	2.7	1.5	1	Breccia [Ftg] on borders	2.12057504
32	B5	block	351855.2673	4947012.66	2266	5	4	3	Breccia	31.415927
33	B17	block	351864.4408	4947011.45	2266	3.1	2.3	1.7	Breccia	6.3465408
34	B18	Foliated basalts (errant)	352397.3743	4947388.906	2322	2	2	2.5	Foliated basalts	5.2359878
35	B19	Foliated basalts (errant)	352394.3898	4947390.197	2324	2	1.5	1	Foliated basalts	1.5707963
36	B20	Foliated basalts (errant)	352393.8501	4947390.876	2324	5	4	1.5	Foliated basalts	15.707963
37	B21	Type3	352409.4281	4947819.185	2326	1.5	1.5	0.5	Ftg blocks (multiple blocks)	0.5890486
38	B22	Type3	352418.2006	4947915.009	2321	1.5	1.5	0.5	Ftg blocks (multiple blocks)	0.5890486
39	B25	Type3	352330.8339	4947906.004	2315	1.5	1.5	0.5	Ftg blocks (multiple blocks)	0.5890486
40	B26	Type3	352298.4497	4947766.153	2350	1.5	1.5	0.5	Ftg blocks (multiple blocks)	0.5890486
41	B27	Type3	352269.4825	4947630.113	2358	1.5	1.5	0.5	Ftg blocks (multiple blocks)	0.5890486
42	B28	Type3	352266.0241	4947621.079	2360	1.5	1.5	0.5	Ftg blocks (multiple blocks)	0.5890486
43	B32	Type2	351304.2819	4946522.299	2267	1.5	1.5	1.5	Breccia [Ftg] on borders	1.76714587
44	B31	Type2	351304.333	4946521.075	2267	4	3	1.5	Breccia [Ftg] on borders	9.42477796
45	B36	Type1	351779.4366	4947515.578	2414	2	1.4	1.2	Breccia	1.7592919
46	B47	Type1	351867.3523	4945747.502	2375	1	1	0.5	Breccia	0.2617994
47	B51	Type1	351853.8997	4945463.047	2364	20	10	5	Breccia	523.59878
48	B52	Type1	351847.0211	4945455.769	2365	4	1.5	1	Breccia	3.1415927
49	B54	Type1	352041.3682	4945378.088	2345	4	3	1.3	Breccia	8.1681409
50	B60	Type1	352334.2141	4946197.489	2346	5	5	4	Breccia	52.359878
51	B61	Type1	352131.1112	4946134.339	2360	2	2	1	Breccia	2.0943951
52	B62	Type3	352523.861	4947585.957	2298	2	2.5	1.5	Ftg block	3.9269908
53	B63	Type3	352238.2496	4947776.421	2337	2	2.5	1.5	Ftg block	3.9269908
54	B65	Type3	352173.5315	4947804.131	2313	2	2.5	1.5	Ftg block	3.9269908
55	B66	Type1	352062.4792	4947661.414	2335	1.5	1.5	1	Breccia	1.1780972
56	B69	Type2	352120.1722	4948154.665	2191	2	2.5	1.7	Breccia [Ftg] on borders	4.45058959
57	B71	Type2	351749.1488	4947714.722	2327	4	2	1.2	Breccia [Ftg] on borders	5.02654825
58	B73+BLOCCO REOLOGICO	Type2	351749.2412	4947867.315	2259	2	1	1.5	Breccia [Ftg] on borders	1.57079633
59		Type2	351785.3441	4948016.637	2209	6.5	5	5	Breccia [Ftg] on borders	85.084801
60		Type3	351672.2498	4948952.145	2349	2	1.5	1.2	Ftg block	1.8849556
61		Type1	351706.3672	4949198.093	2278	4.5	3.5	3	Breccia	24.740042
62	B81	Type1	351688.952	4949202.828	2282	3.7	3	2.5	Breccia	14.529866
63	B82	Type2	351740.477	4949236.654	2258	2.9	2.9	1.6	Breccia [Ftg] on borders	7.04554512

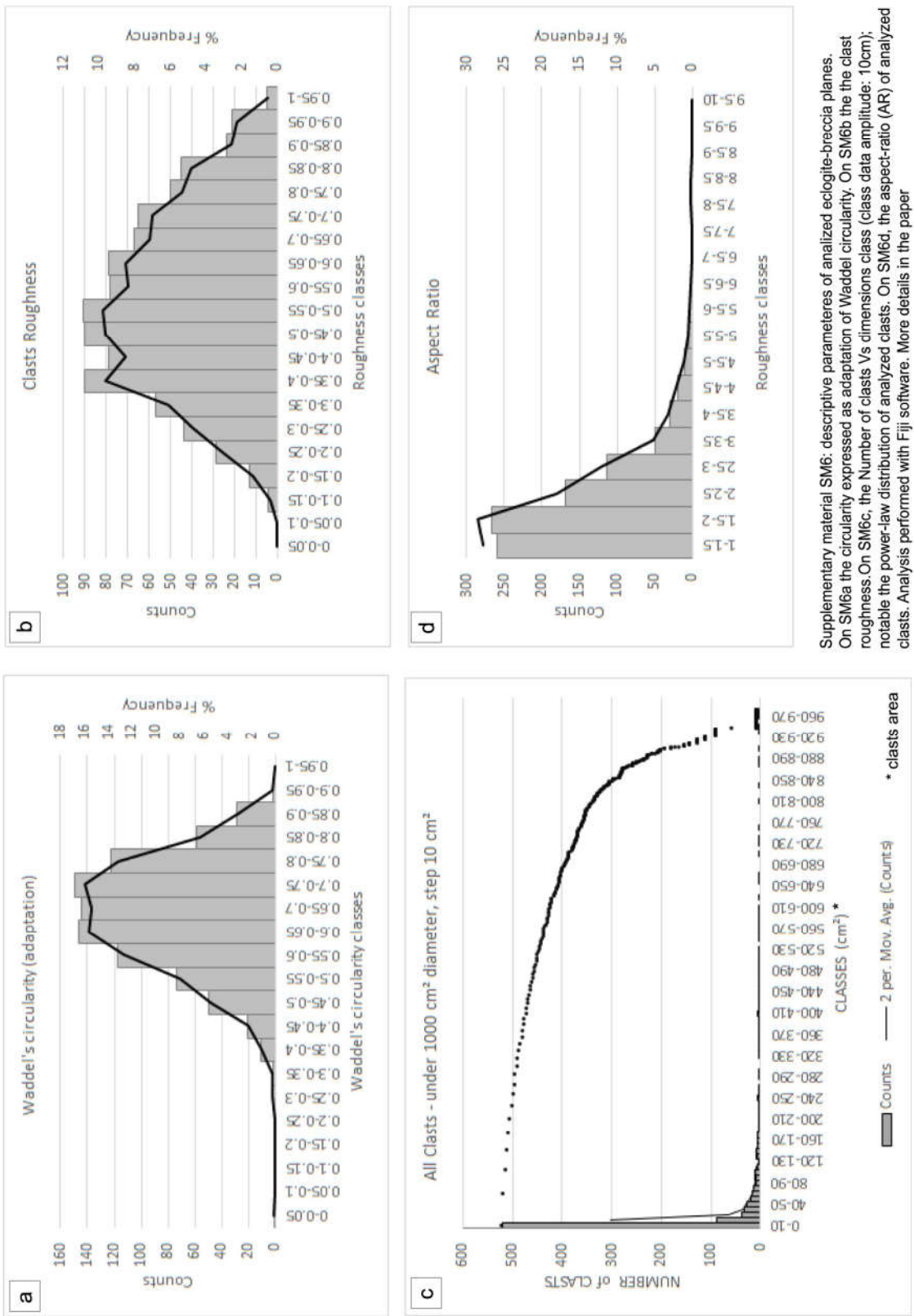
SUPPLEMENTARY MATERIAL (SM5) - catalog of mapped eclogite-facies Fe-Ti and Mg-Al metagabbro blocks from the LSZ and ISZ										
64	B83	Type2	351758.2962	4949228.798	2257	3	3.6	2.7	Breccia [Ftg] on borders	15.2681403
65	B84	Type2	351757.1506	4949234.159	2256	3.2	2.8	3.1	Breccia [Ftg] on borders	14.5434796
66	B144	Type2	351791.9012	4948305.784	2216	4.5	3.9	3.7	Breccia [Ftg] on borders	33.9998865
67	B85	Type1	351688.9212	4949142.813	2298	2.9	2.7	1.6	Breccia	6.5596455
68	B86	Type3	351474.0207	4949810.819	2195	5	4	5	Ftg block	52.359878
69	B87	Type3	351445.3649	4949843.82	2209	5	5	5	Ftg block	65.449847
70	B98	Type3	351401.2257	4949834.5	2219	9	8	6	Ftg block	226.19467
71	B88	Type3	351425.245	4949903.188	2232	10	6	5	Ftg block	157.07963
72	B89	Type3	351160.6465	4950132.567	2327	30	20	10	Ftg block	3141.5927
73	B99	Type3	351150.044	4950140.369	2321	7	6	4	Ftg block	87.964594
74	B90	Type3	351083.9617	4950173.013	2300	10	7	4	Ftg block	146.60766
75	B91	Type3	351072.7348	4950167.493	2296	3	3	2.8	Ftg block	13.194689
76	B92	Type3	351062.5099	4950164.173	2294	1.5	1.5	1.2	Ftg block	1.4137167
77	B96	Type3	350805.9657	4949688.078	2397	1	1	0.7	Ftg block	0.3665191
78	B103	Type1	350291.3234	4949583.074	2343	2.5	2	1.3	Breccia	3.403392
79	B104	Type1	350240.6917	4949557.241	2333	2.7	2.2	1.5	Breccia	4.6652651
80	B106	Foliated basalts (errant)	349779.572	4949862.038	2205	0	0	0	Foliated basalts	0
81	B107	Foliated basalts (errant)	349761.6203	4949847.007	2203	0	0	0	Foliated basalts	0
82	B108	Foliated basalts (errant)	349474.1401	4949752.566	2230	0	0	0	Foliated basalts	0
83	B109	Type1	348431.0804	4950913.528	2315	4	3.5	2	Breccia	14.660766
84	B110	Type2	348471.1242	4951059.074	2328	1.5	1	1	Breccia [Ftg] on borders	0.78539816
85	B111	Type1	348468.4567	4951050.134	2328	2	1.5	1.2	Breccia	1.8849556
86	B120	Type2	351909.0047	4945935.14	2374	2.5	1.8	0.7	Breccia [Ftg] on borders	1.64933614
87	B70	Type2	351769.3935	4947616.706	2371	7	5	5	Breccia [Ftg] on borders	91.6297857
88	B1	Type1	351764.467	4947482.737	2407	8.5	5.5	3.5	Breccia	85.67385
89	B6	Type1	351785.012	4947484.245	2408	1.5	1	0.5	Breccia	0.3926991
90	B2	Type1	351745.1656	4947428.937	2398	7.5	4	1.7	Breccia	26.703538
91	B3	Type1	351752.7857	4947433.699	2398	4.5	2.7	1	Breccia	6.3617251
92	B153	Type2	351687.8717	4947772.281	2298	7	4.5	3.2	Breccia [Ftg] on borders	52.7787566
93	B72	Type1	351656.0775	4947889.664	2251	5	5	5	Breccia	65.449847
94	B64	Type3	352228.5135	4947780.307	2334	2	2.5	1.5	Ftg block	3.9269908
95	B23	Type3	352446.169	4947968.461	2320	1.5	1.5	0.5	Ftg blocks (multiple blocks)	0.5890486
96	B24	Type3	352423.6794	4948024.685	2314	1.5	1.5	0.5	Ftg blocks (multiple blocks)	0.5890486

SUPPLEMENTARY MATERIAL (SM5) - catalog of mapped eclogite-facies Fe-Ti and Mg-Al metagabbro blocks from the LSZ and ISZ										
97	B8	Type1	351774.2604	4947522.446	2415	1.5	1	0.3	Breccia	0.2356194
98	B7	Type2	351556.1318	4946621.083	2262	65	34	25	Breccia [Ftg] on borders	28928.8324
99	B74	Type1	351819.858	4947532.043	2401	25	14	10	Breccia	1832.5957
100	B29	Type1	351815.7221	4947476.742	2413	4.2	2	1.3	Breccia	5.7176986
101	B14	Type2	351779.692	4946960.561	2260	2.8	2.6	1.3	Breccia [Ftg] on borders	4.95533881
102	B15	Type2	351788.7143	4946984.056	2265	2.3	1.6	1.7	Breccia [Ftg] on borders	3.27563394
103	B30	Type2	351364.851	4946642.941	2263	3	2	3	Breccia [Ftg] on borders	9.42477796
104	B33	Type2	351310.942	4946514.287	2263	3	5	1	Breccia [Ftg] on borders	7.85398163
105	B34	Type2	351318.2842	4946521.696	2261	3.2	2.7	3	Breccia [Ftg] on borders	13.5716803
106	B35	Type2	351396.2703	4946521.233	2240	2.5	2.6	2.9	Breccia [Ftg] on borders	9.86983692
107	B37	Type2	351736.2606	4947500.193	2411	1.8	1.2	1.2	Breccia [Ftg] on borders	1.35716803
108	B38	Type1	351568.1175	4946502.315	2248	5	3.5	2	Breccia	18.325957
109	B39	Foliated basalts (errant)			2248	3.2	3	1.5	Foliated basalts	7.5398224
110	B40	Type2	351405.2	4946452.441	2246	2.8	2.3	1.4	Breccia [Ftg] on borders	4.72076656
111	B41	Type2	351421.4058	4946428.298	2259	1.5	2.1	1	Breccia [Ftg] on borders	1.64933614
112	B44	Type1	351871.3968	4945807.518	2381	2	1.5	1	Breccia	1.5707963
113	B42	Type2	351822.4488	4945799.051	2383	24	15	7	Breccia [Ftg] on borders	1319.46891
114	B43	Type3	351865.3114	4945784.499	2384	1	1	0.5	Ftg blocks (multiple blocks)	0.2617994
115	B45	Type1	351821.9196	4945778.149	2389	4	2.5	4	Breccia	20.943951
116	B46	Type1	351838.0592	4945750.632	2378	5	4	3.5	Breccia	36.651914
117	B48	Type1	351817.1571	4945763.068	2386	1.8	2.5	1	Breccia	2.3561945
118	B49	Type1	351796.7842	4945709.092	2367	5	4	3	Breccia	31.415927
119	B50	Type1	351766.0924	4945698.774	2373	10	5	5	Breccia	130.89969
120	B53	Type1	351912.1427	4945409.584	2373	1	0.5	0.2	Breccia	0.0523599
121	B55	Type1	352053.9067	4945346.083	2334	5	3.2	1	Breccia	8.3775804
122	B56	Type1	352068.988	4945381.802	2347	3	2.1	1.2	Breccia	3.9584067
123	B57	Type3	352160.6663	4945479.989	2312	1.5	1	1	Ftg blocks (multiple blocks)	0.7853982
124	B58	Type3	352150.3476	4945520.868	2312	1.2	1	1	Ftg blocks (multiple blocks)	0.6283185
125	B59	Type1	352185.4049	4945533.568	2293	14	10	6.5	Breccia	476.47489
126	B67	Type3	351798.299	4947788.353	2303	2	1.5	1.5	Ftg block	2.3561945
127	B68	Type3	351781.3656	4947809.52	2289	2	1.7	1.6	Ftg block	2.8483773
128	B75	Type1	351640.4486	4947933.663	2242	7	6	4	Breccia	87.964594
129	B78	Type3	351658.3277	4949199.056	2287	5	4.5	3	Breccia [Ftg] on borders	35.342917

SUPPLEMENTARY MATERIAL (SM5) - catalog of mapped eclogite-facies Fe-Ti and Mg-Al metagabbro blocks from the LSZ and ISZ										
130	B76	Type1	351841.8401	4947756.817	2327	1	1	0.5	Breccia	0.2617994
131	B101	Type3	350280.476	4950014.868	2292	1	0.9	0.8	Ftg block	0.3769911
132	B100	Type3	350312.226	4950006.93	2286	0.8	0.9	0.8	Ftg block	0.3015929
133	B128	Type1	352043.8942	4945175.943	2285	3.2	2.7	1.1	Breccia	4.9762828
134	B131	Type1	352060.7615	4945056.218	2242	1.9	1.6	1.1	Breccia	1.7509143
135	B132	Type1	352080.936	4945049.604	2239	5.7	4.2	2.1	Breccia	26.323405
136	B133	Type1	352078.9516	4945063.825	2241	2.1	1.5	0.75	Breccia	1.2370021
137	B134	Type1	352103.4256	4945040.674	2238	3.5	2.8	1.8	Breccia	9.2362824
138	B139	Type2	352775.0756	4943866.476	2267	7	5	5	Breccia [Ftg] on borders	91.6297857
139	B145	Type2	352990.9761	4943268.119	2437	12	4.5	1.3	Breccia [Ftg] on borders	36.756634
140	B146	Type1	352952.2391	4943197.388	2417	17.5	12.6	8.5	Breccia	981.35501
141	B147	Type1	352961.4996	4943134.418	2388	11.7	9.8	7.5	Breccia	450.26877
142	B148	Type1	352886.2371	4943274.718	2434	13	8.5	0.6	Breccia	34.714599
143	B149	Type1	352844.7504	4943270.485	2441	7	7	0.4	Breccia	10.262536
144	B150	Type1	352844.1513	4943203.813	2436	5.8	6.2	0.7	Breccia	13.180028
145	B151	Type1	352772.3073	4943232.728	2463	1.5	1.5	0.5	Breccia	0.5890486
146	B152	Type1	352529.8045	4943233.795	2438	3.2	2.8	1	Breccia	4.691445
147	B93	Type3	351147.8321	4950263.655	2273	1.5	1.5	1.2	Ftg block	1.4137167
148	B95	Type3	350705.4236	4949705.078	2408	1	1.2	0.8	Ftg block	0.5026548
149	B94	Type3	351222.9496	4950274.462	2283	1.5	1.5	1.2	Ftg block	1.4137167
150	B102	Type3	350373.6707	4949969.013	2285	1.1	1.2	0.7	Ftg block	0.4838053
151	B4	Type2	351769.9313	4947473.479	2405	2	1.6	0.9	Breccia [Ftg] on borders	1.50796447
152	B155	Type1	350971.3223	4947761.447	2315	15	5	0.8	Breccia	31.415927
153	B154	Type2	351073.7163	4947877.335	2305	7	4	3.5	Breccia [Ftg] on borders	51.31268
154	B156	Type1	349739.5522	4947850.744	2640	4.5	2	1.8	Breccia	8.4823002
155	B157	Type1	351553.1885	4948842.782	2374	5	3.2	2.9	Breccia	24.294983
156	B158	Type1	351558.4802	4948829.023	2381	8	5.3	4.2	Breccia	93.24247
157	B159	Type1	351487.0426	4948802.565	2380	5.8	4.6	2.8	Breccia	39.114923
158	B160	Type1	351491.8051	4948790.923	2384	5.5	4	3.4	Breccia	39.165188
159	B161	Type1	351478.0467	4948789.865	2387	7.9	6.8	4.7	Breccia	132.20031
160	B162	Type1	351455.2925	4948791.452	2388	9	4.5	4	Breccia	84.823002
161	B163	Type1	351454.7633	4948807.327	2383	4.6	2.6	1.8	Breccia	11.272034
162	B164	Type1	351501.3301	4948763.936	2414	85	25	20	Breccia	22252.948

SUPPLEMENTARY MATERIAL (SM5) - catalog of mapped eclogite-facies Fe-Ti and Mg-Al metagabbro blocks from the LSZ and ISZ										
163	B165	Type1	351497.0968	4948736.419	2413	18	9	5	Breccia	424.11501
164	B166	Type1	351467.9925	4948725.306	2428	29	13	7	Breccia	1381.7772
165	B167	Type1	351451.0592	4948742.24	2424	32	19.5	8	Breccia	2613.8051
166	B168	Type1	351425.6591	4948760.232	2409	22	14	7	Breccia	1128.879
167	B169	Type2	351944.1332	4945859.974	2404	100	60	40	Breccia [Ftg] on borders	125663.706
168	B188	Type1	350423.2875	4949343.76	2436	14.6	7.6	6.5	Breccia	377.64038
169	B172	Type1	350441.6431	4949325.673	2449	10.4	4.8	3.6	Breccia	94.096983
170	B173	Type1	350443.6309	4949318.385	2452	2.7	2.6	1.5	Breccia	5.5134951
171	B174	Type1	350433.692	4949328.986	2447	6.2	4.5	3.8	Breccia	55.511942
172	B175	Type1	350421.1708	4949326.298	2445	14.6	8.2	7.2	Breccia	451.33377
173	B176	Type1	350422.9568	4949314.722	2447	9.4	3.2	2.5	Breccia	39.374628
174	B177	Type1	350409.3969	4949327.951	2437	13.8	10.7	6.9	Breccia	533.47071
175	B178	Type1	350397.1599	4949323.321	2429	10.6	6.4	5.2	Breccia	184.70889
176	B179	Type1	350386.5765	4949314.061	2428	15	12	7.6	Breccia	716.28313
177	B180	Type1	350386.2458	4949330.597	2421	23.2	9.2	6.2	Breccia	692.89292
178	B181	Type1	350379.6312	4949325.967	2420	10.2	7.3	5.3	Breccia	206.63197
179	B182	Type1	350378.3083	4949295.209	2425	24.8	6.4	7.1	Breccia	590.04974
180	B183	Type1	350383.2692	4949276.358	2428	8.9	6.6	4.8	Breccia	147.62972
181	B184	Type1	350385.2536	4949266.436	2431	12.4	4.3	2.5	Breccia	69.795717
182	B185	Type1	350387.238	4949248.246	2437	19.5	6.8	1.7	Breccia	118.02964
183	B186	Type1	350393.5218	4949403.689	2398	10.2	8.2	6.7	Breccia	293.41847
184	B187	Type1	350422.9568	4949402.035	2404	16.7	12.5	8.4	Breccia	918.13045
185	B170	Type1	350475.5428	4949326.298	2452	22.6	4.5	1.5	Breccia	79.874993
186	B171	Type1	350444.1235	4949342.504	2442	21.5	9	4.5	Breccia	455.92363
187	B97	Type3	351021.2907	351021.2907	2269	1.5	1.5	1.2	Ftg block	1.4137167
188	B Gallarino1	Type1	350675.22	4944931.68	2725	2	1	0.5	Breccia	0.5235988
189	B Gallarino 2	Type1	350636.25	4944871.11	2707	2.1	1.2	0.6	Breccia	0.7916813
190	B189	Type2	352963.4	4943053.23	2388	6	4	3	Breccia [Ftg] on borders	37.699112
191	B190	Type2	352994.71	4943110.81	2390	3	2.1	1.5	Breccia [Ftg] on borders	4.9480084
192	B191	Type1	353003.76	4943060.5	2382	1	0.3	0.4	Breccia	0.0628319
193	B192	Type2	352890.91	4943157.63	2418	50	33	24	Breccia [Ftg] on borders	20734.512
194	B193	Type1	352839.06	49431.97	2444	1	0.6	0.2	Breccia	0.0628319
195	B194	Type1	352911.14	4943180.19	2419	1	0.7	3	Breccia	1.0995574

SUPPLEMENTARY MATERIAL (SM6) - descriptive parameters of analyzed clasts from LSZ eclogite breccia



SUPPLEMENTARY MATERIAL (SM7)

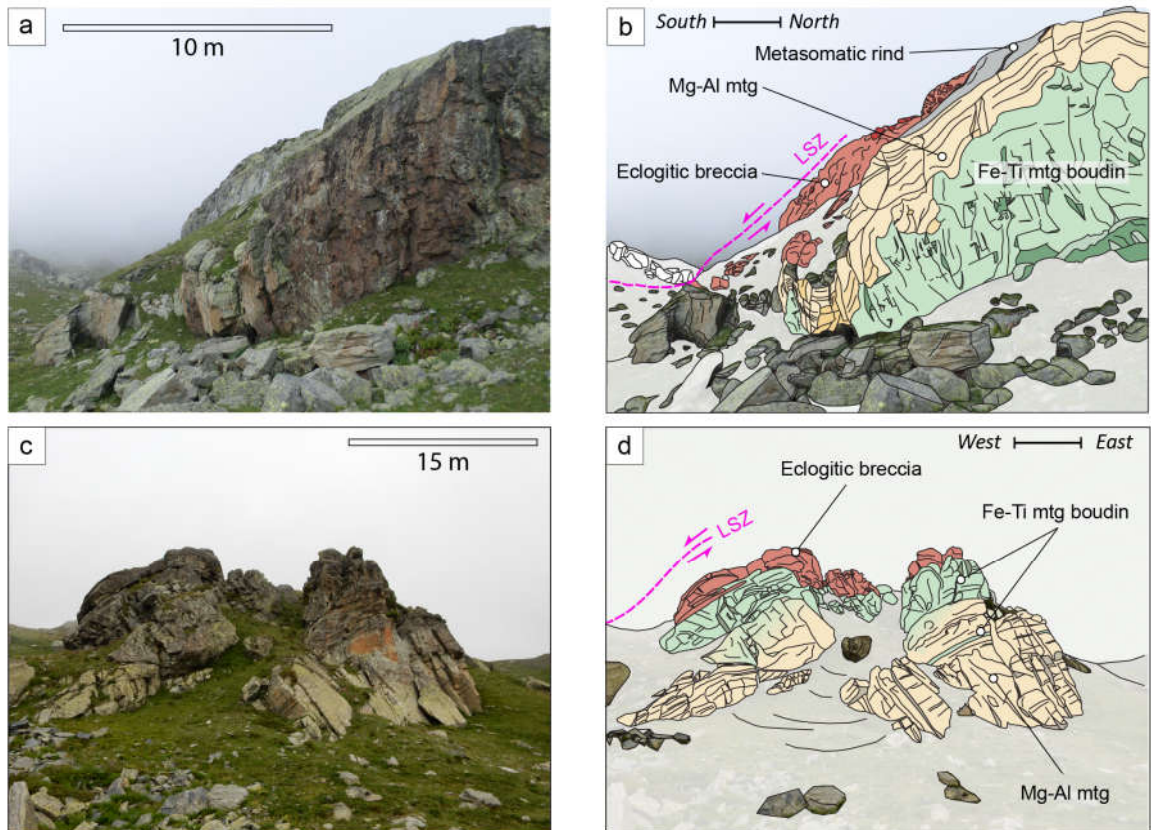


Figure SM7a-d: example of one the big (length > 10 meters) Mg-Al metagabbro slices with eclogite breccia horizon. These slices are characterized by massive, unbrecciated Fe-Ti boudins at the cores (thickness from 0.5 to 8 meters) wrapped by heavily-strained Mg-Al metagabbro. On blocks western flank, eclogite breccia layers unconformably crosscut the Mg-Al metagabbro's mylonitic foliation. SM7a, b: Punta Murel, B69. SM7c, d: Colle di Luca, B192.

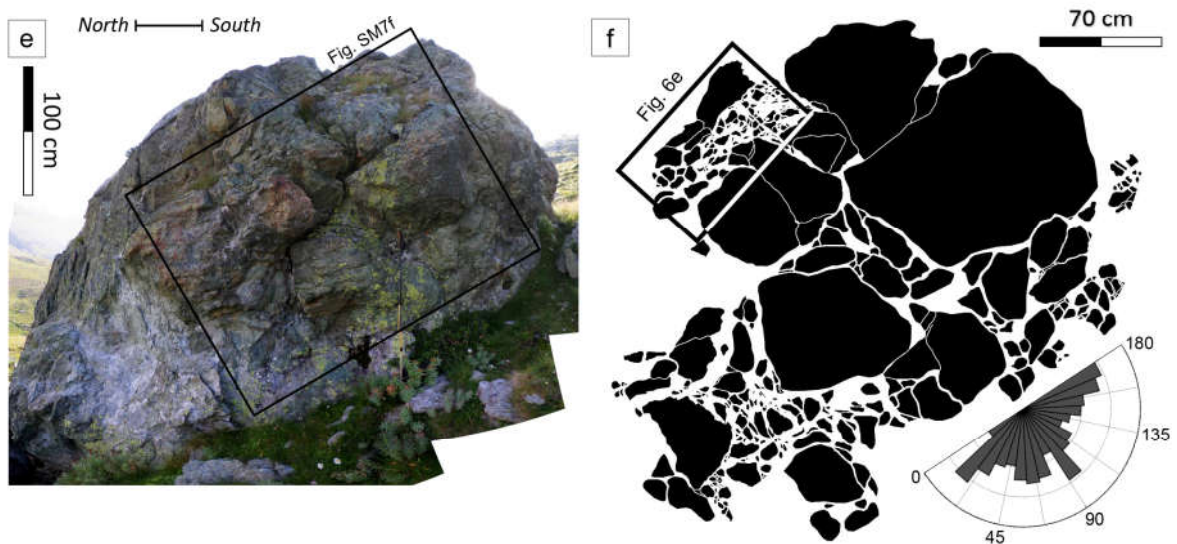


Figure SM7e-f: Characteristic breccia structures in Block B74 (Pra Fiorito Valley). Subdividing the breccia horizons in equal-area sections with increasing degree of deformation (crackle to chaotic) the amount of matrix increase from average 10% of total rock amount to 60%, in agreement to what is observed in shallow-crust fault breccias (Mort et al., 2008).

SUPPLEMENTARY MATERIAL (SM8)

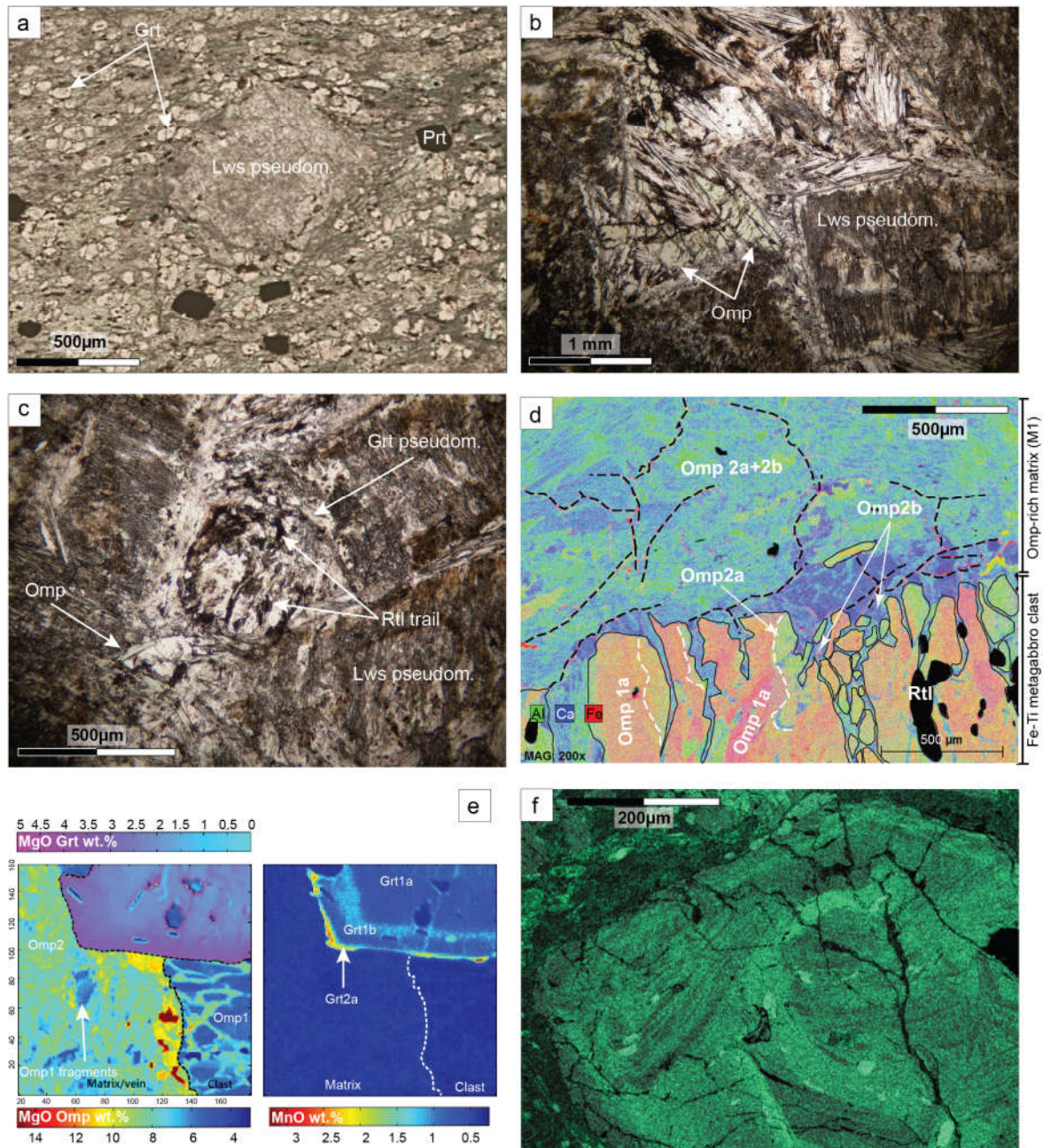


Figure SM8a: a lawsonite pseudomorph (replaced by a microfelt of epidote + phengite) synkinematically grown inside the foliation of a Fe-Ti metagabbro clast from eclogite breccia block (LSZ). In this case the omphacite of the clast is generally replaced by tremolite, with garnet rimmed by chlorite rims derived by retrogression, a typical feature of metagabbros rich in lawsonite. Sample LSZ 14-11c/LA.

Figure SM8b-c: Lawsonite-rich matrix M3, evidences of the pristine mineralogical assemblage Lawsonite + Omphacite + Garnet. The lawsonite appears to be pseudomorphosed by a microfelt composed by epidote + phengite +/- chlorite; interestingly the zonations of the crystals are still visible. In-between, relics of interstitial omphacites are locally preserved (Fig. SM8b). Rounded agglomerate of chlorite, preserving rutile's trails (not observed in the surrounding lawsonite pseudomorphs), are interpreted as former garnets now totally replaced (SM8c). Thin section LSZ 14-12, from block B7 (Lower Shear Zone).

SM8d: typical example of the contact between an Fe-Ti metagabbro clast and the omphacite-rich matrix M1. In the clast are evident the radial-type cracks filled by OMP2b (and subordinate OMP2a) of the matrix (more detail in the paper). In the clast is also distinguishable an area where fragments of OMP1a and OMP1b are displaced and sealed by the omphacites OMP2a and OMP2b (similar to what described as "crushed breccia", more details in the paper). Evident, in the matrix, is the scarcity of the rutiles and the later-stage cracks filled by Iron-rich mineralization. Sample LSZ 14-53, lower shear zone.

Figure SM8e: the typical "zebra-pattern" Cr-zoning inside matrix M2 garnets (generations: Grt2a-b). Sample 63-35, from ISZ.

Figure SM8f: EPMA compositional map of the transition clast-matrix M1. In the clast, well visible the MgO-richer Omp2b crystallizing along infiltration-like patterns. In evidence, in the garnet, the crystallization of a thin outer rim of MnO-richer Grt2a respect to the poorer Grt1a and Grt1b. To be noted that Grt2a rims only crystallize at the contact with the Omp2b of the matrix. Sample LSZ 14-53, Lower shear zone.

SUPPLEMENTARY MATERIAL (SM9) - EPMA geochemical maps (Cameca SX5)

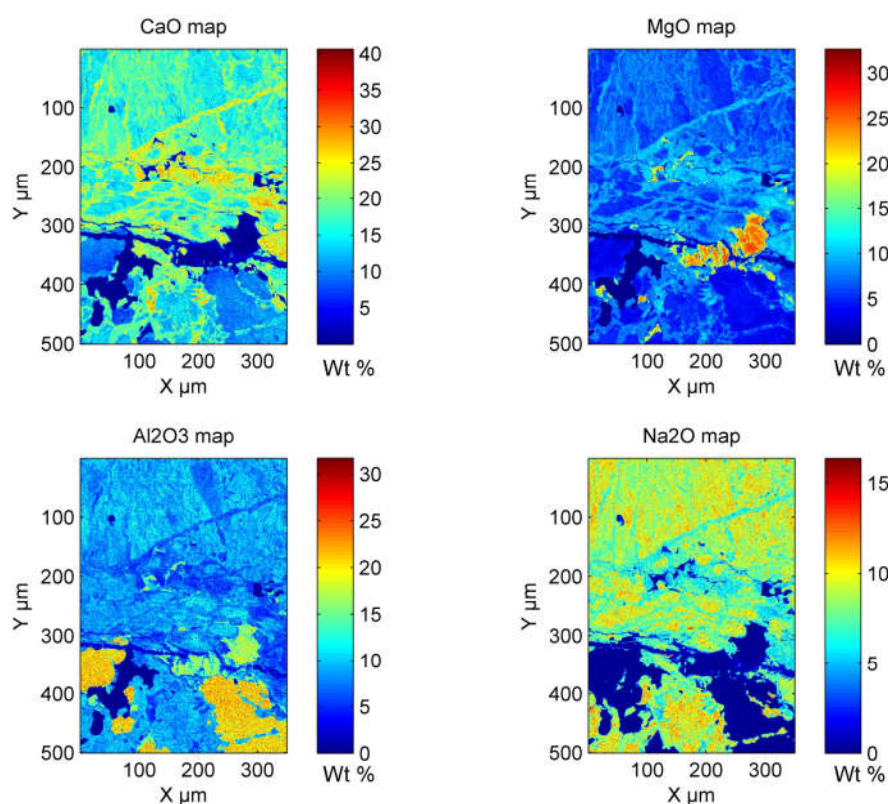


Figure SM9a: EMPA geochemical maps of a "crushed breccia" matrix domain (sample LSZ 15-53)

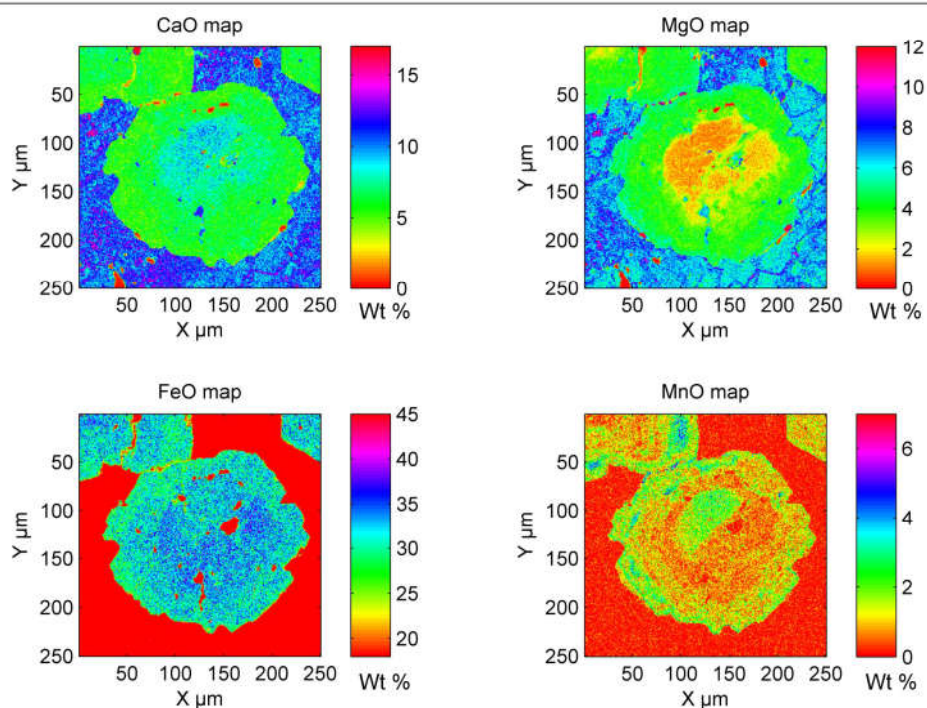


Figure SM9b: EMPA geochemical maps of a complex-zoned garnet from Fe-Ti metagabbro clast (sample LSZ 1550)

10. References:

- Agard, P., Monié P., Jolivet L., Goffé B., 2002. Exhumation of the Schistes Lustrés Complex: In Situ Laser Probe $^{40}\text{Ar}/^{39}\text{Ar}$ Constraints and Implications for the Western Alps. *Journal of Metamorphic Geology* 20 (6): 599–618.
- Angiboust, S., Agard P., 2010. Initial Water Budget: The Key to Detaching Large Volumes of Eclogitized Oceanic Crust along the Subduction Channel?. *Lithos* 120 (3–4): 453–74. doi:10.1016/j.lithos.2010.09.007.
- Angiboust, S., Agard P., Raimbourg H., Yamato P., Huet B., 2011. “Subduction Interface Processes Recorded by Eclogite-Facies Shear Zones (Monviso, W. Alps).” *Lithos* 127 (1–2): 222–38. doi:10.1016/j.lithos.2011.09.004.
- Angiboust, S., Agard P., Yamato P., Raimbourg H., 2012. Eclogite Breccias in a Subducted Ophiolite: A Record of Intermediate-Depth Earthquakes? *Geology* 40 (8): 707–10. doi:10.1130/G32925.1.
- Angiboust, S., Langdon R., Agard P., Waters D., Chopin C., 2012. Eclogitization of the Monviso Ophiolite (W. Alps) and Implications on Subduction Dynamics. *Journal of Metamorphic Geology* 30 (1): 37–61. doi:10.1111/j.1525-1314.2011.00951.x.
- Angiboust, S., Pettke, T., De Hoog, J. C. M., Caron, B., Oncken, O., 2014. Channelized Fluid Flow and Eclogite-Facies Metasomatism along the Subduction Shear Zone. *Journal of Petrology* 55 (5): 883–916. doi:10.1093/petrology/egu010.
- Bachmann, R., Oncken O., Glodny J., Seifert W., Georgieva V., Sudo M., 2009. Exposed Plate Interface in the European Alps Reveals Fabric Styles and Gradients Related to an Ancient Seismogenic Coupling Zone. *Journal of Geophysical Research: Solid Earth* 114 (B5): B05402. doi:10.1029/2008JB005927.
- Balestro, G., Festa A., Tartarotti P., 2015. Tectonic Significance of Different Block-in-Matrix Structures in Exhumed Convergent Plate Margins: Examples from Oceanic and Continental HP Rocks in Inner Western Alps (Northwest Italy). *International Geology Review* 57 (5–8): 581–605. doi:10.1080/00206814.2014.943307.
- Balestro, G., Fioraso G., Lombardo B., 2011. Geological Map of the Upper Pellice Valley (Italian Western Alps). *Journal of Maps* 7 (1): 634–54. doi:10.4113/jom.2011.1213.
- Balestro, G., Fioraso G., Lombardo B., 2013. Geological Map of the Monviso Massif (Western Alps). *Journal of Maps* 9 (4): 623–34. doi:10.1080/17445647.2013.842507.
- Balleve, M., Lagabrielle Y., Merle O., 1990. Tertiary Ductile Normal Faulting as a Consequence of Lithospheric Stacking in the Western Alps. *Mémoires de La Société Géologique de France* 156: 227–36.

- Beltrando, M., Rubatto D., Manatschal G., 2010. From Passive Margins to Orogens: The Link between Ocean-Continent Transition Zones and (Ultra) High-Pressure Metamorphism. *Geology* 38 (6): 559–562.
- Bostock, M.G., Hyndman R.D., Rondenay S., Peacock S.M., 2002. An Inverted Continental Moho and Serpentinization of the Forearc Mantle. *Nature* 417 (6888): 536–538.
- Castelli, D., Rostagno C., Lombardo B., 2002. Jd-Qtz-bearing metaplagiogranite from the monviso meta-ophiolite (western alps). *Ophioliti* 27 (2): 81–90. doi:10.4454/ofioliti.v27i2.178.
- Compagnoni, R., Rolfo F., Manavella F., Salusso F., 2007. Jadeitite in the Monviso Meta-Ophiolite, Piemonte Zone, Italian Western Alps. *Per. Mineral* 76 (2–3): 79–89.
- Coward, M., Dietrich D., 1989. Alpine Tectonics - an Overview. *Geological Society, London, Special Publications* 45 (1): 1–29. doi:10.1144/GSL.SP.1989.045.01.01.
- Dal Piaz, G.V., Bistacchi A., Massironi M., 2003. Geological Outline of the Alps. *Episodes* 26 (3): 175–180.
- Duchêne, S., Blichert-Toft J., Luais B., Télouk P., Lardeaux J. M., Albarède F. and others. 1997. The Lu-Hf Dating of Garnets and the Ages of the Alpine High-Pressure Metamorphism. *Nature* 387 (6633): 586–588.
- Escartín, J., Cannat M., Pouliquen G., Rabain A., Lin J., 2001. Crustal Thickness of V-Shaped Ridges South of the Azores: Interaction of the Mid-Atlantic Ridge (36°–39°N) and the Azores Hot Spot. *Journal of Geophysical Research: Solid Earth* 106 (B10): 21719–35. doi:10.1029/2001JB000224.
- Festa, A., Balestro G., Dilek Y., Tartarotti P., 2015. A Jurassic Oceanic Core Complex in the High-Pressure Monviso Ophiolite (Western Alps, NW Italy). *Lithosphere* 7 (6): 646–52. doi:10.1130/L458.1.
- Fusseis, F., Handy M.R., Schrank C., 2006. Networking of Shear Zones at the Brittle-to-Viscous Transition (Cap de Creus, NE Spain). *Journal of Structural Geology* 28 (7): 1228–43. doi:10.1016/j.jsg.2006.03.022.
- Green, H.W., Houston H., 1995. The Mechanics of Deep Earthquakes. *Annual Review of Earth and Planetary Sciences* 23: 169–214.
- Groppo, C., Castelli D., 2010. Prograde P–T Evolution of a Lawsonite Eclogite from the Monviso Meta-Ophiolite (Western Alps): Dehydration and Redox Reactions during Subduction of Oceanic FeTi-Oxide Gabbro. *Journal of Petrology* 51 (12): 2489–2514. doi:10.1093/petrology/egq065.
- Hacker, B.R., Abers, G.A., Peacock, S.M., 2003. Subduction Factory 1. Theoretical Mineralogy, Densities, Seismic Wave Speeds, and H₂O. *Journal of Geophysical Research: Solid Earth* 108 (B1). doi:10.1029/2001JB001127.

Hacker, B.R., Peacock, S.M., Abers, G.A., Holloway, S.D., 2003. Subduction Factory 2. Are Intermediate-Depth Earthquakes in Subducting Slabs Linked to Metamorphic Dehydration Reactions? *Journal of Geophysical Research: Solid Earth* 108 (B1). doi:10.1029/2001JB001129.

Handy, M.R., Franz L., Heller F., Janott B., Zurbriegen R., 1999. Multistage Accretion and Exhumation of the Continental Crust (Ivrea Crustal Section, Italy and Switzerland). *Tectonics* 18 (6): 1154–77. doi:10.1029/1999TC900034.

Laubscher, H., 1991. The Arc of the Western Alps Today. *Eclogae Geologicae Helvetiae* 84 (3): 359–631.

Ikesawa, E., Sakaguchi A., Kimura, G., 2003. Pseudotachylyte from an Ancient Accretionary Complex: Evidence for Melt Generation during Seismic Slip along a Master Décollement? *Geology* 31 (7): 637–40. doi:10.1130/0091-7613(2003)031<0637:PFAAAC>2.0.CO;2.

Jébrak, M., 1997. Hydrothermal Breccias in Vein-Type Ore Deposits: A Review of Mechanisms, Morphology and Size Distribution. *Ore Geology Reviews* 12 (3): 111–34. doi:10.1016/S0169-1368(97)00009-7.

John, T., Medvedev S., Rüpke, L. H., Andersen, T.B., Podladchikov, Y.Y., Austrheim, H., 2009. Generation of Intermediate-Depth Earthquakes by Self-Localizing Thermal Runaway. *Nature Geoscience* 2 (2): 137–40. doi:10.1038/ngeo419.

Jung, H., Green, H.W., 2004. Experimental Faulting of Serpentinite during Dehydration: Implications for Earthquakes, Seismic Low-Velocity Zones, and Anomalous Hypocenter Distributions in Subduction Zones. *International Geology Review* 46 (12): 1089–1102. doi:10.2747/0020-6814.46.12.1089.

Kirby, S., Engdahl R., Denlinger, R., 1996. Intermediate-depth Intraslab Earthquakes and Arc Volcanism as Physical Expressions of Crustal and Uppermost Mantle Metamorphism in Subducting Slabs. *Subduction Top to Bottom*, 195–214.

Kuge, K., Kase Y., Urata Y., Campos J., Perez, A., 2010. “Rupture Characteristics of the 2005 Tarapaca, Northern Chile, Intermediate-Depth Earthquake: Evidence for Heterogeneous Fluid Distribution across the Subducting Oceanic Plate?” *Journal of Geophysical Research* 115 (B9). doi:10.1029/2009JB007106.

Lagabrielle, Y., Lemoine M., 1997. Alpine, Corsican and Apennine Ophiolites: The Slow-Spreading Ridge Model. *Comptes Rendus de l’Académie Des Sciences - Series IIA - Earth and Planetary Science* 325 (12): 909–20. doi:10.1016/S1251-8050(97)82369-5.

Lissenberg, C. J., Rioux, M., Shimizu, N., Bowring, S.A., Mével, C., 2009. Zircon Dating of Oceanic Crustal Accretion. *Science* 323 (5917): 1048–50. doi:10.1126/science.1167330.

Lombardo, B., Rubatto D., Castelli D., 2002. Ion Microprobe U-PB Dating of Zircon from a Monviso Metaplagiogranite: Implications for the Evolution of the Piedmont-Liguria Tethys in the Western Alps. *Ophioliti* 27 (2): 109–17.

Lombardo, B., Nervo R., Compagnoni R., Messiga B., Kienast J. R., Mevel C., Fiora L., Piccardo, G. P., Lanza, R., 1978. Osservazioni Preliminari Sulle Ofioliti Metamorfiche Del Monviso. *Rendiconti Della Società Italiana Di Mineralogia E Petrologia* 34 (2): 253–305.

Malusà, M.G., Faccenna C., Garzanti E., Polino, R. 2011. Divergence in Subduction Zones and Exhumation of High Pressure Rocks (Eocene Western Alps). *Earth and Planetary Science Letters* 310 (1–2): 21–32. doi:10.1016/j.epsl.2011.08.002.

Means, W.D., 1995. Shear Zones and Rock History. *Tectonophysics*, 30 Years of Tectonophysics a Special Volume in Honour of Gerhard Oertel, 247 (1): 157–60. doi:10.1016/0040-1951(95)98214-H.

Meneghini, F., Di Toro, G., Rowe, C.D., Moore, J. C. , Tsutsumi, A., Yamaguchi, A., 2010. Record of Mega-Earthquakes in Subduction Thrusts: The Black Fault Rocks of Pasagshak Point (Kodiak Island, Alaska). *Geological Society of America Bulletin* 122 (7–8): 1280–97. doi:10.1130/B30049.1.

Messiga, B., Kienast, J.R., Rebay, G., Riccardi M.P., Tribuzio, R., 1999. Cr-Rich Magnesiochloritoid Eclogites from the Monviso Ophiolites (Western Alps, Italy). *Journal of Metamorphic Geology* 17 (3): 287–99. doi:10.1046/j.1525-1314.1999.00198.x.

Montési, L.G.J., Hirth G., 2003. Grain Size Evolution and the Rheology of Ductile Shear Zones: From Laboratory Experiments to Postseismic Creep. *Earth and Planetary Science Letters* 211 (1–2): 97–110. doi:10.1016/S0012-821X(03)00196-1.

Mort, K., Woodcock, N.H., 2008. Quantifying Fault Breccia Geometry: Dent Fault, NW England. *Journal of Structural Geology* 30 (6): 701–9. doi:10.1016/j.jsg.2008.02.005.

Pelletier, L., Müntener, O., 2006. High-Pressure Metamorphism of the Lanzo Peridotite and Its Oceanic Cover, and Some Consequences for the Sesia–Lanzo Zone (Northwestern Italian Alps). *Lithos* 90 (1–2): 111–30. doi:10.1016/j.lithos.2006.01.006.

Philippot, P., 1987. Crack Seal’ Vein Geometry in Eclogitic Rocks. *Geodinamica Acta* 1 (3): 171–81. doi:10.1080/09853111.1987.11105136.

Philippot, P., Kienast J.R., 1989. Chemical-Microstructural Changes in Eclogite-Facies Shear Zones (Monviso, Western Alps, North Italy) as Indicators of Strain History and the Mechanism and Scale of Mass Transfer. *Lithos* 23 (3): 179–200. doi:10.1016/0024-4937(89)90004-2.

Philippot, P., Van Roermund, H.L.M, 1992. Deformation Processes in Eclogitic Rocks: Evidence for the Rheological Delamination of the Oceanic Crust in Deeper Levels of Subduction Zones. *Journal of Structural Geology, Mechanical Instabilities in Rocks and Tectonics*, 14 (8): 1059–77. doi:10.1016/0191-8141(92)90036-V.

Plunder, A., Agard, P., Chopin, C., Okay, A.I., 2013. Geodynamics of the Tavşanlı Zone, Western Turkey: Insights into Subduction/obduction Processes. *Tectonophysics* 608 (November): 884–903. doi:10.1016/j.tecto.2013.07.028.

- Pognante, U., Kienast, J.R., 1987. Blueschist and Eclogite Transformations in Fe-Ti Gabbros: A Case from the Western Alps Ophiolites. *Journal of Petrology* 28 (2): 271–92. doi:10.1093/petrology/28.2.271.
- Raleigh, C.B., 1967. Tectonic Implications of Serpentinite Weakening. *Geophysical Journal International* 14 (1–4): 113–18. doi:10.1111/j.1365-246X.1967.tb06229.x.
- Raleigh, C. B., Paterson, M.S., 1965. Experimental Deformation of Serpentinite and Its Tectonic Implications. *Journal of Geophysical Research* 70 (16): 3965–85. doi:10.1029/JZ070i016p03965.
- Rondenay, S., Abers, G.A., Van Keken, P.E., 2008. Seismic Imaging of Subduction Zone Metamorphism. *Geology* 36 (4): 275. doi:10.1130/G24112A.1.
- Rowe, C.D., Moore, J.C., Meneghini F., McKeirnan, A.W., 2005. Large-Scale Pseudotachylytes and Fluidized Cataclasites from an Ancient Subduction Thrust Fault. *Geology* 33 (12): 937–40. doi:10.1130/G21856.1.
- Rubatto, D., Angiboust, S., 2015. Oxygen Isotope Record of Oceanic and High-Pressure Metasomatism: A P–T–time–fluid Path for the Monviso Eclogites (Italy). *Contributions to Mineralogy and Petrology* 170 (5–6). doi:10.1007/s00410-015-1198-4.
- Rubatto, D., Hermann, J., 2003. Zircon Formation during Fluid Circulation in Eclogites (Monviso, Western Alps): Implications for Zr and Hf Budget in Subduction Zones. *Geochimica et Cosmochimica Acta* 67 (12): 2173–87. doi:10.1016/S0016-7037(02)01321-2.
- Rubatto, D., Regis, D., Hermann, J., Boston, K., Engi, M., Beltrando, M., McAlpine, S.R.B., 2011. Yo-Yo Subduction Recorded by Accessory Minerals in the Italian Western Alps. *Nature Geoscience* 4 (5): 338–42. doi:10.1038/ngeo1124.
- Schindelin, J., Arganda-Carreras, I., Frise, E., Kaynig, V., Longair, M., Pietzsch, T., Preibisch, S., et al., 2012. Fiji: An Open-Source Platform for Biological-Image Analysis. *Nature Methods* 9 (7): 676–82. doi:10.1038/nmeth.2019.
- Schmid, S.M., Kissling, E., 2000. The Arc of the Western Alps in the Light of Geophysical Data on Deep Crustal Structure. *Tectonics* 19 (1): 62–85. doi:10.1029/1999TC900057.
- Schmid, S.M., Fügenschuh, B., Kissling, E., Schuster, R., 2004. Tectonic Map and Overall Architecture of the Alpine Orogen. *Eclogae Geologicae Helvetiae* 97 (1): 93–117. doi:10.1007/s00015-004-1113-x.
- Schrank, C.E., Handy, M. R., Fousseis, F., 2008. Multiscaling of Shear Zones and the Evolution of the Brittle-to-Viscous Transition in Continental Crust. *Journal of Geophysical Research: Solid Earth* 113 (B1): B01407. doi:10.1029/2006JB004833.
- Schwartz, S., Lardeaux J.M., Guillot, S., Tricart, P., 2000. Diversité Du Métamorphisme Éclogitique Dans Le Massif Ophiolitique Du Monviso (Alpes Occidentales, Italie). *Geodinamica Acta* 13 (2–3): 169–88. doi:10.1080/09853111.2000.11105371.

Sibson, R.H., 1977. Fault Rocks and Fault Mechanisms. *Journal of the Geological Society* 133 (3): 191–213. doi:10.1144/gsjgs.133.3.0191.

Sibson, R.H., 1986. Brecciation Processes in Fault Zones: Inferences from Earthquake Rupturing. *Pure and Applied Geophysics* 124 (1–2): 159–75. doi:10.1007/BF00875724.

Spandler, C., Pettke, T., Rubatto, D., 2011. Internal and External Fluid Sources for Eclogite-Facies Veins in the Monviso Meta-Ophiolite, Western Alps: Implications for Fluid Flow in Subduction Zones. *Journal of Petrology* 52 (6): 1207–36. doi:10.1093/petrology/egr025.

Toyoshima, T., 1990. Pseudotachylite from the Main Zone of the Hidaka Metamorphic Belt, Hokkaido, Northern Japan. *Journal of Metamorphic Geology* 8 (5): 507–23. doi:10.1111/j.1525-1314.1990.tb00483.x.

Vannucchi, P., Sage F., Morgan J.P., Remitti, F., Collot, J.Y., 2012. Toward a Dynamic Concept of the Subduction Channel at Erosive Convergent Margins with Implications for Interplate Material Transfer. *Geochemistry, Geophysics, Geosystems* 13 (2): Q02003. doi:10.1029/2011GC003846.

Whitney, D.L., Evans, B.W., 2010. Abbreviations for Names of Rock-Forming Minerals. *American Mineralogist* 95 (1): 185–87. doi:10.2138/am.2010.3371.

Yamasaki, T., Seno, T., 2003. Double Seismic Zone and Dehydration Embrittlement of the Subducting Slab. *Journal of Geophysical Research: Solid Earth* 108 (B4). doi:10.1029/2002JB001918.

4.11 The identification of dynamic fracture networks in coseismic breccia

In absence of pseudotachylite formation, four dominant mechanical processes of rock brecciation are recognized to be potentially linked to seismic activity. Sibson (1986) predicted that continued displacement along a master fault may result in seismic-derived structures as (a) ***attrition breccia***, from progressive frictional wear along principal slip surfaces during both seismic and aseismic sliding, (b) ***distributed crush breccia***, involving microfracturing over broad regions when slip on the principal slip surfaces is impeded by antidilational jogs or other obstructions, and (c) ***implosion breccia***, associated with the sudden creation of void space and fluid-pressure differentials at dilational fault jogs during earthquake rupture propagation. Additionally, Melosh et al. (2014) recognized as seismic-product the (d) ***single slip dilational breccia***, which differs from the implosion breccia (sensu Sibson) by the absence of pressure gradient-driven failure of the fault walls, but rather by the intersection and interaction of dynamic, near-fault, fractures associated with an earthquake rupture. All these brecciation processes were described in rupture surfaces accompanying shallow earthquakes, located in the Seismogenic Zone (up-to 30 km-depth). Nevertheless, such dynamic fault breccias from mid-crustal shear zones were predicted to form through-out the seismogenic crust to the depth (e.g, up to Intermediate Depth, ~70-300 km in subducted slab) in a variety of tectonic settings or rock types (e.g., Melosh et al., 2014). Thus, the structural (*Chapter 3*) and statistical analysis of eclogite-breccia surfaces on blocks from LSZ would help to discriminate between seismic Vs aseismic origin of Monviso eclogite breccia. Hereafter are summarize some of the univocally-defining characteristics of dynamically formed, single-slip seismic breccia.

4.11.1 - Dynamic fracturing: fracture geometry and spacing

Fracture propagation is dynamic when inertia is an important factor in the fracturing process, such as during rapid loading or crack propagation (Freund, 1990). An earthquake is the result of dynamic rupture propagation along a fault plane (Ide & Aochi, 2005). It has been observed in experiments that dynamic ruptures propagating above a critical velocity will produce unique networks of closely spaced secondary tensile fractures (e.g. Sharon & Fineberg, 1996; Griffith et al., 2009b). While the growth of quasi-static extension fractures does not preclude clustering (Delaney et al., 1986), it does encourage localization to fewer main fractures by creating stress shadows (e.g., Pollard & Segall, 1987; Gross, 1993), and limiting failure to the most favorable flaws (Grady & Kipp, 1987).

Because earthquakes are dynamic ruptures they will produce diagnostic fracturing patterns that cannot be explained by static conditions alone (e.g., Melosh et al., 2014). Analog and field studies of the strain rate dependence of fracturing patterns support the formation of clusters of high density fractures and branching fractures at higher strain rates (Sagy et al., 2001; Rockwell et al., 2009; Riley and Tikoff, 2010; Melosh et al., 2014) (Fig. 2A). The geometries of secondary dynamic fractures depend on the mode of primary fracture propagation (e.g. Sharon & Fineberg, 1996; Griffith et al., 2009b).

1.1.1. Subsidiary fractures from a dynamic mode II fracture

Dynamic shear rupture experiments demonstrate that tensile microcracks form at high angles of 87–92° (Rosakis et al., 2000) and 70–80° (Griffith et al., 2009b), on one side of the rupture plane within the tensile quadrant (*Figure 43a*). The difference in angle between the two studies is ascribed to the rupture velocity and static prestress conditions. Microcracks form an acute angle with the direction of rupture propagation, are closely spaced and can be slightly curved (e.g.

Griffith et al., 2009b). These observations match previous laboratory results (Ravi-Chandar & Knauss, 1984) and theoretical predictions (Samudrala et al., 2002; Di Toro et al., 2005). The relation between laboratory-made microcracks and geologic observations of off-fault tensile fractures and pseudotachylyte injection veins was proposed by Rosakis (2002) and supported by Di Toro et al. (2005), Rowe et al. (2012), Griffith et al. (2012), and Ngo et al. (2012).

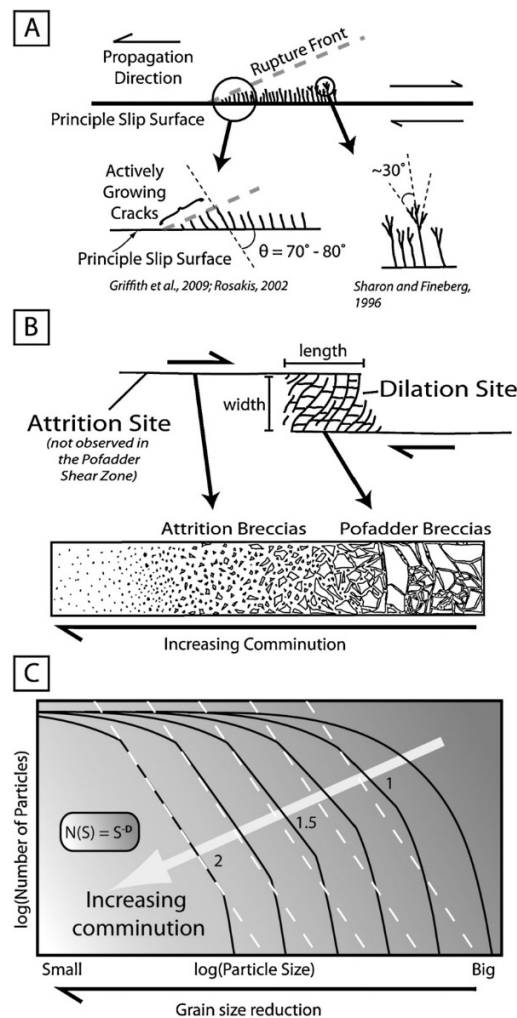


Figure 43: Figure from Melosh et al. (2014) depicting two styles of dynamic fracture geometries. A) schematic drawing of fractures growing behind the rupture front at high angles ($70-80^\circ$) from the principle slip surface, and those growing off mode I parent fractures at low angles of $\sim 30^\circ$. B) Development locus of dilation and attrition breccias on a schematic strike slip fault and associated textures of each C) Model for the evolution of particle size

distributions (PSD) (black lines) with increasing comminution, after Blenkinsop and Fernandes (2000), example D-values are shown. White dashed lines are a reference power-law fit for the PSD at the far left. PSD are meant to roughly correspond to the breccia textures drawn directly above

1.1.2. Subsidiary fractures from a dynamic mode I crack

During primary mode I crack propagation a branching fracture morphology occurs at a critical velocity, above which exists a linear relationship between fracture area and velocity (*Figure 43a*) (Sharon & Fineberg, 1996). Branching of dynamic tensile fractures has been observed in experiments (Isida & Noguchi, 1992; Sharon & Fineberg, 1996), and predicted numerically (Abraham et al., 1994; Xu and Needleman, 1994) with a characteristic preferred branching angle of $\sim 30^\circ$. Sagy et al. (2001) reported a series of clustered fractures with a branching morphology that increase in abundance with proximity to a major strike slip fault. This branching morphology is suggested to form because it is easier for the rock to dissipate energy by forming many branching fractures rather than increasing the propagation velocity on a single fracture (Sharon & Fineberg, 1996). A branching morphology is also observed on a microscale in the densely spaced tabular fracture clusters described by Riley & Tikoff (2010) and in pulverized rocks from deep boreholes (Sagy & Korngreen, 2012).

1.1.3. Fracture spacing

Studies of mode I fracture spacing in layered media find that a “fracture saturation” condition is reached when fracture length (L_f) approaches the fracture spacing (S) (Pollard & Segall, 1987; Wu & Pollard, 1995; Bai & Pollard, 2000a, 2000b). Below a critical value, where $S/L_f \approx 1$, fracture infilling is inhibited. Fracture length can only be as long as the layered medium permits so that at fracture saturation $L_f \approx S \approx$ layer thickness. Extension alone will not form fracture networks with a spacing to length ratio less than half the critical value; for this to occur other mechanisms are

required (Bai & Pollard, 2000a). A dilational stepover between two parallel fault segments may be an analogous setting to a stretching layer bounded by two free surfaces, as modeled by Bai & Pollard (2000a, 2000b), therefore, we use their findings as a quasi-static prediction for fracture spacing.

4.11.2 - Dynamic fracturing summary

In summary, high angle (70–90°) mode I fractures emanate from the surface of a dynamically slipping fault, forming near the rupture tip with an acute angle to the slip surface in the direction of rupture propagation. They form all along the fault during rupture propagation, leaving a set of parallel fractures decorating the wall rock. These tensile fractures may themselves branch, with subsidiary fractures forming angles of ~30° to the primary tensile fracture (e.g. Fig. 2A). Dynamically growing tensile fractures may form in much closer spacing than is theoretically predicted by quasi-static descriptions of elastic solids, creating a metric by which dynamic fracture arrays may be distinguished in field observations. Where these fracture sets interact between multiple fault surfaces, fracture spacing will correspond to particle size in brecciated rock.

4.11.3 Particle size distributions

Particle or grain size distributions are used extensively in fault rock studies in order to quantify the self-similarity of fracturing and fragmentation processes (e.g. Sammis et al., 1987; Biegel et al., 1989; Sammis & Biegel, 1989; Marone & Scholz, 1989; Blenkinsop, 1991; Billi et al., 2003; Monzawa & Otsuki, 2003; Billi & Storti, 2004; Heilbronner & Keulen, 2006). Effects of confining pressure, strain, temperature, permeability and deformation mechanisms are manifested in particle size distributions rendering their analyses an important tool in mechanical fault zone studies

(Allegre et al., 1982; Marone and Scholz, 1989; Storti et al., 2003; Hadizadeh & Johnson, 2003; Heilbronner & Keulen, 2006; Keulen et al., 2007; Luther et al., 2013). A particle size distribution is created in log–log space by plotting the cumulative number of particles against their size, the linear portion of the resulting curve is fit with the equation:

$$N(S)=S^{-D}$$

where S is clast size, N(S) is the number of clasts above size S, and D is the slope of the best fit line (D-value). Typically, only the center of the curve is linear, as the particles in larger size classes are underrepresented where size approaches the total size of the studied sample; particles at the lower size classes are underrepresented due to observational detection limits (e.g. Blenkinsop, 1991). However, many particle distribution curves are not log-linear over any grain size range, and cannot be fit with a power law (e.g. Blenkinsop & Fernandes, 2000).

D-values between 1–3 are commonly measured in three-dimensional analyses, corresponding to values of 0–2 when D- value is estimated from two-dimensional observations (Mandelbrot, 1982; Turcotte, 1986; Glazner & Mills, 2012). D-values measured in this study are two-dimensional, measured on outcrop photographs and thin sections. In order to draw comparisons we converted the 3D D-values of other studies to 2D D-values

$$(D_{3d}=D_{2d}+1) \text{ (Mandelbrot, 1982).}$$

D-values describe the relative abundance of smaller versus larger clasts, so that **increasing the relative abundance of smaller size particles creates a steeper slope and a higher D-value.** Because cataclasis reduces particle size and increases the proportion of fine particles, it follows that **breccias should have lower D-values than cataclasites or gouge** (Figure 43b-c). Typical 2D D-values for fault breccias range from ~1–1.8 (Storti et al., 2003; Billi & Storti, 2004; Billi, 2005), measured in carbonate fault rocks. Clark et al. (2006) report D-values from fluid induced breccias

of 1.17–1.34. Mean D-values of cracked granitoid rock calculated from Table 4 of Keulen et al. (2007) are 1.21 ± 0.11 . Cataclasite and gouge 2D D-values are typically higher, clustering around 1.6–1.7 (Sammis et al., 1987; Biegel et al., 1989; Marone & Scholz, 1989), but reaching values as high as 2.5 (for a review, see Table 1 of Keulen et al., 2007). Despite clustering of D-values near 1.6 (e.g. Sammis et al., 1987) many studies find a progressive **increase in D-value with increasing cataclasite maturity** (Blenkinsop, 1991; Hattori & Yamamoto, 1999; Billi & Storti, 2004; Storti et al., 2007). There is general consensus that **D-value increases with increased fragmentation**, which is correlated to advancing cataclasis during progressive fault slip. Exceptions to this trend have been suggested by studies linking dynamic pulverization to gouge formation and non-fractal particle size distributions (Wilson et al., 2005; Reches & Dewers, 2005). Thus, **dynamically formed breccias are expected to have either low D-values or non-fractal distributions** (Figure 42b-c), due to the many similar sized clasts controlled by the characteristic fracture spacing.

1.3. The eclogite breccias of Monviso metaophiolite and the limitations to of statistical analysis

Above it was proposed to use particle size distributions in order to apply a quantitative method for distinguishing dynamic breccias. We tried to compare the theoretical background of dynamic fracture networks development to the observed grain size distributions for **5 breccia planes** from the LSZ. The goal was to find univocal proxies to discriminate between the seismic Vs aseismic origin of eclogite-facies breccia recognized in the LSZ metagabbro blocks.

Nevertheless, several limitation at the outcrops-scale affected the statistical analysis of clasts:

1. In the larger part of the blocks (>95%), the pervasive cover by late-stage metasomatic rinds (composed by serpentinite and other hydrous phases; more detail in

Angiboust et Al., 2014) strongly reduce the available surface for structural and statistical analysis of breccia layers.

2. The lack of extended, planar, breccia surfaces (due to the roundness of metagabbro blocks) affected the photo-reproduction of outcrops. In many cases the distortion of the photos stitched in panoramic view resulted in deformed representation of clasts and matrix domains, biasing the correct measurement of dimensional parameters.

3. Lichens preferentially grow over the portion of metagabbro blocks/breccia free of metasomatic rinds.

4. The color of weathering patina on metagabbros is often flattening the visual differences between clasts and matrix, resulting in the mismatching of their real surfaces.

5. The general lack of hand-size samples suitable for statistic structural analysis affected the reproducibility of data between outcrop-scale and hand-specimen scale.

6. In best-preserved breccia layers, clasts contain phases similar to those of matrices (e.g., Omp + Grt \pm Lws; e.g., *Figure 36* and *Figure 37*). The same color contrast biased any automated clast-matrix detection, therefore manual outlining of breccia clasts was required.

Taking in account these problems, for every outcrops the clasts were outlined on scaled photographs with the use of a drawing track pad. The resultant black and white images were imported into Fiji© (Windows compilation of Macintosh Image-J software) for the analysis of clasts (1) area, (2) Fereth's lenght, (3) maximum clasts length-width, (4) misorientation angle between clasts elongation axis and inferred brecciation surface and (5) the area ratio between class and matrix. The following

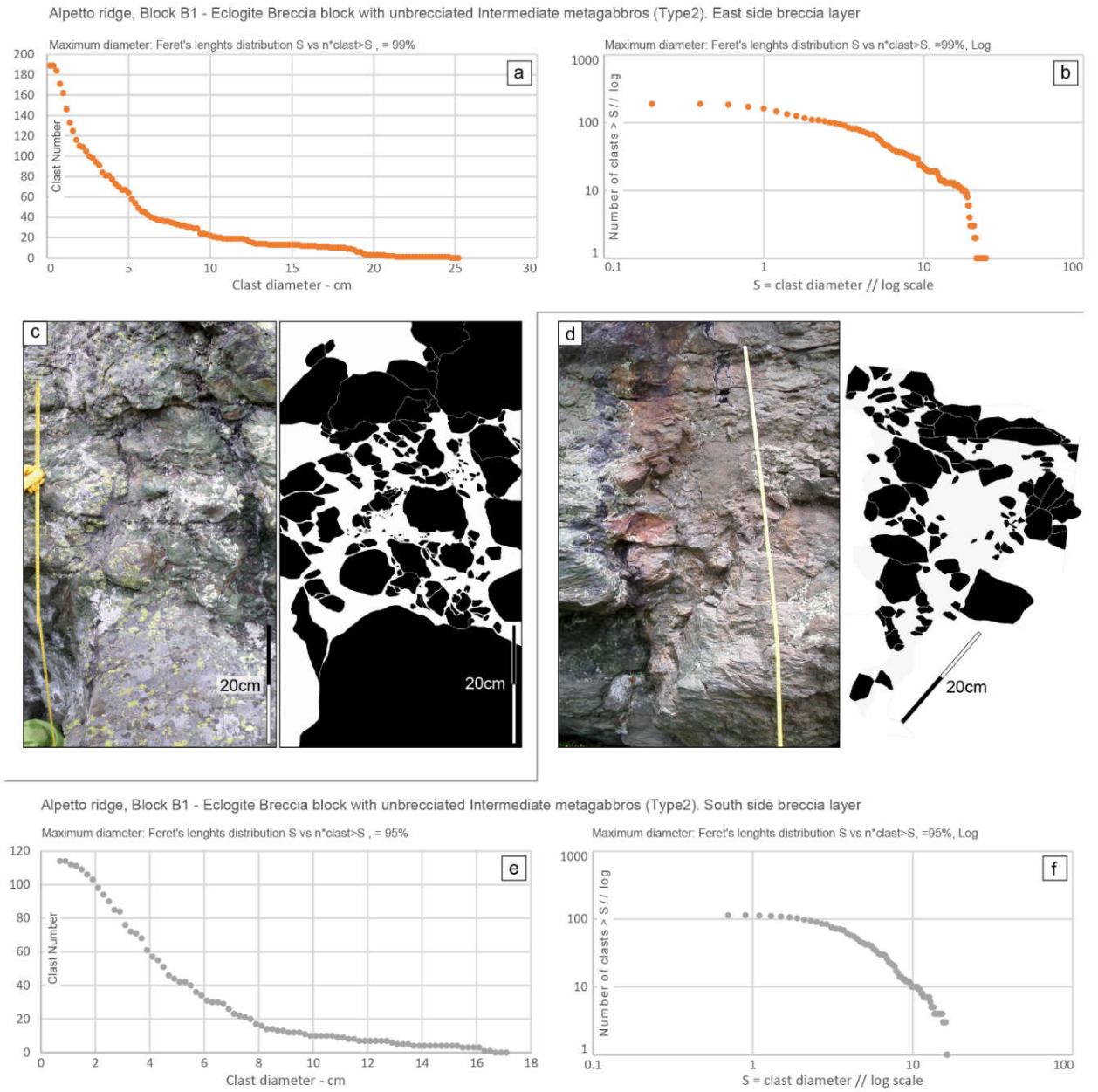


Figure 44: Block B1 (east of Rocce Sbiasere ridge): morphological study of two breccia layers cutting with complex geometries the intact Mg-Al metagabbros. The two breccia layers contain both M2 and M3 matrix.

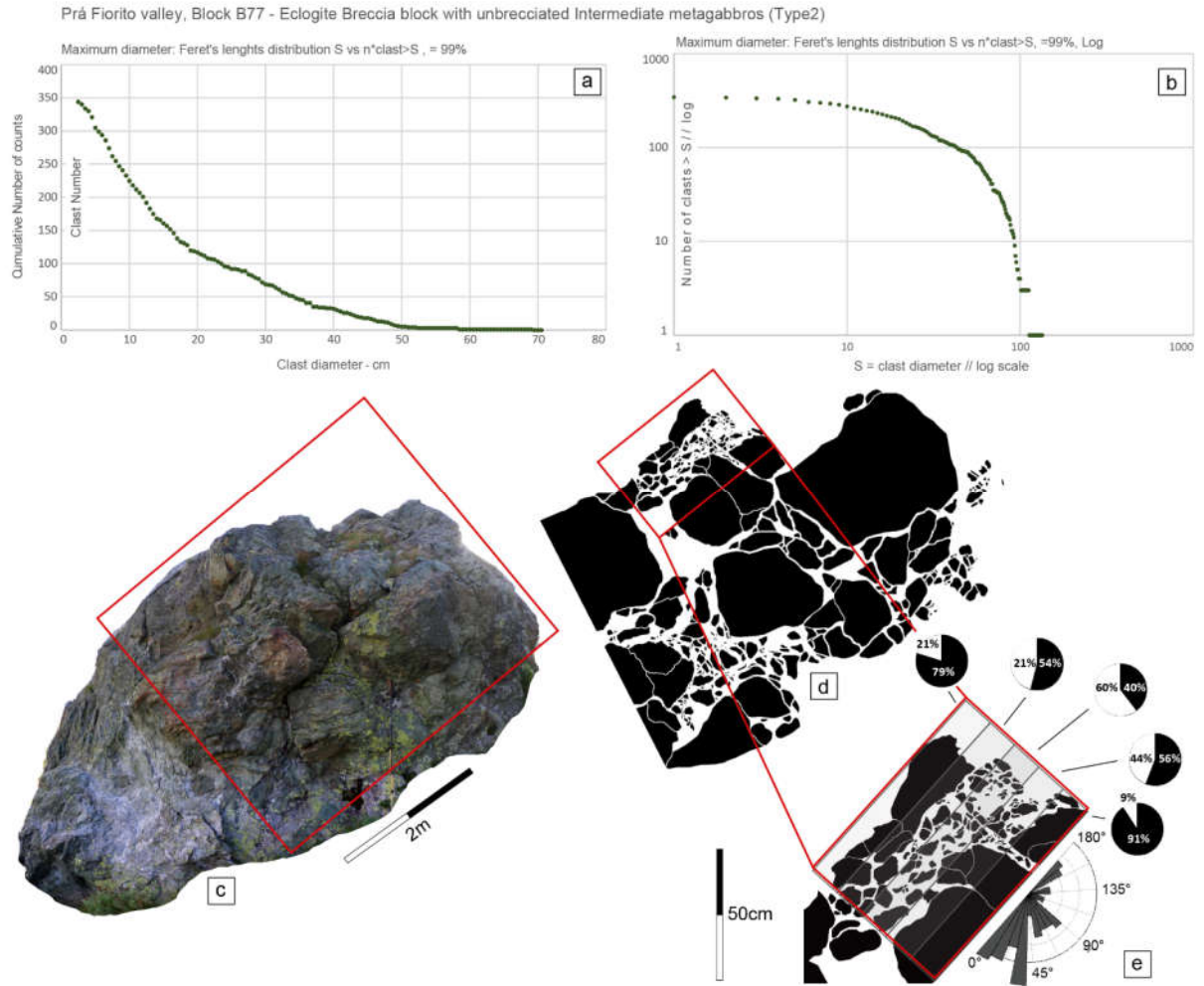


Figure 45: Block 77 (south flank of Prá Fiorito valley): morphological study of two breccia layers cutting with complex geometries the intact Mg-Al metagabbros. Both the breccia layers contains both M2 and M3 matrix. In detail on figure (d) the drawn of the selected area showing the complex geometries of more comminuted breccia planes. The statistical analysis of the misorientation of clasts elongation axis respect to the inferred master fault planes (e) suggested that the angles are not randomly distributed but grouped around $30^{\circ} \pm 10^{\circ}$ and $80^{\circ} \pm 10^{\circ}$. Nevertheless the low AR (aspect-ratio) values of the clasts (generally < 1.2) and high roundness of the clasts risk to bias the real meaning of the angle-distribution analysis. (f) Close-up view of a breccia plane on B77, showing the pervasive lichens + serpentinite coating that in most cases prevent the correct morphological characterization of the breccias.

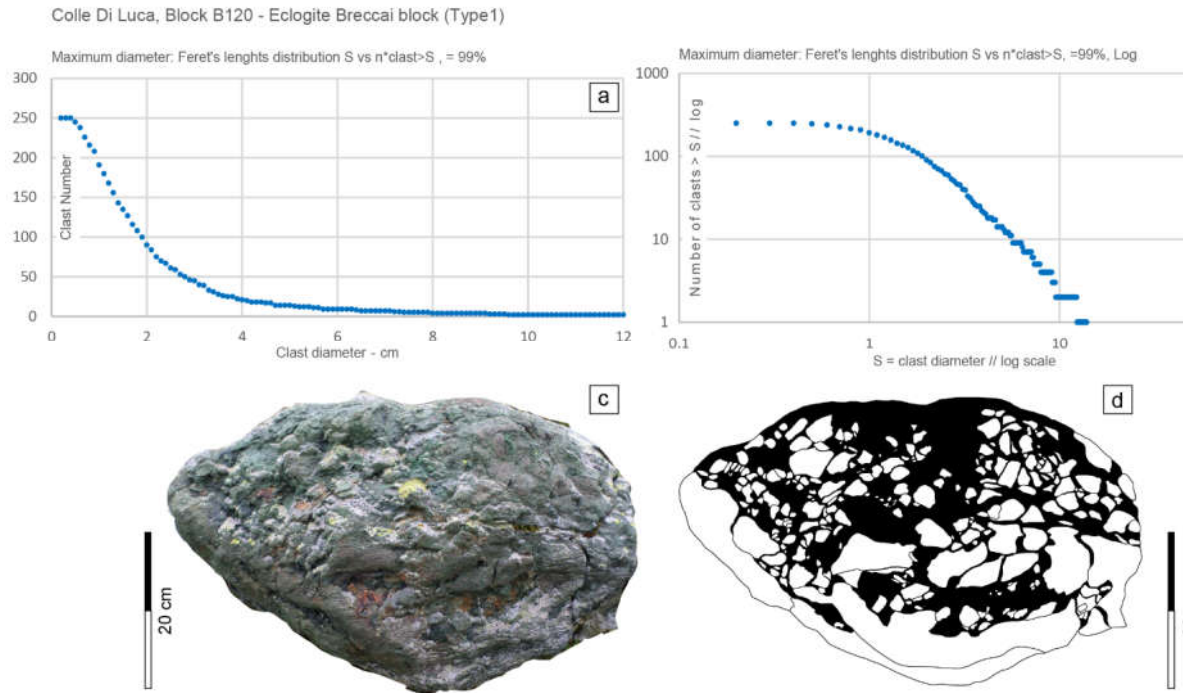


Figure 46: Block B120 (north of Colle di Luca pass): morphological study of the incomplete breccia layer cutting with planar geometry the intact Mg-Al metagabbros (visible at the base of the block). The breccia layer contains both M1 and M2 matrix.

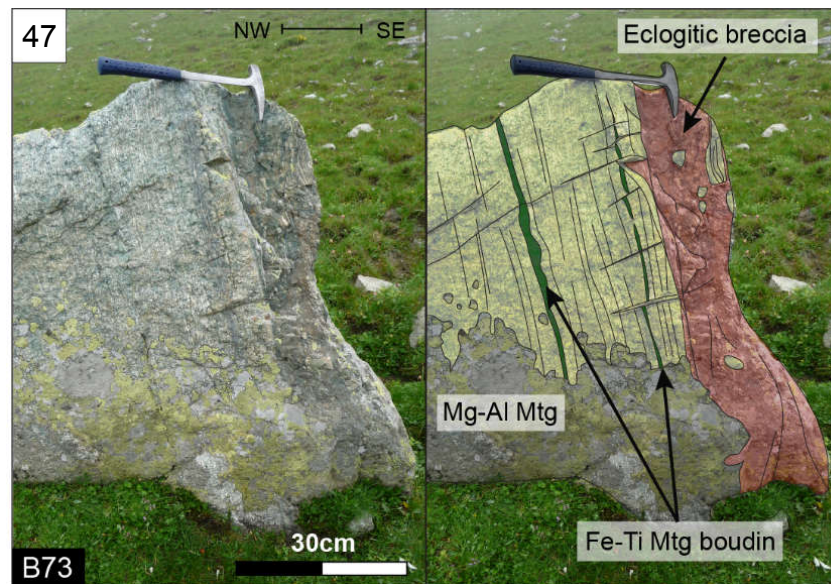


Figure 47: example of “injection veins” sub-perpendicular to the contact between the wall-rock and the breccia layer preserved in block B73 (north flank of Pra Fiorito valley).

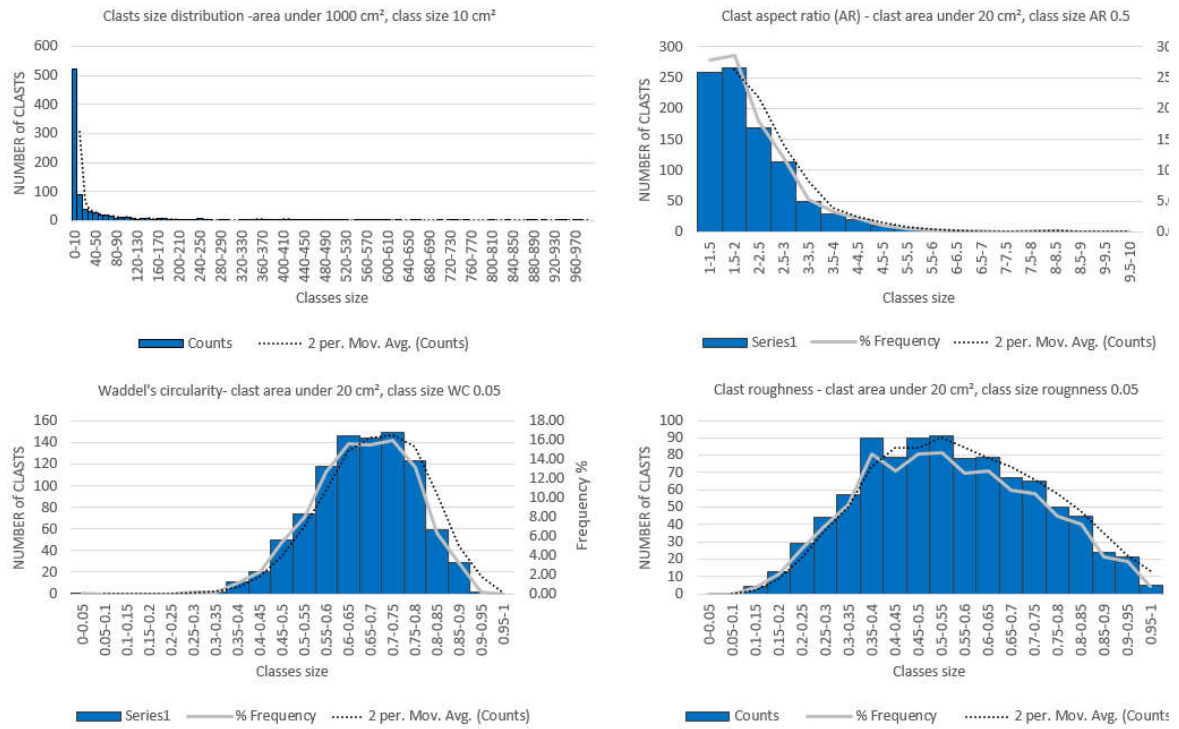


Figure 48: results of statistical analysis. All data with area > 1000 cm² (~99% of analysed clasts)

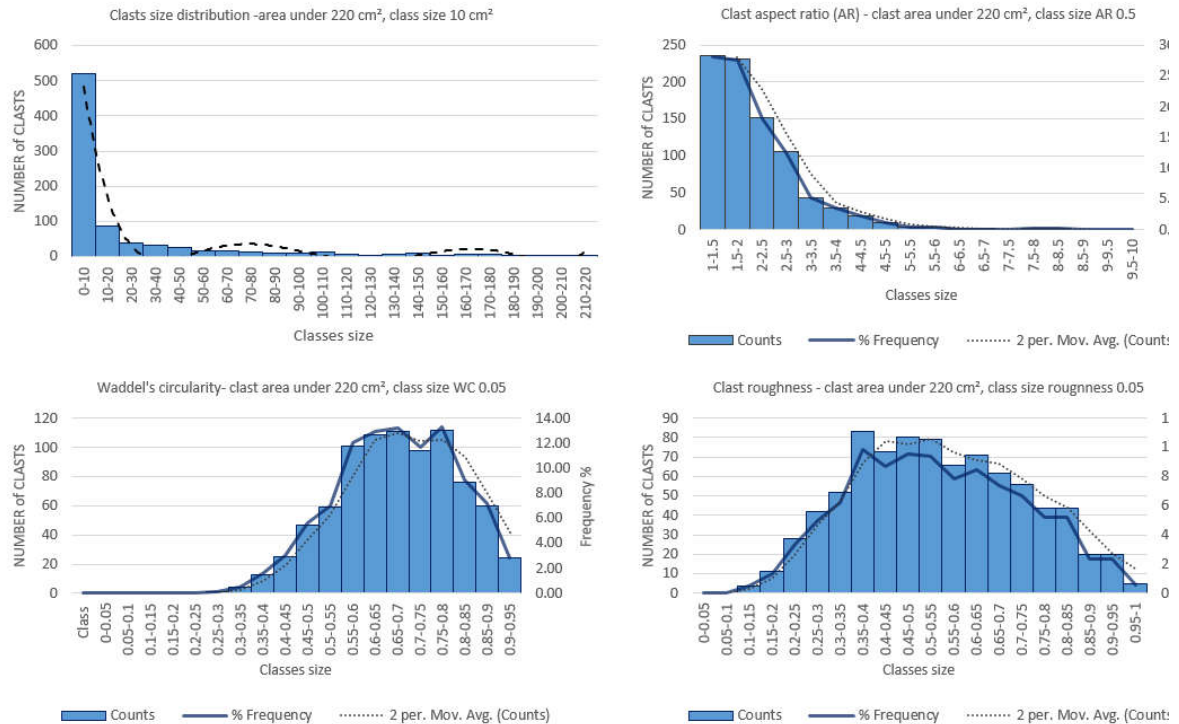


Figure 49: results of statistical analysis. All data with area > 220 cm² (~90% of analysed clasts)

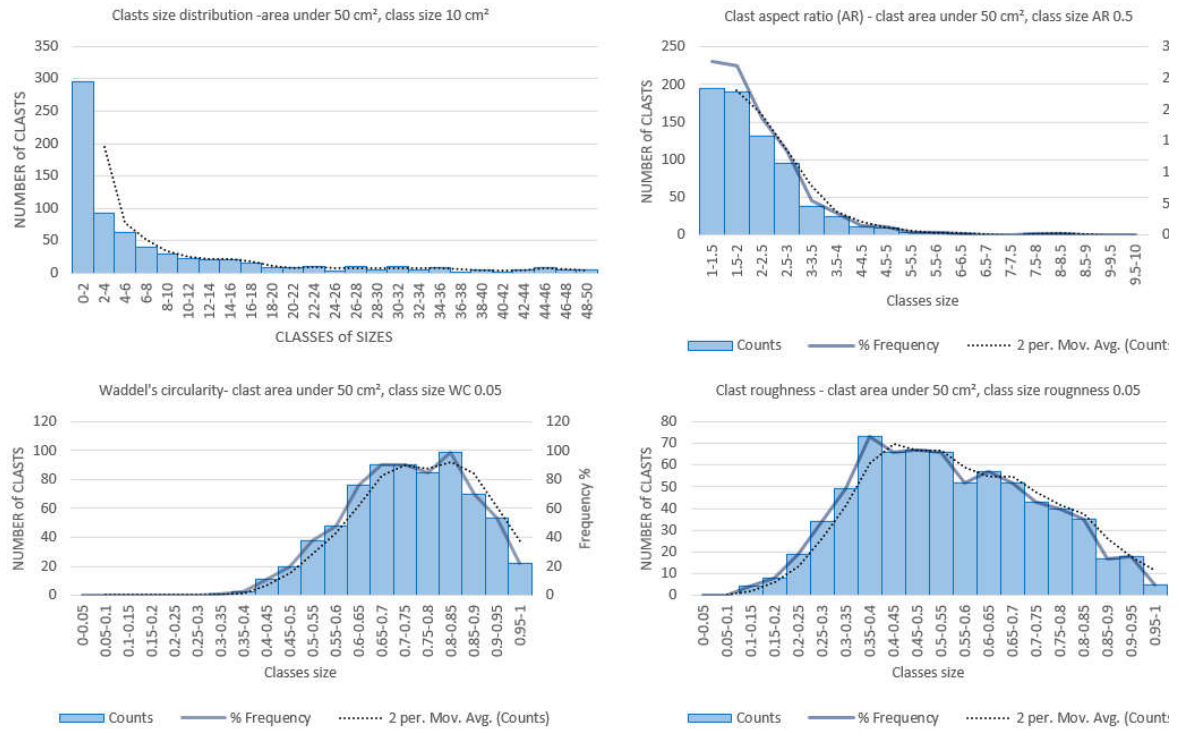


Figure 50: results of statistical analysis. All data with area $> 50 \text{ cm}^2$ ($\sim 75\%$ of analysed clasts)

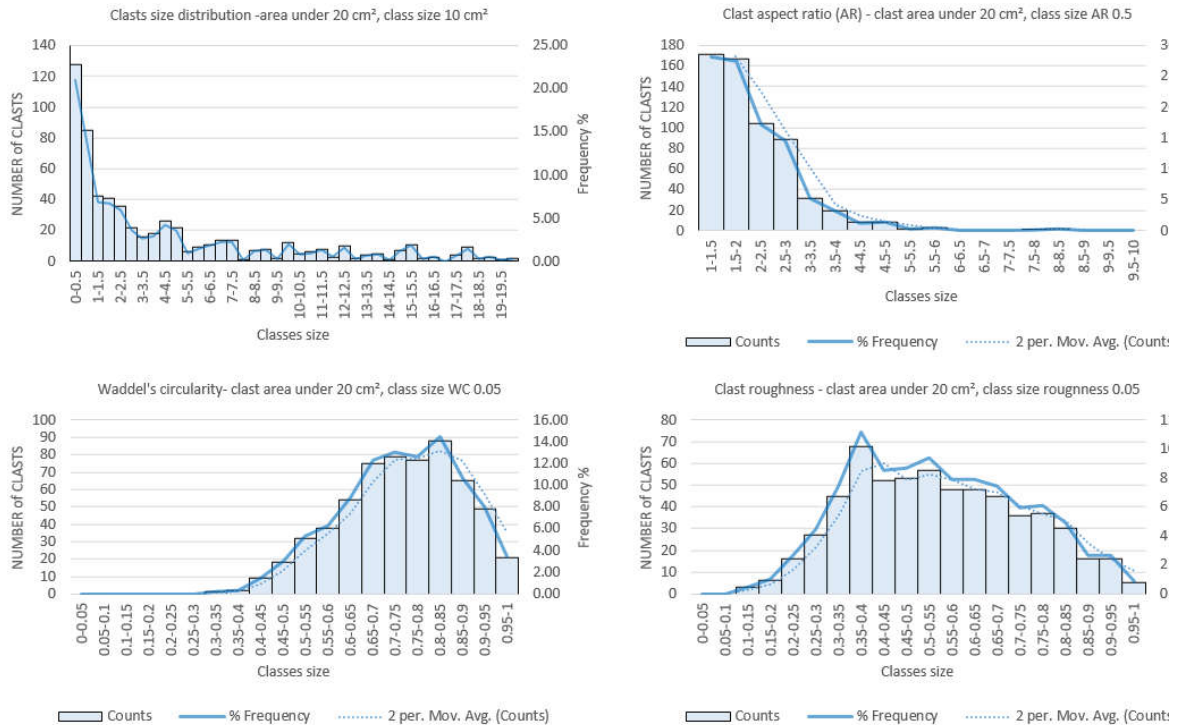


Figure 51: results of statistical analysis. All data with area $> 10 \text{ cm}^2$ ($\sim 50\%$ of analysed clasts)

Monviso eclogite-breccia: can statistic structural analysis unravel onset of seismic activity?

Few of the universally accepted characteristics defining dynamically-formed, single-slip dilational breccias (e.g., Sibson, 1986; Melosh et al., 2014) are observed in the studied Monviso metagabbros. In agreement to their generation by seismic activity there are the rare preserved portion of breccia with exploded jigsaw texture, minimal clast rotation and displacement. As predicted by Melosh et al. (2014) they are composed by monomict, locally sourced clasts (e.g., Fe-Ti metagabbros), are poor of wear products (e.g., host-rock-wall fragments: Intermediate metagabbros), are clast-supported and display abrupt transition from crackle to mosaic breccia textures (more details in chapter 4).

Nevertheless, the eclogitic breccia layers displaying the above listed characteristics are limited in extension (between ~1 and ~3 meters) and rare (observed only in blocks B154 and B770); thus are not representative of the 296 mapped blocks.

As direct consequence of the limited extension of outcrops, (e.g., analysis developed on meter-seized blocks *Chapter 4*, tables of *SM5*) and the short length of rupture surfaces (corresponding to the principle slip surface; e.g., *Figure 43*) was not possible to define the off-fault damage mode (e.g., Wilson et al., 2003; Blenkinsop, 2008; Mitchell & Faulkner 2009) producing brecciation in metagabbros. Thus the discrimination between ***attrition breccias*** and ***dilation breccias***, (the latter considered to be genuine product of seismic activity: e.g., Sibson, 1986; Blenkinsop & Fernandes, 2000; Melosch et al., 2014), was not possible.

Moreover, the fabrics of the best-preserved breccia surface from block B154 (*Figure 36*) corresponds to ***attrition breccia*** rather than ***collapse breccia***, thus suggesting onset of tectonic brecciation in metagabbros but excluding direct correlation to seismicity.

Another limitation in the structural recognition of seismically-induced brecciation in Monviso metagabbros is the lack of outcrops preserving fracture networks in wall-rock, being their **morphology and density** the most important attribute for recognizing dynamically formed breccia (e.g., Melosh et al., 2014). In some cases was possible to recognize some omphacite-bearing veins emanating from the breccia layers inside the intact wall rock (e.g., *Figure 47*). Nevertheless, the propagation of seismic front would produce fractures and not veins (*Figure 43*; e.g., Sibon, 1986; Melosh et al., 2014), being the latter indicative of fluid circulation and thus hydraulic fracturing rather than purely tectonic brecciation. Additionally, some of these veins are clearly ductile-deformed in the hosting metagabbros (in detail, the Intermediate metagabbros) and witness that protracted ductile deformation continued around the brecciated layers. This occurrence, although not excluding the onset of brecciation by seismic event/s, prevent the preservation of any brittle structure in the wall rocks.

Another necessary statement to study the development of seismically-derived fracture networks is to run the morphological and statistical analysis of tectonic breccia on surfaces that are thought to be produced by a **single event** (e.g., Rowe et al., 2011; Melosh et al., 2014). Indeed, the overprint of multiple events would result in the overestimation of the energy leading to the brecciation and in the misunderstanding of mechanisms inducing the rock failure (e.g., multiple events could develop with different mechanisms; Jebrack, 1997). In all the analyzed breccia surfaces, the crosscutting relationships between the different matrices are clearly visible (e.g., *Figure 36c*) with reworking of pre-existing brecciated surfaces by later-stage events. Thus, the occurrence of matrix M3 enveloping clasts composed by metagabbros sealed by M1/M2 matrices prevents any correct and rigorous structural evaluation of the brecciation kinematics. The evaluation of the D values

for eclogitic breccias was thus discarded and, for this reason, the results of the clast-size analysis were used only for the morphological description of brittle rupture at eclogite-facies condition.

The significance of this work is twofold:

1) based on breccia geometry, geologic relationships and particle size distributions it was not possible to recognize, with certainty, paleoseismic fingerprint on the generation of eclogitic breccia from Monviso metaophiolite. The D-values estimation on analyzed samples are not feasible to identify and quantify dynamically-formed breccias, due to the complex interplay and overprinting between of the different matrices (M1, M2 and M3), which potentially developed with different mechanisms. However, eclogitic breccias from Monviso don't appear to be derived by pressure gradient-driven failure of the walls of a void, but rather by the intersection and interaction of dynamic, near-fault fractures (*sensu* Sibson, 1986 and Melosh et al., 2014).

2) Nevertheless, considering (I) the extended serpentinite-coating of outcrops, (II) their diffused retrogression and (III) the limited extension of breccia layers (all elements strongly limiting any macrostructural analysis) it is not possible to exclude with certainty the potential association between brecciation and earthquake rupture at Intermediate Depth.

5.1. Introduction

The structural analysis of the eclogite breccia from the Lower Shear Zone (LSZ) demonstrates their univocal genesis at eclogite-facies conditions, with the development of three successive matrices. Three sets of veins also developed along the prograde PT path. Structural and microstructural evidences showed that brecciation preferentially affected the Fe-Ti metagabbro boudins embedded in Mg-Al metagabbro bodies, suggesting that rheological contrasts controlled and localized the brecciation. In detail, chronological relationships exist between the matrices cementing the eclogite breccia, with matrix M3 (Lws + Omp \pm Tlc \pm Grt) clearly postdating M2 (Omp + Grt \pm Tlc \pm Rtl) and M1 (Omp). The different parageneses suggest slight changes regarding the P-T conditions, but potentially bigger differences among the fluids (amount and composition) present during the brecciation events, as implicated by the presence of talc and other hydrated minerals as lawsonite in some matrices only. However, a petrographic analysis alone cannot describe these variations. As already discussed in the introduction, intermediate-depth earthquakes may be triggered by metamorphic dehydration reactions (e.g., Hacker et al., 2003a, 2003b; Yamasaki and Seno, 2003; Fumagalli and Poli, 2005; Brudzinski et al., 2007); free-fluid production by mineral phase-change and and/or fluid circulation seem to be the main candidates to explain the seismicity at these depths. However, fluid circulation may be very restricted in gabbros at eclogite-facies condition due to the limited porosity of these rocks, which is generally restricted to microfractures, isolated pores, cleavage planes and mineral boundaries (e.g., Mibe et al., 2003) with a connectivity presumed to be very limited (Watson & Brenan, 1987; Davies, 1999) and that is estimated to be six-orders of magnitude lower than for mylonitic serpentinites (10^{-18}m^2 ; Morrow et al., 1984). Nevertheless, evidences of localized fluid circulation has already been

observed in these eclogitic metagabbros (e.g., Philippot & Kienast, 1989; Philippot & Selverstone, 1991; Philippot & van Roermund, 1992; Nadeau et al., 1993; Spandler et al., 2011; Angiboust et al., 2012 and 2014) even if the fluid source (e.g., “internal” Vs “external” to the gabbros) remains debated. In the Fe-Ti metagabbros from Lago Superiore area (Intermediate Shear Zone, ISZ) Philippot & Selverstone (1991) and Nadeau et al. (1993) suggested that the Omp-bearing veins formed in the presence of locally-derived fluids, with migration restricted to the millimetre- to centimetre-scale and no evidences of external fluid involvement during the vein formation. An exception is the kosmochlor-rich clinopyroxene included in some vein garnet or as cores of vein omphacite; on this basis, Philippot & Kienast (1989) suggested that external fluid infiltration may have been involved in the early stage of vein formation. In their work, Spandler et al. (2011) found evidences for externally-derived fluids (likely derived by dehydration reactions in serpentinites) involved in the formation of garnet and omphacite-bearing veins (Type 2 veins, *sensu* Spandler; corresponding to ISZ’s *Veins T2* in our work); nevertheless, formation of both Cr-poor and Cr-rich veins was inferred to be coeval (Philippot & Kienast, 1989; Spandler et al., 2011).

The large dataset and studies on the HP-veins developed in the metagabbros of the ISZ has no equivalent in the Lower Shear Zone; moreover, no studies focused on the geochemical characterization of eclogitic breccia of LSZ, but rather on the late-stage metasomatism that affected metagabbro blocks disseminated in the shear zone matrix (Angiboust et al., 2014). Thus, open questions still remain on:

- (I) The origin of fluids involved in brecciation processes: produced in-situ (then along which reactions?) or externally derived?
- (II) The timing and kinematics of the successive brecciation steps, to better constrain the mechanical parameters controlling the brecciation of Monviso metagabbros (pure mechanical brecciation or hydraulic fracturing?).

(III) The rheological changes induced by the successive crystallization of veins and matrices in the eclogitized metagabbros, to understand why brecciation preferentially developed in Fe-Ti metagabbros boudins, and how breccia planes were subsequently disseminated as blocks in the LSZ and ISZ.

(IV) The kinematics and timing of intraslab brecciation relative to the development of the shear zones (ISZ and LSZ), and to the detachment and exhumation of the Monviso ophiolitic complex.

To address these issues, we performed a detailed geochemical study of clasts, veins and matrices, combining bulk-rock analyses (major and trace elements) to in-situ LA-ICP-MS (trace elements) and microprobe (major) analyses on minerals. We focused our attention on **12** samples from **7** different outcrops for the in-situ trace-element analysis (*Table 5*), while for the bulk-rock geochemistry, **20** samples were analysed (*Table 6*). In addition to the metagabbros (both Mg-Al and Fe-Ti, intact and brecciated), antigorite schists forming the matrix of the shear zones, blocks of massive peridotite, and metasediments pinched-out in the ISZ were studied.

5.2 Analytical techniques

5.2.1 Bulk-rock geochemical analysis

Twenty fist-sized samples of Type-2 veins, Fe-Ti eclogitic host-rock, serpentinite and Mg-Al metagabbro from the Lago Superiore Unit were crushed in a steel jaw crusher and then milled to fine powder in an agate mill. A small amount of crushed, inclusion-free hydrothermal quartz was milled between each sample to prevent cross-contamination. Additionally, a small amount of the rock intended to be milled was crushed for 10', in order to the self-contaminate the mill and fade the signals of precedent samples. Whole rock chemical analyses were performed at the SARM-CRPG (Nancy, France). Major elements were analyzed by inductively coupled plasma-optical emission spectroscopy (ICP-OES) after fusion with LiBO₃ and dissolution in HNO₃. Trace

elements were quantified by inductively coupled plasma mass spectrometry (ICP-MS) following the procedure described by following the procedure described by Carignan et al. (2001).

5.2.2 X-ray mapping and mineral major element analysis

Before the in-situ LA-ICP-MS measurements, the microstructures of the 12 analysed samples were studied at the thin section scale using both optical microscope and SEM (Zeiss Supra 55VP, associated to SSD detector PTG Sahara for EDS analysis; housed at the IStEP institute, UPMC, Paris).

The quantitative major element analyses were performed by EPMA (CAMECA FIVE and SX100) at CAMPARIS (UPMC, Paris). Major element measurements on clinopyroxene, garnet, rutile, apatite and ex-lawsonite (later investigated at LA-ICP-MS for trace elements) and other minerals (chlorite, talc, epidote, plagioclase and phengite) were performed using a 15 kV acceleration voltage and 10 nA beam current, wavelength-dispersive spectroscopy (WDS). Acquired data were processed using j(rZ) corrections and standardized against a set of well-characterized, in-lab standards: Fe₂O₃ (Fe), MnTiO₃ (Mn, Ti), diopside (Mg, Si), CaF₂ (F), orthoclase (Al, K), anorthite (Ca), albite (Na) and silicate (albite, almandine, forsterite, wollastonite).

The in-situ X-ray mapping (major-element mineral compositions) of matrices and clasts minerals were acquired on polished thin sections by wavelength-dispersive spectrometry using the CAMECA FIVE microprobe housed at CAMPARIS (UPMC, Paris). The X-ray mapping of matrices and clast omphacite, garnet and rutile was conducted using a beam at 15 kV acceleration voltage and 10 nA current condition. The mapping was run by point-scanning in steps of 2 µm, with dwell counting time set at 50ms for Si, Ti, Al, Mg, Ca, Mn, Na, K and at 300ms for Cr and Ni. The Fe²⁺ and Fe³⁺ contents of clinopyroxene and garnet were calculated on the basis of charge

balance, assuming perfect stoichiometry. All Fe was assumed to be Fe²⁺ in talc analyses and Fe³⁺ for rutile analyses.

5.2.3 Mineral trace-element analysis

Vein and host-rock minerals were analysed for trace elements in situ on polished thick sections by LA-ICP-MS at the Institute of Geological Sciences, University of Bern, Switzerland, using a Geolas Pro 193 nm ArF Excimer laser (Lambda Physik, Germany) coupled with an ELAN DRCE quadrupole mass spectrometer (QMS; Perkin Elmer, USA). The details on the setup and optimization strategies can be found in Pettke et al. (2012). The laser apparatus was set with a laterally homogeneous energy distribution, tuned to an ablation rate of ca. 0.15 μm per-pulse. A custom-built 20 cm³ ablation cell was used, and the aerosol carrier gas was a He-H₂ mixture. The analytical set-up was tuned for optimum performance across the entire mass range. To lower the detection limits of trace-element, the analyses on omphacite crystals were conducted using mainly 120 μm to 90 μm laser beam (and more rarely 44 μm and 60 μm); these beam diameters are larger than the dimensions of zoning in most crystals of matrices (e.g., *Figures 58a-e*) and mylonitic clasts. Indeed, most of the LA-ICP-MS analyses include multiple zonations and, therefore, direct comparison between trace element geochemistry and single major components (e.g., for omphacite: jadeite, diopside, aegirine) of matrices and veins omphacite is not feasible. Nevertheless, in samples LSZ 14-50, LSZ 14-53, LSZ 63-15b and LSZ 63-15d, it was possible to identify the different signatures of cores and rims for mylonitic clast omphacites as well as for some omphacite crystals of the M1 matrix. However, the calculation of trace-element partition coefficients between the different mineral phases was not possible but, using chemical proxies, the general trace-element behaviours were examined in regards of changes in major element composition of omphacite. In garnets the analyses were run using 120 μm , 90 μm and 60 μm laser

beam, size that permitted in most cases to differentiate between rims and cores, except for the atoll-garnet crystals from samples LSZ 63-15b, ISZ 35-15 and ISZ 38-15 where the zonation thickness is too thin to analyse each rim. Thanks to the exceptional size of the crystals (often >1mm), the analyses on the pseudomorphosed lawsonite were run using 160µm beam size, in order to obtain a bulk of their trace element signature. The pervasive replacement by epidote, plagioclase and mica prevents any rigorous evaluation of the concentration of most of the trace elements but still allows an evaluation of the variation of the elements thought to be poorly mobile, such as Cr, Ni and Co. Laser ablation on apatite crystals, usually run at the end of every measurement session with 90µm and 60µm beam sizes, was conducted with lower laser fluence at the sample site (10J/cm²) and slower repetition rate (8 Hz) to prevent the disruption of the crystals.

Each signal was carefully evaluated during off-line data reduction using SILLIS © program (Guillong et al., 2008), with rigorous limits of detection calculated for each element in every analysis following the formulation detailed in Pettke et al. (2012). Integration intervals were set to avoid contributions from accidentally ablated inclusions and/or cracks. External standardization was carried out using NIST SRM 612 and NIST GSD 1G glasses, which were analysed using a beam diameter of 44 mm and repetition rate of 10 Hz. Internal standardization employed major element concentrations determined by EPMA for minerals, or the sum of measured major element oxides (i.e., 100 % minus H₂O) for the bulk reaction product composition of former lawsonite crystals. Internal standard reference values are presented in *Appendix I*. The analytical conditions minimized mass-load dependent element fractionations (e.g. Kroslakova & Gunter, 2007).

5.3. Outcrops and samples description

The analysed samples of eclogitic breccias and adjacent host rocks were sampled in both the Lower and Intermediate shear zones (respectively LSZ and ISZ, *Figures 52, 53 and Table 5*). The strategy of sampling was to optimize the description of the successive steps leading to the brecciation at eclogite-facies conditions, comparing the processes acting in both shear zones. To achieve this goal, the samples for which it was possible to couple microstructural, petrographic and geochemical data were selected. The following description of the structural characteristics of sampled eclogite breccias does not distinguish between the different blocks, because no significant macro- or micro-scale difference was observed. In contrast, we stress that all the analysed blocks (and brecciated Fe-Ti boudins) are comparable. A particular attention was given to the description of the petrology of breccia layers and associated intact metagabbros (*Figures 54 and 55*), as their composition is crucial to understand the geochemical signature of the different vein and matrix generations and to evaluate the origin/source of the fluids potentially involved in the brecciation events.

5.3.1 Eclogitic breccias in the LSZ

In the LSZ, the largest part of the eclogite-facies breccias crops out as blocks disseminated in the antigorite-rich matrix of the shear zone. All the studied breccias were sampled from blocks completely enclosed within the antigorite schists of the shear zone (B1, B70, B75 and B77, *Figures 52 and 53*), with the exception of those developed in the Fe-Ti metagabbro boudin outcropping W of Punta Forcion (samples 63-15b and 63-15d; *Figures 52 and 53*), which crops out as a boudin embedded in Mg-Al metagabbro, situated in the lowest part of the Mg-Al gabbro cliff. The block B1 (samples 14-10 and 14-11) outcrops near the roof of the LSZ, east of the Rocce Sbiasere ridge. Blocks B77

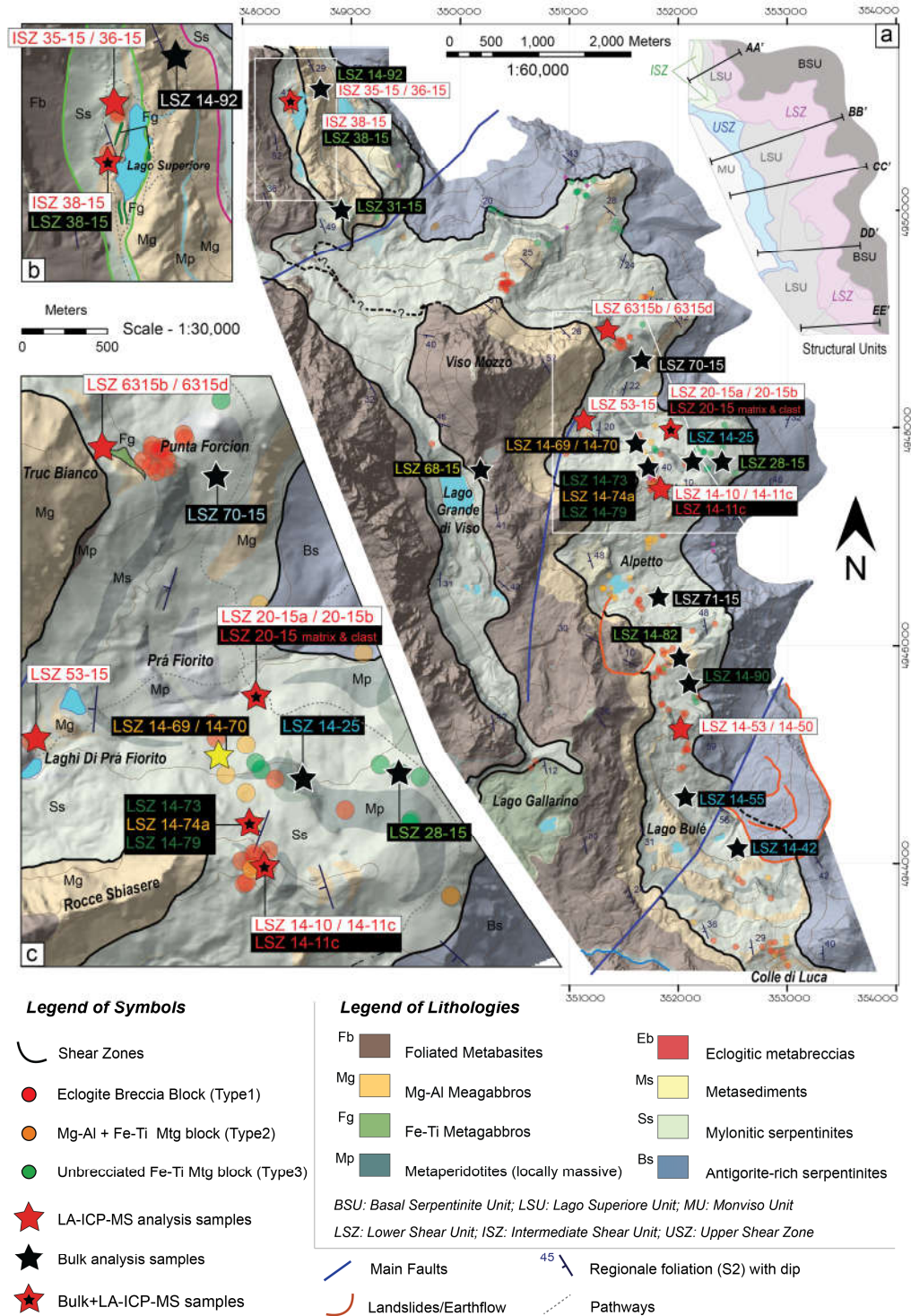


Figure 52: a) Simplified geological map based on our field observations integrated with Lombardo et al. (1978) and Balestro et al. (2013) original maps. The location of samples studied for the mineral in-situ LA-ICP-MS analysis (white boxes) and for bulk-rock analysis (black boxes) are shown together with the metagabbro blocks found in the shear zones. In the insets the detailed maps of (b) Lago Superiore and (c) Prà Fiorito valley.

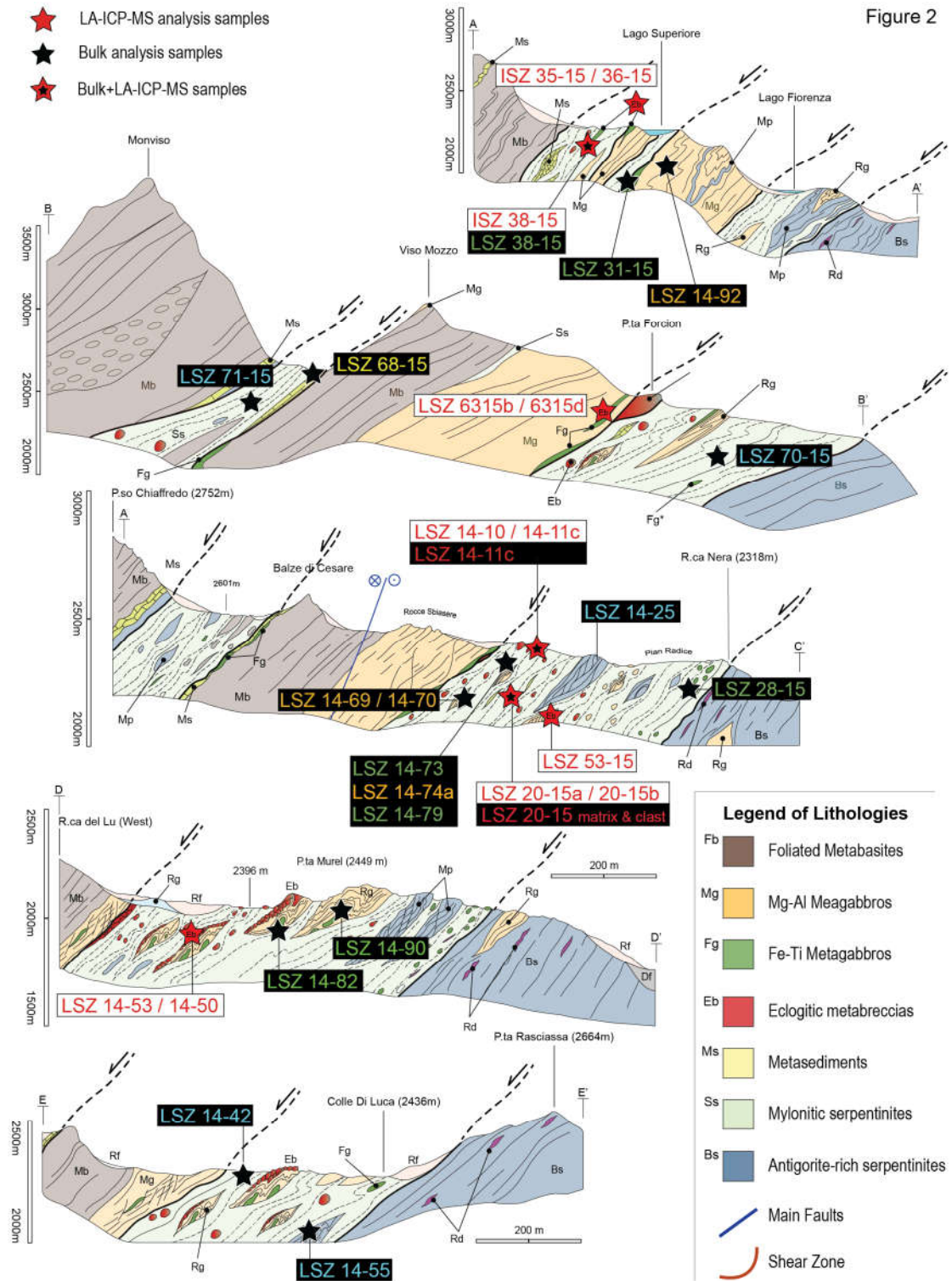


Figure 53: Geological cross-sections across the Monviso metaophiolite complex. Enlightened the location of samples studied for the mineral in-situ LA-ICP-MS analysis (white boxes) and for bulk-rock analysis (black boxes).

Table 5: Description of samples analysed at the LA-ICP-MS

Lower Shear Zone (LSZ)			
Block/Outcrop	GPS	Sample	Sample description
East of Rocce Sbiasere			
B1	44°39'55"N 07°07'46"E	LSZ 14-10	The sample consists of 2/3 of Intermediate-metagabbro (host rock) and 1/3 of M3 matrix. The host-rock is composed by banded eclogite, crystallizing sub-euhedral garnet (~20 Vol%), tabular, sub-millimeter omphacite (~45 Vol%), agglomerate of finely-grained epidote (~30 Vol%) and stringers of coarse (up to 0.5 mm) rutile (~5 Vol%). The M3 matrix is almost completely composed by chlorite + talc + phengite + epidote crystallizing after lawsonites. The pseudomorphosed lawsonites crystals are still recognizable by the peculiar lozenge-shape, with preserved mimetic zonations.
		LSZ 14-11c	The sample is entirely composed by M3 matrix, with the same characteristic of sample LSZ 14-10. In the matrix between ex-lawsonite crystals are preserved rare, tabular omphacite grains (size up-to 0.7 mm) apparently in equilibrium with rare talc crystals.
Southern-flank Prà Fiorito valley			
B77	44°40'12"N 07°08'03"E	LSZ 20-15a	The host rock is composed by fine-grained (0.1-0.6 mm) banded eclogite, strongly folded, crystallizing sub-millimeter garnet (~40 Vol%), omphacite (~50 Vol%), and stringers of coarse (up to 0.5 mm) rutile (~10 Vol%). Omp+Apt+Rtl-bearing veins (Veins 1) cut the host-rock foliation. M1 matrix domain is almost exclusively composed by tabular omphacite (size up-to 0.5 mm), with accessory rutile grains dispersed in the matrix. Subordinate, sub-millimeter thick domains crystallizing acicular omphacite (in equilibrium with M3 matrix) randomly intersect the M1 matrix. All the structures are cut by mm-thick veins crystallizing acicular omphacite + talc. In the brecciated layer, the matrix is locally infiltrated by metasomatic veins, crystallizing Tlc+Grt+Chl+Amph.
		LSZ 20-15b	The sample have similar characteristic respect to LSZ 20-15b.
Prà Fiorito valley			
B75	44°40'08"N 07°15'15"E	LSZ 53-15	The sample consists of 2/3 of Intermediate-metagabbro and Fe-Ti metagabbro (clasts) and 1/3 of M2 matrix. The Intermediate metagabbro is composed by banded eclogite, crystallizing anhedral garnet crystals (~25 Vol%), tabular, sub-millimeter omphacite (~45 Vol%), agglomerate of finely-grained epidote (~30 Vol%) and stringers of coarse (up to 0.5 mm) rutile. Fe-Ti metagabbro clasts consist in fine-grained (0.2-0.5 mm) eclogite crystallizing atoll garnet (~40 Vol%), omphacite (~60 Vol%) with subordinate rutile. The matrix M2 cements the clasts and consist in coarse, tabular omphacite (~80 Vol%) + garnets (up-to 3mm, ~20 Vol%) and accessory talc, pyrite and rutile grains.
East of Truc Bianco			
Boudin*	44°40'36"N 07°07'31"E	LSZ 63-15b	Representative sample of the peculiar clast-in matrix fabrics of eclogite-breccia at millimeter-scale. Clasts are composed by finely-grained (0.2-0.5 mm) banded eclogite, polydeformed, crystallizing sub-millimeter garnet (~45 Vol%), omphacite (~50 Vol%), and stringers of coarse (up to 0.5 mm) rutile (~5 Vol%). The eclogitic-foliation of the clasts is cut by veins crystallizing Omp (~98 Vol%) ± Apt (~2 Vol%) Veins 1). The bulk of matrix is retrogressed to greenschist (actinolite + albite + chlorite ± quartz); nevertheless, preserved matrix portion are found. M1 matrix domain is almost exclusively composed by tabular omphacite (size up-to 0.5 mm), with accessory rutile grains dispersed in the matrix. Matrix M2, which form up to 1/3 of sample, consists in >70 Vol% of coarse, tabular omphacite + ~25 Vol% garnets (up-to 3mm) and accessory talc (~5 Vol%). Rare pyrite and rutile grains are also found. Metasomatic veins intrude the pre-existing Omp ± Grt matrix, leading to crystallization of Grt (up-to 3mm, ~50 Vol%), talc (~30 Vol%) and chlorite.
		LSZ 63-15d	The sample have similar characteristic respect to LSZ 20-15b.
South of Punta Murel			
B54	44°40'02"N 07°07'47"E	LSZ 14-50	Sample composed by a mylonitic Fe-Ti metagabbro clast hosting Omp+Apt+Rtl-bearing veins (Vein 1) cut by M1 matrix domain. The clast corresponds to a banded eclogite, mylonitized, with sub-millimeter garnet (up-to 0.3mm, ~30 Vol%), omphacite (~60 Vol%), and stringers of coarse (up to 0.5 mm) rutile (~5 Vol%). Accessory apatite, pyrite and chlorite complete the assemblage. The vein is composed by finely-grained Omp (~90 Vol%) + Apt (~5 Vol%) and garnet (~5 Vol%). Matrix M1 consists in >95 Vol% of tabular omphacite, with strong grain-size reduction from clast-matrix boundary to the inner portion of M1. Rutile, apatite and chlorite complete the assemblage (~5 Vol%).
		LSZ 14-53	Sample composed by mylonitic Fe-Ti metagabbro clasts hosting Omp + Apt + Rtl-bearing veins (Vein 1) and cemented by M1 matrix. Clasts correspond to banded eclogite, mylonitized, with sub-millimeter garnet (up-to 0.3mm, ~30 Vol%), omphacite (~60 Vol%), and stringers of coarse (up to 0.5 mm) rutile (~5 Vol%). Accessory apatite, pyrite and chlorite complete the assemblage. The vein are composed by fibrous, sintaxial Omp (~100 Vol%) ± accessory apatite and rare pyrite. Locally mylonitic clasts are cemented by "crushed-matrix" domains, composed by Omp + Grt grains (derived from the clasts and undergone to strong grain-size reduction) cemented by µm-thick, newly-formed omphacite. Elsewhere, clasts are cemented by Matrix M1, consisting in >95 Vol% of tabular omphacite. Rutile, apatite and chlorite complete the assemblage (~5 Vol%). Oxide + Chlorite-bearing veins postdate all the pre-existing structures and mainly infiltrate throughout the clast-matrix or clast-veins boundaries.
Intermediate Shear Zone (ISZ)			
Block/Outcrop	GPS	Sample	Sample description
Western side of Lago Superiore			
B110	44°41'38"N 07°05'15"E	ISZ 35-15	The host rock is composed by fine-grained (0.2-0.5 mm) banded eclogite, strongly folded, crystallizing atoll garnet (~38 Vol%), omphacite (~57 Vol%), and stringers of coarse (up to 0.5 mm) rutile (~5 Vol%). Two type of veins cut the samples: Vein T1 and Vein T2. Vein T1 is composed by coarse Omp (~90 Vol%) + Apt (~8 Vol%), while Vein T2 by bladed Omp (~85 Vol%) + Grt (~10 Vol%, up-to 4mm) and Rtl (~5 Vol%). Matrix M2, crosscutting Vein T1, consists in >90 Vol% of coarse, tabular omphacite + ~10 Vol% garnets (up-to 3mm).
		ISZ 36-15	Coarse-grained vein of ~80% fibrous omphacite (zoned) with minor apatite (~15 Vol%) and rutile (~5 Vol%). Retrograde chlorite, epidote, albite and amphibole are present in minor amounts. The host rock is a fine-grained (0.2-0.5 mm) banded eclogite crystallizing atoll garnet (~40 Vol%), omphacite (~57 Vol%), and stringers of rutile (up to 0.5 mm-thick, ~3 Vol%).
B111	44°41'48"N 07°05'15"E	ISZ 38-15	Sample composed by massive Vein T2: ~80% of coarse (up to 0.6mm) bladed omphacite grains + ~20% of garnet (up to 5 mm) and accessory rutile (less than 1 Vol%; size up to 0.5 mm) and pyrite. The host rock is composed by equigranular (0.1-0.5 mm), finely-foliated eclogite crystallizing omphacite (~75 Vol%), atoll-garnet (~20 Vol%), rutile (2 Vol%, aligned on coarse ribbons) and accessory apatite, pyrite (more abundant nearby clast-vein boundary) and rare blue amphibole.

(samples 20-15a and 20-15b) and B75 (sample 73-15) were sampled on the northern flank of the Prà Fiorito valley, while the block B51 (samples 14-50 and 14-53) outcrops E of the Peiro Jauno ridge. It is noteworthy that all sampled blocks outcrop near the roof of the LSZ (*Figures 52 and 53*).

The morphology, structure and mineralogy allow to distinguish two types of brecciated metagabbro blocks with non-random distribution throughout the ~15km-long Lower Shear Zone: (1) completely brecciated Fe-Ti-metagabbros (62% of mapped blocks, Min Vol. 0.05 m³, Max Vol. 2613.81 m³, corresponding to Type1 blocks of *chapters 3 and 4*), scattered in the intermediate to upper levels of the LSZ (*Figures 52 and 53*). These blocks show a peculiar clast-in-matrix structure (*Figure 1*), with clasts almost exclusively made of mylonitic Fe-Ti metagabbros with rare Mg-Al gabbros (10% of modal amount), cemented by an omphacite-rich matrix (+/- garnet and lawsonite). (2) Meter-size blocks and decameter-scale slivers of metagabbros (Type 2 blocks; 22% of mapped blocks, Min Vol. 1.51 m³, Max Vol. 125663.71 m³) made of unbrecciated, foliated Mg-Al metagabbros showing strong internal mylonitization and complex folding, with locally breccia layers of Fe-Ti metagabbros (the latter with textural and petrographic characteristics comparable to Type1 blocks). These Type 2 blocks, scattered in the intermediate part of LSZ (*Figures 52*), show the complete transition from intact to brecciated rocks and were the main target of this study.

5.3.2 Eclogitic breccias in the ISZ

Compared to the LSZ, rare blocks of eclogitic metagabbro are disseminated in the Intermediate Shear Zone matrix. The rare, m-scale eclogite breccias crop out chiefly on the western and eastern side of Lago Superiore (*Figures 52a-b*) as discontinuous layers in Fe-Ti metagabbro boudins, isolated from the surrounding antigorite schist of the ISZ by at least tens of meters of

highly-deformed Mg-Al metagabbros (comparable to the metabreccia boudins east of Truc Bianco, LSZ). Samples ISZ 35-15, ISZ 36-15 (block B110) and ISZ 38-15 (block B111) were sampled W of Lago Superiore, in the only outcrops clearly showing evidences of brecciation (e.g., with clast-in-matrix structure).

5.4 Brecciation patterns

5.4.1 Outcrop scale: structural patterns of eclogitic breccia-bearing blocks (type 2)

Type2 blocks from the LSZ exhibit the complete transition from intact metagabbros to breccia cores (*Figure 54*): four Type 2 blocks were chosen among them to conduct a detailed structural and geochemical analysis (in Prà Fiorito valley, north of Alpetto Lake and in the upper Bulè Valley; *Figure 52*). In average, more than 80% of Type2 blocks are formed by eclogite-facies, mylonitic Mg-Al metagabbro (paragenesis: omphacite + clinozoisite +/- ex-lawsonite and glaucophane) showing tight isoclinal folds (*Figure 54a*) locally embedding cm- to dm-scale boudins of Fe-Ti metagabbros (*Figure 54a-c*). The latter (with the classical omphacite + garnet + rutile +/- lawsonite paragenesis) are crosscut by a network of HP veins (e.g., omphacite- and garnet- bearing, which locally include host-rock fragments) up-to ~1 cm thick, developed almost perpendicular to the foliation in the thinnest boudins (e.g., thickness between ~2 to ~10 cm; *Figure 54c*) and with a radial arrangement in the biggest boudins. The opening geometries vary from crack-seal to tension gashes, similar to geometries of veins crosscutting the Lago Superiore Fe-Ti metagabbros (Philippot & Selverstone, 1991; Spandler et al., 2011). Interestingly, these tapering veins developed in Fe-Ti metagabbros progressively disappear into garnet-bearing Mg-Al metagabbros (e.g., “intermediate metagabbro”; *Figure 54c*) at their contact, being sheared parallel to

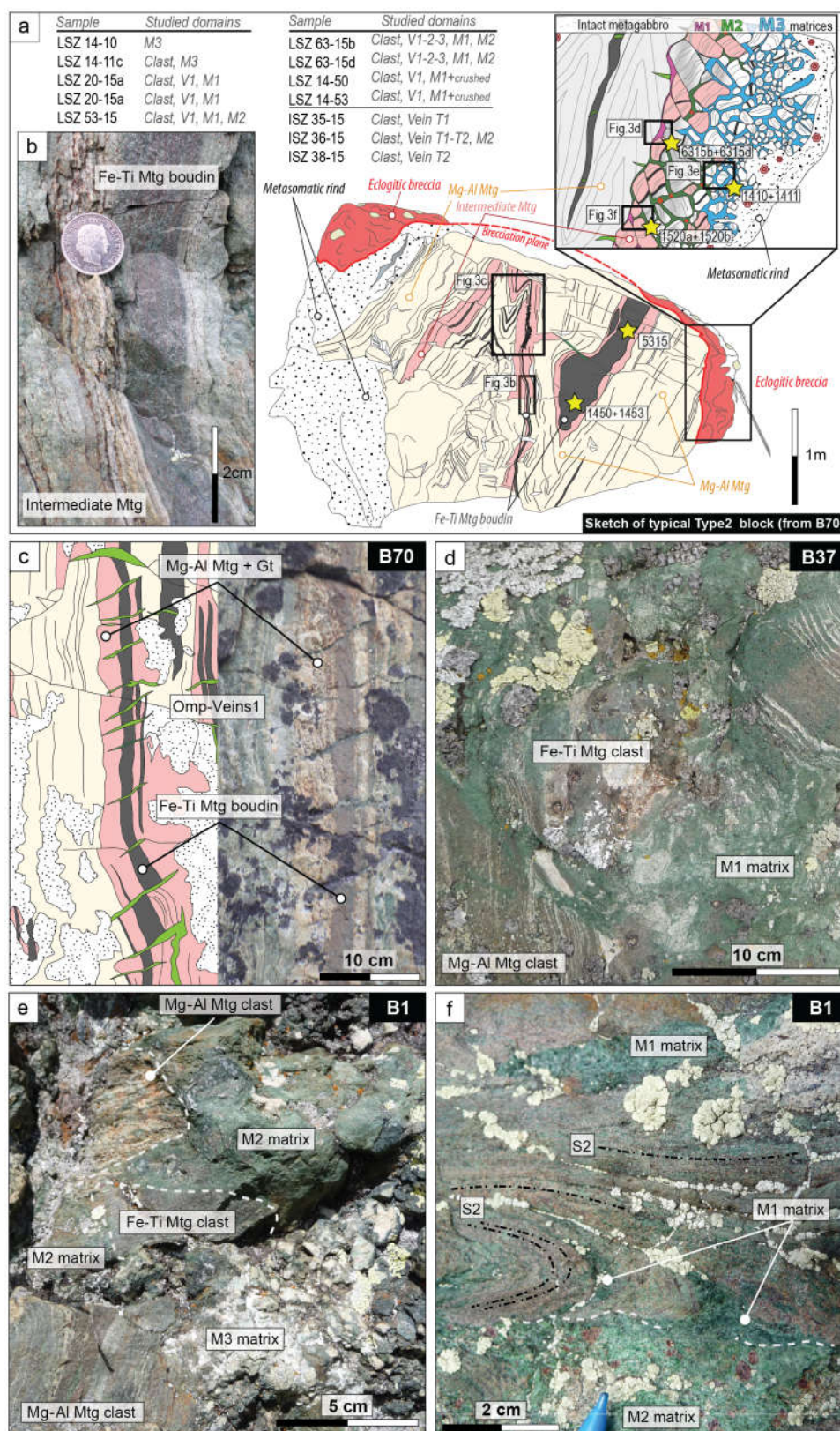


Figure 54

Figure 54: a) Typical m-scale Type2 block. The eclogitic breccia develops crosscutting (here at high angle) the pre-existing mylonitic foliation of the intact Mg-Al metagabbro. To be noted the complex folding of the Fe-Ti boudins in the intact metagabbro. In the inset, a schematic view of the typical structuration of eclogite-breccia layers, with progressive increase of clast comminution and rotation toward the breccia core (M3 matrix -rich). M1 and M2 matrix are preserved nearby intact metagabbro. The position of samples depict their structural domain, but are derived from different outcrops (see Table 5). b) Close-up view of a cm-thick Fe-Ti metagabbro boudin embedded in Intermediate metagabbro; brownish rutile ribbons sup-parallel to the boudin mark the eclogitic S1 foliation. Block 70, Prà Fiorito Valley. c) $\text{Omp} \pm \text{Apt}$ -bearing Veins1 crosscutting sub-perpendicularly a Fe-Ti metagabbro boudin; to be noted the tapering of the veins at the contact with the intermediate metagabbro. Block 70, Prà Fiorito Valley. d) Typical clast-in-matrix appearance of eclogite-facies breccia on fresh surface. Here the rotated metagabbro clasts are cemented by omphacite-rich matrix (M1). Veins in the clasts are filled by fibrous $\text{Omp} \pm \text{Apt}$. Block B37, NW of Alpetto. e) Eclogitic metagabbro clasts (evident the mylonitic foliations) sealed by Lws-rich matrix. Noteworthy, in the upper-center part of the picture, the occurrence of a clast composed by reworked eclogite-facies breccia (mylonitic metagabbro clasts cemented by Omp -rich matrix M1). Block B45, South of Punta Murel. f) Eclogitic Fe-Ti metagabbro (evident the folded mylonitic foliations) sealed by Omp -rich M1 matrix. Noteworthy, in the lower part of the picture, the occurrence of $\text{Omp} + \text{Grt}$ bearing M2 matrix, sharply crosscutting all the previous structures. Block B1, NW of Alpetto.

the eclogitic foliation of the Intermediate metagabbro, suggesting that shearing partly postdates vein formation (refer to *chapter 4* for more details).

Both the eclogite-facies mylonitic foliation of Mg-Al metagabbro and the boudins of Fe-Ti metagabbro (as well as some of the HP veins) are sharply truncated, unconformably, by eclogite-breccia horizons (*Figure 54a*), suggesting that the primary oceanic lithostratigraphic sequence was composed by sills and dykes of Fe-Ti metagabbros intruded in the Mg-Al metagabbros (more details in *Chapters 3 and 4*). In fully-preserved breccia planes, it is possible to observe the complete transition, towards breccia cores, from intact rock to (I) crackle, (II) mosaic and (III) chaotic breccia i.e., the characteristic breccia plane structure (*sensu* Sibson, 1987; e.g., *Figure 36a-b*; refer to *Chapter 4* for more details). This progressive change in breccia fabrics is characterized by the increase in matrix content and angle of clast rotation from intact-rock to chaotic-breccia, with correlated comminution of clasts (which diameter decrease from dm- to m-size; Fig. SM1c)

All the analyzed eclogitic breccia planes show a bimodal clast composition (*Figure 54a, 54d, and 54e*) with ~90% (modal amount) constituted by Fe-Ti metagabbro and rarer (~ 10%) Mg-rich metagabbros.

Mg-Al metagabbro clasts show the same fabrics and composition than Mg-Al metagabbros forming most of **Type 2** blocks, whereas the mylonitized Fe-Ti metagabbro clasts are comparable to the boudins embedded in **Type 2** blocks.

In most cases, rotated clasts were cemented after brecciation by a succession of newly-formed, eclogite-facies matrices (*Figure 54d-f*). Textural and compositional characteristics of the four successive matrix types observed are described below.

5.4.2 Decimeter- to millimeter-scale structures of eclogitic breccia layers

The amount of matrix sealing the metagabbro clasts in the eclogitic breccia planes increases from rims to cores of breccia levels (*e.g.*, *Figure 54a*); crosscutting and textural relationships allow distinguishing four successive matrix types:

(I) At the contact with intact rock, inside the first 10 to 20 cm of brecciated layers, slightly rotated clasts are surrounded by anastomosed, sub-millimeter domains of finely crushed grains (< 100 μm) of Fe-Ti metagabbros (called *crushed-breccia* hereafter; Fig. 7d. (II) Such domains are sealed by small amounts of a light green omphacitic cement (hereafter called *matrix M1*, *Figures 54f* and *55a*), which amount increases (up-to 1 cm-thick mantles around clasts; *Figures 54d* and *54f*) while crushed breccia progressively disappears towards breccia cores. (III) Both the *crushed-breccia* and the *matrix M1* are sealed by the *matrix M2* (*Figure 54f* and *55b*). This omphacite- and garnet-bearing matrix crystallizes around the clasts, forming mantles up-to 3 cm-thick and, in hand-specimen, is well recognizable by the bigger size of garnets with respect to mylonitic Fe-Ti clast garnets (*Figures 54f* and *55b*). Two successive sets of sub-millimeter scale veins (Veins 2: omphacite-bearing; Veins3: omphacite + apatite-bearing) subparallel to the mylonitic foliation of

clasts crosscut all these pre-existing structures (e.g., *Figure 55b*). (IV) In the cores of brecciated layers (i.e., *chaotic breccia fabrics* – Fig. SM1e; refer also to chapter 4), crosscutting relationships show that a late matrix M3 postdates both matrices M1 and M2 and the veins (*Figure 54e* and *55c*). M3 shows penetrative fracturing at the core of breccia layers (*Figure 54e*) and is the most abundant matrix type: it is characterized by impressive euhedral lozenge-shape pseudomorphs after lawsonite (< 2 cm; Figs. *Figure 54e* and *55c*), accompanied by relics of omphacite, talc and *chlorite* + *rutile* aggregates after garnets. In fact, numerous clasts are composed by mylonitic metagabbro and M1+M2 matrices

Figure 55: a) Polished sample of eclogite breccia evidencing the crosscutting relationship between mylonitic clasts, the Omp + Grt matrix (M2) and the metasomatic mineralization (Tlc + Chl + Grt + Amph ± Ca-rich Diop). The darker areas (mainly developed in the matrix portions) are Chl/Amph-rich recrystallization linked to late-stage retrogression under green-schist condition. Evidenced the position of sample LSZ 63-15b + d. Sampled at the base of Truc Bianco cliff. b) Photograph of a thin-section across mylonitic, eclogite-facies Fe-Ti metagabbro and a matrix domain. In evidence the complex succession M1-M2, with the pervasive, late-stage metasomatization developed only at the expenses of matrices. In the box, a detail of the fibrous Omp ± Apt crystals of Veins1; the holes are from laser ablation. Sample LSZ 63-15d. c) Photograph of a thin-section across mylonitic, Lws-bearing Fe-Ti metagabbros sealed by M3 matrix. In evidence (in the boxes) the lawsonite crystals (now pseudomorphosed by Ep + Phg ± Plg) with laser ablation holes. Sample LSZ 14-11. d) Photo of a breccia outcrops from the ISZ, with M2-matrix (Omp + Grt) cementing clasts of Fe-Ti metagabbro hosting fibrous Omp + Apt VeinT1. The pervasive lichens cover of the outcrop is a constant around the Lago Superiore area. e) Scan of sample ISZ 35-15, summing-up the microstructural relationship between mylonitic clast, veins and matrix M2; in the box, a SEM map showing the different Cr concentration between garnet from M2 matrix (enriched) and the atoll garnets from the mylonitic clast. Sample from block B110, W of Lago Superiore.

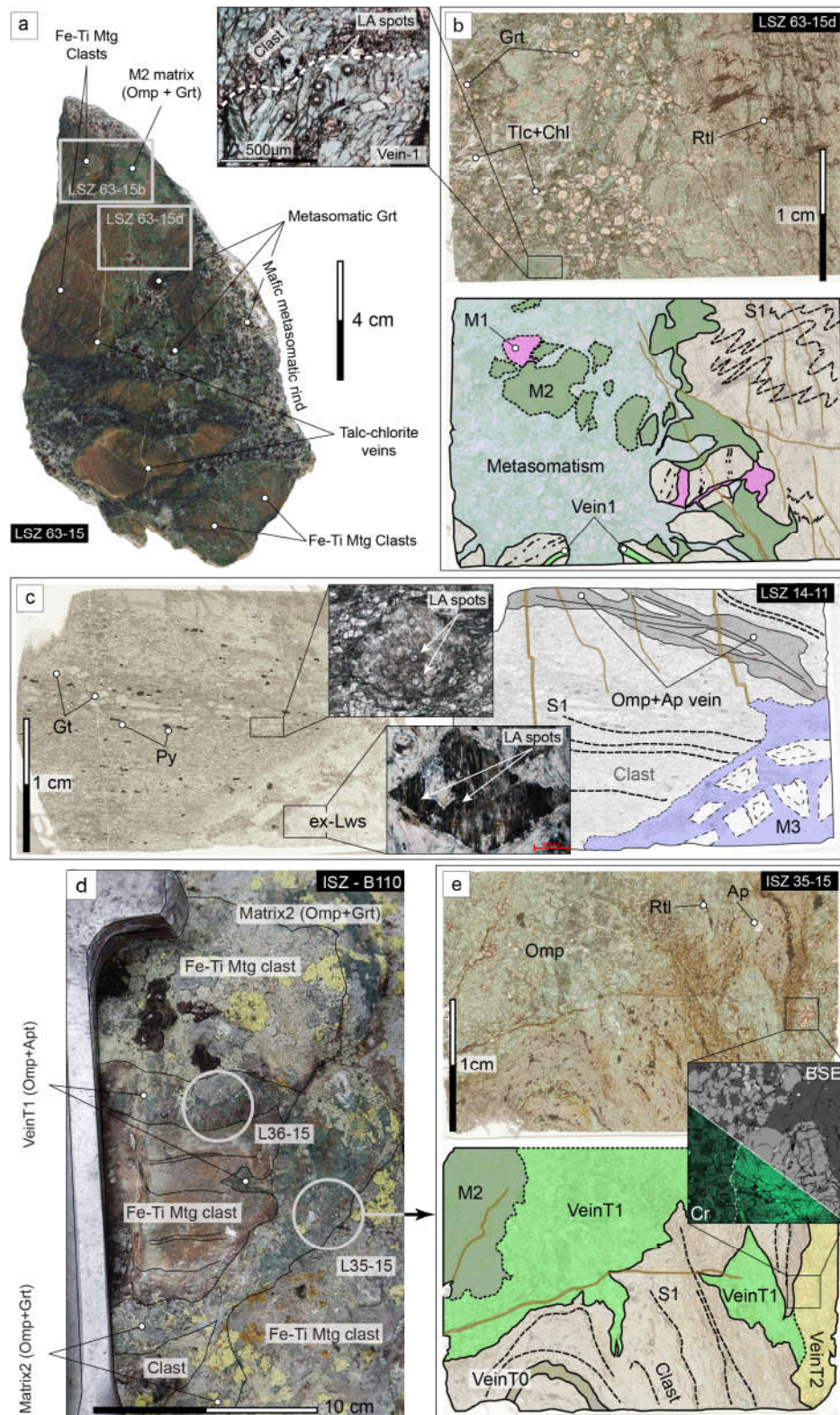


Figure 55

cemented by newly formed M3 (*Figure 54e*), suggesting that M3 emplacement was driven by hydraulic fracturing of pre-existing breccia. Noteworthy, while clasts always show a strong mylonitic foliation, all these matrices lack any evidence of crystal-plastic deformation.

A later-stage set of veins (hereafter *Late-stage veins*), filled with talc and clinopyroxene, sharply crosscuts all the matrices and thus postdates the brecciation events.

In the LSZ, at the contact with the antigorite-rich matrix embedding the blocks, these are rimmed by a hydrated metasomatic rind that can locally reach 0.5 meter-thick (e.g. in Lago Superiore, Pta. Forcion and Colle di Luca). This metasomatic replacement affects both clasts and matrix (*Figure 55a-b*), and thus postdates both the *brecciation* and the emplacement of the *Late-Stage veins*. Matrix M3 is more strongly affected if compared to M1 and M2, suggesting that dehydration reactions accompanying lawsonites breakdown likely promoted the massive metasomatism of M3. Nevertheless, a complex set of sub-millimeter scale veins filled with hydrous minerals nucleated from the metasomatic rinds and radially crosscuts the surrounding clasts as well as M1 and M2 domains (e.g., *Figure 55a-c*).

Note that the eclogite-breccia sampled in the Fe-Ti metagabbro boudin at the base of the Truc Bianco peak (*Figures 52a and 53b*) shows similar structures (i.e., clasts locally crosscut by veins and embedded in matrix, *Figure 55b*) but notably no M3 lawsonite-rich matrix. Similarly in the ISZ, the 4 small eclogitic breccia boudins developed at the expenses of the Fe-Ti metagabbro layers also lack of any evidence for M3 (e.g., *Figure 55d-e*), as well as M1, crystallization. Differently from the LSZ, in the ISZ only two sets of veins predate the crystallization of M2 matrix (*Figure 55d-e*). Veins T1 (paragenesis: Omp + Apt) formed both as massive, irregular-shaped veins with euhedral crystals or as syntaxyal veins (thickness up-to 2 cm) with acicular crystals. Veins T2

(paragenesis Omp + Grt) formed as cm-thick veins crosscutting both the mylonitic foliation of Fe-Ti metagabbro and the Veins T1 (e.g., *Figure 55d-e*).

All the details about structural relationships between clasts and matrices are extensively described in *Chapter 4*.

5.5. Bulk-rock geochemistry

The mylonitic, unbrecciated Fe-Ti metagabbro eclogites that crop out S of Lago Superiore have mafic compositions with high Fe₂O₃ (16.69-21.10 Wt%) and TiO₂ (1.11-4.56 Wt%) and low Cr (7.72-41.86 µg/g), Ni (21.99-60.34 µg/g) and Co (20.12-46.25 µg/g) contents relative to the mid-ocean ridge basalt (MORB; Sun & McDonough, 1989). These compositions are similar to the other Lago Superiore eclogites analysed by Schwartz et al. (2000), Hermann & Rubatto (2003) and Spandler et al. (2011) and can be compared with the fractionated ferrobasalts of the oceanic crust (e.g. Carmichael, 1964; Wood, 1979; Bach, 2001).

The cm- to dm-thick, boudinated Fe-Ti metagabbros in Type2 blocks show comparable contents in Fe₂O₃ (16.69-19.76 Wt%), Cr (32.75-49.61 µg/g), Ni (32.63-45.61 µg/g) and Co (23.42-31.11 µg/g), but higher TiO₂ (4.30-6.20 Wt%) with respect to the unbrecciated Fe-Ti metagabbros (*Figure 56a*). Here the REE show a peculiar trend (*Figure 55c*), with LREE concentrations similar to those of Mg-Al metagabbros and, in contrast, HREE concentrations shifting towards those observed in Fe-Ti and Intermediate metagabbros (*Table 6*).

Figure 56: Trace element variation diagrams for bulks from selected samples. The data are normalized to pyrolite values from McDonough & Sun (1995). b) Selected binary diagram for bulks. Noteworthy the similar geochemical composition of M1-matrix bulk with respect to Intermediate metagabbro; differently, samples of M3-matrix and metasomatic rinds show affinity to serpentinite compositions. Data from other works as shaded areas (legend to abbreviation in the figure). c) Rare earth element variation diagrams for bulks from selected samples. The data are normalized to NMORB values from Sun & McDonough (1989).

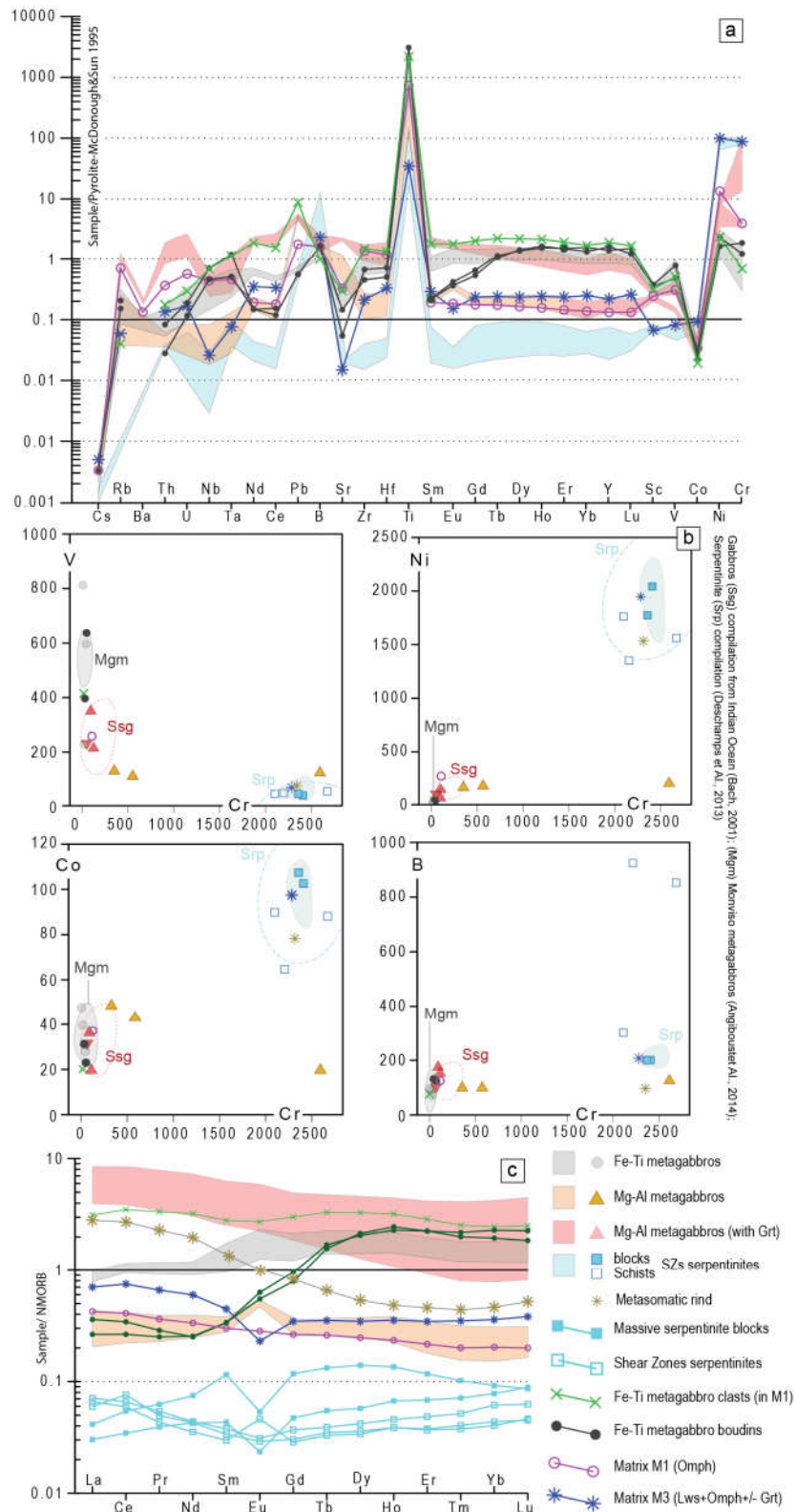


Figure 56

Table 6: Bulk-rock composition

SAMPLE	14-02	13-15	14-03	14-90	139-15	120-15c*	14-79	14-74A	14-69	14-70	14-92	71-15	14-42	70-15	14-55	120-15m**	14-11
Petrology	Fe-Ti Mtg	Fe-Ti Mtg	Fe-Ti Mtg	Fe-Ti Mtg	Fe-Ti Mtg	Int Mtg	Int Mtg	Int Mtg	Mg-Al Mtg	Mg-Al Mtg	Mg-Al Mtg	Serpentinite SZ matrix	Serpentinite SZ matrix	Serpentinite SZ matrix	Serpentinite Block	Fe-Ti Mtg M1 matrix	ex-Lw matrix M3 matrix
Comment	Host Rock	Host Rock	Boudlin	Boudlin	Clast	Clast	Clast	Host Rock	Host Rock	Host Rock	Host Rock	Serpentinite SZ matrix	Serpentinite SZ matrix	Serpentinite SZ matrix	Block	M1 matrix	M3 matrix
Major element oxides (XRF-Wt%)																	
SiO ₂	46.29	44.65	43.09	44.32	44.53	46.59	47.77	43.41	50.82	51.34	51.00	37.77	39.24	38.94	41.26	53.51	41.67
TiO ₂	4.46	1.11	6.20	4.30	4.44	1.55	1.52	1.73	0.86	0.38	0.25	0.05	0.07	0.29	0.03	1.51	0.07
Al ₂ O ₃	11.64	13.30	13.15	12.60	13.36	16.55	16.41	18.39	12.03	12.56	17.29	1.48	1.74	1.55	1.46	7.18	2.59
Fe ₂ O ₃	16.75	21.10	19.76	16.69	19.08	7.81	6.81	11.69	7.80	7.07	2.13	11.77	7.93	8.35	7.21	6.75	8.96
FeO	10.37	15.00	13.71	12.61	13.48	3.80	2.43	7.17	4.40	4.13	1.36	3.92	2.97	2.72	3.96	2.62	6.78
Fe Tot	27.12	36.10	33.47	29.30	32.56	11.61	9.24	18.86	12.20	11.20	3.49	15.69	10.90	11.07	11.17	9.88	15.74
MnO	0.34	0.39	0.45	0.57	0.36	0.13	0.07	0.24	0.17	0.12	0.03	0.11	0.11	0.17	0.09	0.06	0.13
MgO	6.18	6.02	5.09	7.21	5.48	6.10	6.30	6.55	11.04	11.23	9.26	36.17	37.61	37.73	37.72	10.16	33.97
CaO	9.27	10.51	8.32	11.47	7.98	13.28	13.85	12.80	9.40	10.23	14.37	0.07	0.05	0.04	<L.D.	13.23	1.48
Na ₂ O	4.45	2.73	3.75	2.50	4.39	4.03	4.09	1.81	2.83	3.02	3.00	<L.D.	<L.D.	<L.D.	<L.D.	4.57	0.04
K ₂ O	0.03	0.03	<L.D.	<L.D.	<L.D.	0.16	0.20	<L.D.	0.06	0.06	<L.D.	<L.D.	<L.D.	<L.D.	<L.D.	0.11	<L.D.
P ₂ O ₅	<L.D.	<L.D.	<L.D.	<L.D.	0.41	<L.D.	<L.D.	0.47	<L.D.	<L.D.	<L.D.	<L.D.	<L.D.	<L.D.	<L.D.	<L.D.	<L.D.
Total	100.17	99.81	98.80	98.89	99.15	100.07	100.22	99.87	100.10	100.22	99.97	99.63	98.96	98.99	100.09	100.16	99.46
LOI %	0.77	-0.02	-0.35	-0.76	-0.67	3.48	3.21	2.78	5.10	4.21	2.64	12.21	12.21	11.91	11.94	3.10	10.56
CO ₂ %	0.54	0.34	0.36	0.38	0.41	1.13	1.25	0.30	0.83	0.52	0.40	0.92	0.57	0.43	0.46	0.85	0.20
H ₂ O %	1.52	1.41	0.79	0.54	0.36	2.78	2.30	3.09	5.05	4.20	2.49	12.07	11.93	11.83	11.84	2.40	11.10
S %	0.02	<0.01	<0.01	<0.01	0.03	0.22	0.07	0.19	0.01	<0.01	0.01	0.02	<0.01	<0.01	<0.01	0.17	<0.01
MgO#	37.35	28.63	27.06	36.36	28.91	61.63	72.18	47.75	71.50	73.11	87.19	90.22	92.68	93.28	90.74	79.51	83.36
Trace elements (XRF-ppm)																	
Li	25.00	12.80	16.50	18.40	26.00	34.00	18.40	9.70	7.60	8.40	3.30	0.50	0.50	0.50	0.50	40.00	0.50
B	4.00	3.00	5.00	5.00	3.00	7.00	6.00	4.00	4.00	4.00	5.00	34.00	12.00	37.00	8.00	5.00	7.00
P	0.00	0.00	0.00	0.00	1789.32	0.00	0.00	2051.17	0.00	0.00	0.00	0.00	0.00	0.00	0.00	0.00	0.00
Sc	45.61	50.65	61.15	57.07	52.15	36.36	36.24	39.08	30.82	32.08	39.77	11.79	11.64	12.70	10.65	40.30	10.79
V	597.22	228.11	812.36	637.41	415.11	351.76	224.03	227.94	130.91	107.27	122.95	54.07	45.15	46.10	37.42	258.08	66.87
Cr	41.86	22.07	49.61	32.75	18.09	95.22	104.74	55.70	349.53	563.49	2592.41	2672.65	2088.30	2203.42	2408.99	106.14	2283.09
Co	28.33	39.57	46.25	31.11	20.12	35.32	20.70	30.36	48.32	43.76	19.93	88.16	89.73	64.73	102.60	36.31	97.46
Ni	60.34	50.89	32.63	45.61	46.21	67.24	139.25	86.34	162.09	179.37	201.57	1561.12	1761.93	1263.31	2042.73	267.64	1947.19
As	<L.D.	<L.D.	<L.D.	<L.D.	<L.D.	0.50	<L.D.	<L.D.	0.64	<L.D.	<L.D.	2.23	1.71	1.87	1.27	<L.D.	<L.D.
Rb	1.77	1.64	0.51	1.23	0.24	5.67	7.55	0.76	1.51	1.43	0.23	<L.D.	<L.D.	<L.D.	<L.D.	4.31	0.35
Sr	28.83	38.10	10.82	28.64	59.18	409.34	409.59	406.60	86.68	114.47	236.68	<L.D.	<L.D.	<L.D.	<L.D.	66.52	2.96
Y	42.81	54.97	60.79	69.96	82.81	27.78	57.22	121.45	9.79	8.73	5.64	0.95	1.28	0.92	1.60	5.76	9.43
Zr	103.70	58.09	70.16	47.56	157.97	95.94	185.90	578.66	20.49	28.21	10.58	<L.D.	1.58	<L.D.	<L.D.	148.39	22.32
Nb	2.83	0.99	2.01	4.79	4.67	1.65	3.93	5.05	0.56	0.29	0.12	<L.D.	0.02	0.02	0.19	3.05	0.18
Sb	0.08	<L.D.	0.07	0.08	<L.D.	0.08	<L.D.	<L.D.	<L.D.	<L.D.	<L.D.	0.08	0.11	0.06	<L.D.	0.06	<L.D.
Cs	0.11	0.03	0.03	0.11	<L.D.	0.10	0.09	0.06	0.12	0.10	0.05	<L.D.	0.03	<L.D.	0.02	0.07	0.10
Ba	6.84	7.20	<L.D.	<L.D.	<L.D.	12.80	6.50	<L.D.	<L.D.	<L.D.	<L.D.	<L.D.	<L.D.	<L.D.	<L.D.	8.92	<L.D.
La	2.07	1.96	0.90	0.66	7.83	9.89	16.28	21.26	1.04	0.91	0.51	0.17	0.18	0.15	0.08	1.06	1.76
Ce	7.13	7.06	2.57	1.99	26.30	29.05	45.09	64.02	3.12	2.90	1.66	0.45	0.49	0.57	0.26	3.07	5.61
Pr	1.22	1.37	0.38	0.33	4.42	4.53	6.45	10.36	0.52	0.51	0.30	0.06	0.07	0.07	0.05	0.48	0.87

Chapter 5 - The geochemical signature of Eclogitic Breccia

Ni	6.75	8.71	8.65	1.83	1.86	23.59	22.63	29.72	53.26	2.87	2.82	1.80	0.26	0.32	0.31	0.31	0.55	2.45	4.36
Sn	2.52	4.62	3.38	0.88	0.89	7.38	6.68	8.62	16.55	1.00	1.01	0.73	0.08	0.10	0.09	0.11	0.30	0.79	1.17
Tu	1.29	2.34	1.74	0.64	0.56	2.79	2.31	2.62	6.02	0.55	0.56	0.48	0.05	0.03	0.03	0.02	0.05	0.29	0.24
Gd	4.50	7.94	5.10	3.53	2.91	11.09	6.87	9.68	18.19	1.31	1.29	0.98	0.11	0.14	0.11	0.17	0.43	0.97	1.27
Tb	1.00	1.52	0.94	1.14	1.06	2.22	1.04	1.71	3.20	0.25	0.24	0.18	0.02	0.03	0.02	0.04	0.09	0.17	0.24
Dy	7.13	10.20	6.42	9.41	9.79	14.98	5.80	10.66	20.85	1.71	1.58	1.14	0.15	0.19	0.16	0.26	0.64	1.12	1.57
Ho	1.64	2.19	1.45	2.32	2.49	3.24	1.10	2.17	4.51	0.38	0.35	0.23	0.04	0.05	0.04	0.07	0.14	0.24	0.36
Er	4.70	5.81	3.86	6.70	6.71	8.54	2.74	5.45	12.42	1.03	0.92	0.53	0.11	0.14	0.11	0.20	0.35	0.64	1.02
Tm	0.71	0.82	0.55	1.00	0.92	1.17	0.36	0.73	1.88	0.14	0.13	0.07	0.02	0.02	0.02	0.03	0.05	0.09	0.16
Yb	4.98	5.50	3.67	7.02	5.96	7.53	2.38	4.61	12.88	0.94	0.86	0.46	0.12	0.19	0.13	0.24	0.28	0.62	1.09
Lu	0.79	0.87	0.54	1.03	0.85	1.14	0.37	0.68	2.05	0.14	0.13	0.07	0.02	0.03	0.02	0.04	0.04	0.09	0.17
Hf	3.01	1.65	2.89	2.01	1.42	3.87	2.24	5.44	14.42	0.55	0.72	0.32	<L.D.	0.07	<L.D.	<L.D.	0.14	3.46	0.93
Ta	0.26	0.09	0.21	0.45	0.19	0.43	0.10	0.45	0.44	0.05	0.03	0.01	<L.D.	<L.D.	<L.D.	0.01	0.04	0.17	0.03
Pb	0.92	<L.D.	<L.D.	<L.D.	0.83	13.21	7.27	6.62	6.03	<L.D.	<L.D.	7.45	0.64	0.92	1.12	<L.D.	<L.D.	2.78	<L.D.
Bi	0.05	<L.D.	<L.D.	<L.D.	<L.D.	0.05	0.11	0.25	0.19	0.09	0.09	0.17	0.06	<L.D.	<L.D.	0.09	0.12	0.26	0.29
Th	0.12	0.04	0.09	0.07	0.02	0.14	1.51	0.67	0.42	0.05	0.03	<L.D.	<L.D.	<L.D.	<L.D.	<L.D.	0.03	0.30	0.11
U	0.06	0.02	0.04	0.04	0.02	0.06	0.22	0.54	0.85	0.02	0.01	<L.D.	<L.D.	0.01	<L.D.	<L.D.	<L.D.	0.12	0.03
W	<L.D.	<L.D.	1.14	1.13	<L.D.	1.10	<L.D.	<L.D.	<L.D.	<L.D.	<L.D.	<L.D.	<L.D.	<L.D.	<L.D.	<L.D.	<L.D.	0.83	<L.D.
Zn	73.50	131.12	78.34	49.05	34.04	118.57	32.56	30.15	43.23	63.92	60.43	26.57	49.11	48.17	52.80	57.98	44.20	61.42	70.14
Sn	2.11	0.78	1.49	2.08	2.35	1.68	2.14	3.52	3.66	0.82	0.85	<L.D.	<L.D.	<L.D.	<L.D.	<L.D.	<L.D.	2.52	0.56
Mo	<L.D.	<L.D.	<L.D.	<L.D.	<L.D.	<L.D.	<L.D.	<L.D.	<L.D.	<L.D.	<L.D.	<L.D.	<L.D.	<L.D.	<L.D.	<L.D.	<L.D.	<L.D.	<L.D.
Cu	8.62	19.87	20.86	6.64	5.42	6.01	7.61	2.21	<L.D.	26.54	39.21	57.83	17.88	5.58	39.54	35.89	11.29	9.45	5.38
Cd	0.20	0.29	0.11	0.33	0.25	0.24	0.16	0.12	0.22	0.12	0.92	0.04	0.04	<L.D.	0.05	0.03	0.03	0.13	0.04
Be	0.62	0.50	0.50	0.47	0.79	0.70	1.12	1.60	0.80	0.20	0.20	0.13	<L.D.	0.06	<L.D.	0.08	0.13	1.94	0.22
Ga	17.81	22.33	17.72	15.24	8.93	22.54	19.88	20.86	22.23	10.26	10.10	11.09	152	1.66	1.61	1.84	2.96	13.57	4.62
Ge	1.65	1.94	1.44	1.74	1.90	1.66	1.43	1.35	1.95	1.06	1.15	0.99	0.81	0.78	0.81	0.99	1.05	1.10	0.82
In	0.12	0.15	0.11	0.11	0.08	0.15	0.06	0.06	0.08	0.04	0.03	<L.D.	<L.D.	<L.D.	<L.D.	<L.D.	<L.D.	0.08	<L.D.

Rock-types: *Fe-Ti Mig*, Fe-Ti metagabbro; *Mg-Al Mig*, Mg-Al metagabbro; *Int.Mig*, Intermediate (garnet-bearing) Mg-Al metagabbro in Mg-Al metagabbro in eclogitic breccia layers; *SZ matrix*, antigorite-rich matrix of Lower and Intermediate Shear Zone; *MJ* and *M3 matrix*, matrices cementing eclogite-breccia. * *L20-15*, core portion of sample L20-15; ** *L20-15m*, M3 matrix portion of sample L20-15; <L.D., lower than Detection Limit; L.D.: Loss of Ignition; *Mg#*, magnesium number, calculated using the formula $MgO/(MgO+FeO)*100$.

The Fe-Ti clast enveloped in M2 matrix from block B70 (sample LSZ 14-73) show comparable contents in LILEs, REE, Ni and Cr if compared to the unbrecciated Fe-Ti metagabbros (*Figure 56a*). Sensible enrichment in Nb, Ta, Nd, Ce and Pb is observed, with concentrations comparable to Intermediate metagabbros (Fig. 5a), while Sr, Zr and Hf correlate to M1 matrix (*Figure 56a*).

Intermediate metagabbros, found as cm-thick bands of garnet-bearing Mg-Al metagabbros at the transition with the Fe-Ti metagabbro boudins, have similar contents in Fe₂O₃, Na₂O, Al₂O₃ and CaO, but lower MgO (6.10-6.55 µg/g) compared to the Mg-Al metagabbros (*Table 6* and *Figure 56a*). In contrast, incompatible elements such as Rb, Ba, Th, U, Nb, Ta, Nd, Ce, Pb, B and HFSE are enriched (with higher concentration in REE consistent with the crystallization of garnet, preferential host-mineral for HREE; *Table 6* and *Figure 56c*).

The 3 analysed **Mg-Al metagabbro** samples from the LSU have mafic compositions, with high Fe₂O₃ (2.13-7.80 Wt%), TiO₂ (0.25-0.86 Wt%), Ni (162.09-201.57 µg/g) and Co (19.93-48.32 µg/g) contents relative to the mid-ocean ridge basalt (MORB; Sun & McDonough, 1989). Cr content is relatively high (*Table 6*; *Figure 56a-b*) and varies from 349.53 µg/g to 563.49 µg/g in the LSZ's Type2 blocks to a maximum of 2592.41 µg/g in the eclogitic metagabbro cropping out E of Lago Superiore (*Table 6*). The chromium enrichment in this sample is related to the crystallization of cm-size, Cr-rich omphacite (kosmochlor). If compared to the eclogitic Fe-Ti metagabbros (*Table 6*), the Mg-Al metagabbros are richer in MgO, Al₂O₃, CaO, Cr, Ni and Sr (e.g., *Figure 56a-b*), but have lower contents of Fe₂O₃, TiO₂ and most incompatible elements (*Figure 56c*). These chemical characteristics and the occurrence of positive Eu anomalies (that, interestingly, is not observed for the Intermediate metagabbros; *Table 6* and *Figure 56a*) are consistent with a plagioclase-rich cumulate protolith.

Five serpentinite samples were analysed: 3 samples from the antigorite-rich schists of the LSZ and 2 from the massive blocks dispersed in the shear zone matrix (*Table 6* and *Figure 56*). Both the blocks and the matrix serpentinites have compositions typical of hydrated mantle rocks (e.g., high MgO, Cr, Ni and LOI), as well as high concentrations of As (1.27-2.23 µg/g) B (12-37 µg/g) and Sb (0.064-0.11 µg/g) relative to typical mantle peridotite (*Table 6* and). These data are consistent with the Monviso serpentinite data of Hattori & Guillot (2007), Spandler et al. (2011) and Angiboust et al. (2014). The negative Eu anomaly observed in the massive serpentinite blocks (*Table 6* and *Figure 56c*) suggests plagioclase fractionation in the protolith, interpreted as intrusion of plagiogranite in peridotites.

The bulk major element composition of the M1 matrix reflects the high modal abundance of omphacite (*Table 6* and *Figure 56*). M1 matrix trace element patterns are broadly close to those of Fe-Ti and Intermediate gabbros. Compared to Fe-Ti metagabbros and clasts it surrounds, M1 matrix shows a distinct enrichment in Cr (up-to one order of magnitude, with concentrations up-to values of Intermediate metagabbro), Ni (one order of magnitude higher than Fe-Ti megabbro and higher than Intermediate metagabbro) with concentrations comparable to those of Mg-Al metagabbro, and Co to a lesser extent (*Table 6* and *Figure 56*). Rubidium, Th, U and Pb to a lesser extent are also enriched in M1 compared to Fe-Ti metagabbros, whereas Ce, Nd and all REE are depleted, reaching values of Mg-Al metagabbros, nevertheless without Eu anomaly (*Table 6* and *Figure 56*). Nevertheless, the comparison between the geochemical signature of the bulks of M1 matrix and the metagabbros (e.g., Fe-Ti, Mg-Al and Intermediate metagabbro) is difficult due to the mono-mineralic composition of M1 (>99 Vol.% of omphacite, which is classically poor in trace-elements compared to other phases such as lawsonite or garnet). Thus, this strong

mineralogical control has to be taken in account in the interpretation of M1 matrix geochemistry, by comparing in-situ omphacite crystal measurements.

The bulk of M3 matrix clearly shows lower contents of TiO_2 (0.07 wt%), Fe_2O_3 (8.96 wt%) and CaO (1.48 wt%) than both Mg-Al and Fe-Ti metagabbros, but MgO (33.97 wt%) is strongly enriched with respect to all the other lithologies (*Table 6* and *Figure 56c*). Both the major element contents and the high contents in Cr (2283.04 $\mu\text{g/g}$), Ni (1947.19 $\mu\text{g/g}$), Co (97.46 $\mu\text{g/g}$) and B (7 $\mu\text{g/g}$) are comparable to those of the analysed serpentinite samples (*Table 6* and *Figure 56c*), although the LREE and HREE concentrations are similar to that of Fe-Ti and Mg-Al metagabbros respectively. In contrast, the M3 matrix concentration of HFSE and LILE does not show any clear pattern (*Figure 56a*), although they are generally lower than in M1 matrix and Fe-Ti metagabbros, with particular depletions in Sr, Nb, Ta that reach values of serpentinites.

5.6. Textural generations and mineral geochemistry: major elements

The SEM and EPMA analyses suggest that the major element composition of mylonitic clinopyroxene and garnet (*Figure 57a-b*; *Tables 7* and *8*) present only minor differences between Mg-Al and Fe-Ti metagabbro clasts. Similarly, the major element composition of matrices M1, M2 and M3 does not show any striking difference between the different samples, so their mineral analysis are presented together in the following (*Figure 57a-b*).

The representative major element compositions for omphacite, garnet and ex-lawsonite are presented in *Tables 7*, *8* and *9* respectively. The full set of major element data of minerals is presented in the Appendix 1.

5.6.1 – Clast mineral chemistry: Major elements

In the clasts, omphacite crystals (Figure 57a) show clear core-to-rim chronological relationships (e.g., Omp1a and Omp1b of Chapter 4). In the mylonitic Fe-Ti metagabbro clasts, the first generation of omphacite (Omp1a, $\text{Di}_{45}\text{Jd}_{30}\text{Ae}_{25}$; Figure 57a) forms bright porphyroclasts, rimmed by a second omphacite generation (Omp1b, $\text{Di}_{40}\text{Jd}_{38}\text{Ae}_{22}$; Figure 58a-b) crystallizing also

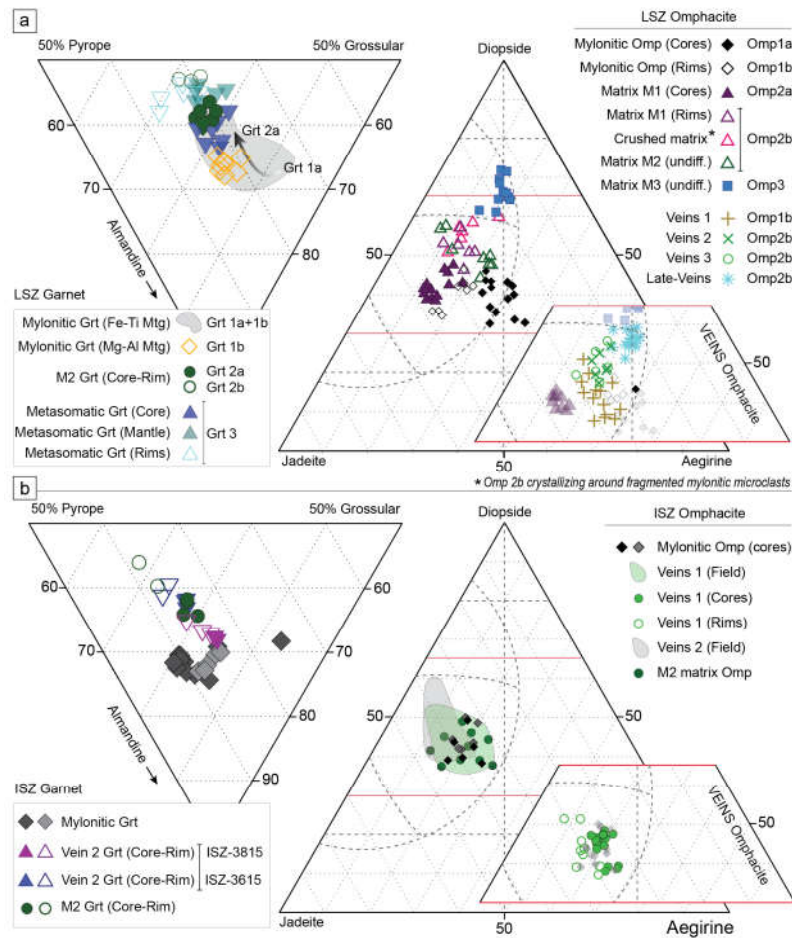


Figure 57: MA composition of minerals analyzed at the LA-ICP-MS: a) LSZ: Ternary-plot for selected omphacite (Jad-Diop-Aeg) and Ternary-plot for selected garnets (Grs-Alm-Prp). b) ISZ: Ternary-plot for selected omphacite (Jad-Diop-Aeg) and Ternary-plot for selected garnets (Grs-Alm-Prp). For the comparison with previous data from Groppo & Castelli (2011); Spandler et Al. (2011); Angiboust et Al. (2012a, 2014) please refer to figure 4.10.

as newly formed crystals aligned in the mylonitic foliation. Garnet is also zoned (*Figures 57b, 58a and 58c*), with darker cores (Grt1a, Grs₂₄Prp₅Alm₇₁; *Figure 58a*) and lighter rims (Grt1b, Grs₁₇Prp₁₃Alm₇₀; *Figure 58a and 58c*). Interestingly, garnet cores (Grt1a) have numerous Omp1a inclusions, whereas the rims (Grt1b) only contain few inclusions of Omp1b, showing that omphacite and garnet compositions evolved jointly during mylonitization. Locally, garnets with smaller size (< 100 µm) of Grt1b composition are scattered in the foliation.

Veins I (i.e., crosscutting clasts but predating brecciation; *Figure 55b*) are almost completely filled with unzoned Omp1b omphacite.

5.6.2 – Matrix mineral chemistry: Major elements

Fragmented omphacite and garnet crystals compose the bulk of the crushed-matrix domains (*Figure 58d*), with compositions and zonations comparable to the mylonitic clast minerals (i.e., Omp1a cores rimmed by Omp1b compositions and Grt1a rimmed by Grt1b. Interstitial Omp2a omphacite (*Figure 58d*) seals these crushed-matrix domains, and fragmented Grt1 garnets in contact with Omp2a layers are overgrown by thin (<20 µm) Mn-rich mantles of Grt2a composition. Anastomosed layers of Omp2b (< 70 µm thick), with infiltration-like pattern departing from M1 matrix domains, seal both interstitial Omp2a and the crushed minerals (*Figure 58d*).

With respect to clasts and crushed-matrix, in M1 and M2 matrices the zonation of omphacite crystals are more complex with transitions difficult to unravel (e.g., Omp2a to Omp2b; *Figures 57a and 58a*). The M1 matrix (omphacite-bearing) is composed by about 60 vol.% of Omp2b crystals surrounding flake-shaped remnants of corroded, Al-richer Omp2a crystals (35 vol.%, *Figure 57a*). The intergrowth of the two generations results in an extremely intricate mesh of both generations (e.g., MgO concentration of M1 matrix shown in *Figure 57a*), in which are included

rare remnant crystals of Omp1 omphacite and rutile (~5 vol.%). M2 matrix (omphacite- and garnet-bearing) is largely made of tabular omphacite crystals of Omp2b composition, with subordinate Omp2a (mainly as crystal cores) and rare, clastic-shape, relics of Omp1a-b (*Figures 58e*); composition of Omp2b is similar to the one analyzed in crushed and M1 matrix but locally noticeably enriched in Cr₂O₃ (up to 0.35 wt.% vs < 0.1 wt.% in the mylonitic clasts; *Table 7*). Garnet cores (Grt2a composition, *Figures 57b and 58f*) are rimmed by almandine-poorer garnet (Grt2b; Grs₂₀Prp₂₅Alm₄₅).

In the next page:

Figure58: a) SEM image of the complex zonation of omphacite crystals at the transition from mylonitic clast to M1-matrix domain. In the box (i) the quantified EPMA map of MgO enlightening the mylonitic Omp1a and Omp1b of sealed at the clast edge by a third generation of omphacite Omp2a. In the box (ii) the EPMA map of MnO, showing its strong enrichment in the garnet rims at the contact with M1-matrix. Sample LSZ 14-53. b) SEM image of the complex zonation of omphacite crystals developed in mylonitic Fe-Ti metagabbro clasts with the FEG-SEM quantified Ca (Green), Fe (Purple) and Mg (Blue) map of the same area. Sample LSZ 14-53. (c) FEG-SEM quantified maps of a garnet from a mylonitic Fe-Ti metagabbro clast. Sample LSZ 63-15d. (d) cross-polarized light microphotography of a Crushed-Matrix domain developed between a mylonitic metagabbro clasts (lower part of the figure) and an Omp+Apt-bearing Veins1 (upper part of the figure). The quantified EPMA map of MgO enlighten the “infiltration” pattern of the MgO-richer Omp2b. Sample LSZ 14-53. (e) plane-polarized light microphotography of the transition between M2-matrix and mylonitic Fe-Ti metagabbro clast. In the box (iii) the quantified EPMA map of MgO enlightening the complex zonation of omphacite grains. Sample LSZ 63-15d. (f) FEG-SEM quantified maps of a garnet from M2-matrix. Noteworthy the Cr zonation of garnet shows an oscillatory, dissymmetric pattern which has no equal in mylonitic and metasomatic garnet. Sample LSZ 63-15d. (g) FEG-SEM quantified maps of a garnet from a metasomatized portion of sample LSZ 63-15d M2-matrix. Chrome is strongly enriched about, differently from M2 garnet, shows symmetric zonation. Sample LSZ 63-15b

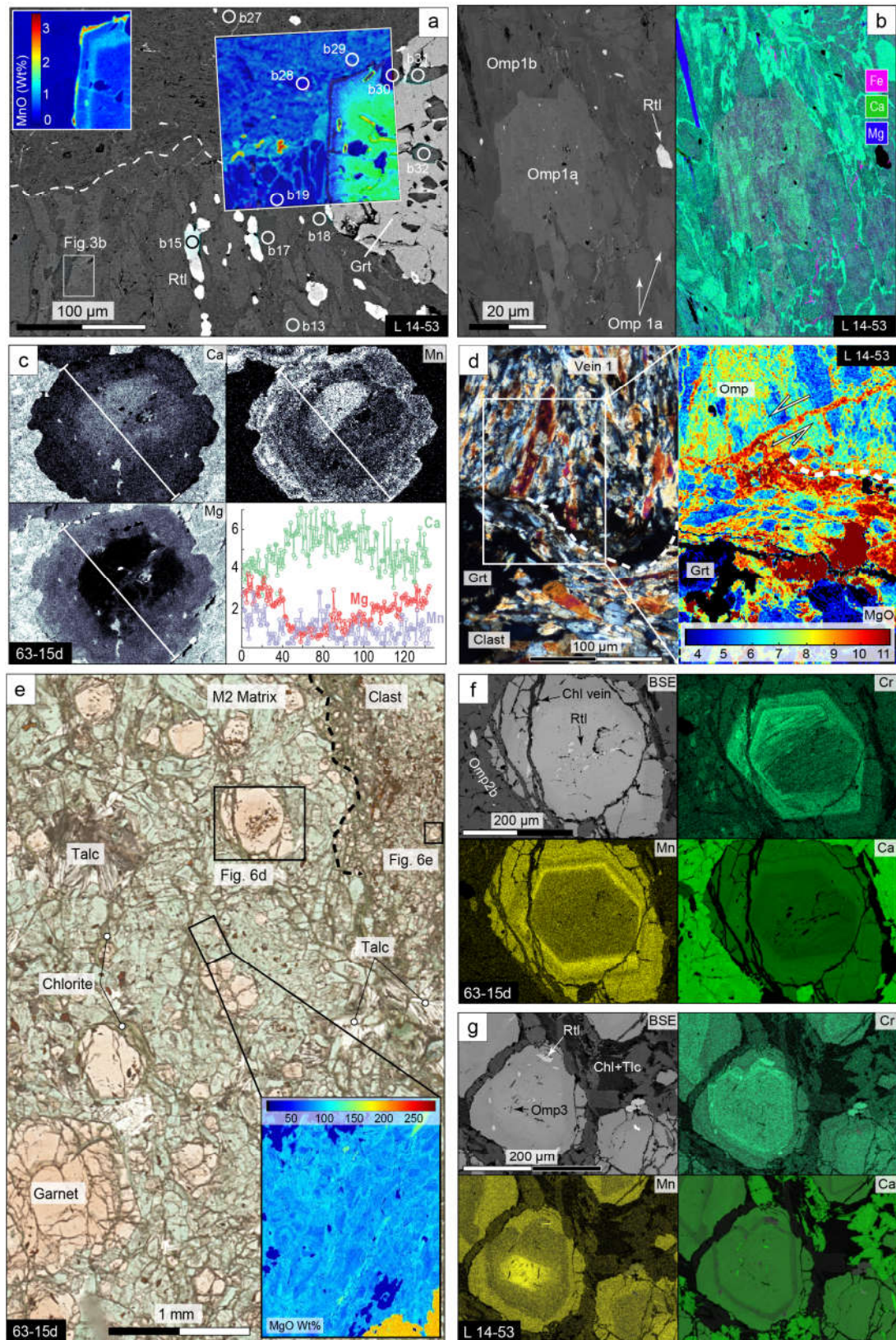


Figure 58

Both are enriched in Cr₂O₃ (up to 0.30 wt%, *Table 8*, with peculiar sectorial enrichment pattern: *Figure 58f*) compared to mylonitic clast Grt1 (where Cr content is up-to 0.1 wt.%). In Grt2a, the included omphacite have Omp2a compositions, while Grt2b appear to be equilibrated with inclusions of Omp2b. Analysis of the M3 matrix eclogite-facies assemblage is difficult due to the strong greenschist retrogression (*Figure 55c*), which lead to pervasive recrystallization of tremolite/actinolite + plagioclase after omphacite and chlorite ± phengite after garnets (as also locally observed in M2 matrix; e.g. *Figures 58g*). The rare omphacite relicts dispersed in this mesh have a distinct Omp3 composition (Di₆₈Jd₁₅Ae₁₇; *Figure 57a*). No major-element analysis could be made on lawsonite, which is now completely pseudomorphosed by clinozoisite, plagioclase and chlorite (e.g., *Figure 55c*).

Late-stage veins postdate both the mylonitization of metagabbros and the matrices: here the composition of clinopyroxene (crystallizing at equilibrium with talc) is Di₅₇Jd₂₂Ae₂₁. Its major element composition is close to both Omp2b and Omp3, but microstructural and geochemical evidences permit to distinguish it as a later generation.

In the metasomatic rinds, the newly-formed garnets have a distinct core-mantle-rim zonation (respectively: Grs₁₇Prp₂₂Alm₆₁, Grs₁₉Prp₂₆Alm₅₅ and Grs₁₈Prp₂₉Alm₅₃; *Figure 57b*).

5.6.3 – Intermediate Shear Zone

In the ISZ, the clasts of brecciated Fe-Ti metagabbros display the same mylonitic Omp1a-Omp1b zonation observed in the LSZ. In contrast to the LSZ, no analogue of the omphacite-bearing M1 matrix could be found, whereas two generations of veins crystallized prior to the M2 brecciation event. The first set of veins (Vein T1) contains omphacite (+ apatite) with composition Di₄₀Jd₃₈Ae₂₂ (directly comparable to the Vein I of LSZ Fe-Ti metagabbros; Omp 1b); omphacite

from Vein T2 has composition $\text{Di}_{50}\text{Jd}_{40}\text{Ae}_{10}$ (comparable to Omp2b from LSZ), and additionally contains garnets with composition that can be compared to Grt2a (cores, $\text{Grs}_{15}\text{Prp}_{22}\text{Alm}_{63}$) and Grt2b (rims, $\text{Grs}_{13}\text{Prp}_{27}\text{Alm}_{60}$). The M2 matrix is composed by Omp2b in equilibrium with garnet, whose composition is comparable to Grt2a (cores) and Grt2b (rims) but slightly depleted in grossular and almandine (*Figure 57b*). Locally, Cr content of M2 omphacite and garnet is enriched with respect to those in M1, clasts and veins of the LSZ (1.02 wt.% vs 0.35 wt.% respectively) and are directly comparable to the Cr concentration of M2-matrix crystals from LSZ (*Table 8*).

5.6.4 – Note on omphacite composition

It is interesting to note that omphacite compositions are supposed to present an immiscibility gap between diopside and jadeite components (e.g., Carpenter, 1980; Nakamura & Banno, 1997; Tsujimori et al., 2005; Green et al; 2007) at P-T conditions corresponding to the peak of 2.6 Gpa, 550°C (Angiboust et al., 2012a) reached by the LSU. The implication is that only two omphacites of different composition (close to end-member jadeite and diopside compositions, plotted on Fig. 6a) are supposed to coexist at each step. Even if the omphacite-diopside gap is expected to become narrower with a little increase of Kosmochlor-component (only 10 mol% Ko reduce the gap of 1 order of magnitude; Tsujimori & Liou, 2004), the miscibility is anyhow not expected.

The composition of the Monviso omphacite presented in Fig. 6a is therefore controversial. Indeed, omphacite crystals from both mylonitic clasts and matrix domains rather present intermediate compositions that do not fit with the theoretical miscibility gap. Moreover, textural analysis clearly show successive omphacite generations rimming or replacing each other (*Figure*

57a-b) with compositions evolving through time, likely related to the evolution in P-T conditions (see chapter 4 for detailed P-T path). Thus this occurrence, already reported from other localities with similar PT conditions (e.g., Brovarone et al., 2011a), does not have at the state of the art a valid explanation.

5.7. Mineral geochemistry: trace elements

The geochemical signature of omphacite, garnet, ex-lawsonite and apatite from the eclogitic breccia of Monviso metaophiolite reflects the great complexity of zonations and major-element composition of these minerals.

To assess the trace element chemistry in detail we acquired nearly 210 omphacite (approximately 70% from LSZ samples, 30% from the ISZ), 80 garnet, 15 ex-lawsonite and 15 apatite trace element analyses. For comparative purposes, we analysed the trace element compositions of the different generations of minerals in clasts, HP veins, matrices and host eclogite adjacent to eclogite-breccia layers. The complete dataset is presented in the Appendix 1.

5.7.1 Lower Shear Zone - LSZ

Omphacite

The omphacite from mylonitic clasts and the Veins I (samples LSZ 14-50, LSZ 14-53, LSZ 63-15b, LSZ 63-15d and ISZ 35-15, ISZ 37-15, ISZ 38-15) have similar trace-element patterns (*Table 7* and *Figure 59*). In all samples, host-rock omphacite grains have similar core and rim concentrations in Sr, Pb and V, with extremely low contents in Nb (generally under 0.04 µg/g at the cores and 0.07 µg/g at the rims), As (cores: 0.01-0.23µg/g; rims: 0.14-0.24µg/g) and Sb (7-25µg/g at the core and 10-39µg at the rim). In the cores, Cr contents are almost exclusively less

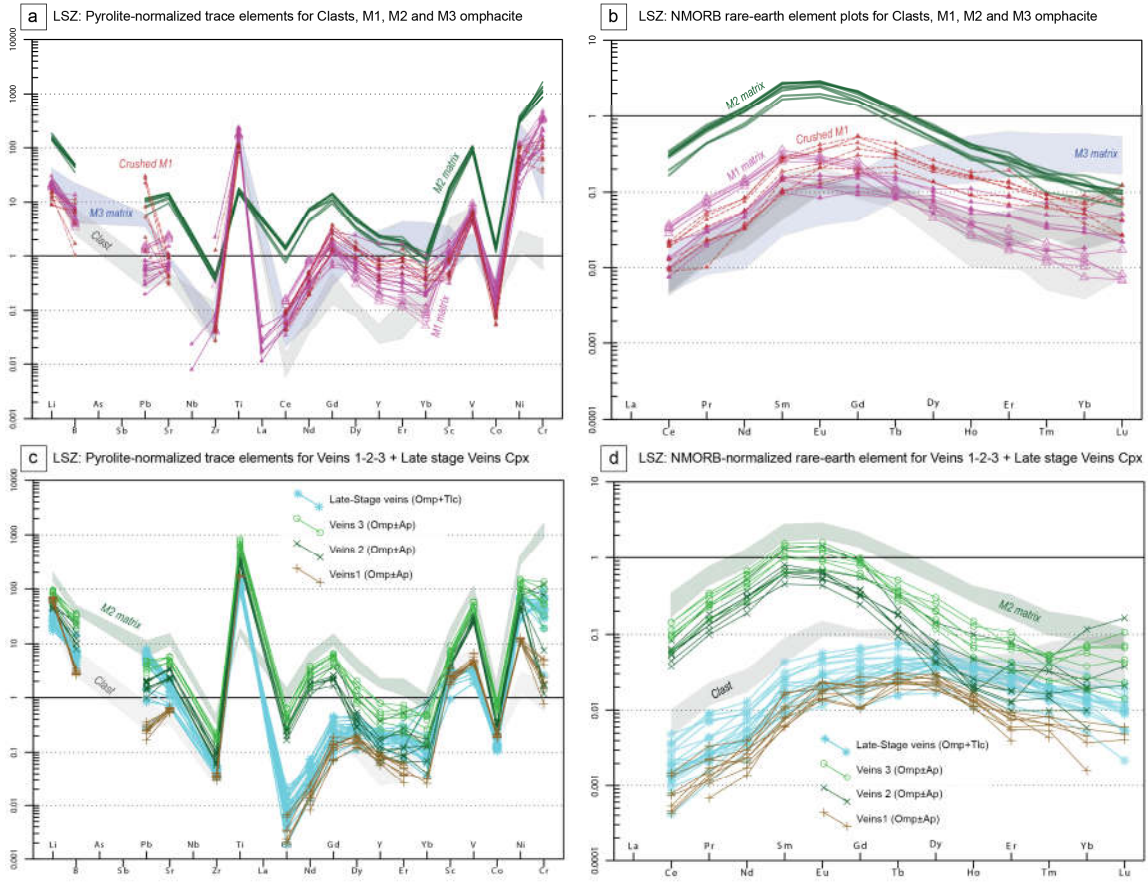


Figure 59: LSZ: omphacite crystals from clasts and matrices; a) trace element variation diagrams (data normalized to pyrolite values from McDonough & Sun; 1995). b) Rare earth elements variation diagrams (normalized to NMORB values from Sun & McDonough; 1989).

LSZ: omphacite crystals from veins; c) trace element variation diagrams (data normalized to pyrolite values from McDonough & Sun; 1995). d) Rare earth elements variation diagrams (normalized to NMORB values from Sun & McDonough; 1989).

than 15 $\mu\text{g/g}$ (Table 7, Figures 59a and 60a-d), while in the rims Cr can reach 67 $\mu\text{g/g}$. Boron contents range from 0.3 to 2 $\mu\text{g/g}$ in the cores of mylonitic omphacites and is slightly enriched in crystals from Mg-Al metagabbro clasts (Table 7; Figures 59a and 60). Mylonitic clast omphacite from samples 6315b and 6315d (Fe-Ti boudin W of P.ta Forcion) are slightly richer in REE + Y + Ni + Sr and poorer in Co compared to those from other samples (Table 7; Figs. 59b, 60a-d and 61). Nevertheless, the HREE appear to be depleted in the mylonitic omphacite rims of all samples respect to the cores (Table 7; Figs. 59b).

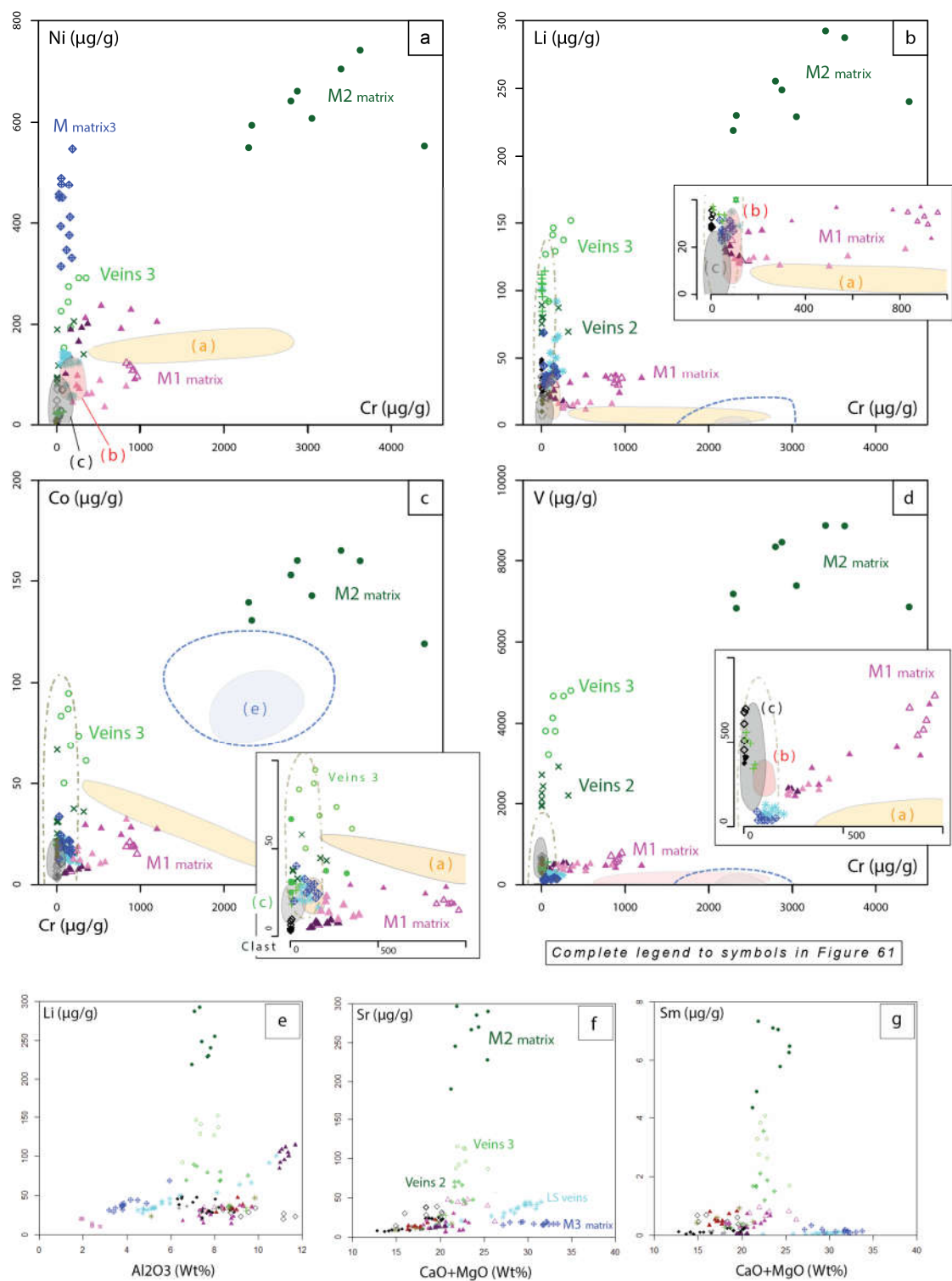


Figure 60

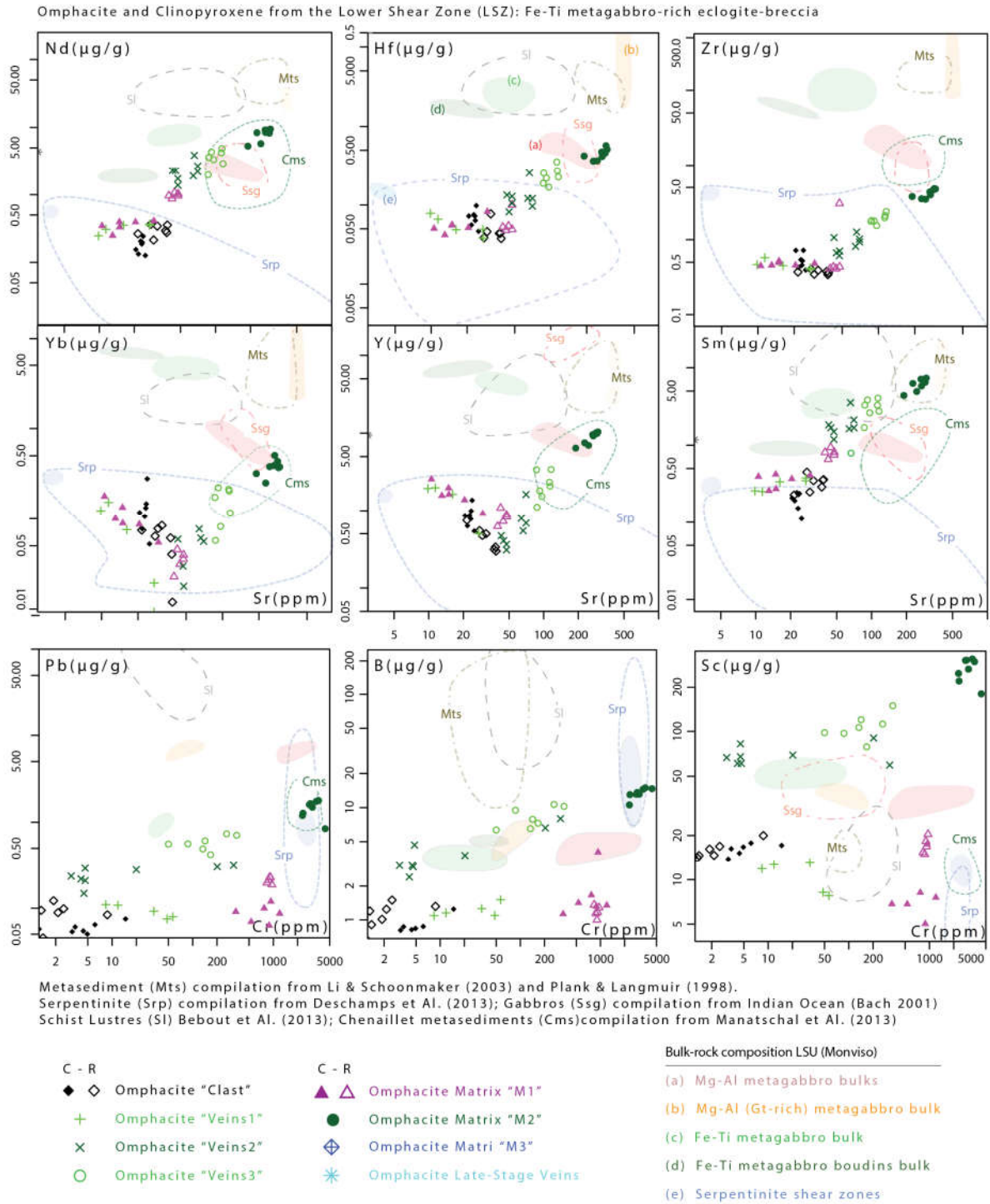


Figure 61

Figure 60: Selected trace element characteristics of clasts, veins and matrices omphacite compared with (a) Mg-Al metagabbros (b) Intermediate metagabbros and (c) Fe-Ti metagabbro (shaded areas). a) Ni vs Cr; b) Li vs Cr; c) Co vs Cr; d) V vs Cr; e) Li vs Al₂O₃; f) Sr vs CaO + MgO; Sm vs CaO + MgO. It should be noted that only linear scale is used in this figure.

Figure 61: Selected trace element characteristics of omphacite crystals from clasts, veins and matrices compared to the bulk-rock composition of lithologies from Monviso metaophiolite (full-colored areas) and from data compilation of other studies (dotted-lines areas); legend in the figure. a) Nd vs Sr; b) Hf vs Sr; c) Zr vs Sr; d) Yb vs Sr; e) Y vs Sr; f) Sm vs Sr; g) Pb vs Cr; h) B vs Cr; i) Sc vs Cr. It should be noted that only logarithmic scale is used in this figure.

In Vein I omphacite crystals, the concentrations of all trace elements is directly comparable to those of the rims of mylonitic clast grains with the exception of REE, depleted of one-order of magnitude, and a slight increase in Li and Ni (Table 7; Figures 59c-d, 60 and 61).

Omphacite grains from the *crushed matrix* domains and M1 matrix show very similar compositions. More precisely, the analysed omphacites of crushed matrix are mainly Omp2b (growth as interstitial between crushed grains). They show slightly higher Y and HREE contents (Table 7; Figures 59c-d and 60) compared to M1 omphacite rims (Omp2b). The trace element spectra of crushed and M1 matrix omphacite are comparable to those of clasts and Vein I omphacite (Table 7; Figures 59c-d and 60), except for a strong enrichment in Cr and Ni, and slight enrichment in Pb, Sr and REE. The increase of lithium and Al₂O₃ contents are correlated in both crushed- and M1-matrix omphacite (as well as in mylonitic clasts; Figure 60e), showing that Li substitutes into pyroxene as spodumene (LiAlSi₂O₆) component. Broad positive correlations with CaO + MgO (Figure 60f) indicate that Sr, light to middle REE (LREE-MREE), Co and Ni partition with the diopside component of the pyroxenes.

The trace element patterns of M2 matrix omphacites are quite parallel to those of clast, M1 and crushed omphacites, but almost all elements are enriched by 0.5 to 1 order of magnitude. The sole exception is Ti, which is 1 order of magnitude lower than for all other omphacites. The highest enrichments concern Cr, Ni, Co and V (Table 7; Figure 59a-d) plus LREE, while HREE are clearly less enriched (almost comparable to M1 cores, Fig. 8b). The Cr contents of M2 matrix

omphacite measured by LA-ICP-MS reach wt.% levels (2293-4398 $\mu\text{g/g}$), which agrees with electron microprobe analyses. Veins 2 and Veins 3, which texturally postdate both the mylonitic stage and the crystallization of M1 matrix, but are crosscut by M2, show omphacite trace element patterns very similar to those of M2 omphacite, except that they do not show any Ti drop, and that concentrations of all elements are lower, in particular in Cr. Ti and Ni contents are similar to M1 omphacite. In fact, there seems to be a progressive enrichment in almost all trace elements along the successive generations M1, Vein2, Vein 33, M2 (*Table 7; Figures 59c-d*). Li vs Al_2O_3 contents in both M2-matrix and Veins2/Veins3 omphacite do not correlate with the spodumene trend, contrary to those in clasts and M1 matrix (*Figure 60e*). Additionally, the lack of correlation of Sr and Sm with $\text{CaO} + \text{MgO}$ (*Figure 60f-g*) suggests that the partitioning of these elements (and light to middle REE) did not follow the diopside component of the pyroxenes.

The trace element pattern of relict omphacite crystals found in the metasomatized M3 matrix (sample LSZ 14-10, block B1) is close to those of mylonitic clasts and M1 matrix (*Table 7; Fig. 59a-b*). However, M3 omphacites are enriched in As, Sb (+/- B), Ni and HREE but depleted in Cr compared to M1 matrix (*Table 7; Figures 59a-d, 60 and 61*). Lithium and Al_2O_3 contents broadly correlate, as well as $\text{CaO} + \text{MgO}$ correlate with Sr (*Figure 60e-f*), though the respective patterns are different from those observed for mylonitic and M1 matrix omphacite.

Late-stage vein omphacite is directly comparable to those of Veins1, with a slight enrichment in most elements except Sc, V, Co and Li that are depleted (*Table 7; Fig. 59c-d*). Ni, Cr, Pb, Sr and B show the highest enrichments compared to mylonitic clast and Veins I omphacite (*Table 7; Figures 59a-d, 60 and 61*) and their contents reach those of Veins2/3 and M3. Lithium readily substitutes into pyroxene as a spodumene ($\text{LiAlSi}_2\text{O}_6$; *Figure 60e*) component; the positive correlations with $\text{CaO} + \text{MgO}$ (*Figure 60f-g*) indicate that Sr, Co and, in lesser extent, light to middle REE (LREE-MREE), partition with the diopside component of the pyroxenes.

Chapter 5 - The geochemical signature of Eclogitic Breccia

Table 7 (a): representative major (Wt%) and trace element (µg/g) analysis of omphacite from LSZ (Clasts and matrices)

Sample	LSZ 1453	LSZ 1453	LSZ 1453	LSZ 1453	LSZ 6315b	LSZ 6315b	LSZ 1453	LSZ 1453	LSZ 1450	LSZ 1452
Petrology	Fe-Ti Mtg Clast C	Fe-Ti Mtg Clast C	Fe-Ti Mtg Clast R	Fe-Ti Mtg Clast R	Fe-Ti Mtg Clast C	Fe-Ti Mtg Clast C	Crush (M1) matrix	Crush (M1) matrix	M1 matrix	M1 matrix
<i>Major element analysis (Wt%)</i>										
<i>SiO2</i>	55.46	55.02	56.13	56.84	56.05	56.36	56.86	56.91	55.62	55.00
<i>TiO2</i>	0.09	0.07	0.08	0.02	0.04	0.08	0.03	0.09	0.03	0.05
<i>Al2O3</i>	6.50	7.18	11.15	11.70	7.76	8.66	7.49	7.82	8.07	8.44
<i>Cr2O3</i>	0.02	0.01	0.01	0.01	0.08	0.00	0.11	0.02	0.03	0.12
<i>FeO</i>	15.36	14.10	7.38	7.24	9.67	9.36	7.08	7.27	11.29	8.97
<i>MnO</i>	0.05	0.06	0.03	0.06	0.06	0.02	0.08	0.06	0.04	0.03
<i>MgO</i>	4.94	4.95	6.20	5.86	7.67	6.91	9.14	8.92	6.92	7.71
<i>CaO</i>	9.56	8.69	9.71	9.04	12.63	11.43	13.67	13.26	10.77	11.73
<i>Na2O</i>	8.55	9.37	9.11	9.49	7.46	8.29	6.76	7.00	8.35	8.06
<i>K2O</i>	0.01	<0.0086	0.00	0.01	0.00	0.04	0.02	0.02	0.00	0.01
<i>NiO</i>	0.00	0.00	0.00	0.00	0.00	0.00	0.00	0.00	0.01	0.01
<i>P2O5</i>	0.00	0.00	0.00	0.00	0.04	0.00	0.00	0.00	0.00	0.00
<i>Total</i>	100.53	99.47	99.80	100.27	101.46	101.15	101.23	101.36	101.15	100.13
<i>MgO#</i>	24.35	25.99	45.68	44.76	44.23	42.48	56.38	55.10	38.01	46.25
<i>Trace element analysis (µg/g)</i>										
<i>Li</i>	46.44	47.44	20.16	23.36	29.84	35.52	14.34	25.21	28.46	32.54
<i>B</i>	0.75	0.81	5.96	15.68	0.87	1.24	1.86	1.13	2.26	4.42
<i>Na</i>	61219.10	61865.61	43483.75	46834.57	57242.63	63135.27	32925.05	39937.85	61938.14	59795.21
<i>P</i>	-	-	-	-	3.65	2.49	-	-	8.43	5.33
<i>K</i>	-	-	-	-	5.51	<4.14	-	-	37.29	48.49
<i>Sc</i>	34.70	45.20	14.41	16.15	16.27	14.69	14.28	7.73	24.45	20.32
<i>Ti</i>	160.33	158.69	409.43	103.95	329.80	213.57	123.99	132.16	208.51	277.69
<i>V</i>	305.40	538.21	400.33	354.52	376.18	510.66	525.30	494.74	502.25	498.56
<i>Cr</i>	1.45	2.64	67.27	49.60	3.49	2.14	298.04	149.21	203.75	839.36
<i>Mn</i>	59.92	103.80	343.87	266.31	172.63	148.58	381.49	301.55	335.33	252.10
<i>Co</i>	19.13	17.78	12.80	10.44	3.84	8.97	8.89	8.19	12.70	34.72
<i>Ni</i>	3.38	2.27	69.27	27.31	8.51	48.04	193.22	137.96	45.05	79.42
<i>As</i>	0.07	0.13	0.29	0.44	<0.01	<0.03	<0.02	<0.17	<0.03	0.03
<i>Rb</i>	0.02	0.04	0.13	0.08	<0.01	<0.02	0.19	0.06	0.13	0.08
<i>Sr</i>	8.61	6.67	30.00	13.59	22.73	27.67	19.94	7.76	12.79	21.70
<i>Y</i>	0.15	0.15	3.12	2.05	0.87	0.55	3.75	2.93	2.45	3.37
<i>Zr</i>	0.31	0.28	1.67	161.56	0.54	0.40	0.53	0.45	0.77	0.84
<i>Nb</i>	0.01	0.01	0.07	0.05	<0.00	0.00	0.01	0.01	<0.01	0.02
<i>Sb</i>	0.06	0.11	0.36	0.95	<0.02	<0.05	0.15	0.16	<0.04	0.01
<i>Cs</i>	0.01	0.02	0.05	0.06	<0.00	<0.01	0.06	0.03	<0.01	0.01
<i>Ba</i>	0.08	0.15	0.36	0.34	0.05	<0.05	0.10	0.46	0.19	0.81
<i>La</i>	0.01	0.01	0.04	0.03	0.01	<0.01	0.01	0.01	0.03	0.02
<i>Ce</i>	0.01	0.01	0.10	0.11	0.06	0.09	0.16	0.07	0.14	0.14
<i>Pr</i>	0.00	0.00	0.09	0.06	0.02	0.04	0.07	0.03	0.04	0.05
<i>Nd</i>	0.06	0.05	0.74	0.35	0.21	0.36	0.60	0.23	0.35	0.62
<i>Sm</i>	0.04	0.04	0.69	0.68	0.24	0.45	0.74	0.39	0.37	0.81
<i>Eu</i>	0.05	0.03	0.43	0.10	0.11	0.19	0.42	0.21	0.19	0.45
<i>Gd</i>	0.07	0.08	1.67	0.84	0.40	0.45	1.96	1.11	0.63	1.68
<i>Tb</i>	0.02	0.02	0.16	0.07	0.06	0.05	0.29	0.18	0.12	0.22
<i>Dy</i>	0.07	0.08	0.59	0.66	0.30	0.17	1.18	0.83	0.58	0.97
<i>Ho</i>	0.01	0.01	0.15	0.08	0.03	0.03	0.18	0.15	0.10	0.15
<i>Er</i>	0.01	0.02	0.17	0.16	0.09	0.05	0.57	0.41	0.28	0.39
<i>Tm</i>	0.01	0.01	0.07	0.03	0.01	0.01	0.04	0.04	0.03	0.05
<i>Yb</i>	0.04	0.07	0.10	0.17	0.11	0.06	0.22	0.27	0.24	0.33
<i>Lu</i>	0.00	0.00	0.03	0.05	0.01	<0.01	0.06	0.03	0.04	0.05
<i>Hf</i>	0.04	0.04	0.11	4.45	0.08	0.04	0.06	0.10	0.07	0.08
<i>Ta</i>	0.01	0.01	0.03	0.03	<0.00	<0.00	0.01	0.00	<0.00	0.00
<i>Pb</i>	0.04	0.07	0.28	0.24	0.06	0.09	4.40	4.01	0.08	0.18
<i>Bi</i>	0.03	0.04	0.10	0.12	<0.00	<0.01	0.02	0.04	<0.01	0.00
<i>Th</i>	0.01	0.02	0.03	0.03	0.01	<0.00	0.01	0.01	0.01	0.00
<i>U</i>	0.01	0.01	0.03	0.03	0.01	<0.01	0.01	0.00	<0.01	0.00
<i>W</i>	-	-	-	-	-	-	-	-	0.88	5.84

Table 7 (a): follows

Sample	LSZ 6315b	LSZ 6315b	LSZ 6315d	LSZ 6315d	LSZ 6315d	LSZ 14-10	LSZ 14-10	LSZ 1520a
Petrology	M1	M1	M2	M2	M2	M3	M3	M3
	matrix	matrix	matrix	matrix	matrix	matrix	matrix	matrix
<i>Major element analysis (Wt%)</i>								
<i>SiO₂</i>	56.52	55.82	55.71	55.74	55.27	54.27	54.63	56.16
<i>TiO₂</i>	0.00	0.03	0.04	0.01	0.01	0.03	0.02	0.05
<i>Al₂O₃</i>	7.50	7.57	7.80	7.31	7.08	3.85	3.78	5.94
<i>Cr₂O₃</i>	0.09	0.16	0.09	0.05	0.06	0.02	0.03	0.00
<i>FeO</i>	5.04	6.42	6.21	6.32	6.48	6.26	6.97	7.18
<i>MnO</i>	0.07	0.02	0.01	0.03	0.04	0.08	0.08	0.07
<i>MgO</i>	10.49	9.18	7.65	7.74	11.13	11.89	12.01	10.63
<i>CaO</i>	14.87	13.96	13.59	14.15	14.31	19.92	20.35	17.31
<i>Na₂O</i>	6.20	6.83	7.18	6.67	6.36	3.71	3.67	5.07
<i>K₂O</i>	0.02	0.01	0.01	0.02	0.00	0.00	0.00	0.00
<i>NiO</i>	0.03	0.08	0.04	0.04	0.01	0.05	0.07	0.06
<i>P₂O₅</i>	0.01	0.08				0.00	0.00	0.00
<i>Total</i>	100.82	100.13	98.22	97.94	100.76	100.07	101.62	102.47
<i>MgO#</i>	67.57	58.84	55.18	55.03	63.22	65.51	63.29	59.69
<i>Trace element analysis (µg/g)</i>								
<i>Li</i>	34.74	29.59	240.32	292.50	287.42	39.56	36.18	68.77
<i>B</i>	1.36	1.17	14.70	14.54	14.96	1.47	6.85	2.44
<i>Na</i>	57477.41	52447.31	60100.47	54392.39	52737.09	27510.58	27241.49	37614.03
<i>P</i>	4.01	4.09	0.37	0.49	0.52	4.23	3.37	5.46
<i>K</i>	1.89	4.33	7.11	6.94	7.59	9.63	17.14	17.10
<i>Sc</i>	15.40	16.85	178.30	309.74	297.08	9.62	12.78	56.25
<i>Ti</i>	204.29	191.90	18.83	22.11	21.66	163.70	105.58	286.72
<i>V</i>	704.91	631.92	6863.36	8889.24	8875.22	174.65	141.53	97.83
<i>Cr</i>	833.34	918.29	4397.54	3399.61	3628.74	157.70	187.56	26.31
<i>Mn</i>	162.67	185.10	724.72	971.99	985.03	610.70	637.77	563.04
<i>Co</i>	18.82	19.09	119.07	165.34	159.79	21.30	17.42	12.85
<i>Ni</i>	123.79	109.31	553.20	705.09	741.69	412.13	547.68	456.96
<i>As</i>	0.01	<0.00	<0.06	0.07	0.06	<0.01	<0.02	<0.03
<i>Rb</i>	0.00	<0.00	0.07	0.04	0.04	<0.01	0.14	<0.02
<i>Sr</i>	39.69	47.64	190.25	296.62	290.40	15.37	16.17	18.58
<i>Y</i>	0.62	0.83	6.42	10.40	9.89	5.00	5.38	12.14
<i>Zr</i>	0.41	0.43	3.77	4.76	4.82	0.32	0.27	0.93
<i>Nb</i>	0.00	0.00	<0.02	0.02	0.03	0.01	0.02	<0.01
<i>Sb</i>	<0.02	<0.01	<0.08	<0.08	<0.08	<0.02	<0.02	<0.04
<i>Cs</i>	<0.00	<0.00	<0.01	<0.02	<0.02	<0.00	0.03	<0.01
<i>Ba</i>	0.03	<0.02	0.20	<0.10	0.11	0.26	0.38	0.59
<i>La</i>	0.02	0.02	0.13	0.25	0.22	0.02	0.01	0.02
<i>Ce</i>	0.24	0.25	1.45	2.47	2.13	0.10	0.06	0.15
<i>Pr</i>	0.10	0.10	0.57	0.91	0.82	0.03	0.01	0.04
<i>Nd</i>	0.97	1.03	5.30	9.46	8.28	0.20	0.14	0.38
<i>Sm</i>	0.81	0.81	4.38	7.34	6.48	0.19	0.09	0.34
<i>Eu</i>	0.28	0.30	1.84	2.85	2.78	0.07	0.04	0.13
<i>Gd</i>	0.78	0.84	5.11	7.81	7.98	0.33	0.23	0.65
<i>Tb</i>	0.07	0.08	0.52	0.86	0.81	0.09	0.07	0.21
<i>Dy</i>	0.21	0.28	2.11	3.23	3.47	0.83	0.81	1.93
<i>Ho</i>	0.03	0.04	0.28	0.43	0.42	0.19	0.19	0.55
<i>Er</i>	0.05	0.07	0.48	0.77	0.98	0.67	0.87	1.85
<i>Tm</i>	0.01	0.01	0.07	0.08	0.07	0.12	0.14	0.26
<i>Yb</i>	0.02	0.04	0.32	0.38	0.37	0.86	0.91	1.78
<i>Lu</i>	0.00	0.00	0.04	0.04	0.05	0.10	0.11	0.24
<i>Hf</i>	0.05	0.05	0.42	0.51	0.57	0.03	0.02	0.09
<i>Ta</i>	<0.00	<0.00	<0.01	<0.00	<0.01	<0.00	<0.00	<0.00
<i>Pb</i>	0.20	0.23	0.84	1.74	1.78	0.64	0.75	0.63
<i>Bi</i>	0.01	0.00	<0.01	0.01	<0.01	0.00	<0.00	<0.01
<i>Th</i>	<0.00	<0.00	<0.00	0.02	<0.01	0.01	0.00	0.02
<i>U</i>	0.00	<0.00	0.01	<0.01	<0.01	0.01	0.01	0.01
<i>W</i>	-	-	-	-	-	2.81	3.06	1.07

Table 7 (b): representative major (Wt%) and trace element ($\mu\text{g/g}$) analysis of omphacite from LSZ (Veins 1, 2 and 3)

PETROLOGY	LSZ 6315b	LSZ 6315b	LSZ 6315d	LSZ 6315d	LSZ 6315d	LSZ 6315d	LSZ 1520a	LSZ 1520a
Comment	Vein 1	Vein 1	Vein 2	Vein 2	Vein 3	Vein 3	Late-Stage Vein	Late-Stage Vein
Major element analysis (Wt%)								
SiO ₂	56.14	56.71	56.39	56.39	55.09	55.33	56.33	55.83
TiO ₂	0.03	0.03	0.06	0.06	0.03	0.00	0.03	0.03
Al ₂ O ₃	0.00	8.69	8.26	8.26	8.15	7.37	10.50	8.12
Cr ₂ O ₃	0.00	0.00	0.00	0.00	0.00	0.01	0.03	0.02
FeO	8.22	8.16	7.49	7.49	6.79	7.92	5.70	8.30
MnO	0.00	0.09	0.02	0.02	0.04	0.04	0.03	0.04
MgO	6.93	7.73	8.60	8.60	8.73	8.56	8.35	8.63
CaO	11.07	12.20	13.01	13.01	13.23	13.56	12.53	13.77
Na ₂ O	8.29	7.72	7.35	7.35	7.15	6.95	7.65	7.21
K ₂ O	0.00	0.00	0.01	0.01	0.00	0.01	0.00	0.00
NiO	0.00	0.03	0.00	0.00	0.15	0.14	0.01	0.01
P ₂ O ₅	0.04	0.04	0.00	0.00	0.03	0.03	0.00	0.00
Total	100.17	101.44	101.20	101.20	98.95	99.89	101.14	101.95
MgO#	45.77	48.65	53.45	53.45	56.25	51.95	59.44	50.98
Trace element analysis ($\mu\text{g/g}$)								
Li	33.68	37.17	80.27	69.61	151.89	141.14	91.87	53.83
B	1.51	1.09	3.77	7.97	10.25	6.53	1.21	2.11
Na	60897.54	57596.64	54952.57	56537.78	53031.29	52865.57	56743.65	53495.47
P	7.14	3.20	7.27	7.90	37.96	16.82	4.44	6.94
K	7.07	4.37	<7.40	18.90	64.15	38.09	<9.04	4.52
Sc	7.80	11.87	68.58	59.43	148.62	106.21	34.66	15.29
Ti	341.30	215.05	385.03	364.44	916.17	801.63	201.18	188.75
V	367.60	519.17	2430.20	2203.64	4808.85	4131.75	285.18	153.15
Cr	56.71	8.38	20.00	321.42	351.26	133.70	179.51	109.99
Mn	114.82	157.49	362.31	331.08	929.50	621.38	222.39	307.97
Co	29.94	18.69	31.17	36.11	61.38	87.04	14.54	13.53
Ni	267.62	135.98	118.60	140.87	291.93	244.05	57.02	77.94
As	<0.01	<0.01	<0.06	<0.04	<0.07	0.03	<0.07	<0.02
Rb	<0.01	<0.00	<0.03	<0.02	<0.04	0.03	<0.05	<0.01
Sr	11.40	27.17	70.20	64.37	115.80	92.17	14.32	20.51
Y	1.98	0.50	0.69	0.79	3.41	1.81	0.70	0.64
Zr	0.57	0.40	0.94	0.81	2.37	1.78	0.51	0.58
Nb	<0.00	<0.00	<0.01	<0.00	<0.02	<0.00	<0.02	0.01
Sb	<0.01	<0.01	<0.08	<0.06	<0.10	<0.03	<0.09	<0.02
Cs	<0.00	<0.00	<0.016	<0.01	<0.03	<0.00	<0.02	<0.00
Ba	0.06	<0.02	<0.18	<0.13	<0.21	0.14	0.36	0.17
La	0.01	0.01	0.03	0.04	0.07	0.09	<0.01	<0.00
Ce	0.06	0.07	0.45	0.42	0.74	0.85	0.01	0.01
Pr	0.02	0.03	0.17	0.17	0.31	0.38	<0.00	0.00
Nd	0.31	0.36	2.18	1.92	2.92	4.35	0.03	0.05
Sm	0.25	0.38	1.68	1.65	2.74	3.84	<0.09	0.03
Eu	0.08	0.18	0.62	0.54	0.96	1.38	0.03	0.03
Gd	0.36	0.51	1.23	1.20	2.87	3.23	0.16	0.14
Tb	0.06	0.06	0.12	0.12	0.34	0.24	0.02	0.03
Dy	0.42	0.18	0.25	0.36	1.37	0.60	0.19	0.13
Ho	0.08	0.02	0.02	0.05	0.15	0.07	0.03	0.02
Er	0.19	0.03	0.12	0.10	0.21	0.19	<0.05	0.05
Tm	0.02	0.00	0.01	0.01	0.02	0.02	0.01	0.01
Yb	0.15	0.02	0.06	0.08	0.12	0.22	<0.07	0.03
Lu	0.03	<0.00	<0.01	0.02	0.02	0.05	<0.01	<0.00
Hf	0.07	0.04	0.10	0.12	0.23	0.22	<0.05	0.06
Ta	<0.00	<0.00	<0.01	<0.00	<0.01	<0.00	<0.01	<0.00
Pb	0.08	0.11	0.28	0.31	0.71	0.49	0.13	0.22
Bi	<0.00	<0.00	<0.02	<0.01	<0.01	<0.01	<0.02	<0.00
Th	0.00	<0.00	<0.01	<0.00	0.02	0.01	<0.01	<0.00
U	0.00	<0.00	<0.0145	<0.01	0.01	0.00	<0.01	0.00
W	-	-	-	-	-	-	0.57	2.37

Garnet

Garnets from Fe-Ti metagabbro clasts are classically enriched Y and HREE (*Table 8; Figure 62a-d*), elements classically hosted in garnet (Spandler et al., 2003). Clast garnets are also enriched in metallic elements such as Mn, Ti and V, while Co, Ni and Cr present very low concentrations. Most of LILE are also depleted in garnets. Compared to Fe-Ti metagabbro garnets (*Table 8; Figure 62c-d*), those crystallizing in the *Intermediate Metagabbros* (or garnet-bearing Mg-Al metagabbros; *Table 8; Figure 62a-b*) are slightly depleted in most LILE and LREE to MREE while enriched in HREE, Y and Sr. Cr is also enriched compared to Fe-Ti metagabbro garnet rims but similar to compositions in garnet rims.

Absent in M1-matrix, Veins1, Veins2 and Veins3, garnets from M2 matrix show patterns close to those of clast garnets, although depleted in Ti and enriched in B, As (+/- Li), Sc, V, Co and Cr (+/- Ni). Cr shows the highest enrichment (2-3 orders of magnitude) and reaches concentrations up-to the weight percent with cores generally richer than rims (*Table 8; Figure 62a*). The strong Cr enrichment and Ti drop (compared to clast garnets) is comparable to what was observed for M2 omphacite. Concerning HREE and Y, M2 garnets show a distinct zonation, with cores poorer than rims, which present concentrations comparable to Intermediate metagabbros garnets (*Table 8; Figure 62a-d*). On the contrary, core to rim decrease in HREE was observed for M2 omphacite. Garnet MgO content directly correlates with Co, Y and REE concentration while the CaO broadly correlates with V.

The trace element composition of the metasomatic garnet cores, mantles and rims are characterized by similar patterns and concentrations (*Table 8; Figure 62c-d*), except for REE. Indeed, garnet cores show higher contents in LREE (except Ce; *Table 8; Figure 62d*), while MREE are enriched in both mantles and cores and HREE are enriched in the rims, for which clinopyroxene

inclusions suggest a coeval crystallization with the late-stage HP omphacite crystals. Ti content is high (up-to one order of magnitude richer than M2 matrix garnet), similar to clast garnets, as well as Cr that is up-to two order of magnitude richer than in mylonitic clast garnets but lower than in M2 garnets (Table 8; Figure 62c-d).

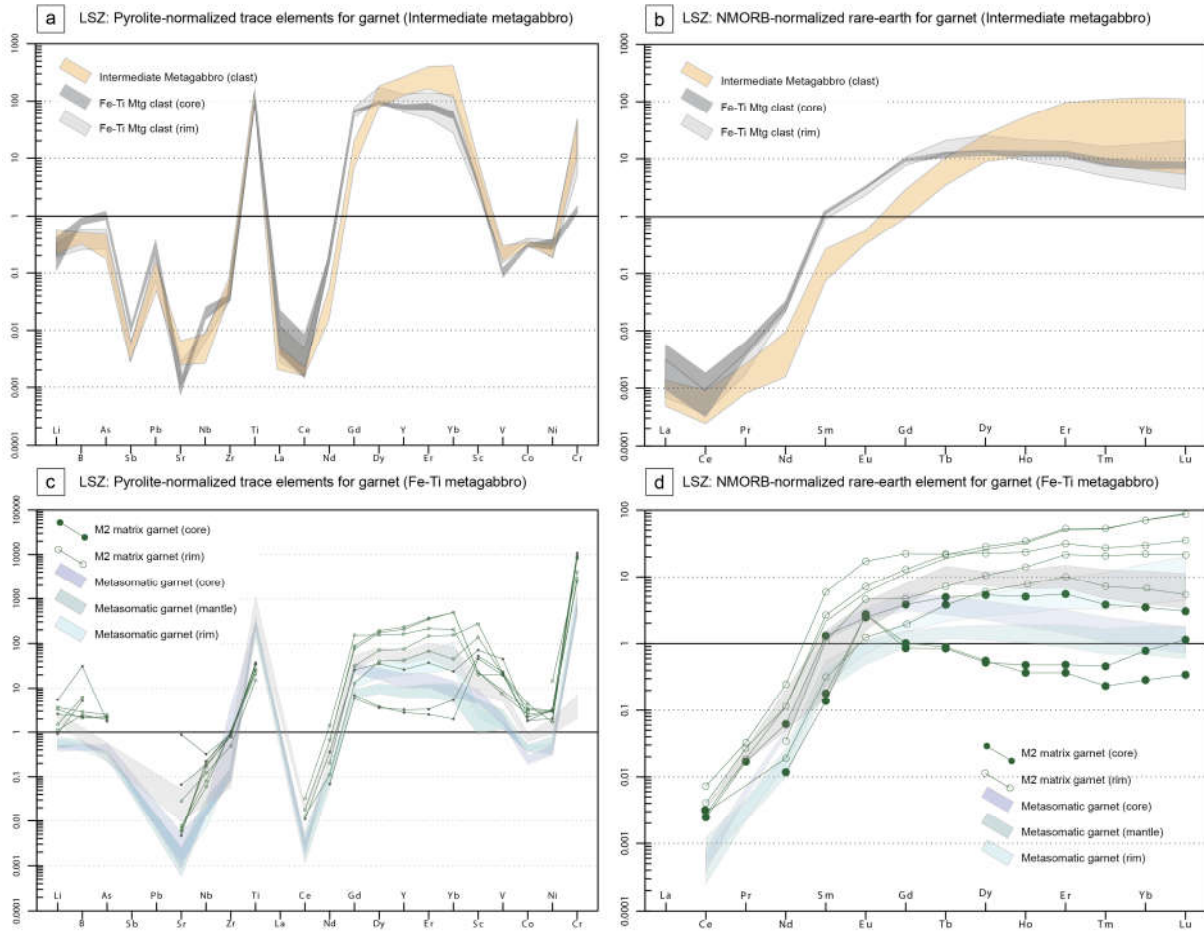


Figure 62: LSZ: garnet crystals from sample LSZ 53-15, hosting both Intermediate metagabbro and Fe-Ti metagabbros clasts; a) trace element variation diagrams (data normalized to pyrolite values from McDonough & Sun; 1995). b) Rare earth elements variation diagrams (normalized to NMORB values from Sun & McDonough; 1989).

LSZ: garnet crystals from the other samples, hosting only Fe-Ti metagabbro clasts; c) trace element variation diagrams (data normalized to pyrolite values from McDonough & Sun; 1995). d) Rare earth elements variation diagrams (normalized to NMORB values from Sun & McDonough; 1989).

Table 8 (a): representative major (Wt%) and trace element ($\mu\text{g/g}$) analysis of garnet from LSZ

Sample	LSZ 6315d	LSZ 6315d	LSZ 6315b	LSZ 6315b	LSZ 6315d	LSZ 6315d	LSZ 6315b	LSZ 6315b	LSZ 6315b	LSZ 5315	LSZ 5315
Petrology	Fe-Ti Mtg Clast	Fe-Ti Mtg Clast	Fe-Ti Mtg Clast	Fe-Ti Mtg Clast	M2 matrix	M2 matrix	Metasom	Metasom	Metasom	Intermediate Mtg Clast	Intermediate Mtg Clast
<i>Major element analysis (Wt%)</i>											
<i>SiO₂</i>	37.68	38.14	38.75	38.30	37.25	37.25	38.49	40.71	39.01	38.52	39.15
<i>TiO₂</i>	0.10	0.03	0.03	0.03	0.01	0.01	0.08	0.06	0.03	0.03	0.02
<i>Al₂O₃</i>	20.99	21.42	22.05	21.17	19.88	19.88	21.54	20.76	22.21	21.86	21.99
<i>Cr₂O₃</i>	0.00	0.01	0.01	0.00	0.39	0.39	0.40	0.05	0.22	0.01	0.00
<i>FeO</i>	29.16	28.57	28.02	27.44	32.82	32.82	27.99	25.66	25.35	30.42	31.20
<i>MnO</i>	0.48	0.82	0.89	1.25	0.15	0.15	0.30	0.83	0.93	0.56	0.35
<i>MgO</i>	2.52	5.17	5.89	4.05	3.60	3.60	5.22	6.36	7.19	3.70	4.06
<i>CaO</i>	9.41	5.64	5.97	7.63	5.82	5.82	7.38	6.61	6.67	6.56	6.22
<i>Na₂O</i>	0.00	0.02	0.04	0.05	0.02	0.02	0.00	0.09	0.02	0.07	0.05
<i>K₂O</i>	0.01	0.02	0.02	0.02	0.01	0.01	0.00	0.00	0.02	0.00	0.00
<i>NiO</i>	0.01	0.06	0.02	0.13	0.04	0.04	0.00	0.06	0.03	0.00	0.00
<i>P₂O₅</i>	0.03	0.05	0.01	0.05			0.03	0.00	0.03	0.00	0.00
<i>Total</i>	100.40	99.90	101.65	99.98	99.98	99.98	101.43	101.19	101.73	101.74	103.05
<i>MgO#</i>	7.96	15.33	17.36	12.86	9.88	9.88	15.71	19.87	22.10	10.83	11.52
<i>Trace element analysis ($\mu\text{g/g}$)</i>											
<i>Li</i>	2.80	4.37	0.95	0.46	8.71	1.47	0.72	0.81	0.74	0.60	0.24
<i>B</i>	<0.91	<1.30	<0.58	<0.46	9.28	1.54	0.14	<0.38	<0.37	0.15	0.09
<i>Na</i>	368.94	898.24	332.62	71.23	1064.54	122.98	60.89	69.78	94.13	527.96	394.95
<i>P</i>	25.22	31.88	13.36	9.49	4.25	4.05	19.38	31.61	33.71	10.12	13.27
<i>K</i>	38.16	<16.82	<8.61	14.92	451.27	77.75	11.62	<5.69	<5.63	26.11	24.99
<i>Sc</i>	118.67	302.02	86.64	79.52	851.46	740.69	153.66	42.03	56.60	99.31	102.36
<i>Ti</i>	1284.43	387.35	156.26	550.65	45.16	41.66	299.65	253.38	402.54	164.87	147.99
<i>V</i>	782.65	406.62	111.60	133.90	1899.78	1606.64	196.01	163.37	94.30	18.05	16.20
<i>Cr</i>	6.86	14.85	12.26	<2.33	28534.13	21456.76	2769.21	1418.32	1363.14	54.30	32.28
<i>Mn</i>	11133.12	14646.99	4344.91	3048.01	5000.98	5165.81	2609.04	3255.30	6084.76	4371.47	2689.77
<i>Co</i>	64.42	93.55	35.47	24.59	188.27	193.17	24.66	45.40	43.08	29.95	34.74
<i>Ni</i>	1.98	3.63	<0.78	1.95	6.34	3.94	0.95	0.96	1.13	0.38	0.34
<i>As</i>	<0.08	<0.12	<0.08	<0.05	0.09	<0.09	0.02	<0.05	<0.05	0.01	0.01
<i>Rb</i>	0.04	<0.05	<0.03	0.04	12.38	0.49	0.01	<0.03	0.03	0.39	0.17
<i>Sr</i>	0.40	1.03	0.10	0.04	17.50	1.32	0.02	0.01	0.04	0.22	0.07
<i>Y</i>	185.72	149.29	43.56	114.58	13.78	11.95	56.41	46.95	140.46	1456.57	1075.06
<i>Zr</i>	1.25	0.59	0.26	0.49	9.28	8.35	0.94	1.05	1.36	0.61	0.61
<i>Nb</i>	<0.01	<0.01	<0.01	0.04	0.22	0.13	0.01	<0.01	<0.01	0.00	0.00
<i>Sb</i>	<0.12	<0.17	<0.10	<0.08	<0.13	<0.13	0.03	<0.07	<0.07	0.01	0.02
<i>Cs</i>	<0.02	<0.03	<0.02	<0.01	2.19	0.10	<0.01	<0.01	<0.01	0.00	0.01
<i>Ba</i>	<0.14	<0.19	<0.13	<0.16	2.27	0.18	<0.02	<0.07	<0.07	0.02	0.03
<i>La</i>	0.01	<0.01	<0.01	<0.01	0.03	<0.02	0.00	<0.01	<0.01	0.00	0.00
<i>Ce</i>	0.03	<0.02	0.02	0.02	<0.02	<0.02	0.01	0.01	<0.01	0.00	0.00
<i>Pr</i>	<0.01	0.02	<0.01	<0.01	<0.01	<0.01	0.01	<0.01	<0.01	0.00	0.00
<i>Nd</i>	<0.09	0.57	0.14	0.03	0.09	<0.08	0.35	0.10	0.11	0.04	0.04
<i>Sm</i>	1.62	4.10	1.19	0.28	0.36	0.47	3.35	1.07	0.67	0.34	0.59
<i>Eu</i>	2.29	4.29	1.00	0.56	2.78	2.73	2.51	0.78	0.71	0.35	0.55
<i>Gd</i>	28.93	25.15	6.02	5.03	3.14	3.74	12.58	5.04	5.60	5.90	9.08
<i>Tb</i>	9.61	5.20	1.27	1.81	0.57	0.60	2.06	1.15	1.80	5.26	6.97
<i>Dy</i>	54.28	33.10	7.82	17.94	2.39	2.54	12.46	8.50	18.45	114.96	120.97
<i>Ho</i>	8.91	6.58	1.61	4.36	0.49	0.37	2.43	1.91	5.14	54.48	40.21
<i>Er</i>	20.32	20.08	4.72	13.59	1.44	1.10	6.80	5.47	20.98	285.51	139.64
<i>Tm</i>	2.15	2.93	0.64	1.78	0.21	0.11	0.85	0.75	3.72	50.07	16.79
<i>Yb</i>	11.82	18.39	4.14	11.30	2.39	0.88	5.58	5.50	32.19	357.68	91.36
<i>Lu</i>	1.51	2.80	0.56	1.62	0.52	0.16	0.81	0.82	6.10	50.76	10.99
<i>Hf</i>	0.03	0.02	<0.04	0.01	0.11	0.10	0.01	<0.03	<0.03	0.01	0.01
<i>Ta</i>	<0.02	<0.02	<0.01	<0.01	<0.02	<0.01	<0.00	<0.00	<0.00	0.00	0.00
<i>Pb</i>	<0.09	<0.13	<0.08	<0.06	<0.07	<0.07	<0.01	<0.05	<0.05	0.01	0.01
<i>Bi</i>	<0.02	<0.02	<0.02	<0.01	<0.03	<0.03	0.04	<0.01	<0.01	0.00	0.00
<i>Th</i>	<0.02	<0.03	<0.02	<0.02	<0.03	<0.02	<0.00	<0.01	<0.01	0.00	0.00
<i>U</i>	<0.02	<0.03	<0.02	<0.00	<0.01	<0.01	0.00	<0.00	<0.00	0.00	0.00

Table 8 (b): representative major (Wt%) and trace element ($\mu\text{g/g}$) analysis of garnet from ISZ

Sample	ISZ 3615	ISZ 3615	ISZ 3815	ISZ 3815	ISZ 3615	ISZ 3615	ISZ 3815	ISZ 3815
Petrology	Fe-Ti Mtg Clast	Fe-Ti Mtg Clast	Fe-Ti Mtg Clast	Fe-Ti Mtg Clast	M2 matrix	M2 matrix	Vein T2	Vein T2
Major element analysis (Wt%)								
SiO ₂	36.00	36.38	39.27	38.87	37.47	38.09	39.38	39.91
TiO ₂	0.03	0.08	0.06	0.04	0.09	0.04	0.04	0.04
Al ₂ O ₃	20.95	20.25	20.61	20.84	20.95	21.28	21.11	20.55
Cr ₂ O ₃	0.00	0.01	0.00	0.00	0.22	0.11	0.60	0.79
FeO	31.76	29.91	30.64	30.62	28.70	27.52	29.02	29.41
MnO	1.00	0.75	0.76	0.73	0.26	0.21	0.15	0.17
MgO	4.30	1.64	3.59	3.48	5.71	6.70	5.32	4.20
CaO	3.54	8.51	5.05	5.39	5.48	5.13	4.96	5.69
Na ₂ O	0.02	0.04	0.02	0.02	0.01	0.03	0.01	0.01
K ₂ O	0.01	0.01	0.00	0.01	0.00	0.02	0.00	0.00
NiO	0.00	0.04	0.00	0.00	0.04	0.04	0.00	0.00
P ₂ O ₅	0.03	0.01	0.00	0.00	0.01	0.01	0.01	0.00
Total	97.57	97.53	100.00	100.00	98.93	99.18	100.59	100.79
MgO#	11.92	5.20	10.48	10.20	16.59	19.58	15.49	12.50
Trace element analysis ($\mu\text{g/g}$)								
Li	0.39	0.45	0.56	0.62	0.89	1.18	0.26	0.30
B	<0.18	<0.14	<0.10	<0.13	0.53	0.77	0.06	0.06
Na	173.82	224.70	165.16	158.66	98.95	143.81	94.63	110.04
P	19.44	8.32	14.16	12.35	1.81	5.58	36.26	16.85
K	29.10	32.26	35.15	43.12	0.83	1.26	20.27	25.34
Sc	66.44	96.19	68.04	62.20	886.90	179.20	104.62	272.48
Ti	128.32	249.98	332.89	242.95	19.86	24.23	229.29	247.93
V	37.01	70.65	146.19	140.15	1477.93	1756.49	393.10	374.03
Cr	6.39	5.78	4.59	4.29	3997.34	8141.77	4073.03	5399.44
Mn	5303.07	4154.25	5891.66	5670.45	3721.40	1958.24	1143.90	1346.92
Co	17.61	12.09	18.80	17.94	166.17	192.76	27.82	23.32
Ni	0.77	0.61	0.70	0.71	4.02	4.78	1.05	1.59
As	<0.03	<0.02	<0.02	<0.02	0.07	0.07	0.02	<0.01
Rb	0.03	0.02	0.02	0.02	0.10	0.06	0.01	0.01
Sr	0.04	0.04	0.04	0.04	0.07	0.20	0.01	0.02
Y	145.19	146.71	196.21	171.19	526.51	72.93	11.25	17.42
Zr	0.20	4.09	5.49	0.29	6.98	13.04	1.21	0.69
Nb	<0.01	0.01	0.02	<0.01	0.02	0.11	0.02	0.02
Sb	<0.04	<0.03	0.03	<0.02	0.06	0.10	0.02	<0.01
Cs	<0.01	<0.01	<0.01	<0.01	<0.01	<0.01	<0.01	<0.01
Ba	<0.06	<0.04	<0.04	<0.06	0.03	0.04	<0.01	<0.02
La	<0.01	0.00	0.00	0.01	<0.01	<0.01	<0.01	<0.01
Ce	0.01	0.01	0.02	0.03	0.02	0.05	0.00	0.00
Pr	<0.01	0.01	0.01	0.01	0.06	0.06	0.01	0.01
Nd	0.23	0.13	0.22	0.27	2.21	1.88	0.30	0.22
Sm	1.67	1.37	2.16	2.56	15.79	10.32	1.83	2.04
Eu	1.80	1.77	2.39	2.90	9.70	5.95	0.97	1.56
Gd	12.04	15.51	19.86	23.43	64.69	24.84	4.97	5.40
Tb	2.82	4.62	5.23	5.81	15.40	3.47	0.69	0.74
Dy	22.20	31.36	37.73	36.83	109.06	17.19	3.38	4.21
Ho	4.93	5.39	7.43	6.37	21.93	3.12	0.52	0.75
Er	14.06	12.62	21.12	17.11	67.71	10.12	1.29	1.85
Tm	1.85	1.43	2.63	2.08	7.00	1.02	0.16	0.22
Yb	12.47	8.05	16.71	13.60	41.05	6.08	1.00	1.25
Lu	1.84	1.12	2.31	1.90	5.05	0.83	0.14	0.17
Hf	<0.02	0.13	0.13	<0.01	0.08	0.15	0.02	0.00
Ta	<0.01	<0.01	<0.01	<0.01	<0.01	<0.01	0.00	<0.01
Pb	<0.03	<0.02	<0.02	<0.03	<0.03	<0.02	0.01	<0.01
Bi	<0.01	<0.01	0.01	<0.01	0.01	0.04	0.00	<0.01
Th	<0.01	<0.01	0.00	<0.01	<0.01	0.01	<0.01	0.00
U	<0.01	<0.01	<0.01	<0.01	<0.01	0.01	<0.01	0.00

Lawsonite pseudomorphs

The lawsonite pseudomorphs embedded in the mylonitic foliation of clasts poorly partitioned **Cr**, **Ni** and **Co** (*Table 9; Figure 63a-b*). Elements that classically strongly partition into lawsonite, such as **REE**, show a general enrichment of **LREE** and **MREE** respect to the **HREE** (*Figure 63b*). Fluid mobile elements such as **Li**, **B**, **As** are generally enriched (*Table 9; Figure 63a*), except for **Sb** that shows a strong negative anomaly. **Pb** and **Sr** are enriched (*Table 9; Figure 63a*), in agreement to their preferential partitioning in lawsonite (Spandler et Al., 2003; Martin et Al., 2013; Spandler & Pirard, 2013).

In M3 matrix, the lawsonite pseudomorphs have distinct zonations which correspond to three different geochemical signature. M3 lawsonite patterns are close to those of clast lawsonite, except for **Cr** and **Ni** contents that are enriched up-to 2 orders of magnitude, and **Li**, **B**, **Pb** (+/- **Sr**) that are also enriched (sample LSZ 14-11c; *Table 9; Figure 63a*). **REE** present linear patterns very different from those of clast lawsonite, with lower **LREE** and **MREE** contents (*Figure 63a-b*). **REE** content in the rims is lower (1 order of magnitude) than in cores and mantles, but present **Eu** positive anomaly (*Table 9; Figure 63b*), possibly linked to recrystallization of plagioclase after lawsonite. **Titanium** concentrations show a large range of values, with a broad decrease from cores to rims (*Table 9; Figure 63a*).

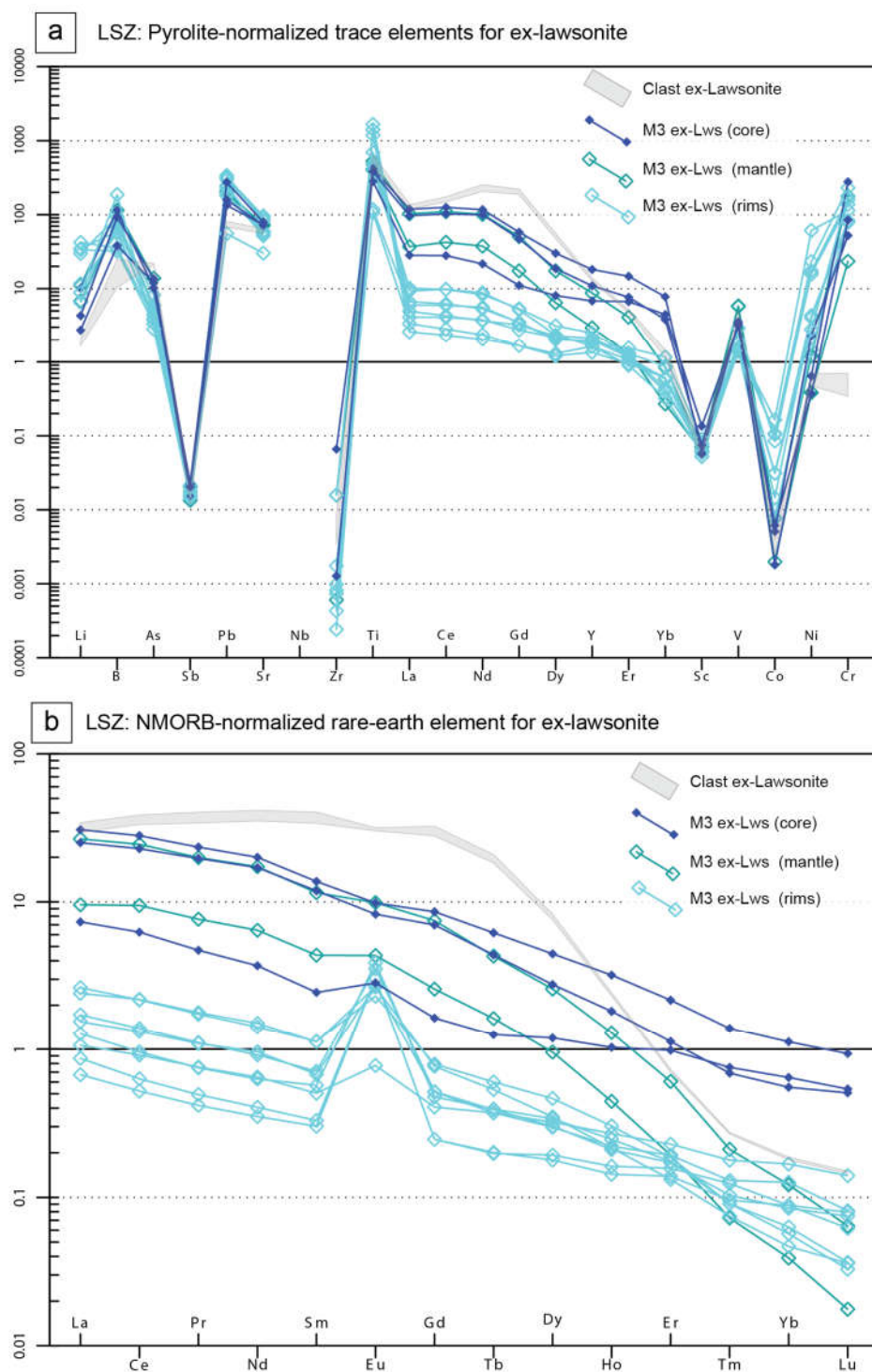


Figure 63: a) LSZ: ex-lawsonite crystals from mylonitic clasts (sample LSZ 14-11) compared to ex-lawsonite crystals from M3 matrix (sample LSZ 14-10). a) Trace element variation diagrams (data normalized to pyrolite values from McDonough & Sun; 1995). b) Rare earth elements variation diagrams (normalized to NMORB values from Sun & McDonough; 1989).

Table 9: representative major (Wt%) and trace element ($\mu\text{g/g}$) analysis of ex-lawsonite in host-rock and M3

Sample	LSZ 1410	LSZ 1411c	LSZ 1410	LSZ 1410	LSZ 1410	LSZ 1410	LSZ 1411c	LSZ 1411c
Petrology	M3 matrix (core)	M3 matrix (core)	M3 matrix (mantle)	M3 matrix (mantle)	M3 matrix (rim)	M3 matrix (rim)	Mg-Al Mtg clast	M3 matrix (core)
Major element analysis (Wt%)								
SiO ₂	36.62	37.63	35.71	36.61	36.86	35.36	36.94	37.83
TiO ₂	0.06	0.09	0.08	0.11	0.10	0.14	0.12	0.08
Al ₂ O ₃	29.06	29.45	27.44	28.92	28.82	27.11	29.80	29.21
Cr ₂ O ₃	0.11	0.00	0.01	0.07	0.06	0.04	0.00	0.03
FeO	0.82	1.89	1.16	1.31	2.07	2.75	1.75	1.74
MnO	0.01	0.08	0.02	0.03	0.03	0.04	0.06	0.05
MgO	0.15	0.13	0.19	0.50	4.30	7.38	0.32	0.35
CaO	20.39	19.09	22.29	19.21	15.22	15.83	19.37	16.49
Na ₂ O	1.15	0.53	1.37	1.10	0.87	0.22	0.24	1.04
K ₂ O	0.73	0.12	0.74	1.20	0.74	0.18	0.39	2.23
NiO	0.00	0.00	0.00	0.00	0.00	0.02	0.00	0.00
P ₂ O ₅	0.01	0.00	0.00	0.01	0.01	0.00	0.00	0.00
Total	89.11	89.00	89.01	89.07	89.06	89.06	89.00	89.03
Trace element analysis ($\mu\text{g/g}$)								
Li	16.14	2.69	10.89	17.80	47.78	67.61	3.33	6.89
B	34.49	3.14	22.78	34.48	27.91	10.62	7.47	27.89
P	33.06		11.80	40.95	33.42	17.15		
Sc	2.19	0.79	1.01	1.14	0.96	1.01	1.15	1.22
V	257.56	331.31	471.12	478.66	239.43	127.03	404.60	275.67
Cr	728.99	0.90	61.65	467.20	417.38	299.61	1.82	221.62
Co	0.19	0.27	0.21	0.80	8.91	17.28	0.36	0.65
Ni	1.26	0.98	0.75	2.36	33.99	119.71	1.35	0.73
As	0.51	1.09	0.30	0.69	0.25	0.20	1.06	0.68
Rb	9.92	1.59	13.06	17.24	10.69	2.92	5.06	21.49
Sr	1574.13	1185.81	1454.04	1427.78	1033.17	1103.76	1289.27	1436.90
Y	29.30	55.26	12.66	37.56	7.03	8.52	54.53	46.88
Zr	<0.01	0.08	0.17	0.01	0.01	0.01	0.04	0.69
Nb	0.00	0.02	0.00	0.00	<0.01	<0.01	0.04	0.02
Sb	0.13	0.07	0.07	0.11	0.08	0.09	0.10	0.11
Cs	0.11	0.01	0.11	0.11	0.23	0.32	0.03	0.11
Ba	41.10	2.15	24.72	59.93	54.30	15.40	3.02	31.93
La	18.32	85.67	23.93	66.62	6.03	4.30	73.38	62.81
Ce	46.88	289.32	71.01	183.82	16.44	10.43	250.37	171.62
Pr	6.22	53.00	10.09	26.30	2.36	1.46	45.11	25.96
Nd	27.03	302.63	46.99	126.23	11.01	6.67	257.66	124.53
Sm	6.43	106.17	11.48	30.39	2.95	1.86	89.46	31.27
Eu	2.89	30.89	4.43	10.08	2.72	3.61	31.66	8.43
Gd	6.02	119.34	9.47	27.50	2.82	1.90	102.97	25.73
Tb	0.84	13.97	1.09	2.88	0.36	0.26	12.31	2.94
Dy	5.43	37.58	4.35	11.73	1.59	1.38	34.59	12.58
Ho	1.04	2.36	0.45	1.31	0.22	0.21	2.34	1.84
Er	2.92	2.08	0.57	1.80	0.39	0.51	2.10	3.35
Tm	0.34	0.12	0.03	0.10	0.03	0.05	0.12	0.31
Yb	1.96	0.54	0.12	0.37	0.14	0.26	0.55	1.69
Lu	0.24	0.07	0.01	0.03	0.02	0.03	0.06	0.23
Hf	<0.01	<0.01	0.00	<0.01	<0.01	0.00	<0.01	0.02
Ta	<0.01	0.00	<0.01	<0.01	0.00	0.00	0.00	0.00
Pb	41.03	10.46	28.77	30.84	29.26	36.99	10.99	23.75
Bi	0.40	0.09	0.41	0.64	0.48	0.51	0.07	0.44
Th	0.01	0.02	0.02	0.32	0.02	0.04	0.04	0.92
U	0.01	0.06	0.05	1.61	0.10	0.25	0.09	0.25

5.7.2 Intermediate Shear Zone

Omphacite

In the ISZ, clast omphacites show trace element patterns similar to those of LZS clasts. Three types of veins were recognized with peculiar petrographic and geochemical signature. Omphacite from *Veins-T0* (developed subparallel to the eclogitic foliation, with paragenesis: Omp + Apt; *Figure 55e*), has the same trace element composition as mylonitic clast (*Figure 64a-d*), like Veins1 in the LSZ. The omphacite from *Veins-T1* (crosscutting at high angle the mylonitic foliations of clasts, *Figure 55e*) shows core-to-rim geochemical zonation; the composition of the cores is totally comparable to the mylonitic clast omphacite (*Table 7* and *Figure 64c-d*) with only slight enrichment in *Ni* and *Li* (*Figure 64c*) and depletion in *Co*. The rims, instead, show enrichments in *Sc*, *V* and *Cr* (*Table 7* and *Figure 64c-d*); *REE* concentrations of both cores and rims show enrichments, in particular in HREE (*Figure 64d*), with *Veins-T1* rims composition quite comparable to the LSZ M1-matrix patterns. Omphacite crystals from the garnet-bearing *Veins-T2* (crosscutting at various angles all the pre-existing structures; *Figure 55e*) are enriched in *Ni* and *Cr* but depleted in *Ti* compared to both *Veins-T0/Veins-T1* and mylonitic clasts (*Table 7* and *Figure 64c-d*). *REE* patterns are similar to *Vein1* rim patterns (*Table 7* and *Figure 64d*).

The omphacite crystals from the matrix M2 do not show any detectable core-rim trace element zonation; the trends are in general comparable to mylonitic clast omphacite patterns, but with higher concentrations, in particular *Sc*, *V*, *Cr* and *Ni* (similar to those of ISZ *Veins-T2* and M2-

matrix from LSZ), with strong depletion in **Ti** (similar to M2-matrix from the LSZ; Table 7 and Figure 59a vs Figure 64c).

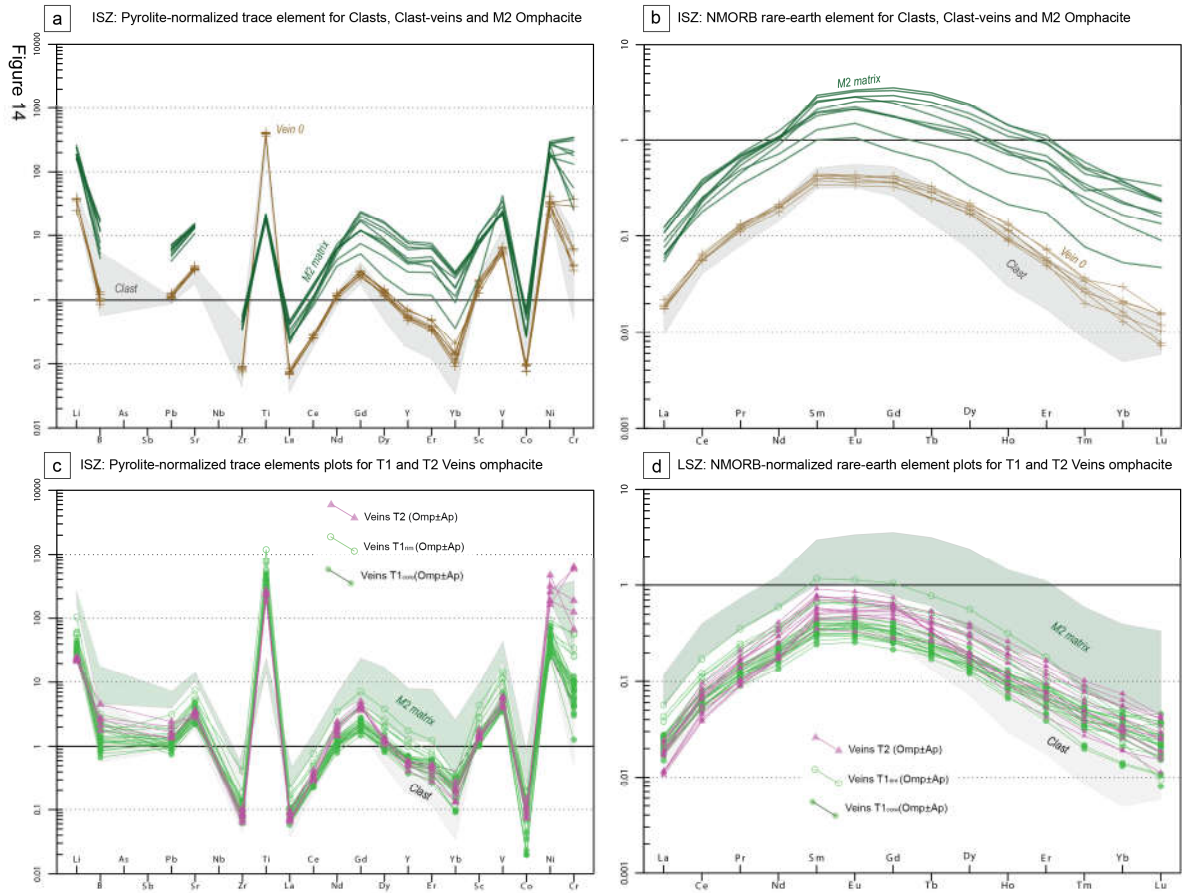


Figure 64, ISZ: omphacite crystals from clasts VeinsT0 and matrices; a) trace element variation diagrams (data normalized to pyrolite values from McDonough & Sun; 1995). b) Rare earth elements variation diagrams (normalized to NMORB values from Sun & McDonough; 1989). The choice to plot VeinsT0 in this graph is due to ISZ: omphacite crystals from VeinsT1 (Omp+Ap) and VeinsT2 (Omp+Grt); c) trace element variation diagrams (data normalized to pyrolite values from McDonough & Sun; 1995). d) Rare earth elements variation diagrams (normalized to NMORB values from Sun & McDonough; 1989).

Garnet

In the ISZ, garnets crystallize only in mylonitic clasts (usually as atoll-garnet with diameters <50 μm), Veins-T2 and matrix M2 (Figure 55f). The geochemical signature of Veins-T2 garnet is comparable to of the the mylonitic clast garnets, but shows a marked enrichment in **Cr** (more than 3 orders of

magnitude; Table 8 and Figure 65a), and lower concentration in **HREE**. The latter have a **LREE/HREE** ratio that strongly varies between the analysed blocks, with marked **HREE** depletion in sample ISZ 35-15, which also shows a peculiar **V** and (in lesser extent) **B** positive anomaly if compared to other samples (Table 8 and Figure 65a). In matrix M2, both rims and cores show enrichments in most elements compared to Veins-T2 and mylonitic clasts (Table 8 and Figure 65a-b), with preferential enrichments in **Cr**, **Ni**, **Co**, **Li**, **B** and **As**; on the contrary, **Ti** is strongly depleted (more than one order of magnitude). This geochemical signature is comparable to that M2-matrix garnets from LSZ (Table 8; Figure 62). With respect to mylonitic clasts, **HREE** are slightly enriched in M2-matrix garnet cores, while concentration in rims are totally comparable (Table 8; Figure 63b). Interestingly, the **V** concentration of both cores and rims are similar, with one-order of magnitude enrichment with respect to Veins-T2 and mylonitic clasts (Table 8; Figure 63a).

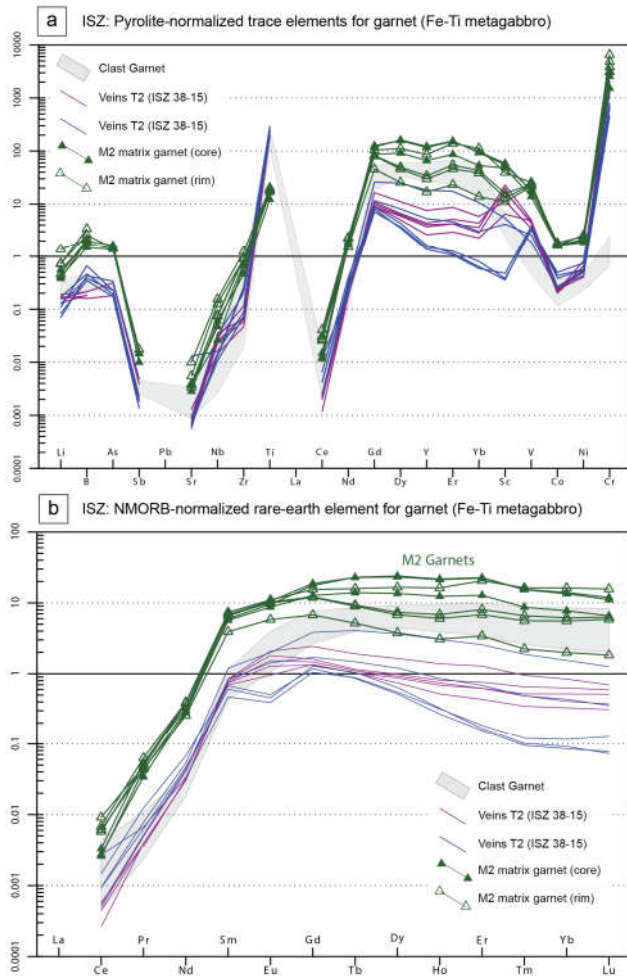


Figure 65; ISZ: garnet crystals compositions from mylonitic clasts, VeinsT2 and M2-matrix. a) Trace element variation diagrams (data normalized to pyrolite values from McDonough & Sun; 1995). b) Rare earth elements variation diagrams (normalized to NMORB values from Sun & McDonough; 1989).

5.8 Discussion

The trace element redistribution between host-rock, vein and matrix minerals is mainly influenced by three parameters: (1) the major element composition of minerals, influencing the trace-element affinity for each mineral phase; (2) the composition of the fluid phases involved in metamorphic reactions and (3) the mineral/fluid partitioning coefficient.

In our dataset, although some element enrichments seem to correlate with Cr contents in both omphacite and garnet, enrichment patterns are complex and often far from linear, suggesting that trace elemental distribution in minerals cannot be solely controlled by the chemical effects induced by high Cr contents. In the following, we will combine the different element signals for each vein and matrix in order to decipher the source (i.e., local versus external) of fluid that potentially accompanied both veining and brecciation.

5.8.1 Formation of Veins 1 and Matrix M1: evidences for closed-system fluid circulation

The first vein generation, enclosed in clasts and predating brecciation, i.e., crosscut by M1 matrix (i.e., Veins 1 in LSZ and Veins T0 and T1 in ISZ) are usually little deformed and consist largely of omphacite (with subordinate apatite, *Figure 55b*). Opening geometries suggest that they developed **as syn-deformation, syntaxial crack-seal fractures** (*Figures 54c and 55b*). The omphacites crystallizing in these veins have major element compositions similar to those of omphacite rims from the adjacent host-rock and mylonitic clasts (Omp1b, *Figure 57a*), which present the highest jadeitic content of all omphacite generations, suggesting that they formed at eclogite-facies PT conditions (for more details see chapter 4 and refer to Angiboust et Al., 2012a). Even if trace-element characteristics may slightly vary between different vein/host-rock pairs, trace element patterns for vein omphacite are very similar to those of clast omphacite rims. Only

slight Li and Ni enrichment and REE enrichment or depletion were observed for LSZ *Veins1* and ISZ *Veins-T1* cores (e.g., *Figure 60a-d*). **These observations support the hypothesis of chemical equilibrium between the omphacite in the first vein sets and host-rocks, at least at the centimetre scale, which suggests that Veins1 formation was assisted by fluids locally derived, i.e., from the adjacent Fe-Ti metagabbros, likely by dissolution-precipitation processes.** Our conclusions for the first vein set (LSZ *Veins1* and ISZ *VeinT0* and *T1* cores) are in agreement with the previous works that investigated the formation processes of HP veins hosted in the eclogitic metagabbros from the ISZ. In their works, Philippot & Selverstone (1991), Philippot & van Roermund (1992) and Nadeau et al. (1993), suggested that these veins formed in presence of locally-derived fluids, with no evidence of external fluid involvement during the vein formation. The growth of minerals by a combination of repetitive crack-sealing cycles and diffusional mass transfer in immobile fluid is analogue to the processes proposed by Philippot & Selverstone (1991), Philippot & van Roermund, (1992) and Spandler et al. (2011) for the fibrous omphacite-bearing veins in the ISZ (or “Type1”, *sensu* Spandler; *Veins-T1* in this work).

The trace element concentration of M1-matrix bulk is very close to that of Fe-Ti and intermediate metagabbros, with concentrations in between both for most elements. However, direct comparison is biased by the monomineralic content of M1-matrix compared to host-rocks: omphacite generally hosts only small amounts of trace elements compared to other host-rock forming minerals such as garnet and lawsonite, richer in REE among others (Spandler et al., 2003). The main signal is that M1 bulk composition does not show any specific enrichment compared to surrounding clasts, except for *Ni* and *Cr*. This signal is confirmed by both crushed and M1 matrix omphacite analyses (Omp2a and 2b; *Figure 57a*), which are similar to clast omphacite patterns except for *Cr* and *Ni* (and to a lesser extent *Pb*, *Sr* and *REE*) enrichments (*Table 7*; *Figures 59a-b*

and 60a-d). Such specific enrichments are likely explained by fluid infiltration from the Mg-Al or Intermediate metagabbros (which show suitable Cr, Ni and Pb content; Table 6 and Figure 60a-d) systematically surrounding the breccia layers. Nevertheless, the positive correlation between Li and Al₂O₃ contents in omphacite shows a common trend between grains from mylonitic clasts, Veins1 and M1-matrix (Figure 60e). The same pattern is observed also in the broad correlation between Sm and (CaO+MgO) or Sr and (CaO+MgO), as well as B-Cr and Sc-Cr (Figure 60f-g): all these evidences indicate a crystallization in a system with common geochemical characteristics.

ISZ breccias do not show any M1 matrix. However, *VeinsT1* omphacite rims show trace element patterns comparable to those of LSZ M1 matrix, i.e., enrichments in Cr only compared to clast omphacites. Thus we suggest that:

- (I) The first vein set (LSZ: *Vein1*; ISZ: *VeinT0*) formed in the presence of locally-derived fluids (**mm- to cm-scale mass-transfer in Fe-Ti metagabbros**).
- (II) The LSZ *Crushed-* and *M1-matrix* (recovered only in the rims of breccia planes where incipient brecciation was not overprinted by later-stage M2 or M3 matrix) **formed by the interplay between fluids locally-derived (like Vein1) and proximal Mg-Al/Intermediate metagabbros (dm- to m-scale mass transfer)**. Thus, still local mass transfer in closed system at the meter-scale. The same can be said for ISZ *VeinsT1* omphacite rims.

5.8.2 Matrices M2, M3 and late-stage veins: evidences for dm- to km-scale external fluid infiltration

M2 matrix

The M2 matrix is composed of omphacite, garnet, and accessory talc. M2 matrix is characterized by a general enrichment in most trace elements in both omphacite and garnet compared to Fe-Ti clast minerals, and a drop in Ti amount in both minerals, in both LSZ and ISZ. Main enrichments concern Cr, Ni, V and Co, plus B and As (these latter mostly in garnet; Figures

59 and 62). Contrary to omphacite from clasts, Veins1 and M1-matrix, M2 omphacite lacks any correlation between trace elements and omphacite major components (e.g., spodumene and diopside; *Figure 60e*), and rather presents abrupt enrichments for Li, B, Sc, Zr, Hf and Pb. Both this lack of correlation and the strong enrichments in trace elements likely attest a change in the geochemistry (and thus source) of fluids present during brecciation.

The strongest enrichment concerns Cr (1-3 orders of magnitude in both omphacite and garnet), which can reach 2-4 wt%. Furthermore, EPMA major-element mapping and elemental cross-sections on garnet and omphacite from M2-matrix point out complex Cr zoning, with both sectorial enrichments and oscillatory Cr contents that have no equivalents in the enclosing host eclogite, mylonitic metagabbro clasts and M1 matrix (e.g., *Figures 58c, 58f and 58g*). In ultramafic geological settings, Cr-rich omphacite is frequently interpreted to be the product of static replacement of Cr-rich spinel (e.g. Ikehata & Arai, 2004; Tsujimori & Liou, 2004). Furthermore, Martin (2009) proposed that in semi-pelitic schist, highly localized sourcing of components from precursor mineral phases in the rock matrix would lead to the growth of garnet crystals. However, such local and static replacement of Cr-rich minerals is unlikely for M2-matrix minerals, for both compositional and textural considerations. Indeed, clast relicts are rare, and most M2-matrix minerals are newly-formed, as M2-matrix is associated to brecciation event and lacks any deformation. Moreover, even considering clast relicts in M2-matrix, Fe-Ti metagabbros are Cr-poor, and even magnetite, which was probably part of the original igneous paragenesis (see *Chapter 3*), likely had a low Cr-content (e.g., Natland et al., 1991; Arai, 1992). So **the presence of any Cr-rich precursor in this lithology is unlikely**. Moreover, Cr (and Ni, Co, B) contents in both omphacite and garnet from M2-matrix (*Tables 7 and 8*) are higher than mylonitic Mg-Al

metagabbros embedding the breccias (*Figures 59a-d, 60a-d, 62a-d, 64a-d and 65a-b*), suggesting that a Mg-Al metagabbro-derived fluid only would not explain these strong Cr enrichments.

In both omphacite and garnet, Cr enrichment can occur in any sector of the crystals, with no exception between grain cores or rims, and does not correlate with omphacite/garnet major-elements (*Figures 57a and 58e*), suggesting that M2-matrix minerals crystallization was accompanied by multiple pulses of Cr-bearing fluids. Both omphacite and garnet crystals show two distinct Cr-enrichment textures: fracture-like and oscillatory textures. The first-one, observed in samples ISZ 35-15, ISZ 38-15 and LSZ 63-15b, probably developed during multiple stages of crack-sealing of the grains during fluid circulation. Cr oscillatory zoning of garnet (and in lesser extent omphacite) in samples ISZ 35-15 and LSZ 63-15d likely formed by precipitation of solutes diffusing through fluid that was wetting grain boundaries (*Figure 58f*). This scenario (already suggested by Philippot & van Roermund, 1992 and Spandler et Al., 2011) requires relatively low external fluid fluxes, while crack-sealing would imply higher fluid pressure. Therefore, M2-matrix crystallization was accompanied by pulses of external Cr-rich fluid infiltration, suggesting an opening of the system compared to Veins I and M1 matrix event. Interestingly, veins postdating M1 but ante-M2 matrix (i.e., Veins 2-3 in LSZ and Veins T2 in ISZ) also show Cr and Ni enrichments, although lower than in M2. This suggests a progressive opening of the system to external fluid infiltration from M1 to veins to M2, similar to what proposed by Spandler et Al. (2011) for the Grt +Omp-bearing veins (or Type 2, *sensu* Spandler) from the ISZ.

M3 matrix

The trace element trends and concentrations for bulk composition of M3-matrix are considerably different with respect to those of neighbouring Mg-Al and Fe-Ti metagabbros. Indeed, M3 is clearly enriched in Cr, Ni, Co and B compared to Fe-Ti and Mg-Al metagabbros, and these elements reach values typical of serpentinites (*Table 6* and *Figure 56*). Moreover, the M3-matrix concentrations of HFSE and LILE are generally lower than in Fe-Ti metagabbros, with particular depletions in Sr, Nb and Ta (*Table 6* and *Figure 56*). These trace element signatures, coupled to the strong MgO enrichments, suggest the infiltration of an external fluid, potentially serpentinite-derived. Moreover, the large volume of M3 matrix (forming ~80% of the breccia volume) and its high amount of lawsonite (11.5 vol% of H₂O; Pawley, 1994) suggest infiltration of large volumes of fluid during M3-matrix formation. However, considering that M3 matrix formed at the beginning of the retrograde path (see *Chapter 4* for detailed P-T path based on omphacite and garnet compositions and refer also to Angiboust et Al., 2012a), the already dry surrounding metagabbros cannot be the source for such fluids (no more dehydration reaction post peak), which also calls for external fluid infiltration.

The M3-matrix texture also suggests massive external fluid infiltration. Indeed, the emplacement of M3 appears to be driven by hydraulic fracturing of pre-existing breccia, as demonstrated by the occurrence of numerous clasts composed by mylonitic metagabbro and M1+M2 matrices cemented by newly formed M3 (e.g., *Figure 54e*) and penetrative fracturing at the core of breccia layers. Moreover, the strong enrichment in Cr, Ni, B and Co result in complex, sectorial crystals zonations, suggesting long-lived crystallization via discrete pulses of externally-derived fluids, likely sustaining the opening of M3 breccia planes.

Late-stage veins

For the same reason, large volumes of fluid circulation is invoked to permit the formation of the late-stage, omphacite + talc \pm chlorite-bearing veins and metasomatic domains. These developed as randomly oriented fractures crosscutting all the pre-existing structures (e.g., *Figure 55a*). High fluid pressure is required to overcome the strength of the rock and long-lasting circulation to sustain the growth of the big, idiomorphic omphacite crystals which do not show any evidences for Cr oscillatory zoning (e.g., *Figure 58g*) at the opposite of grains in M2-matrix (e.g., *Figure 58f*). The presence of chlorite, talc and in lesser extent rutile and pyrope-rich garnet in the veins also indicates mobilization of Mg and HFSE (as previously noted by Philippot & Selverstone, 1991; Rubatto & Hermann, 2003 and Spandler et Al., 2011), characteristics not observed in the other matrices (e.g., *Figure 56a and 56c*).

Chapter 6:

Discussion

6.1 - Monviso metabreccia: evidence for brittle rupture at eclogite-facies conditions

6.1.2 Eclogitic or Pre-Alpine breccias?

The recognition of metabreccia ascribed to **eclogite-facies conditions** (Angiboust et Al., 2012a) and their hypothesized link to seismic activity (Angiboust et Al., 2012b) has resulted in considerable debate around the origin of these rocks and their link to the regional evolution of the Monviso metaophiolite complex (*Table 10*).

Authors and year	Main findings on veins/breccia formation and fluids circulation at eclogite-facies conditions	Target and results of this study
Philippot (1987)	* ISZ: recognition of HP veins. Peak P at ~40 km	* Mapping of blocks and analysis of their distribution in LSU shear zones.
Philippot & Selverstone (1990)	* ISZ veins feeded by local fluids (fluid inclusions)	* Analysis of breccia blocks and characterization of brecciation pattern.
Nadeau et al. (1992)	* ISZ veins feeded by local fluids (stable isotopes)	
Messiga et al. (1999)	* LSU veins: feeded by local fluids	* Confirm the eclogitic origin of brecciation (by microstructural and structural analysis).
Spandler et al. (2011)	* identification of two type of veins in the ISZ * geochemical analysis: one set of veins crystallize by serpentinite-derived fluids	* Identification of the locus of brecciation and origin of blocks in LSZ (Fe-Ti Mtg within and at the base of LSU). No transportation from ISZ.
Angiboust et al. (2012a)	* LSZ: recognition of eclogitic breccia blocks (by petrographic evidence) * Inferred blocks origin: Fe-Ti Mtg from ISZ * discrete pulses of fluids through LSZ (origin?)	* Recognition of various steps of veining and brecciation, leading to the channellization of fluids flux (from M2 event to metasomatic stage). * Investigation of fluid sources leading to brecciation and their potential migration pathways (bulk + in-situ trace element analysis).
Angiboust et al. (2012b)	* proposed seismic origin for eclogitic breccia	* Comparison between ISZ and LSZ eclogite-breccia and HP veins.
Angiboust et al. (2014)	* recognized antigorite dehydration as source of fluids metasomatizing blocks in the LSZ	* Structural, microstructural and (attempted) statistical analysis of eclogitic breccia layers to unveil the potential coseismic origin.

Table 10: on the left column, a brief resume of the main results achieved by precedent works investigating the Monviso metaophiolite complex. Major focus is given to the studies that investigate the fluid-rock interaction processes and the eclogitic breccias. On the right, the target of this PhD thesis.

Several authors challenged their “**eclogitic origin**”, ascribing them either to (I) sedimentary processes or (II) tectonic breccias inherited from a Tethyan Oceanic Core Complex (e.g., Balestro et al., 2014a-b and Festa et al., 2015). Structural, microstructural and petrographic evidence reported here (Chapter 4) nevertheless demonstrate that the studied breccia blocks disseminated in the Monviso Lower Shear Zone (LSZ) and Intermediate Shear Zone (ISZ) equilibrated at eclogite-facies conditions. This assertion is supported by the occurrence of mylonitic clasts and matrices both composed by the classical eclogite facies paragenesis *omphacite* + *garnet* ± *lawsonites* (+

rutile in the clasts), and textural observation ruling out that these breccias could represent former brecciated mylonites statically overprinted by eclogite facies minerals.

Major element mineral compositions presented in this work (*Chapter 4* and *5*) match those previously published on Monviso meta-ophiolite (*Figure 66*). The mylonitic omphacite generations (Omp1a cores and Omp1b rims; *Chapter 4*) fall in the same compositional field than mylonitic omphacite analysed by Groppo & Castelli (2011) and Angiboust et al. (2012a), with trends towards higher jadeitic content corresponding to the prograde eclogitic path of the Lago Superiore unit. The onset of a first, localized eclogitic brecciation (developing the crushed and M1 matrix) is associated to Omp2a crystallization in the LSZ and to Omp1b in the M1 matrix of ISZ (*Figure 66*), whose compositions are directly comparable to the peak omphacite of Angiboust et al. (2012a; $\text{Di}_{45}\text{Jd}_{43}\text{Ae}_{12}$) and Spandler et al. (2011; i.e., host-rock omphacite crystals, $\text{Di}_{43}\text{Jd}_{47}\text{Ae}_{10}$). Therefore the onset of the first eclogitic brecciation can be ascribed to the peak P-T conditions reached by the LSU (2.5 GPa, 550°C: Groppo & Castelli, 2011; 2.6 GPa, 550°C: Angiboust et al., 2012a).

Furthermore, structural and microstructural evidence allows to differentiate the eclogite-facies breccia blocks from the metasedimentary breccias found in the LSZ (the latter found as meter-scale lenses dispersed in metasedimentary slivers mainly composed by calcschists and marbles, metamorphosed under eclogite facies P-T conditions; *Figure 67*). In the **fully preserved eclogitic breccia planes** the classical, undisturbed rim-to-core sequence showing continuous transition from intact metagabbro to chaotic breccia (e.g., Sibson, 1986) is preserved, advocating for dynamic fracturing rather than sedimentary processes.

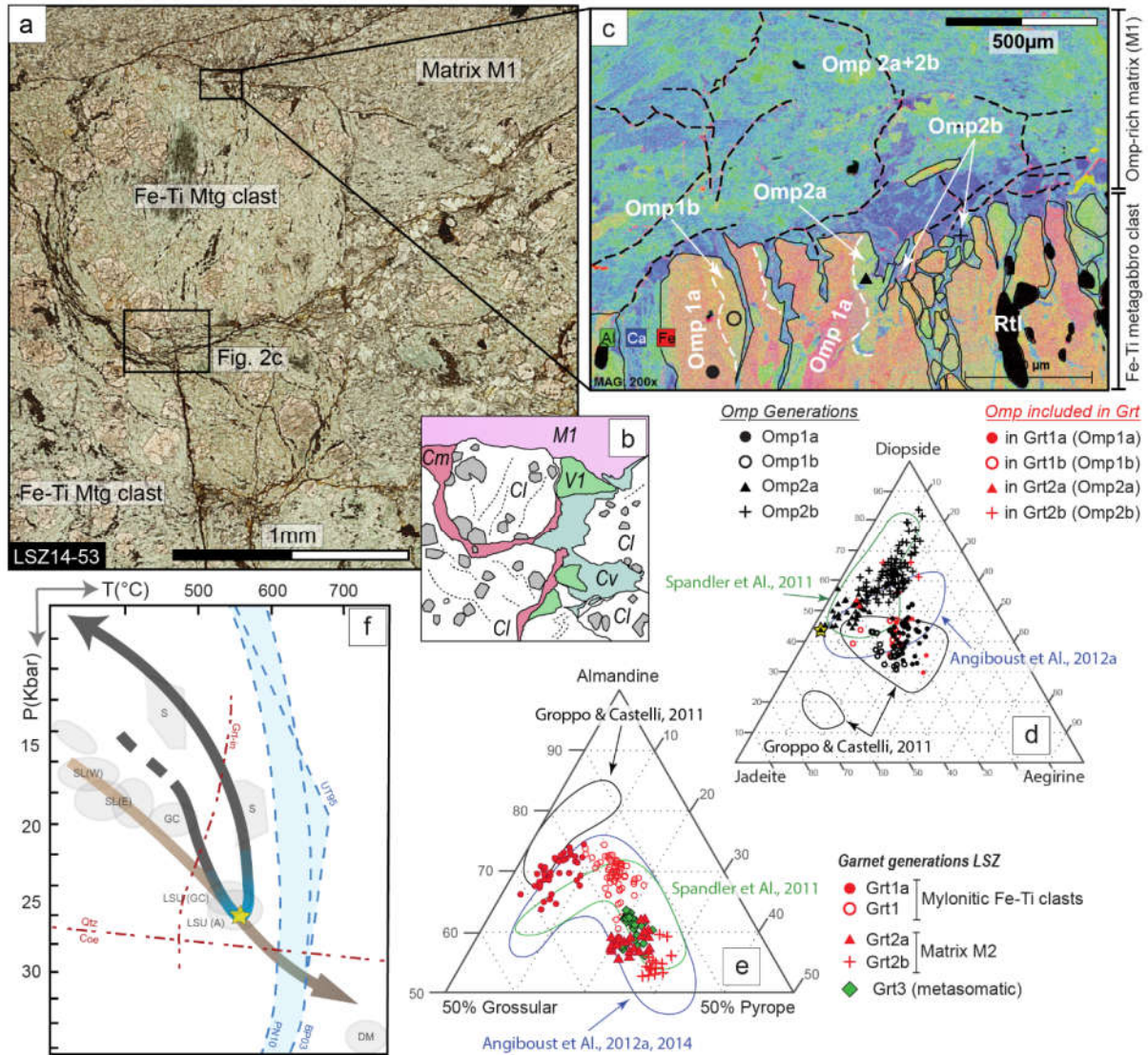


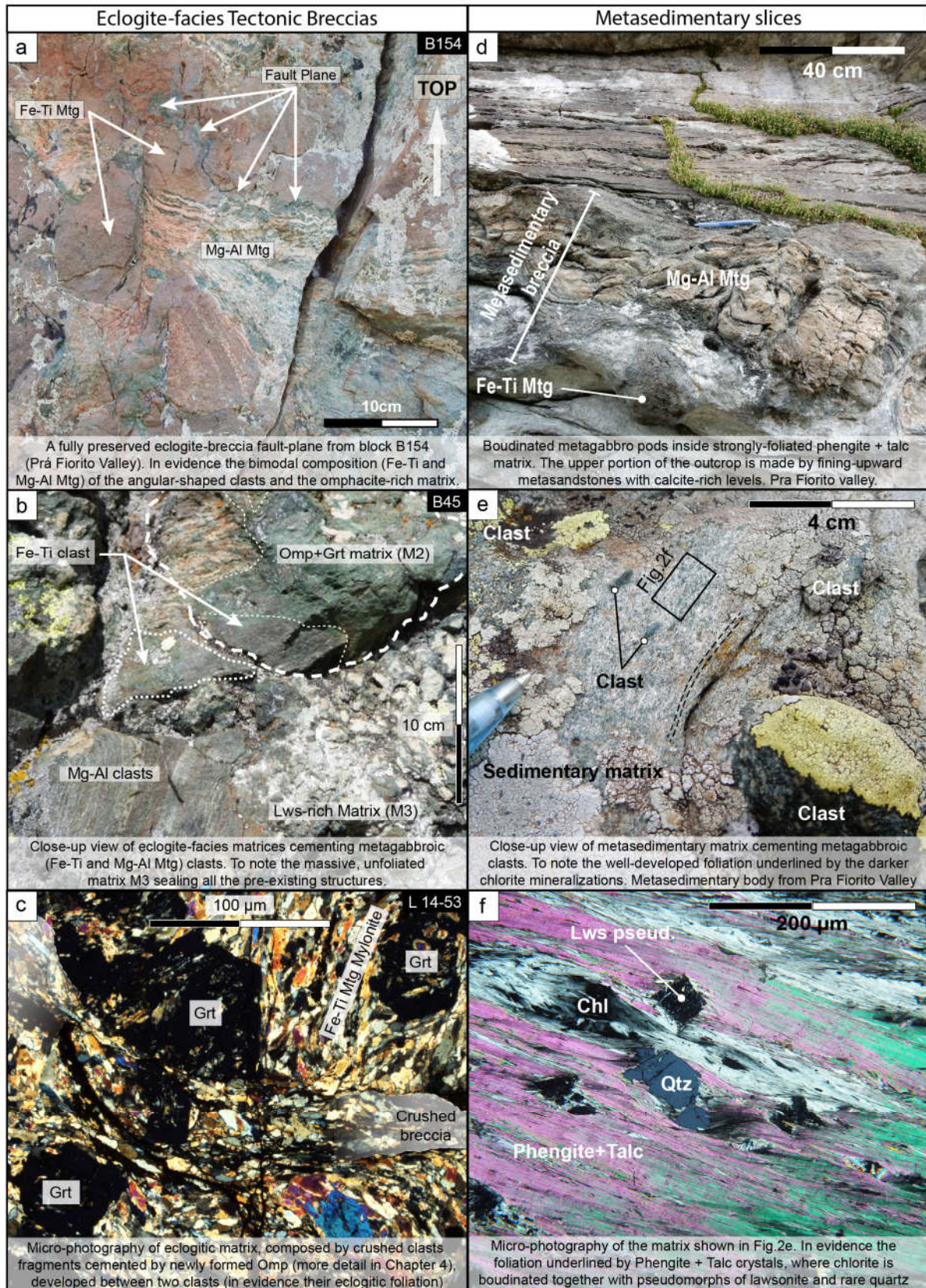
Figure 66: a) plane polarized light microphotograph of a brittle-deformed Fe-Ti metagabbro. The prominent rotation of a metagabbro microclast (Cl) is evidenced by its foliation, sub-perpendicular to those of intact rock (lower in the picture). Clast and intact rock are sealed by Omp-bearing matrix (M1), together with fragmented Omp+Apt bearing Veins1 (V1). Between the clast and intact rock is developed a 50µm-thick domain of Crushed-Matrix (Cm), composed by comminute Omp and Grt grains from clast/intact rock (composition: Omp1a-b and Grt1a-b) cemented by newly formed Omp2a and finally sealed by Omp2b. Late-stage veins of chlorite (Cv) preferentially crystallise at the expenses of crushed-matrix and Veins1. Sample 14-53, block B51. b) sketch of the microstructure shown in Figure 66a. c) FEG-SEM quantified map showing the transition Clast-M1 matrix, with the evident “radial-shape” fractures filled with Omp2a-2b (similar to what described for the Crushed-breccia). Notable the absence of Rt from M1. d) Ternary-plot (Jad-Diop-Aeg) for selected omphacite from the LSZ; EPMA analysis. e) Ternary-plot (Grs-Alm-Prp) for selected garnets from the LSZ; EPMA analysis. Comparison with data from Groppo & Castelli (2011); Spandler et Al. (2011); Angiboust et Al. (2012a, 2014) is shown. f) P-T path diagram for the LSU modified after Angiboust et al. (2012), evidencing the trajectory of slab (brown arrow) and LSU (black arrow). The yellow star depict the inferred PT-condition of eclogite-facies brecciation, at LSU metamorphic peak. More detail in Chapter 4.

In this breccia planes the clast composition is almost monogenic (metagabbros, both Fe-Ti and Mg-Al; *Figure 67a-c*), whereas in metasedimentary breccias it would be expected to be polymictic, as locally observed in metasedimentary outcrops from LSU (e.g., *Figure 67d*). Moreover, in eclogitic breccias the matrices cementing clasts are always non sedimentary (e.g., no detrital matrices or quartz/calcite-bearing cements), contrary to what is observed in metasedimentary outcrops (*Figure 67e-f*). Finally, all breccia planes preserved in eclogitic blocks (which line up the LSZ for ~15 km along strike) cut across the mylonitic, eclogite facies foliation of intact Mg-Al metagabbros. This observation, which can be made at both macro- and microscale (where brecciation cuts across syn-kinematic, mylonitic garnet), demonstrates that brecciation postdates the eclogitic mylonitization of LSU metagabbros.

It is therefore possible to univocally ascribe the formation of these Fe-Ti metagabbro breccia blocks to processes occurring at eclogite-facies conditions. A few distinct blocks (scattered in both the LSZ and ISZ) nevertheless hint to earlier disruption (e.g., *Figure 67d*) and may correspond to the pre-alpine sedimentary or tectonic breccias (e.g., upper Pellice Valley; northern part of Monviso metaophiolite complex) ascribed to detachment faulting by Festa et al. (2015) and Balestro et al. (2014a-b and 2015).

Next Page:

Figure 67: plate of pictures depicting the main structural and microstructural differences between eclogite-facies breccia developed on metagabbros (Figure 68a-c) and metasedimentary/metabasic tectonic slices (Figure 69d-f) preserving breccias ascribed either to sedimentary processes or Pre-Alpine tectonic brecciation. The highlighted dualism between eclogitic breccia and Pre-Alpine tectonic/sedimentary breccia is a necessary statement to understand the different (and complex) processes leading to evolution of the LSU and its shear zones.



6.2 Chronology of brecciation steps and origin of fluids

A fundamental difference between breccias recognized as eclogitic and those thought to be Pre-Alpine is the identification of several discrete brecciation steps in the eclogitic metagabbros from both the LSZ and ISZ (e.g., Figure 67b; § 4). Based on the successive omphacite and garnet compositions (and fluid producing reactions) these steps are shown here to span the time between prograde to peak mylonitization (Omp2a-Omp2b, matching compositions used for published P-T evolutions; e.g., Groppo & Castelli, 2010; Angiboust et al., 2012a) and early retrograde stage linked to exhumation (as suggested by the jadeite-poorer Omp3).

6.2.1 - STEP (I) Pre-brecciation eclogitization, mylonitization and veining

Fe-Ti and Mg-Al gabbros, either within the crustal sequence or intruded into the peridotitic mantle, underwent prograde eclogitization up to 530-550°C/23-27.5 kbar associated to intense mylonitization (Lombardo et al., 1979; Philippot et al., 1987, 1990, 1991; Schwartz et al., 2000; Angiboust et al., 2011, 2012a; Balestro et al., 2014). In the Fe-Ti metagabbros, prograde deformation (e.g., folding underlined by rutile trails; Figure 67c) was accompanied by grain size reduction, fracturing and dismembering of the magmatic clinopyroxene relicts into the newly formed, eclogite-facies mylonitic foliation consisting of *omphacite* + *garnet* + *rutile* ± *apatite* and accessory *glaucofane* (chapters 3 and 4). Pre-peak metamorphism was accompanied, mainly in Fe-Ti metagabbros (e.g., Figure 70), by the transient development of *omphacite*- ± *apatite*-bearing Veins1. Dissolution-precipitation processes leading to the formation of these veins induced minor changes in omphacite trace element composition (Chapter 5, Figures 59a-d and 60). Their enrichment in Li, Co and Cr and depletion in V is negligible (of the order of few µg/g, Figure 70), with substitution trends between Li and Al₂O₃ (as well as between Sm or Sr and CaO+MgO) readily correlating between Veins1 and mylonitic clast omphacite (Chapter 5, Figure 60e-g).

These findings suggest chemical equilibrium between percolating fluids forming Veins1 and the host-rock (neighbouring Fe-Ti metagabbros) and thus support the hypothesis of fluid flow limited to the millimetre to centimetre scale. These findings concord with those of several earlier works on *Omp* \pm *Grt* bearing veins near the ISZ (Philippot & Kienast, 1989; Philippot & Selverstone, 1991; Philippot & van Roermund, 1992; Nadeau et al., 1993).

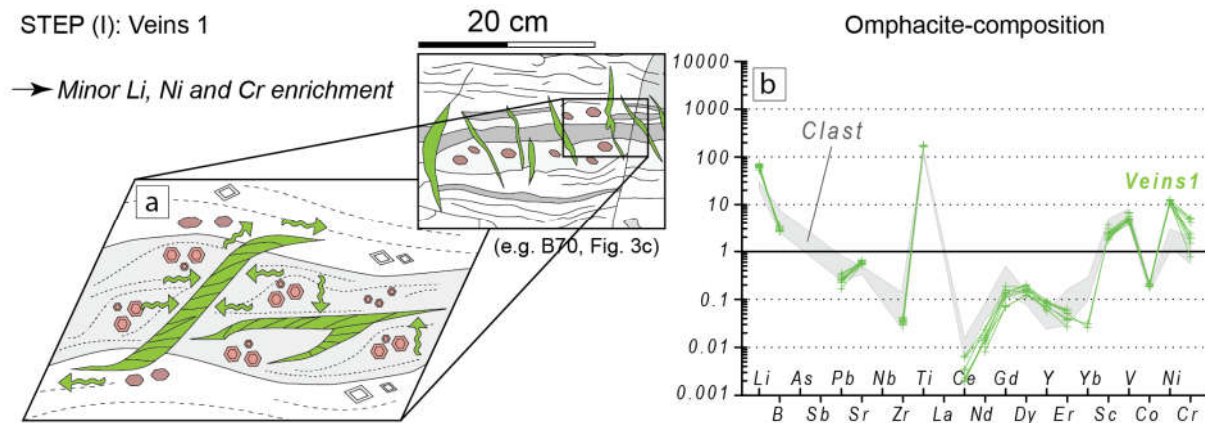


Figure 70: a) schematic representation of the development of *Omp* \pm *Apt*-bearing Veins1 in Fe-Ti metagabbros. Their major- and trace-element (b) composition, equilibrated to the host-rock (Fe-Ti metagabbro) is suggestive of fluid flow limited to the millimetre to centimetre scale. To be noted the tapered-geometry of these veins, which disappear at the contact with the intermediate metagabbro. Notable examples are in Block B70, Prà Fiorito Valley.

6.2.2 - STEP (II) Brecciation M1

The first brecciation event is marked by the relative rotation of clasts of Fe-Ti (and rare Intermediate) metagabbros sealed either by thin ($< 200 \mu\text{m}$ -thick) inter-clast domains filled with crushed eclogitic minerals ("crushed matrix") or newly crystallized, idiomorphic omphacite-rich (Omp2a) M1 matrix (with Omp2a composition in LSZ). This stage, in the ISZ, is witnessed by the crystallization of garnet+omphacite Veins-T2.

Newly formed Omp2a presents the highest jadeitic content among all analyzed omphacite crystals (Figure 66d) and can be ascribed to peak conditions (Angiboust et al. (2012a) and Spandler

et al. (2011), showing that the onset of brecciation in the LSU took place at or close to peak P-T conditions (*Figure 66f*). The complex overgrowth of Omp2b over Omp2a (e.g., *Figure 58a*), whereby both generations form an intricate mesh, suggests that both the crushed and M1 matrix were later infiltrated by fluids that partially replaced Omp2a by Omp2b. The wide compositional range of M1 matrix omphacite (*Figure 66d*), as well as the complex trace element zonations (e.g., core-to-rim depletion in HREE and Pb, with Ni enrichment; *Table 7 and Figure 59a-b*) suggests protracted fluid activity.

Hydrofracturing likely caused the brecciation witnessed by the Crushed and M1 matrices but, contrary to prograde Veins1, fluids are not internally derived from the Fe-Ti metagabbros. In the LSZ, potential ‘external’ fluid sources are either the nearby *Mg-Al metagabbro* or *serpentinites*, but the former is more likely for the following reasons:

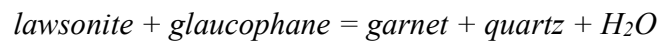
- 1) the absolute M1 matrix concentration of *Cr* and *Ni*, even if enriched (*Figure 71 and Table 7*), remains considerably lower than for serpentinites (*Figures 59a-b and 60a-d*; see also Hattori & Guillot, 2007 and Spandler et Al., 2011; Deschamps et al 2013).
- 2) Serpentine is a preferential host for *B*, *Nb*, *As* and *Sb* (*Table 6*; see also Hattori & Guillot, 2007; Spandler et Al., 2011; Angiboust et Al., 2014), for which no significant enrichment can be detected in M1 matrix.

As for the bulk composition of M1 matrix (*Figure 71*), Mg-Al metagabbros have indeed relatively low B, As and Sb contents (*Table 6 and Figure 56a-b*; see also Hattori & Guillot, 2007 or Spandler et Al., 2011) and high concentrations in Mg, Cr, Ni as well as *Sc*, *Pb*, *Sr*, *Sm* and *Nd* (*Figure 56a-b*).

The peak metamorphic assemblage for Mg-Al metagabbros consists in Cr-rich *omphacite* + *rutile* + *lawsonite* (preferential host for *Pb*, *Sr*, *Sm* and *Nd*; e.g., Spandler et Al., 2003; Martin et

Al, 2011) ± *glaucophane* (preferential host for *Sc*; e.g., Spandler et Al., 2003). Additionally, *garnet* crystallizes in the cm- to dm-thick layers of Intermediate metagabbro at the contact with Fe-Ti boudins and eclogite-breccia layers (e.g. *Fig. 54b-c*).

Given peak metamorphic conditions for the LSU it is likely that the continuous reaction involving *glaucophane* and *lawsonite* (simplified from Poli & Schmidt, 1995)



resulted in the progressive production of garnet and a free fluid phase (enriched in *Sc*, *Pb*, *Sr*, *Sm* and *Nd*; *Figure 71*) which promoted the crystallization of the M1 matrix. Sequestration of HREE by newly formed garnet crystals in Intermediate metagabbros may account for the increasing LREE/HREE ratio observed in M1-matrix omphacite rims (*Table 7 and Figure 59b*).

It is proposed that preferential pathways for such cm to m scale fluid transfer were the Veins1/host-rock borders, as suggested by the infiltration-like geometries of Omp2a and Omp2b overgrowing the Crushed-matrix developed between Veins1 and mylonitic host-rock (e.g., *Figures 58d and Figure 66a-b*).

The complex overgrowth of Omp2b over Omp2a (e.g., *Figure 66b*), both generations forming an intricate mesh, suggests that both crushed and M1 matrix were later infiltrated by fluids that allowed partial replacement of pre-existing Omp2a by Omp2b omphacite. The wide compositional range of M1 matrix omphacite (*Figure 66d*) as well as the complex trace element zonations (e.g., core-to-rim depletion in HREE and Pb, with Ni enrichment) suggests protracted fluid activity.

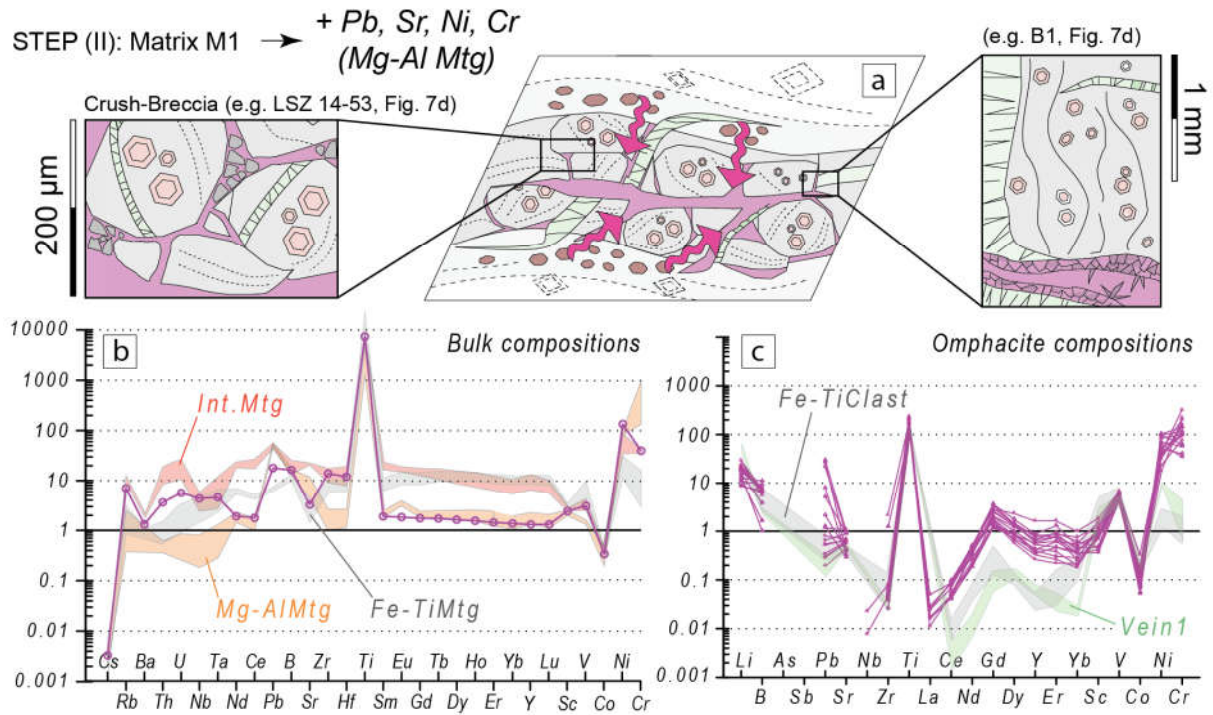


Figure 71: schematic representation of the development of M1-matrix. It crystallizes both idiomorphic omphacite grains (a) or as newly-formed, “infiltrating” omphacite generation (Omp2b) sealing comminute mylonitic fragments (Omp1a-b, the “crushed-breccia” domains). Trace-element composition (b and c) with their enrichment in Pb, Sr, Sm, Nd and Sc suggests that fluids promoting M1 crystallization were derived from Mg-Al metagabbros, rather than Fe-Ti metagabbros or serpentinites.

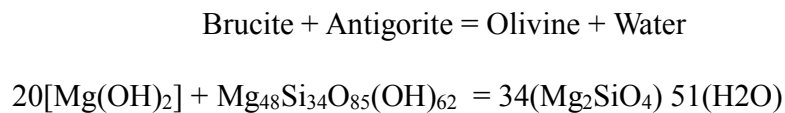
6.2.3 - STEP (III) Brecciation M2

Formation of the M2 matrix was assisted by (i) continuous dehydration occurring in the Mg-Al metagabbros (as witnessed by V, Sc and Sr anomalies in the M2-matrix) coupled to (ii) infiltration of serpentinite derived fluids (as suggested by the strong, typically ultramafic enrichment in Mg, Ni and Cr, as well as B and LREE/MREE; Figure 72 and Tables 7 and 8). The latter component was detected by Hattori & Guillot (2007) and Spandler et al. (2011) for the Monviso, and is commonly observed in similar geological settings (e.g., Scambelluri et al., 2004; Tenthorey & Hermann, 2004; Savov et al., 2005; Hattori & Guillot, 2007; Deschamps et al., 2013). In the light

of our results, we speculate that the M1 brecciation increased the porosity of the Fe-Ti metagabbros, thereby creating a preferential pathway for fluid infiltration.

M2 brecciation therefore marks the transition from a “*closed*” system, with circulation of Intermediate metagabbro-derived fluid, to an “*open*” system with influx of at least some serpentinite-derived fluids.

Two continuous, olivine-producing reactions accompany serpentinite dehydration: the (i) antigorite-out reaction, expected to take place at about 630°-700°C at 2.5-3.0 GPa (e.g., Ulmer & Trommsdorff, 1999), which is clearly beyond the peak of metamorphism inferred for the Lago Superiore Unit¹ (600°C, 2.4 GPa: Schwartz et al., 2000; 550°C, 2.6 GPa: Groppo & Castelli, 2010; 550°, 2.5 GPa: Angiboust et al., 2012a), and (ii) the **brucite-out reaction**, occurring at ~500C and 1.5-2.0 GPa (Ulmer & Trommsdorff, 1999). The balanced (Ulmer & Trommsdorff, 1999; Scambelluri et al., 2001) reaction is as follows:



¹ Structural and petrographic evidences (like the development in both LSU and BSU of coeval S1, eclogite-facies foliation overprinted by the regional, exhumation-related S2 foliation) suggest that the serpentinite of BSU and the mafic rocks of the LSU likely experienced the same PT-path evolution from peak metamorphism to exhumation (in agreement with the findings of [Blake et al., 1995](#) and [Schwartz et al., 2001](#)). Thus, local dehydration of Monviso serpentinite under antigorite-out condition have to be excluded as potential source of fluids.

Rare olivine-bearing veins (expected as a reaction of antigorite breakdown; e.g., Scambelluri et al., 2001) cutting across the serpentinite were identified (i) in some massive blocks scattered in the LSZ (Groppo & Compagnoni, 2007), and more recently (ii) in the basal serpentinites (Gilio, 2017; PhD thesis), advocating for effective local serpentinite dehydration in both LSZ and BSU. Unfortunately, exhumation-related deformation (i.e., the pervasive S2 and S3 deformation) affecting the mylonitic antigorite-schist of LSZ and ISZ have obliterated much of the pre-existing structures and mineral evidence (*Chapter 3*). The complex oscillatory *Cr*-enrichment patterns observed in the M2-matrix (from both ISZ and LSZ; *Figures 55e and 58f*) points to several pulses sustaining the brecciation event. The chemical and petrological affinity between the various M2-matrix samples indicates that fluids were derived from a common serpentinite source, with only minor contribution/anomalies from the nearby Intermediate metagabbro (e.g., different *Dy-Y-Er* trends between ISZ and LSZ omphacite; *Figure 72*). M2-matrix brecciation thus coincides with the onset of brecciation over the entire length of the shear zones, i.e. along ~15 km (*Figures 52 and 53*)

In the next page:

Figure 72: a) schematic representation of the development of M2-matrix. On samples, M2 is recognizable by its paragenesis of omphacite and garnet, the latter absent in M1-matrix. Formation M2 matrix was assisted either by continuous Mg-Al metagabbros dehydration (as shown by V, Sc and Sr anomalies) and serpentinite dehydration (as evidenced by the strong, typically ultramafic enrichment in Mg, Ni and Cr, as well as B and LREE/MREE). These enrichment trends are observed in both garnet (b) and omphacite (c) from ISZ and LSZ. M2-matrix marks therefore the transition from a “closed” system, with circulation of Intermediate metagabbro-derived fluid, to an “open” system with influx of at least some serpentinite-derived fluids, with brecciation over the entire length of the shear zones.

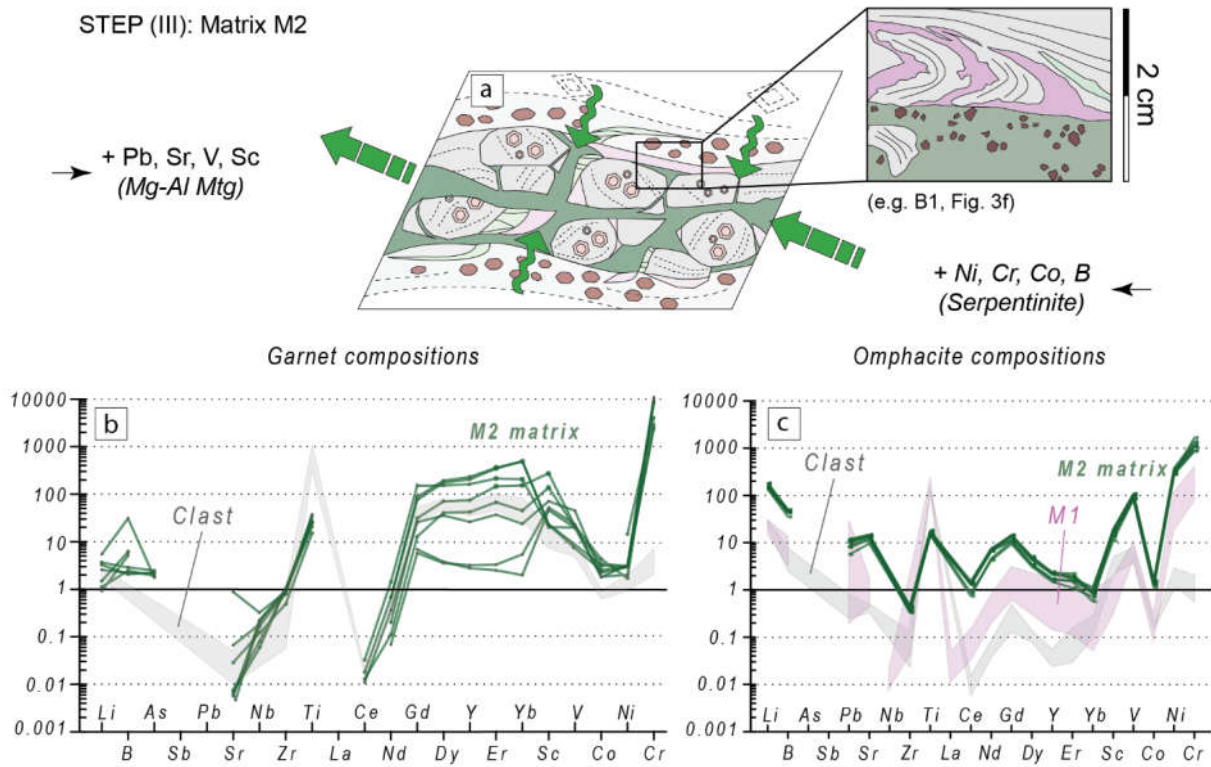


Figure 72

6.2.4 - STEP (IV) Brecciation M3

The third, volumetrically dominant (80 vol%) lawsonite-rich M3 matrix crosscuts all preexisting structures of the LSZ eclogitic breccia blocks (e.g., Figure 67b) but is never observed in the ISZ and in the undetached breccia layers of Truc Bianco. The extreme abundance of lawsonite in M3 (up to ~40 vol% in places) compared to the rather dry assemblages of M1 and even M2 advocates for massive fluid infiltration. High **Ni**, **Cr**, **Co** and **B** concentration, with no **V**, **Sc**, **Li**, **Pb** and **Sr** anomalies (only found in breccia blocks dispersed in the LSZ), support the hypothesis that M3 matrix was generated by externally- serpentinite-derived fluids (e.g., Ulmer & Trommsdorff, 1999; Scambelluri et al., 2001 and 2004; Tenthorey & Hermann, 2004; Hattori & Guillot, 2007). Whether the serpentinite-source of fluids change between M2 and M3 matrices can

unfortunately not (yet) be determined on the basis of geochemistry. The lack of analysis for the bulk composition of the M2-matrix and the fact of having only one for the M3-matrix make the interpretation of **Cr, Ni, Co** and REE concentration in single mineral phases rather uncertain.

Nevertheless, the hydrated M3 matrix assemblage consisting of **lawsonite** (that may retain up-to 11.5 wt.% of water; Pawley, 1994) + **omphacite** \pm **talc** \pm **garnet** suggest that fluids circulating at this stage were richer in H₂O (as well as **Ca, Al, B, U, Th** and partly **LILE**) than those leading to the formation of the almost anhydrous M2 matrix with **omphacite** + **garnet** \pm **rutile** \pm **talc**. The lack of evidence for massive dehydration in the antigorite-bearing LSZ and BSU, which would account for the strong volumetric increase from M2 to M3 matrix, point to deeper antigorite-breakdown fluids percolating through the porosity already opened by the M2 brecciation event. Interestingly, such M3 matrix is absent in the ISZ and from undetached breccia layers of Truc Bianco (LSZ), still included at the base of the Mg-Al metagabbro cliff. This observation suggests that the massive M3 serpentinite-derived fluid infiltration occurred in m- to km-scale interconnected breccia planes formed as a result of M2 matrix brecciation in the LSZ, and further contributed to the formation of weak planes, later fracturation and incorporation of breccia blocks into the LSZ.

In the next page:

Figure 73: a) from blocks scattered in the LSZ is evident that the Lws-rich matrix M3 seals all the pre-existing breccia-structures, postdating the brecciation event M1 and M2. In the bulk, the high Ni and Cr concentrations (b) as well as Co and B (c) with no V, Sc, Li, Pb and Sr anomalies support the hypothesis that M3 matrix was generated only by externally- serpentinite-derived fluids. The unexpected low Ni and Cr concentrations of M3 omphacite (d) are to be attributed to the “matrix effect” of lawsonite crystals, which sequester the larger part of these elements. Noteworthy M3 matrix is observed only in the eclogitic breccia blocks dispersed in the LSZ, while is absent in the ISZ.

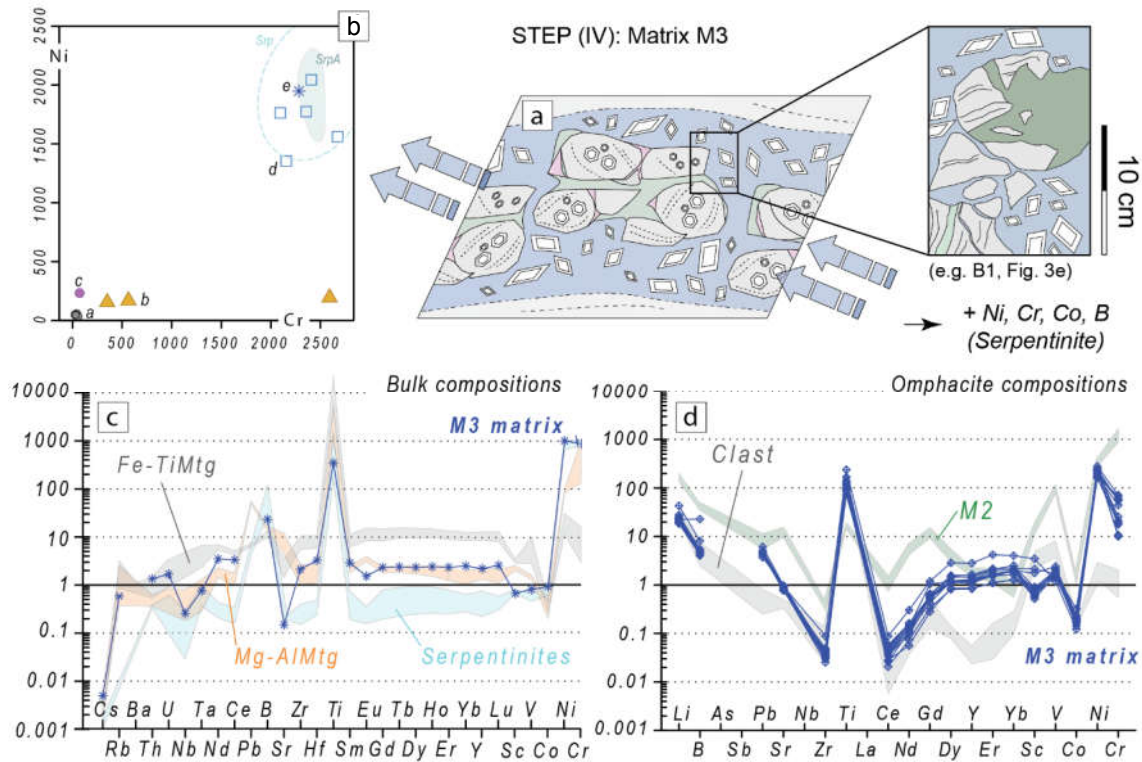


Figure 6

6.2.5 - STEP (V) Post-brecciation evolution

After the M3 brecciation event, protracted fluid circulation continued throughout the shear zones (especially the LSZ), leading to (I) formation of new HP ‘Late-stage veins’ and (II) to the extensive ultramafic metasomatism that affected brecciated blocks with prominent rind formation (up to 0.5 m thick) at their contact with the antigorite-rich matrix embedding them in the shear zones (Angiboust et al., 2014).

The formation of Late-stage veins is associated with serpentinite-derived fluids quite similar to those of the M3 stage, as suggested by **Cr**, **Ni**, **Co** and **B** enrichments (

Figure 74) and the absence of any other geochemical anomaly. Vein patterns denote processes of hydraulic fracturing. Later metasomatic replacement affects both clasts and matrix and postdates

brecciation. In the rims of metagabbro block, the preexisting eclogitic facies assemblage was replaced by a mafic to ultramafic assemblage (talc, chlorite, metasomatic garnet Grt3, sodic amphibole and diopside plus albite, epidote and rare phengite after lawsonite), suggesting an interaction with ultramafic fluid (the likely carrier of Cr, Ni, and Mg, as also suggested by the presence of talc) and LILE from metasediments (Angiboust et al., 2014). The degree of metasomatism rapidly decreases from block rims to cores. These metasomatic rinds are thought to form shortly after peak burial and brecciation, during the onset of exhumation (see also Angiboust et al., 2014).

STEP (V): Late-stage veins + metasomatism

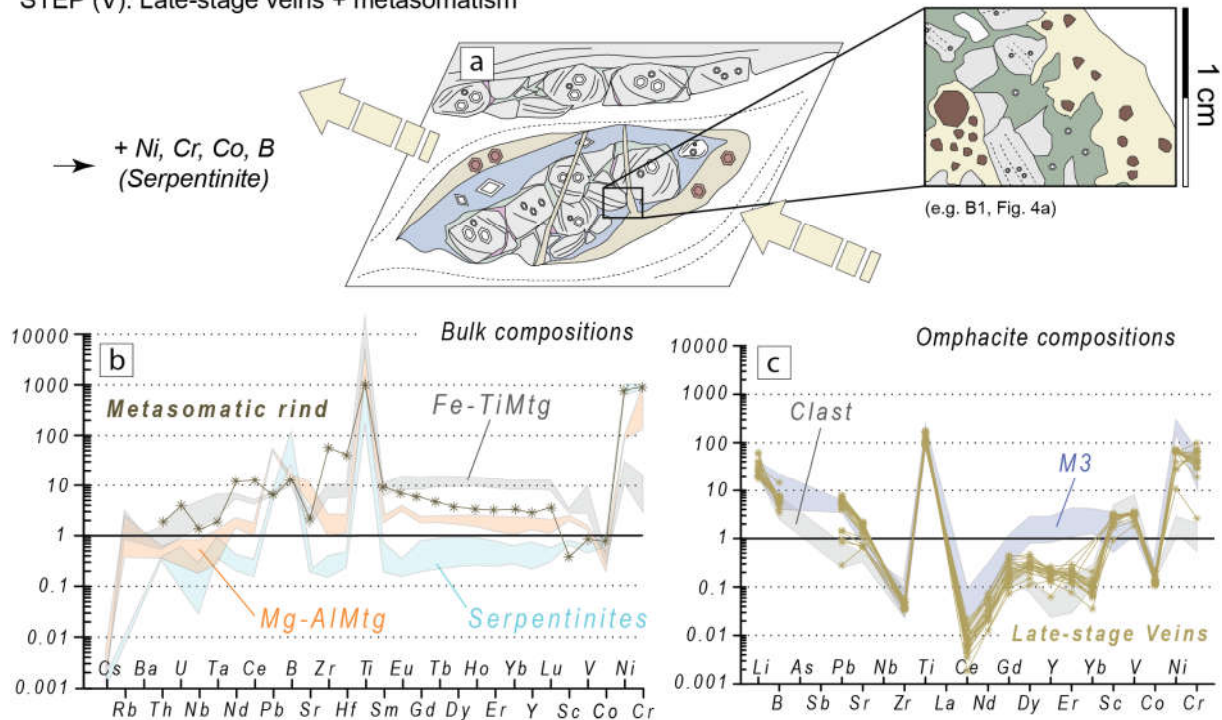


Figure 74: a) the protracted fluid circulation throughout the shear zones (especially the LSZ), led to (I) formation of new HP 'Late-stage veins' and (II) to the extensive ultramafic metasomatism that affected brecciated blocks with prominent rind formation. The interaction with ultramafic fluid (the likely carrier of Cr, Ni, and Mg) is suggested for the formation of both metasomatic rinds (b) and Late-stage veins (c), as also suggested by the presence of talc. In Late-stage veins (b) the enrichment in Cr, Ni, Co and B suggests the persistence of serpentinite-derived fluids (quite similar to those of the M3 stage) circulating in the shear zones.

6.3 – Strain localization in Fe-Ti gabbro horizons

Although eclogite facies ductile deformation chiefly controlled the evolution of Monviso metaophiolite (as demonstrated by the polyphase deformation affecting Mg-Al and Fe-Ti metagabbros), concomitant brittle deformation is clearly witnessed by eclogitic breccias and HP-veins. Veining and brecciation in Fe-Ti metagabbros horizons (to a lesser extent in neighboring Intermediate metagabbros) as well as massive fluid circulation throughout the metagabbros is rather counterintuitive however when considering known rheological properties of such metagabbros.

At peak PT conditions of the LSU, the strength of Mg-Al metagabbros, if approximated by diabase (owing to its initial assemblage of Ca-rich plagioclase and clinopyroxene; Mackwell et al., 1995), can reach 1.3 GPa (e.g., Angiboust et al., 2012a), while that of eclogitic Fe-Ti metagabbros, if approximated by an eclogite flow law (owing to its high garnet content), may reach up to 7 GPa (see Jin et al., 2001 for a comparable assemblage made of 50% garnet, 40% omphacite and 10% quartz). The strength of Fe-Ti metagabbros would thus be predicted to exceed that of both Mg-Al metagabbros and serpentinite (whose effective viscosity is notoriously low, ~4 orders of magnitude lower than metagabbros; e.g., Hilairet et al., 2007) and deformation can thus be expected to localize in the weaker serpentinite (and Mg-Al metagabbros). Fe-Ti metagabbro boudins embedded inside the Mg-Al gabbros nevertheless represent a strong rheological contrast that may explain strain localization, as seen at the boundaries between multi-layered lithologies/media with different competency (e.g., Strömgård, 1973; Treagus, 1981).

It should also be noted that the behaviour of multi-phase material is not very well known, and that monomineralic layers may deviate largely from available flow laws: the strength of pure omphacite (the “*omphacitite*”) is for example twice lower than that of eclogite and four-time lower

than garnetite (e.g.; Jin et al., 2001). Ongoing reactions are likely to change these rheologies — i.e., the growth of garnet (along with fluid release) in Intermediate metagabbros likely increased the strength (and brecciation potential) of this lithology. Finally, “semi-brittle” modes of deformation, involving mechanical failure at the contact between monomineralic and polyminerale media, have also been observed in experiments on clinopyroxene and garnet (Kirby and Kronenberg, 1984; Philippot and Van Roermund, 1992; Rutter, 1986).

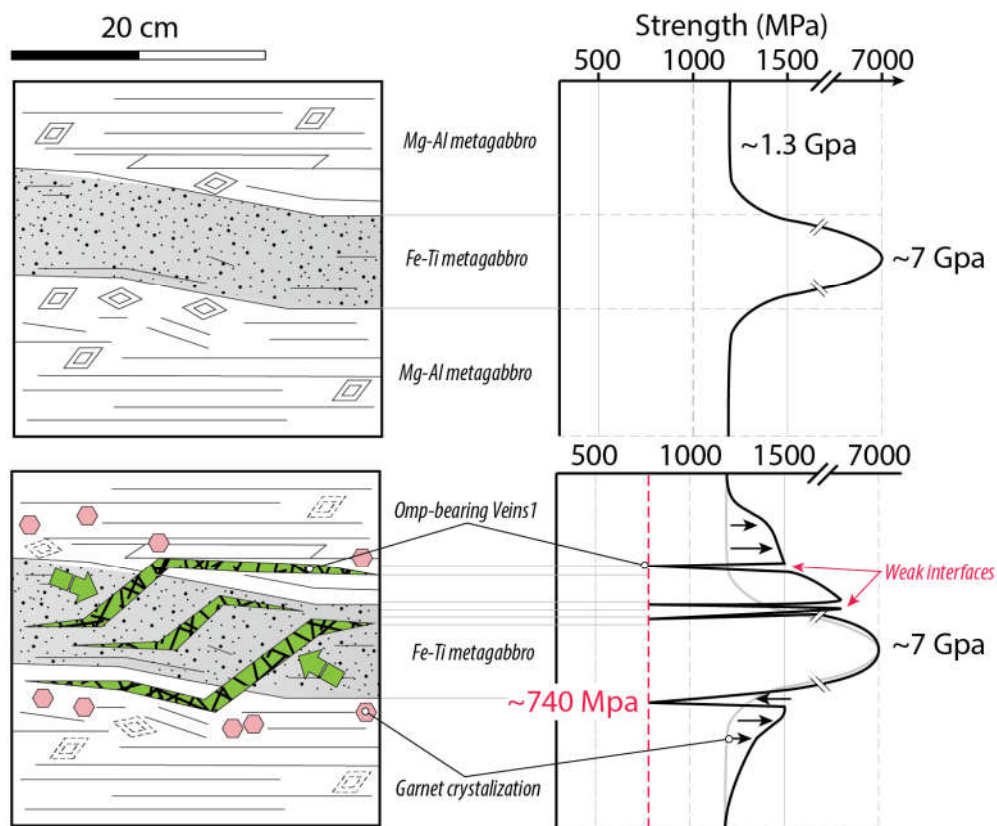


Figure 75: simplified plot of the expected differential strength (thick line) across a Fe-Ti metagabbro boudin embedded in Intermediate metagabbros before (a) and after (b) the nucleation of omphacite-bearing veins (and later-on, matrices), which likely acted as weaker layers in the multi-phase material. In Intermediate metagabbros the growth of garnet (along with fluid release) likely increased the strength (and brecciation potential) of this lithology. Adopted flow laws: gabbros Fe-Ti (eclogite: Jin et al., 2001), gabbros Mg-Al (diabase: Mackwell et al., 1995), omphacite veins (omphacitite: Jin et al., 2001) at 550 °C and with a strain rate of 10–14. More details in the text.

In our rocks, an analogue of “*omphacitite*” are the Omp-bearing veins (*Figure 75*) observed in both LSZ (*Veins1, Chapter 4 and 5*) and ISZ (*VeinsT0, Chapter 5*) that generally predate the crystallization of crushed and M1 matrix (e.g., *Figure 66a*). The crushed matrix preferentially developed at the boundaries between mylonitic clasts and veins (*Figure 66a*), suggesting that in Fe-Ti metagabbros, omphacite-bearing veins likely acted as weaker layers where deformation focused (*Figure 75*). Thus even at the small scale, strain obviously localized at boundaries between layers with contrasting competency (e.g., Treagus, 1981).

Heterogeneous fluid release in contrasting lithologies (with different strength and/or porosity-permeability) may also have influenced brittle strain localization: at an early stage fluid release inside the Fe-Ti metagabbro boudins only (via the garnet-in reaction) resulted in fluid expulsion and veining towards the embedding Intermediate gabbros (*Vein1* formation), whereas at peak conditions (i.e., when Fe-Ti metagabbros were rather dry) the fluid produced by the garnet-in dehydration reaction in the cm to dm-thick Intermediate gabbro layers triggered M1 brecciation inside the Fe-Ti gabbro boudins.

The succession of M1 to M3 matrices suggests that brecciation likely increased rock porosity and effective permeability in Fe-Ti metagabbros and surrounding Intermediate metagabbros. This must have been a crucial step, since the permeability of eclogites is extremely low (up to six orders of magnitude lower than for serpentinite mylonites: 10^{-18} m^2 ; Morrow et al., 1984; Mibe et al., 2003) and restricted to mineral boundaries, isolated pores, cleavage planes, and microfractures (which connectivity is expected to be very limited; e.g., Davies, 1999; Watson & Brenan, 1987).

Structural, petrographic and geochemical evidences for circulation of serpentinite-derived fluids along both the LSZ and the ISZ suggest that the M2 brecciation event achieved full interconnection along the entire length of the shear zones. Later, more pervasive fluid pulses

focused on the pre-brecciated metagabbros (e.g., M3 matrix, Late-stage veins and metasomatic fluids) indicating that at this stage eclogitic breccias chiefly controlled the permeability in metagabbros, promoting further fluid channelization: subsequent brecciation, fluid circulation and late-stage metasomatism were thus a direct consequence of localization of strain and fluid circulation in Fe-Ti metagabbros.

6.4 – Strain localization in the LSU

The Lago Superiore metaophiolite was affected by intense shearing dominantly accommodated along three major shear zones (the LSZ, ISZ and USZ) defined by eclogite-facies mylonites and/or serpentinite slivers (*Figure 76a*).

In the LSZ, distribution of the largest part of *Type1* blocks and *Type2* blocks (both preserving eclogitic breccia) stratigraphically above the big slivers of retrogressed Mg-Al metagabbro of Punta Murel, Colle di Luca and Alpetto Lake (e.g., *Figures 52 and 53*; refer to the *Geological Map* for further details), while unbrecciated Type 3 blocks are restricted to a 30-100 m thick band at the base of the LSZ, suggests limited tectonic mixing.

In detail, the preserved eclogite-breccia layers in the biggest Type2 blocks and lenses (e.g., Punta Murel, Colle di Luca and Alpetto Lake; *Figures 35 and SM7a-d, §4*) are systematically oriented towards the cliff of intact Mg-Al metagabbros, subparallel to the dip-direction of the LSZ roof, indicating small rotation of the blocks inside the shear zone. This finding, supported by the evidence of decreasing volumes of brecciated Type1 and Type2 blocks from the roof of the shear zone towards the footwall, suggests that the LSZ developed by network widening (e.g., *sensu* Schrank et al., 2008) and not as a subduction *mélange* (e.g., *sensu* Festa et al., 2010) formed by extensive mixing along the subduction interface (Blake et al., 1995; Guillot et al., 2004).

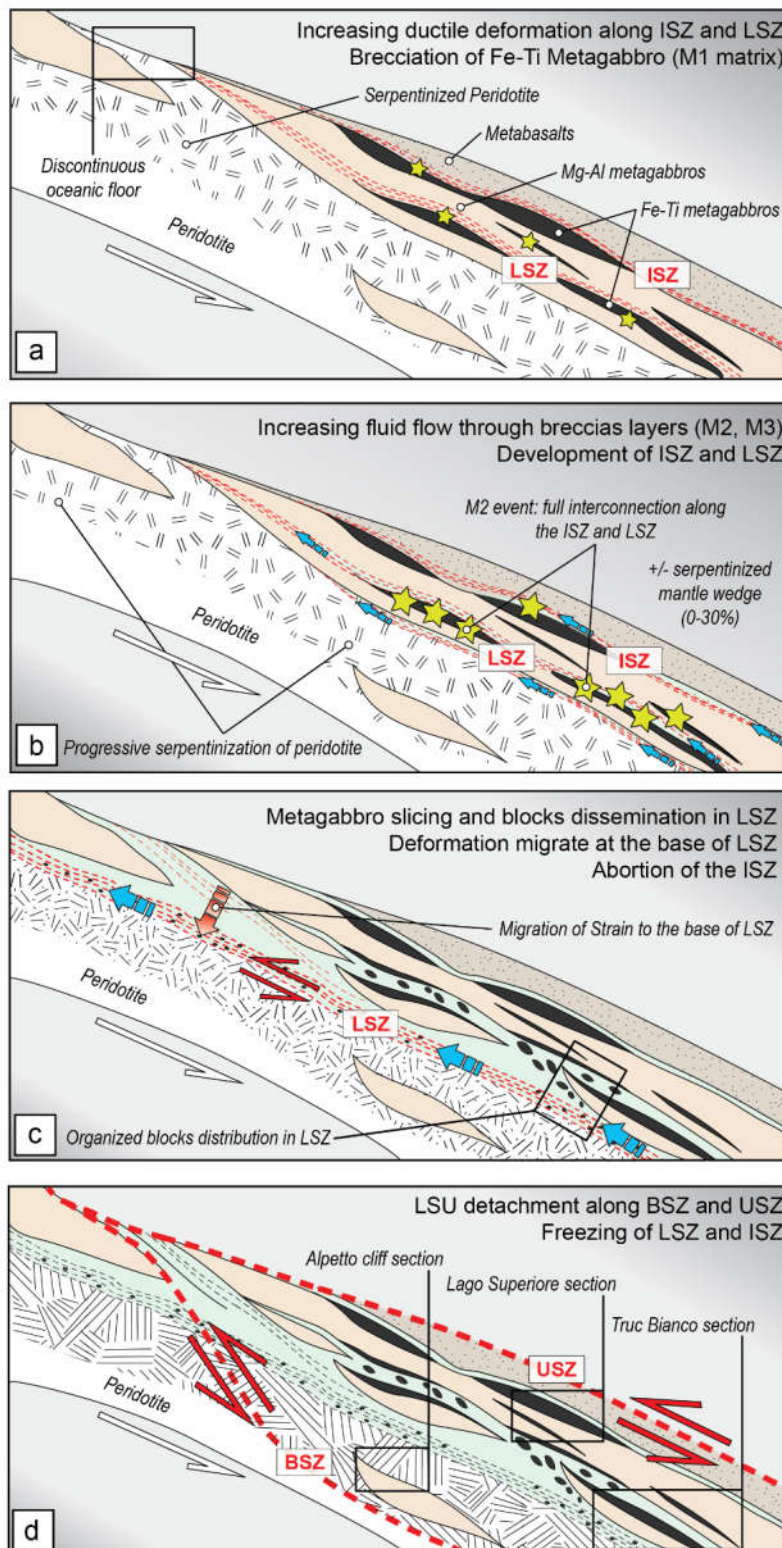


Figure 76

Figure 76: Sketch representing the LSU and the BSU from the onset of mylonitization to the dissemination of breccia blocks in the LSZ. a) During subduction the LSU the increasing deformation coupled to the rheological contrast between Fe-Ti and Mg-Al metagabbros culminated at peak-burial conditions (eclogite-facies) in the brittle failure both in LSZ and ISZ (M1-matrix, pure Omp). b) As suggested by the crystallization of matrices progressively richer in water (M2, Omp + Grt) brecciation likely promoted the generation the porosity that permitted the successive external fluid infiltration. Noteworthy, M2 marks the onset of brecciation over the entire length of the shear zones. c) Field evidence shows that further deformation and fluids circulation migrated towards the base of the LSZ. M3-matrix (70% Lws + Omp \pm Grt), indeed, is absent in the ISZ and is found only in eclogitic breccia blocks disseminated in the LSZ. The interplay between on-going deformation and the massive, fluid-assisted mafic metasomatism likely further decreased the strength of the rock, promoting the detachment and dissemination of blocks and slivers in LSZ. d) Final strain localization in the BSZ (and abortion of ISZ and LSZ) was probably driven by increasing contrast between a largely serpentized BSU and a dryer underlying peridotite. The progressive, prograde serpentization of the BSU peridotite would explain why, despite the presence of supposedly weak a thick serpentine, both LSZ and ISZ (as well as the bulk of the metabasalt and metagabbro) were pervasively deformed before final strain localization on the BSZ. Juxtaposition with the adjacent Monviso Unit (MU) occurred in the epidote blueschist facies during exhumation in the subduction channel (Schwartz et al., 2000).

The evolution of the Lago Superiore Unit before its detachment from the subducting slab remains somewhat speculative but our results suggest that it is closely linked to the development of brittle rupture at eclogite facies. The onset of brecciation (*Figure 76a*) channelized increasing amount of fluids throughout the metagabbros, leading to the crystallization of matrices M1, M2 and M3 (*Figure 76b*) and creating weaker horizons where deformation preferentially focused (i.e., LSZ: M1 to M3; ISZ: M1 to M2; *Figure 76b*). The crystallization of M2 matrix coincided with interconnection at shear-zone scale, as suggested by similar petrography/element composition in both LSZ and ISZ, but more pronounced for the LSZ (*Figure 76b*). The absence of M3 matrix and Late-Stage Veins in the ISZ indeed demonstrates that later fluid circulation was focused in the LSZ (e.g., at the base of LSU; *Figure 76c*). In the LSZ, the widespread occurrence of eclogitic breccia blocks with preserved M3 matrix and Late Stage Veins suggest that M3 and late vein crystallization

strongly contributed to the detachment of the blocks (i.e., probably through weaker layers formed by lawsonite-rich matrix percolated by talc + omphacite-bearing veins).

After detachment of the LSU from the slab, during the earlier stage of exhumation (Angiboust et al., 2014), ingress of ultramafic fluids in the LSZ promoted the progressive metasomatization of disseminated blocks and neighbouring metagabbros (*Figure 76c*).

As observed on the LSZ blocks (*Figure 76c*; more details in *Chapter 4*), metasomatic chemical exchange at the block rinds further enhanced disaggregation (e.g., Bebout and Barton, 2002; Catlos and Sorensen, 2003; Breeding et al., 2004). Fortunately, however, the comparably low permeability of the blocks with respect to the serpentinized shear zone matrix sheltered their eclogite-facies structures from deep infiltration and metasomatism (e.g., Ague, 2007). The observation of limited tectonic mixing and block rotation also suggests that the detachment of eclogitic blocks from the LSU marked the moment when deformation migrated from the LSZ towards the base of the serpentinite sole, freezing-in (and preserving) the LSZ. We speculate that strain localization at the BSZ was probably driven by the increasing contrast, with time, between a largely serpentinized BSU and a dryer underlying peridotite: only sparse initial serpentinization of the BSU peridotite would explain why, in spite of the presence of a thick serpentine sole supposedly so weak as to accommodate all the deformation, the LSZ, ISZ, and also the bulk of the metabasalt unit were pervasively deformed before final strain localization on the BSZ.

6.5 - Are Monviso eclogite-breccia seismically derived?

The switch from ductile to brittle regime documented by eclogite brecciation can result from a change in strain rate (i.e., as a consequence of an earthquake) and/or in fluid pressure (whether or not related to ‘dehydration embrittlement’; Hacker et al., 2003a). Massive water ingress recorded by the M3 lawsonite-rich matrix (Lws~40 vol%) could thus be seen either as a consequence or as the trigger for strain localization.

Whether brecciation represent former seismic event(s), as hypothesized by Angiboust et al. (2012a), was one of the objectives of the present work. In any case, the sequence of M1 to M3 events reported here demonstrate that this cannot have been one single large earthquake only. Unlike for pseudotachylites, regarded as the unequivocal evidence for past seismic activity (e.g., di Toro et al., 2005?), assessing the seismic origin of the Monviso eclogitic breccias is difficult (and pseudotachylite formation is notably hampered by the presence of free-fluids, as in the LSU; e.g., Philpotts, 1964; Deseta et al., 2014). Several arguments support an instantaneous, major brittle rupture phase at eclogite-facies conditions preluding to the formation of a km-scale fault zone that subsequently localized deformation:

1. The sharp, M1-matrix bearing breccia planes crosscutting the eclogitic mylonitic foliation, indicating instantaneous deformation at the expenses of Fe-Ti metagabbros (e.g., *Figure 66a-b* and *Figure 67b*).
2. The formation, at the mm-scale, of a crushed matrix (*Figure 67c*), witness of tectonic comminution of wall-rock fragments during brecciation.
3. The existence of minerals fractured and offset along omphacite-bearing planes (e.g., garnets; *Figures 38d-e*, Chapter 4).
4. The formation of crackle-breccia with relative displacement, and the full transition from crackle to chaotic breccia, indicating tectonic brecciation at M2 rather than hydraulic fracturing (*Figures 36a-b*, Chapter 4).

5. The length scale of breccia block recovery, on 15 km along strike of the LSZ, indicating coeval brecciation and connection of the breccia planes at the km scale (M2 event), forming a major fault zone inside the metagabbros that later concentrated both strain and fluid circulation.

Unfortunately, macrostructural characteristics that univocally define dynamically-formed, single-slip dilational breccias are hindered by both the limited extension of most breccia planes now occurring as meter size blocks, and the ubiquitous ultramafic rind coating most outcrops.

Indeed, rupture surfaces (corresponding to the principle slip surface; e.g., *Figures 36a-b*) on most meter-sized blocks (*Chapter 4*, tables of *SM5*) were too limited to define the off-fault damage mode (e.g., Wilson et al., 2003; Blenkinsop, 2008; Mitchell & Faulkner 2009), i.e., to discriminate between *attrition breccias* and *dilation breccias* (the latter considered to be the genuine product of seismic activity: e.g., Sibson, 1986; Blenkinsop & Fernandes, 2000; Melosh et al., 2014). Similarly, there is a lack of outcrops preserving fracture networks in wall-rocks, although their *morphology and density* is the most important attribute for recognizing dynamically formed breccias (e.g., Melosh et al., 2014). Only omphacite-bearing veins propagating from the breccia layers inside the intact wall-rock (*Figure 34g, Chapter 4*) were locally observed, but their shearing in the Intermediate gabbro wall-rock suggests that the post-brecciation ductile deformation prevents the preservation of any brittle structure in the wall rocks. Moreover, the study of seismically-derived fracture networks requires a morphological and statistical analysis of tectonic breccias performed on surfaces produced by a *single event* (e.g., Rowe et al., 2011; Melosh et al., 2014). Indeed, the overprint of multiple events would result in the overestimation of the energy leading to the brecciation and in the misunderstanding of mechanisms inducing the rock failure (e.g., multiple events could develop with different mechanisms; Jebrack, 1997). In our case, the clear crosscutting relationships between the different matrices, in particular with M3 matrix

reworking M1-M2 pre-existing brecciated surfaces (*Figure 67b*; more details in *Chapter 4*), prevent a rigorous structural evaluation of the brecciation kinematics.

However, although only observed on rather small (~1 and ~3 meters) and limited number of blocks (only in blocks B154 and B770), some of the universally accepted characteristics defining dynamically-formed, single-slip dilational breccias (e.g., Sibson, 1986; Melosh et al., 2014) are observed in the studied Monviso metagabbros. Evidence for seismically-derived breccias include the rare preserved portions of breccia with exploded jigsaw texture, and minimal clast rotation and displacement. As predicted by Melosh et al. (2014), breccias are composed by monomict, locally sourced clasts (e.g., Fe-Ti metagabbros), are poor in wear products (e.g., host-rock-wall fragments: Intermediate metagabbros), are clast-supported and display an abrupt transition from crackle to mosaic breccia textures (more details in chapter 4). However, the fabrics of the best-preserved breccia surface from block B154 (refer to *Fig. 36a-b* of *Chapter 4* for more details) correspond to *attrition breccia* rather than *collapse breccia*, thus suggesting onset of tectonic brecciation in metagabbros... but excluding a direct correlation to seismicity.

Thus, although some macrostructural (and microstructural) evidence support the hypothesis of seismically-derived breccias, they are at present too scarce to univocally assess such a seismic origin. Whether M1 and M2 stages were seismic cannot at present be demonstrated given outcrop/block sizes and discontinuity but the recognizable patterns of M1-M2 along the whole LSZ (and more moderately ISZ) indicate that these processes are not random but occur through brittle comminution along a given plane developing into a major fault zone. Further microstructural investigation would be essential to better constrain the link between this brecciation events, particularly the M2 brecciation which appears as a critical step in the history of strain localization, and earthquake rupture and/or creep processes at Intermediate Depth.

Chapter 7:

Conclusions and Perspectives

7.1 – Conclusions

It is perhaps worth recalling what was known at the start of this work (i.e., PhD work of Samuel Angiboust and related papers; 2011; 2012a, b; 2014): brecciation was regarded as most likely eclogitic (e.g., as inferred from the eclogitic cement), found along the LSZ for 15 km, and at least some of the fluids accompanying brecciation were derived from serpentinites (e.g., Mg buffering of garnets), possibly as pulses (e.g., cracks in garnets; oscillatory zoning). These conclusions were preliminary, however, and their interpretation in terms of intermediate-depth process was challenged by several authors (Festa; Ballestro; Müntener pers. comm.). If eclogitic, whether or not brecciation was related to any seismic activity (and, if seismic, whether or not to one or several earthquakes) was completely unknown.

At the outcome of a detailed structural and petrological investigation of the Lago Superiore Unit, this study has documented progressive strain localization within the slab into the gabbroic crust during and prior to the detachment of this large slab fragment, and the following conclusions can be highlighted:

(1) The vast majority of **breccia blocks outcropping inside the LSZ formed by brittle rupture under eclogite-facies conditions**. Occurrence of eclogite-facies mylonitic Fe-Ti and Mg-Al metagabbro clasts exclude an origin by sedimentary deposition in paleo-oceanic basins or high-pressure overprinting of breccia formed at shallow crustal depths. The lack of deformation in the matrix between eclogitic clasts contrasts with the reworked matrix of some (rare) metasedimentary blocks dispersed in the shear zone.

(2) **Brecciation is stepwise, as demonstrated by existence of (at least) three generations of HP-veins and three successive types of matrix**. In breccias from LSZ, the sharp increase in fluid-

content observed from M2-matrix to the lawsonite-rich M3-matrix, points to embrittlement then fluid ingression.

(3) **Trace element composition of the three, successive matrices of LSZ depicts the progressive change in the fluids involved in the brecciation**, reflecting a progressive opening of the system. In detail, **M1 matrix crystallized during percolation of fluids buffered by the Intermediate metagabbros** (Grt-bearing Mg-Al metagabbros), **M2 matrix by a mixing of fluids derived from the surrounding Intermediate metagabbros and from serpentinites**, and **M3 matrix from external fluids buffered by serpentinites**.

(4) Similarly to the matrices, the three generations of HP-veins from LSZ reflect a progressive **transition from “closed” geochemical system** (pre-brecciation Veins-1, with trace element composition similar to that of the host Fe-Ti metagabbros) **to “open” system** (syn-brecciation Veins-2 and Veins-3, progressively enriched in serpentine-buffered trace elements).

(5) In the **poorly-developed breccia from ISZ**, the occurrence of a M2 matrix with petrographic and geochemical characteristics similar to those of LSZ M2 suggests coeval brecciation in both shear zones. However, a major difference is the limited extension of M2 and complete lack of M3 in the ISZ, compared to the km-scale connection in the LSZ. Pervasive fluid ingression during M3 matrix formation is thus restricted to areas of extensive M2 brecciation, which in turn could be controlled by the extent of M1 brecciation (absent in the ISZ). The absence of the Lws + Omp-bearing M3 matrix in the ISZ also suggests that breccia blocks disseminated in the LSZ were not derived from the ISZ, contrary to the earlier hypothesis of Angiboust et al. (2012a-b).

(6) The occurrence, at the base of the coherent Mg-Al metagabbros of Lago Superiore Unit, of meter-thick layers of eclogite breccias (with M1 and M2 but lacking M3 matrix) confirm that the

metagabbro blocks dispersed in the LSZ were locally detached from the base of the Mg-Al metagabbro cliff and not transported away from the ISZ. Moreover, the occurrence of M3 matrix in the detached blocks/slivers, whereas it is absent from the undetached sliver mentioned above, suggests that **detachment only occurs in places affected by the M3 brecciation event (and already fragmented and inter-connected by the M2 event).**

(7) **Brecciation controlled the initial stages of strain localization within the LSZ.** It preferentially occurred in Fe-Ti gabbros embedded in Mg-Al metagabbros, suggesting that the onset of brecciation was controlled by the rheological contrast between the two metagabbros, rheological changes induced by metamorphic reactions, and heterogeneous fluid release in neighboring contrasted lithologies.

(8) **After eclogite-facies brecciation (M1 to M3 matrix crystallization) further strain localization into the LSZ, marked by the incorporation of unbrecciated mafic and ultramafic blocks** and by shear zone network widening, was promoted by fluids and metasomatism.

(9) **The distribution of breccia-blocks and metagabbros slivers in the LSZ is not chaotic but clearly structured,** with only minor block rotation inside the shear zone matrix. Blocks comminution and disaggregation is observed only at the footwall of the LSZ, between the base of the bigger Mg-Al metagabbros slivers and the more coherent serpentinite of the BSU.

(10) Observation on preserved breccia planes of the full transition from intact metagabbro to crackle, mosaic and chaotic breccia, together with the presence of crushed matrix and the occurrence of minerals fractured and offset along omphacite-bearing planes **suggest that Monviso eclogite breccias were generated by instantaneous brittle rupture.** Nevertheless, the limited extension of breccia outcrops and the impossibility to run statistical analysis on their descriptive

parameters (clasts size, sphericity, and fracture-network geometry) **do not permit to ascribe with certainty the generation of Monviso eclogite-breccia to coseismic events.**

7.2 – Perspectives

Further investigations will be necessary to better constrain the brecciation kinematics at eclogite-facies conditions.

- **More detailed PT estimations** (by pseudosection modeling) are required to better constrain the PT conditions of the successive brecciation events. In particular, determining precisely which steps can be ascribed to peak versus incipient retrograde path is necessary to precise the timing of the shift of deformation localization, from inside the Monviso slice (LSZ) to the base of the slice (leading to its exhumation). Such pseudosection should be run on both Mg-Al and Fe-Ti metagabbro compositions, corresponding to the blocks analysed in this study, in order to validate the order of reactions leading to each brecciation event (e.g., the mineral apparition/destabilization deduced by trace element patterns in matrices/veins) and to better constrain the timing and extent of fluid release.

- **HP-HT deformation experiments (Griggs apparatus, ENS, collab. A. Schubnel)** will be designed to test the hypotheses derived from field observations. A first set of experiments will be run on Fe-Ti gabbro only and Fe-Ti / Mg-Al gabbro sandwiches, with and without serpentinite, in PT conditions allowing serpentinite dehydration, at different strain rates. The aim is to evaluate the respective influence of fluid production, rheological contrasts and strain rate in the brecciation process. The geochemical study of the newly-formed matrix minerals will help track the reactions and determining the impact of the serpentinite-derived fluid on mineral trace element signature.

Chemical experiments following the *wet eclogite* → *dry eclogite* transition (e.g., the glaucophane + lawsonite = garnet + omphacite + quartz + H₂O dehydration reactions leading to localized M1 brecciation) are also envisioned. The aim is to monitor the kinetics, order of reactions and fluids produced as a function of the (I) *initial lithology*, (II) *presence/absence of initial fluid*, (III) *fluid pressure* and (IV) *strain rate*. The goal of this study would be to characterize the amount, the kinematics of fluid production (pulse versus continuous fluid liberation) and the trace element redistribution (among *reactants* / *products* / *trapped fluids*), in order to better track fluid sources during the brecciation process.

- Finally, on selected samples displaying garnet offsets along omphacite-bearing fractures, a microstructural analysis (SEM + EBSD) could be run to evaluate the potential seismic deformation, following on the recent findings of Austrheim et al. (2017) about garnet fragmentation during deep crustal earthquakes.

Bibliography

- Abers, G. A., Nakajima, J., van Keken, P. E., Kita, S., & Hacker, B. R. (2013). Thermal–petrological controls on the location of earthquakes within subducting plates. *Earth and Planetary Science Letters*, 369, 178–187. <https://doi.org/10.1016/j.epsl.2013.03.022>
- Abers, G. A., van Keken, P. E., Kneller, E. A., Ferris, A., & Stachnik, J. C. (2006). The thermal structure of subduction zones constrained by seismic imaging: Implications for slab dehydration and wedge flow. *Earth and Planetary Science Letters*, 241(3), 387–397. <https://doi.org/10.1016/j.epsl.2005.11.055>
- Agard, P., Jolivet, L., & Goffé, B. (2001). Tectonometamorphic evolution of the Schistes Lustrés Complex; implications for the exhumation of HP and UHP rocks in the Western Alps. *Bulletin de La Société Géologique de France*, 172(5), 617–636. <https://doi.org/10.2113/172.5.617>
- Agard, P., Monié, P., Jolivet, L., & Goffé, B. (2002). Exhumation of the Schistes Lustrés complex: in situ laser probe $^{40}\text{Ar}/^{39}\text{Ar}$ constraints and implications for the Western Alps. *Journal of Metamorphic Geology*, 20(6), 599–618.
- Ague, J. J. (2007). Models of permeability contrasts in subduction zone mélange: Implications for gradients in fluid fluxes, Syros and Tinos Islands, Greece. *Chemical Geology*, 239(3), 217–227. <https://doi.org/10.1016/j.chemgeo.2006.08.012>
- Ampferer, O. (1906). *über das Bewegungsbild von Faltengebirgen*. Verlag der kk geologischen Reichsanstalt.
- Ampferer, O. (1925). Über Kontinentverschiebungen. *Naturwissenschaften*, 13(31), 669–675.
- Ampferer, O. (1941). *Gedanken über das Bewegungsbild des atlantischen Raumes*. Hölder-Pichler-Tempsky [Abt. Akad. d. Wiss.]. Retrieved from http://www.zobodat.at/stable/pdf/SBAWW_150_0019-0035.pdf
- Ampferer, O., & Hammer, W. (1911). *Geologischer Querschnitt durch die Ostalpen vom Allgäu zum Gardasee*. Verlag der kk Geologischen Reichsanstalt in Kommission bei R. Lechner (W. Müller), k. u. k. Hofbuchhandlung (IS).
- Amstutz, A. (1951). Sur l'évolution des structures alpines. *Arch. Sci*, 4(5), 323–329.
- Andersen, T. B., & Austrheim, H. (2006). Fossil earthquakes recorded by pseudotachylytes in mantle peridotite from the Alpine subduction complex of Corsica. *Earth and Planetary Science Letters*, 242(1), 58–72. <https://doi.org/10.1016/j.epsl.2005.11.058>
- Angiboust, S., & Agard, P. (2010). Initial water budget: The key to detaching large volumes of eclogitized oceanic crust along the subduction channel? *Lithos*, 120(3–4), 453–474. <https://doi.org/10.1016/j.lithos.2010.09.007>
- Angiboust, S., Agard, P., Raimbourg, H., Yamato, P., & Huet, B. (2011). Subduction interface processes recorded by eclogite-facies shear zones (Monviso, W. Alps). *Lithos*, 127(1–2), 222–238. <https://doi.org/10.1016/j.lithos.2011.09.004>

- Angiboust, S., Agard, P., Yamato, P., & Raimbourg, H. (2012). Eclogite breccias in a subducted ophiolite: A record of intermediate-depth earthquakes? *Geology*, 40(8), 707–710. <https://doi.org/10.1130/G32925.1>
- Angiboust, S., Langdon, R., Agard, P., Waters, D., & Chopin, C. (2012). Eclogitization of the Monviso ophiolite (W. Alps) and implications on subduction dynamics: MONVISO ECLOGITES AND SUBDUCTION DYNAMICS. *Journal of Metamorphic Geology*, 30(1), 37–61. <https://doi.org/10.1111/j.1525-1314.2011.00951.x>
- Angiboust, S., Pettke, T., Hoog, J. C. M. D., Caron, B., & Oncken, O. (2014). Channelized Fluid Flow and Eclogite-facies Metasomatism along the Subduction Shear Zone. *Journal of Petrology*, 55(5), 883–916. <https://doi.org/10.1093/petrology/egu010>
- Arai, S. (1992). Chemistry of chromian spinel in volcanic rocks as a potential guide to magma chemistry. *Mineralogical Magazine*, 56(383), 173–184.
- Arcay, D., Tric, E., & Doin, M.-P. (2005). Numerical simulations of subduction zones. *Physics of the Earth and Planetary Interiors*, 149(1), 133–153. <https://doi.org/10.1016/j.pepi.2004.08.020>
- Argand, E., Blösch, E., Heim, A., & Heim, A. (1911). *I. Les nappes de recouvrement des Alpes pennines et leurs prolongements structuraux*. In Kommission bei A. Francke (vorm. Schmid & Francke).
- Bach, W., Alt, J. C., Niu, Y., Humphris, S. E., Erzinger, J., & Dick, H. J. B. (2001). The geochemical consequences of late-stage low-grade alteration of lower ocean crust at the SW Indian Ridge: results from ODP Hole 735B (Leg 176). *Geochimica et Cosmochimica Acta*, 65(19), 3267–3287. [https://doi.org/10.1016/S0016-7037\(01\)00677-9](https://doi.org/10.1016/S0016-7037(01)00677-9)
- Bachmann, R., Oncken, O., Glodny, J., Seifert, W., Georgieva, V., & Sudo, M. (2009). Exposed plate interface in the European Alps reveals fabric styles and gradients related to an ancient seismogenic coupling zone. *Journal of Geophysical Research: Solid Earth*, 114(B5), B05402. <https://doi.org/10.1029/2008JB005927>
- Balestro, G., Festa, A., & Tartarotti, P. (2015). Tectonic significance of different block-in-matrix structures in exhumed convergent plate margins: examples from oceanic and continental HP rocks in Inner Western Alps (northwest Italy). *International Geology Review*, 57(5–8), 581–605. <https://doi.org/10.1080/00206814.2014.943307>
- Balestro, G., Fioraso, G., & Lombardo, B. (2011). Geological map of the upper Pellice Valley (Italian Western Alps). *Journal of Maps*, 7(1), 634–654. <https://doi.org/10.4113/jom.2011.1213>
- Balestro, G., Fioraso, G., & Lombardo, B. (2013). Geological map of the Monviso massif (Western Alps). *Journal of Maps*, 9(4), 623–634. <https://doi.org/10.1080/17445647.2013.842507>
- Balestro, G., Lombardo, B., Vaggelli, G., Borghi, A., Festa, A., & Gattiglio, M. (2014). Tectonostratigraphy of the northern Monviso Meta-ophiolite Complex (Western Alps). *Italian Journal of Geosciences*, 133(3), 409–426. <https://doi.org/10.3301/IJG.2014.13>
- Ballevre, M., Lagabriele, Y., & Merle, O. (1990). Tertiary ductile normal faulting as a consequence of lithospheric stacking in the western Alps. *Mémoires de La Société Géologique de France*, 156, 227–236.

- Bebout, G. E. (2007). Metamorphic chemical geodynamics of subduction zones. *Earth and Planetary Science Letters*, 260(3), 373–393. <https://doi.org/10.1016/j.epsl.2007.05.050>
- Bebout, G. E., & Barton, M. D. (2002). Tectonic and metasomatic mixing in a high-T, subduction-zone mélange—insights into the geochemical evolution of the slab–mantle interface. *Chemical Geology*, 187(1), 79–106. [https://doi.org/10.1016/S0009-2541\(02\)00019-0](https://doi.org/10.1016/S0009-2541(02)00019-0)
- Beltrando, M., Rubatto, D., & Manatschal, G. (2010). From passive margins to orogens: The link between ocean-continent transition zones and (ultra) high-pressure metamorphism. *Geology*, 38(6), 559–562.
- Bertrand, M. A. (1894). *Sur la structure des Alpes françaises et récurrence de certains faciès sédimentaires*.
- Blake, M. C., & Jayko, A. S. (1990). Uplift of very high pressure rocks in the western Alps : evidence for structural attenuation along low-angle faults. In *Mémoires de la Société géologique de France* (Vol. 156, pp. 237–246). Société géologique de France. Retrieved from <http://cat.inist.fr/?aModele=afficheN&cpsidt=4985750>
- Blake Jr, M. C., Moore, D. E., & Jayko, A. S. (1995). The role of serpentinite melanges in the unroofing of UHPM rocks: An example from the Western Alps of Italy. *Ultrahigh Pressure Metamorphism*, 182–205.
- Bolfan-Casanova, N. (2016). Water in the Earth’s mantle. *Mineralogical Magazine*, 69(3), 229–257. <https://doi.org/10.1180/0026461056930248>
- Bonatti, E. (1976). Serpentinite protrusions in the oceanic crust. *Earth and Planetary Science Letters*, 32(2), 107–113. [https://doi.org/10.1016/0012-821X\(76\)90048-0](https://doi.org/10.1016/0012-821X(76)90048-0)
- Bostock, M. G., Hyndman, R. D., Rondenay, S., & Peacock, S. M. (2002). An inverted continental Moho and serpentinitization of the forearc mantle. *Nature*, 417(6888), 536–538.
- Bousquet, R., Goffé, B., Le Pichon, X., de Capitani, C., Chopin, C., & Henry, P. (2005). Comment on “Subduction factory: 1. Theoretical mineralogy, densities, seismic wave speeds, and H₂O contents” by Bradley R. Hacker, Geoffrey A. Abers, and Simon M. Peacock. *Journal of Geophysical Research: Solid Earth*, 110(B2), B02206. <https://doi.org/10.1029/2004JB003450>
- Breeding, C. M., Ague, J. J., & Bröcker, M. (2004). Fluid–metasedimentary rock interactions in subduction-zone mélange: Implications for the chemical composition of arc magmas. *Geology*, 32(12), 1041–1044. <https://doi.org/10.1130/G20877.1>
- Brovarone, A. V., Groppo, C., Hetényi, G., Compagnoni, R., & Malavieille, J. (2011). Coexistence of lawsonite-bearing eclogite and blueschist: phase equilibria modelling of Alpine Corsica metabasalts and petrological evolution of subducting slabs. *Journal of Metamorphic Geology*, 29(5), 583–600. <https://doi.org/10.1111/j.1525-1314.2011.00931.x>
- Bruce Watson, E., & Brenan, J. M. (1987). Fluids in the lithosphere, 1. Experimentally-determined wetting characteristics of CO₂H₂O fluids and their implications for fluid transport, host-rock physical properties, and fluid inclusion formation. *Earth and Planetary Science Letters*, 85(4), 497–515. [https://doi.org/10.1016/0012-821X\(87\)90144-0](https://doi.org/10.1016/0012-821X(87)90144-0)
- Brudzinski, M. R., Thurber, C. H., Hacker, B. R., & Engdahl, E. R. (2007). Global Prevalence of Double Benioff Zones. *Science*, 316(5830), 1472–1474. <https://doi.org/10.1126/science.1139204>

- Butler, J. P., Beaumont, C., & Jamieson, R. A. (2013). The Alps 1: A working geodynamic model for burial and exhumation of (ultra)high-pressure rocks in Alpine-type orogens. *Earth and Planetary Science Letters*, 377, 114–131. <https://doi.org/10.1016/j.epsl.2013.06.039>
- Carignan, J., Hild, P., Mevelle, G., Morel, J., & Yeghicheyan, D. (2001). Routine Analyses of Trace Elements in Geological Samples using Flow Injection and Low Pressure On-Line Liquid Chromatography Coupled to ICP-MS: A Study of Geochemical Reference Materials BR, DR-N, UB-N, AN-G and GH. *Geostandards Newsletter*, 25(2–3), 187–198. <https://doi.org/10.1111/j.1751-908X.2001.tb00595.x>
- Carmichael, I. S. E. (1964). The Petrology of Thingmuli, a Tertiary Volcano in Eastern Iceland. *Journal of Petrology*, 5(3), 435–460. <https://doi.org/10.1093/petrology/5.3.435>
- Carpenter, M. A. (1982). Time-temperature-transformation (TTT) analysis of cation disordering in omphacite. *Contributions to Mineralogy and Petrology*, 78(4), 433–440. <https://doi.org/10.1007/BF00375205>
- Castelli, D., Rolfo, F., Groppo, C., & Compagnoni, R. (2007). Impure marbles from the UHP Brossasco-Isasca Unit (Dora-Maira Massif, western Alps): evidence for Alpine equilibration in the diamond stability field and evaluation of the X(CO₂) fluid evolution. *Journal of Metamorphic Geology*, 25(6), 587–603. <https://doi.org/10.1111/j.1525-1314.2007.00716.x>
- Castelli, D., Rostagno, C., & Lombardo, B. (2002). JD-QTZ-BEARING METAPLAGIOGRANITE FROM THE MONVISO META-OPHIOLITE (WESTERN ALPS). *Ophioliti*, 27(2), 81–90. <https://doi.org/10.4454/ofioliti.v27i2.178>
- Catlos, E. J., & Sorensen, S. S. (2003). Phengite-Based Chronology of K- and Ba-Rich Fluid Flow in Two Paleosubduction Zones. *Science*, 299(5603), 92–95. <https://doi.org/10.1126/science.1076977>
- Cavallera, G. (1978). *Le ofioliti metamorfiche del Lonvisonelle alto valli Po e del Guil*. Università di Torino, Istituto di Geologia Università di Torino.
- Chernak, L. J., & Hirth, G. (2010). Deformation of antigorite serpentinite at high temperature and pressure. *Earth and Planetary Science Letters*, 296(1), 23–33. <https://doi.org/10.1016/j.epsl.2010.04.035>
- Chinner, G. A., & Dixon, J. E. (1973). Some High-pressure Parageneses of the Allalin Gabbro, Valais, Switzerland. *Journal of Petrology*, 14(2), 185–202. <https://doi.org/10.1093/petrology/14.2.185>
- Chopin, C. (1984). Coesite and pure pyrope in high-grade blueschists of the Western Alps: a first record and some consequences. *Contributions to Mineralogy and Petrology*, 86(2), 107–118. <https://doi.org/10.1007/BF00381838>
- Chopin, C. (2003). Ultrahigh-pressure metamorphism: tracing continental crust into the mantle. *Earth and Planetary Science Letters*, 212(1), 1–14. [https://doi.org/10.1016/S0012-821X\(03\)00261-9](https://doi.org/10.1016/S0012-821X(03)00261-9)
- Coleman, R. G., & Wang, X. (2005). *Ultrahigh Pressure Metamorphism*. Cambridge University Press.
- Compagnoni, R., Rolfo, F., Manavella, F., & Salusso, F. (2007). Jadeitite in the Monviso meta-ophiolite, Piemonte Zone, Italian western Alps. *Per. Mineral*, 76(2–3), 79–89.
- Coward, M., & Dietrich, D. (1989). Alpine tectonics — an overview. *Geological Society, London, Special Publications*, 45(1), 1–29. <https://doi.org/10.1144/GSL.SP.1989.045.01.01>

- Daemen, J. J. K., & Schultz, R. A. (1995). *Rock Mechanics: Proceedings of the 35th US Symposium on Rock Mechanics*. CRC Press.
- Dal Piaz, G. V., Bistacchi, A., & Massironi, M. (2003). Geological outline of the Alps. *Episodes*, 26(3), 175–180.
- Davies, J. H. (1999). The role of hydraulic fractures and intermediate-depth earthquakes in generating subduction-zone magmatism. *Nature*, 398(6723), 142–145. <https://doi.org/10.1038/18202>
- De La Pierre, F., Lozar, F., & Polino, R. (n.d.). L'utilizzo della tettonostratigrafia per la rappresentazione cartografica delle successioni metasedimentarie nelle aree di catena. *Mem. Soc. Geol.*, 49, 195–206.
- Debret, B., Nicollet, C., Andreani, M., Schwartz, S., & Godard, M. (2013). Three steps of serpentinization in an eclogitized oceanic serpentization front (Lanzo Massif – Western Alps). *Journal of Metamorphic Geology*, 31(2), 165–186. <https://doi.org/10.1111/jmg.12008>
- Deschamps, F., Godard, M., Guillot, S., & Hattori, K. (2013). Geochemistry of subduction zone serpentinites: A review. *Lithos*, 178, 96–127. <https://doi.org/10.1016/j.lithos.2013.05.019>
- Deseta, N., Ashwal, L. D., & Andersen, T. B. (2014). Initiating intermediate-depth earthquakes: Insights from a HP–LT ophiolite from Corsica. *Lithos*, 206, 127–146. <https://doi.org/10.1016/j.lithos.2014.07.022>
- Dewey, J. F., & Bird, J. M. (1970). Mountain belts and the new global tectonics. *Journal of Geophysical Research*, 75(14), 2625–2647. <https://doi.org/10.1029/JB075i014p02625>
- Dobson, D. P., Meredith, P. G., & Boon, S. A. (2002). Simulation of Subduction Zone Seismicity by Dehydration of Serpentine. *Science*, 298(5597), 1407–1410. <https://doi.org/10.1126/science.1075390>
- Dragert, H., Wang, K., & James, T. S. (2001). A Silent Slip Event on the Deeper Cascadia Subduction Interface. *Science*, 292(5521), 1525–1528. <https://doi.org/10.1126/science.1060152>
- Duchêne, S., Blichert-Toft, J., Luais, B., Télouk, P., Lardeaux, J. M., Albarède, F., & others. (1997). The Lu–Hf dating of garnets and the ages of the Alpine high-pressure metamorphism. *Nature*, 387(6633), 586–588.
- Dutto, F., Godone, F., & Mortara, G. (1991). L'écroulement du glacier supérieur de Coolidge. (Paroi nord du Mont Viso, Alpes occidentales). *Revue de géographie alpine*, 79(2), 7–18. <https://doi.org/10.3406/rga.1991.3597>
- Escartin, J., Cannat, M., Pouliquen, G., Rabain, A., & Lin, J. (2001). Crustal thickness of V-shaped ridges south of the Azores: Interaction of the Mid-Atlantic Ridge (36°–39°N) and the Azores hot spot. *Journal of Geophysical Research: Solid Earth*, 106(B10), 21719–21735. <https://doi.org/10.1029/2001JB000224>
- Ewerling, K., Obermüller, G., Kirst, F., Froitzheim, N., Nagel, T., & Sandmann, S. (2013). The continental Etna-Levaz slice (Western Alps, Italy): Tectonometamorphic evolution of an extensional allochthon (Vol. 15, p. EGU2013-7921). Presented at the EGU General Assembly Conference Abstracts. Retrieved from <http://adsabs.harvard.edu/abs/2013EGUGA..15.7921E>

- Ferrand, T. P., Hilairret, N., Incel, S., Deldicque, D., Labrousse, L., Gasc, J., ... Schubnel, A. (2017). Dehydration-driven stress transfer triggers intermediate-depth earthquakes. *Nature Communications*, 8, ncomms15247. <https://doi.org/10.1038/ncomms15247>
- Festa, A., Balestro, G., Dilek, Y., & Tartarotti, P. (2015). A Jurassic oceanic core complex in the high-pressure Monviso ophiolite (western Alps, NW Italy). *Lithosphere*, 7(6), 646–652. <https://doi.org/10.1130/L458.1>
- Festa, A., Pini, G. A., Dilek, Y., & Codegone, G. (2010). Mélanges and mélange-forming processes: a historical overview and new concepts. *International Geology Review*, 52(10–12), 1040–1105. <https://doi.org/10.1080/00206810903557704>
- Fiora, L. (1970). *Geologia delle alte valli del Guil e della Vallanta* (Relazione di rilevamento). Istituto di Geologia Università di Torino.
- Franchi, S. (n.d.). Ancora sull'età mesozoica delle pietre verdi nelle Alpi Occidentali e nell'Appennino Ligure. *B.C.G.I.*, 35, 125–179.
- Fumagalli, P., & Poli, S. (2005). High pressure behaviour of hydrates and carbonates: experimental constraints in mafic and ultramafic systems. Presented at the Advances in Petrology : a meeting in honour of prof. Ezio Callegari. Retrieved from <https://air.unimi.it/handle/2434/8597#.WW4r0ITyiVM>
- Fusseis, F., Handy, M. R., & Schrank, C. (2006). Networking of shear zones at the brittle-to-viscous transition (Cap de Creus, NE Spain). *Journal of Structural Geology*, 28(7), 1228–1243. <https://doi.org/10.1016/j.jsg.2006.03.022>
- Gabudianu Radulescu, I., Rubatto, D., Gregory, C., & Compagnoni, R. (2009). The age of HP metamorphism in the Gran Paradiso Massif, Western Alps: A petrological and geochronological study of “silvery micaschists.” *Lithos*, 110(1), 95–108. <https://doi.org/10.1016/j.lithos.2008.12.008>
- Gastaldi, B. (n.d.). Spaccato geologico lungo le valli superiori del Po e delle Varaita. *B.C.G.I.*, 7, 104–111.
- Gebauer, D., Schertl, H.-P., Brix, M., & Schreyer, W. (1997). 35 Ma old ultrahigh-pressure metamorphism and evidence for very rapid exhumation in the Dora Maira Massif, Western Alps. *Lithos*, 41(1), 5–24. [https://doi.org/10.1016/S0024-4937\(97\)82002-6](https://doi.org/10.1016/S0024-4937(97)82002-6)
- Goffe, B., & Chopin, C. (1986). High-pressure metamorphism in the Western Alps: zoneography of metapelites, chronology and consequences. In *Schweizerische Mineralogische und Petrographische Mitteilungen* (Vol. 66, pp. 41–52). Leemann. Retrieved from <http://cat.inist.fr/?aModele=afficheN&cpsidt=7948123>
- Green, H. W., & Houston, H. (1995). The mechanics of deep earthquakes. *Annual Review of Earth and Planetary Sciences*, 23, 169–214.
- Groppo, C., & Castelli, D. (2010). Prograde P–T Evolution of a Lawsonite Eclogite from the Monviso Meta-ophiolite (Western Alps): Dehydration and Redox Reactions during Subduction of Oceanic FeTi-oxide Gabbro. *Journal of Petrology*, 51(12), 2489–2514. <https://doi.org/10.1093/petrology/egq065>

- Groppo, C., & Compagnoni, R. (2007). Metamorphic veins from the serpentinites of the Piemonte Zone, western Alps, Italy: a review. *Periodico Di Mineralogia*, 76, 127–153.
- Groppo, C., Lombardo, B., Castelli, D., & Compagnoni, R. (2007). Exhumation History of the UHPM Brossasco-Isasca Unit, Dora-Maira Massif, as Inferred from a Phengite-Amphibole Eclogite. *International Geology Review*, 49(2), 142–168. <https://doi.org/10.2747/0020-6814.49.2.142>
- Guillong, M., Meier, D. L., Allan, M. M., Heinrich, C. A., & Yardley, B. W. (2008). Appendix A6: SILLS: A MATLAB-based program for the reduction of laser ablation ICP-MS data of homogeneous materials and inclusions. *Mineralogical Association of Canada Short Course*, 40, 328–333.
- Guillot, S., Schwartz, S., Hattori, K., Auzende, A., & Lardeaux, J. (2004). The Monviso ophiolitic massif (Western Alps), a section through a serpentinite subduction channel. *Journal of the Virtual Explorer*, 16, 17 pages.
- Hacker, B. R., & Abers, G. A. (2004). Subduction Factory 3: An Excel worksheet and macro for calculating the densities, seismic wave speeds, and H₂O contents of minerals and rocks at pressure and temperature. *Geochemistry, Geophysics, Geosystems*, 5(1), Q01005. <https://doi.org/10.1029/2003GC000614>
- Hacker, B. R., Abers, G. A., & Peacock, S. M. (2003). Subduction factory 1. Theoretical mineralogy, densities, seismic wave speeds, and H₂O contents: SUBDUCTION ZONE MINERALOGY AND PHYSICAL PROPERTIES. *Journal of Geophysical Research: Solid Earth*, 108(B1). <https://doi.org/10.1029/2001JB001127>
- Hacker, B. R., Peacock, S. M., Abers, G. A., & Holloway, S. D. (2003). Subduction factory 2. Are intermediate-depth earthquakes in subducting slabs linked to metamorphic dehydration reactions?: SUBDUCTION ZONE EARTHQUAKES AND DEHYDRATION. *Journal of Geophysical Research: Solid Earth*, 108(B1). <https://doi.org/10.1029/2001JB001129>
- Handy, M. R., Franz, L., Heller, F., Janott, B., & Zurrbruggen, R. (1999). Multistage accretion and exhumation of the continental crust (Ivrea crustal section, Italy and Switzerland). *Tectonics*, 18(6), 1154–1177. <https://doi.org/10.1029/1999TC900034>
- Hans, L. (1991). The arc of the Western Alps today. *Eclogae Geologicae Helvetiae*, 84(3), 359–631.
- Harry W. Green, & Houston, H. (1995). The Mechanics of Deep Earthquakes. *Annual Review of Earth and Planetary Sciences*, 23(1), 169–213. <https://doi.org/10.1146/annurev.ea.23.050195.001125>
- Hattori, K. H., & Guillot, S. (2007). Geochemical character of serpentinites associated with high- to ultrahigh-pressure metamorphic rocks in the Alps, Cuba, and the Himalayas: Recycling of elements in subduction zones. *Geochemistry, Geophysics, Geosystems*, 8(9), Q09010. <https://doi.org/10.1029/2007GC001594>
- Hawemann, F., Mancktelow, N., Wex, S., Camacho, A., & Pennacchioni, G. (2015). Natural constraints on the rheology of the lower continental crust (Musgrave Ranges, Central Australia) (Vol. 17, p. 2718). Presented at the EGU General Assembly Conference Abstracts. Retrieved from <http://adsabs.harvard.edu/abs/2015EGUGA..17.2718H>

- Hermann, J., Spandler, C., Hack, A., & Korsakov, A. V. (2006). Aqueous fluids and hydrous melts in high-pressure and ultra-high pressure rocks: Implications for element transfer in subduction zones. *Lithos*, 92(3), 399–417. <https://doi.org/10.1016/j.lithos.2006.03.055>
- Hilaret, N., Reynard, B., Wang, Y., Daniel, I., Merkel, S., Nishiyama, N., & Petitgirard, S. (2007). High-Pressure Creep of Serpentine, Interseismic Deformation, and Initiation of Subduction. *Science*, 318(5858), 1910–1913. <https://doi.org/10.1126/science.1148494>
- Ikehata, K., & Arai, S. (2015). Metasomatic formation of kosmochlor-bearing diopside in peridotite xenoliths from North Island, New Zealand. *American Mineralogist*, 89(10), 1396–1404. <https://doi.org/10.2138/am-2004-1006>
- Ikesawa, E., Sakaguchi, A., & Kimura, G. (2003). Pseudotachylyte from an ancient accretionary complex: Evidence for melt generation during seismic slip along a master décollement? *Geology*, 31(7), 637–640. [https://doi.org/10.1130/0091-7613\(2003\)031<0637:PFAAAC>2.0.CO;2](https://doi.org/10.1130/0091-7613(2003)031<0637:PFAAAC>2.0.CO;2)
- Incel, S., Hilaret, N., Labrousse, L., John, T., Deldicque, D., Ferrand, T., ... Schubnel, A. (2017). Laboratory earthquakes triggered during eclogitization of lawsonite-bearing blueschist. *Earth and Planetary Science Letters*, 459, 320–331. <https://doi.org/10.1016/j.epsl.2016.11.047>
- Iwamori, H. (2004). Phase relations of peridotites under H₂O-saturated conditions and ability of subducting plates for transportation of H₂O. *Earth and Planetary Science Letters*, 227(1), 57–71. <https://doi.org/10.1016/j.epsl.2004.08.013>
- Jébrak, M. (1997). Hydrothermal breccias in vein-type ore deposits: A review of mechanisms, morphology and size distribution. *Ore Geology Reviews*, 12(3), 111–134. [https://doi.org/10.1016/S0169-1368\(97\)00009-7](https://doi.org/10.1016/S0169-1368(97)00009-7)
- Jiao, W., Silver, P. G., Fei, Y., & Prewitt, C. T. (2000). Do intermediate- and deep-focus earthquakes occur on preexisting weak zones? An examination of the Tonga subduction zone. *Journal of Geophysical Research: Solid Earth*, 105(B12), 28125–28138. <https://doi.org/10.1029/2000JB900314>
- Jin, Z.-M., Zhang, J., Green, H. W., & Jin, S. (2001). Eclogite rheology: Implications for subducted lithosphere. *Geology*, 29(8), 667–670. [https://doi.org/10.1130/0091-7613\(2001\)029<0667:ERIFSL>2.0.CO;2](https://doi.org/10.1130/0091-7613(2001)029<0667:ERIFSL>2.0.CO;2)
- John, T., Gussone, N., Podladchikov, Y. Y., Bebout, G. E., Dohmen, R., Halama, R., ... Seitz, H.-M. (2012). Volcanic arcs fed by rapid pulsed fluid flow through subducting slabs. *Nature Geoscience*, 5(7), 489–492. <https://doi.org/10.1038/ngeo1482>
- John, T., Medvedev, S., Rüpke, L. H., Andersen, T. B., Podladchikov, Y. Y., & Austrheim, H. (2009). Generation of intermediate-depth earthquakes by self-localizing thermal runaway. *Nature Geoscience*, 2(2), 137–140. <https://doi.org/10.1038/ngeo419>
- John, T., Scambelluri, M., Frische, M., Barnes, J. D., & Bach, W. (2011). Dehydration of subducting serpentinite: Implications for halogen mobility in subduction zones and the deep halogen cycle. *Earth and Planetary Science Letters*, 308(1), 65–76. <https://doi.org/10.1016/j.epsl.2011.05.038>
- John, T., & Schenk, V. (2006). Interrelations between intermediate-depth earthquakes and fluid flow within subducting oceanic plates: Constraints from eclogite facies pseudotachylytes. *Geology*, 34(7), 557–560. <https://doi.org/10.1130/G22411.1>

- Jung, H., & Green, H. W. (2004). Experimental Faulting of Serpentine during Dehydration: Implications for Earthquakes, Seismic Low-Velocity Zones, and Anomalous Hypocenter Distributions in Subduction Zones. *International Geology Review*, 46(12), 1089–1102. <https://doi.org/10.2747/0020-6814.46.12.1089>
- Kawamoto, T., Hervig, R. L., & Holloway, J. R. (1996). Experimental evidence for a hydrous transition zone in the early Earth's mantle. *Earth and Planetary Science Letters*, 142(3), 587–592. [https://doi.org/10.1016/0012-821X\(96\)00113-6](https://doi.org/10.1016/0012-821X(96)00113-6)
- Kawano, S., Katayama, I., & Okazaki, K. (2011). Permeability anisotropy of serpentinite and fluid pathways in a subduction zone. *Geology*, 39(10), 939–942. <https://doi.org/10.1130/G32173.1>
- Kelemen, P. B., & Hirth, G. (2007). A periodic shear-heating mechanism for intermediate-depth earthquakes in the mantle. *Nature*, 446(7137), 787–790. <https://doi.org/10.1038/nature05717>
- Kessel, R., Schmidt, M. W., Ulmer, P., & Pettke, T. (2005). Trace element signature of subduction-zone fluids, melts and supercritical liquids at 120–180 km depth. *Nature*, 437(7059), 724–727. <https://doi.org/10.1038/nature03971>
- Kirby, S., Engdahl, R., & Denlinger, R. (1996). Intermediate-depth intraslab earthquakes and arc volcanism as physical expressions of crustal and uppermost mantle metamorphism in subducting slabs. *Subduction Top to Bottom*, 195–214.
- Kirby, S. H., & Kronenberg, A. K. (1984). Deformation of clinopyroxenite: Evidence for a transition in flow mechanisms and semibrittle behavior. *Journal of Geophysical Research: Solid Earth*, 89(B5), 3177–3192. <https://doi.org/10.1029/JB089iB05p03177>
- Kita, S., Okada, T., Nakajima, J., Matsuzawa, T., & Hasegawa, A. (2006). Existence of a seismic belt in the upper plane of the double seismic zone extending in the along-arc direction at depths of 70–100 km beneath NE Japan. *Geophysical Research Letters*, 33(24), L24310. <https://doi.org/10.1029/2006GL028239>
- Kroslakova, I., & Günther, D. (2007). Elemental fractionation in laser ablation-inductively coupled plasma- mass spectrometry : evidence for mass load induced matrix effects in the ICP during ablation of a silicate glass. *Journal of Analytical Atomic Spectrometry*, 22(1), 51–62. <https://doi.org/10.1039/B606522H>
- Kuge, K., Kase, Y., Urata, Y., Campos, J., & Perez, A. (2010). Rupture characteristics of the 2005 Tarapaca, northern Chile, intermediate-depth earthquake: Evidence for heterogeneous fluid distribution across the subducting oceanic plate? *Journal of Geophysical Research: Solid Earth*, 115(B9), B09305. <https://doi.org/10.1029/2009JB007106>
- Lagabrielle, Y., & Cannat, M. (1990). Alpine Jurassic ophiolites resemble the modern central Atlantic basement. *Geology*, 18(4), 319–322. [https://doi.org/10.1130/0091-7613\(1990\)018<0319:AJORTM>2.3.CO;2](https://doi.org/10.1130/0091-7613(1990)018<0319:AJORTM>2.3.CO;2)
- Lagabrielle, Y., & Lemoine, M. (1997). Alpine, Corsican and Apennine ophiolites: the slow-spreading ridge model. *Comptes Rendus de l'Académie Des Sciences - Series IIA - Earth and Planetary Science*, 325(12), 909–920. [https://doi.org/10.1016/S1251-8050\(97\)82369-5](https://doi.org/10.1016/S1251-8050(97)82369-5)
- Lapen, T. J., Johnson, C. M., Baumgartner, L. P., Piaz, G. V. D., Skora, S., & Beard, B. L. (2007). Coupling of oceanic and continental crust during Eocene eclogite-facies metamorphism: evidence

- from the Monte Rosa nappe, western Alps. *Contributions to Mineralogy and Petrology*, 153(2), 139–157. <https://doi.org/10.1007/s00410-006-0144-x>
- Lardeaux, J. M., Nisio, P., & Boudeulle, M. (1987). Deformational and metamorphic history at the Lago Superiore area of the Monviso ophiolitic complex (Italian Western Alps): a record of subduction–collision cycle. *Ophioliti*, 12(3), 479–502.
- Lardeaux, J. m., Schwartz, S., Tricart, P., Paul, A., Guillot, S., Béthoux, N., & Masson, F. (2006). A crustal-scale cross-section of the south-western Alps combining geophysical and geological imagery. *Terra Nova*, 18(6), 412–422. <https://doi.org/10.1111/j.1365-3121.2006.00706.x>
- Laubscher, H. (1991). The arc of the Western Alps today. *Eclogae Geologicae Helvetiae*, 84(3), 359–631.
- Leporati, P. (1968). *Studio geologico del territorio compreso tra Confine e Sampeire (media Val Varaita)*. Università di Torino, Istituto di Geologia Università di Torino.
- Linde, A. T., & Silver, P. G. (1989). Elevation changes and the Great 1960 Chilean Earthquake: Support for aseismic slip. *Geophysical Research Letters*, 16(11), 1305–1308. <https://doi.org/10.1029/GL016i011p01305>
- Liou, J. G., Tsujimori, T., Zhang, R. Y., Katayama, I., & Maruyama, S. (2004). Global UHP Metamorphism and Continental Subduction/Collision: The Himalayan Model. *International Geology Review*, 46(1), 1–27. <https://doi.org/10.2747/0020-6814.46.1.1>
- Lissenberg, C. J., Rioux, M., Shimizu, N., Bowring, S. A., & Mével, C. (2009). Zircon Dating of Oceanic Crustal Accretion. *Science*, 323(5917), 1048–1050. <https://doi.org/10.1126/science.1167330>
- Lombardo, B. (1969). *Geologia dell'alta Valle Lenta* (Relazione di rilevamento). Istituto di Geologia Università di Torino.
- Lombardo, B., Nervo, R., Compagnoni, R., Messiga, B., Kienast, J.-R., Mevel, C., ... Lanza, R. (1978). Osservazioni preliminari sulle ofioliti metamorfiche del Monviso. *Rendiconti Della Società Italiana Di Mineralogia E Petrologia*, 34(2), 253–305.
- Lombardo, B., Rubatto, D., & Castelli, D. (2002). Ion microprobe U-PB dating of zircon from a Monviso metaplagiogranite: Implications for the evolution of the Piedmont-Liguria tethys in the Western Alps. *Ophioliti*, 27(2), 109–117.
- Lucchesi, S., Fioraso, G., Bertotto, S., & Chiarle, M. (2014). Little Ice Age and contemporary glacier extent in the Western and South-Western Piedmont Alps (North-Western Italy). *Journal of Maps*, 10(3), 409–423. <https://doi.org/10.1080/17445647.2014.880226>
- Lyakhovsky, V., Ben-Zion, Y., & Agnon, A. (2001). Earthquake cycle, fault zones, and seismicity patterns in a rheologically layered lithosphere. *Journal of Geophysical Research: Solid Earth*, 106(B3), 4103–4120. <https://doi.org/10.1029/2000JB900218>
- Mainprice, D., & Ildefonse, B. (2009). Seismic Anisotropy of Subduction Zone Minerals–Contribution of Hydrous Phases. In *Subduction Zone Geodynamics* (pp. 63–84). Springer, Berlin, Heidelberg. Retrieved from https://link.springer.com/chapter/10.1007/978-3-540-87974-9_4

- Malusà, M. G., Faccenna, C., Garzanti, E., & Polino, R. (2011). Divergence in subduction zones and exhumation of high pressure rocks (Eocene Western Alps). *Earth and Planetary Science Letters*, 310(1), 21–32. <https://doi.org/10.1016/j.epsl.2011.08.002>
- Marot, D., Bendahmane, F., & Nguyen, H. H. (2012). Influence of angularity of coarse fraction grains on internal erosion process. *La Houille Blanche*, (6), 47–53. <https://doi.org/10.1051/lhb/2012040>
- Martin, A. J. (2009). Sub-millimeter Heterogeneity of Yttrium and Chromium during Growth of Semi-pelitic Garnet. *Journal of Petrology*, 50(9), 1713–1727. <https://doi.org/10.1093/petrology/egp050>
- Martin, L. a. J., Hermann, J., Gauthiez-Putallaz, L., Whitney, D. L., Vitale Brovarone, A., Fornash, K. F., & Evans, N. J. (2014). Lawsonite geochemistry and stability – implication for trace element and water cycles in subduction zones. *Journal of Metamorphic Geology*, 32(5), 455–478. <https://doi.org/10.1111/jmg.12093>
- McDonough, W. F., & Sun, S. -s. (1995). The composition of the Earth. *Chemical Geology*, 120(3), 223–253. [https://doi.org/10.1016/0009-2541\(94\)00140-4](https://doi.org/10.1016/0009-2541(94)00140-4)
- McKenzie, D. P., & Parker, R. L. (1967). The North Pacific: an example of tectonics on a sphere. *Nature*, 216(5122), 1276–1280.
- Means, W. D. (1995). Shear zones and rock history. *Tectonophysics*, 247(1), 157–160. [https://doi.org/10.1016/0040-1951\(95\)98214-H](https://doi.org/10.1016/0040-1951(95)98214-H)
- Meffan-Main, S., Cliff, R. A., Barnicoat, A. C., Lombardo, B., & Compagnoni, R. (2004). A Tertiary age for Alpine high-pressure metamorphism in the Gran Paradiso massif, Western Alps: a Rb–Sr microsampling study. *Journal of Metamorphic Geology*, 22(4), 267–281. <https://doi.org/10.1111/j.1525-1314.2004.00512.x>
- Meneghini, F., Toro, G. D., Rowe, C. D., Moore, J. C., Tsutsumi, A., & Yamaguchi, A. (2010). Record of mega-earthquakes in subduction thrusts: The black fault rocks of Pasagshak Point (Kodiak Island, Alaska). *GSA Bulletin*, 122(7–8), 1280–1297. <https://doi.org/10.1130/B30049.1>
- Messiga, Kienast, Rebay, Riccardi, & Tribuzio. (1999). Cr-rich magnesiochloritoid eclogites from the Monviso ophiolites (Western Alps, Italy). *Journal of Metamorphic Geology*, 17(3), 287–299. <https://doi.org/10.1046/j.1525-1314.1999.00198.x>
- Mibe, K., Yoshino, T., Ono, S., Yasuda, A., & Fujii, T. (2003). Connectivity of aqueous fluid in eclogite and its implications for fluid migration in the Earth's interior. *Journal of Geophysical Research: Solid Earth*, 108(B6), 2295. <https://doi.org/10.1029/2002JB001960>
- Michard, A. (n.d.). Etudes géologique dans les zones internes des Alpes Cottiennes. *Ed. Du CNRS*, 447p.
- Michibayashi, K., Abe, N., Okamoto, A., Satsukawa, T., & Michikura, K. (2006). Seismic anisotropy in the uppermost mantle, back-arc region of the northeast Japan arc: Petrophysical analyses of Ichinomegata peridotite xenoliths. *Geophysical Research Letters*, 33(10), L10312. <https://doi.org/10.1029/2006GL025812>
- Michibayashi, K., & Murakami, M. (2007). Development of a shear band cleavage as a result of strain partitioning. *Journal of Structural Geology*, 29(6), 1070–1082. <https://doi.org/10.1016/j.jsg.2007.02.003>

- Michibayashi, K., Tasaka, M., Ohara, Y., Ishii, T., Okamoto, A., & Fryer, P. (2007). Variable microstructure of peridotite samples from the southern Mariana Trench: Evidence of a complex tectonic evolution. *Tectonophysics*, 444(1), 111–118. <https://doi.org/10.1016/j.tecto.2007.08.010>
- Migliardi, G. (1969). *Geologia del versante sinistro della Valle Varaita fra Cima delle Lobbie e Cima di Crosa* (Relazione di rilevamento). Istituto di Geologia Università di Torino.
- Montési, L. G. J., & Hirth, G. (2003). Grain size evolution and the rheology of ductile shear zones: from laboratory experiments to postseismic creep. *Earth and Planetary Science Letters*, 211(1–2), 97–110. [https://doi.org/10.1016/S0012-821X\(03\)00196-1](https://doi.org/10.1016/S0012-821X(03)00196-1)
- Moreno, M. S., Bolte, J., Klotz, J., & Melnick, D. (2009). Impact of megathrust geometry on inversion of coseismic slip from geodetic data: Application to the 1960 Chile earthquake. *Geophysical Research Letters*, 36(16), L16310. <https://doi.org/10.1029/2009GL039276>
- Morrow, C. A., Shi, L. Q., & Byerlee, J. D. (1984). Permeability of fault gouge under confining pressure and shear stress. *Journal of Geophysical Research: Solid Earth*, 89(B5), 3193–3200. <https://doi.org/10.1029/JB089iB05p03193>
- Mort, K., & Woodcock, N. H. (2008). Quantifying fault breccia geometry: Dent Fault, NW England. *Journal of Structural Geology*, 30(6), 701–709. <https://doi.org/10.1016/j.jsg.2008.02.005>
- Nadeau, S., Philippot, P., & Pineau, F. (1993). Fluid inclusion and mineral isotopic compositions (HCO) in eclogitic rocks as tracers of local fluid migration during high-pressure metamorphism. *Earth and Planetary Science Letters*, 114(4), 431–448. [https://doi.org/10.1016/0012-821X\(93\)90074-J](https://doi.org/10.1016/0012-821X(93)90074-J)
- Nakajima, J., Hasegawa, A., & Kita, S. (2011). Seismic evidence for reactivation of a buried hydrated fault in the Pacific slab by the 2011 M9.0 Tohoku earthquake. *Geophysical Research Letters*, 38(7), L00G06. <https://doi.org/10.1029/2011GL048432>
- Nakajima, J., Matsuzawa, T., Hasegawa, A., & Zhao, D. (2001). Three-dimensional structure of Vp, Vs, and Vp/Vs beneath northeastern Japan: Implications for arc magmatism and fluids. *Journal of Geophysical Research: Solid Earth*, 106(B10), 21843–21857. <https://doi.org/10.1029/2000JB000008>
- Nakajima, J., Tsuji, Y., & Hasegawa, A. (2009). Seismic evidence for thermally-controlled dehydration reaction in subducting oceanic crust. *Geophysical Research Letters*, 36(3), L03303. <https://doi.org/10.1029/2008GL036865>
- Nakajima, J., Tsuji, Y., Hasegawa, A., Kita, S., Okada, T., & Matsuzawa, T. (2009). Tomographic imaging of hydrated crust and mantle in the subducting Pacific slab beneath Hokkaido, Japan: Evidence for dehydration embrittlement as a cause of intraslab earthquakes. *Gondwana Research*, 16(3), 470–481. <https://doi.org/10.1016/j.gr.2008.12.010>
- Nakamura, D., & Banno, S. (1997). Thermodynamic modelling of sodic pyroxene solid-solution and its application in a garnet-omphacite-kyanite-coesite geothermobarometer for UHP metamorphic rocks. *Contributions to Mineralogy and Petrology*, 130(1), 93–102. <https://doi.org/10.1007/s004100050352>
- Novarese, V. (n.d.). Nomenclature e sistematica delle rocce verdi nelle Alpi Occidentali. *B.C.G.I.*, 26, 164–181.

- Obara, K., Hirose, H., Yamamizu, F., & Kasahara, K. (2004). Episodic slow slip events accompanied by non-volcanic tremors in southwest Japan subduction zone. *Geophysical Research Letters*, 31(23), L23602. <https://doi.org/10.1029/2004GL020848>
- Oberhänsli, R., Bousquet, R., Engi, M., Goffé, B., Gosso, G., Handy, M. R., ... Polino, R. (2004). Metamorphic Structure of the Alps. *CCGM (Commission of the Geological Maps of the World)*, Paris.
- Ohtani, E., Litasov, K., Hosoya, T., Kubo, T., & Kondo, T. (2004). Water transport into the deep mantle and formation of a hydrous transition zone. *Physics of the Earth and Planetary Interiors*, 143, 255–269. <https://doi.org/10.1016/j.pepi.2003.09.015>
- Okazaki, K., & Hirth, G. (2016). Dehydration of lawsonite could directly trigger earthquakes in subducting oceanic crust. *Nature*, 530(7588), 81–84. <https://doi.org/10.1038/nature16501>
- Omori, S., Komabayashi, T., & Maruyama, S. (2004). Dehydration and earthquakes in the subducting slab: empirical link in intermediate and deep seismic zones. *Physics of the Earth and Planetary Interiors*, 146(1), 297–311. <https://doi.org/10.1016/j.pepi.2003.08.014>
- Pawley, A. R. (1994). The pressure and temperature stability limits of lawsonite: implications for H₂O recycling in subduction zones. *Contributions to Mineralogy and Petrology*, 118(1), 99–108. <https://doi.org/10.1007/BF00310614>
- Pawley, A. R., Redfern, S. A. T., & Holland, T. J. B. (2015). Volume behavior of hydrous minerals at high pressure and temperature: I. Thermal expansion of lawsonite, zoisite, clinozoisite, and diaspore. *American Mineralogist*, 81(3–4), 335–340. <https://doi.org/10.2138/am-1996-3-407>
- Pelletier, L., & Müntener, O. (2006). High-pressure metamorphism of the Lanzo peridotite and its oceanic cover, and some consequences for the Sesia–Lanzo zone (northwestern Italian Alps). *Lithos*, 90(1), 111–130. <https://doi.org/10.1016/j.lithos.2006.01.006>
- Perrone, G., Morelli, M., Piana, F., Fioraso, G., Nicolò, G., Mallen, L., ... Tallone, S. (2013). Current tectonic activity and differential uplift along the Cottian Alps/Po Plain boundary (NW Italy) as derived by PS-InSAR data. *Journal of Geodynamics*, 66, 65–78. <https://doi.org/10.1016/j.jog.2013.02.004>
- Pettke, T., Oberli, F., Audétat, A., Guillong, M., Simon, A. C., Hanley, J. J., & Klemm, L. M. (2012). Recent developments in element concentration and isotope ratio analysis of individual fluid inclusions by laser ablation single and multiple collector ICP-MS. *Ore Geology Reviews*, 44, 10–38. <https://doi.org/10.1016/j.oregeorev.2011.11.001>
- Philippot, P. (1987). “Crack seal” vein geometry in eclogitic rocks. *Geodinamica Acta*, 1(3), 171–181. <https://doi.org/10.1080/09853111.1987.11105136>
- Philippot, P. (1990). Opposite vergence of Nappes and crustal extension in the French-Italian western Alps. *Tectonics*, 9(5), 1143–1164. <https://doi.org/10.1029/TC009i005p01143>
- Philippot, P., & Kienast, J.-R. (1989). Chemical-microstructural changes in eclogite-facies shear zones (Monviso, Western Alps, north Italy) as indicators of strain history and the mechanism and scale of mass transfer. *Lithos*, 23(3), 179–200. [https://doi.org/10.1016/0024-4937\(89\)90004-2](https://doi.org/10.1016/0024-4937(89)90004-2)

- Philippot, P., & Selverstone, J. (1991). Trace-element-rich brines in eclogitic veins: implications for fluid composition and transport during subduction. *Contributions to Mineralogy and Petrology*, 106(4), 417–430. <https://doi.org/10.1007/BF00321985>
- Philippot, P., & van Roermund, H. L. M. (1992). Deformation processes in eclogitic rocks: evidence for the rheological delamination of the oceanic crust in deeper levels of subduction zones. *Journal of Structural Geology*, 14(8), 1059–1077. [https://doi.org/10.1016/0191-8141\(92\)90036-V](https://doi.org/10.1016/0191-8141(92)90036-V)
- Philpotts, A. R. (1964). Origin of pseudotachylites. *American Journal of Science*, 262(8), 1008–1035. <https://doi.org/10.2475/ajs.262.8.1008>
- Pittarello, L., Di Toro, G., Bizzarri, A., Pennacchioni, G., Hadizadeh, J., & Cocco, M. (2008). Energy partitioning during seismic slip in pseudotachylite-bearing faults (Gole Larghe Fault, Adamello, Italy). *Earth and Planetary Science Letters*, 269(1–2), 131–139. <https://doi.org/10.1016/j.epsl.2008.01.052>
- Plafker, G. (1965). Tectonic Deformation Associated with the 1964 Alaska Earthquake. *Science*, 148(3678), 1675–1687. <https://doi.org/10.1126/science.148.3678.1675>
- Platt, J. P., Cunningham, P. C., Weston, P., Lister, G. S., Peel, F., Baudin, T., & Dondey, H. (1989). Thrusting and backthrusting in the Briançonnais domain of the western Alps. *Geological Society, London, Special Publications*, 45(1), 135–152. <https://doi.org/10.1144/GSL.SP.1989.045.01.07>
- Plunder, A., Agard, P., Chopin, C., & Okay, A. I. (2013). Geodynamics of the Tavşanlı zone, western Turkey: Insights into subduction/obduction processes. *Tectonophysics*, 608, 884–903. <https://doi.org/10.1016/j.tecto.2013.07.028>
- Pognante, U., & Kienast, J.-R. (1987). Blueschist and Eclogite transformations in Fe-Ti Gabbros: A Case from the Western Alps Ophiolites. *Journal of Petrology*, 28(2), 271–292. <https://doi.org/10.1093/petrology/28.2.271>
- Poli, S., & Schmidt, M. W. (1998). The high-pressure stability of zoisite and phase relationships of zoisite-bearing assemblages. *Contributions to Mineralogy and Petrology*, 130(2), 162–175. <https://doi.org/10.1007/s004100050357>
- Poli, S., & Schmidt, M. W. (2002). Petrology of Subducted Slabs. *Annual Review of Earth and Planetary Sciences*, 30(1), 207–235. <https://doi.org/10.1146/annurev.earth.30.091201.140550>
- POLINO, R. (1990). Tectonic erosion at the Adria margin and accretionary processes for the Cretaceous orogeny of the Alps. *Memoire de La Societe Geologique de France*, 156, 345–367.
- Preston, L. A., Creager, K. C., Crosson, R. S., Brocher, T. M., & Trehu, A. M. (2003). Intraslab Earthquakes: Dehydration of the Cascadia Slab. *Science*, 302(5648), 1197–1200. <https://doi.org/10.1126/science.1090751>
- Raimbourg, H., Goffé, B., & Jolivet, L. (2007). Garnet reequilibration and growth in the eclogite facies and geodynamical evolution near peak metamorphic conditions. *Contributions to Mineralogy and Petrology*, 153(1), 1–28. <https://doi.org/10.1007/s00410-006-0130-3>
- Raimbourg, H., Jolivet, L., & Leroy, Y. (2007). Consequences of progressive eclogitization on crustal exhumation, a mechanical study. *Geophysical Journal International*, 168(1), 379–401. <https://doi.org/10.1111/j.1365-246X.2006.03130.x>

- Raleigh, C. B. (1967). Tectonic Implications of Serpentinite Weakening. *Geophysical Journal International*, 14(1–4), 113–118. <https://doi.org/10.1111/j.1365-246X.1967.tb06229.x>
- Raleigh, C. B., & Paterson, M. S. (1965). Experimental deformation of serpentinite and its tectonic implications. *Journal of Geophysical Research*, 70(16), 3965–3985. <https://doi.org/10.1029/JZ070i016p03965>
- Ranero, C. R., Phipps Morgan, J., McIntosh, K., & Reichert, C. (2003). Bending-related faulting and mantle serpentinization at the Middle America trench. *Nature*, 425(6956), 367–373. <https://doi.org/10.1038/nature01961>
- Ravna, E. J. K., Andersen, T. B., Jolivet, L., & De CAPITANI, C. (2010). Cold subduction and the formation of lawsonite eclogite – constraints from prograde evolution of eclogitized pillow lava from Corsica. *Journal of Metamorphic Geology*, 28(4), 381–395. <https://doi.org/10.1111/j.1525-1314.2010.00870.x>
- Ricou, L. E., & Siddans, A. W. B. (1986). Collision tectonics in the Western Alps. *Geological Society, London, Special Publications*, 19(1), 229–244. <https://doi.org/10.1144/GSL.SP.1986.019.01.13>
- Rietbrock, A., & Waldhauser, F. (2004). A narrowly spaced double-seismic zone in the subducting Nazca plate. *Geophysical Research Letters*, 31(10), L10608. <https://doi.org/10.1029/2004GL019610>
- Roering, C., van Reenen, D. D., Smit, C. A., & Du Toit, R. (1995). Deep Crustal Embrittlement and Fluid Flow during Granulite Metamorphism in the Limpopo Belt, South Africa. *The Journal of Geology*, 103(6), 673–686. <https://doi.org/10.1086/629787>
- Roger, G., & Dragert, H. (2003). Episodic Tremor and Slip on the Cascadia Subduction Zone: The Chatter of Silent Slip. *Science*, 300(5627), 1942–1943.
- Rondenay, S., Abers, G. A., & van Keken, P. E. (2008). Seismic imaging of subduction zone metamorphism. *Geology*, 36(4), 275. <https://doi.org/10.1130/G24112A.1>
- Rowe, C. D., Moore, J. C., Meneghini, F., & McKeirnan, A. W. (2005). Large-scale pseudotachylytes and fluidized cataclasites from an ancient subduction thrust fault. *Geology*, 33(12), 937–940. <https://doi.org/10.1130/G21856.1>
- Rubatto, D., & Angiboust, S. (2015). Oxygen isotope record of oceanic and high-pressure metasomatism: a P–T–time–fluid path for the Monviso eclogites (Italy). *Contributions to Mineralogy and Petrology*, 170(5–6). <https://doi.org/10.1007/s00410-015-1198-4>
- Rubatto, D., & Hermann, J. (2003). Zircon formation during fluid circulation in eclogites (Monviso, Western Alps): implications for Zr and Hf budget in subduction zones. *Geochimica et Cosmochimica Acta*, 67(12), 2173–2187. [https://doi.org/10.1016/S0016-7037\(02\)01321-2](https://doi.org/10.1016/S0016-7037(02)01321-2)
- Rubatto, D., Regis, D., Hermann, J., Boston, K., Engi, M., Beltrando, M., & McAlpine, S. R. B. (2011). Yo-yo subduction recorded by accessory minerals in the Italian Western Alps. *Nature Geoscience*, 4(5), 338–342. <https://doi.org/10.1038/ngeo1124>
- Ruff, L., & Kanamori, H. (1980). Seismicity and the subduction process. *Physics of the Earth and Planetary Interiors*, 23(3), 240–252. [https://doi.org/10.1016/0031-9201\(80\)90117-X](https://doi.org/10.1016/0031-9201(80)90117-X)
- Rutter, E. H. (1986). On the nomenclature of mode of failure transitions in rocks. *Tectonophysics*, 122(3), 381–387. [https://doi.org/10.1016/0040-1951\(86\)90153-8](https://doi.org/10.1016/0040-1951(86)90153-8)

- Savov, I. P., Ryan, J. G., D'Antonio, M., Kelley, K., & Mattie, P. (2005). Geochemistry of serpentinized peridotites from the Mariana Forearc Conical Seamount, ODP Leg 125: Implications for the elemental recycling at subduction zones. *Geochemistry, Geophysics, Geosystems*, 6(4), Q04J15. <https://doi.org/10.1029/2004GC000777>
- Scambelluri, M., Fiebig, J., Malaspina, N., Müntener, O., & Pettke, T. (2004). Serpentinite Subduction: Implications for Fluid Processes and Trace-Element Recycling. *International Geology Review*, 46(7), 595–613. <https://doi.org/10.2747/0020-6814.46.7.595>
- Scambelluri, M., Müntener, O., Hermann, J., Piccardo, G. B., & Trommsdorff, V. (1995). Subduction of water into the mantle: History of an Alpine peridotite. *Geology*, 23(5), 459–462. [https://doi.org/10.1130/0091-7613\(1995\)023<0459:SOWITM>2.3.CO;2](https://doi.org/10.1130/0091-7613(1995)023<0459:SOWITM>2.3.CO;2)
- Scambelluri, M., & Philippot, P. (2001). Deep fluids in subduction zones. *Lithos*, 55(1), 213–227. [https://doi.org/10.1016/S0024-4937\(00\)00046-3](https://doi.org/10.1016/S0024-4937(00)00046-3)
- Scambelluri, M., Strating, E. H. H., Piccardo, G. B., Vissers, R. L. M., & Rampone, E. (1991). Alpine olivine- and titanian clinohumite-bearing assemblages in the Erro-Tobbio peridotite (Voltri Massif, NW Italy). *Journal of Metamorphic Geology*, 9(1), 79–91. <https://doi.org/10.1111/j.1525-1314.1991.tb00505.x>
- Schardt, H. (1898). *Les régions exotiques du versant Nord des Alpes suisses: (Préalpes du Chablais et du Stockhorn et les Klippes): leurs relations avec l'origine des blocs et brèches exotiques et la formation du Flysch*. Impr. Corbaz.
- Schertl, H.-P., Schreyer, W., & Chopin, C. (1991). The pyrope-coesite rocks and their country rocks at Parigi, Dora Maira Massif, Western Alps: detailed petrography, mineral chemistry and PT-path. *Contributions to Mineralogy and Petrology*, 108(1–2), 1–21. <https://doi.org/10.1007/BF00307322>
- Schindelin, J., Arganda-Carreras, I., Frise, E., Kaynig, V., Longair, M., Pietzsch, T., ... Cardona, A. (2012). Fiji: an open-source platform for biological-image analysis. *Nature Methods*, 9(7), 676–682. <https://doi.org/10.1038/nmeth.2019>
- Schmid, S. M., Fügenschuh, B., Kissling, E., & Schuster, R. (2004). Tectonic map and overall architecture of the Alpine orogen. *Eclogae Geologicae Helvetiae*, 97(1), 93–117. <https://doi.org/10.1007/s00015-004-1113-x>
- Schmid, S. M., & Kissling, E. (2000). The arc of the western Alps in the light of geophysical data on deep crustal structure. *Tectonics*, 19(1), 62–85. <https://doi.org/10.1029/1999TC900057>
- Schmid, S. M., Pfiffner, O. A., Froitzheim, N., Schönborn, G., & Kissling, E. (1996). Geophysical-geological transect and tectonic evolution of the Swiss-Italian Alps. *Tectonics*, 15(5), 1036–1064. <https://doi.org/10.1029/96TC00433>
- Schmidt, M. W., & Poli, S. (1998). Experimentally based water budgets for dehydrating slabs and consequences for arc magma generation. *Earth and Planetary Science Letters*, 163(1), 361–379. [https://doi.org/10.1016/S0012-821X\(98\)00142-3](https://doi.org/10.1016/S0012-821X(98)00142-3)
- Schrank, C. E., Boutelier, D. A., & Cruden, A. R. (2008). The analogue shear zone: From rheology to associated geometry. *Journal of Structural Geology*, 30(2), 177–193. <https://doi.org/10.1016/j.jsg.2007.11.002>

- Schrank, C. E., Handy, M. R., & Füsseis, F. (2008). Multiscaling of shear zones and the evolution of the brittle-to-viscous transition in continental crust. *Journal of Geophysical Research: Solid Earth*, 113(B1), B01407. <https://doi.org/10.1029/2006JB004833>
- Schwartz, S., Lardeaux, J.-M., Guillot, S., & Tricart, P. (2000). Diversité du métamorphisme éclogitique dans le massif ophiolitique du Monviso (Alpes occidentales, Italie). *Geodinamica Acta*, 13(2–3), 169–188. <https://doi.org/10.1080/09853111.2000.11105371>
- Shelly, D. R., Beroza, G. C., Ide, S., & Nakamura, S. (2006). Low-frequency earthquakes in Shikoku, Japan, and their relationship to episodic tremor and slip. *Nature*, 442, 188–191. <https://doi.org/10.1038/nature04931>
- Shiina, T., Nakajima, J., & Matsuzawa, T. (2013). Seismic evidence for high pore pressures in the oceanic crust: Implications for fluid-related embrittlement. *Geophysical Research Letters*, 40(10), 2006–2010. <https://doi.org/10.1002/grl.50468>
- Shillington, D. J., Becel, A., Nedimović, M. R., Kuehn, H., Webb, S. C., Abers, G. A., ... Delescluse, M. (2015). Link between plate fabric, hydration and subduction zone seismicity in Alaska. *Nature Geoscience*, 8, 961–964. <https://doi.org/10.1038/NGEO2586>
- Sibson, R. H. (1977). Fault rocks and fault mechanisms. *Journal of the Geological Society*, 133(3), 191–213. <https://doi.org/10.1144/gsjgs.133.3.0191>
- Sibson, R. H. (1986). Brecciation processes in fault zones: Inferences from earthquake rupturing. *Pure and Applied Geophysics*, 124(1–2), 159–175. <https://doi.org/10.1007/BF00875724>
- Simons, M., Minson, S. E., Sladen, A., Ortega, F., Jiang, J., Owen, S. E., ... Webb, F. H. (2011). The 2011 Magnitude 9.0 Tohoku-Oki Earthquake: Mosaicking the Megathrust from Seconds to Centuries. *Science*, 332(6036), 1421–1425. <https://doi.org/10.1126/science.1206731>
- Soarzana, P. F. (1969). *Geologia dell'Alta Valle Po fra il Pian Melzé ed il Monviso* (Relazione di rilevamento). Istituto di Geologia Università di Torino.
- Spalla, M. I., Lardeaux, J. M., Piazz, G., Vittorio D., Gosso, G., & Messiga, B. (1996). Tectonic significance of Alpine eclogites. *Journal of Geodynamics*, 21(3), 257–285. [https://doi.org/10.1016/0264-3707\(95\)00033-X](https://doi.org/10.1016/0264-3707(95)00033-X)
- Spandler, C., Hermann, J., Arculus, R., & Mavrogenes, J. (2003). Redistribution of trace elements during prograde metamorphism from lawsonite blueschist to eclogite facies; implications for deep subduction-zone processes. *Contributions to Mineralogy and Petrology*, 146(2), 205–222. <https://doi.org/10.1007/s00410-003-0495-5>
- Spandler, C., Pettke, T., & Rubatto, D. (2011). Internal and External Fluid Sources for Eclogite-facies Veins in the Monviso Meta-ophiolite, Western Alps: Implications for Fluid Flow in Subduction Zones. *Journal of Petrology*, 52(6), 1207–1236. <https://doi.org/10.1093/petrology/egr025>
- Spandler, C., & Pirard, C. (2013). Element recycling from subducting slabs to arc crust: A review. *Lithos*, 170, 208–223. <https://doi.org/10.1016/j.lithos.2013.02.016>
- Stella, A. (n.d.). Sul rilevamento geologico eseguito nel 1894 in valle Varaita (Alpi Cozie). *B.C.G.I.*, 26, 283–313.
- Stern, R. J. (2002). Subduction Zones. *Reviews of Geophysics*, 40(4), 1012. <https://doi.org/10.1029/2001RG000108>

- Strömgård, K.-E. (1973). Stress distribution during formation of boudinage and pressure shadows. *Tectonophysics*, 16(3), 215–248. [https://doi.org/10.1016/0040-1951\(73\)90013-9](https://doi.org/10.1016/0040-1951(73)90013-9)
- Sue, C., Thouvenot, F., Fréchet, J., & Tricart, P. (1999). Widespread extension in the core of the western Alps revealed by earthquake analysis. *Journal of Geophysical Research: Solid Earth*, 104(B11), 25611–25622. <https://doi.org/10.1029/1999JB900249>
- Sun, S. —., & McDonough, W. F. (1989). Chemical and isotopic systematics of oceanic basalts: implications for mantle composition and processes. *Geological Society, London, Special Publications*, 42(1), 313–345. <https://doi.org/10.1144/GSL.SP.1989.042.01.19>
- Tenthorey, E., & Hermann, J. (2004). Composition of fluids during serpentinite breakdown in subduction zones: Evidence for limited boron mobility. *Geology*, 32(10), 865–868. <https://doi.org/10.1130/G20610.1>
- Terry, M. P., & Heidelbach, F. (2006). Deformation-enhanced metamorphic reactions and the rheology of high-pressure shear zones, Western Gneiss Region, Norway. *Journal of Metamorphic Geology*, 24(1), 3–18. <https://doi.org/10.1111/j.1525-1314.2005.00618.x>
- Thatcher, W. (1982). Seismic triggering and earthquake prediction. *Nature*, 299, 12–13. <https://doi.org/10.1038/299012a0>
- Tilton, G. R., Schreyer, W., & Schertl, H.-P. (1991). Pb–Sr–Nd isotopic behavior of deeply subducted crustal rocks from the Dora Maira Massif, Western Alps, Italy-II: what is the age of the ultrahigh-pressure metamorphism? *Contributions to Mineralogy and Petrology*, 108(1–2), 22–33. <https://doi.org/10.1007/BF00307323>
- Toyoshima, T. (1990). Pseudotachylite from the Main Zone of the Hidaka metamorphic belt, Hokkaido, northern Japan. *Journal of Metamorphic Geology*, 8(5), 507–523. <https://doi.org/10.1111/j.1525-1314.1990.tb00483.x>
- Treagus, S. H. (1981). A theory of stress and strain variations in viscous layers, and its geological implications. *Tectonophysics*, 72(1), 75–103. [https://doi.org/10.1016/0040-1951\(81\)90088-3](https://doi.org/10.1016/0040-1951(81)90088-3)
- Tsuji, Y., Nakajima, J., & Hasegawa, A. (2008). Tomographic evidence for hydrated oceanic crust of the Pacific slab beneath northeastern Japan: Implications for water transportation in subduction zones. *Geophysical Research Letters*, 35(14), L14308. <https://doi.org/10.1029/2008GL034461>
- Tsujimori, T., & Liou, J. G. (2015). Coexisting chromian omphacite and diopside in tremolite schist from the Chugoku Mountains, SW Japan: The effect of Cr on the omphacite-diopside immiscibility gap. *American Mineralogist*, 89(1), 7–14. <https://doi.org/10.2138/am-2004-0102>
- Tsujimori, T., Sisson, V. B., Liou, J. G., Harlow, G. E., & Sorensen, S. S. (2006). Very-low-temperature record of the subduction process: A review of worldwide lawsonite eclogites. *Lithos*, 92(3), 609–624. <https://doi.org/10.1016/j.lithos.2006.03.054>
- Ulmer, P., & Trommsdorff, V. (1995). Serpentine Stability to Mantle Depths and Subduction-Related Magmatism. *Science*, 268(5212), 858–861.
- Ulmer, P., & Trommsdorff, V. (1999). Phase relations of hydrous mantle subducting to 300 km. *Mantle Petrology: Field Observations and High Pressure Experimentation: A Tribute to Francis R.(Joe) Boyd*, 6, 259–281.

- van Keken, P. E., Hacker, B. R., Syracuse, E. M., & Abers, G. A. (2011). Subduction factory: 4. Depth-dependent flux of H₂O from subducting slabs worldwide. *Journal of Geophysical Research: Solid Earth*, 116(B1), B01401. <https://doi.org/10.1029/2010JB007922>
- Vannucchi, P., Sage, F., Phipps Morgan, J., Remitti, F., & Collot, J.-Y. (2012). Toward a dynamic concept of the subduction channel at erosive convergent margins with implications for interplate material transfer. *Geochemistry, Geophysics, Geosystems*, 13(2), Q02003. <https://doi.org/10.1029/2011GC003846>
- Vialon, P. (1966, June). *Etude géologique du massif cristallin Dora-Maira : Alpes cottiennes internes : Italie* (Theses). Université de Grenoble. Retrieved from <https://tel.archives-ouvertes.fr/tel-00723197>
- Von Herzen, R., Robinson, P. T., & et al. (Eds.). (1991). *Proceedings of the Ocean Drilling Program, 118 Scientific Results* (Vol. 118). Ocean Drilling Program. Retrieved from http://www-odp.tamu.edu/publications/118_SR/118TOC.HTM
- Waldhauser, F., & Schaff, D. P. (2008). Large-scale relocation of two decades of Northern California seismicity using cross-correlation and double-difference methods. *Journal of Geophysical Research: Solid Earth*, 113(B8), B08311. <https://doi.org/10.1029/2007JB005479>
- Wegener, A. (1912). Die Entstehung der Kontinente. *Geologische Rundschau*, 3(4), 276–292. <https://doi.org/10.1007/BF02202896>
- White, A. J. R., Jakes, P., & Christie, D. M. (1971). Composition of greenstones and the hypothesis of sea-floor spreading in the Archaean. *Geological Society of Australia, Special Publication*, 3, 47–56.
- White, W. M. (1985). Sources of oceanic basalts: Radiogenic isotopic evidence. *Geology*, 13(2), 115–118. [https://doi.org/10.1130/0091-7613\(1985\)13<115:SOOBRI>2.0.CO;2](https://doi.org/10.1130/0091-7613(1985)13<115:SOOBRI>2.0.CO;2)
- White, W. M., Dupré, B., & Vidal, P. (1985). Isotope and trace element geochemistry of sediments from the Barbados Ridge-Demerara Plain region, Atlantic Ocean. *Geochimica et Cosmochimica Acta*, 49(9), 1875–1886. [https://doi.org/10.1016/0016-7037\(85\)90082-1](https://doi.org/10.1016/0016-7037(85)90082-1)
- Whitney, D. L., & Evans, B. W. (2010). Abbreviations for names of rock-forming minerals. *American Mineralogist*, 95(1), 185–187. <https://doi.org/10.2138/am.2010.3371>
- Wilson, J. T. (1973). Mantle plumes and plate motions. *Tectonophysics*, 19(2), 149–164. [https://doi.org/10.1016/0040-1951\(73\)90037-1](https://doi.org/10.1016/0040-1951(73)90037-1)
- Wood, D. A. (1979). A variably veined suboceanic upper mantle—Genetic significance for mid-ocean ridge basalts from geochemical evidence. *Geology*, 7(10), 499–503. [https://doi.org/10.1130/0091-7613\(1979\)7<499:AVVSUM>2.0.CO;2](https://doi.org/10.1130/0091-7613(1979)7<499:AVVSUM>2.0.CO;2)
- Yamasaki, T., & Seno, T. (2003). Double seismic zone and dehydration embrittlement of the subducting slab. *Journal of Geophysical Research: Solid Earth*, 108(B4), 2212. <https://doi.org/10.1029/2002JB001918>
- Yang, J.-J., Huang, M.-X., Wu, Q.-Y., & Zhang, H.-R. (2014). Coesite-bearing eclogite breccia: implication for coseismic ultrahigh-pressure metamorphism and the rate of the process. *Contributions to Mineralogy and Petrology*, 167(6), 1013. <https://doi.org/10.1007/s00410-014-1013-7>
- Zaccagna, D. (n.d.). Sulla gelogia delle Alpi Occidentali. *B.C.G.I.*, 18, 346–417.
- Zhang, Z. (Jenny), Paulino, G. H., & Celes, W. (2007). Extrinsic cohesive modelling of dynamic fracture and microbranching instability in brittle materials. *International Journal for Numerical Methods in Engineering*, 72(8), 893–923. <https://doi.org/10.1002/nme.2030>

APPENDIX 1 (a): EPMA ANALYSIS of SELECTED OMPHACITE CRYSTALS with the COMPLETE TRACE-ELEMENTS DATASET

Samples from the Lower Shear Zone: Breccia blocks with only Fe-Ti metagabbro clasts

# Analysis	Microstrucrtal domain	Sample	EPMA analysis (internal standard) wt%														LA-ICP-MS concentration (µg/g)											
			SiO2	TiO2	Al2O3	Cr2O3	FeO	MnO	MgO	CaO	Na2O	K2O	NiO	P2O5	Total	MgO#	Li	B	Na	Mg	Al	Si	P	K	Ca	Sc	Ti	
B07	Mylonitic Clast- core Omp	LSZ 53-15	55.46	0.09	6.50	0.02	15.36	0.05	4.94	9.56	8.55	0.01	0.00	0.00	100.53	24.35	46.44	0.75	61219.10	41652.21	259232.98			58663.74	34.70	160.33		
B08	Mylonitic Clast- core Omp	LSZ 53-15	55.02	0.07	7.18	0.01	14.10	0.06	4.95	8.69	9.37	-0.01	0.00	0.00	99.46	25.99	47.44	0.81	61865.61	39992.27	257217.26			52645.96	45.20	158.69		
B09	Mylonitic Clast- core Omp	LSZ 53-15	55.62	0.01	8.20	0.01	13.35	0.01	4.78	8.02	9.46	0.00	0.00	0.00	99.45	26.37	34.87	2.05	59057.66	40874.25	259996.35			50153.45	73.51	139.36		
B10	Mylonitic Clast- core Omp	LSZ 53-15	55.51	0.07	8.04	0.00	12.57	-0.02	5.08	9.06	8.93	0.03	0.00	0.00	99.25	28.77	45.46	1.42	59355.67	40376.31	259472.32			48819.01	81.82	137.98		
B12	Mylonitic Clast- core Omp	LSZ 53-15	56.00	0.03	7.01	0.00	13.54	-0.02	5.64	9.58	8.97	-0.01	0.00	0.00	100.73	29.42	41.62	1.85	55328.56	37983.19	261771.31			47914.55	71.68	131.53		
B13	Mylonitic Clast- core Omp	LSZ 53-15	54.99	0.00	6.51	0.00	14.09	0.01	5.60	10.04	8.51	0.01	0.00	0.00	99.76	28.46	48.87	0.96	56961.23	43483.10	257046.17			43913.99	44.74	132.29		
B14	Mylonitic Clast- core Omp	LSZ 53-15	55.31	0.05	6.31	0.01	13.63	0.02	5.95	10.57	8.31	-0.01	0.00	0.00	100.16	30.40	45.72	1.34	55968.76	37058.22	258534.11			46950.21	40.58	135.62		
B19	Mylonitic Clast- rim Omp	LSZ 53-15	56.13	0.08	11.15	0.01	7.38	0.03	6.20	9.71	9.11	0.00	0.00	0.00	99.80	45.68	20.16	5.96	43483.75	40064.13	262381.82			55131.71	14.41	409.43		
B30	Omp inclusion in Grt	LSZ 53-15	55.06	0.02	5.14	0.00		0.01		4.46	5.06		0.00	0.00	69.76	-	29.28	2.84	37547.57	27229.55	255329.64			31861.77	41.86	83.92		
B31	Omp inclusion in Grt	LSZ 53-15	54.99	0.07	5.50	0.00		0.01		4.59	4.99		0.00	0.00	70.15	-	33.36	2.34	37027.19	29086.30	251215.94			32840.24	24.10	87.12		
B27	M1 matrix	LSZ 53-15	55.15	0.00	4.99	0.01	7.67	0.07	10.66	15.57	5.52	0.01	0.00	0.00	99.64	58.16	29.41	4.94	33887.68	34637.95	257807.21			43638.38	10.57	188.71		
B28	Crushed matrix - Omp2b	LSZ 53-15	56.43	0.02	6.54	0.00	7.81	0.11	9.19	14.03	6.43	0.00	0.00	0.00	100.57	54.05	17.53	2.78	35065.76	29764.93	263790.30			38674.53	13.03	123.19		
B29	Crushed matrix - Omp2b	LSZ 53-15	56.86	0.03	7.49	0.11	7.08	0.08	9.14	13.67	6.76	0.02	0.00	0.00	101.23	56.38	14.34	1.86	32925.05	30395.20	265804.14			42653.53	14.28	123.99		
B31	Crushed matrix - Omp2b	LSZ 53-15	56.91	0.09	7.82	0.02	7.27	0.06	8.92	13.26	7.00	0.02	0.00	0.00	101.36	55.10	25.21	1.13	39937.85	38684.04	266028.52			30663.24	7.73	132.16		
B34	Crushed matrix - Omp2b	LSZ 53-15	56.55	0.03	8.77	0.00	6.87	0.01	8.34	12.29	8.00	0.00	0.00	0.00	100.85	54.81	20.53	3.30	41077.80	36070.65	264333.96			24199.74	6.72	96.19		
B36	Crushed matrix - Omp2b	LSZ 53-15	56.55	0.03	8.77	0.00	6.87	0.01	8.34	12.29	8.00	0.00	0.00	0.00	100.85	54.81	13.80	2.09	30929.60	26893.44	264333.96			35184.52	12.36	95.47		
B35	Crushed matrix - Omp2b	LSZ 53-15	56.17	0.09	8.87	0.11	6.89	0.10	8.11	12.45	7.31	0.01	0.00	0.00	100.11	54.06	23.12	0.30	40939.74	40779.57	262552.92			24277.39	5.89	118.27		
B37	Crushed matrix - Omp2b	LSZ 53-15	56.31	0.02	7.42	0.01	6.73	0.08	9.12	13.44	6.66	0.02	0.00	0.00	99.83	57.55	19.17	0.49	34637.37	33452.95	263247.10			27763.44	7.50	117.50		
A16	Mylonitic Clast- core Omp	LSZ 53-15	56.84	0.02	11.70	0.01	7.24	0.06	5.86	9.04	9.49	0.01	0.00	0.00	100.27	44.76	23.36	15.68	46834.57	51730.60	265707.37			42096.90	16.15	103.95		
A18	Mylonitic Clast- core Omp	LSZ 53-15	56.54	0.73	9.19	0.02	6.80	0.12	7.77	11.74	8.03	0.01	0.00	0.00	100.97	53.34	23.51	130.22	44827.67	51283.52	264304.98			40860.89	16.97	110.39		
A20	Mylonitic Clast- core Omp	LSZ 53-15	56.63	0.02	11.16	0.01	7.98	0.05	5.98	9.08	9.50	0.02	0.00	0.00	100.42	42.85	26.48	92.18	43589.61	50026.57	260051.04			37959.28	13.54	139.40		
B06	Mylonitic Clast- core Omp	LSZ 14-50	54.86	0.04	6.74	0.00	13.91	0.01	6.18	11.61	8.29	0.00	0.00	0.00	101.65	30.76	36.41	0.68	61499.79	37272.66	35662.30	256451.56	3.21	13.50	82975.14	29.63	251.01	
B13	Mylonitic Clast- core Omp	LSZ 14-50	54.52	0.04	6.38	0.00	14.26	0.02	6.14	11.92	8.03	0.00	0.00	0.00	101.32	30.08	33.74	1.15	59587.28	37001.89	33771.47	254862.17	3.12	25.49	85157.87	81.90	257.19	
B15	Mylonitic Clast- core Omp	LSZ 14-50	55.10	0.04	8.08	0.00	11.76	0.02	6.26	10.06	8.69	0.00	0.00	0.00	100.00	34.74	28.57	2.08	64491.09	37741.77	42757.25	257548.33	3.63	8.79	71908.04	33.61	214.17	
B16	Mylonitic Clast- core Omp	LSZ 14-50	55.21	0.03	8.72	0.00	11.16	0.02	6.24	10.44	8.75	0.00	0.00	0.00	100.59	35.87	31.95	1.91	64940.66	37654.62	46171.07	258087.69	3.74	12.73	74588.41	73.44	208.53	
B17	Mylonitic Clast- core Omp	LSZ 14-50	54.44	0.05	6.41	0.00	13.68	0.04	5.96	11.85	7.57	0.00	0.00	0.00	100.00	30.37	26.13	2.38	56140.27	35972.01	33938.34	254497.60	5.79	25.63	84661.07	136.99	284.31	
B23	M1 matrix	LSZ 14-50	55.62	0.03	8.07	0.03	11.29	0.04	6.92	10.77	8.35	0.00	0.01	0.00	101.15	38.01	28.46	2.26	61938.14	41760.84	42703.48	260004.29	8.43	37.29	76956.51	24.45	208.51	
B28	M1 matrix	LSZ 14-50	55.00	0.05	8.44	0.12	8.97	0.03	7.71	11.73	8.06	0.01	0.01	0.00	100.13	46.25	32.54	4.42	59795.21	46528.68	44667.59	257093.02	5.33	48.49	83846.30	20.32	277.69	
B29	M1 matrix	LSZ 14-50	55.38	0.04	9.06	0.09	10.58	0.05	6.20	10.08	8.69	0.00	0.00	0.00	100.18	36.94	47.24	1.65	64486.44	37392.97	47940.49	258854.33	3.56					

APPENDIX 1 (a-follow): EPMA ANALYSIS of SELECTED OMPHACITE CRYSTALS with the COMPLETE TRACE-ELEMENTS DATASET

Samples from the Lower Shear Zone: Breccia blocks with only Fe-Ti metagabbro clasts

# Analysis	Microstrucrtal domain	Sample	EPMA analysis (internal standard) wt%														LA-ICP-MS concentration (µg/g)											
			SiO2	TiO2	Al2O3	Cr2O3	FeO	MnO	MgO	CaO	Na2O	K2O	NiO	P2O5	Total	MgO#	Li	B	Na	Mg	Al	Si	P	K	Ca	Sc	Ti	
B20	M1 matrix	LSZ 63-15b	56.20	0.05	9.73	0.07	7.35	0.02	7.03	11.04	8.35	0.01	0.11	0.02	99.90	48.88	34.73	1.35	59715.07	49966.36	50902.98	262701.57	4.55	-2.22	89532.63	7.57	257.43	
B21	M1 matrix	LSZ 63-15b	56.07	0.06	9.15	0.02	7.59	0.02	7.22	11.41	7.91	0.01	0.08	0.01	99.50	48.76	37.00	1.32	61744.50	48969.97	50820.64	262090.12	4.61	3.43	85636.58	5.02	270.54	
B23	M1 matrix	LSZ 63-15b	56.10	0.04	8.32	0.05	7.93	0.10	7.71	12.07	7.63	0.01	0.06	0.01	99.68	49.30	36.74	1.42	57270.02	49594.87	48231.17	262224.75	5.38	-2.13	86044.63	6.83	273.48	
B26	M1 matrix	LSZ 63-15b	55.64	0.03	7.32	0.05	8.78	0.01	8.42	12.95	7.15	0.02	0.09	0.08	100.36	48.97	31.07	1.13	55434.81	50393.45	46066.32	260111.34	4.01	-2.24	89306.16	6.84	227.47	
B27	M1 matrix	LSZ 63-15b	55.68	0.02	8.42	0.10	6.89	0.04	8.33	12.51	7.49	0.00	0.18	0.03	99.60	54.74	32.95	1.00	55763.42	55043.97	48301.88	260277.76	3.93	-1.08	92952.80	18.32	212.54	
B29	M1 matrix	LSZ 63-15b	57.54	0.02	8.99	0.23	5.27	0.03	9.23	13.47	7.16	0.00	0.02	0.02	101.99	63.65	30.83	1.14	53561.89	56488.49	47393.21	268976.83	4.35	1.41	100826.03	14.97	206.82	
B35	M1 matrix	LSZ 63-15b	55.77	0.07	7.30	0.01	8.12	0.04	8.37	13.14	7.08	0.02	0.12	0.07	99.74	50.75	23.69	4.04	49715.93	55058.27	41870.31	260725.13	4.64	-7.02	88998.95	17.48	196.48	
D07	Vein3 Omp	LSZ 63-15d	54.93	0.05	7.14	0.02	7.46	0.09	8.70	13.95	6.78	0.03	0.00	0.04	99.17	53.82	146.38	7.88	50817.17	211059.01	44844.29	256782.52	19.04	100.13	99247.79	119.80	921.18	
D08	Vein3 Omp	LSZ 63-15d	54.93	0.05	7.14	0.02	7.46	0.09	8.70	13.95	6.78	0.03	0.00	0.04	99.17	53.82	146.38	7.88	50817.17	211059.01	44844.29	256782.52	19.04	100.13	99247.79	119.80	921.18	
D09	Vein3 Omp	LSZ 63-15d	55.09	0.03	8.15	0.00	6.79	0.04	8.73	13.23	7.15	0.00	0.15	0.03	98.95	56.25	151.89	10.25	53031.29	205793.67	46721.75	257513.64	37.96	64.15	92457.66	148.62	916.17	
D10	Vein3 Omp	LSZ 63-15d	55.33	0.00	7.37	0.01	7.92	0.04	8.56	13.56	6.95	0.01	0.14	0.03	99.89	51.95	141.14	6.53	52865.57	198707.87	45127.56	258662.67	16.82	38.09	96297.60	106.21	801.63	
D11	Vein3 Omp	LSZ 63-15d	55.69	0.01	8.18	0.01	6.55	0.04	9.01	13.82	6.97	0.00	0.03	0.01	100.18	57.91	137.49	10.65	53905.73	191901.55	45278.09	260347.41	20.31	27.33	91307.75	112.15	1013.13	
D13	Vein3 Omp	LSZ 63-15d	55.96	0.02	7.99	0.01	7.08	0.01	8.51	13.24	7.11	0.01	0.03	0.01	99.88	54.58	126.88	6.35	51251.01	180774.96	45004.51	261595.55	15.86	8.36	99009.55	98.04	726.11	
D14	Vein3 Omp	LSZ 63-15d	55.95	0.01	7.35	0.02	6.99	0.11	9.20	13.70	6.76	0.04	0.09	0.01	100.22	56.85	129.33	7.29	53854.00	174538.97	46847.95	261551.60	13.79	12.04	98819.56	78.70	700.86	
D15	Vein3 Omp	LSZ 63-15d	55.95	0.01	7.35	0.02	6.99	0.11	9.20	13.70	6.76	0.04	0.09	0.01	100.22	56.85	129.33	7.29	53854.00	174538.97	46847.95	261551.60	13.79	12.04	98819.56	78.70	700.86	
D16	Vein3 Omp	LSZ 63-15d	55.84	0.01	6.53	0.01	6.82	0.16	10.15	15.31	6.06	0.01	0.09	0.05	100.70	59.78	92.04	9.49	49171.41	185114.94	39503.40	261027.58	15.55	-7.64	102545.08	97.07	550.17	
D20	Vein2 Omp	LSZ 63-15d	55.08	0.01	7.18	0.03	7.81	0.09	8.48	13.62	6.90	0.02	0.06	0.04	98.94	52.03	87.39	6.53	53040.22	131241.91	41213.33	257460.35	11.43	-11.71	96047.88	90.23	505.19	
D23	Vein2 Omp	LSZ 63-15d	56.84	0.05	7.04	0.04	7.91	0.01	8.74	13.75	5.78	0.07	0.00	0.01	100.24	52.50	89.33	4.70	57347.19	117598.93	47162.37	265700.83	12.72	55.12	102056.74	60.74	665.50	
D24	Vein2 Omp	LSZ 63-15d	56.39	0.06	8.26	0.00	7.49	0.02	8.60	13.01	7.35	0.01	0.00	0.00	101.20	53.45	80.27	3.77	54952.57	115095.62	40846.21	263602.38	7.27	-7.40	111726.62	68.58	385.03	
D25	Vein2 Omp	LSZ 63-15d	56.39	0.06	8.26	0.00	7.49	0.02	8.60	13.01	7.35	0.01	0.00	0.00	101.20	53.45	69.61	7.97	56537.78	111036.19	41997.73	263602.38	7.90	18.90	102270.80	59.43	364.44	
D26	Vein2 Omp	LSZ 63-15d	56.38	0.00	6.71	0.02	8.27	0.00	9.25	14.47	6.43	0.00	0.04	0.02	101.58	52.80	69.73	3.00	57063.24	103378.80	41904.35	263568.72	6.79	-5.46	100592.74	82.77	362.55	
D27	Vein2 Omp	LSZ 63-15d	56.83	0.00	9.52	0.06	6.18	0.01	8.51	12.78	7.56	0.00	0.00	0.03	101.47	57.94	75.48	3.06	57475.63	97364.29	42420.98	265662.96	6.51	10.28	106990.10	67.21	441.26	
D28	Vein2 Omp	LSZ 63-15d	56.35	0.00	8.23	0.03	6.45	0.05	9.05	13.84	7.29	0.00	0.00	0.00	101.28	58.38	68.69	3.03	56886.29	99336.62	40406.01	263429.41	7.11	23.10	106343.00	66.51	368.55	
D29	Vein2 Omp	LSZ 63-15d	57.06	0.14	7.67	0.00	7.05	0.00	9.10	13.50	7.12	0.00	0.03	0.00	101.67	56.34	79.83	2.41	58385.76	89238.33	42237.35	266714.29	5.24	14.88	106461.75	60.33	325.06	
C15	M2 matrix	LSZ 63-15d	55.71	0.04	7.80	0.09	6.21	0.01	7.65	13.59	7.18	0.01	0.04		98.22	55.18	240.32	14.70	60100.47	71602.70	51094.28	260425.01	0.37	7.11	100250.67	178.30	18.83	
C16	M2 matrix	LSZ 63-15d	55.83	0.07	7.71	0.11	5.78	0.06	7.83	13.84	6.81	0.02	0.04		97.97	57.53	230.12	13.00	55239.24	81163.09	47684.23	260985.97	0.37	8.41	107769.40	220.39	17.89	
C19	M2 matrix	LSZ 63-15d	55.97	0.02	6.95	0.04	6.85	0.12	11.00	14.40	6.38	0.00	0.03		101.71	61.62	219.05	10.56	54453.29	85250.93	44645.17	261640.42	0.57	5.83	98028.01	248.03	17.52	
C20	M2 matrix	LSZ 63-15d	54.39	0.01	7.67	0.03	6.40	0.00	10.58	13.77	6.89	0.01	0.01		99.69	62.31	229.21	13.15	53072.14	85683.97	43066.20	254254.47	0.42	-1.35	103891.35	264.71	17.36	
C25	M2 matrix	LSZ 63-15d	55.84	0.00	8.00	0.08	6.09	0.02	10.28	13.27	7.20	0.00	0.03		100.81	62.79	255.33	13.10	54169.75	95941.51	45951.51	261032.72	0.51	12.86	102476.91	302.92	20.33	
C26	M2 matrix	LSZ 63-15d	55.94	0.01	7.41	0.10	6.98	0.03	10.59	13.56	6.67	0.01	0.05		101.26	60.27	248.81	13.61	88216.03	95579.91	44583.04	261500.18	0.49	11.02	100219.71	304.37	20.20	
C29	M2 matrix	LSZ 63-15d	55.27	0.01	7.08	0.06	6.48	0.04	11.13	14.31	6.36	0.00	0.01		100.76	63.22	287.42	14.96	52737.09	100893.13	45964.04	258368.16	0.52	7.59	103940.18	297.08	21.66	

Trace element data with (-) are below their respective detection limit (method: Pettke et Al., 2012)

APPENDIX 1 (a): EPMA ANALYSIS of SELECTED OMPHACITE CRYSTALS with the COMPLETE TRACE-ELEMENTS DATASET

Samples from the Lower Shear Zone: Breccia blocks with only Fe-Ti metagabbro clasts

# Analysis	Microstructural domain	Sample	LA-ICP-MS concentration (µg/g)																							
			V	Cr	Mn	Fe	Co	Ni	As	Rb	Sr	Y	Zr	Nb	Sb	Cs	Ba	La	Ce	Pr	Nd	Sm	Eu	Gd	Tb	Dy
B07	Mylonitic Clast- core Omp	LSZ 53-15	305.40	1.45	59.92		19.13	3.38	0.07	0.02	8.61	0.15	0.31	0.01	0.06	0.01	0.08	0.01	0.01	0.00	0.06	0.04	0.05	0.07	0.02	0.07
B08	Mylonitic Clast- core Omp	LSZ 53-15	538.21	2.64	103.80		17.78	2.27	0.13	0.04	6.67	0.15	0.28	0.01	0.11	0.02	0.15	0.01	0.01	0.00	0.05	0.04	0.03	0.08	0.02	0.08
B09	Mylonitic Clast- core Omp	LSZ 53-15	644.76	5.37	76.28		18.30	3.44	0.23	0.08	7.55	0.16	0.24	0.03	0.20	0.05	0.21	0.01	0.03	0.01	0.11	0.11	0.06	0.27	0.03	0.10
B10	Mylonitic Clast- core Omp	LSZ 53-15	660.49	5.12	82.97		18.11	5.72	0.22	0.07	7.61	0.17	0.29	0.03	0.19	0.04	0.18	0.01	0.02	0.01	0.10	0.10	0.07	0.12	0.02	0.09
B12	Mylonitic Clast- core Omp	LSZ 53-15	630.42	5.64	80.40		17.67	3.70	0.23	0.09	8.35	0.24	0.32	0.04	0.25	0.03	0.27	0.02	0.02	0.02	0.10	0.09	0.04	0.13	0.02	0.08
B13	Mylonitic Clast- core Omp	LSZ 53-15	642.03	2.95	72.93		15.34	4.40	0.12	0.05	9.97	0.20	1.42	0.02	0.13	0.02	0.14	0.01	0.03	0.01	0.05	0.10	0.07	0.27	0.02	0.05
B14	Mylonitic Clast- core Omp	LSZ 53-15	487.30	3.84	76.90		17.00	3.60	0.16	0.07	8.14	0.11	0.28	0.03	0.18	0.02	0.20	0.02	0.02	0.02	0.08	0.08	0.06	0.13	0.04	0.07
B19	Mylonitic Clast- rim Omp	LSZ 53-15	400.33	67.27	343.87		12.80	69.27	0.29	0.13	30.00	3.12	1.67	0.07	0.36	0.05	0.36	0.04	0.10	0.09	0.74	0.69	0.43	1.67	0.16	0.59
B30	Omp inclusion in Grt	LSZ 53-15	420.72	8.68	72.47		11.96	99.98	0.22	0.31	5.39	0.15	0.23	0.04	0.79	0.03	0.07	0.02	0.01	0.01	0.08	0.05	0.03	0.13	0.01	0.08
B31	Omp inclusion in Grt	LSZ 53-15	350.45	6.52	56.54		10.96	65.06	0.17	0.25	5.82	0.19	0.23	0.03	0.61	0.02	0.08	0.02	0.01	0.01	0.07	0.05	0.03	0.19	0.01	0.08
B27	M1 matrix	LSZ 53-15	418.75	171.40	358.48		6.62	783.72	0.07	0.07	19.73	6.67	108.44	0.02	0.14	0.01	0.14	0.01	0.11	0.03	0.38	0.52	0.27	1.46	0.21	1.15
B28	Crushed matrix - Omp2b	LSZ 53-15	538.13	261.62	336.05		7.58	166.04	0.19	0.07	17.64	3.39	0.55	0.02	0.04	0.04	0.15	0.02	0.15	0.06	0.54	0.66	0.37	1.60	0.20	0.98
B29	Crushed matrix - Omp2b	LSZ 53-15	525.30	298.04	381.49		8.89	193.22	-0.02	0.19	19.94	3.75	0.53	0.01	0.15	0.06	0.10	0.01	0.16	0.07	0.60	0.74	0.42	1.96	0.29	1.18
B31	Crushed matrix - Omp2b	LSZ 53-15	494.74	149.21	301.55		8.19	137.96	-0.17	0.06	7.76	2.93	0.45	0.01	0.16	0.03	0.46	0.01	0.07	0.03	0.23	0.39	0.21	1.11	0.18	0.83
B34	Crushed matrix - Omp2b	LSZ 53-15	367.48	105.55	199.84		5.81	101.07	-0.03	0.08	6.39	1.50	0.27	0.03	0.14	0.09	0.15	0.02	0.07	0.01	0.27	0.25	0.21	0.73	0.15	0.61
B36	Crushed matrix - Omp2b	LSZ 53-15	457.73	369.55	288.85		7.86	201.23	-0.03	0.05	18.50	2.52	0.40	0.02	0.15	0.06	0.15	0.02	0.14	0.06	0.60	0.72	0.35	1.93	0.23	0.94
B35	Crushed matrix - Omp2b	LSZ 53-15	346.72	90.85	191.74		5.49	124.95	-0.06	0.05	5.78	1.78	0.40	0.01	0.03	0.02	0.25	0.02	0.09	0.03	0.23	0.28	0.13	0.65	0.12	0.61
B37	Crushed matrix - Omp2b	LSZ 53-15	490.93	165.19	273.05		7.42	190.05	-0.01	0.03	8.50	2.83	12.91	0.01	0.00	0.03	0.08	0.03	0.14	0.05	0.41	0.48	0.24	1.35	0.21	0.89
A16	Mylonitic Clast- core Omp	LSZ 53-15	354.52	49.60	266.31		10.44	27.31	0.44	0.08	13.59	2.05	161.56	0.05	0.95	0.06	0.34	0.03	0.11	0.06	0.35	0.68	0.10	0.84	0.07	0.66
A18	Mylonitic Clast- core Omp	LSZ 53-15	318.80	29.61	246.01		11.94	19.54	0.14	0.04	12.89	1.83	6.92	0.01	7.47	0.02	0.11	0.02	0.08	0.03	0.33	0.59	0.17	0.73	0.08	0.44
A20	Mylonitic Clast- core Omp	LSZ 53-15	325.47	23.01	194.68		12.79	15.59	0.24	0.06	10.02	1.63	0.58	0.01	13.05	0.03	0.17	0.02	0.07	0.02	0.21	0.46	0.14	0.60	0.07	0.38
B06	Mylonitic Clast- core Omp	LSZ 14-50	278.31	2.60	70.17	108125.24	21.42	4.14	-0.01	-0.01	9.38	0.94	15.99	0.01	-0.02	0.00	0.05	0.01	0.03	0.01	0.06	0.07	0.06	0.18	0.03	0.19
B13	Mylonitic Clast- core Omp	LSZ 14-50	585.07	6.38	138.71	110864.03	18.70	5.10	-0.01	0.01	9.57	0.64	0.68	0.01	-0.01	0.00	0.19	0.01	0.03	0.01	0.07	0.07	0.05	0.14	0.03	0.14
B15	Mylonitic Clast- core Omp	LSZ 14-50	499.49	10.73	117.44	91396.29	15.48	10.17	-0.03	-0.02	14.20	1.28	0.64	-0.01	-0.04	-0.01	0.18	0.01	0.05	0.01	0.16	0.13	0.12	0.33	0.05	0.26
B16	Mylonitic Clast- core Omp	LSZ 14-50	615.08	7.43	135.09	86763.04	13.54	9.20	-0.02	-0.01	13.59	0.59	23.20	0.00	-0.02	-0.01	0.07	0.01	0.03	0.01	0.13	0.14	0.11	0.29	0.04	0.15
B17	Mylonitic Clast- core Omp	LSZ 14-50	484.00	11.68	281.90	106308.01	16.37	7.67	0.03	0.04	7.85	1.21	1.94	0.03	-0.02	-0.01	0.49	2.42	8.41	1.34	6.56	1.39	0.28	0.80	0.06	0.24
B23	M1 matrix	LSZ 14-50	502.25	203.75	335.33	87779.70	12.70	45.05	-0.03	0.13	12.79	2.45	0.77	-0.01	-0.04	-0.01	0.19	0.03	0.14	0.04	0.35	0.37	0.19	0.63	0.12	0.58
B28	M1 matrix	LSZ 14-50	498.56	839.36	252.10	69695.62	34.72	79.42	0.03	0.08	21.70	3.37	0.84	0.02	0.01	0.01	0.81	0.02	0.14	0.05	0.62	0.81	0.45	1.68	0.22	0.97
B29	M1 matrix	LSZ 14-50	530.63	583.90	384.63	82268.25	10.95	34.90	-0.02	-0.01	9.17	1.75	0.46	0.00	-0.02	0.00	0.07	0.01	0.08	0.03	0.32	0.33	0.17	0.73	0.10	0.49
B31	Late-Stage Vein	LSZ 14-50	645.64	2358.02	499.92	66452.96	18.48	85.58	-0.02	0.04	17.00	6.96	0.66	0.01	-0.02	-0.01	0.35	0.02	0.18	0.07	0.65	0.92	0.44	1.80	0.30	1.69
B32	Late-Stage Vein	LSZ 14-50	480.23	726.25	439.53	85599.09	10.41	56.14	-0.03	-0.02	8.58	3.80	0.71	-0.01	-0.05	-0.01	-0.07	0.02	0.12	0.04	0.44	0.42	0.24	0.94	0.15	0.86
B33																										

APPENDIX 1 (a-follow): EPMA ANALYSIS of SELECTED OMPHACITE CRYSTALS with the COMPLETE TRACE-ELEMENTS DATASET

Samples from the Lower Shear Zone: Breccia blocks with only Fe-Ti metagabbro clasts

# Analysis	Microstructural domain	Sample	LA-ICP-MS concentration (μg/g)																							
			V	Cr	Mn	Fe	Co	Ni	As	Rb	Sr	Y	Zr	Nb	Sb	Cs	Ba	La	Ce	Pr	Nd	Sm	Eu	Gd	Tb	Dy
B20	M1 matrix	LSZ 63-15b	471.17	1198.32	124.18	58267.32	27.52	204.96	-0.02	-0.01	14.88	1.97	0.50	0.01	-0.03	-0.01	0.07	0.01	0.10	0.04	0.39	0.42	0.15	0.63	0.11	0.46
B21	M1 matrix	LSZ 63-15b	420.38	887.65	141.39	61556.53	28.31	229.12	-0.01	0.00	10.56	2.55	0.45	0.01	-0.01	0.00	0.02	0.01	0.07	0.04	0.35	0.39	0.12	0.60	0.10	0.50
B23	M1 matrix	LSZ 63-15b	427.49	530.90	159.60	64587.30	27.87	236.89	-0.02	0.01	14.96	1.62	0.52	-0.01	-0.03	0.00	-0.04	0.01	0.07	0.03	0.33	0.27	0.12	0.34	0.06	0.36
B26	M1 matrix	LSZ 63-15b	346.33	341.95	130.35	66034.12	29.51	212.57	-0.02	-0.01	13.01	1.57	0.46	-0.01	-0.03	-0.01	0.02	0.01	0.06	0.03	0.25	0.26	0.09	0.37	0.06	0.41
B27	M1 matrix	LSZ 63-15b	575.59	903.03	195.09	50682.48	18.68	107.58	-0.01	-0.01	47.49	0.88	3.06	0.01	-0.01	0.00	0.01	0.02	0.24	0.09	0.96	0.75	0.27	0.72	0.07	0.30
B29	M1 matrix	LSZ 63-15b	543.93	874.29	176.78	55387.46	20.99	118.81	0.01	-0.01	42.25	1.09	0.43	0.00	-0.01	0.00	0.04	0.02	0.21	0.08	0.88	0.66	0.25	0.74	0.07	0.31
B35	M1 matrix	LSZ 63-15b	726.13	932.74	191.04	44454.60	18.97	90.09	-0.06	-0.03	29.51	0.92	0.48	-0.01	-0.09	-0.02	0.34	-0.01	0.16	0.04	0.41	0.41	0.17	0.56	0.05	0.24
DO7	Vein3 Omp	LSZ 63-15d	4673.30	142.19	715.15	224374.44	94.68	274.57	0.05	0.19	113.53	2.08	2.10	-0.01	-0.03	-0.01	0.71	0.09	1.06	0.46	4.88	4.06	1.63	3.62	0.27	0.92
DO8	Vein3 Omp	LSZ 63-15d	4673.30	142.19	715.15	224374.44	94.68	274.57	0.05	0.19	113.53	2.08	2.10	-0.01	-0.03	-0.01	0.71	0.09	1.06	0.46	4.88	4.06	1.63	3.62	0.27	0.92
DO9	Vein3 Omp	LSZ 63-15d	4808.85	351.26	929.50	205924.14	61.38	291.93	-0.07	-0.04	115.80	3.41	2.37	-0.02	-0.10	-0.03	-0.21	0.07	0.74	0.31	2.92	2.74	0.96	2.87	0.34	1.37
D10	Vein3 Omp	LSZ 63-15d	4131.75	133.70	621.38	221870.00	87.04	244.05	0.03	0.03	92.17	1.81	1.78	0.00	-0.03	-0.01	0.14	0.09	0.85	0.38	4.35	3.84	1.38	3.23	0.24	0.60
D11	Vein3 Omp	LSZ 63-15d	4672.61	262.86	707.20	194447.33	73.61	292.13	-0.07	-0.03	112.51	2.33	1.96	-0.02	-0.10	-0.02	0.29	0.06	1.07	0.42	4.25	3.28	1.17	3.08	0.22	0.91
D13	Vein3 Omp	LSZ 63-15d	3812.40	50.15	513.60	199381.58	83.58	226.05	-0.03	-0.02	87.49	1.11	1.80	-0.01	-0.05	-0.01	-0.07	0.06	0.71	0.32	3.61	3.28	1.31	3.46	0.20	0.54
D14	Vein3 Omp	LSZ 63-15d	3809.38	166.75	596.06	172588.92	68.86	194.08	-0.03	-0.01	96.46	1.53	1.54	-0.01	-0.05	-0.01	0.08	0.07	0.66	0.30	3.36	2.62	0.91	2.29	0.18	0.70
D15	Vein3 Omp	LSZ 63-15d	3809.38	166.75	596.06	172588.92	68.86	194.08	-0.03	-0.01	96.46	1.53	1.54	-0.01	-0.05	-0.01	0.08	0.07	0.66	0.30	3.36	2.62	0.91	2.29	0.18	0.70
D16	Vein3 Omp	LSZ 63-15d	3209.75	86.94	927.84	167628.48	50.25	153.54	-0.05	-0.03	86.57	3.38	1.76	-0.01	-0.09	-0.02	-0.10	0.04	0.45	0.21	1.97	1.69	0.72	2.07	0.24	1.15
D20	Vein2 Omp	LSZ 63-15d	2914.20	203.93	465.72	161490.79	37.55	205.87	-0.08	-0.04	70.27	1.62	1.02	-0.02	-0.12	-0.02	-0.22	0.08	0.48	0.24	2.67	2.10	0.68	2.04	0.22	0.65
D23	Vein2 Omp	LSZ 63-15d	2714.14	4.67	296.94	115638.62	66.78	189.82	-0.05	-0.02	65.95	0.54	1.26	-0.01	-0.06	-0.01	-0.08	0.07	0.63	0.32	3.81	3.55	1.47	3.29	0.14	0.32
D24	Vein2 Omp	LSZ 63-15d	2430.20	20.00	362.31	120440.96	31.17	118.60	-0.05	-0.03	70.20	0.69	0.94	-0.01	-0.08	-0.02	-0.18	0.03	0.45	0.17	2.18	1.68	0.62	1.23	0.12	0.25
D25	Vein2 Omp	LSZ 63-15d	2203.64	321.42	331.08	109419.04	36.11	140.87	-0.04	-0.02	64.37	0.79	0.81	0.00	-0.06	-0.01	-0.13	0.04	0.42	0.17	1.92	1.65	0.54	1.20	0.12	0.36
D26	Vein2 Omp	LSZ 63-15d	2265.57	4.58	264.18	118443.53	31.04	82.07	-0.03	-0.02	47.57	0.31	0.69	0.00	-0.05	-0.01	-0.10	0.01	0.28	0.13	1.37	1.49	0.52	1.40	0.08	0.13
D27	Vein2 Omp	LSZ 63-15d	2110.07	4.52	289.40	112351.33	30.85	93.67	-0.03	-0.01	44.87	0.41	0.67	0.01	-0.04	-0.01	-0.05	0.03	0.41	0.20	2.28	1.67	0.66	1.15	0.08	0.27
D28	Vein2 Omp	LSZ 63-15d	1967.98	3.12	287.09	110181.64	31.46	89.47	-0.01	0.01	42.76	0.47	1.07	0.00	-0.02	0.00	0.08	0.03	0.46	0.21	2.27	1.87	0.67	1.38	0.08	0.20
D29	Vein2 Omp	LSZ 63-15d	1938.46	4.18	284.62	103475.35	25.35	90.80	-0.01	-0.01	47.36	0.37	0.60	0.00	-0.02	0.00	0.03	0.02	0.34	0.15	1.71	1.18	0.44	0.90	0.06	0.19
C15	M2 matrix	LSZ 63-15d	6863.36	4397.54	724.72	70958.78	119.07	553.20	-0.06	0.07	190.25	6.42	3.77	-0.02	-0.08	-0.01	0.20	0.13	1.45	0.57	5.30	4.38	1.84	5.11	0.52	2.11
C16	M2 matrix	LSZ 63-15d	6833.77	2332.41	752.69	73017.27	130.62	594.19	0.07	0.03	245.21	6.98	3.48	-0.01	-0.07	-0.01	-0.09	0.11	1.24	0.58	5.76	4.93	2.02	5.80	0.62	2.30
C19	M2 matrix	LSZ 63-15d	7180.25	2293.36	730.00	75347.51	139.51	550.39	0.07	0.05	227.57	7.51	3.52	-0.01	-0.05	-0.01	-0.06	0.24	2.27	0.87	8.39	6.28	2.50	5.90	0.60	2.33
C20	M2 matrix	LSZ 63-15d	7381.30	3050.87	832.37	75357.26	142.85	608.05	0.08	-0.05	269.93	9.20	3.98	-0.03	-0.12	-0.02	-0.15	0.23	2.27	0.87	8.45	5.79	2.61	6.55	0.73	2.92
C25	M2 matrix	LSZ 63-15d	8358.82	2800.06	839.17	83992.85	152.96	641.87	0.07	0.08	266.88	9.59	4.35	0.02	0.06	-0.01	0.13	0.25	2.24	0.93	9.19	7.11	2.92	7.27	0.81	3.25
C26	M2 matrix	LSZ 63-15d	8476.04	2876.10	849.05	85370.28	160.05	661.10	0.07	0.10	285.13	10.10	4.64	0.01	0.04	-0.01	0.16	0.30	2.57	1.00	9.24	7.06	2.97	7.72	0.77	3.03
C29	M2 matrix	LSZ 63-15d	8875.22	3628.74	985.03	88544.15	159.79	741.69	0.06	0.04	290.40	9.89	4.82	0.03	-0.08	-0.02	0.11	0.22	2.13	0.82	8.28	6.48	2.78	7.98	0.81	3.47

Trace element data with (-) are below their respective detection limit (method: Pettke et Al., 2012)

APPENDIX 1 (a): EPMA ANALYSIS of SELECTED OMPHACITE CRYSTALS with the COMPLETE TRACE-ELEMENTS DATASET
Samples from the Lower Shear Zone: Breccia blocks with only Fe-Ti metagabbro clasts

Ho	# Analysis	Microstructural domain	Sample	LA-ICP-MS concentration (µg/g)									
				Er	Tm	Yb	Lu	Hf	Ta	Pb	Bi	Th	U
0.01	B07	Mylonitic Clast- core Omp	LSZ 53-15	0.01	0.01	0.04	0.00	0.04	0.01	0.04	0.03	0.01	0.01
0.01	B08	Mylonitic Clast- core Omp	LSZ 53-15	0.02	0.01	0.07	0.00	0.04	0.01	0.07	0.04	0.02	0.01
0.02	B09	Mylonitic Clast- core Omp	LSZ 53-15	0.05	0.03	0.12	0.02	0.09	0.02	0.12	0.07	0.03	0.03
0.02	B10	Mylonitic Clast- core Omp	LSZ 53-15	0.04	0.03	0.10	0.02	0.08	0.02	0.12	0.06	0.03	0.03
0.02	B12	Mylonitic Clast- core Omp	LSZ 53-15	0.07	0.02	0.10	0.02	0.03	0.01	0.12	0.07	0.03	0.01
0.01	B13	Mylonitic Clast- core Omp	LSZ 53-15	0.04	0.01	0.05	0.01	0.03	0.00	0.06	0.04	0.01	0.00
0.02	B14	Mylonitic Clast- core Omp	LSZ 53-15	0.06	0.01	0.08	0.01	0.05	0.01	0.09	0.05	0.02	0.01
0.15	B19	Mylonitic Clast- rim Omp	LSZ 53-15	0.17	0.07	0.10	0.03	0.11	0.03	0.28	0.10	0.03	0.03
0.02	B30	Omp inclusion in Grt	LSZ 53-15	0.04	0.02	0.08	0.01	0.03	0.02	0.09	0.08	0.03	0.01
0.01	B31	Omp inclusion in Grt	LSZ 53-15	0.04	0.02	0.07	0.01	0.03	0.01	0.08	0.07	0.03	0.01
0.21	B27	M1 matrix	LSZ 53-15	0.50	0.06	0.31	0.05	2.27	0.00	0.18	0.02	0.03	0.07
0.17	B28	Crushed matrix - Omp2b	LSZ 53-15	0.38	0.04	0.18	0.05	0.09	0.01	3.28	0.07	0.01	0.02
0.18	B29	Crushed matrix - Omp2b	LSZ 53-15	0.57	0.04	0.22	0.06	0.06	0.01	4.40	0.02	0.01	0.01
0.15	B31	Crushed matrix - Omp2b	LSZ 53-15	0.41	0.04	0.27	0.03	0.10	0.00	4.01	0.04	0.01	0.00
0.09	B34	Crushed matrix - Omp2b	LSZ 53-15	0.20	0.03	0.16	0.01	0.10	0.02	1.19	0.05	0.03	0.03
0.16	B36	Crushed matrix - Omp2b	LSZ 53-15	0.33	0.04	0.11	0.01	0.06	0.01	0.77	0.03	0.02	0.02
0.09	B35	Crushed matrix - Omp2b	LSZ 53-15	0.27	0.03	0.16	0.02	0.10	0.00	0.19	0.00	0.01	0.01
0.16	B37	Crushed matrix - Omp2b	LSZ 53-15	0.34	0.04	0.21	0.04	0.70	0.01	0.32	0.01	0.02	0.01
0.08	A16	Mylonitic Clast- core Omp	LSZ 53-15	0.16	0.03	0.17	0.05	4.45	0.03	0.24	0.12	0.03	0.03
0.07	A18	Mylonitic Clast- core Omp	LSZ 53-15	0.13	0.03	0.13	0.01	0.33	0.01	0.10	0.03	0.01	0.01
0.06	A20	Mylonitic Clast- core Omp	LSZ 53-15	0.13	0.03	0.13	0.03	0.06	0.01	0.11	0.05	0.01	0.01
0.04	B06	Mylonitic Clast- core Omp	LSZ 14-50	0.13	0.02	0.22	0.04	0.45	0.00	0.03	0.00	0.00	0.00
0.03	B13	Mylonitic Clast- core Omp	LSZ 14-50	0.08	0.01	0.08	0.01	0.08	0.00	0.04	0.00	0.00	0.00
0.04	B15	Mylonitic Clast- core Omp	LSZ 14-50	0.16	0.03	0.12	0.03	0.09	0.00	0.10	-0.01	-0.01	-0.01
0.03	B16	Mylonitic Clast- core Omp	LSZ 14-50	0.06	0.01	0.07	0.01	0.70	0.00	0.05	0.00	0.00	0.00
0.05	B17	Mylonitic Clast- core Omp	LSZ 14-50	0.17	0.02	0.15	0.03	0.15	0.00	0.07	0.00	0.04	0.01
0.10	B23	M1 matrix	LSZ 14-50	0.28	0.03	0.24	0.04	0.07	0.00	0.08	-0.01	0.01	-0.01
0.15	B28	M1 matrix	LSZ 14-50	0.39	0.05	0.33	0.05	0.08	0.00	0.18	0.00	0.00	0.00
0.06	B29	M1 matrix	LSZ 14-50	0.14	0.02	0.13	0.02	0.05	0.00	0.03	-0.01	0.00	0.00
0.28	B31	Late-Stage Vein	LSZ 14-50	0.68	0.09	0.41	0.05	0.08	0.00	0.11	0.00	0.00	0.00
0.14	B32	Late-Stage Vein	LSZ 14-50	0.42	0.07	0.34	0.04	0.06	0.00	-0.05	0.01	-0.01	-0.01
0.46	B33	Late-Stage Vein	LSZ 14-50	1.34	0.17	1.10	0.15	0.35	0.02	0.22	0.00	0.01	0.01
0.13	B34	Late-Stage Vein	LSZ 14-50	0.38	0.05	0.41	0.05	0.10	-0.01	0.19	-0.01	0.04	0.01
0.27	B35	M1 matrix	LSZ 14-50	0.73	0.09	0.44	0.05	0.07	0.00	0.12	-0.01	0.00	-0.01
0.07	B36	M1 matrix	LSZ 14-50	0.17	0.02	0.09	0.01	0.03	0.00	0.05	-0.01	0.00	-0.01
0.10	B37	M1 matrix	LSZ 14-50	0.21	0.03	0.17	0.02	0.07	0.00	0.08	-0.01	0.00	0.00
0.06	B38	M1 matrix	LSZ 14-50	0.12	0.02	0.08	0.01	0.04	0.00	0.04	-0.01	0.00	0.00
0.14	B39	M1 matrix	LSZ 14-50	0.33	0.03	0.16	0.02	0.06	-0.01	0.10	-0.01	0.00	-0.01
0.04	B40	M1 matrix	LSZ 14-50	0.10	0.01	0.10	0.02	0.46	-0.01	0.05	-0.01	0.00	-0.01
0.03	A12	Mylonitic Clast- core Omp	LSZ 63-15b	0.07	0.01	0.13	0.01	0.07	-0.01	0.05	-0.01	-0.01	0.00
0.02	A13	Mylonitic Clast- rim Omp	LSZ 63-15b	0.05	0.00	0.06	0.01	0.04	0.00	0.09	-0.01	-0.01	0.00
0.04	A14	Mylonitic Clast- core Omp	LSZ 63-15b	0.10	0.01	0.12	0.02	0.07	0.00	0.05	0.00	0.00	0.00
0.03	A15	Mylonitic Clast- core Omp	LSZ 63-15b	0.06	0.01	0.05	0.01	0.05	0.00	0.06	0.00	0.00	0.00
0.02	A16	Mylonitic Clast- rim Omp	LSZ 63-15b	0.07	0.01	0.08	0.01	0.08	0.00	0.10	-0.01	0.00	0.00
0.02	A17	Mylonitic Clast- core Omp	LSZ 63-15b	0.05	0.01	0.08	0.02	0.06	0.00	0.05	-0.01	0.00	0.00
0.02	A18	Mylonitic Clast- rim Omp	LSZ 63-15b	0.09	0.01	0.07	0.03	-0.04	-0.01	0.08	-0.02	-0.02	-0.01
0.03	A19	Mylonitic Clast- rim Omp	LSZ 63-15b	0.05	0.01	0.06	0.00	0.04	0.00	0.09	-0.01	0.00	-0.01
0.01	A20	Mylonitic Clast- rim Omp	LSZ 63-15b	0.03	0.00	0.01	0.00	0.04	0.00	0.09	0.00	0.00	0.00
0.03	A21	Mylonitic Clast- core Omp	LSZ 63-15b	0.09	0.01	0.11	0.01	0.08	0.00	0.06	0.00	0.01	0.01
0.04	A22	Mylonitic Clast- core Omp	LSZ 63-15b	0.11	0.02	0.15	0.03	0.06	0.00	0.06	0.00	0.01	0.00
0.02	A23	Mylonitic Clast- rim Omp	LSZ 63-15b	0.06	0.01	0.08	0.01	0.05	0.00	0.05	-0.01	0.00	0.00
0.05	A24	Mylonitic Clast- core Omp	LSZ 63-15b	0.17	0.04	0.28	0.05	0.10	0.00	0.08	-0.01	0.00	0.00
0.01	A25	Mylonitic Clast- rim Omp	LSZ 63-15b	0.04	0.00	0.04	-0.01	0.04	0.00	0.12	-0.01	-0.01	0.00
0.08	A26	Vein1 Omp	LSZ 63-15b	0.19	0.02	0.15	0.03	0.07	0.00	0.08	0.00	0.00	0.00
0.02	A27	Vein1 Omp	LSZ 63-15b	0.03	0.00	0.02	0.00	0.04	0.00	0.11	0.00	0.00	0.00
0.02	A28	Vein1 Omp	LSZ 63-15b	0.03	0.00	0.01	0.00	0.05	0.00	0.11	0.00	0.00	0.00
0.07	A29	Vein1 Omp	LSZ 63-15b	0.14	0.02	0.08	0.01	0.05	0.00	0.09	0.00	0.00	0.00
0.09	A30	Vein1 Omp	LSZ 63-15b	0.21	0.03	0.12	0.01	0.08	0.00	0.08	-0.01	0.00	0.00
0.03	B16	M1 matrix	LSZ 63-15b	0.05	0.01	0.02	0.00	0.05	0.00	0.20	0.01	0.00	0.00
0.04	B17	M1 matrix	LSZ 63-15b	0.07	0.01	0.04	0.00	0.05	0.00	0.23	0.00	0.00	0.00
0.03	B18	M1 matrix	LSZ 63-15b	0.05	0.01	0.03	0.00	0.05	0.00	0.19	-0.01	0.00	0.00
0.05	B19	M1 matrix	LSZ 63-15b	0.14	0.02	0.09	0.01	0.05	0.00	0.10	0.01	0.00	0.00

APPENDIX 1 (a-follow): EPMA ANALYSIS of SELECTED OMPHACITE CRYSTALS with the COMPLETE TRACE-ELEMENTS DATASET
Samples from the Lower Shear Zone: Breccia blocks with only Fe-Ti metagabbro clasts

Ho	# Analysis	Microstructural domain	Sample	LA-ICP-MS concentration (µg/g)									
				Er	Tm	Yb	Lu	Hf	Ta	Pb	Bi	Th	U
0.07	B20	M1 matrix	LSZ 63-15b	0.19	0.02	0.13	0.02	0.06	0.00	0.09	-0.01	0.00	0.00
0.11	B21	M1 matrix	LSZ 63-15b	0.25	0.03	0.18	0.02	0.05	0.00	0.06	0.00	0.00	0.00
0.06	B23	M1 matrix	LSZ 63-15b	0.14	0.01	0.09	0.01	0.06	0.00	0.07	-0.01	0.00	0.00
0.06	B26	M1 matrix	LSZ 63-15b	0.15	0.02	0.10	0.01	0.04	0.00	0.09	-0.01	0.00	0.00
0.04	B27	M1 matrix	LSZ 63-15b	0.06	0.01	0.04	0.00	0.10	0.00	0.23	0.00	0.00	0.00
0.04	B29	M1 matrix	LSZ 63-15b	0.09	0.01	0.05	0.01	0.05	0.00	0.21	0.00	0.00	0.00
0.04	B35	M1 matrix	LSZ 63-15b	0.06	0.01	0.05	-0.01	0.08	-0.01	0.12	0.01	-0.02	-0.01
0.09	DO7	Vein3 Omp	LSZ 63-15d	0.22	0.02	0.20	0.03	0.27	0.00	0.61	0.00	0.00	0.00
0.09	DO8	Vein3 Omp	LSZ 63-15d	0.22	0.02	0.20	0.03	0.27	0.00	0.61	0.00	0.00	0.00
0.15	DO9	Vein3 Omp	LSZ 63-15d	0.21	0.02	0.12	0.02	0.23	-0.01	0.71	-0.01	0.02	0.01
0.07	D10	Vein3 Omp	LSZ 63-15d	0.19	0.02	0.22	0.05	0.22	0.00	0.49	-0.01	0.01	0.00
0.09	D11	Vein3 Omp	LSZ 63-15d	0.27	0.02	0.21	0.03	0.36	-0.01	0.74	-0.03	-0.01	-0.01
0.05	D13	Vein3 Omp	LSZ 63-15d	0.10	-0.01	0.06	0.01	0.25	0.00	0.56	-0.01	0.00	0.00
0.07	D14	Vein3 Omp	LSZ 63-15d	0.13	0.01	0.08	0.01	0.17	0.00	0.42	-0.01	0.00	-0.01
0.07	D15	Vein3 Omp	LSZ 63-15d	0.13	0.01	0.08	0.01	0.17	0.00	0.42	-0.01	0.00	-0.01
0.13	D16	Vein3 Omp	LSZ 63-15d	0.32	0.02	0.17	0.02	0.19	0.00	0.56	-0.02	-0.01	-0.01
0.10	D20	Vein2 Omp	LSZ 63-15d	0.23	0.02	0.35	0.07	0.12	-0.02	0.30	-0.02	-0.01	-0.02
0.02	D23	Vein2 Omp	LSZ 63-15d	0.04	0.02	0.06	-0.01	0.26	-0.01	0.29	0.01	-0.01	0.00
0.02	D24	Vein2 Omp	LSZ 63-15d	0.12	0.01	0.06	-0.01	0.10	-0.01	0.28	-0.02	-0.01	-0.01
0.05	D25	Vein2 Omp	LSZ 63-15d	0.10	0.01	0.08	0.02	0.12	0.00	0.31	-0.01	0.00	-0.01
0.02	D26	Vein2 Omp	LSZ 63-15d	0.04	0.01	0.02	-0.01	0.13	0.00	0.15	-0.01	0.00	-0.01
0.02	D27	Vein2 Omp	LSZ 63-15d	0.05	-0.01	-0.03	-0.01	0.08	-0.01	0.21	-0.01	-0.01	-0.01
0.03	D28	Vein2 Omp	LSZ 63-15d	0.05	0.01	0.06	0.01	0.13	0.00	0.23	0.00	0.00	0.00
0.02	D29	Vein2 Omp	LSZ 63-15d	0.03	0.00	0.03	0.00	0.10	0.00	0.22	0.00	0.00	0.00
0.28	C15	M2 matrix	LSZ 63-15d	0.48	0.07	0.32	0.04	0.42	-0.01	0.84	-0.01	-0.01	0.01
0.27	C16	M2 matrix	LSZ 63-15d	0.70	0.07	0.38	0.05	0.37	-0.01	1.27	-0.02	0.01	-0.01
0.30	C19	M2 matrix	LSZ 63-15d	0.66	0.04	0.25	0.03	0.36	0.00	1.20	0.01	0.01	-0.01
0.42	C20	M2 matrix	LSZ 63-15d	0.76	0.08	0.50	0.05	0.42	0.00	1.49	-0.02	-0.02	-0.02
0.38	C25	M2 matrix	LSZ 63-15d	0.85	0.07	0.39	0.03	0.48	-0.01	1.59	0.04	0.02	0.01
0.38	C26	M2 matrix	LSZ 63-15d	0.84	0.09	0.43	0.04	0.46	-0.01	1.64	0.01	0.01	0.01
0.42	C29	M2 matrix	LSZ 63-15d	0.98	0.07	0.37	0.05	0.57	-0.01	1.78	-0.01	-0.01	-0.01

Trace element data with (-) are below their respective detection limit (method: Pettke et Al., 2012)

APPENDIX 1 (b): EPMA ANALYSIS of SELECTED OMPHACITE CRYSTALS with the COMPLETE TRACE-ELEMENTS DATASET

Samples from the Lower Shear Zone: Breccia blocks with Mg-Al + Fe-Ti metagabbro clasts

# Analysis	Microstrucrtal domain	Sample	EPMA analysis (internal standard) wt%														LA-ICP-MS concentration (µg/g)										
			SiO2	TiO2	Al2O3	Cr2O3	FeO	MnO	MgO	CaO	Na2O	K2O	NiO	P2O5	Total	MgO#	Li	B	Na	Mg	Al	Si	P	K	Ca		
C04	M3 matrix Omp	LSZ 14-10	55.29	0.02	3.46	0.01	7.18	0.09	12.15	19.96	3.48	0.00	0.05	0.00	101.68	62.86	34.01	1.27	25794.77	73264.74	18290.63	258461.66	4.78	31.11	142619.17		
C05	M3 matrix Omp	LSZ 14-10	55.71	0.03	4.49	0.02	7.36	0.08	11.54	19.13	4.24	0.00	0.05	0.00	102.67	61.07	43.81	1.64	31460.01	69627.55	23786.84	260425.01	5.17	12.17	136733.36		
C06	M3 matrix Omp	LSZ 14-10	54.91	0.03	3.76	0.02	6.40	0.08	12.25	20.69	3.64	0.00	0.06	0.00	101.84	65.69	38.39	1.47	26990.62	73888.55	19907.28	256685.29	4.19	16.34	147863.31		
C07	M3 matrix Omp	LSZ 14-10	54.27	0.03	3.85	0.02	6.26	0.08	11.89	19.92	3.71	0.00	0.05	0.00	100.07	65.51	39.56	1.47	27510.58	71697.58	20380.17	253659.75	4.23	9.63	142348.05		
C08	M3 matrix Omp	LSZ 14-10	54.63	0.02	3.78	0.03	6.97	0.08	12.01	20.35	3.67	0.00	0.07	0.00	101.62	63.29	36.18	6.85	27241.49	72445.89	20030.99	255376.39	3.37	17.14	145472.45		
C09	M3 matrix Omp	LSZ 14-10	54.95	0.02	3.79	0.02	6.54	0.08	12.17	19.96	3.79	0.01	0.04	0.00	101.38	65.02	31.71	1.35	28141.36	73370.47	20083.61	256872.27	3.93	77.30	142630.59		
C10	M3 matrix Omp	LSZ 14-10	54.95	0.02	4.89	0.03	6.86	0.08	11.04	18.37	4.60	0.00	0.04	0.00	100.89	61.69	39.87	1.48	34162.22	66606.22	25866.10	256872.27	3.99	18.17	131287.50		
C11	M3 matrix Omp	LSZ 14-10	54.45	0.02	3.75	0.01	6.64	0.08	11.94	19.87	3.52	0.00	0.06	0.00	100.34	64.24	36.05	1.26	26085.55	71997.35	19847.15	254534.95	3.49	4.33	142008.27		
C12	M3 matrix Omp	LSZ 14-10	54.65	0.02	3.84	0.01	6.50	0.08	11.95	19.75	3.67	0.00	0.06	0.00	100.54	64.77	37.22	1.54	27240.36	72049.69	20346.91	255469.88	4.00	9.68	141187.43		
C13	M3 matrix Omp	LSZ 14-10	55.01	0.02	3.19	0.01	7.03	0.09	12.55	20.87	3.12	0.00	0.06	0.00	101.96	64.09	31.45	1.47	23151.75	75699.21	16875.40	257152.75	5.50	13.48	149185.52		
C08	Mylonitic Clast- core Omp	LSZ 14-11	55.92	0.00	6.38	0.01	6.07	-0.02	10.29	16.18	5.49	-0.03	0.00	0.00	100.28	62.91	38.35	7.01	29500.08		28341.27	257352.83			108216.99		
C10	Mylonitic Clast- core Omp	LSZ 14-11	54.33	0.04	1.25	0.01	6.32	0.06	13.54	22.13	1.67	0.01	0.00	0.00	99.35	68.18	48.73	4.37	29899.44		27560.84	253989.42			97582.61		
C11	Mylonitic Clast- core Omp	LSZ 14-11	55.70	0.01	6.40	0.01	6.72	0.03	9.94	15.25	5.90	0.01	0.00	0.00	99.96	59.66	23.56	9.15	18203.62		15050.73	260375.93			127850.05		
C12	Mylonitic Clast- core Omp	LSZ 14-11	55.04	0.19	1.14	-0.01	5.92	0.07	13.89	22.61	1.35	0.03	0.00	0.00	100.22	70.10	26.74	3.93	28621.14		25704.15	257278.97			99169.27		
C13	Mylonitic Clast- core Omp	LSZ 14-11	56.20	0.10	5.51	0.00	6.15	0.03	10.67	16.62	4.99	0.01	0.00	0.00	100.28	63.44	33.21	12.04	24126.13		24554.52	262723.07			89603.77		
C07	Mylonitic Clast- Omp (selvage)	LSZ 14-11	55.05	0.03	5.45	0.01	6.49	0.10	10.29	16.69	4.67	-0.01	0.00	0.00	98.77	61.32	32.27	7.09	34305.42		30897.90	261405.29			106138.32		
C09	Mylonitic Clast- Omp (selvage)	LSZ 14-11	55.21	0.04	2.04	0.00	6.54	0.08	12.97	21.16	2.10	0.00	0.00	0.00	100.14	66.49	29.01	4.84	32195.00		28162.50	258108.72			102247.97		
C15	Mylonitic Clast- Omp (selvage)	LSZ 14-11	54.66	0.02	4.82	0.01	6.98	0.06	10.89	17.09	4.02	0.01	0.00	0.00	98.56	60.95	17.48	-12.49	23634.96		23996.26	255499.33			71502.06		
C16	Vein1 Omp (shear vein)	LSZ 14-11	55.16	0.00	1.96	0.01	5.43	0.04	13.98	21.15	2.14	0.00	0.00	0.00	99.87	72.02	20.24	-1.83	24451.56		25610.13	257864.70			77000.17		
C17	Vein1 Omp (shear vein)	LSZ 14-11	55.60	0.01	1.89	0.00	5.24	0.00	13.96	21.37	1.99	0.00	0.00	0.00	100.06	72.70	20.04	-1.67	25353.74		25961.29	259904.72			78112.76		
C18	Vein1 Omp (shear vein)	LSZ 14-11	55.36	0.05	2.40	0.00	5.45	0.00	13.40	20.36	2.63	0.02	0.00	0.00	99.67	71.10	13.73	-2.15	19603.08		19778.40	258773.92			57089.66		
C19	Vein1 Omp (shear vein)	LSZ 14-11	55.36	0.05	2.40	0.00	5.45	0.00	13.40	20.36	2.63	0.02	0.00	0.00	99.67	71.10	10.81	-1.93	16294.20		16327.13	258773.92			61574.36		
C20	Vein1 Omp (shear vein)	LSZ 14-11	55.37	-0.02	2.77	0.00	5.38	-0.01	13.07	20.21	2.85	0.01	0.00	0.00	99.64	70.82	10.25	-0.05	15649.91		18911.76	258838.90			49402.76		
A04	Late-Stage Vein	LSZ 1520a	54.66	0.02	4.78	0.01	6.80	0.05	11.77	18.43	4.49	0.00	0.02	0.00	101.04	63.37	31.65	1.71	33343.98	70958.36	25305.48	255515.22	4.15	14.92	131733.71		
A05	Late-Stage Vein	LSZ 1520a	55.31	0.02	5.25	0.02	6.85	0.05	11.58	18.12	4.86	0.00	0.02	0.00	102.07	62.82	34.64	1.86	36041.13	69811.74	27793.76	258520.56	3.81	12.20	129501.38		
A06	Late-Stage Vein	LSZ 1520a	55.32	0.02	5.58	0.02	6.96	0.05	11.25	17.67	5.14	0.00	0.02	0.00	102.04	61.77	39.56	1.86	38150.09	67844.20	29549.42	258595.82	3.79	22.49	126274.52		
A07	Late-Stage Vein	LSZ 1520a	55.50	0.02	5.17	0.01	6.46	0.04	12.13	18.89	4.70	0.00	0.02	0.00	102.95	65.26	34.05	1.85	34904.46	73154.23	27369.85	259445.67	3.88	20.22	135005.47		
A08	Late-Stage Vein	LSZ 1520a	55.25	0.02	5.17	0.02	6.76	0.05	11.64	18.70	4.82	0.00	0.02	0.00	102.44	63.26	33.91	1.74	35753.42	70176.91	27365.35	258254.57	3.53	18.20	133668.89		
A09	Late-Stage Vein	LSZ 1520a	54.68	0.02	5.11	0.01	6.75	0.05	11.43	18.31	4.72	0.00	0.02	0.00	101.10	62.86	33.72	2.30	34992.56	68918.48	27061.38	255577.40	4.00	26.53	130883.52		
A10	Late-Stage Vein	LSZ 1520a	54.90	0.02	4.70	0.01	6.96	0.04	12.26	19.25	4.30	0.00	0.02	0.00	102.47	63.78	27.46	2.01	31883.13	73928.97	24889.97	256644.62	4.16	16.90	137566.73		
A11	Late-Stage Vein	LSZ 1520a	54.88	0.03	9.14	0.02	8.06	0.03	7.49	12.01	7.65	0.00	0.01	0.00	99.32	48.16	63.86	1.40	56749.37	45165.69	48375.48	256526.35	3.69	-4.59	85807.52		
A13	Late-Stage Vein																										

APPENDIX 1 (b): EPMA ANALYSIS of SELECTED OMPHACITE CRYSTALS with the COMPLETE TRACE-ELEMENTS DATASET
Samples from the Lower Shear Zone: Breccia blocks with Mg-Al + Fe-Ti metagabbro clasts

# Analysis	Microstructural domain	Sample	LA-ICP-MS concentration (µg/g)																						
			Sc	Ti	V	Cr	Mn	Fe	Co	Ni	As	Rb	Sr	Y	Zr	Nb	Sb	Cs	Ba	La	Ce	Pr	Nd	Sm	Eu
C04	M3 matrix Omp	LSZ 14-10	10.06	124.93	123.09	46.66	680.48	55781.22	18.29	393.73	-0.04	-0.03	19.42	6.42	0.45	-0.01	-0.05	-0.01	0.60	0.01	0.04	0.01	0.13	0.14	0.05
C05	M3 matrix Omp	LSZ 14-10	14.22	201.74	164.21	149.31	650.52	57208.48	17.46	376.21	-0.03	-0.02	16.51	6.10	0.49	-0.01	-0.04	-0.01	0.18	0.02	0.07	0.01	0.16	0.12	0.06
C06	M3 matrix Omp	LSZ 14-10	9.36	163.47	167.66	144.99	624.92	49734.77	21.96	476.59	-0.01	-0.01	16.27	4.69	0.34	0.00	-0.02	0.00	0.19	0.01	0.09	0.03	0.20	0.11	0.06
C07	M3 matrix Omp	LSZ 14-10	9.62	163.70	174.65	157.70	610.70	48649.89	21.30	412.13	-0.01	-0.01	15.37	5.00	0.32	0.01	-0.02	0.00	0.26	0.02	0.10	0.03	0.20	0.19	0.07
C08	M3 matrix Omp	LSZ 14-10	12.78	105.58	141.53	187.56	637.77	54159.17	17.42	547.68	-0.02	0.14	16.17	5.38	0.27	0.02	-0.02	0.03	0.38	0.01	0.06	0.01	0.14	0.09	0.04
C09	M3 matrix Omp	LSZ 14-10	12.53	108.08	128.55	116.40	624.67	50872.43	17.30	346.86	-0.01	0.27	19.19	3.58	0.38	0.01	-0.02	0.01	0.35	0.01	0.03	0.01	0.09	0.09	0.04
C10	M3 matrix Omp	LSZ 14-10	14.82	145.95	145.80	178.89	585.77	53321.80	15.00	331.31	-0.01	0.01	19.07	3.69	0.44	0.01	-0.02	0.00	0.44	0.01	0.05	0.01	0.07	0.07	0.04
C11	M3 matrix Omp	LSZ 14-10	8.44	123.58	133.31	67.50	597.60	51644.06	21.13	450.62	-0.03	-0.02	15.81	4.91	0.35	-0.01	-0.04	-0.01	0.12	0.01	0.08	0.03	0.16	0.13	0.06
C12	M3 matrix Omp	LSZ 14-10	11.25	138.35	148.71	55.16	620.82	50518.36	19.28	477.87	-0.01	-0.01	15.39	4.85	0.40	0.00	-0.02	0.00	0.21	0.02	0.08	0.02	0.18	0.13	0.06
C13	M3 matrix Omp	LSZ 14-10	13.94	111.99	127.51	53.23	716.91	54657.06	20.45	489.76	-0.03	0.05	17.04	5.13	0.48	0.01	-0.04	-0.01	0.33	0.01	0.06	0.02	0.12	0.12	0.06
C08	Mylonitic Clast- core Omp	LSZ 14-11	63.03	236.99	134.98	35.40	618.47		13.95	308.16	0.06	0.09	17.76	7.73	0.68	0.01	0.05	0.01	0.69	0.01	0.09	0.02	0.15	0.20	0.08
C10	Mylonitic Clast- core Omp	LSZ 14-11	60.32	434.84	70.17	26.15	508.14		9.59	314.47	0.07	0.01	12.51	8.64	0.64	0.00	0.03	0.01	0.38	0.01	0.05	0.01	0.10	0.08	0.04
C11	Mylonitic Clast- core Omp	LSZ 14-11	67.10	157.38	61.61	20.73	518.20		15.78	418.92	0.26	0.21	23.45	6.77	0.35	0.01	0.16	0.03	12.01	0.01	0.07	0.02	0.19	0.15	0.06
C12	Mylonitic Clast- core Omp	LSZ 14-11	45.65	211.46	208.10	26.42	303.02		11.75	244.39	0.24	0.05	18.58	3.56	0.57	0.01	0.14	0.02	2.92	0.01	0.08	0.01	0.19	0.19	0.06
C13	Mylonitic Clast- core Omp	LSZ 14-11	84.65	866.09	65.94	49.87	385.12		14.38	459.40	-0.13	0.01	11.49	8.22	0.66	0.01	0.07	0.01	0.30	0.02	0.09	0.02	0.20	0.16	0.06
C07	Mylonitic Clast- Omp (selvage)	LSZ 14-11	24.25	180.87	311.16	10.42	195.27		9.07	112.82	0.04	0.08	22.94	1.05	0.73	0.01	0.03	0.00	1.22	0.02	0.09	0.03	0.25	0.21	0.08
C09	Mylonitic Clast- Omp (selvage)	LSZ 14-11	22.26	170.08	302.52	9.62	195.28		10.01	123.41	0.15	0.04	21.52	0.57	0.71	0.02	0.12	0.02	0.56	0.01	0.07	0.03	0.21	0.23	0.08
C15	Mylonitic Clast- Omp (selvage)	LSZ 14-11	25.38	960.54	228.24	6.72	140.87		9.26	131.26	-0.08	0.03	15.30	0.78	0.70	0.03	0.58	0.03	0.18	0.01	0.05	0.01	0.17	0.13	0.06
C16	Vein1 Omp (shear vein)	LSZ 14-11	25.08	1002.57	233.74	4.24	161.55		11.09	125.73	-0.03	0.41	18.74	0.76	0.73	0.01	0.17	0.03	9.19	0.01	0.05	0.02	0.12	0.11	0.05
C17	Vein1 Omp (shear vein)	LSZ 14-11	31.36	919.53	231.30	8.38	165.44		11.00	141.19	-0.03	0.04	18.20	1.02	0.69	0.01	0.17	0.01	0.47	0.01	0.07	0.01	0.16	0.12	0.06
C18	Vein1 Omp (shear vein)	LSZ 14-11	30.07	-3.64	194.26	4.81	98.93		3.17	116.52	0.01	0.08	15.62	1.31	0.63	0.05	0.27	0.08	0.51	0.02	0.07	0.02	0.19	0.13	0.07
C19	Vein1 Omp (shear vein)	LSZ 14-11	30.65	-3.18	173.68	4.29	126.95		12.37	156.27	0.08	0.07	14.04	1.06	0.67	0.04	0.02	0.07	0.77	0.01	0.05	0.01	0.12	0.09	0.02
C20	Vein1 Omp (shear vein)	LSZ 14-11	30.56	-0.06	161.45	2.96	93.21		9.37	139.07	0.00	0.31	13.79	0.85	0.71	0.01	-0.01	0.31	4.96	0.01	0.03	0.01	0.12	0.07	0.03
A04	Late-Stage Vein	LSZ 1520a	49.74	105.30	233.22	101.50	414.40	52871.09	15.31	138.79	-0.01	0.02	43.95	1.01	0.39	0.00	-0.02	0.00	1.33	0.00	0.01	0.00	0.04	0.05	0.02
A05	Late-Stage Vein	LSZ 1520a	50.03	117.62	243.02	112.49	405.96	53250.28	13.69	133.87	-0.01	0.01	40.17	0.91	0.43	0.01	-0.01	0.00	0.34	0.00	0.01	0.00	0.03	0.04	0.02
A06	Late-Stage Vein	LSZ 1520a	48.71	133.59	257.96	109.59	396.90	54125.41	14.00	132.98	0.01	0.02	37.83	0.93	0.52	0.00	-0.01	0.00	0.71	0.00	0.01	0.00	0.03	0.06	0.02
A07	Late-Stage Vein	LSZ 1520a	46.67	124.62	291.71	79.23	330.45	50189.92	15.30	140.18	0.01	0.02	41.62	1.00	0.45	0.00	0.01	0.00	0.70	0.00	0.03	0.01	0.09	0.11	0.06
A08	Late-Stage Vein	LSZ 1520a	50.22	114.56	244.02	108.66	387.44	52524.91	13.68	132.66	0.01	0.02	40.82	0.89	0.39	0.00	0.01	0.00	0.69	0.00	0.01	0.00	0.03	0.04	0.02
A09	Late-Stage Vein	LSZ 1520a	49.56	117.03	244.18	101.13	393.32	52487.38	14.77	130.57	0.01	0.05	41.48	0.86	0.48	0.00	-0.02	0.00	4.09	0.00	0.02	0.00	0.04	0.05	0.03
A10	Late-Stage Vein	LSZ 1520a	48.31	102.52	281.91	76.64	340.93	54102.13	17.89	144.57	-0.04	-0.02	44.58	0.93	0.35	-0.01	-0.05	-0.01	0.26	-0.01	0.04	0.01	0.06	0.07	0.05
A11	Late-Stage Vein	LSZ 1520a	27.38	198.43	190.20	163.80	238.06	62654.02	11.78	55.50	-0.03	-0.02	13.18	0.63	0.42	-0.01	-0.05	-0.01	0.13	0.00	0.01	0.00	0.04	-0.05	0.01
A13	Late-Stage Vein	LSZ 1520a	34.66	201.18	285.18	179.51	222.39	44284.73	14.54	57.02	-0.07	-0.05	14.32	0.70	0.51	-0.02	-0.09	-0.02	0.36	-0.01	0.01	-0.01	0.03	-0.09	0.03
A14	Late-Stage Vein	LSZ 1520a	15.29	188.75	153.15	109.99	307.97	64497.09	13.53	77.94	-0														

APPENDIX 1 (b): EPMA ANALYSIS of SELECTED OMPHACITE CRYSTALS with the COMPLETE TRACE-ELEMENTS DATASET

Samples from the Lower Shear Zone: Breccia blocks with Mg-Al + Fe-Ti metagabbro clasts

# Analysis	Microstructural domain	Sample	LA-ICP-MS concentration (µg/g)														
			Gd	Tb	Dy	Ho	Er	Tm	Yb	Lu	Hf	Ta	Pb	Bi	Th	U	W
C04	M3 matrix Omp	LSZ 14-10	0.36	0.08	0.97	0.25	0.92	0.14	1.11	0.15	0.05	0.00	0.92	-0.01	-0.01	-0.01	
C05	M3 matrix Omp	LSZ 14-10	0.29	0.08	1.03	0.24	0.92	0.15	1.11	0.15	0.05	0.00	0.65	-0.01	-0.01	-0.01	
C06	M3 matrix Omp	LSZ 14-10	0.31	0.08	0.78	0.20	0.69	0.11	0.72	0.10	0.03	0.00	0.67	-0.01	0.02	0.00	
C07	M3 matrix Omp	LSZ 14-10	0.33	0.09	0.83	0.19	0.67	0.12	0.86	0.10	0.03	0.00	0.64	0.00	0.01	0.01	
C08	M3 matrix Omp	LSZ 14-10	0.23	0.07	0.81	0.19	0.87	0.14	0.91	0.11	0.02	0.00	0.75	0.00	0.00	0.01	
C09	M3 matrix Omp	LSZ 14-10	0.18	0.05	0.55	0.14	0.49	0.08	0.56	0.08	0.04	0.00	0.65	-0.01	0.01	0.01	
C10	M3 matrix Omp	LSZ 14-10	0.15	0.06	0.57	0.13	0.48	0.09	0.57	0.09	0.04	0.00	0.56	-0.01	0.01	0.01	
C11	M3 matrix Omp	LSZ 14-10	0.32	0.08	0.79	0.21	0.67	0.13	0.88	0.09	0.03	0.00	0.68	-0.01	0.02	0.01	
C12	M3 matrix Omp	LSZ 14-10	0.28	0.07	0.75	0.20	0.73	0.12	0.88	0.13	0.05	0.00	0.66	-0.01	0.01	0.00	
C13	M3 matrix Omp	LSZ 14-10	0.30	0.09	0.74	0.24	0.75	0.13	0.81	0.12	0.06	-0.01	0.75	-0.01	-0.01	-0.01	
C08	Mylonitic Clast- core Omp	LSZ 14-11	0.50	0.16	1.21	0.32	0.97	0.15	0.98	0.14	0.07	0.01	0.59	0.01	0.01	0.01	
C10	Mylonitic Clast- core Omp	LSZ 14-11	0.27	0.13	1.04	0.34	1.15	0.21	1.67	0.19	0.04	0.00	0.49	0.01	0.00	0.01	
C11	Mylonitic Clast- core Omp	LSZ 14-11	0.34	0.13	1.03	0.28	0.83	0.13	1.10	0.13	0.03	0.00	1.58	0.01	0.01	0.01	
C12	Mylonitic Clast- core Omp	LSZ 14-11	0.25	0.08	0.70	0.15	0.42	0.04	0.63	0.06	0.05	0.01	0.52	0.02	0.02	0.02	
C13	Mylonitic Clast- core Omp	LSZ 14-11	0.30	0.16	1.15	0.32	0.93	0.16	1.72	0.15	0.05	0.00	0.61	0.01	0.02	0.02	
C07	Mylonitic Clast- Omp (selvage)	LSZ 14-11	0.32	0.06	0.25	0.04	0.07	0.01	0.06	0.01	0.06	0.00	0.37	0.02	0.00	0.00	
C09	Mylonitic Clast- Omp (selvage)	LSZ 14-11	0.42	0.04	0.26	0.03	0.06	0.00	0.03	0.01	0.07	0.01	0.31	0.02	0.01	0.02	
C15	Mylonitic Clast- Omp (selvage)	LSZ 14-11	0.19	0.05	0.16	0.03	0.04	0.01	0.04	0.00	0.06	0.01	0.48	0.01	0.00	0.01	
C16	Vein1 Omp (shear vein)	LSZ 14-11	0.19	0.04	0.15	0.02	0.04	0.01	0.04	0.00	0.05	0.00	0.70	0.01	0.00	0.00	
C17	Vein1 Omp (shear vein)	LSZ 14-11	0.22	0.05	0.21	0.04	0.07	0.01	0.07	0.01	0.05	0.00	0.48	0.01	0.00	0.00	
C18	Vein1 Omp (shear vein)	LSZ 14-11	0.29	0.08	0.17	0.04	0.10	0.03	0.37	0.03	0.10	0.03	0.30	0.02	0.02	0.01	
C19	Vein1 Omp (shear vein)	LSZ 14-11	0.23	0.03	0.11	0.03	0.11	0.02	0.32	0.02	0.09	0.02	0.71	0.02	0.01	0.01	
C20	Vein1 Omp (shear vein)	LSZ 14-11	0.13	0.04	0.12	0.03	0.03	0.00	0.10	0.00	0.04	0.00	1.64	0.00	0.00	0.00	
A04	Late-Stage Vein	LSZ 1520a	0.13	0.03	0.23	0.04	0.11	0.01	0.05	0.01	0.05	0.00	0.96	0.00	0.00	0.00	2.49
A05	Late-Stage Vein	LSZ 1520a	0.09	0.03	0.20	0.04	0.09	0.01	0.05	0.00	0.04	0.00	0.81	0.00	0.00	0.00	4.26
A06	Late-Stage Vein	LSZ 1520a	0.09	0.03	0.20	0.03	0.10	0.01	0.04	0.00	0.06	0.00	0.76	0.00	0.00	0.00	4.25
A07	Late-Stage Vein	LSZ 1520a	0.25	0.05	0.28	0.04	0.07	0.01	0.03	0.00	0.05	0.00	1.11	0.00	0.00	0.00	7.19
A08	Late-Stage Vein	LSZ 1520a	0.08	0.02	0.20	0.04	0.08	0.01	0.04	0.00	0.05	0.00	0.83	0.00	0.00	0.00	7.37
A09	Late-Stage Vein	LSZ 1520a	0.13	0.03	0.19	0.03	0.08	0.01	0.04	0.00	0.06	0.00	0.88	0.00	0.00	0.00	2.48
A10	Late-Stage Vein	LSZ 1520a	0.23	0.05	0.32	0.04	0.06	-0.01	-0.04	0.00	0.02	-0.01	1.19	-0.01	0.00	-0.01	1.32
A11	Late-Stage Vein	LSZ 1520a	0.07	0.02	0.17	0.03	0.06	0.00	0.03	-0.01	0.05	0.00	0.15	-0.01	0.01	-0.01	0.96
A13	Late-Stage Vein	LSZ 1520a	0.16	0.02	0.19	0.03	-0.05	0.01	-0.07	-0.01	-0.05	-0.01	0.13	-0.02	-0.01	-0.01	0.57
A14	Late-Stage Vein	LSZ 1520a	0.14	0.03	0.13	0.02	0.05	0.01	0.03	0.00	0.06	0.00	0.22	0.00	0.00	0.00	2.37
A18	Late-Stage Vein	LSZ 1520a	0.11	0.03	0.23	0.04	0.08	0.01	0.06	0.01	0.05	0.00	0.21	-0.01	0.00	0.00	1.97
A20	Late-Stage Vein	LSZ 1520a	0.05	0.01	0.10	0.01	-0.02	-0.01	-0.03	-0.01	0.04	-0.01	0.04	-0.01	-0.01	-0.01	0.87
A21	Late-Stage Vein	LSZ 1520a	0.11	0.02	0.18	0.03	0.09	0.01	0.04	0.01	0.07	0.00	0.60	0.00	0.00	0.00	4.15
A22	Late-Stage Vein	LSZ 1520a	0.18	0.03	0.17	0.02	0.03	0.00	0.02	0.00	0.04	0.00	1.06	0.00	0.00	0.00	4.24
A23	Late-Stage Vein	LSZ 1520a	0.20	0.04	0.26	0.04	0.06	0.01	0.03	0.00	0.03	0.00	1.10	0.00	0.00	0.00	2.35
A24	Late-Stage Vein	LSZ 1520a	0.17	0.03	0.22	0.05	0.13	0.02	0.09	0.01	0.07	0.00	0.79	0.00	0.00	-0.01	2.30
B04	Matrix M1 Omp	LSZ 1520b	0.08	0.02	0.14	0.01	0.02	0.00	-0.02	0.00	0.05	0.00	0.03	-0.01	0.00	0.00	2.11
B05	Matrix M1 Omp	LSZ 1520b	0.10	0.02	0.12	0.01	-0.02	-0.01	-0.03	-0.01	0.05	0.00	-0.04	-0.01	-0.01	-0.01	0.89
B06	Matrix M1 Omp	LSZ 1520b	0.04	0.01	0.10	0.01	0.02	0.00	0.00	0.00	0.04	0.00	0.05	-0.01	0.00	0.00	2.00
B07	Matrix M1 Omp	LSZ 1520b	0.04	0.01	0.08	0.01	0.02	0.00	0.01	0.00	0.04	0.00	0.03	-0.01	0.00	0.00	1.93
B08	Matrix M1 Omp	LSZ 1520b	0.07	0.01	0.11	0.01	0.02	0.00	-0.02	0.00	0.05	0.00	0.04	-0.01	0.00	0.00	1.99
B09	Matrix M1 Omp	LSZ 1520b	0.09	0.02	0.09	0.01	0.01	0.00	-0.01	0.00	0.05	0.00	0.04	0.00	0.00	0.00	1.93
B10	Matrix M1 Omp	LSZ 1520b	0.04	0.02	0.08	0.01	0.03	0.00	-0.01	0.00	0.05	0.00	0.05	-0.01	0.00	0.00	1.94
B12	Late-Stage Vein	LSZ 1520b	0.07	0.02	0.16	0.03	0.06	0.01	0.05	0.00	0.05	0.00	0.69	0.00	0.00	0.00	4.26
B13	Late-Stage Vein	LSZ 1520b	0.07	0.02	0.19	0.03	0.07	0.01	0.05	0.00	0.04	0.00	0.80	-0.01	0.00	0.00	2.50
B15	Matrix M1 Omp	LSZ 1520b	0.07	0.02	0.11	0.02	0.02	0.00	0.01	0.00	0.06	0.00	0.04	0.00	0.00	0.00	3.62
B16	Matrix M1 Omp	LSZ 1520b	0.07	0.02	0.13	0.02	0.03	0.00	-0.02	0.00	0.05	0.00	0.04	0.00	0.00	0.00	1.99
B17	Matrix M1 Omp	LSZ 1520b	0.06	0.02	0.10	0.01	0.03	0.00	-0.02	0.00	0.04	0.00	0.04	0.00	0.00	0.00	1.90
B20	Matrix M3 Omp	LSZ 1520b	0.34	0.13	1.06	0.28	0.95	0.14	0.97	0.13	0.04	-0.01	0.65	-0.03	-0.02	0.01	0.35
B21	Matrix M3 Omp	LSZ 1520b	0.57	0.11	0.81	0.22	0.73	0.12	0.87	0.10	0.03	-0.01	0.76	-0.04	0.02	0.01	0.35
B22	Late-Stage Vein	LSZ 1520b	0.06	0.02	0.16	0.04	0.08	0.01	0.04	0.00	0.06	0.00	0.63	-0.01	-0.01	-0.01	1.10
B23	Late-Stage Vein	LSZ 1520b	0.09	0.02	0.18	0.03	0.09	0.01	0.04	0.00	0.05	0.00	0.91	0.00	0.00	0.00	2.59
B24	Late-Stage Vein	LSZ 1520b	0.04	0.01	0.08	0.02	0.08	0.01	0.07	0.01	0.05	-0.01	0.60	-0.01	-0.01	0.00	1.10
B25	Matrix M3 Omp	LSZ 1520b	0.65	0.21	1.93	0.55	1.85	0.26	1.78	0.24	0.09	-0.01	0.63	-0.01	0.02	0.01	1.07

Trace element data with (-) are below their respective detection limit (method: Pettke et Al., 2012)

APPENDIX 1 (c): EPMA ANALYSIS of SELECTED OMPHACITE CRYSTALS with the COMPLETE TRACE-ELEMENTS DATASET

Samples from the Intermediate Shear Zone: Breccia blocks with only Fe-Ti metagabbro clasts

Trace element data with (-) are below their respective detection limit (method: Pettke et Al., 2012)

# Analysis	Microstrucrtal domain	Sample	EPMA analysis (internal standard) wt%														LA-ICP-MS concentration (µg/g)									
			SiO2	TiO2	Al2O3	Cr2O3	FeO	MnO	MgO	CaO	Na2O	K2O	NiO	P2O5	Total	MgO#	Li	B	Na	Mg	Al	Si	P	K	Ca	
B24	Mylonitic Clast Omp	ISZ 35-15	54.71	0.07	8.29	0.01	8.94	0.00	7.00	10.70	8.35	0.02	0.02	0.05	98.11	43.93	45.67	0.44	61877.74	37333.57	53273.91	255729.32	3.86	4.96	70813.30	
B25	Mylonitic Clast Omp	ISZ 35-15	55.06	0.11	9.33	0.00	9.12	0.04	6.31	9.50	8.68	0.02	0.02	0.02	98.15	40.91	63.00	0.32	62264.63	36192.05	53613.20	257367.32	11.43	13.65	68066.83	
B26	Mylonitic Clast Omp	ISZ 35-15	56.60	0.17	8.20	0.01	9.71	0.03	7.60	12.15	7.52	0.00	0.00	0.06	102.05	43.92	62.20	0.35	65823.08	41087.80	55517.90	264592.00	6.87	22.59	86176.94	
B27	Mylonitic Clast Omp	ISZ 35-15	56.63	0.08	8.60	0.00	9.64	0.03	7.12	11.17	8.32	0.02	0.11	0.07	101.77	42.49	63.97	0.36	67201.88	42068.76	54057.84	264719.15	7.78	36.74	83588.16	
B30	Mylonitic Clast Omp	ISZ 35-15	56.67	0.03	10.32	0.07	8.40	0.11	6.16	9.76	9.02	0.00	0.01	0.02	100.56	42.28	73.60	0.29	69234.99	41408.26	53598.22	264923.90	4.96	80.93	87741.49	
B31	Mylonitic Clast Omp	ISZ 35-15	56.23	0.12	9.46	0.04	8.75	0.06	6.74	10.89	8.26	0.00	0.00	0.04	100.59	43.52	69.49	0.30	68455.38	40710.89	52451.36	262864.71	7.98	107.77	82934.38	
B07	VeinT1 Omp	ISZ 35-15	54.78	0.04	8.15	0.01	7.61	0.09	7.80	12.30	7.39	0.02	0.08	0.02	98.21	50.59	47.13	0.35	53545.82	48809.24	44875.67	256067.77	4.18	16.23	92103.54	
B08	VeinT1 Omp	ISZ 35-15	54.78	0.04	8.15	0.01	7.61	0.09	7.80	12.30	7.39	0.02	0.08	0.02	98.21	50.59	47.13	0.35	53545.82	48809.24	44875.67	256067.77	4.18	16.23	92103.54	
B09	VeinT1 Omp	ISZ 35-15	54.60	0.04	7.65	0.00	8.03	0.06	7.96	12.84	7.03	0.01	0.18	0.02	98.38	49.79	48.13	0.43	55586.64	45862.10	47399.28	255249.23	11.70	16.51	84388.30	
B10	VeinT1 Omp	ISZ 35-15	54.55	0.08	8.06	0.01	8.07	0.02	7.80	11.61	7.46	0.03	0.03	0.00	97.68	49.15	47.36	0.36	54255.18	47081.47	48197.29	254979.51	5.11	9.38	85078.43	
B15	VeinT1 Omp	ISZ 35-15	54.71	0.00	8.64	0.02	8.96	0.18	6.96	10.52	8.25	0.01	0.05	0.04	98.22	43.74	36.05	0.66	52114.86	42213.19	44384.37	255736.80	11.69	-1.51	77099.86	
B16	VeinT1 Omp	ISZ 35-15	54.87	0.04	7.92	0.02	8.04	0.06	7.86	11.54	7.60	0.01	0.08	0.01	98.02	49.46	38.25	0.71	55868.07	40763.87	43259.77	256514.66	9.09	-2.35	76762.03	
B17	VeinT1 Omp	ISZ 35-15	54.22	0.03	8.05	0.04	8.30	0.05	8.07	11.64	7.71	0.02	0.21	0.04	98.31	49.31	41.77	0.54	53587.66	44123.78	45167.85	253464.92	7.34	12.92	78595.88	
B18	VeinT1 Omp	ISZ 35-15	54.67	0.04	8.37	0.03	8.30	0.01	6.90	10.31	8.09	0.03	0.09	0.02	96.74	45.39	43.10	0.82	62977.07	41553.63	44983.83	255581.60	7.48	14.57	72029.55	
B19	VeinT1 Omp	ISZ 35-15	55.05	0.10	8.45	0.00	8.12	0.02	7.59	11.61	7.59	0.03	0.05	0.00	98.46	48.32	52.55	0.67	54725.28	46970.32	46758.92	257321.98	9.49	11.12	83245.26	
B20	VeinT1 Omp	ISZ 35-15	54.85	0.06	8.05	0.01	8.64	0.02	7.67	11.42	7.53	0.01	0.06	0.04	98.23	47.05	41.29	0.57	54605.09	45316.95	47589.90	256417.43	6.31	4.80	82478.92	
B21	VeinT1 Omp	ISZ 35-15	54.00	0.04	7.33	0.01	9.05	0.06	7.62	11.89	7.21	0.01	0.08	0.01	97.10	45.70	47.36	0.34	55683.11	41659.45	47457.61	252444.44	5.68	12.31	75897.07	
B22	VeinT1 Omp	ISZ 35-15	54.26	0.09	8.76	0.00	8.00	0.04	7.32	11.42	7.97	0.01	0.18	0.04	97.63	47.77	41.91	0.38	55157.13	42268.09	48968.56	253669.67	5.32	6.01	78265.30	
B23	VeinT1 Omp	ISZ 35-15	53.49	0.06	8.02	0.01	9.68	0.05	6.82	10.72	7.95	0.03	0.02	0.01	96.68	41.31	41.34	0.20	57970.69	37789.20	48222.48	250026.24	4.52	7.44	71701.16	
C17	VeinT1 Omp	ISZ 35-15	56.50	0.07	8.95	0.03	8.68	0.03	7.24	11.45	8.16	0.00	0.00	0.00	101.10	45.48	58.78	0.41	58326.69	56874.14	49059.51	264125.47	18.24	9.37	80076.17	
C18	VeinT1 Omp	ISZ 35-15	56.97	0.02	9.93	0.03	8.34	0.04	6.71	10.22	8.64	0.01	0.00	0.03	100.93	44.60	72.41	0.53	63336.78	52352.30	55098.48	266296.38	4.31	-1.29	73160.91	
D07	VeinT0 Omp	ISZ 35-15	55.95	0.08	8.34	0.01	9.80	0.05	6.78	11.06	8.12	0.01	0.00	0.00	100.20	40.90	51.34	0.26	60787.48	41451.46	53327.25	261540.85	4.82	20.90	80132.70	
D08	VeinT0 Omp	ISZ 35-15	55.41	0.00	9.60	0.00	8.47	0.03	6.46	10.56	7.63	0.00	0.09	0.16	98.42	43.28	53.40	0.25	62379.68	38732.79	56523.51	259018.41	3.99	8.78	77810.85	
D09	VeinT0 Omp	ISZ 35-15	57.12	0.08	8.94	0.00	9.40	0.07	6.86	11.02	7.87	0.04	0.00	0.00	101.40	42.21	65.80	0.30	63910.23	44182.05	55475.17	267007.39	5.66	13.77	85562.24	
D10	VeinT0 Omp	ISZ 35-15	56.56	0.09	9.90	0.00	7.78	0.04	7.16	11.12	8.32	0.00	0.00	0.00	100.97	47.91	55.29	0.34	62845.38	44043.97	54360.21	264393.33	4.77	14.87	83883.91	
D11	VeinT0 Omp	ISZ 35-15	57.03	0.11	9.69	0.03	8.35	0.01	6.93	10.66	8.52	0.00	0.04	0.01	101.38	45.33	64.68	0.28	63311.92	42203.33	58023.56	266600.70	4.45	12.96	84450.57	
D12	VeinT0 Omp	ISZ 35-15	56.56	0.05	8.60	0.02	8.68	0.06	7.14	11.16	8.16	0.01	0.00	0.01	100.45	45.12	58.26	0.34	66022.13	43665.14	54404.74	264414.83	5.25	10.15	84384.55	
D13	VeinT0 Omp	ISZ 35-15	56.																							

APPENDIX 1 (c): EPMA ANALYSIS of SELECTED OMPHACITE CRYSTALS with the COMPLETE TRACE-ELEMENTS DATASET

Samples from the Intermediate Shear Zone: Breccia blocks with only Fe-Ti metagabbro clasts

Trace element data with (-) are below their respective detection limit (method: Pettke et Al., 2012)

# Analysis	Microstructural domain	Sample	LA-ICP-MS concentration (µg/g)																						
			Sc	Ti	V	Cr	Mn	Fe	Co	Ni	As	Rb	Sr	Y	Zr	Nb	Sb	Cs	Ba	La	Ce	Pr	Nd	Sm	Eu
B24	Mylonitic Clast Omp	ISZ 35-15	30.43	417.05	526.35	4.66	238.25	62414.51	7.52	58.52	-0.01	0.00	54.31	1.46	0.64	0.00	-0.01	0.00	-0.02	0.03	0.30	0.12	1.12	0.88	0.32
B25	Mylonitic Clast Omp	ISZ 35-15	26.48	538.33	519.94	23.87	313.74	65079.63	7.29	64.18	-0.01	0.00	44.62	2.78	1.29	0.00	-0.01	0.00	-0.02	0.04	0.40	0.13	1.27	0.89	0.36
B26	Mylonitic Clast Omp	ISZ 35-15	24.64	518.36	509.24	6.97	315.40	73697.54	8.76	59.33	-0.01	-0.01	62.85	2.54	0.90	0.00	-0.01	0.00	-0.02	0.05	0.39	0.16	1.45	0.93	0.36
B27	Mylonitic Clast Omp	ISZ 35-15	26.31	509.44	489.03	25.82	270.48	68241.25	8.43	64.85	-0.01	0.01	53.49	2.27	0.92	0.00	-0.01	0.00	0.04	0.05	0.45	0.16	1.45	1.06	0.40
B30	Mylonitic Clast Omp	ISZ 35-15	25.39	541.35	557.65	11.25	331.64	74021.35	9.14	59.04	-0.01	-0.01	59.48	2.34	4.67	0.00	-0.01	0.00	-0.02	0.04	0.40	0.15	1.42	0.90	0.35
B31	Mylonitic Clast Omp	ISZ 35-15	23.21	500.79	489.56	11.01	285.84	70985.13	8.40	56.38	0.01	0.01	56.14	2.49	0.92	0.00	-0.01	0.00	0.04	0.04	0.41	0.15	1.29	0.94	0.37
B07	VeinT1 Omp	ISZ 35-15	16.43	348.38	304.12	27.83	236.33	60934.73	14.36	132.63	0.01	0.00	68.53	2.79	0.81	0.00	0.01	0.00	0.03	0.06	0.49	0.17	1.52	1.02	0.38
B08	VeinT1 Omp	ISZ 35-15	16.43	348.38	304.12	27.83	236.33	60934.73	14.36	132.63	0.01	0.00	68.53	2.79	0.81	0.00	1.01	0.00	0.03	0.06	0.49	0.17	1.52	1.02	0.38
B09	VeinT1 Omp	ISZ 35-15	17.69	390.12	310.43	10.76	222.98	58217.76	11.02	101.05	0.01	0.01	63.79	2.37	0.80	0.00	0.01	0.00	0.06	0.05	0.47	0.16	1.32	0.83	0.32
B10	VeinT1 Omp	ISZ 35-15	16.54	375.96	280.48	7.89	216.31	55391.77	13.28	108.55	0.01	0.01	64.27	2.40	0.76	0.00	0.01	0.00	0.02	0.06	0.47	0.16	1.34	0.77	0.31
B15	VeinT1 Omp	ISZ 35-15	19.24	299.28	356.23	21.20	215.23	61485.66	4.63	106.44	0.02	-0.01	53.70	2.41	0.74	0.00	-0.01	0.00	0.05	0.05	0.49	0.15	1.45	0.91	0.35
B16	VeinT1 Omp	ISZ 35-15	21.29	336.30	329.88	14.73	231.97	60868.72	2.42	90.12	-0.02	-0.01	47.62	2.81	1.10	-0.01	-0.02	-0.01	-0.04	0.06	0.47	0.16	1.52	1.00	0.40
B17	VeinT1 Omp	ISZ 35-15	27.34	348.92	413.73	11.05	182.47	56056.50	2.08	78.46	0.01	0.00	44.50	1.80	1.46	0.00	0.02	0.00	-0.01	0.06	0.56	0.19	1.58	1.01	0.41
B18	VeinT1 Omp	ISZ 35-15	21.80	317.45	308.20	25.45	221.36	62001.15	2.08	85.78	0.01	0.01	43.91	2.98	0.79	0.00	0.01	0.00	0.03	0.05	0.47	0.16	1.38	0.93	0.37
B19	VeinT1 Omp	ISZ 35-15	18.35	377.17	313.41	14.29	226.30	58746.23	13.55	148.49	0.01	0.00	59.86	2.86	1.14	0.00	-0.01	0.00	0.03	0.07	0.59	0.20	1.64	1.07	0.41
B20	VeinT1 Omp	ISZ 35-15	24.74	366.76	399.11	11.68	196.94	58451.82	3.64	86.04	0.01	0.00	47.28	2.11	1.45	0.00	-0.01	0.00	0.02	0.06	0.59	0.20	1.70	1.14	0.44
B21	VeinT1 Omp	ISZ 35-15	22.14	453.25	327.98	19.45	268.27	61001.15	10.60	79.50	0.01	0.01	55.11	2.72	0.86	0.01	0.01	0.00	-0.01	0.05	0.39	0.12	0.99	0.64	0.26
B22	VeinT1 Omp	ISZ 35-15	20.05	392.23	323.81	19.83	237.37	57374.36	9.77	96.00	0.01	0.00	54.99	2.42	0.86	0.00	-0.01	0.00	-0.01	0.05	0.42	0.13	1.12	0.70	0.29
B23	VeinT1 Omp	ISZ 35-15	29.43	460.06	358.90	3.34	253.70	66644.62	7.16	49.12	0.01	0.00	53.35	2.25	0.96	0.00	-0.01	0.00	-0.01	0.04	0.37	0.13	1.30	0.94	0.39
C17	VeinT1 Omp	ISZ 35-15	23.81	577.20	476.63	27.22	312.21	80446.88	15.10	68.48	-0.01	0.01	93.77	2.71	1.19	0.00	0.01	0.00	0.03	0.07	0.57	0.19	1.48	0.91	0.44
C18	VeinT1 Omp	ISZ 35-15	25.48	584.12	549.09	26.81	339.84	79245.21	12.70	83.78	0.01	0.01	79.99	2.95	0.94	0.00	-0.01	0.00	-0.02	0.05	0.51	0.19	1.74	1.21	0.48
D07	VeinT0 Omp	ISZ 35-15	21.16	483.66	425.69	12.80	255.47	67671.28	11.17	57.69	0.01	0.01	64.42	2.18	0.78	0.00	0.02	0.00	-0.01	0.05	0.40	0.15	1.23	0.82	0.32
D08	VeinT0 Omp	ISZ 35-15	22.48	494.87	428.96	32.44	281.77	61760.41	9.76	58.15	-0.01	0.00	66.62	1.62	0.64	0.00	-0.01	0.00	-0.02	0.04	0.39	0.16	1.26	0.92	0.38
D09	VeinT0 Omp	ISZ 35-15	19.95	477.45	396.01	16.52	260.10	66803.12	11.27	55.35	-0.01	0.00	64.65	2.27	0.86	0.00	-0.01	0.00	0.02	0.06	0.42	0.14	1.33	0.91	0.36
D10	VeinT0 Omp	ISZ 35-15	21.18	494.78	330.84	8.73	253.97	67891.35	11.05	71.34	-0.01	0.00	76.91	3.09	0.92	0.00	-0.01	0.00	-0.01	0.06	0.59	0.20	1.84	1.17	0.48
D11	VeinT0 Omp	ISZ 35-15	24.44	481.28	391.83	18.91	256.85	62533.54	8.98	68.30	0.01	0.00	76.95	2.68	0.72	0.00	-0.01	0.00	0.00	0.05	0.47	0.17	1.60	1.06	0.42
D12	VeinT0 Omp	ISZ 35-15	22.54	455.80	484.15	24.34	279.08	69168.23	11.80	71.19	-0.01	-0.01	62.97	2.31	0.83	0.00	-0.02	0.00	0.01	0.05	0.41	0.15	1.28	0.85	0.40
D13	VeinT0 Omp	ISZ 35-15	19.14	480.43	390.76	23.52	251.77	67505.25	11.48	54.98	0.01	0.01	60.13	2.15	0.80	0.00	0.01	0.00	0.01	0.04	0.40	0.14	1.23	0.80	0.31
C07	VeinT1 Omp	ISZ 36-15	44.63	1435.33	1152.80	68.66	699.69	155714.92	20.49	136.01	0.03	0.02	101.30	5.49											

APPENDIX 1 (c): EPMA ANALYSIS of SELECTED OMPHACITE CRYSTALS with the COMPLETE TRACE-ELEMENTS DATASET

Samples from the Intermediate Shear Zone: Breccia blocks with only Fe-Ti metagabbro clasts

# Analysis	Microstructural domain	Sample	LA-ICP-MS concentration (µg/g)													
			Gd	Tb	Dy	Ho	Er	Tm	Yb	Lu	Hf	Ta	Pb	Bi	Th	U
B24	Mylonitic Clast Omp	ISZ 35-15	1.17	0.14	0.57	0.06	0.07	0.01	0.02	0.00	0.07	0.00	0.15	0.00	0.00	0.00
B25	Mylonitic Clast Omp	ISZ 35-15	1.17	0.18	0.86	0.11	0.17	0.02	0.05	0.00	0.12	0.00	0.13	0.00	0.00	0.00
B26	Mylonitic Clast Omp	ISZ 35-15	1.36	0.20	0.86	0.12	0.16	0.01	0.05	0.01	0.12	0.00	0.16	0.00	0.00	0.00
B27	Mylonitic Clast Omp	ISZ 35-15	1.35	0.19	0.90	0.11	0.17	0.01	0.05	0.01	0.13	0.00	0.15	0.00	0.00	0.00
B30	Mylonitic Clast Omp	ISZ 35-15	1.24	0.17	0.83	0.10	0.17	0.01	0.05	0.01	0.25	0.00	0.18	0.00	0.00	0.00
B31	Mylonitic Clast Omp	ISZ 35-15	1.18	0.17	0.84	0.11	0.22	0.02	0.18	0.03	3.26	0.00	0.15	0.00	0.01	0.02
B07	VeinT1 Omp	ISZ 35-15	1.22	0.16	0.82	0.12	0.24	0.02	0.12	0.01	0.08	0.00	0.21	0.00	0.00	0.00
B08	VeinT1 Omp	ISZ 35-15	1.22	0.16	0.82	0.12	0.24	0.02	0.12	0.01	0.08	0.00	0.21	0.00	0.00	0.00
B09	VeinT1 Omp	ISZ 35-15	0.95	0.13	0.69	0.10	0.21	0.02	0.10	0.01	0.09	0.00	0.20	0.00	0.00	0.00
B10	VeinT1 Omp	ISZ 35-15	0.99	0.13	0.68	0.10	0.19	0.02	0.10	0.01	0.09	0.00	0.17	0.00	0.00	0.00
B15	VeinT1 Omp	ISZ 35-15	1.02	0.14	0.57	0.08	0.18	0.01	0.09	0.01	0.06	0.00	0.13	0.00	0.00	0.00
B16	VeinT1 Omp	ISZ 35-15	1.24	0.16	0.77	0.12	0.27	0.02	0.13	0.02	0.11	0.00	0.15	0.00	0.00	0.00
B17	VeinT1 Omp	ISZ 35-15	1.22	0.14	0.60	0.07	0.11	0.01	0.04	0.00	0.13	0.00	0.11	0.01	0.00	0.00
B18	VeinT1 Omp	ISZ 35-15	1.24	0.16	0.79	0.12	0.26	0.03	0.14	0.02	0.07	0.00	0.15	0.00	0.00	0.00
B19	VeinT1 Omp	ISZ 35-15	1.35	0.17	0.87	0.12	0.25	0.02	0.11	0.01	0.13	0.00	0.18	0.00	0.00	0.00
B20	VeinT1 Omp	ISZ 35-15	1.36	0.16	0.70	0.09	0.15	0.02	0.08	0.01	0.13	0.00	0.13	0.00	0.00	0.00
B21	VeinT1 Omp	ISZ 35-15	0.80	0.13	0.69	0.10	0.23	0.02	0.09	0.01	0.08	0.00	0.15	0.00	0.00	0.00
B22	VeinT1 Omp	ISZ 35-15	0.93	0.14	0.63	0.09	0.20	0.02	0.10	0.01	0.10	0.00	0.16	0.00	0.00	0.00
B23	VeinT1 Omp	ISZ 35-15	1.30	0.18	0.82	0.08	0.14	0.01	0.04	0.00	0.10	0.00	0.15	0.00	0.00	0.00
C17	VeinT1 Omp	ISZ 35-15	1.09	0.15	0.72	0.11	0.20	0.02	0.12	0.01	0.10	0.00	0.24	0.00	0.00	0.00
C18	VeinT1 Omp	ISZ 35-15	1.52	0.21	0.91	0.12	0.21	0.02	0.09	0.01	0.09	0.00	0.17	0.00	0.00	0.00
D07	VeinT0 Omp	ISZ 35-15	1.00	0.15	0.68	0.09	0.16	0.01	0.06	0.01	0.10	0.00	0.16	0.01	0.00	0.00
D08	VeinT0 Omp	ISZ 35-15	1.05	0.12	0.55	0.07	0.13	0.01	0.04	0.00	0.09	0.00	0.18	0.00	0.00	0.00
D09	VeinT0 Omp	ISZ 35-15	1.16	0.16	0.78	0.10	0.23	0.02	0.10	0.02	0.11	0.00	0.16	0.00	0.00	0.00
D10	VeinT0 Omp	ISZ 35-15	1.49	0.21	1.04	0.14	0.27	0.03	0.15	0.02	0.10	0.00	0.19	0.00	0.00	0.00
D11	VeinT0 Omp	ISZ 35-15	1.37	0.20	0.90	0.12	0.20	0.02	0.11	0.01	0.08	0.00	0.17	0.00	0.00	0.00
D12	VeinT0 Omp	ISZ 35-15	1.18	0.18	0.79	0.10	0.16	0.02	0.09	0.01	0.10	0.00	0.15	0.00	0.00	0.00
D13	VeinT0 Omp	ISZ 35-15	0.94	0.13	0.65	0.09	0.19	0.02	0.08	0.01	0.09	0.00	0.14	0.00	0.00	0.00
C07	VeinT1 Omp	ISZ 36-15	2.42	0.35	1.75	0.23	0.36	0.03	0.13	0.01	0.40	0.00	0.29	0.00	0.00	0.00
C08	VeinT1 Omp	ISZ 36-15	3.85	0.52	2.57	0.32	0.54	0.04	0.16	0.01	0.23	0.00	0.47	0.00	0.00	0.00
C11	VeinT1 Omp	ISZ 36-15	2.12	0.29	1.31	0.17	0.28	0.02	0.08	0.01	0.15	0.00	0.31	0.00	0.00	0.00
C13	VeinT1 Omp	ISZ 36-15	2.10	0.29	1.39	0.17	0.25	0.02	0.07	0.00	0.15	0.00	0.23	0.00	0.00	0.00
C14	VeinT1 Omp	ISZ 36-15	2.18	0.34	1.36	0.19	0.32	0.04	0.14	0.02	0.13	0.00	0.26	0.00	0.00	0.00
D14	VeinT0 Omp	ISZ 36-15	1.49	0.21	1.00	0.13	0.22	0.02	0.06	0.01	0.11	0.00	0.19	0.00	0.00	0.00
D15	VeinT0 Omp	ISZ 36-15	1.47	0.19	0.92	0.11	0.17	0.01	0.06	0.01	0.11	0.00	0.18	0.00	0.00	0.00
D16	VeinT0 Omp	ISZ 36-15	1.56	0.22	0.95	0.14	0.21	0.02	0.09	0.01	0.11	0.00	0.19	0.00	0.00	0.00
D17	VeinT0 Omp	ISZ 36-15	1.20	0.17	0.87	0.12	0.17	0.02	0.06	0.01	0.10	0.00	0.16	0.00	0.00	0.00
D18	VeinT0 Omp	ISZ 36-15	1.36	0.17	0.77	0.09	0.14	0.01	0.04	0.00	0.09	0.00	0.16	0.00	0.00	0.00
D19	VeinT0 Omp	ISZ 36-15	1.31	0.19	0.84	0.10	0.15	0.01	0.05	0.00	0.11	0.00	0.17	0.00	0.00	0.00
D20	VeinT0 Omp	ISZ 36-15	1.33	0.17	0.78	0.09	0.16	0.01	0.05	0.00	0.11	0.00	0.17	0.00	0.00	0.00
A07	Matrix M2 Omp	ISZ 36-15	9.06	1.22	5.89	0.75	1.44	0.10	0.40	0.04	0.59	0.00	0.93	0.03	0.00	0.00
A08	Matrix M2 Omp	ISZ 36-15	6.40	0.99	5.61	0.86	2.04	0.15	0.67	0.08	0.60	0.01	1.06	0.02	0.01	0.00
A09	Matrix M2 Omp	ISZ 36-15	6.56	0.89	4.72	0.71	1.77	0.16	0.70	0.07	0.74	0.00	0.83	0.02	0.01	0.00
A10	Matrix M2 Omp	ISZ 36-15	2.83	0.41	1.51	0.22	0.52	0.03	0.16	0.02	0.60	-0.01	0.60	-0.02	0.02	0.01
A11	Matrix M2 Omp	ISZ 36-15	6.46	0.91	5.10	0.78	1.77	0.14	0.96	0.10	0.65	-0.01	0.99	-0.01	0.01	0.01
A15	Matrix M2 Omp	ISZ 36-15	4.04	0.59	3.18	0.46	1.17	0.12	0.50	0.06	0.47	0.00	0.75	0.01	0.00	0.00
A16	Matrix M2 Omp	ISZ 36-15	10.91	1.68	8.56	1.25	2.72	0.23	1.05	0.11	0.43	0.00	1.07	0.02	-0.01	0.00
A17	Matrix M2 Omp	ISZ 36-15	9.56	1.52	7.61	1.10	2.80	0.20	1.12	0.11	0.42	-0.01	0.71	-0.02	-0.02	0.00
A18	Matrix M2 Omp	ISZ 36-15	12.29	2.01	10.40	1.45	3.01	0.27	1.14	0.11	0.44	-0.01	0.89	0.01	0.01	-0.01
A19	Matrix M2 Omp	ISZ 36-15	13.11	2.12	10.88	1.43	3.30	0.24	1.21	0.15	0.53	-0.01	0.90	0.01	0.00	-0.01
B33	VeinT2 Omp	ISZ 36-15	1.83	0.27	1.36	0.20	0.35	0.04	0.17	0.02	0.07	0.00	0.20	0.00	0.00	0.00
B34	VeinT2 Omp	ISZ 36-15	2.30	0.35	1.80	0.26	0.49	0.05	0.22	0.02	0.07	0.00	0.21	0.00	0.00	0.00
B39	VeinT2 Omp	ISZ 36-15	2.11	0.31	1.66	0.22	0.43	0.04	0.19	0.02	0.06	0.00	0.16	0.00	0.00	0.00
B40	VeinT2 Omp	ISZ 36-15	1.67	0.24	1.15	0.16	0.28	0.03	0.12	0.01	0.07	0.00	0.14	0.00	0.00	0.00
B41	VeinT2 Omp	ISZ 36-15	1.04	0.18	0.91	0.13	0.23	0.02	0.10	0.01	0.09	0.00	0.12	0.00	0.00	0.00
C04	Mylonitic Clast Omp - core	ISZ 38-15	1.86	0.22	0.88	0.10	0.17	0.01	0.04	0.00	0.10	0.00	0.15	0.01	0.00	0.00
C05	Mylonitic Clast Omp - core	ISZ 38-15	1.74	0.21	0.82	0.09	0.15	0.01	0.05	0.01	0.12	0.00	0.13	0.00	0.00	0.00
C06	Mylonitic Clast Omp - core	ISZ 38-15	1.77	0.20	0.78	0.07	0.12	0.01	0.06	0.00	0.12	0.00	0.15	0.01	0.00	0.00
C07	Mylonitic Clast Omp - core	ISZ 38-15	1.53	0.15	0.53	0.07	0.11	0.01	0.04	0.00	0.12	-0.01	0.18	0.01	-0.01	0.00
C08	Mylonitic Clast Omp - core	ISZ 38-15	1.94	0.23	0.74	0.08	0.10	0.01	0.05	0.00	0.11	0.00	0.14	-0.01	0.00	0.00
C12	Mylonitic Clast Omp - rim	ISZ 38-15	1.97	0.27	1.33	0.18	0.32	0.03	0.13	0.01	0.12	0.00	0.21	0.01	0.00	0.00
C13	Mylonitic Clast Omp - rim	ISZ 38-15	2.05	0.28	1.46	0.20	0.39	0.03	0.17	0.02	0.11	0.00	0.19	0.00	0.00	0.00
C14	Mylonitic Clast Omp - rim	ISZ 38-15	1.64	0.19	0.80	0.11	0.22	0.02	0.09	0.01	0.09	0.00	0.23	0.00	0.00	0.00
C15	VeinT2 Omp	ISZ 38-15	2.23	0.22	0.90	0.11	0.23	0.02	0.11	0.01	0.09	0.00	0.20	0.00	0.00	0.00
C18	VeinT2 Omp	ISZ 38-15	2.38	0.22	0.72	0.08	0.12	0.01	0.06	0.01	0.06	0.00	0.36	0.00	0.00	0.00
C19	VeinT2 Omp	ISZ 38-15	2.71	0.25	0.90	0.11	0.20	0.02	0.09	0.01	0.07	0.00	0.30	0.00	0.00	0.00
C23	VeinT2 Omp	ISZ 38-15	2.18	0.23	0.83	0.09	0.16	0.01	0.06	0.01	0.07	0.00	0.25	0.00	0.00	0.00
C24	VeinT2 Omp	ISZ 38-15	2.36	0.22	0.83	0.09	0.19	0.02	0.08	0.01	0.10	0.00	0.20	0.00	0.00	0.00
C27	Mylonitic Clast Omp - core	ISZ 38-15	1.42	0.12	0.33	0.03	0.05	0.00	0.02	0.00	0.05	0.00	0.15	0.00	0.00	0.00
C28	Mylonitic Clast Omp - core	ISZ 38-15	1.00	0.09	0.34	0.04	0.11	0.01	0.14	0.03	1.11	0.00	0.13	0.00	0.00	0.01
C29	Mylonitic Clast Omp - core	ISZ 38-15	0.97	0.09	0.40	0.05	0.10	0.01	0.04	0.01	0.36	0.00	0.13	0.00	0.01	0.00
C30	Mylonitic Clast Omp - core	ISZ 38-15	1.16	0.11	0.37	0.04	0.08	0.01	0.03	0.00	0.08	0.00	0.13	-0.01	0.00	0.00

APPENDIX 1 (d): EPMA ANALYSIS of SELECTED GARNET CRYSTALS with the COMPLETE TRACE-ELEMENTS DATASET

Samples from the Lower Shear Zone: Breccia blocks with only Fe-Ti metagabbro clasts

# Analysis	Microstructural domain	Sample	EPMA analysis (internal standard) wt%														LA-ICP-MS concentration (µg/g)									
			SiO2	TiO2	Al2O3	Cr2O3	FeO	MnO	MgO	CaO	Na2O	K2O	NiO	P2O5	Total	MgO#	Li	B	Na	Mg	Al	Si	P	K	Ca	
C07	M2 matrix Grt - rim	ISZ 63-15d	38.61	0.10	21.30	0.14	26.62	0.37	7.37	6.93	0.01	0.00	0.02		101.42	21.67	6.32	-0.57	122.73	42021.56	113412.98	180488.42	2.93	13.52	47900.41	
C08	M2 matrix Grt - rim	ISZ 63-15d	38.44	0.07	20.97	0.34	27.41	0.24	6.32	7.40	0.02	0.00	0.03		101.24	18.74	2.39	1.83	95.64	34854.98	112991.43	179693.73	1.35	91.92	48956.87	
C09	M2 matrix Grt - core	ISZ 63-15d	38.19	0.12	20.42	0.01	29.75	0.19	5.52	6.62	0.00	0.01	0.04		100.77	15.65	0.34	0.65	52.97	31272.77	112692.14	178525.06	1.81	27.67	44093.31	
C10	M2 matrix Grt - core	ISZ 63-15d	37.99	0.12	20.81	0.02	29.22	0.11	6.03	6.56	0.02	0.02	0.03		100.83	17.10	0.78	0.50	46.15	34355.71	112248.16	177590.13	1.60	28.58	44730.20	
C11	M2 matrix Grt - rim	ISZ 63-15d	39.31	0.05	22.41	0.43	24.50	0.80	6.80	7.76	0.00	0.00	0.01	0.00		102.05	21.72	5.22	0.62	101.04	50183.04	119349.53	183753.20	2.99	23.47	49747.69
C13	M2 matrix Grt - core	ISZ 63-15d	38.36	0.09	19.80	0.91	28.60	0.16	4.92	7.71	0.00	0.01	0.08		100.62	14.67	4.10	0.66	100.99	35927.38	118394.90	179319.75	2.22	18.77	50891.44	
C21	M2 matrix Grt - core	ISZ 63-15d	37.25	0.01	19.88	0.39	32.82	0.15	3.60	5.82	0.02	0.01	0.04		99.98	9.88	8.71	9.28	1064.54	27100.60	114705.14	174130.89	4.25	451.27	37701.91	
C22	M2 matrix Grt - core	ISZ 63-15d	37.25	0.01	19.88	0.39	32.82	0.15	3.60	5.82	0.02	0.01	0.04		99.98	9.88	1.47	1.54	122.98	27687.57	112192.88	174130.89	4.05	77.75	36006.93	
C23	M2 matrix Grt - rim	ISZ 63-15d	37.12	0.08	20.03	0.12	32.75	0.21	3.68	5.61	0.00	0.01	0.04		99.62	10.09	5.83	0.86	83.60	49903.20	114351.15	173523.18	2.66	41.48	44109.89	
C24	M2 matrix Grt - rim	ISZ 63-15d	37.50	0.06	19.67	1.05	27.05	0.43	5.26	7.72	0.03	0.01	0.04		98.72	16.29	1.78	0.74	112.23	42889.69	114716.45	175299.55	2.86	36.72	49872.05	
D17	Mylonitic clast Grt	ISZ 63-15d	37.68	0.10	20.99	0.00	29.16	0.48	2.52	9.41	0.00	0.01	0.01	0.03		100.40	7.96	2.80	-0.91	368.94	46872.82	176131.17	25.22	38.16	55579.30	
D18	Mylonitic clast Grt	ISZ 63-15d	38.14	0.03	21.42	0.01	28.57	0.82	5.17	5.64	0.02	0.02	0.06	0.05		99.90	15.33	4.37	-1.30	898.24	78859.58	97159.42	178273.10	31.88	-16.82	35246.38
D19	Mylonitic clast Grt	ISZ 63-15d	37.36	0.05	21.01	0.02	30.42	0.47	1.91	9.52	0.03	0.01	0.01	0.02		100.81	5.91	2.68	-0.55	446.55	62808.67	104661.99	174664.27	26.06	59.70	44246.91
A07	Metasomatic Grt - core	ISZ 63-15b	38.49	0.08	21.54	0.40	27.99	0.30	5.22	7.38	0.00	0.00	0.00	0.03		101.43	15.71	0.72	0.14	60.89	30978.66	112276.08	179918.58	19.38	11.62	44759.89
A09	Metasomatic Grt - mantle	ISZ 63-15b	40.71	0.06	20.76	0.05	25.66	0.83	6.36	6.61	0.09	0.00	0.06	0.00		101.19	19.87	0.81	-0.38	69.78	35275.96	101404.94	190284.16	31.61	-5.69	42141.54
A10	Metasomatic Grt - rim	ISZ 63-15b	39.01	0.03	22.21	0.22	25.35	0.93	7.19	6.67	0.02	0.02	0.03	0.03		101.73	22.10	0.74	-0.37	94.13	36920.66	99700.47	182375.11	33.71	-5.63	44026.01
A11	Metasomatic Grt - core	ISZ 63-15b	39.07	0.08	21.92	0.21	26.64	2.64	5.15	6.51	0.05	0.00	0.00	0.00		102.26	16.20	0.75	0.14	65.98	31412.49	116557.89	182622.86	18.09	10.35	47021.74
B07	Metasomatic Grt - core	ISZ 63-15b	39.26	0.12	21.81	0.44	27.92	0.76	5.89	6.14	0.02	0.00	0.02	0.06		102.44	17.43	0.74	0.13	270.22	29666.73	115790.54	183538.16	18.76	18.11	48842.00
B08	Metasomatic Grt - rim	ISZ 63-15b	39.83	0.08	22.33	0.19	25.46	0.73	6.64	6.98	0.04	0.00	0.03	0.00		102.31	20.69	1.09	0.13	155.93	42375.32	118103.39	186209.26	44.96	19.06	43726.00
B10	Metasomatic Grt - rim	ISZ 63-15b	39.74	0.02	21.88	0.46	26.18	0.26	7.94	5.26	0.05	0.04	0.03	0.00		101.88	23.26	0.98	-0.14	119.18	42694.86	114452.81	185789.01	42.92	12.16	41083.87
B11	Metasomatic Grt - core	ISZ 63-15b	39.10	0.02	21.64	0.24	28.61	0.34	4.72	6.96	0.03	0.00	0.00	0.01		101.66	14.17	0.81	0.14	273.78	32527.13	115672.58	182779.00	18.70	16.34	45300.13
B12	Metasomatic Grt - rim	ISZ 63-15b	39.27	0.04	22.00	0.53	27.00	0.34	7.67	4.65	0.03	0.00	0.02	0.01		101.56	22.13	0.75	0.12	91.44	43761.74	120259.99	183573.69	40.70	10.44	44068.40
B13	Metasomatic Grt - rim	ISZ 63-15b	39.27	0.04	22.00	0.53	27.00	0.34	7.67	4.65	0.03	0.00	0.02	0.01		101.56	22.13	0.79	0.16	101.13	40255.94	119906.58	183573.69	37.89	12.99	49765.77
B14	Metasomatic Grt - core	ISZ 63-15b	38.52	0.06	21.44	0.41	29.04	1.37	4.55	6.59	0.00	0.00	0.00	0.03		102.01	13.54	0.69	0.12	59.89	27466.16	115743.01	180050.87	18.62	16.91	44793.38
B15	Metasomatic Grt - rim	ISZ 63-15b	39.56	0.09	21.64	0.69	26.15	0.32	7.19	6.65	0.00	0.00	0.02	0.01		102.31	21.56	0.89	0.14	113.01	42293.99	123867.64	184909.24	46.54	17.09	52186.46
B30	Metasomatic Grt - mantle	ISZ 63-15b	39.04	0.09	21.81	0.45	26.78	0.35	6.23	7.18	0.04	0.01	0.01	0.03		102.02	18.88	0.68	-0.10	63.39	40914.20	109738.25	182508.80	28.60	11.77	38296.10
B31	Metasomatic Grt - mantle	ISZ 63-15b	39.19	0.10	21.84	0.43	25.84	0.20	6.79	7.27	0.03	0.02	0.00	0.00		101.72	20.81	0.80	0.16	54.12	37786.02	112160.03	183220.29	26.60	16.93	47264.55
B22	Metasomatic Grt - mantle	ISZ 63-15b	38.97	0.09	21.32	0.52	25.14	0.33	5.83	7.90	0.02	0.01	0.13	0.04		99.92	18.84	0.94	-0.10	125.70	35982.34	114220.35	182185.78	39.77	12.69	47062.73
B24	Metasomatic Grt - mantle	ISZ 63-15b	38.71	0.08	21.46	0.05	23.84	0.89	6.47	6.97	0.01	0.01	0.02	0.00		98.49	21.36	1.05	-0.18	122.87	33585.23	105910.22	180977.39	34.64	9.85	42418.55
B25	Metasomatic Grt - core	ISZ 63-15b	38.88	0.01	20.85	0.39	28.90	0.46	5.28	6.08	0.00	0.00	0.01	0.01		100.83	15.45	0.61	-0.18	79.37	29377.58	103936.91	181756.65	17.65	-2.87	41088.70
B28	Metasomatic Grt - mantle	ISZ 63-15b	38.37	0.10	21.05	0.69	24.36	0.39	5.45	8.43	0.02	0.02	0.04	0.06		98.74	18.28	1.15	0.19	265.21	33645.28	106426.33	179377.25	35.84	10.45	44994.67
A04	Intermediate Mtg Clast - Grt	ISZ 53-15	38.93	0.03	21.47	0.00	29.09	0.62	4.06	6.16	0.05	0.01	0.00	0.00												

APPENDIX 1 (d): EPMA ANALYSIS of SELECTED GARNET CRYSTALS with the COMPLETE TRACE-ELEMENTS DATASET

Samples from the Lower Shear Zone: Breccia blocks with only Fe-Ti metagabbro clasts

# Analysis	Microstrucrtal domain	Sample																						
			Sc	Ti	V	Cr	Mn	Fe	Co	Ni	As	Rb	Sr	Y	Zr	Nb	Sb	Cs	Ba	La	Ce	Pr	Nd	Sm
C07	M2 matrix Grt - rim	ISZ 63-15d	371.67	29.85	597.65	7497.15	15861.01	204951.93	262.84	5.83	0.11	0.19	0.15	882.83	10.25	0.06	-0.12	-0.02	-0.09	-0.02	0.03	0.04	0.83	5.62
C08	M2 matrix Grt - rim	ISZ 63-15d	2238.68	18.17	1626.36	10661.22	4560.09	237143.19	292.61	28.31	-0.10	4.89	0.57	180.99	5.21	0.08	-0.13	1.49	0.44	-0.02	0.02	0.00	0.14	0.81
C09	M2 matrix Grt - core	ISZ 63-15d	541.10	30.36	3839.61	99.49	2713.21	250368.26	200.86	1.46	0.12	0.04	0.06	39.37	7.42	0.01	-0.08	-0.02	-0.06	0.00	0.02	0.04	1.93	16.78
C10	M2 matrix Grt - core	ISZ 63-15d	42.55	30.12	3923.30	968.75	3363.73	248935.94	255.93	1.90	0.11	0.04	0.06	15.98	134.92	0.02	-0.08	-0.02	-0.06	0.00	0.02	0.04	1.87	13.18
C11	M2 matrix Grt - rim	ISZ 63-15d	373.93	31.89	715.78	6377.67	18078.68	233359.80	331.74	5.74	0.11	0.20	0.14	987.51	11.19	0.04	0.10	-0.01	-0.07	-0.01	0.02	0.02	0.84	6.98
C13	M2 matrix Grt - core	ISZ 63-15d	1149.28	41.15	3675.55	24817.33	3027.37	282012.40	233.69	5.74	0.11	0.05	0.09	112.45	9.31	0.15	0.10	-0.01	0.06	-0.01	0.02	0.02	0.45	3.43
C21	M2 matrix Grt - core	ISZ 63-15d	851.46	45.16	1899.78	28534.13	5000.98	355513.38	188.27	6.34	0.09	12.38	17.50	13.78	9.28	0.22	-0.13	2.19	2.27	0.03	-0.02	-0.01	0.09	0.36
C22	M2 matrix Grt - core	ISZ 63-15d	740.69	41.66	1606.64	21456.76	5165.81	360161.26	193.17	3.94	-0.09	0.49	1.32	11.95	8.35	0.13	-0.13	0.10	0.18	-0.02	-0.02	-0.01	-0.08	0.47
C23	M2 matrix Grt - rim	ISZ 63-15d	326.31	25.15	1626.83	22478.24	18857.70	318560.46	361.51	6.03	0.12	0.13	0.12	697.79	9.45	0.11	-0.10	-0.02	0.06	-0.02	0.05	0.04	1.80	15.30
C24	M2 matrix Grt - rim	ISZ 63-15d	4449.55	39.74	1753.03	23531.71	12646.87	322205.66	455.77	3.31	0.09	0.10	0.11	322.14	10.48	0.15	-0.11	-0.02	0.04	-0.02	-0.01	-0.01	0.25	2.88
D17	Mylonitic clast Grt	ISZ 63-15d	118.67	1284.43	782.65	6.86	11133.12	597378.92	64.42	1.98	-0.08	0.04	0.40	185.72	1.25	-0.01	-0.12	-0.02	-0.14	0.01	0.03	-0.01	-0.09	1.62
D18	Mylonitic clast Grt	ISZ 63-15d	302.02	387.35	406.62	14.85	14646.99	562206.19	93.55	3.63	-0.12	-0.05	1.03	149.29	0.59	-0.01	-0.17	-0.03	-0.19	-0.01	-0.02	0.02	0.57	4.10
D19	Mylonitic clast Grt	ISZ 63-15d	244.03	745.10	399.20	18.27	11894.24	496865.44	76.74	2.74	-0.06	-0.04	0.44	179.29	1.12	-0.02	-0.10	-0.01	0.12	-0.01	-0.01	-0.01	0.37	2.76
A07	Metasomatic Grt - core	ISZ 63-15b	153.66	299.65	196.01	2769.21	2609.04	218012.72	24.66	0.95	0.02	0.01	0.02	56.41	0.94	0.01	0.03	0.00	-0.02	0.00	0.01	0.01	0.35	3.35
A09	Metasomatic Grt - mantle	ISZ 63-15b	42.03	253.38	163.37	1418.32	3255.30	196083.49	45.40	0.96	-0.05	-0.03	0.01	46.95	1.05	-0.01	-0.07	-0.01	-0.07	0.00	0.01	-0.01	0.10	1.07
A10	Metasomatic Grt - rim	ISZ 63-15b	56.60	402.54	94.30	1363.14	6084.76	188247.42	43.08	1.13	-0.05	0.03	0.04	140.46	1.36	-0.01	-0.07	-0.01	-0.07	0.00	0.00	-0.01	0.11	0.67
A11	Metasomatic Grt - core	ISZ 63-15b	92.04	320.75	175.68	2005.32	3489.10	223647.24	24.63	0.87	0.02	0.02	0.03	49.14	41.99	0.02	0.03	0.00	0.01	0.00	0.01	0.01	0.34	3.19
B07	Metasomatic Grt - core	ISZ 63-15b	85.38	329.05	171.43	2366.90	3472.86	228059.95	22.60	0.75	0.02	0.01	0.11	56.34	0.93	0.01	0.02	0.00	0.01	0.00	0.00	0.01	0.35	3.60
B08	Metasomatic Grt - rim	ISZ 63-15b	46.32	360.56	99.89	1300.67	5560.14	201496.01	49.40	1.17	0.01	0.02	0.05	119.67	1.50	0.01	0.02	0.00	-0.01	0.00	0.00	0.00	0.11	0.87
B10	Metasomatic Grt - rim	ISZ 63-15b	34.58	268.03	133.01	1541.68	4474.50	188404.85	50.81	1.15	-0.02	0.01	0.03	83.42	1.45	0.01	-0.03	0.00	-0.03	0.00	0.00	0.00	0.12	0.94
B11	Metasomatic Grt - core	ISZ 63-15b	74.51	268.02	179.92	1256.73	2699.58	219549.09	26.92	1.00	0.02	0.01	0.11	44.17	0.86	0.01	0.02	0.00	0.02	0.00	0.01	0.01	0.30	2.99
B12	Metasomatic Grt - rim	ISZ 63-15b	34.21	341.43	100.81	1727.67	5079.09	184465.31	46.29	0.98	0.02	0.02	0.03	124.29	1.55	0.01	0.02	0.00	0.03	0.00	0.00	0.00	0.13	0.87
B13	Metasomatic Grt - rim	ISZ 63-15b	45.22	431.50	106.79	1021.72	6440.04	184004.64	41.77	1.10	0.02	0.03	0.03	177.05	1.55	0.00	0.02	0.00	-0.03	0.00	0.01	0.00	0.13	1.00
B14	Metasomatic Grt - core	ISZ 63-15b	71.55	338.29	132.96	2313.67	9288.21	217095.75	20.24	0.60	0.02	0.01	0.02	62.23	0.91	0.01	0.02	0.00	-0.02	0.00	0.01	0.01	0.33	3.69
B15	Metasomatic Grt - rim	ISZ 63-15b	53.31	491.22	113.13	1382.16	6887.84	191582.68	40.55	1.02	0.01	0.05	0.04	205.12	1.91	0.01	0.02	0.00	-0.01	0.00	0.00	0.01	0.14	1.03
B30	Metasomatic Grt - mantle	ISZ 63-15b	14.41	174.78	153.90	2127.90	2934.22	188766.49	47.73	0.91	0.01	-0.01	0.01	39.37	0.86	0.01	0.02	0.00	-0.02	0.00	0.01	0.01	0.16	1.30
B31	Metasomatic Grt - mantle	ISZ 63-15b	94.22	262.14	263.60	4094.63	1895.85	190179.82	38.57	0.64	-0.02	-0.01	0.02	30.08	1.24	0.02	-0.02	-0.01	-0.02	0.00	0.00	0.00	0.19	1.43
B22	Metasomatic Grt - mantle	ISZ 63-15b	47.30	379.21	97.18	1595.54	2763.57	198561.96	50.09	1.28	-0.01	0.01	0.03	35.89	1.65	0.01	-0.02	0.00	-0.02	0.00	0.00	0.00	0.07	0.53
B24	Metasomatic Grt - mantle	ISZ 63-15b	48.90	311.10	112.23	1684.25	2243.39	189122.82	43.44	1.49	-0.03	-0.01	0.02	24.74	1.37	0.01	-0.03	0.00	0.04	0.00	0.01	0.00	0.16	0.89
B25	Metasomatic Grt - core	ISZ 63-15b	92.92	297.56	144.36	1811.42	3284.04	192299.62	29.69	0.64	0.03	0.02	0.04	92.63	0.89	0.01	-0.03	-0.01	-0.04	-0.01	-0.01	0.00	0.32	3.05
B28	Metasomatic Grt - mantle	ISZ 63-15b	52.12	373.37	121.37	2179.91	2293.31	183405.80	41.89	1.58	-0.01	0.01	0.05	26.24	1.53	0.01	-0.02	0.00	0.02	0.00	0.01	0.00	0.14	0.88
A04	Intermediate Mtg Clast - Grt	ISZ 53-15	73.59	154.13	15.11	26.12	4795.82	226117.60	35.24	0.51	-0.01	0.18	0.09	949.42	0.60	0.00	-0.02	0.00	-0.03	0.00	0.00	0.00	0.04	0.44
A05	Intermediate Mtg Clast - Grt	ISZ 53-15	115.02	114.41	24.67	109.61	3444.23	229193.12	37.15	0.39	-0.02	0.17	0.07	874.87	18.67	0.00	-0.02	0.00	-0.03	0.00	0.00	0.00	0.03	0.41
A06	Intermediate Mtg Clast - Grt	ISZ 53-15	66.57	116.98	12.76	42.45	3551.40	233051.26	37.18	0.42	-0.02	0.14	0.06	907.20	0.42	0.00	-0.03	-0.01						

APPENDIX 1 (d): EPMA ANALYSIS of SELECTED GARNET CRYSTALS with the COMPLETE TRACE-ELEMENTS DATASET

Samples from the Lower Shear Zone: Breccia blocks with only Fe-Ti metagabbro clasts

Analysis: Microstructural domain Sample																	
			Eu	Gd	Tb	Dy	Ho	Er	Tm	Yb	Lu	Hf	Ta	Pb	Bi	Th	U
C07	M2 matrix Grt - rim	ISZ 63-15d	5.84	41.16	12.69	117.45	32.49	151.35	23.71	216.67	40.75	0.14	-0.02	-0.06	-0.03	-0.02	-0.02
C08	M2 matrix Grt - rim	ISZ 63-15d	1.26	6.99	2.51	27.44	7.72	29.69	3.23	19.79	2.44	0.07	-0.02	-0.07	-0.03	-0.02	-0.03
C09	M2 matrix Grt - core	ISZ 63-15d	11.38	28.94	2.44	10.83	1.68	4.87	0.51	3.14	0.54	0.07	0.00	-0.05	0.04	-0.01	0.00
C10	M2 matrix Grt - core	ISZ 63-15d	8.78	20.09	1.48	4.71	0.54	1.09	0.12	0.85	0.19	3.69	0.00	-0.05	0.02	-0.01	0.01
C11	M2 matrix Grt - rim	ISZ 63-15d	7.20	47.57	14.33	129.71	34.50	157.96	24.25	215.51	39.37	0.16	-0.01	0.05	0.01	0.00	0.01
C13	M2 matrix Grt - core	ISZ 63-15d	2.48	13.98	3.29	23.97	5.04	16.22	1.73	10.48	1.37	0.12	0.00	0.03	0.03	-0.01	0.00
C21	M2 matrix Grt - core	ISZ 63-15d	2.78	3.14	0.57	2.39	0.49	1.44	0.21	2.39	0.52	0.11	-0.02	-0.07	-0.03	-0.03	-0.01
C22	M2 matrix Grt - core	ISZ 63-15d	2.73	3.74	0.60	2.54	0.37	1.10	0.11	0.88	0.16	0.10	-0.01	-0.07	-0.03	-0.02	-0.01
C23	M2 matrix Grt - rim	ISZ 63-15d	17.49	81.94	14.82	102.69	23.77	93.45	12.44	90.51	16.01	0.11	-0.01	-0.04	-0.02	0.00	0.01
C24	M2 matrix Grt - rim	ISZ 63-15d	4.64	17.02	4.71	47.37	14.14	64.06	9.39	67.45	9.75	0.10	-0.01	-0.05	-0.02	-0.01	-0.01
D17	Mylonitic clast Grt	ISZ 63-15d	2.29	28.93	9.61	54.28	8.91	20.32	2.15	11.82	1.51	0.03	-0.02	-0.09	-0.02	-0.02	-0.02
D18	Mylonitic clast Grt	ISZ 63-15d	4.29	25.15	5.20	33.10	6.58	20.08	2.93	18.39	2.80	0.02	-0.02	-0.13	-0.02	-0.03	-0.03
D19	Mylonitic clast Grt	ISZ 63-15d	3.17	23.16	6.17	41.67	7.78	21.30	2.75	16.91	2.69	0.08	-0.01	-0.06	-0.02	-0.01	-0.01
A07	Metasomatic Grt - core	ISZ 63-15b	2.51	12.58	2.06	12.46	2.43	6.80	0.85	5.58	0.81	0.01	0.00	-0.01	0.04	0.00	0.00
A09	Metasomatic Grt - mantle	ISZ 63-15b	0.78	5.04	1.15	8.50	1.91	5.47	0.75	5.50	0.82	-0.03	-0.01	-0.05	-0.01	-0.01	0.00
A10	Metasomatic Grt - rim	ISZ 63-15b	0.71	5.60	1.80	18.45	5.14	20.98	3.72	32.19	6.10	-0.03	-0.01	-0.05	-0.01	-0.01	0.00
A11	Metasomatic Grt - core	ISZ 63-15b	2.51	12.90	2.04	11.39	2.03	4.96	0.55	3.17	0.39	0.96	0.00	0.01	0.02	0.00	0.01
B07	Metasomatic Grt - core	ISZ 63-15b	2.82	14.47	2.28	13.07	2.27	5.37	0.59	3.30	0.43	0.01	0.00	0.01	0.01	0.00	0.00
B08	Metasomatic Grt - rim	ISZ 63-15b	0.83	5.51	1.64	14.33	3.91	15.37	2.71	24.37	4.42	0.02	0.00	0.01	0.00	0.00	0.00
B10	Metasomatic Grt - rim	ISZ 63-15b	0.82	5.60	1.42	11.77	2.85	9.81	1.47	11.86	2.00	0.02	0.00	-0.02	-0.01	0.00	0.00
B11	Metasomatic Grt - core	ISZ 63-15b	2.35	11.48	1.79	10.30	1.78	4.24	0.48	2.68	0.33	0.01	0.00	0.03	0.01	0.00	0.00
B12	Metasomatic Grt - rim	ISZ 63-15b	0.79	5.65	1.67	15.45	4.08	15.66	2.76	23.09	4.35	0.02	0.00	-0.01	0.00	0.00	0.00
B13	Metasomatic Grt - rim	ISZ 63-15b	0.94	6.92	2.22	21.65	6.19	24.18	4.30	36.49	6.74	0.02	0.00	-0.01	0.00	0.00	0.00
B14	Metasomatic Grt - core	ISZ 63-15b	3.40	20.30	3.41	16.63	2.34	4.77	0.52	3.13	0.44	0.01	0.00	-0.01	0.00	0.00	0.00
B15	Metasomatic Grt - rim	ISZ 63-15b	1.05	7.79	2.52	24.47	7.01	28.86	5.31	47.94	9.22	0.03	0.00	-0.01	0.00	0.00	0.00
B30	Metasomatic Grt - mantle	ISZ 63-15b	0.97	5.59	1.05	6.49	1.35	4.02	0.58	4.46	0.71	0.01	0.00	-0.01	0.01	0.00	0.00
B31	Metasomatic Grt - mantle	ISZ 63-15b	1.12	5.47	1.07	6.62	1.21	2.93	0.36	2.10	0.26	0.01	0.00	-0.02	0.00	0.00	0.00
B22	Metasomatic Grt - mantle	ISZ 63-15b	0.50	3.19	0.83	6.10	1.28	3.55	0.44	2.87	0.41	0.02	0.00	-0.01	0.00	0.00	0.00
B24	Metasomatic Grt - mantle	ISZ 63-15b	0.57	3.89	0.83	5.16	1.00	2.67	0.33	2.14	0.30	-0.01	0.00	-0.03	-0.01	-0.01	-0.01
B25	Metasomatic Grt - core	ISZ 63-15b	2.30	15.08	3.01	19.28	3.58	9.32	1.12	6.32	0.80	0.01	0.00	-0.03	-0.01	0.00	-0.01
B28	Metasomatic Grt - mantle	ISZ 63-15b	0.60	3.73	0.79	5.09	1.02	2.87	0.37	2.56	0.34	0.01	0.00	-0.01	0.00	0.00	0.00
A04	Intermediate Mtg Clast - Grt	ISZ 53-15	0.44	6.63	5.16	93.73	34.32	137.30	18.99	113.17	13.85	0.02	0.00	-0.01	-0.01	0.00	0.00
A05	Intermediate Mtg Clast - Grt	ISZ 53-15	0.39	5.94	4.89	90.27	32.16	119.50	15.82	93.79	12.34	0.48	0.00	-0.01	-0.01	0.00	0.01
A06	Intermediate Mtg Clast - Grt	ISZ 53-15	0.46	7.49	5.95	98.46	31.30	103.75	12.50	68.66	8.48	0.01	0.00	-0.02	-0.01	0.00	-0.01
A07	Intermediate Mtg Clast - Grt	ISZ 53-15	0.35	5.90	5.26	114.96	54.48	285.51	50.07	357.68	50.76	0.01	0.00	-0.01	0.00	0.00	0.00
A08	Intermediate Mtg Clast - Grt	ISZ 53-15	0.55	9.08	6.97	120.97	40.21	139.64	16.79	91.36	10.99	0.01	0.00	-0.01	0.00	0.00	0.00
A09	Intermediate Mtg Clast - Grt	ISZ 53-15	0.40	3.43	2.51	40.68	11.46	33.39	3.67	19.79	2.46	0.01	0.00	-0.01	0.00	0.00	0.00
A10	Intermediate Mtg Clast - Grt	ISZ 53-15	0.58	10.49	7.31	123.01	43.54	175.32	26.28	184.18	27.14	0.01	0.00	-0.01	0.00	0.00	0.00
A11	Intermediate Mtg Clast - Grt	ISZ 53-15	0.35	3.49	2.91	55.16	19.82	71.84	9.17	50.99	6.47	-0.01	0.00	-0.02	-0.01	-0.01	0.00
A12	Intermediate Mtg Clast - Grt	ISZ 53-15	0.38	3.72	2.82	52.67	20.09	82.43	11.75	74.72	10.21	0.03	0.00	-0.01	0.00	0.00	0.00
A15	FeTi Mtg Clast - Grt	ISZ 53-15	3.27	32.34	7.73	56.74	13.32	39.52	4.55	27.84	4.05	0.01	-0.01	-0.03	-0.01	0.00	-0.01
A16	FeTi Mtg Clast - Grt	ISZ 53-15	3.05	33.04	8.37	53.82	11.07	30.09	3.42	20.68	3.12	-0.02	-0.01	-0.04	-0.01	0.00	0.00
A20	FeTi Mtg Clast - Grt	ISZ 53-15	3.21	32.80	8.57	64.21	13.29	36.23	4.29	26.39	3.91	-0.02	-0.01	-0.04	-0.01	-0.01	-0.01
A21	FeTi Mtg Clast - Grt	ISZ 53-15	3.35	32.18	8.03	59.07	12.30	32.00	3.70	23.42	3.46	0.02	-0.01	-0.05	-0.01	0.00	0.00
A24	M2 Matrix - Grt	ISZ 53-15	3.06	34.99	9.55	66.64	13.19	39.66	5.04	29.69	3.66	0.01	0.00	-0.02	-0.01	0.00	0.00
A25	M2 Matrix - Grt	ISZ 53-15	2.41	27.19	8.63	70.12	15.32	51.49	7.87	58.65	9.41	-0.01	0.00	-0.02	-0.01	0.00	0.00
A26	M2 Matrix - Grt	ISZ 53-15	2.86	33.82	10.20	61.93	9.32	21.41	2.28	11.81	1.35	0.01	0.00	-0.01	0.00	0.00	0.00
A27	M2 Matrix - Grt	ISZ 53-15	3.09	40.57	14.69	115.35	22.44	60.96	7.71	55.65	9.14	-0.02	0.00	-0.03	-0.01	-0.01	0.00
A13	M2 Matrix - Grt	ISZ 53-15	2.57	32.85	11.35	88.14	16.39	42.00	5.16	33.87	5.15	0.01	0.00	-0.01	-0.01	0.00	0.00
A14	M2 Matrix - Grt	ISZ 53-15	3.09	39.00	12.82	94.93	17.04	42.39	5.14	32.91	4.90	0.02	0.00	-0.01	-0.01	0.00	0.00

Trace element data with (-) are below their respective detection limit (method: Pettke et Al., 2012)

APPENDIX 1 (e): EPMA ANALYSIS of SELECTED GARNET CRYSTALS with the COMPLETE TRACE-ELEMENTS DATASET

Samples from the Lower Shear Zone: Breccia blocks with MG-Al and Fe-Ti metagabbro clasts

# Analysis	Microstructral domain	Sample	EPMA analysis (internal standard) wt%														LA-ICP-MS concentration (µg/g)							
			SiO2	TiO2	Al2O3	Cr2O3	FeO	MnO	MgO	CaO	Na2O	K2O	NiO	P2O5	Total	MgO#	Li	B	Na	Mg	Al	Si	P	K
A04	Intermediate Mtg Clast - Grt	ISZ 53-15	38.93	0.03	21.47	0.00	29.09	0.62	4.06	6.16	0.05	0.01	0.00	0.00	100.41	12.24	0.89	0.11	357.21	24476.54	113631.15	181984.31	15.61	50.89
A05	Intermediate Mtg Clast - Grt	ISZ 53-15	38.81	0.02	21.72	0.02	29.49	0.44	4.12	5.96	0.05	0.01	0.00	0.00	100.62	12.25	0.48	0.13	352.73	24822.71	114943.55	181423.35	10.52	47.48
A06	Intermediate Mtg Clast - Grt	ISZ 53-15	38.96	0.02	22.06	0.01	29.98	0.46	4.46	6.27	0.04	0.00	0.00	0.00	102.27	12.96	0.44	-0.15	296.81	26928.14	116733.02	182124.55	10.52	30.49
A07	Intermediate Mtg Clast - Grt	ISZ 53-15	38.52	0.03	21.86	0.01	30.42	0.56	3.70	6.56	0.07	0.00	0.00	0.00	101.74	10.83	0.60	0.15	527.96	22291.05	115717.90	180067.70	10.12	26.11
A08	Intermediate Mtg Clast - Grt	ISZ 53-15	39.15	0.02	21.99	0.00	31.20	0.35	4.06	6.22	0.05	0.00	0.00	0.00	103.05	11.52	0.24	-0.09	394.95	24496.76	116373.05	183012.73	13.27	24.99
A09	Intermediate Mtg Clast - Grt	ISZ 53-15	38.51	0.02	21.89	0.01	30.49	0.45	4.22	6.20	0.03	0.00	0.00	0.00	101.82	12.15	0.32	0.10	194.78	25434.58	115838.37	180020.95	12.78	24.36
A10	Intermediate Mtg Clast - Grt	ISZ 53-15	37.76	0.02	21.46	0.01	29.24	0.81	3.71	6.93	0.05	0.00	0.00	0.00	100.01	11.26	0.76	0.10	393.81	22390.18	113559.93	176517.75	8.41	23.68
A11	Intermediate Mtg Clast - Grt	ISZ 53-15	38.72	0.02	21.56	0.01	30.47	0.43	4.17	6.03	0.03	0.00	0.00	0.00	101.45	12.05	0.34	0.27	238.66	25167.51	114106.63	181002.63	12.70	30.26
A12	Intermediate Mtg Clast - Grt	ISZ 53-15	38.41	0.02	21.72	0.02	29.84	0.62	4.15	6.27	0.04	0.00	0.00	0.00	101.09	12.20	0.67	0.13	279.41	24999.32	114939.99	179553.49	12.95	31.44
A15	FeTi Mtg Clast - Grt	ISZ 53-15	38.09	0.02	18.70	0.00	27.10	0.78	3.14	5.46	0.03	0.00	0.00	0.00	93.32	10.40	0.23	-0.26	189.73	18963.80	98970.83	178057.60	10.26	13.00
A16	FeTi Mtg Clast - Grt	ISZ 53-15	38.02	0.02	17.77	0.00	26.62	0.69	2.82	5.18	0.02	0.00	0.00	0.00	91.14	9.57	0.17	-0.26	171.08	16996.52	94045.68	177730.37	9.90	21.19
A20	FeTi Mtg Clast - Grt	ISZ 53-15	38.23	0.02	18.94	0.00	26.76	0.79	3.25	5.62	0.03	0.00	0.00	0.00	93.64	10.83	0.66	-0.21	190.39	19597.87	100254.46	178712.05	10.07	29.71
A21	FeTi Mtg Clast - Grt	ISZ 53-15	41.37	0.02	20.13	0.00	28.66	0.79	3.06	5.93	0.03	0.00	0.00	0.00	100.00	9.65	0.27	-0.24	194.66	18464.37	106548.68	193396.59	12.07	34.17
A24	M2 Matrix - Grt	ISZ 53-15	38.82	0.03	20.96	0.00	29.41	0.75	3.74	6.25	0.03	0.00	0.00	0.00	100.00	11.28	0.52	0.13	209.05	22564.69	110923.52	181449.18	14.29	23.99
A25	M2 Matrix - Grt	ISZ 53-15	38.69	0.02	20.11	0.01	28.79	0.82	3.94	5.44	0.03	0.00	0.00	0.00	97.87	12.04	0.52	-0.11	220.85	23764.59	106454.02	180862.39	11.36	33.32
A26	M2 Matrix - Grt	ISZ 53-15	38.51	0.03	20.63	0.00	29.62	0.69	3.33	6.04	0.02	0.00	0.00	0.00	98.88	10.10	0.40	0.08	184.24	20069.27	109180.40	180020.95	13.46	36.36
A27	M2 Matrix - Grt	ISZ 53-15	38.49	0.02	21.11	0.01	29.76	0.68	3.78	6.12	0.04	0.00	0.00	0.00	100.01	11.26	0.49	-0.15	275.93	22771.34	111728.30	179896.69	10.75	36.86
A13	M2 Matrix - Grt	ISZ 53-15	37.96	0.02	21.32	0.02	29.83	0.78	3.88	5.72	0.03	0.00	0.00	0.00	99.56	11.51	0.36	0.13	220.60	23392.70	112829.86	177449.89	13.38	30.71
A14	M2 Matrix - Grt	ISZ 53-15	38.54	0.03	21.97	0.01	30.58	0.73	3.86	5.75	0.03	0.00	0.00	0.00	101.51	11.22	0.30	0.17	228.82	23299.00	116259.50	180161.19	14.26	31.53

Trace element data with (-) are below their respective detection limit (method: Pettke et Al., 2012)

APPENDIX 1 (e): EPMA ANALYSIS of SELECTED GARNET CRYSTALS with the COMPLETE TRACE-ELEMENTS DATASET

Samples from the Lower Shear Zone: Breccia blocks with MG-Al and Fe-Ti metagabbro clasts

# Analysis	Microstructural domain	Sample	LA-ICP-MS concentration (µg/g)																						
			Ca	Sc	Ti	V	Cr	Mn	Fe	Co	Ni	As	Rb	Sr	Y	Zr	Nb	Sb	Cs	Ba	La	Ce	Pr	Nd	Sm
A04	Intermediate Mtg Clast - Grt	ISZ 53-15	44007.00	73.59	154.13	15.11	26.12	4795.82	226117.60	35.24	0.51	-0.01	0.18	0.09	949.42	0.60	0.00	-0.02	0.00	-0.03	0.00	0.00	0.00	0.04	0.44
A05	Intermediate Mtg Clast - Grt	ISZ 53-15	42575.98	115.02	114.41	24.67	109.61	3444.23	229193.12	37.15	0.39	-0.02	0.17	0.07	874.87	18.67	0.00	-0.02	0.00	-0.03	0.00	0.00	0.00	0.03	0.41
A06	Intermediate Mtg Clast - Grt	ISZ 53-15	44809.87	66.57	116.98	12.76	42.45	3551.40	233051.26	37.18	0.42	-0.02	0.14	0.06	907.20	0.42	0.00	-0.03	-0.01	-0.05	0.00	-0.01	0.00	0.05	0.54
A07	Intermediate Mtg Clast - Grt	ISZ 53-15	46898.62	99.31	164.87	18.05	54.30	4371.47	236436.82	29.95	0.38	-0.01	0.39	0.22	1456.57	0.61	0.00	0.01	0.00	-0.02	0.00	0.00	0.00	0.04	0.34
A08	Intermediate Mtg Clast - Grt	ISZ 53-15	44424.72	102.36	147.99	16.20	32.28	2689.77	242518.01	34.74	0.34	-0.01	0.17	0.07	1075.06	0.61	0.00	-0.02	-0.01	-0.03	0.00	0.00	0.00	0.04	0.59
A09	Intermediate Mtg Clast - Grt	ISZ 53-15	44305.04	147.74	136.52	13.88	84.73	3510.40	236963.23	37.59	0.37	0.01	0.05	0.02	330.49	0.54	0.00	0.01	0.00	-0.01	0.00	0.00	0.00	0.01	0.21
A10	Intermediate Mtg Clast - Grt	ISZ 53-15	49563.61	49.71	145.62	14.70	74.87	6240.67	227322.27	35.75	0.42	0.01	0.23	0.13	1108.94	0.47	0.00	0.01	0.00	0.01	0.00	0.00	0.00	0.07	0.71
A11	Intermediate Mtg Clast - Grt	ISZ 53-15	43089.63	112.45	123.96	12.09	67.89	3342.09	236809.51	37.96	0.58	-0.02	0.09	0.05	576.81	0.48	-0.01	0.02	0.00	-0.04	0.00	0.00	0.00	-0.02	0.23
A12	Intermediate Mtg Clast - Grt	ISZ 53-15	44796.97	148.56	140.64	18.39	128.06	4808.84	231920.24	35.15	0.37	-0.02	0.10	0.08	539.12	0.95	0.00	-0.02	0.00	0.10	0.00	0.00	0.00	0.02	0.24
A15	FeTi Mtg Clast - Grt	ISZ 53-15	38993.76	59.43	116.70	9.39	3.33	6017.98	210655.44	29.88	-0.71	-0.04	0.04	0.03	360.72	0.41	-0.01	-0.06	-0.01	-0.10	0.00	0.00	-0.01	0.21	3.03
A16	FeTi Mtg Clast - Grt	ISZ 53-15	37006.00	56.67	113.54	6.74	2.91	5344.12	206884.05	32.92	-0.66	-0.05	0.04	-0.01	303.88	0.34	-0.02	-0.06	-0.01	-0.09	0.00	-0.01	-0.01	0.24	2.46
A20	FeTi Mtg Clast - Grt	ISZ 53-15	40153.11	50.28	115.98	8.59	3.60	6148.01	207982.07	29.91	-0.48	-0.04	0.04	0.03	358.15	0.41	-0.01	-0.05	-0.01	-0.08	-0.01	0.01	-0.01	0.26	2.61
A21	FeTi Mtg Clast - Grt	ISZ 53-15	42353.56	63.49	127.13	8.46	3.80	6126.21	222788.73	31.99	-0.61	-0.05	-0.03	0.02	336.86	0.41	-0.02	-0.06	-0.01	-0.07	-0.01	0.00	0.00	0.16	2.83
A24	M2 Matrix - Grt	ISZ 53-15	44660.98	39.84	189.69	21.09	13.48	5837.87	228631.54	38.57	0.44	-0.02	0.05	0.04	369.44	0.72	0.00	-0.03	-0.01	-0.03	0.00	0.01	0.00	0.22	2.83
A25	M2 Matrix - Grt	ISZ 53-15	38910.38	61.16	121.41	13.03	80.15	6330.24	223815.04	39.81	0.71	-0.02	0.07	0.04	422.65	0.41	-0.01	-0.03	0.00	-0.03	0.00	0.00	0.00	0.18	2.31
A26	M2 Matrix - Grt	ISZ 53-15	43173.84	38.58	180.33	21.21	22.79	5308.26	230234.68	37.52	0.35	-0.01	0.03	0.02	264.73	0.65	0.00	-0.02	0.00	-0.02	0.00	0.00	0.00	0.17	2.45
A27	M2 Matrix - Grt	ISZ 53-15	43758.11	93.12	115.68	15.90	62.23	5287.09	231319.56	38.50	0.45	-0.03	0.08	0.05	561.31	0.34	-0.01	-0.03	-0.01	-0.05	-0.01	-0.01	0.01	0.16	2.55
A13	M2 Matrix - Grt	ISZ 53-15	40863.10	100.97	134.06	16.06	103.28	6042.42	231843.97	41.55	0.43	-0.01	0.05	0.03	434.19	0.54	0.00	-0.02	0.00	-0.03	0.00	0.00	0.00	0.18	2.42
A14	M2 Matrix - Grt	ISZ 53-15	41114.91	101.12	158.09	14.63	53.84	5640.06	237709.29	41.58	0.41	-0.01	0.05	0.04	456.91	0.70	0.00	0.02	-0.01	-0.03	0.00	0.00	0.00	0.19	2.88

Trace element data with (-) are below their respective detection limit (method: Pettke et Al., 2012)

APPENDIX 1 (e): EPMA ANALYSIS of SELECTED GARNET CRYSTALS with the COMPLETE TRACE-ELEMENTS DATASET

Samples from the Lower Shear Zone: Breccia blocks with MG-Al and Fe-Ti metagabbro clasts

# Analysis	Microstructural domain	Sample	LA-ICP-MS concentration (µg/g)														
			Eu	Gd	Tb	Dy	Ho	Er	Tm	Yb	Lu	Hf	Ta	Pb	Bi	Th	U
A04	Intermediate Mtg Clast - Grt	ISZ 53-15	0.44	6.63	5.16	93.73	34.32	137.30	18.99	113.17	13.85	0.02	0.00	-0.01	-0.01	0.00	0.00
A05	Intermediate Mtg Clast - Grt	ISZ 53-15	0.39	5.94	4.89	90.27	32.16	119.50	15.82	93.79	12.34	0.48	0.00	-0.01	-0.01	0.00	0.01
A06	Intermediate Mtg Clast - Grt	ISZ 53-15	0.46	7.49	5.95	98.46	31.30	103.75	12.50	68.66	8.48	0.01	0.00	-0.02	-0.01	0.00	-0.01
A07	Intermediate Mtg Clast - Grt	ISZ 53-15	0.35	5.90	5.26	114.96	54.48	285.51	50.07	357.68	50.76	0.01	0.00	-0.01	0.00	0.00	0.00
A08	Intermediate Mtg Clast - Grt	ISZ 53-15	0.55	9.08	6.97	120.97	40.21	139.64	16.79	91.36	10.99	0.01	0.00	-0.01	0.00	0.00	0.00
A09	Intermediate Mtg Clast - Grt	ISZ 53-15	0.40	3.43	2.51	40.68	11.46	33.39	3.67	19.79	2.46	0.01	0.00	-0.01	0.00	0.00	0.00
A10	Intermediate Mtg Clast - Grt	ISZ 53-15	0.58	10.49	7.31	123.01	43.54	175.32	26.28	184.18	27.14	0.01	0.00	-0.01	0.00	0.00	0.00
A11	Intermediate Mtg Clast - Grt	ISZ 53-15	0.35	3.49	2.91	55.16	19.82	71.84	9.17	50.99	6.47	-0.01	0.00	-0.02	-0.01	-0.01	0.00
A12	Intermediate Mtg Clast - Grt	ISZ 53-15	0.38	3.72	2.82	52.67	20.09	82.43	11.75	74.72	10.21	0.03	0.00	-0.01	0.00	0.00	0.00
A15	FeTi Mtg Clast - Grt	ISZ 53-15	3.27	32.34	7.73	56.74	13.32	39.52	4.55	27.84	4.05	0.01	-0.01	-0.03	-0.01	0.00	-0.01
A16	FeTi Mtg Clast - Grt	ISZ 53-15	3.05	33.04	8.37	53.82	11.07	30.09	3.42	20.68	3.12	-0.02	-0.01	-0.04	-0.01	0.00	0.00
A20	FeTi Mtg Clast - Grt	ISZ 53-15	3.21	32.80	8.57	64.21	13.29	36.23	4.29	26.39	3.91	-0.02	-0.01	-0.04	-0.01	-0.01	-0.01
A21	FeTi Mtg Clast - Grt	ISZ 53-15	3.35	32.18	8.03	59.07	12.30	32.00	3.70	23.42	3.46	0.02	-0.01	-0.05	-0.01	0.00	0.00
A24	M2 Matrix - Grt	ISZ 53-15	3.06	34.99	9.55	66.64	13.19	39.66	5.04	29.69	3.66	0.01	0.00	-0.02	-0.01	0.00	0.00
A25	M2 Matrix - Grt	ISZ 53-15	2.41	27.19	8.63	70.12	15.32	51.49	7.87	58.65	9.41	-0.01	0.00	-0.02	-0.01	0.00	0.00
A26	M2 Matrix - Grt	ISZ 53-15	2.86	33.82	10.20	61.93	9.32	21.41	2.28	11.81	1.35	0.01	0.00	-0.01	0.00	0.00	0.00
A27	M2 Matrix - Grt	ISZ 53-15	3.09	40.57	14.69	115.35	22.44	60.96	7.71	55.65	9.14	-0.02	0.00	-0.03	-0.01	-0.01	0.00
A13	M2 Matrix - Grt	ISZ 53-15	2.57	32.85	11.35	88.14	16.39	42.00	5.16	33.87	5.15	0.01	0.00	-0.01	-0.01	0.00	0.00
A14	M2 Matrix - Grt	ISZ 53-15	3.09	39.00	12.82	94.93	17.04	42.39	5.14	32.91	4.90	0.02	0.00	-0.01	-0.01	0.00	0.00

Trace element data with (-) are below their respective detection limit (method: Pettke et Al., 2012)

APPENDIX 1 (f): EPMA ANALYSIS of SELECTED GARNET CRYSTALS with the COMPLETE TRACE-ELEMENTS DATASET

Samples from the Intermediate Shear Zone: Breccia blocks with only Fe-Ti metagabbro clasts

# AnalysisMicrostructral domainSample			EPMA analysis (internal standard) wt%														LA-ICP-MS concentration (µg/g)							
			SiO2	TiO2	Al2O3	Cr2O3	FeO	MnO	MgO	CaO	Na2O	K2O	NiO	P2O5	Total	MgO#	Li	B	Na	Mg	Al	Si	P	K
B26	Mylonitic clast Grt	ISZ 35-15	36.00	0.03	20.95	0.00	31.76	1.00	4.30	3.54	0.02	0.01	0.00	0.03	97.57	11.92	0.39	-0.18	173.82	24369.16	106849.94	168295.98	19.44	29.10
B27	Mylonitic clast Grt	ISZ 35-15	36.38	0.08	20.25	0.01	29.91	0.75	1.64	8.51	0.04	0.01	0.04	0.01	97.53	5.20	0.45	-0.14	224.70	15298.94	100068.17	170051.32	8.32	32.26
B28	Mylonitic clast Grt	ISZ 35-15	37.01	0.02	20.98	0.01	31.75	0.81	4.75	3.50	0.01	0.01	0.07	0.02	98.74	13.03	0.54	-0.20	381.73	23199.01	101869.46	173011.31	23.29	32.93
B30	Mylonitic clast Grt	ISZ 35-15	36.06	0.02	20.50	0.02	33.69	0.60	3.20	4.31	0.01	0.02	0.06	0.00	98.39	8.68	0.31	0.13	215.86	19605.91	107617.08	168570.85	17.65	39.80
B31	Mylonitic clast Grt	ISZ 35-15	36.61	0.06	20.44	0.04	32.91	0.97	3.80	3.72	0.00	0.02	0.25	0.01	98.74	10.36	0.31	0.13	164.91	18914.47	104434.76	171156.40	30.55	51.39
D21	VeinT2 - Grt	ISZ 35-15	38.72	0.08	21.62	0.01	32.51	0.74	4.30	3.36	0.05	0.01	0.00	0.07	101.48	11.68	0.29	0.07	139.14	21126.06	121871.82	180990.48	18.68	101.52
D22	VeinT2 - Grt	ISZ 35-15	38.19	0.06	22.15	0.00	31.47	0.62	3.79	5.63	0.01	0.00	0.10	0.02	102.04	10.76	0.26	-0.10	121.82	19226.93	117901.31	178511.51	16.35	65.25
D24	VeinT2 - Grt	ISZ 35-15	38.55	0.21	21.20	0.04	30.82	0.76	4.73	3.48	0.10	0.00	0.02	0.00	99.91	13.30	0.53	-0.20	173.44	24370.21	106664.69	180230.84	22.76	-12.34
D25	Mylonitic clast Grt	ISZ 35-15	38.50	0.16	21.82	0.00	32.07	0.79	4.81	3.47	0.04	0.01	0.09	0.01	101.75	13.05	0.39	-0.11	148.84	22671.64	117129.45	179967.19	19.68	24.10
D28	Mylonitic clast Grt	ISZ 35-15	38.55	0.00	22.08	0.00	33.24	0.82	4.78	3.12	0.04	0.02	0.00	0.00	102.65	12.58	0.34	-0.24	191.93	23898.72	114744.72	180194.85	16.54	165.79
D29	Mylonitic clast Grt	ISZ 35-15	38.72	0.03	22.21	0.05	32.77	0.81	5.02	3.11	0.06	0.00	0.05	0.00	102.82	13.28	0.42	-0.23	192.77	24323.43	107805.77	180984.87	19.88	121.36
A20	M2 matrix Grt - core	ISZ 35-15	37.47	0.09	20.95	0.22	28.70	0.26	5.71	5.48	0.01	0.00	0.04	0.01	98.93	16.59	0.61	0.59	93.82	2966.02	50249.94	175138.28	1.74	2.70
A21	M2 matrix Grt - core	ISZ 35-15	37.36	0.02	20.97	0.08	29.55	0.15	5.51	5.37	0.00	0.02	0.01	0.04	98.98	15.72	0.66	0.44	76.55	2916.45	49605.79	174645.57	1.37	2.48
A22	M2 matrix Grt - core	ISZ 35-15	37.47	0.09	20.95	0.22	28.70	0.26	5.71	5.48	0.01	0.00	0.04	0.01	98.93	16.59	0.89	0.53	98.95	2466.87	44716.51	175138.28	1.81	0.83
B32	M2 matrix Grt - core	ISZ 35-15	38.38	0.10	20.91	0.36	28.96	0.04	5.61	4.91	0.00	0.03	0.09	0.01	99.16	16.22	0.11	0.13	61.60	28517.56	106021.38	179404.36	18.96	40.80
B35	M2 matrix Grt - core	ISZ 35-15	37.81	0.06	20.70	0.49	28.71	0.47	5.04	5.51	0.02	0.02	0.04	0.01	98.71	14.93	0.20	0.11	155.97	28083.56	113725.26	176735.14	18.50	38.30
B37	M2 matrix Grt - core	ISZ 35-15	38.05	0.12	21.14	0.44	28.05	0.33	5.73	5.47	0.02	0.01	0.06	0.02	99.44	16.97	0.27	0.14	106.13	35518.55	113156.75	177877.16	86.26	23.18
B38	M2 matrix Grt - core	ISZ 35-15	38.05	0.12	21.14	0.44	28.05	0.33	5.73	5.47	0.02	0.01	0.06	0.02	99.44	16.97	0.13	0.10	101.50	38661.41	116105.81	177877.16	95.36	21.29
A12	M2 matrix Grt - rim	ISZ 35-15	37.83	0.05	20.92	0.29	28.20	0.09	6.67	4.52	0.01	0.02	0.07	0.01	98.68	19.13	0.74	0.64	91.31	6540.23	71978.17	176845.46	2.35	6.30
A13	M2 matrix Grt - rim	ISZ 35-15	37.83	0.05	20.92	0.29	28.20	0.09	6.67	4.52	0.01	0.02	0.07	0.01	98.68	19.13	1.15	1.02	92.81	6686.18	74359.31	176845.46	2.38	9.03
A14	M2 matrix Grt - rim	ISZ 35-15	37.83	0.05	20.92	0.29	28.20	0.09	6.67	4.52	0.01	0.02	0.07	0.01	98.68	19.13	2.18	0.63	109.57	5297.70	68304.45	176845.46	2.43	6.65
A23	M2 matrix Grt - rim	ISZ 35-15	38.09	0.04	21.28	0.11	27.52	0.21	6.70	5.13	0.03	0.02	0.04	0.01	99.18	19.58	1.18	0.77	143.81	2588.05	42986.33	178052.92	5.58	1.26
B42	M2 matrix Grt - rim	ISZ 35-15	38.36	0.05	21.40	0.78	28.23	0.14	7.09	4.70	0.03	0.03	0.09	0.05	100.88	20.08	0.21	1.66	115.49	39868.48	106351.07	179298.72	96.57	30.08
B43	M2 matrix Grt - rim	ISZ 35-15	38.28	0.05	21.41	0.58	25.47	0.00	8.20	4.27	0.04	0.02	0.24	0.01	98.53	24.36	0.17	0.20	133.92	40379.24	106232.22	178940.17	101.60	30.65
C08	Mylonitic clast Grt	ISZ 38-15	41.22	0.02	19.62	0.00	30.77	0.91	3.71	3.72	0.02	0.00	0.00	0.00	100.00	10.76	0.38	-0.25	171.75	22367.17	103863.05	192657.60	14.64	21.48
C10	Mylonitic clast Grt	ISZ 38-15	39.27	0.06	20.61	0.00	30.64	0.76	3.59	5.05	0.02	0.00	0.00	0.00	100.00	10.48	0.56	-0.10	165.16	21632.25	109066.21	183583.66	14.16	35.15
C11	Mylonitic clast Grt	ISZ 38-15	38.87	0.04	20.84	0.00	30.62	0.73	3.48	5.39	0.02	0.01	0.00	0.00	100.00	10.20	0.62	-0.13	158.66	20984.97	110312.28	181679.69	12.35	43.12
C25	Mylonitic clast Grt	ISZ 38-15	39.67	0.02	20.77	0.00	30.88	0.69	3.61	4.33	0.02	0.00	0.00	0.00	100.00	10.46	0.37	0.10	147.44	21752.87	109917.70	185455.65	14.30	18.91
C26	Mylonitic clast Grt	ISZ 38-15	39.57	0.03	20.78	0.00	31.09	0.84	3.57	4.08	0.02	0.00	0.00	0.00	100.00	10.31	0.49	0.08	171.93	21555.85	109998.54	184955.65	16.31	32.91
C16	VeinT2 - Grt	ISZ 38-15	38.93	0.04	21.12	0.25	30.06	0.27	3.88	5.68	0.01	0.00	0.00	0.00	100.25	11.43	0.25	0.05	104.58	23383.19	111784.52	181981.93	12.62	36.53
C17	VeinT2 - Grt	ISZ 38-15	39.38	0.04	21.11	0.60	29.02	0.15	5.32	4.96	0.01	0.00	0.00	0.01	100.59	15.49	0.26	0.06	94.63	32080.54	111721.23	184095.40	36.26	20.27
C21	VeinT2 - Grt	ISZ 38-15	39.91	0.04	20.55	0.79	29.41	0.17	4.20	5.69	0.01	0.00	0.00	0.00	100.79	12.50	0.30	0.06	110.04	25336.99	108777.96	186551.89	16.85	25.34
C31	VeinT2 - Grt	ISZ 38-15	39.79	0.04	20.58	0.57	29.57	0.12	4.43	5.43	0.01	0.00	0.00	0.00	100.57	13.04	0.21	0.06	105.72	26741.53	108926.18	186011.56	18.77	32.23
C32	VeinT2 - Grt	ISZ 38-15	39.31	0.05	20.68	0.47	29.98	0.21	4.03	5.72	0.01	0.00	0.00	0.00	100.47	11.86	0.27	0.05	107.77	24334.37	109470.56	183727.57	15.28	37.92

Trace element data with (-) are below their respective detection limit (method: Pettke et Al., 2012)

APPENDIX 1 (f): EPMA ANALYSIS of SELECTED GARNET CRYSTALS with the COMPLETE TRACE-ELEMENTS DATASET

Samples from the Intermediate Shear Zone: Breccia blocks with only Fe-Ti metagabbro clasts

# Analysis	Microstructural domain	Sample	LA-ICP-MS concentration (μg/g)																									
			Ca	Sc	Ti	V	Cr	Mn	Fe	Co	Ni	As	Rb	Sr	Y	Zr	Nb	Sb	Cs	Ba	La	Ce	Pr	Nd	Sm	Eu	Gd	Tb
B26	Mylonitic clast Grt	ISZ 35-15	22046.77	66.44	128.32	37.01	6.39	5303.07	201772.00	17.61	0.77	-0.03	0.03	0.04	145.19	0.20	-0.01	-0.04	-0.01	-0.06	0.00	0.01	0.00	0.23	1.67	1.80	12.04	2.82
B27	Mylonitic clast Grt	ISZ 35-15	41578.06	96.19	249.98	70.65	5.78	4154.25	193140.18	12.09	0.61	-0.02	0.02	0.04	146.71	4.09	0.01	-0.03	-0.01	-0.04	0.00	0.01	0.01	0.13	1.37	1.77	15.51	4.62
B28	Mylonitic clast Grt	ISZ 35-15	20797.49	64.57	167.25	42.12	6.34	5469.04	203436.86	19.61	0.57	-0.03	0.03	0.06	138.74	0.30	-0.01	-0.03	-0.01	-0.05	-0.01	0.01	0.00	0.19	1.35	1.41	10.11	2.64
B30	Mylonitic clast Grt	ISZ 35-15	22945.72	54.12	146.11	37.55	3.27	5740.15	210278.52	18.32	0.47	0.01	0.02	0.04	129.18	0.22	0.00	0.01	0.00	0.06	0.00	0.00	0.00	0.22	1.89	2.06	13.82	2.84
B31	Mylonitic clast Grt	ISZ 35-15	24332.15	38.58	188.07	38.88	2.58	5035.25	208836.75	17.48	0.53	0.01	0.02	0.03	115.08	0.28	0.00	-0.02	0.00	0.05	0.00	0.01	0.01	0.21	2.15	2.40	17.41	3.35
D21	VeinT2 - Grt	ISZ 35-15	27199.22	37.25	200.48	49.84	2.49	4836.28	237743.53	21.17	0.49	0.01	0.03	0.02	166.34	0.25	0.00	-0.01	0.00	-0.02	0.00	0.01	0.01	0.21	2.17	2.16	20.65	5.03
D22	VeinT2 - Grt	ISZ 35-15	28621.52	38.46	199.94	51.49	1.92	4607.79	236413.57	20.31	0.44	-1.27E-02	0.02	0.02	163.54	0.23	0.00	-0.02	0.00	-0.02	0.00	0.01	0.01	0.25	2.47	2.51	23.90	5.74
D24	VeinT2 - Grt	ISZ 35-15	22359.66	66.19	180.63	48.81	2.15	5305.74	221191.74	23.25	0.83	-3.31E-02	0.04	0.02	160.94	0.23	-0.01	-0.04	-0.01	-0.06	-0.01	0.01	0.01	0.22	1.45	1.45	12.97	3.16
D25	Mylonitic clast Grt	ISZ 35-15	22762.98	48.38	179.82	42.34	2.52	5587.65	231777.61	23.33	0.82	-1.74E-02	0.03	0.03	161.81	0.20	0.00	-0.02	0.00	-0.03	0.00	0.01	0.01	0.18	1.13	1.07	9.85	2.74
D28	Mylonitic clast Grt	ISZ 35-15	24647.95	57.74	182.34	52.82	2.46	5267.26	239680.11	19.56	0.41	-3.02E-02	0.03	0.06	148.22	0.18	-0.01	-0.04	-0.01	-0.07	-0.01	0.00	0.01	0.21	1.58	1.57	14.27	3.50
D29	Mylonitic clast Grt	ISZ 35-15	22259.46	50.28	175.99	49.25	1.71	5229.68	229492.06	20.99	0.52	-2.95E-02	0.03	0.04	143.17	0.21	-0.01	-0.04	-0.01	-0.07	-0.01	0.02	0.01	0.22	1.46	1.39	12.18	3.20
A20	M2 matrix Grt - core	ISZ 35-15	39783.22	951.45	21.55	1450.81	6723.28	3538.08	4428.96	169.27	3.68	0.08	0.12	0.08	501.54	7.70	0.03	0.08	-0.01	0.04	0.00	0.02	0.07	2.41	18.02	10.80	68.89	15.27
A21	M2 matrix Grt - core	ISZ 35-15	38548.04	773.68	14.81	1139.59	8266.14	3180.42	4459.46	166.43	4.01	0.07	0.07	0.06	284.12	4.85	0.04	0.08	-0.01	0.04	0.00	0.02	0.05	2.06	14.99	8.88	46.86	9.31
A22	M2 matrix Grt - core	ISZ 35-15	39902.68	886.90	19.86	1477.93	3997.34	3721.40	3838.60	166.17	4.02	0.07	0.10	0.07	526.51	6.98	0.02	0.06	-0.01	0.03	-0.01	0.02	0.06	2.21	15.79	9.70	64.69	15.40
B32	M2 matrix Grt - core	ISZ 35-15	32951.05	67.23	301.78	212.16	1205.64	1715.60	203827.07	28.19	0.84	0.02	0.01	0.01	22.63	0.76	0.01	0.03	0.00	-0.01	0.00	0.00	0.01	0.32	2.18	1.46	6.29	0.99
B35	M2 matrix Grt - core	ISZ 35-15	35351.69	86.98	284.83	156.59	1701.91	2483.24	201731.95	25.87	0.98	0.01	0.02	0.26	78.71	0.93	0.01	0.01	0.00	-0.01	0.00	0.01	0.01	0.39	3.16	2.03	14.13	2.73
B37	M2 matrix Grt - core	ISZ 35-15	29486.66	7.72	345.40	309.46	2055.95	725.06	196574.65	40.39	1.08	0.01	0.01	0.01	5.84	2.60	0.01	0.01	0.00	-0.01	0.00	0.01	0.02	0.49	1.78	0.52	4.35	0.58
B38	M2 matrix Grt - core	ISZ 35-15	30476.92	5.78	353.44	308.75	1834.71	572.45	194464.07	45.73	1.10	0.01	0.01	0.01	7.05	2.73	0.01	0.01	0.00	-0.01	0.00	0.01	0.01	0.34	1.60	0.46	4.74	0.70
A12	M2 matrix Grt - rim	ISZ 35-15	34907.72	638.54	22.48	2084.09	17136.58	2259.27	10497.11	168.83	4.23	-0.09	0.10	0.11	368.78	9.42	0.09	-0.11	-0.02	-0.15	0.01	0.04	0.07	2.89	19.37	11.21	56.83	10.65
A13	M2 matrix Grt - rim	ISZ 35-15	33364.01	258.55	22.09	1919.44	12737.80	2263.92	10759.37	176.58	4.05	-0.09	0.05	0.07	146.74	9.74	0.05	-0.11	-0.02	-0.15	0.01	0.05	0.08	2.90	17.27	10.48	44.80	6.25
A14	M2 matrix Grt - rim	ISZ 35-15	33279.92	211.64	21.39	1889.16	10100.89	2971.36	8341.47	170.58	5.06	-0.09	0.06	0.08	127.96	9.57	0.05	-0.10	-0.02	-0.11	-0.02	0.07	0.06	2.79	17.89	10.19	43.78	6.03
A23	M2 matrix Grt - rim	ISZ 35-15	40096.98	179.20	24.23	1756.49	8141.77	1958.24	3179.81	192.76	4.78	0.07	0.06	0.20	72.93	13.04	0.11	0.10	-0.01	0.04	-0.01	0.05	0.06	1.88	10.32	5.95	24.84	3.47
B42	M2 matrix Grt - rim	ISZ 35-15	28080.65	6.14	267.53	263.52	3368.69	495.84	184680.61	52.27	1.46	0.03	0.01	0.11	6.40	37.94	0.02	0.01	0.00	2.30	0.01	0.02	0.01	0.24	1.23	0.40	3.86	0.59
B43	M2 matrix Grt - rim	ISZ 35-15	25222.45	7.99	234.05	149.07	4013.41	1083.66	192579.15	58.04	1.22	0.01	0.01	0.02	6.88	2.11	0.02	0.01	0.00	0.05	0.00	0.01	0.00	0.04	0.24	0.24	1.19	0.28
C08	Mylonitic clast Grt	ISZ 38-15	26616.04	78.76	148.92	80.32	3.97	7021.08	239150.96	20.13	0.79	-0.05	0.03	0.03	145.08	0.20	-0.01	-0.05	-0.01	-0.06	-0.01	0.01	0.01	0.24	2.71	3.04	19.37	3.58
C10	Mylonitic clast Grt	ISZ 38-15	36070.98	68.04	332.89	146.19	4.59	5891.66	238151.21	18.80	0.70	-0.02	0.02	0.04	196.21	5.49	0.02	0.03	0.00	-0.04	0.00	0.02	0.01	0.22	2.16	2.39	19.86	5.23
C11	Mylonitic clast Grt	ISZ 38-15	38489.41	62.20	242.95	140.15	4.29	5670.45	238032.58	17.94	0.71	-0.02	0.02	0.04	171.19	0.29	-0.01	-0.02	-0.01	-0.06	0.01	0.03	0.01	0.27	2.56	2.90	23.43	5.81
C25	Mylonitic clast Grt	ISZ 38-15	30969.86	74.95	143.84	40.76	3.97	5340.23	240012.56	39.32	0.61	-0.02	0.01	0.02	144.20	0.23	-0.01	-0.02	-0.01	-0.03	0.00	0.01	0.01	0.23	2.98	4.04	28.20	5.88
C26	Mylonitic clast Grt	ISZ 38-15	29181.88	76.67	156.27	41.05	4.09	6497.69	241703.72	37.77	0.88	-0.01	0.04	0.03	261.91	0.22	-0.01	-0.02	0.00	-0.02	0.00	0.01	0.00	0.18	1.88	2.29	16.43	4.69
C16	VeinT2 - Grt	ISZ 38-15	40605.01	183.72	227.89	285.03	1716.72	2112.72	233627.02	21.23	1.12	-0.01	0.01	0.03	32.48	0.49	0.01	0.02	0.00	-0.02	0.00	0.00	0.01	0.22	2.22	2.13	8.94	1.28
C17	VeinT2 - Grt	ISZ 38-15	35437.25	104.62	229.29	393.10	4073.03	1143.90	225565.56	27.82	1.05	0.02	0.01	0.01	11.25	1.21	0.02	0.02	0.00	-0.01	0.00	0.00	0.01	0.30	1.83	0.97	4.97	0.69
C21	VeinT2 - Grt	ISZ 38-15	40639.78	272.48	247.93	374.03	5399.44	1346.92	228626.63	23.32	1.59	-0.01	0.01	0.02	17.42	0.69	0.02	-0.01	0.00	-0.02	0.00	0.00	0.01	0.22	2.04	1.56	5.40	0.74
C31	VeinT2 - Grt	ISZ 38-15	38832.92	371.53	269.22	410.84	3891.37	954.02	229822.88	24.76	0.79	-0.01	-0.01	0.01	15.96	0.74	0.02	0.01	0.00	-0.02	0.00	0.00	0.00	0.24	1.96	1.31	4.89	0.69
C32	VeinT2 - Grt	ISZ 38-15	40903.94	285.50	273.72	358.42	3235.45	1589.47	233027.73	22.26	1.28	0.01	0.01	0.01	18.83	0.63	0.02	0.01	0.00	-0.01	0.00	0.00	0.01	0.23	2.18	1.85	5.91	0.77

Trace element data with (-) are below their respective detection limit (method: Pettke et Al., 2012)

APPENDIX 1 (f): EPMA ANALYSIS of SELECTED GARNET CRYSTALS with the COMPLETE TRACE-ELEMENTS DATASET

Samples from the Intermediate Shear Zone: Breccia blocks with only Fe-Ti metagabbro clasts

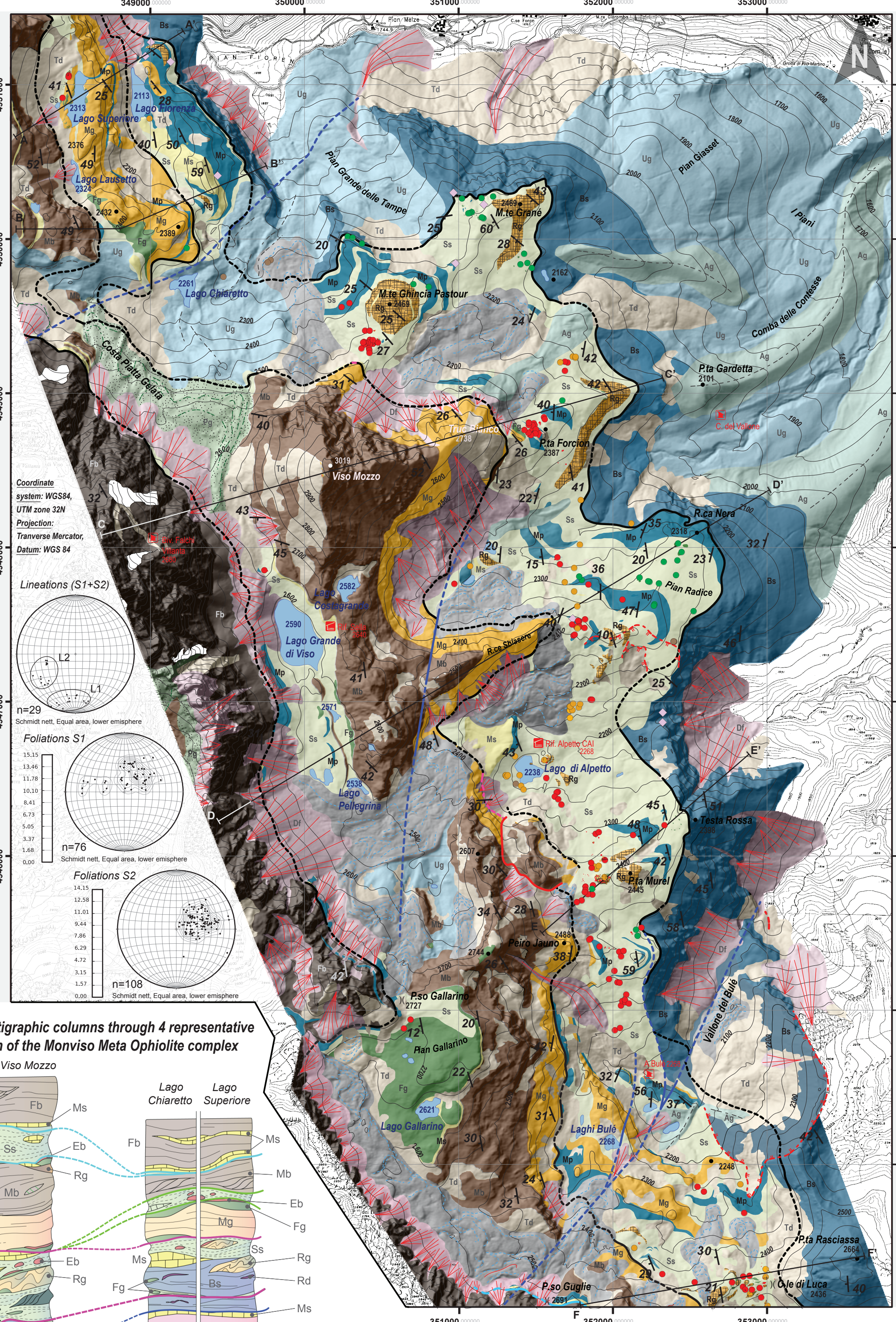
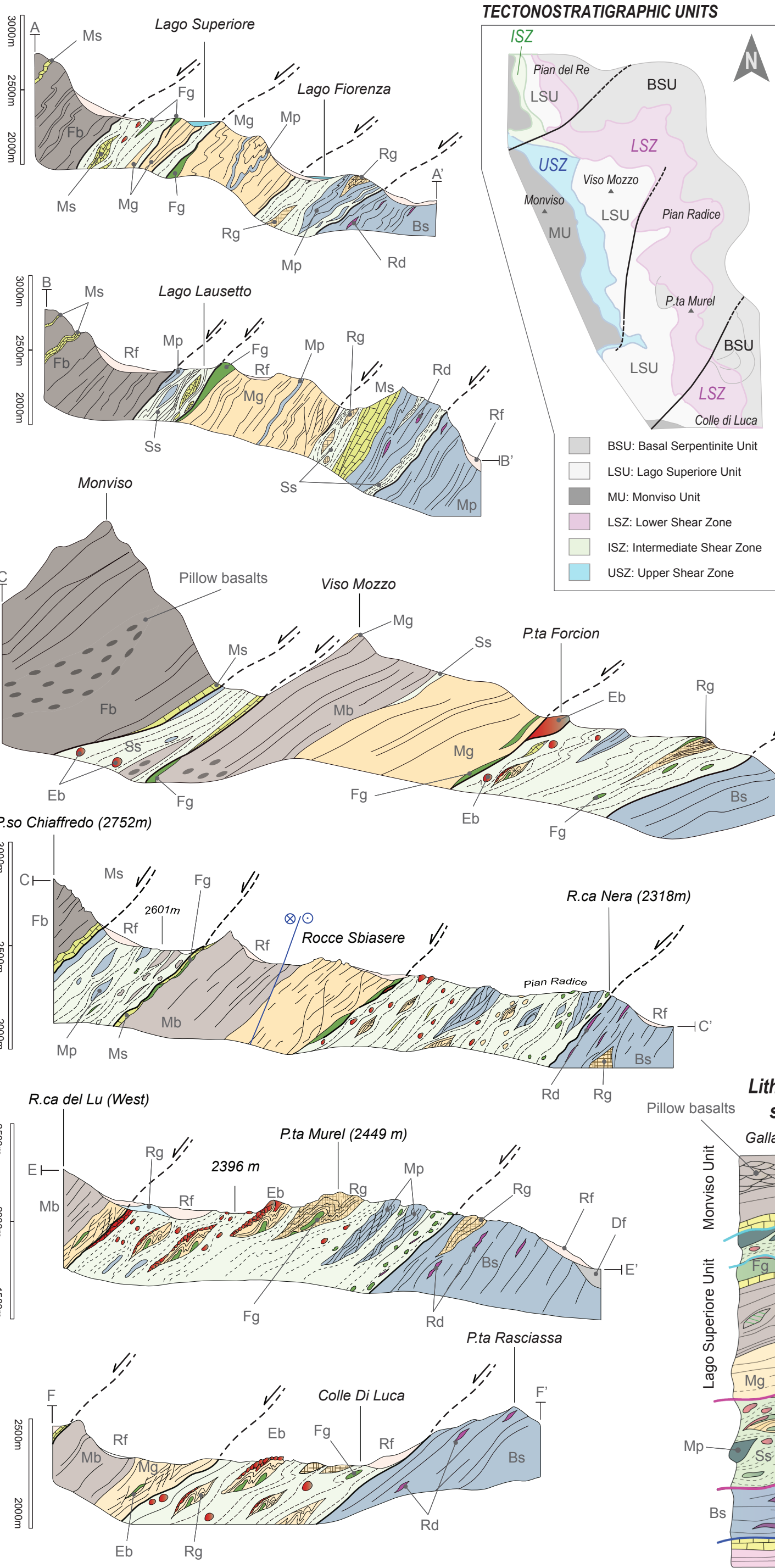
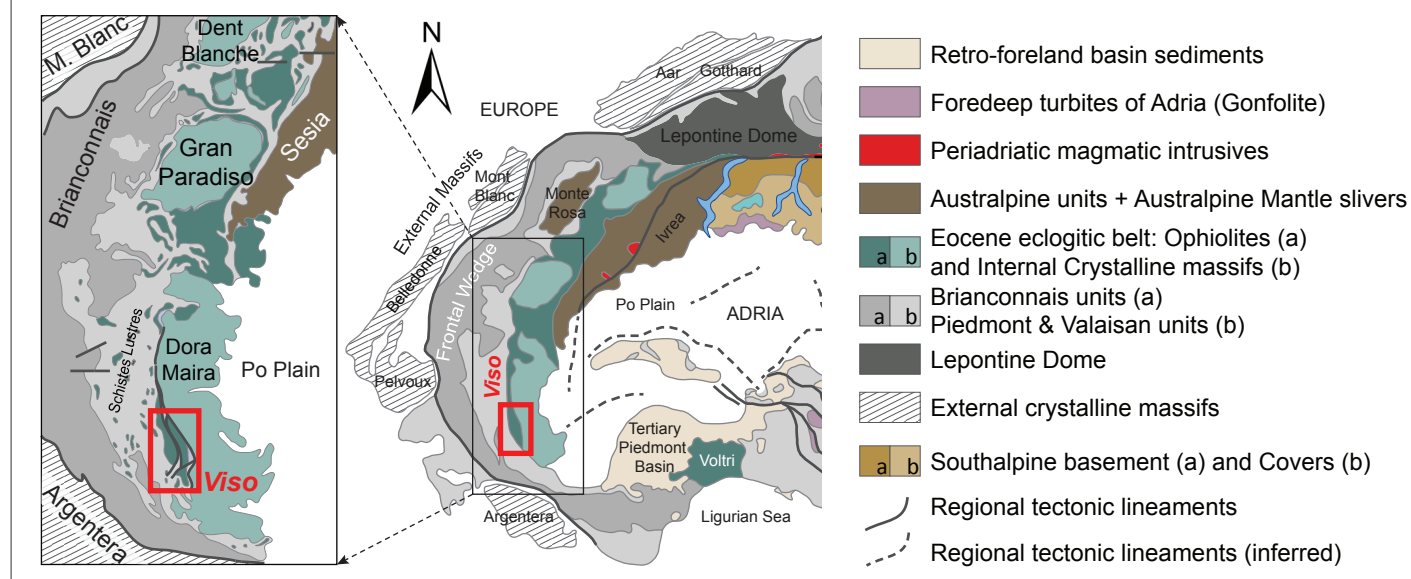
# Analysis	Microstructural domain	Sample	LA-ICP-MS concentration (µg/g)											
			Dy	Ho	Er	Tm	Yb	Lu	Hf	Ta	Pb	Bi	Th	U
B26	Mylonitic clast Grt	ISZ 35-15	22.20	4.93	14.06	1.85	12.47	1.84	-0.02	0.00	-0.03	-0.01	0.00	0.00
B27	Mylonitic clast Grt	ISZ 35-15	31.36	5.39	12.62	1.43	8.05	1.12	0.13	0.00	-0.02	-0.01	0.00	0.00
B28	Mylonitic clast Grt	ISZ 35-15	21.47	4.91	14.13	1.90	12.26	1.87	0.01	0.00	-0.02	-0.01	0.00	0.00
B30	Mylonitic clast Grt	ISZ 35-15	20.25	4.45	12.62	1.64	10.02	1.44	0.00	0.00	0.04	0.00	0.00	0.00
B31	Mylonitic clast Grt	ISZ 35-15	20.76	3.94	10.17	1.18	6.76	0.92	0.01	0.00	0.02	0.00	0.00	0.00
D21	VeinT2 - Grt	ISZ 35-15	32.48	6.47	15.93	1.72	9.35	1.21	0.00	0.00	0.01	0.00	0.00	0.00
D22	VeinT2 - Grt	ISZ 35-15	34.18	6.41	15.45	1.61	8.38	1.05	-0.01	0.00	-0.01	0.00	0.00	0.00
D24	VeinT2 - Grt	ISZ 35-15	24.43	6.32	20.89	2.65	17.42	2.49	-0.02	0.00	-0.02	-0.01	-0.01	0.00
D25	Mylonitic clast Grt	ISZ 35-15	25.50	6.48	19.22	2.40	15.00	2.10	-0.01	0.00	-0.01	0.00	0.00	0.00
D28	Mylonitic clast Grt	ISZ 35-15	24.35	5.81	16.66	2.04	12.29	1.68	0.01	0.00	-0.02	-0.01	0.00	0.00
D29	Mylonitic clast Grt	ISZ 35-15	24.81	5.89	16.46	2.04	11.56	1.71	0.01	0.00	-0.02	0.00	0.00	0.00
A20	M2 matrix Grt - core	ISZ 35-15	105.76	21.45	66.46	7.09	42.72	5.43	0.08	0.01	0.02	0.04	0.00	0.01
A21	M2 matrix Grt - core	ISZ 35-15	61.88	12.50	38.03	3.97	23.60	2.99	0.04	0.00	0.02	0.03	0.00	0.00
A22	M2 matrix Grt - core	ISZ 35-15	109.06	21.93	67.71	7.00	41.05	5.05	0.08	-0.01	-0.03	0.01	0.00	-0.01
B32	M2 matrix Grt - core	ISZ 35-15	5.47	0.87	2.04	0.22	1.33	0.16	0.01	0.00	0.01	0.01	0.00	0.00
B35	M2 matrix Grt - core	ISZ 35-15	16.71	3.09	7.62	0.86	4.71	0.57	0.01	0.00	0.01	0.00	0.00	0.00
B37	M2 matrix Grt - core	ISZ 35-15	2.36	0.27	0.47	0.04	0.26	0.04	0.03	0.00	0.00	0.00	0.00	0.00
B38	M2 matrix Grt - core	ISZ 35-15	2.91	0.33	0.50	0.05	0.28	0.03	0.03	0.00	0.00	0.00	0.00	0.00
A12	M2 matrix Grt - rim	ISZ 35-15	75.53	16.41	61.09	7.44	49.61	7.15	0.11	-0.01	-0.05	-0.03	-0.01	0.00
A13	M2 matrix Grt - rim	ISZ 35-15	33.37	6.93	23.93	3.01	18.80	2.86	0.14	-0.01	-0.06	-0.03	-0.01	0.01
A14	M2 matrix Grt - rim	ISZ 35-15	30.96	6.09	20.26	2.55	16.96	2.66	0.19	0.00	-0.06	-0.02	-0.01	-0.01
A23	M2 matrix Grt - rim	ISZ 35-15	17.19	3.12	10.12	1.02	6.08	0.83	0.15	0.00	-0.02	0.04	0.01	0.01
B42	M2 matrix Grt - rim	ISZ 35-15	2.50	0.32	0.55	0.05	0.35	0.06	0.99	0.00	3.09	0.00	0.00	0.02
B43	M2 matrix Grt - rim	ISZ 35-15	1.71	0.30	0.71	0.09	0.50	0.09	0.03	0.00	0.10	0.00	0.00	0.00
C08	Mylonitic clast Grt	ISZ 38-15	22.79	5.30	16.92	2.37	15.52	2.37	0.01	-0.01	-0.04	-0.02	-0.01	-0.01
C10	Mylonitic clast Grt	ISZ 38-15	37.73	7.43	21.12	2.63	16.71	2.31	0.13	0.00	-0.02	0.01	0.00	0.00
C11	Mylonitic clast Grt	ISZ 38-15	36.83	6.37	17.11	2.08	13.60	1.90	-0.01	-0.01	-0.03	0.00	0.00	0.00
C25	Mylonitic clast Grt	ISZ 38-15	31.78	5.51	15.47	1.97	13.42	2.17	0.01	0.00	-0.01	-0.01	-0.01	0.00
C26	Mylonitic clast Grt	ISZ 38-15	41.84	9.66	29.68	3.92	26.06	3.78	0.01	0.00	0.01	0.00	0.00	0.00
C16	VeinT2 - Grt	ISZ 38-15	7.49	1.40	3.81	0.43	2.57	0.32	0.01	0.00	0.01	0.00	0.00	0.00
C17	VeinT2 - Grt	ISZ 38-15	3.38	0.52	1.29	0.16	1.00	0.14	0.02	0.00	0.01	0.00	0.00	0.00
C21	VeinT2 - Grt	ISZ 38-15	4.21	0.75	1.85	0.22	1.25	0.17	0.00	0.00	-0.01	0.00	0.00	0.00
C31	VeinT2 - Grt	ISZ 38-15	3.98	0.70	1.85	0.24	1.58	0.23	0.02	0.00	-0.01	0.00	0.00	0.00
C32	VeinT2 - Grt	ISZ 38-15	4.48	0.82	2.26	0.30	1.92	0.27	0.01	0.00	0.01	0.00	0.00	0.00

Trace element data with (-) are below their respective detection limit (method: Pettke et Al., 2012)

Geological Map of the Southern Monviso Metaophiolite Complex

Michele Locatelli, L. Federico, A. Verlaquet and P. Agard

GEOLOGICAL and GEOGRAPHICAL SETTING



LEGEND TO THE GEOLOGICAL MAPS, LITHOSTRATIGRAPHIC COLUMNS and GEOLOGICAL CROSS-SECTIONS

QUATERNARY DEPOSITS

- Df: Alluvial and debris flow deposits, composed by gravely cobbles and sandy gravels clast-supported, well stratified to massive, sometimes containing decimetric to metric-scale boulders. Late Upper Pleistocene – Present
- Td: Recent talus deposits, composed by centimetric to decimetric angular fragments and blocks, usually clast supported, without visible stratifications. Upper Pleistocene – Present
- Ag: Undifferentiated glacial deposits (Ag), made up of diamiction with silty-sandy matrix and chaotic blocks accumulation. Blocks are locally devoid of lichens. Pg: Little Ice-Age moraines. Holocene-Present
- Ug: Undifferentiated glacial deposits, made up of diamiction and chaotic blocks accumulation with silty-sandy matrix (Ug). Upper Pleistocene
- Rg: Inactive rock glacier, formed by poorly sorted angular to sub-angular blocks at surface, with progressive passage to blocks-in-matrix texture below the surface. Characteristic the coverage of blocks by lichens. Holocene
- Lakes and ponds

LITHOLOGIES - Lago Superiore Unit (LSU)

- Ms: Fine-to-medium grained lawsonite-bearing calcschists (Mc) interbedded with quartz-rich and mica-rich cm-to-dm levels; locally with decimetric to metric-size bodies of metabasite (a). Late Jurassic? Cretaceous?
- Mb: Finely banded epidote-rich metabasites, with pervasive blueschist foliation, locally strongly retrogressed to greenschists (Mb). Middle Jurassic? - Late Jurassic?
- Fg: Blocks of massive-to-foliated Eclogitic Fe-Ti metagabbros, usually strongly retrogressed to greenschist facies. Middle Jurassic?
- Eb: Eclogitic metabreccias (Punta Forcion, SW of Testa Rossa, Colle di Luca, W of Rocca Nera), composed by strongly foliated Fe-Ti and subordinate Mg-Al metagabbro clasts on fine-grained omphacite-matrix, locally with ex-lawsonite-rich domains. Middle Jurassic?
- Rg: Bodies of Mg-Al metagabbros, frequently retrogressed in green-schist facies, with cm-to-meter Fe-Ti gabbro boudins, and locally (W of P.ta Murel, W-NW of R.ca Nera) with preserved eclogitic metabreccias. Middle Jurassic?
- Mg: Mg-Al metagabbros, locally strongly foliated and folded. Middle Jurassic?
- Ss: Strongly deformed mylonitic serpentinite schists, locally interbedded with centimetric to decimetric-thick layers of talcschist. Internal structures are chaotic, usually dismembered by recent erosion. Middle Jurassic?
- Mp: Massive metaperidotites (Lago Fiorenza), locally interbedded as slices in the mylonitic serpentinites (N Colle di Luca, W of R.ca Nera, Lago Grande di Viso). Middle Jurassic?
- Bs: Foliated to massive antigorite serpentinites with subordinates antigorite schists. Middle Jurassic?

LITHOLOGIES - Monviso Unit (MU)

- Ms: Fine-to-medium grained lawsonite-bearing calcschists interbedded with quartz-rich (metachert) and mica-rich cm-to-dm levels. Late Jurassic? Cretaceous?
- Fb: Finely banded epidote-rich metabasites, with pervasive blueschist foliation, locally retrogressed to greenschist facies. Pillow-structures, generally strongly deformed, are observed NW of Passo delle Segnette. Middle Jurassic? Late Jurassic?

LINEAR ELEMENTS

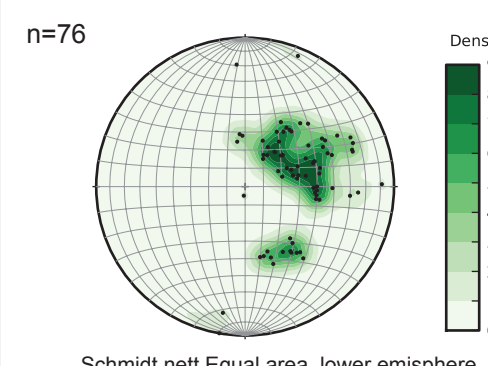
- Major tectonic contacts
- Landslide escarpments
- Regional Fault
- Regional Fault (inferred)
- Regional foliation (with dip angle)
- Geological cross-sections
- Isolines
- Fe-Ti metagabbro breccia blocks (Type 1)
- Mg-Al metagabbro blocks with eclogitic breccia (Type 2)
- Unbrecciated Fe-Ti metagabbro blocks (Type 3)
- Massive rodingite dykes (Rd). Middle Jurassic?

INTERPRETATIVE GEOLOGICAL MAP of THE SOUTHERN MONVISO METAOPHIOLITE COMPLEX

SHEAR ZONES LIMITS

- LSZ (Lower Shear Zone)
- ISZ (Intermediate Shear Zone)
- USZ (Upper Shear Zone)
- Regional Faults
- Landslide escarpments

REGIONAL (S2) FOLIATION of the LSZ mylonitic serpentinite schists



DISTRIBUTION of the METAGABBRO BLOCKS in the LSZ

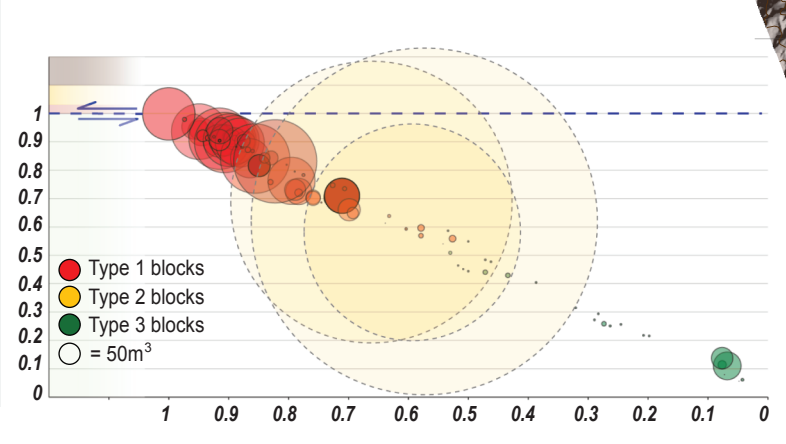
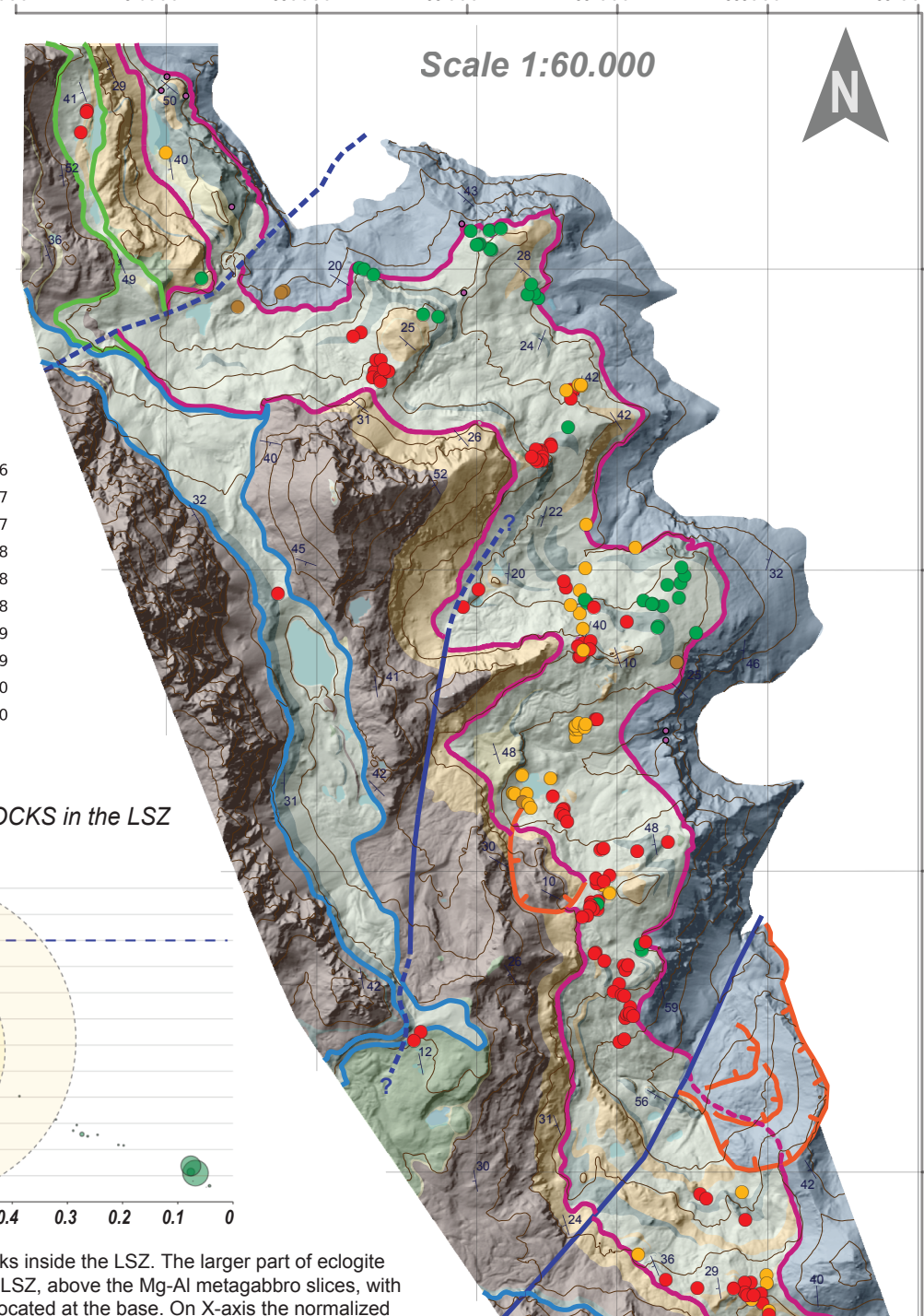


Diagram showing the distribution of metagabbro blocks inside the LSZ. The larger part of eclogite breccia blocks (Type 1) outcrops in the upper part of LSZ, above the Mg-Al metagabbro slices, with the unbrecciated Fe-Ti metagabbro blocks (Type 3) located at the base. On X-axis the normalized horizontal distance of blocks from the base of LSZ and on Y-axis the normalized vertical distance of blocks from the base of LSZ.



0 500 1,000 2,000 Meters Scale 1:20.000